X-ray Study of Rapid Variability in TeV Blazars and the Implications on Particle Acceleration in Jets

Jun KATAOKA

Doctoral Thesis

Department of Physics

Faculty of Science

University of Tokyo

December 1999

Abstract

Four TeV blazars, Mrk 421, Mrk 501, PKS 2155−304, and 1ES 2344+514, have been studied with the X−ray satellites $ASCA$ and $RXTE$. Because spectral energy distributions of TeV blazars cover all observable bands, and their fluxes vary rapidly, we conducted a number of multi-frequency campaigns. In particular, our observations of Mrk 421 and Mrk 501 in both X-ray and TeV γ-ray bands provide the first truly simultaneous data sets in various phases of source activity. The overall νL_ν spectra of TeV blazars show two broad pronounced peaks in the spectral energy distribution; one is located between the radio and X-ray bands, and another in the γ-ray regime. We found that variability in the X-ray and TeV bands is well correlated on time scale of a day to years. The amplitude of flux variation was comparable in both enengy bands for Mrk 421 ([X-ray flux] $\propto$ [TeV flux]), while quadratic for Mrk 501 ([X-ray flux]^2 $\propto$ [TeV flux]). The data considered here support the currently popular models where the low energy peak is produced via the synchrotron process, and the high energy peak is produced by Comptonization of the synchrotron photons by the *same* electrons that produced the synchrotron photons (the SSC model). The physical parameters relevant for the emission were successfully constrained from the observational properties of each TeV blazar.

Analysis of the X-ray data indicated five principal results. First, we detected the peak of the synchrotron component for all TeV blazars. We found that the position of the synchrotron peak shifted from lower to higher energy when the source became brighter. This correlation is best studied for Mrk 421 and Mrk 501. The relationship between the peak energy and luminosity showed quite different behavior in the two sources. Data for Mrk 421 indicated very little change in the peak position (0.5−2 keV), while Mrk 501 revealed the lagest shift ever observed in blazars (1−100 keV). Second, seven day uninterrupted observation of Mrk 421 revealed day-by-day flares, which were strongly correlated from the UV to the hard X-ray bands. We found that the characteristic time scales of individual flare events are similar for all TeV blazars ($\sim$ 1 day), but are slightly different in each object. Below this time scale, rapid variability appears strongly suppressed, indicating 'strong red-noise' type behavior ($\propto f^{-2} \sim f^{-3}$ in the Power Spectrum Density). Third, from the analysis of light curves of the blazar Mrk 421, we found the presence of 'hard-lag' flares, where soft X-ray variations *precede* those in the hard X-rays. More remarkably, time-lags in various X-ray energy bands changed flare by flare, and hence the *paradigm* of 'soft-lag' does not always apply. Fourth, we detected the general trend that the amplitude of variation becomes larger at increasing photon energy. A few exceptions were found in which variation in the lower energy X-ray band is larger or comparable to that in the higher energy band. Fifth, time profiles of each flare event were almost *symmetric*,

meaning that they are characterized by nearly equal rise-time and decay-time. From the detailed temporal analysis, we discovered that the symmetry of the time profiles tends to break down at lower energies.

Clear correlations of synchrotron peak energy with peak luminosity, found in Mrk 421 and Mrk 501, suggest that flaring behavior is repeatable and reproduced in these objects. However, very different spectral evolution of Mrk 421 and Mrk 501 probably indicates some differences in the electron acceleration mechanism at work during the flares. Our result strongly supports the idea that the variability of TeV blazars is most probably due to the changes in the injected electron number and/or maximum Lorentz factor (γ_{max}). Data for Mrk 421 indicate that the flux variability is associated with an increase in the number of electrons, while only small changes are implied for γ_{max}. On the other hand, the flare of Mrk 501 is mostly due to the large changes in γ_{max} while keeping the electron number almost conservative. Interestingly, our X-ray data and interpretation suggest that the origin of the flares may be associated with what is expected from the VLBI observations of superluminal motion.

From the X-ray study of TeV blazars, we suggest that at least four dynamical time scales must be taken into account to understand the observed time variabilities. These are (1) electron accerelation time, t_{acc}, (2) electron cooling time, t_{cool}, (3) source light travel time, t_{crs} and (4) electron injection time, t_{inj}. We show that all the variability patterns in blazars are well understood by the balance of those time scales. To confirm our knowledge of spectral evolution and rapid variability in blazars more *quantitatively*, we have developed a new time-dependent SSC code, incorporating the radiative cooling and acceleration process, as well as light travel time effects properly. That is because we deemed the popular SSC model based on *steady state* emission as inadequate for our case, given the detection of the *rapid flux and spectral time variability* in blazars. By using the code developed by us, we simulated various types of flares for TeV blazars. We confirmed that 'soft-lag' will be expected when the acceleration time of electrons is much shorter than cooling time, while 'hard-lag' can be observed when the acceleration time is nearly equal to the cooling time, which is only expected around γ_{max}.

Contents

List of Figures

List of Tables

Chapter 1

Introduction

Active Galactic Nuclei (AGN) produce enormous power ($10^{40} \sim 10^{46}$ erg/s) from extremely compact volumes. They are commonly variable, and large luminosity variations on time scales of hours to years have been observed. From the combination of high luminosities and rapid time variability, it is generally believed that the ultimate source of power in AGN is accretion onto massive black holes ($10^7 \sim 10^{10} M_\odot$) which exist at the centers of these powerhouses. The recent discovery of the clear, broad, skewed fluorescent iron line in the spectrum of MCG 6-30-15 with *ASCA* (Tanaka et al. 1995), as well as the high rotation velocities in a sub-parsec region of NGC 4258 (Miyoshi et al. 1995) from water-maser observation confirmed the existence of those massive black holes in AGN, and in some cases, allowed us to estimate their masses.

Blazars, a subclass of AGNs, have outstanding properties in several aspects. They exhibit the most rapid and the largest amplitude variations of all AGNs (Stein et al. 1976). Recent observations with the EGRET instrument (30 MeV$-$30 GeV; Thompson et al. 1993) on-board the *Compton Gamma-Ray Observatory* (*CGRO*) reveal that more than 60 AGNs are bright γ–ray emitters (e.g., Mukherjee et al. 1997). Remarkably, all AGNs detected by EGRET were classified as blazars. Observations with ground-based Cherenkov telescopes further confirmed γ-ray emission extending up to TeV energies for four nearby blazars: Mrk 421 ($z = 0.031$; Punch et al. 1992), Mrk 501 ($z = 0.034$; Quinn et al. 1996), 1ES 2344+514 ($z = 0.044$; Catanese et al. 1998) and PKS 2155$-$304 ($z = 0.117$; Chadwick et al. 1999).

It has been reported that the overall spectra of blazars (plotted as νF_ν) have at least two pronounced continuum components: one peaking between IR and X–rays, and another in the γ–ray regime (e.g., von Montigny et al. 1995). The strong polarization observed in the radio and optical bands (Angel & Stockman 1980) implies that the lower energy component is most likely produced by synchrotron radiation of relativistic electrons in

magnetic fields, while inverse-Compton scattering by the same electrons is believed to be the dominant process responsible for the high energy γ–ray emission (Ulrich, Maraschi, & Urry 1997; Ghisellini et al. 1998; see also § 2). This non-thermal radiation is thought to be emitted in a relativistic jet pointing close to our line of sight (e.g., Urry & Padovani 1995).
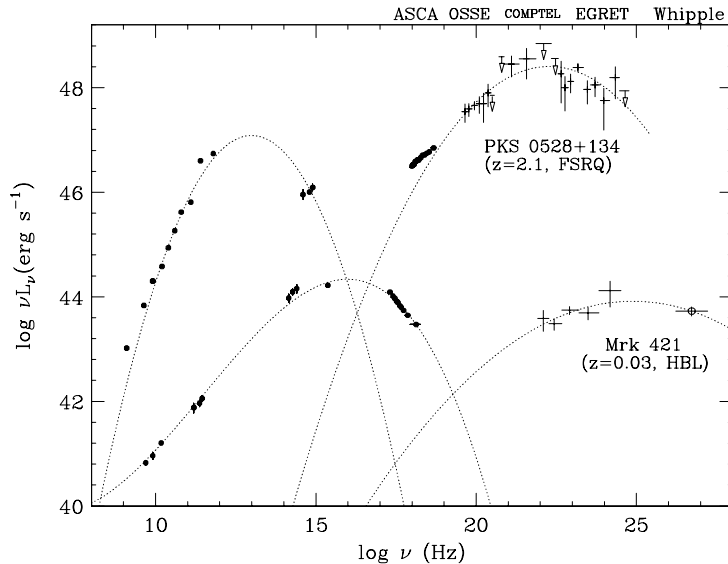
Figure 1.1: The multi-frequency spectra obtained from the contemporaneous observations of Mrk 421 and PKS 0528+134 (Kubo et al. 1998). The dotted line (intended as a guide to the eyes) shows the fit to a third-order polynomial function.

Multi-frequency spectra of blazars indicate their variety. Figure 1.1 shows the spectral energy distributions of Mrk 421 and PKS 0528+134, respectively. Mrk 421 is the proto-type of TeV γ-ray emitting blazars, while PKS 0528+134 is the one of the brightest GeV emitting blazars that was observed by EGRET but has not been detected at TeV energies. One can find significant differences in their luminosities and peak positions of low-energy (LE) and high-energy (HE) components. Also note that the LE luminosity is larger than that of HE for Mrk 421, while the reverse applies for PKS 0528+134. Several authors have interpreted the difference as due to the different 'seed' photons for inverse-Compton scattering. Kubo et al (1998) suggested that the multi-frequency spectrum of Mrk 421 is well explained by the synchrotron-Self-Compton (SSC) scenario, in which the source of the 'seed' photons for the Compton process is pure synchrotron radiation internal to the jet (Jones et al. 1974; Marscher 1980; Kőnigl 1981; Marscher & Gear 1985; Ghisellini & Maraschi 1989; Maraschi et al. 1992; Marscher & Travis 1996), while seed photons external to the jet play an important role for the case of PKS 0528+134 and other objects

showing strong broad emission lines (External Radiation Compton (ERC) model: Dermer & Schlickeiser 1993; Sikora, Begelman, & Rees 1994).

There are indications that particles are accelerated more efficiently in blazars having lower luminosities (e.g., Ghisellini et al. 1998; Kubo et al. 1998). In fact, the luminosity of Mrk 421 is significantly lower than that of PKS 0528+134, while the peaks of LE/HE components are located at much higher frequencies (Figure 1.1). In low luminosity objects, energy loss by radiative cooling would not be effective because there are less ambient photons to be Compton scattered to higher energies. Thus the TeV blazars gives an important opportunity to study the particle acceleration in blazar jets.

The first multi-frequency campaign of Mrk 421 including TeV energies was conducted in 1994 (Macomb et al. 1995; Takahashi et al. 1996). The contemporaneous observations implied correlated variability between the keV X–ray and TeV γ–ray emission, while the GeV flux and the radio to UV fluxes showed less variability. The results from this campaign are important because it suggested the possibility that a single electron population is responsible for both the X–rays and TeV γ–rays, qualitatively agreeing with the SSC scenario. However, the fact that the X-ray and TeV observations were separated by one day, could introduce uncertainties to draw concrete pictures. In fact, we now know that both X-ray and TeV γ-ray fluxes of Mrk 421 can vary significantly within a day. Simultaneous, uninterrupted observations are crucial to understand the blazar phenomenon.

In this thesis we intensively study the four TeV blazars, with an emphasis on the observations with the X-ray satellites $ASCA$ and $RXTE$. Our main goal is to understand $both$ the rapid time variability and spectral evolution of TeV blazars based on the high quality X-ray data. We analyze all the $ASCA$ data obtained in $1993-1998$, which covers the energy range $0.5-10$ keV. To increase data samples in different states of source activity, we have also analyzed all the archival data of $RXTE$ obtained in $1996-1998$, where the energy range covered by the Proportional Counter Array (PCA) on-board $RXTE$ is 2.5 keV to $\sim$20 keV.

Importantly, 30 observations presented in this thesis were conducted truly simultaneously with the $Whipple$ Cherenkov telescope (TeV γ-ray) and 7 observations were simultaneous with EGRET (GeV γ-ray). In particular, an unprecedented campaign of Mrk 421 (7 days) is extremely valuable since this provides for the first time an uninterrupted and simultaneous data set including $EUVE$, X-ray ($ASCA$ and $RXTE$) and TeV γ-ray energy bands. We also report another big campaign for PKS $2155-304$ for 12 days by $RXTE$.

Unlike most of the previous work which focused on the photon spectral properties and/or classification of blazars, we also study the rapid time variability in blazars. Photon

spectra are important since they provide information on the distribution of relativistic electrons and the physical environment around the jet. On the other hand, the time variability gives us different constraints on the dynamics operating in blazar jets, such as the acceleration, radiative cooling and particle escape. It also gives us an information on the size of the emission region. To understand the observational data deeply, we develop a time-dependent numerical code that follows the time evolution of radiation from particles based on the one-zone homogeneous SSC model. Using the code, we compare the observational data directly to the prediction of the time-dependent model. Such a comparison is an important ingredient in the study of blazar activity.

In this thesis, we present the review of the past study on the AGNs and blazars in § 2. We give a brief description for theoretical frameworks which can be a guide to understand the radiation mechanism in blazars in § 3. We describe the instruments on-board *ASCA* satellite in § 4 and *RXTE* satellite in § 5. The log of *ASCA* and *RXTE* observations of four TeV blazars are described in § 6. We report the analysis and results of *ASCA* observations in § 7 and *RXTE* observations in § 8. The multiband properties of TeV blazars are described in § 9. We discuss our observational results and their implications in § 10. We develop a 'new' time-dependent SSC model in § 11 and compare it to the observational data. Finally, the conclusions are presented in § 12. Details are described in appendixes.

Chapter 2

Observational Properties of Blazars

2.1 Unifying Active Galactic Nuclei (AGN)

2.1.1 Classification of AGN

The Universe is made up of galaxies, many containing more than a hundred thousand million stars. $1-10$ % of galaxies are called 'active' galaxies and possess an amazing source of energy at its nucleus (e.g., Ormes et al. 1996; Figure 2.1), generating the power comparable to that emitted by a thousand of galaxies. They are called an active galactic nuclei (AGNs).

AGNs produce enormous luminosities in extremely compact volumes. The combination of high luminosities ($10^{40}\sim10^{46}$ erg/s) and short variability time scales ($\leq$ 1 day) implies that the power of AGN is produced in more efficient way than ordinary stellar processes (e.g., nuclear fusion). This leads us to the hypothesis – which is widely believed – that the massive black holes are present in the central powerhouses, and that the accretion of matter onto such black holes is the origin of their high radiation power.

In general, an AGN emits not only visible light, but their emission spans a wide spectral range from radio to γ-rays. Furthermore, the most rapid time variability in AGN is observed in the X-ray and γ-ray energy bands. Since the integrated stellar light from a galaxy is emitted mainly in the IR/optical bands and relatively little of it is in the X-ray band, X-ray observations are an extremely important tool to 'look' inside the active galaxies.

In the broadest sense, galaxies in general are classified into two types, ellipticals or spirals. Independently, on the spectral grounds AGNs are classified into 'radio loud' and 'radio quiet' objects by their activity and/or luminosity in the radio band (Figure 2.1). About 10 % of AGNs are radio loud, and a 'jet' structure most frequently appears in the

radio VLBI image. Jets usually extend in opposite directions from the central core of the galaxy (see, Figure 2.2). BL Lac objects, the subject of this thesis, have strong radio emission, but also generally 'inhabit' elliptical galaxies. About 1000 blazars are known so far (see, also Veron-Cetty & Veron 1993).
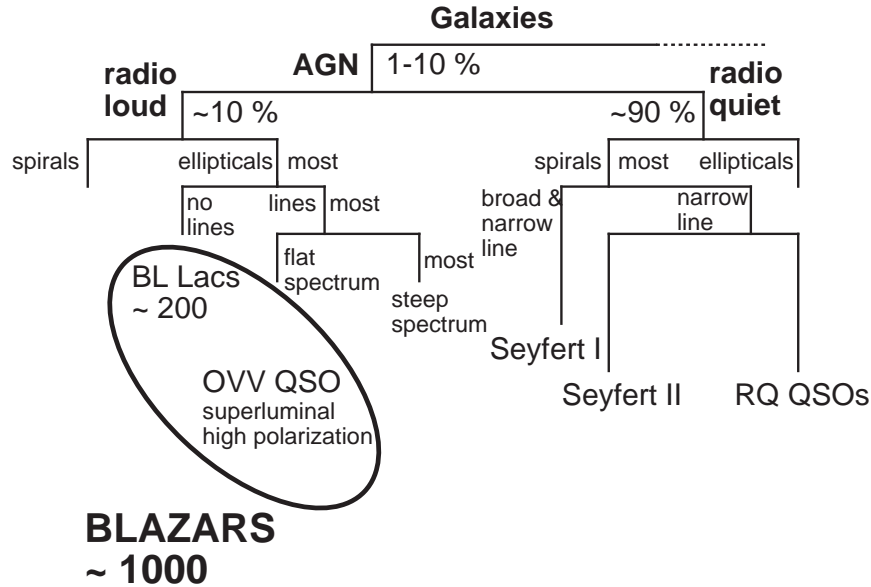
Figure 2.1: A categorization of active galactic nuclei (AGN). About 1−10 % of galaxies have active nucleus in their center. AGNs are furter classified into radio loud/quiet objects. Figure adopted from Ormes et al (1996).

2.1.2   Unified Picture of AGN

The radio quiet AGNs which are *not* associated with jet structure include Seyfert galaxies and radio quiet quasars as shown in Figure 2.1. The precise classification of Seyfert I, Seyfert II and the intermediate categories are discussed by Osterbrock (1981).

Recent intensive studies to unify AGNs can successfully impose some order on many types of AGN classes (e.g., Antonucci & Miller 1985; Antonucci 1993). Figure 2.2 shows a schematic picture of the unifying scheme of AGNs. The left panel summarizes the radio loud objects with jets, while the right is for the case of radio quiet objects without jets. The black hole, the accretion disk and the broad line region are surrounded by a molecular torus. Narrow line region (NLR) is thought to be the place that emits optical lines with narrow width. Broad line region (BLR) is believed to be inner part of the NLR. Due to the high velocity of clouds, optical lines emitted from this region form broad line structure. When the line of sight is between the jet axis and the torus plane, both the broad line

region and the narrow line region are visible; for galaxies with radio emission, these would be classified as broad line radio galaxies. When the broad line region is obscured by the torus, an object is observed as a narrow line galaxy. In this context, the observational differences between Seyfert I and II galaxies (and this holds independently of their radio loudness) are interpreted by the difference of line of sight between the jet axis and torus plane (e.g., Antonucci 1993).
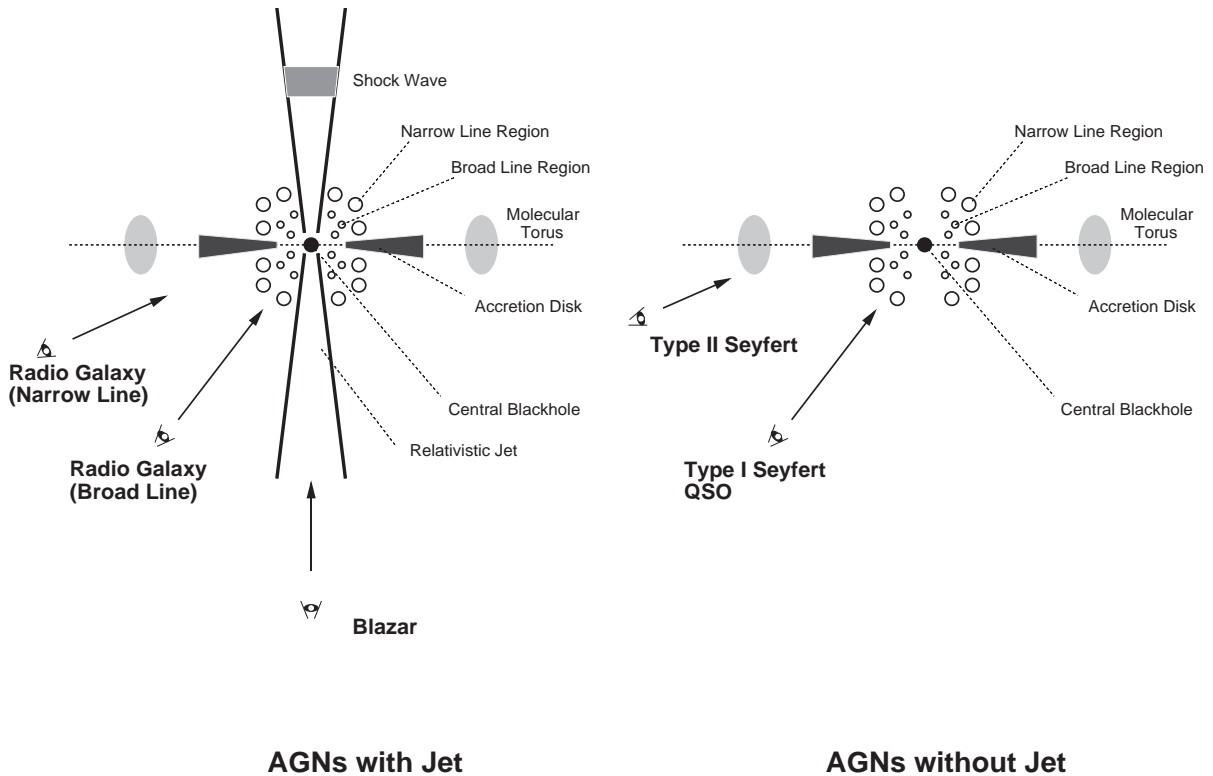
Figure 2.2: Unified scheme of all types of AGNs. *left panel*: AGNs having the jet, *right panel*: AGNs in absence of the jet.

2.1.3 Blazars – Roles in All AGN Classes

As it was mentioned above, some galaxies show strong radio emission, and those are called radio galaxies. We believe that most if not all radio galaxies have relativistic jets. However, the emission from the relativistic jet, due to the effects of relativistic light aberation (see, e.g., Rybicki and Lightman 1979), is only visible (and strongly amplified) if it is pointing close to our line of sight, and could be invisible if viewed close to the line of sight perpendicular to the direction of the jet. Blazars are the AGNs in which the line of sight lies close to the jet axis (Figure 2.2). VLBI observations reveal that many blazars

show superluminal motion of their jets; the apparent velocity of the blob sometimes well exceeds the light velocity ($v/c = 5 \sim 10$; Vermeulen & Cohen 1994). The superluminal motion can be explained by motion with speed close to c of the blobs at a small angle towards the observer (e.g., Blanford & König 1979).

Blazars are thus very different from other types of AGNs in a sense that the emission from the very inner part of the system (e.g., accretion disk, line emission region) is mostly overwhelmed by the strong jet emission. In fact, thermal X-ray emission from the accretion disk often observed in Seyfert galaxies and Galactic black holes (e.g., Dotani et al. 1997) is *not* observed in blazars, suggesting that the non-thermal jet emission is dominant for these sources. Polarization observed in the radio and optical band (Angel & Stockman 1980) further implies that most of the radiation in the radio - to UV band is non-thermal synchrotron radiation of relativistic electrons in the magnetic field.

The synchrotron radiation from radio to UV and sometimes X-ray bands indicates that the distribution of the relativistic electrons exists in the blazars' jets; these electrons cannot be mono-energetic. In some objects, an existence of extremely relativistic electrons with Lorentz factor $\gamma_{\mathrm{max}} \sim 10^6$ (see below) is implied. Such high-energy electrons should rapidly cool via synchrotron radiation, hence continuous acceleration must occur. These acceleration/deceleration processes are very likely related to the large amplitude, rapid time variability often observed in blazars (see, § 2.2.2). Therefore, blazars are the only class of AGNs which provide information of dynamics operating in relativistic jets.

2.2 Observations of Blazars

2.2.1 Spectral Energy Distribution

Figure 2.3 shows the multi-frequency spectra of the well-studied TeV blazar Mrk 421 (Macomb et al. 1995; § 2.4.3). Open circles are data compiled from the archive, while filled diamonds are the data from the multi-wavelengh campaign in 1994 May (Macomb et al. 1995; see also below). Conveniently, the data points are plotted as $\mathrm{Log}(\nu)$ versus $\mathrm{Log}(\nu L_{\nu})$, often used for multi-wavelength astronomy. This gives the source power per logarithmic frequency interval and thereby directly shows the relative energy output in each frequency band (Gehrels 1997). In this figure, the data taken within a week are plotted as 'simultaneous'.

One can find two important features from this figure. First, the multiband spectra of blazars, when plotted as νL_{ν}, show two pronounced continuum components. This is a common feature of all blazars detected with EGRET (von Montigny et al. 1995;

Mukherjee et al. 1997). The low energy component (hereafter LE component) extends from the radio to UV, and sometimes extends to the X-ray bands. It is generally belived that the LE component is due to the synchrotron emission of relativistic electrons in magnetic field. The higher component (hereafter HE component) covers from the hard X-ray to TeV γ-ray energy bands, but its origin is less well understood. One promising explanation is inverse-Compton scattering of ambient photons, either internal or external to the jet. We will discuss various emission models which explain the HE component in § 2.3.

Blazars vary in all observable bands with large amplitude, and important clues to their structure and radiative properties lie in the correlations of flux variability in various spectral bands. For example, in the blazar Mrk 421, the keV X–ray and TeV γ–ray emission varied by an order of magnitude from their base values, while GeV γ–ray flux observed by EGRET, as well as the radio and UV fluxes, showed less variability than the keV or TeV bands. However, clear conclusions from the inter-band correlation could not be drawn because the X-ray observation by *ASCA* in this campaign was conducted one day after the TeV observation, and thus was not exactly simultaneous (Takahashi et al. 1996; 1999). In spite of the non-simultaneity of the observations, this campaign played an important role to give a strong motivation for subsequent multi-frequency campaigns of blazars.
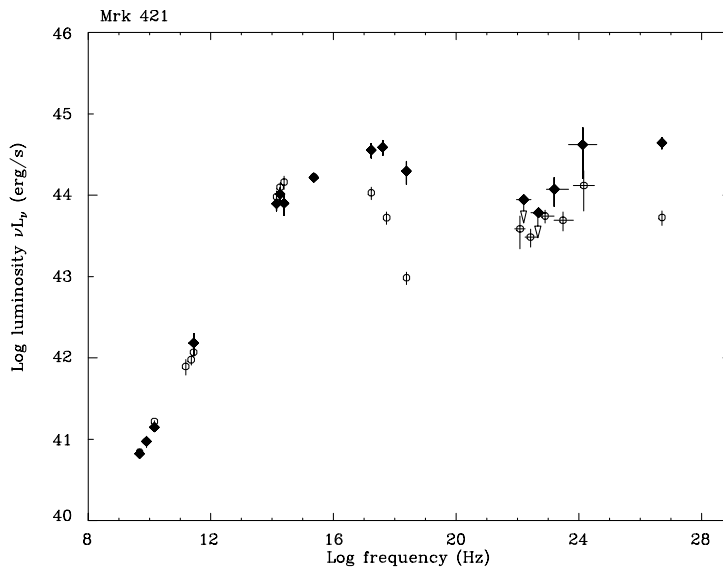
Figure 2.3: Spectral Energy Distribution of the TeV blazar Mrk 421 at multiple epochs including faint to flare states. Open circles are data taken before 1994 May in the quiescent state, while filled diamonds are data obtained in 1994 campaign (May 10−17) and plotted as 'simultaneous'. Figure from Macomb et al (1995).

2.2.2   Time Variability

One of the main characteristics of blazars is their rapid time variability with large amplitude. Flares have been observed in most wavelengths. Figure 2.4 shows time variation of TeV γ-rays of Mrk 501 from Quinn et al (1999). One can see that the large flux variations on time-scales from days to years. In particular, this source was in the historical high state during 1997 observations (see § 2.4.3). The maximum flux reached to $\sim$ 4 Crab, which is about a factor 40 increase from the average flux of 1995 (Quinn et al. 1996). Most rapid time variability were found for this source whose doubling time of a few hours in 1997 data (Quinn et al. 1999).
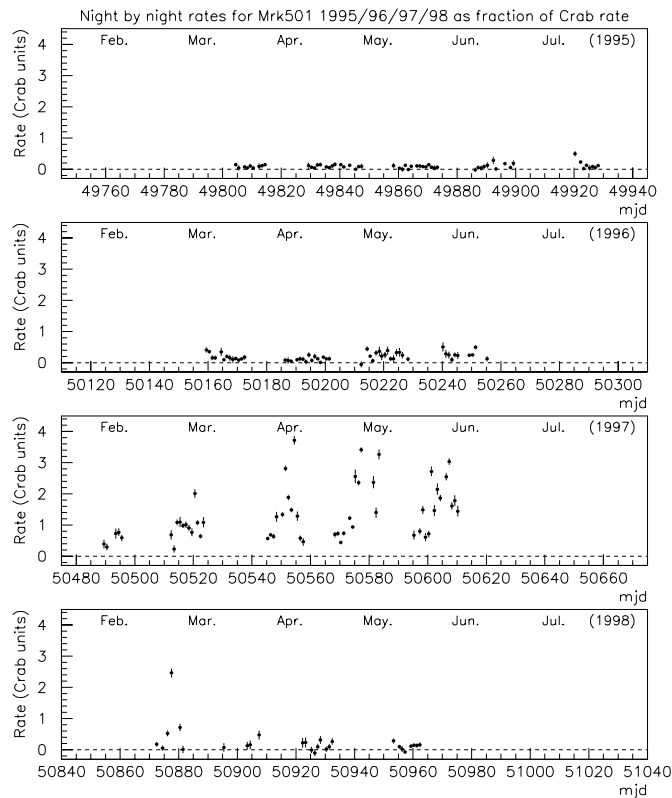
Figure 2.4: Average TeV γ-ray rates on daily time-scales for Mrk 501 between 1995 and 1998. Figure adapted from Quinn et al (1999).

Figure 2.5 show the X-ray light curves of PKS 2155$-$304 obtained with *BeppoSAX* in 1997 (Maraschi et al. 1999a; Zhang et al. 1999). Well-defined flare is clearly seen in the center, whose doubling time is about 3×10^4 sec (0.3 day). One can see the factor two variation in the lower energy X-rays (0.1$-$1.5 keV), and a factor three variation for higher energy X-rays (3.5$-$10 keV). The origin of the flare is completely unknown.
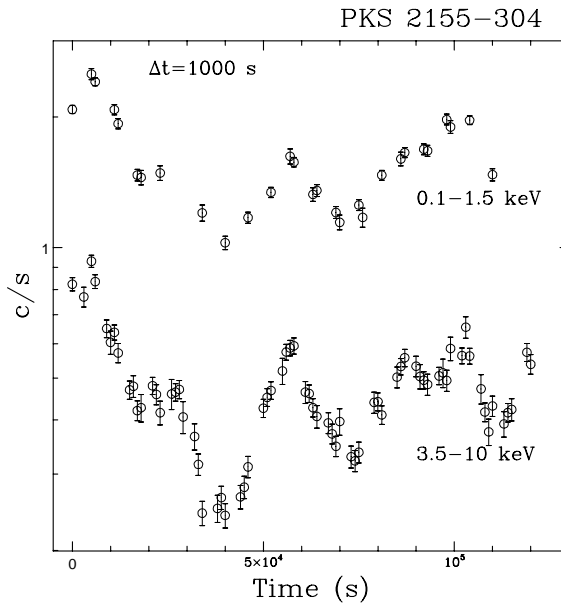
Figure 2.5: Light curves obtained from Nov 1997 observation of PKS2155-304 with *BeppoSax*. Quasi-symmetric flares are seen. Figure from Maraschi et al (1999).

2.2.3 X-ray Spectral Evolution

Another important discovery is the detection of the time lag between the soft X-ray and the hard X-ray band variations. This behaviour was first pointed out by Tashiro (1992) using the light curves from *GINGA* observations. He found that most of the X-ray variations exihibit canonical 'clockwise' hysteresis when plotted in flux versus photon index plane, which can be interpreted that the soft X-ray variation lags behind the hard X-ray variations both in an increasing and decreasing phases of intensity. This behaviour is expected for objects in which the X-ray emission is dominated by the synchrotron radiation.

This idea was verified during the *ASCA* observation of Mrk 421 in 1994, which was conducted as a part of the multi-frequency observations (Figure 2.3). The result indicated that the soft X-ray (≤ 1 keV) flux variation lagged behind that in the hard X-ray band (~ 2 keV) by 4 ksec. X-ray spectral evolution tracked a clearest 'clockwise' loop ever observed in the X-ray energy bands (Figure 2.6). Takahashi et al. (1996) associated the soft lag with the energy dependence of the synchrotron cooling time, deriving a magnetic field strength $B \sim 0.2$ G for $\delta = 5$. Importantly, this was the first case where the magnetic field was calculated only from the observed X-ray spectral variability.

The similar behavior was also detcted in other blazars (Kohmura et al. 1994; Tashiro

et al. 1995), leading to the *paradigm* that soft X-rays always lag behind the hard X-ray variations. However, the other types of the variations, e.g., *anti*-clockwise motion (e.g., PKS 2155−304; Sembey et al. 1993) or very small time-lag (e.g., PKS 2155−304; Edelson et al. 1995) have also been detected. Such an event was completely forgotten in the theoretical field until very recently (Kirk, Rieger & Mastichiadis 1998; see also § 2.3).
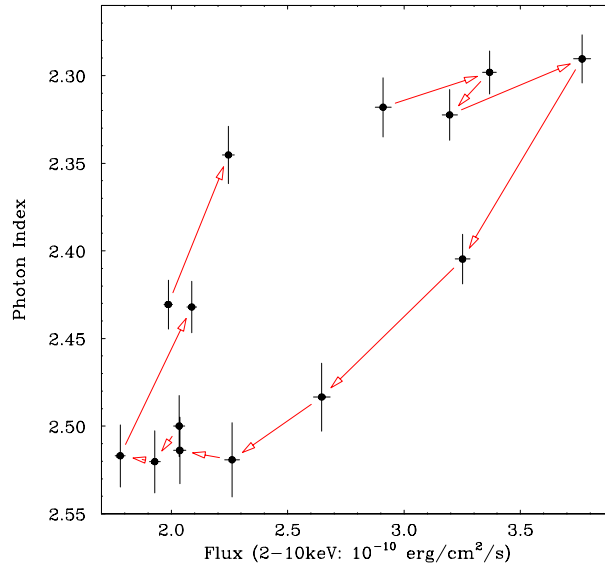
Figure 2.6: Hysteresis in a correlation between the flux and the photon index. A 'clockwise loop' is clearly seen. Figure from Takahashi et al (1996).

2.2.4   Implications on the Relativistic Beaming

Relativistic beaming is also suggested to avoid the so called "$\tau_{\gamma-\gamma}$" problem, related to the excessive optical depth (τ) to pair production for X-ray and γ-ray photons if one uses the variability time scale observed in blazars as the indicator of their size. In particular, several blazars detected by EGRET were extremely bright, whose isotropic luminosity would amount to $\sim 10^{49}$ (erg/s) (e.g., Figure 1.1). For these γ-ray bright blazars, if we assume that the radiation is isotropic and all photons are created in the same region of the size implied by the variability time scale, the value of τ well exceeds unity, hence γ-ray would *not* be observed. In order for GeV γ-rays to escape, emission region should be transparent to the γ-rays. This can be satisfied when the radiation is anisotropic, i.e., strongly beamed in a certain direction. For example, Mattox et al (1993) derived the lower limit of Doppler beaming factor as $\delta > 7.6$ for OVV quasar 1633+382.

Assume that there is an emission blob which radiates isotropically in the rest frame. In the observer's frame, the blob is moving with relativistic speed $\beta = v/c$ (~ 1), and the

radiation is strongly anisotropic (e.g., Rybicki & Lightman 1979). Three important effects are expected (for more detail, see § 3.7). First, in the observer's frame, photons emitted from the moving source are concentrated in a narrow cone of half angle $\theta \sim 1/\Gamma$, where Γ is the Lorentz factor of emission blob in the observer's frame. Second, because of the difference in emission and arrival time intervals, the observed time scale is shortened by factor $\sim 1/\Gamma$. Third, since frequencies are the inverse of times, observed photon frequencies is blue-shifted by Γ.

Beaming factor δ is related with Γ as $\delta = [\Gamma(1-\beta\cos\theta)]^{-1}$ (see, § 3.7). If the observer lies close to the angles $\theta \sim 1/\Gamma$ from the jet axis, we have the relation of $\delta \simeq \Gamma$. Combining these relations, the total observed luminosity is enhanced by δ^4. The origin of this enhancement factor is easily understood as follows; factor δ^2 comes from the light aberration in solid angle, factor δ due to the blue shift of the frequency, and factor δ from the time dilation.

2.3 Jet Models for Blazar Emission

In this section, we summarize the emission models of blazars based on *leptonic* jet scenario. In the leptonic jet scenario, the electrons and positrons (hereafter, the term "electrons" refers to both electrons and positrons) are accelerated in the relativistic jets and produce both low-energy (LE) and high-energy (HE) components. Most of the current models agree in that the LE component is due to the synchrotron radiation of those high-energy electrons, while the source of the 'seed' photons for the Compton process producing HE component is a matter of debate. Various authors have considered various origin of the seed photons. These models are briefly summarized in the following and Figure 2.7.

There are completely different scenario in which *protons* are the primarily accelerated particles in the jet. This framework is called *hadronic* jet scenario. Even in the hadronic jet scenario, LE component is thought to be the synchrotron radiation from the electrons produced of hadronic cascade. Although the hadronic jet model is not considered in this thesis, we will briefly describe this model in § 2.3.3.

2.3.1 Leptonic Jet Models

SSC (Synchrotron-Self-Compton) Model

The first candidate for the 'seed' photons is the synchrotron radiation (i.e., LE component) produced in the jet (Jones et al. 1974; Marscher 1980; Königl 1981; Ghisellini & Maraschi 1989; Marscher & Travis 1996). In a most simple scenario, a single homogeneous
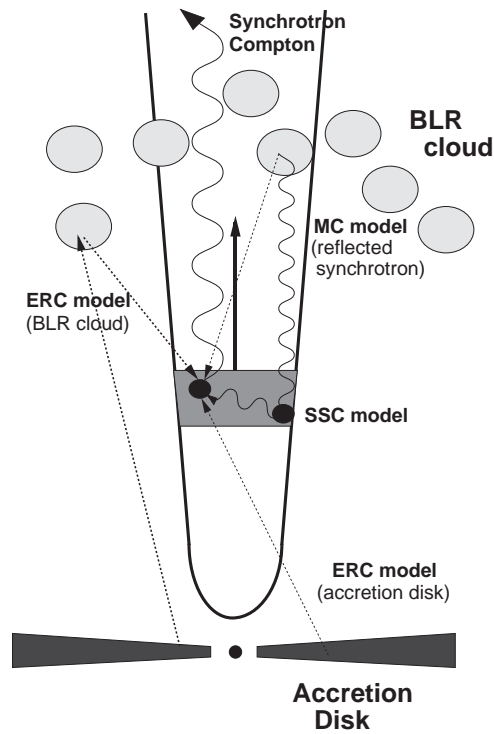
Figure 2.7: Illustration of the model geometry and the relevant γ-ray radiation mechanisms for leptonic jet models

region (spherical or slab geometry) emits both the synchrotron and inverse-Compton radiation (one-zone homogeneous model), as suggested by Gould (1979), Band & Grindlay (1985), and Inoue & Takahara (1996). More sophisticated model takes into account the inhomogeneity of the source, e.g., radial profile of the magnetic field and/or the propagating disturbance in the plasma jet flow (Marscher 1980; Marscher & Travis 1996; Georganopoulos & Marscher 1999).

Various authors have successfully interpreted the multi-frequency spectra of TeV emitting blazars by a simple one-zone homogeneous SSC model (e.g., Mastichiadis & Kirk 1997; Pian et al. 1998; Kataoka et al. 1999a). However, for the γ-ray bright OVV quasars, the γ-ray flux severely dominates the radiative output (e.g., PKS 0528+134; Figure 1.1), and an extremely strong beaming ($\delta \geq 100$) is necessary to account for the multiband spectra. Considering the *reasonable* beaming factor suggested by the VLBI observations ($5 < \delta < 30$), SSC scenario is thus highly unlikely for these bright OVV quasars (Kubo et al. 1998).

In OVV quasars, both X-ray and the γ-ray spectra are considered to be the Compton radiation from relativistic electrons. However, their multi-frequency spectra often show that the X-ray and the γ-ray spectra are not connected smoothly (e.g.,Figure 1.1; see

also Madejski et al. 1999 and Tanihata et al. 2000). This implies that both emissions are produced by the Compton process, but their seed photons are different. One of the candidates of the seed photons is the photons external to the jet, as discussed below.

ERC (External-Radiation-Compton) Model

The energy density of radiation produced externally to the emission blob may also be important for Compton scattering, since it is enhanced by relativistic beaming effect in the blob frame. In fact, the beaming pattern produced by radiation emitted isotropically in the blob frame (e.g., SSC process) is $\propto \delta^4$, while in the scattering of an external isotropic radiation field goes as $\propto \delta^6$ (Dermer 1995).

Various contributions for the *external* seed photons has been proposed; the radiation produced by an accretion disk (Dermer & Schlickeiser 1993), or reprocessed by the Broad Line Region (BLR) and/or scattered by material surrounding the jet (Sikora, Begelman, & Rees 1994; Blanford & Levinson 1995). Multi-frequency spectra of OVV quasars are well explained as the combination of SSC process and ERC process, with a reasonable beaming factor of $\delta \sim 10$ (Inoue & Takahara. 1996; Kubo et al. 1998; Takahashi et al. 1999).

MC (Mirror-Compton) Model

A portion of the broad line region (BLR; see § 2.7) could be illuminated by the beamed jet radiation, provided that some broad line clouds (or scattering material) exist in the vicinity of the jet (Ghisellini & Madau 1996). In different with other Compton scattering scenarios, this model predicts the flare in the γ-ray band (i.e., HE component) to lag the synchrotron outburst by $\sim L/c$, where L is the distance from the blob to the BLR region. It also predicts almost simultaneous variability at all γ-ray energies.

2.3.2   Time Dependent SSC Model

Theoretical models in previous sections have brought much success to understand the multi-frequency spectra of blazars from radio to γ-ray bands. However, we must note that these models are basically constructed on the *steady* state assumption, while blazars are highly variable in various energy bands (§ 2.2.2). Next step for the theoretical works is to understand the rapid time variability of blazars. It is only recently that several authors start to consider unified picture of blazars, taking both temporal and spectral evolutions into account. Successful results have been obtained for the simplest one-zone SSC model, but an application to the ERC and/or the MC models remains a future work.

Mastichiadis & Kirk (1997) and Dermer (1998) considered time-dependent SSC models where the variability is on time scales longer than R/c, R being the size of the emission region. One example of such calculations is illustrated in Figure 2.8 (Mastichiadis & Kirk 1997). Observational data come from Macomb et al. (1995; Figure 2.3). Assuming that electron injection spectrum is suddenly changed and then left constant, they calculated the time evolution of the electron and photon spectra for an arbitrary time. Left panel shows the time evolution of multi-frequency spectra, while right panel shows the changes in flux in various energy bands. In this particular case, they assumed that maximum Lorentz factor (γ_{max}) of the electron population changed by factor of 5 in the 'new' equilibrium state.

Kirk, Rieger & Mastichiadis (1998) considered more sophisticated scenario where a thin shock front propagates through the emission region with a finite velocity v_{s}, supplying freshly accelerated electrons only in the front's vicinity. Most important discovery of their model is that the balance of acceleration and cooling processes plays an important role to determine blazar's variability, in particular at $\gamma \sim \gamma_{\mathrm{max}}$. They found that not only the usual clockwise hysteresis (Figure 2.6), but also the *anti*-clockwise hysteresis could be observed if the acceleration time is comparable with the cooling time scale.
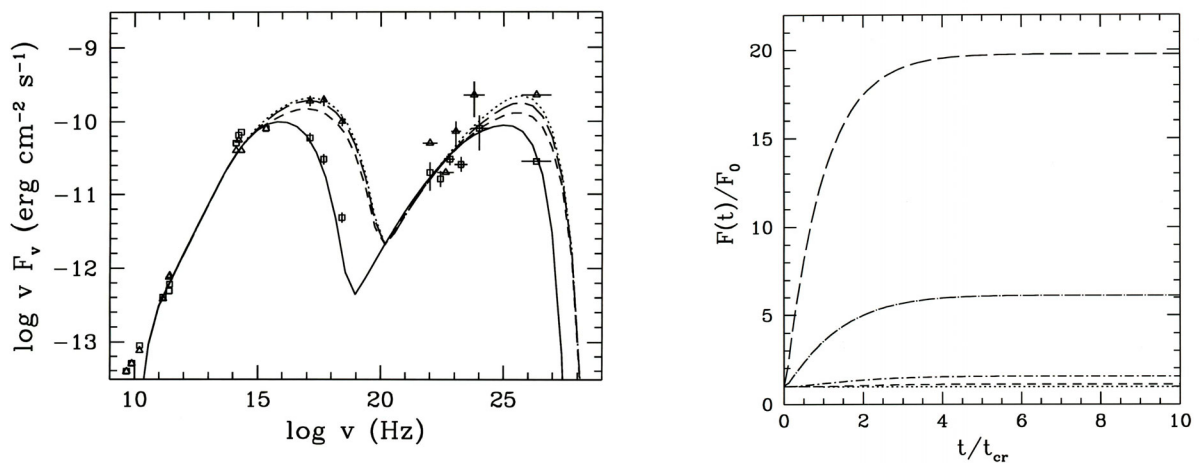
Figure 2.8: Time-dependent model for multi-wavelength spectrum and light curves of Mrk 421. Electron injection spectrum is assumed to be suddenly changed and then left constant. In this figure, maximum Lorentz factor of injected electron population are changed by factor of 5. *left*: Evolutions of multi-wavelength spectrum. Solid line is an initial state, while dotted line is the 'new' equilibrium state. *right*: Plot of the flux at various frequencies. The large dash line is $2-10$ keV X-rays, while large dot-dash line is > 500 GeV γ-rays. Figure from Mastichiadis & Kirk (1997).

2.3.3 Comment on the Hadronic Jet Model

Finally, we must note that there exists an alternative (or additional) scenario that AGN jets consists of normal hadronic matter ("proton jet" model; Mannheim & Biermann 1992; Mannheim 1993; Dar & Laor 1997). In this scenario, relativistic electrons can be injected by relativistic protons following nuclear interactions and/or photo-meson production process. Since the column densities in the jet plasma are too low to provide target for nuclear interactions, an external target has been proposed (Bednarek 1993). Such a model, however, may include several shortcomings as discussed in Sikora (1994) and Sikora et al. (1997).

First, the extremely low magnetic field in the target are required to avoid isotropization of accelerated protons before nuclear interactions. Second, in this scenario, it is only the third generation of particles which produces synchrotron radiation in the observable energy range. In this case, very fine tuning must be at work in order to obtain a third generation radiation component in the radio to X-ray bands. Third, such a compact region is expected to be opaque for GeV photons. Only for protons with energies above $\sim 10^9$ GeV, the radiation fields become opaque for photo-meson production process (Mannheim 1993). Following photo-meson production triggered by such protons, the synchrotron pair cascade develops. In this model, the break between X-rays and γ-rays is postulated to correspond with the break in the pair injection function. This model predicts the γ-ray energy index to be $\alpha_\gamma \geq 1$, which cannot explain steep γ-ray spectra observed with EGRET.

Finally, we should note that the prediction from the leptonic scenario is quite consistent with the observational data from radio to TeV γ-ray bands. Additional contribution from the accelerated protons, even if it exists, seems not very important. For these reasons, we do not consider the hadronic jet model in this thesis. Following discussion assumes the jet includes only leptons (i.e., electrons and positrons), or at least, radiation originated in hadronic interactions is assumed to be negligibly small.

2.4 TeV Blazars – Clue to the Jet Physics

2.4.1 Unifying Blazar Classes

As we see briefly in the previous section, blazars are classified into BL lac objects and OVV quasars. BL lac objects that have low-energy peaks in the IR/optical bands are called LBLs (low-energy peaked BL lacs), while BL lacs that have the peaks in the UV/X-ray band are called HBLs (high-energy peaked BL lacs) (e.g., Padovani & Giommi. 1995).

The first attempt to find regularities in the spectral energy distribution (SED) of blazars including γ-ray data, are performed by Kubo et al (1997; 1998) and Fossati et al (1998).

Kubo et al. (1997; 1998) fit the multi-frequency spectra of 18 blazars observed with *ASCA* by a cubic, leading to a conclusion that the difference of three types of blazars (HBLs, LBLs and OVV quasars) are primarily due to the different maximum Lorentz factors (γ_{max}) of electrons. γ_{max} of OVV quasars were derived to be 10^3-10^4, while they were 10^5-10^6 for HBLs. They also found that the multiband spectra of HBLs are well explained by a simple SSC process, while the ERC process must be dominant for OVV quasars. Since BL lac objects is characterized with the lack of any emission lines in the optical band (Figure 2.1), contribution from the external radiation field should be much less than that in the OVV quasars. In such situation, they found that pure Synchrotron-Self-Compton (SSC) process is expected to be dominant.

Fossati et al (1998) collect data from literature for more than 50 sources and construct the SED of all these blazars. They divided the all sources in radio luminosity bins, averaging the data of the sources belonging to the same luminosity bin. The result is shown in Figure 2.9. Importantly, there seems a clear trend that as the total power decreases, both LE and HE components shift to the higher frequencies, and at the same time the γ-ray luminosity decreases its relative importance, reducing the bolometric output.
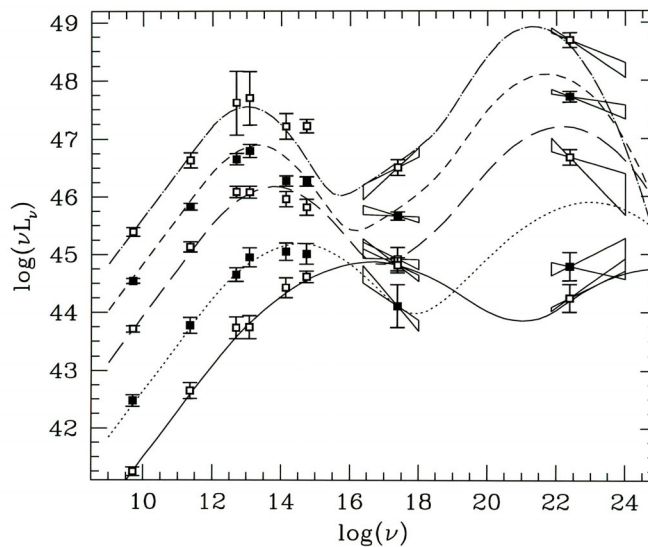
Figure 2.9: Unified picture of spectral energy distribution for all types of blazars. Figure from Fossati et al (1998).

Ghisellini et al. (1998) have collected a larger samples of 51 blazars and applied more

stringent theoretical models for blazars. They also associated the difference of three blazar classes with the difference in electron Lorentz factors. They found a tight correlation between the γ_{peak} ($\sim \gamma_{\mathrm{max}}$) and the amount of energy density U (both magnetic and radiative); $\gamma_{\mathrm{peak}} \propto U^{-0.6}$ (Figure 2.10). Importantly, this means that the energy loss rate of electrons ($\propto \gamma^2 U$; see § 3) is, at γ_{peak}, nearly the same for all types of blazars. Since the acceleration and cooling is expected to be balanced at γ_{peak}, this suggests the presence of some *universal* acceleration mechanism in blazar jets.
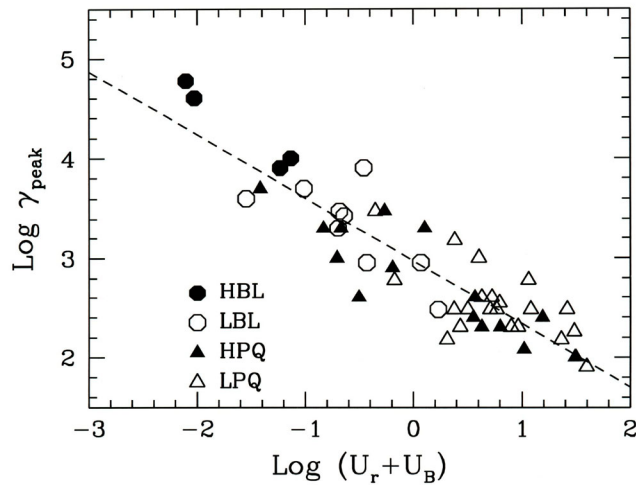
Figure 2.10: Correlation between γ_{peak} and the total (magnetic plus radiative) energy density. A tight correlation, $\gamma_{\mathrm{peak}} \propto U^{-0.6}$ was found. In this figure, QSO hosted blazars (QHBs) are defined as LPQ plus HPQ. Figure from Ghisellini et al (1998).

2.4.2 Extreme Particle Accelerators – TeV Blazars

As was suggested by Kubo et al. (1998) and Ghisellini et al. (1998), the typical values of γ_{max} are $\sim 10^3$ for OVV quasars, $\sim 10^4$ for LBLs and $\sim 10^5$ for HBLs, respectively. The unified picture of these blazar classes is illustrated in Figure 2.11. This figure represents the relation between luminosity (in the source frame) versus maximum Lorentz factor of electrons (Ghisellini et al. 1998). One can see that the HBLs are less luminous but have large γ_{max}, which indicates that particle acceleration process is working most efficiently in HBLs.

Four TeV blazars are classified into HBLs, because their LE component reaches to the X–ray energy band. Detection of TeV γ-rays suggests a presence of electrons accelerated to extremely high energies, up to $\gamma_{\mathrm{max}} \geq 10^6$. This can be easily understood as follows.
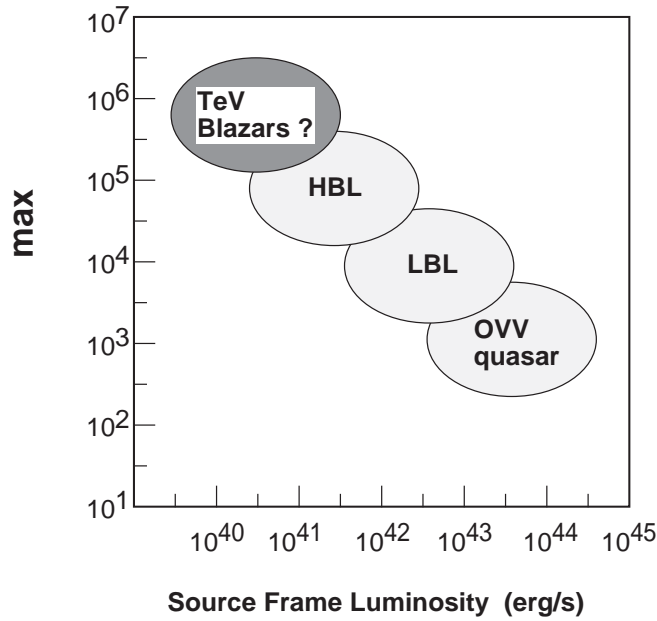
Figure 2.11: Unified scheme of all types of blazars. Figure adapted from Ghisellini et al (1998).

The maximum energy of high energy electrons is given as $\gamma_{max}\, m_e c^2$. From the argument of energy conservation between an electron and photon, this must be larger than the observed maximum photon energy measured in the source frame, i.e., $h\nu_{max}/\delta$. Since we have detected TeV γ-rays from these sources, the relation becomes $\gamma_{max}\delta \geq 10^7$. Assuming $\delta \sim 10$ for beaming factor, we expect that electrons are accelerated to more than $\gamma_{max} \sim 10^6$ at least in these TeV sources.

Since the cooling time when an electron loses its half of energy by synchrotron radiation is proportional to γ^{-1} (§ 3.3), most rapid variations can be observed for these TeV blazars. Any changes, such as variations in acceleration rate and/or the magnetic field, will be most sensitively observed at γ_{max}. Importantly, in the photon frequency space, this corresponds to the X-ray band for LE component and TeV band for HE component, both of which are known to show very steep spectra and large amplitude variability (§ 2.2.2). Thus the study of variability patterns and the spectral evolutions in X-ray and TeV bands provides direct information on dynamics operating in the jet (e.g., Kirk, Rieger,& Mastichiadis 1998).

A similar study could be also possible for QHBs and LBLs, but would probably be less conclusive, as these sub-classes of blazars exhibit a greater variety of spectral behavior. In particular, the X-ray and γ-ray bands (GeV regine in this case) corresponds to the lowest and the highest part of HE component, respectively, and thus *they sample different ends of the electron population*, which is in contrast to HBLs. In fact, X-ray variability

of QHBs and LBLs is known to be slower and less variable on short time scales (e.g., Kubo et al. 1998). TeV blazars promise to provide richest – but reasonably well measured – variety of both temporal and spectral evolution which at the same time is reasonably well understood in the context of the relatively simple SSC model, which points to diverse but relatively well-determined physical conditions in the jet rather than including additional effects due to geometry (e.g., beaming and orientation).

2.4.3   Individual Target

Mrk 421

Mrk 421 is very bright and highly variable in the X-ray band. Rapid variability in time scales as short as ≤ 1 day was repeatedly observed (e.g., Makino et al. 1987; George et al. 1988). X-ray spectrum is very steep, such that the photon energy spectrum in the X-ray band is well-described by a power law with the photon index $\sim 2 - 3$, although the spectral shape changes significantly during individual observations (Giommi et al. 1990; Makino et al. 1992; Comastri et al. 1997). It was also shown that the energy spectrum from radio to X-ray band connects smoothly, suggesting that the same emission mechanism (i.e., synchrotron radiation) is responsible for the radiative output from the entire radio - to X-ray regime (e.g., Urry 1984; Makino et al. 1987).

The advent of EGRET instrument and the observations by *Whipple* Cherenkov telescope brought a dramatical progress in the multifrequency study of this object. The γ-ray emission was first detected in the GeV band in 1991, but was very faint. The GeV flux was comparable to that of EGRET detection limit (Lin et al. 1992). Importantly, the spectral photon index in the GeV band was flat (≤ 2) and *not* connected smoothly to the X-ray spectrum. This was the first case which suggested that the both emissions have different origins, as predicted by the SSC scenario (see § 2.3).

After the EGRET detection, Mrk 421 was detected at TeV energies (Punch et al. 1992) by *Whipple* collaboration, being the *first* extragalactic TeV source detected at that time. The initial detection indicated a 6 σ excess and the flux was approximately 30 % of the flux of the Crab Nebula above 500 GeV (Punch et al. 1992). TeV emission from Mrk 421 has now been confirmed by several other collaborations (e.g., Petry et al. 1996 for the *HEGRA* detection). The TeV spectrum was measured to be very steep, indicating the spectral photon index of ~ 3 (Petry et al. 1996; Aharonian et al. 1999). Many authors associated the peculiarity of Mrk 421 with the distance to the source. In fact, it is the closest BL lac objects whose redshift is 0.031, and thus least affected by DIRB (extragalactic diffuse Infrared background) absorption (see § 2.5).

The first multiwavelength campaign of Mrk 421, including γ-ray detectors, was conducted in 1994 from radio to TeV bands (Macomb et al. 1995; 1996). This campaign provided the best-sampled data ever known for Mrk 421. During this campaign, a TeV flare was detected, but the *ASCA* observation was conducted one day after the TeV flare (Kerrick et al. 1995; Takahashi et al. 1996). The EGRET also observed Mrk 421 for a week, but no significant variation in flux was detected (Figure 2.3). Another Mrk 421 multiwavelength campaign performed in 1995 revealed another coincident keV/TeV flare (Buckley et al. 1996; Takahashi et al. 1996b). Although the relative amplitudes of variability are different, the UV and optical bands also showed correlation during the flares. Unfortunately, the X-ray data were too sparsely sampled to resolve the rapid time variability during the observation (see, e.g., Figure 7.2).

Mrk 501

Mrk 501 was known to be a fainter and less variable BL lac object than Mrk 421 in the X-ray band. Except for an *EXOSAT* observation in 1986 (Giommi et al.1990), the variation time scale was always longer than one day. X-ray spectrum was steep, such that the photon energy spectrum was well-described by a power law with the photon index of ~ 2.6 (Makino et al. 1992; Comastri et al. 1997). The energy spectrum from radio to X-ray bands connected smoothly, again suggesting that same emission mechanism is dominant for the radiation in both energy bands (e.g., Urry 1984).

From 1991 to 1992, EGRET observed Mrk 501 three times, but no significant γ-ray emission was detected ($\leq 2\ \sigma$). Thus only upper limit on flux was available in the 2nd EGRET source catalogue (Fichtel et al. 1994). In parallel with EGRET observations, Mrk 501 was also part of an active program of observing extragalactic sources by the *Whipple* collaboration. Prior to the detection in the GeV band, in 1995, it was detected as the *second* extragalactic source that emits TeV γ-rays (Quinn et al. 1996). The sum of 1995 data indicated the marginal evidence for detection at $9\ \sigma$ level and the flux was approximately 10 % of the flux of the Crab Nebula above 350 GeV (Quinn et al. 1996). The TeV spectrum was measured to be steep, but flatter than Mrk 421. The spectral photon index was ~ 2.5 (Petry et al. 1997; Samuelson al. 1998). Notably, Mrk 501 is the second closest TeV-emitting BL Lac object ($z = 0.034$).

The first multiwavelength observations of Mrk 501, which included γ-ray detectors, were conducted in 1996 (Kataoka et al. 1999a). The observations were conducted with optical, *ASCA* , EGRET, and *Whipple* telescopes, although the GeV γ-ray was not detected at that time. The observations were well-scheduled and simultaneous from optical to TeV bands. The X-ray flux observed with *ASCA* was five times higher than that obtained

with *GINGA* (Makino et al. 1992) and the photon energy spectrum was harder. More importantly, during this campaign, EGRET detected Mrk 501 with a significance of 3.5 σ above 100 MeV (Kataoka et al. 1999a). Follow up observations established more strongly the detection of Mrk 501 by EGRET, with a marginal significance of 4.0 σ above 100 MeV but a significance of 5.2 σ above 500 MeV, indicating a hard GeV photon spectrum of the photon index of 1.3±0.5.

The multiwavelength observations of Mrk 501 including TeV telescopes repeated after the success in 1996. During 1997 April campaign, a dramatical flare was observed in both X-ray and TeV bands (e.g., Catanese et al. 1997; Pian et al. 1998). Those results implied that the keV and TeV variations are well correlated, and X-ray spectrum becomes hardest among the HBLs (photon index at 2 – 10 keV was $\sim$ 1.7; Pian et al. 1998). Pian et al (1998) pointed out the shift of synchrotron peak (peak of LE component) by a factor of 100, which is the largest shift ever observed in blazars.

PKS 2155−304

PKS 2155−304 is a bright X-ray blazar, showing a rapid variability on time-scale of hours (e.g. Treves et al. 1989; Tagliaferri et al. 1991; Chiapetti et al. 1999; Zhang et al. 1999). It is also one of the brightest extragalactic EUV sources. A large number of intensive multiwavelength campaigns have been conducted, but those observations did not include γ-ray detectors (e.g., Edelson et al. 1995; Urry et al. 1997). The energy spectrum from radio to X-ray band connects very smoothly, suggesting that both emissions are due to the same origin (e.g., Urry 1984; Treves et al. 1989). The photon energy spectrum is well-described by a power law with the photon index $\sim 2 - 3$, but highly variable (e.g., Sembay et al. 1993)

EGRET observed PKS 2155−304 six times from 1991 to 1993, but no significant emission was detected. However, during 1994 observation, it was detected for the first time at 6 σ level (Vestrand, Stacy, & Sreekumar 1995). Furthermore, higher GeV flux was observed during 1997 observation, implying a GeV flux increase by a factor of 3 (Sreekumar & Vestrand. 1997). The spctral photon index in the GeV band was measured to be 1.7 ± 0.2, more flatter than that of the X-ray spectrum (Vestrand, Stacy & Sreekumar. 1995).

The TeV emission from PKS 2155−304 was detected only recently, probably due to its southern location (Chadwick et al. 1999). *Durham Mark 6* Cherenkov telescope repeatedly observed PKS 2155−304 from 1996 to 1997, and obtained an evidence for TeV emission with marginal significance of 6.8 σ. Although other telescopes located in the Southern Hemisphere, e.g., CANGAROO collaboration, have not confirmed the detection, PKS 2155−304 is now believed to be the *fourth* TeV emitting blazar. It should be noted

that PKS 2155−304 is more distant ($z = 0.117$) than Mrk 421 and Mrk 501, and thus the most crucial test on DIRB will be achieved for this source in the future work.

Since both GeV and TeV emission was detected only recently, no multiwavelength campaign including γ-ray detectors was reported. The time variability was greatly different in different epochs. During 1991 campaign, 10 % flux change was observed *coherently* from optical to X-ray bands, with no significant time lags (Edelson et al. 1995). However in 1994 campaign, the amplitude of variation was strongly frequency dependent – flare of a factor 2 in the X-ray band, while smaller amplitude variations in UV bands were observed with significant time lags (Urry et al.1997). Considering the latter campaign has only short coverage between UV and X-ray observations, it seems speculative to put emphasis on the time lag. However, these observations suggest the variety of flares which are probably due to the different physical origin.

1ES 2344−514

1ES 2344+514 is one of the few known BL lac objects. It was first detected in the *Einstein* Slew Survey (Elvis et al. 1992). 1ES 2344+514 was only recently identified as a BL lac object (Perlman et al. 1996), by the lack of optical emission lines whose equivalent width greater than 5Åand its Ca II 'break strength' being smaller than 25 %. The former eliminates the possibility of the source as a quasar, while the latter criteria is indicative of the presence of a power law continuum. Perlman et al. (1996) determined the redshift of this object ($z = 0.044$) based on absorption lines, since it had no evident emission lines.

1ES 2344+514 is identified as the third closest known BL Lac object, after Mrk 421 and Mrk 501. Perlman et al. (1996) derive a 2 keV X-ray flux as roughly 1/3 the flux detected for Mrk 421 and Mrk 501. Measurements taken with the Very Large Array radio interferometer indicate that its radio emission is 'point-like,' with more than 80% of its flux being from an unresolved point source (Patanik et al. 1992; Perlman et al. 1996). The 5 GHz radio flux is about 1/3 and 1/4 of the flux of Mrk 421 and Mrk 501, respectively.

The EGRET observed 1ES 2344+514, but has not detected it. The preliminary upper limit on the GeV flux, derived from the private communication with the EGRET team, is presented in Catanese et al. (1998). 1ES 2344+514 was, however, detected by *Whipple* collaboration as the *third* extragalactic source succeeding to Mrk 501 (Catanese et al. 1998). The evidence for emission from 1ES 2344+514 comes mostly from an apparent flare on 1995, with a significance of 6 σ excess. This corresponds to about the 60 % of the Crab flux. However, follow up observations taken between 1995 and 1996 showed a fainter flux, cresponding to 10 % of the Crab Nebula, and no significant flux was observed

between 1996 to 1997, indicating the source is highly variable in the TeV energy band.

Although no simultaneous campaigns have been conducted so far, best quality data in the X-ray band were obtained very recently by *BeppoSAX* observations (Giommi et al. 1999). They detected a flux variation on a time scale as short as ≤ 1 day. The X-ray photon spectrum was well represented by a power law form, with photon index ranged from 1.8 to 2.3.

2.5 Effects by the DIRB

There exist HBLs whose multiband properties are very similar to those of TeV blazars, but which are *not* detected at TeV energies yet. It should be noted that four TeV blazars detected at present are all low-redshift BL Lac objects. In fact, Mrk 421 is the closest BL lac objects ever known. This naturally suggests that the detectability at TeV energy band may be dependent on the distance to the source. Many authors pointed out that TeV γ-rays from the high-redshift sources are probably absorbed by the interaction with extragalactic diffuse infrared background (DIRB; e.g., Stecker et al. 1992). This interpretation is very likely, however, main difficulty is that the flux of the DIRB has not been determined experimentally due to large systematic errors driven by local effects (Figure 2.12). Some authors suggest that the TeV energy spectrum of blazars can be viable to derive the upper limit on DIRB, but this still involves large systematic errors in the estimation (e.g., Funk et al. 1998; Figure 2.12).

Thus the effects of DIRB on the photon spectra of TeV emitting blazars is now still under debate. We show one example presented by Stecker et al. (1998) in Figure 2.13. According to their model, optical depth for TeV−IR absorption is less than unity below 10 TeV for Mrk 421 and Mrk 501, both at redshift of ~ 0.03. This indicates that no significant curvature would be appearent in the TeV γ-ray spectra obtained with ground-based Cherenkov telescopes. However, the intrinsic spectra of these sources should be harder by amounts of ~ 0.25 to 0.45 in the spectral index (in the 1 to 10 TeV range), with an intergalactic absorption cutoff above 20 TeV.

In this thesis, we proceed under the assumption that the effect of absorption by DIRB is negligibly small for all TeV blazars. This approximation is probably valid for *Whipple* observations of Mrk 421 and Mrk 501 ($z \simeq 0.03$), because the energy threshold of the detector is 0.35 TeV and most of the photons are detected below 1 TeV (Figure 2.13). However, for the most distant TeV blazar PKS 2155−304 (z = 0.117), optical depth becomes ~ 1 at 1 TeV (Figure 2.13), which may lead to an underestimation of absolute TeV flux by factor ~ 2, altough this is still consistent within the measurement error (Chadwick

et al. 1999).

We also note that, even if absorption by DIRB is more important than the estimation given by Stecker et al. (1998), *relative* amplitude of variation in the TeV flux is *not* affected unless DIRB itself is variable in time. Thus the study of inter-band correlation between X-ray and TeV γ-rays described in § 9 is not affected by the DIRB absorption.
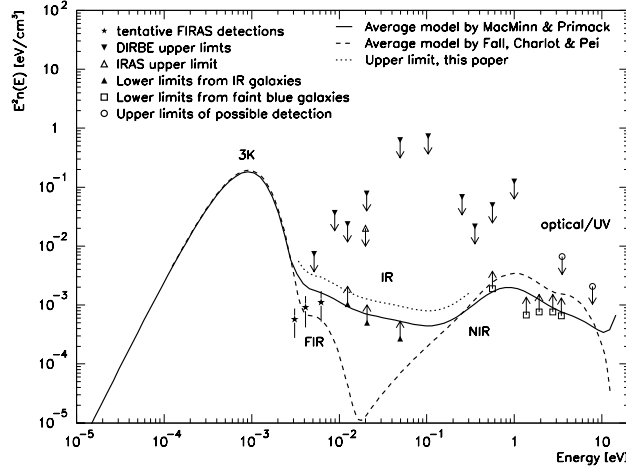
Figure 2.12: Energy density of the DIRB. *Solid line* and *dashed line* : theoretical models for DIRBs. *Dotted line* : upper limit from the TeV energy spectra of Mrk 501. Figure from Funk et al (1998).
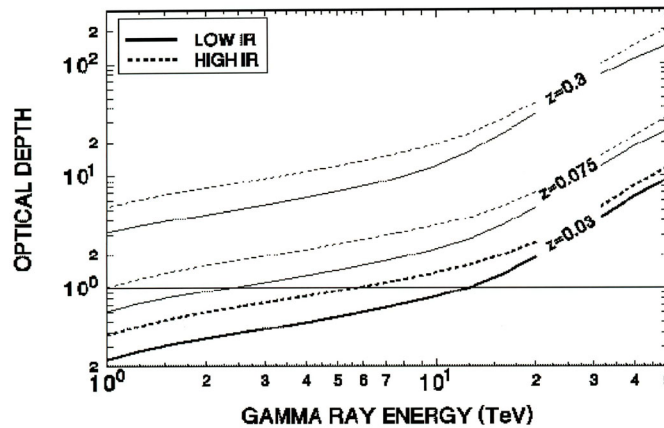
Figure 2.13: Optical depth vs energy for γ-rays originating at various redshifts. Figure from Stecker et al (1998).

Chapter 3

Emission Mechanism of Blazars

3.1 Energy Gain Processes

In this section, a simple theory for particle acceleration at a shock front is introduced as a possible energy gain process of electrons in blazar jets. The following treatment of Fermi acceleration is based on Gaisser (1990) and Protheroe (1996). More detailed and rigorous treatments are given in the literature (e.g., Blanford & Eichler 1987).

3.1.1 2nd order Fermi Acceleration

Assume that there are magnetized clouds moving with speed V (Figure 3.1). A charged particle enters the cloud and scatters off irregularities in the magnetic field which is tied to the cloud. In the frame comoving with cloud, there is no change in energy of the particle because the scattering is collisionless, however, the direction of the particle is randomized by the scattering with clouds in a random direction. We consider a charged particle entering a cloud with energy E_1, momentum p_1, moving in a direction θ_1 related to the cloud's direction. After scattering has occured, it emerges with E_2, momentum p_2, in a direction θ_2 relative to cloud's direction. By applying Lorentz transformations between the observer's frame (unprimed) and the cloud frame (primed), we obtain the fractional energy change in particle energy $(E_2 - E_1)/E_1$,

$$\frac{\Delta E}{E} = \frac{1 - \beta\cos\theta_1 + \beta\cos\theta_2' - \beta^2\cos\theta_1\cos\theta_2'}{1 - \beta^2} - 1, \qquad (3.1)$$

where $\beta = V/c$. Since particles and clouds move randomly in direction, average values of $\cos\theta_1$ and $\cos\theta_2'$ are important. Inside the cloud, the direction of the charged particle will be completely randomized by multiple scatterings, such that $<\cos\theta_2'> = 0$. The average value of $\cos\theta_1$ depends on the rate of collision, which is proportional to the relative velocity

between the cloud and particle. Thus probability per unit solid angle of having a collision at angle θ_1 is proportional to $v - V\cos\theta_1$, where v $(\simeq c)$ is the velocity of particle. We obtain

$$< \cos\theta_1 > = \int \cos\theta_1 \frac{dP}{d\Omega_1} d\Omega_1 / \int \frac{dP}{d\Omega_1} d\Omega_1 = -\frac{\beta}{3}, \qquad (3.2)$$

giving

$$\frac{< \Delta E >}{E} = \frac{1 + \beta^2/3}{1 - \beta^2} - 1 \simeq \frac{4}{3}\beta^2. \qquad (3.3)$$

This result shows the particle gains energy from the cloud, but the average gain is small because $\beta \ll 1$ in ordinary cases.
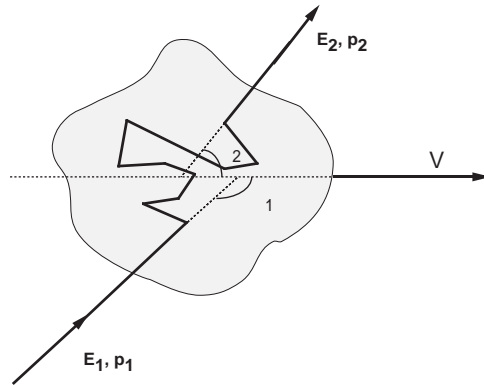
Figure 3.1: Schematic view of 2nd order Fermi Acceleration.

3.1.2   1st order Fermi Acceleration

More efficient acceleration (1st order in β) can take place when a shock propagates through the plasma, and charged particles cross the shock front iteratively from downstream to upstream, and upstream to downstream. This situation is expected in many astrophysical situations, such as supernova explosion in the interstellar medium or relativistic jets associated with extragalactic and/or galactic sources. A schematic view of acceleration at shock front is given in Figure 3.2. In this case, the probability per unit solid angle of having a collision at angle θ_1 is proportional to $\cos\theta_1$, while the probability is proportional to $\cos\theta_2'$ after the scattering. Thus we obtain $<\cos\theta_1> = -2/3$ and $<\cos\theta_2'> = 2/3$. In this case, one finds from equation (3.1)

$$\frac{< \Delta E >}{E} \simeq \frac{4(R - 1)}{3R} \frac{V_s}{c} \simeq \frac{4}{3}\beta, \qquad (3.4)$$

where V_s is the shock velocity, $R = u_1/u_2$ is the compression ratio, $u_1 = V_s$ and u_2 are the upstream and downstream velocities in the rest frame of the shock. For a strong shock in

a mono-atomic gas (e.g., fully ionized plasma), $R_c = 4$ is expected from Rankine-Hugoniot relation.
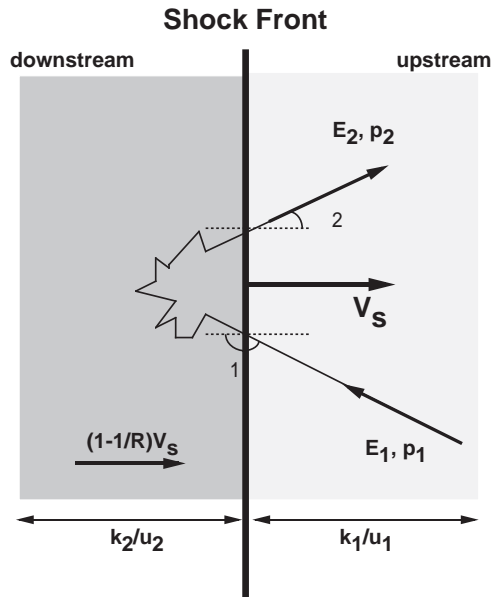
Shock Front

Figure 3.2: Schematic view of 1st order Fermi Acceleration.

3.1.3 Acceleration Rate

A net flow of the energetic particles, which are escaping from the shock front, is calculated as

$$r_{\rm loss} = n_{\rm cp}u_2 = n_{\rm cp}\frac{V_{\rm s}}{R}, \tag{3.5}$$

where $n_{\rm cp}$ is the number density of particles at the shock. In the upstream of the shock, a charged particle moving at speed v at angle θ to the shock normal (in the observer's frame) approaches the shock with speed $V_{\rm s}+v\cos\theta$ in the shock frame. To cross the shock, $\cos\theta > -V_{\rm s}/v$ is required. Thus the rate at which particles cross the shock from upstream to downstream is calculated assuming isotropic distributions of particles

$$r_{\rm cross} = n_{\rm cp}\frac{1}{4\pi}\int_{-V_{\rm s}/v}^{1}(V_{\rm s} + v\cos\theta)d(\cos\theta)\int_{0}^{2\pi}d\phi = n_{\rm cp}\frac{v}{4}. \tag{3.6}$$

We obtain the probability of crossing the shock front once and then escaping from the acceleration process as the ratio of these two rates,

$$\text{Prob(escape)} = \frac{r_{\rm loss}}{r_{\rm cross}} = \frac{4}{R}\frac{V_{\rm s}}{v}. \tag{3.7}$$

By defining the time $t_{\rm cycle}$ for one complete cycle, i.e., from crossing the shock from upstream to downstream, diffusing back towards the shock and crossing from downstream

to upstream, with enegy gain $<\Delta E>$, we can define the acceleration rate and escape rate per shock crossing as

$$r_{\mathrm{acc}} = \frac{1}{E}\frac{dE}{dt} = \frac{<\Delta E>}{E}\frac{1}{t_{\mathrm{cycle}}}, \tag{3.8}$$

$$r_{\mathrm{esc}} = \frac{\mathrm{Prob(escape)}}{t_{\mathrm{cycle}}} \simeq \frac{4}{R}\frac{V_{\mathrm{s}}}{c}\frac{1}{t_{\mathrm{cycle}}}. \tag{3.9}$$

Combined this with equation (3.4), one obtains the relation

$$\frac{r_{\mathrm{esc}}}{r_{\mathrm{acc}}} \simeq \frac{3}{R-1}. \tag{3.10}$$

Note that for a strong shock case ($R = 4$), the two rates are equal.

3.1.4   Diffusion Coefficient

The cycle time for the acceleration process depends on particle diffusion, as well as the shock velocity. We first consider the diffusion in the downstream direction. The typical distance of a particle diffusion in time t is given as $\sqrt{k_2 t}$, where k_2 is the diffusion coefficient in the downstream region. The distance advected in this time is simply $u_2 t$. If $\sqrt{k_2 t} \gg u_2 t$, it is very probable that the particle will return to the shock, but if $\sqrt{k_2 t} \ll u_2 t$, the particle will never come back. By setting $\sqrt{k_2 t} = u_2 t$, we obtain the boundary distance $d = k_2/u_2$ from the shock front in the downstream direction, where inside of this, the particle will effectively return to the shock front. There exist $n_{\mathrm{cp}} k_2/u_2$ particles per unit area, between the shock front and this boundary. Dividing this by the ratio r_{cross}, one finds the average time spent downstream before returning to the shock

$$t_{\mathrm{cycle}}^{\mathrm{down}} \simeq \frac{4}{c}\frac{k_2}{u_2}. \tag{3.11}$$

Similary, the other half of the cycle after the particle has crossed the shock from downstream to upstream is easily obtained. In this case, one can define a boundary at a distance k_1/u_1 upstream of the shock, leading to

$$t_{\mathrm{cycle}}^{\mathrm{up}} \simeq \frac{4}{c}\frac{k_1}{u_1}. \tag{3.12}$$

Thus the total cycle time t_{cycle}, the acceleration rate r_{acc}, and the acceleration time t_{acc} ($\equiv 1/r_{\mathrm{acc}}$) are respectively

$$t_{\mathrm{cycle}} \simeq \frac{4}{c}\Big(\frac{k_1}{u_1} + \frac{k_2}{u_2}\Big), \tag{3.13}$$

$$r_{\mathrm{acc}} \simeq \frac{(R-1)u_1}{3R}\Big(\frac{k_1}{u_1} + \frac{k_2}{u_2}\Big)^{-1}, \tag{3.14}$$

$$t_{\mathrm{acc}} \simeq \frac{3R}{(R-1)u_1}\Big(\frac{k_1}{u_1} + \frac{k_2}{u_2}\Big). \tag{3.15}$$

3.1.5 Energy Spectrum

Assume that the diffusion coefficients upstream and downstream have the same power law dependence ξ on energy, i.e.,

$$k_1 \propto k_2 \propto E^\xi, \tag{3.16}$$

then the acceleration rate r_{acc} and the escape rate r_{esc} also have a power law dependence (see equation (3.10) and (3.14)),

$$r_{\mathrm{acc}} \propto r_{\mathrm{esc}} \propto E^{-\xi}. \tag{3.17}$$

In the following, we consider the case of ignoring losses due to radiative cooling (e.g., synchrotron cooling) or any other processes. We define the acceleration/escape rate

$$r_{\mathrm{acc}} = aE^{-\xi}, \tag{3.18}$$

$$r_{\mathrm{esc}} = cE^{-\xi}, \tag{3.19}$$

where a and c are constants. From equation (3.8), the particle energy at time t is determined from a differential equation

$$dE/dt = aE^{1-\xi}, \tag{3.20}$$

giving

$$E(t) = (E_0^\xi + \xi a t)^{1/\xi}, \tag{3.21}$$

where E_0 is the particle energy at time t=0. The number of particles remaining inside the shock front at time t after injection is calclulated by solving

$$dN/dt = -N(t)r_{\mathrm{esc}} = -N(t)cE(t)^{-\xi}. \tag{3.22}$$

The solution of this equation is

$$N(t) = N_0[E(t)/E_0]^{-c/a}. \tag{3.23}$$

Since $N_0 - N(t)$ particles have escaped from the shock front before time t, having energies between E_0 and $E(t)$, the differential energy spectrum of particles which have escaped from the shock front is given as

$$dN/dE = N_0(s-1)E_0^{-1}(E/E_0)^{-s}, \qquad (E_0 < E < E(t)) \tag{3.24}$$

where $s = (1 + c/a)$ is the differential spectral index. It should be noted that for the strong shock case ($r_{\mathrm{esc}} = r_{\mathrm{acc}}$), one obtains the standard result for shock acceleration, $s = 2$.

3.2   Energy Loss Processes

While the electrons gain energy from the shock, they also suffer from many kind of energy-loss processes. Because of the very wide energy distribution of electrons and the different dependence on energy of each cooling process, it is important to discuss which process cools electrons more effectively. We first consider four cooling processes – (1) synchrotron cooling, (2) inverse Compton scattering, (3) Coulomb losses, and (4) bremsstrahlung. In the following, we evaluate the energy losses $b(\gamma)$, for a single electron.

High-energy electrons in a magnetic field emit synchrotron radiation (e.g., Rybicki & Lightman (1979); see also equation (3.34))

$$b_{\mathrm{sync}} = \frac{4\sigma_{\mathrm{T}}\gamma^2 U_B}{3m_e c} = 1.29 \times 10^{-9} B^2 \gamma^2 \qquad [\mathrm{s}^{-1}], \tag{3.25}$$

where U_{B} is the energy density in the magnetic field and σ_{T} is the Thomson cross section.

Similarly, the inverse Compton cooling rate b_{IC} is given by (e.g., Rybicki & Lightman 1979; see also equation (3.47))

$$b_{\mathrm{IC}} \simeq \frac{4\sigma_{\mathrm{T}}\gamma^2 U_{\mathrm{ph}}}{3m_e c} \qquad [\mathrm{s}^{-1}], \tag{3.26}$$

where U_{ph} is the soft photon density to be up-scattered.

The relativistic electrons will also lose their energy by interactions with the thermal plasma. The Coulomb losses due to collisions with charged particles give a loss rate which is approximately (e.g., Rephaeli 1979),

$$b_{\mathrm{Coul}} \simeq 1.2 \times 10^{-12} n_e [1.0 + \frac{\ln(\gamma/n_e)}{75}] \qquad [\mathrm{s}^{-1}], \tag{3.27}$$

where n_e is the thermal electron density in the plasma.

The same collisions between high energy electrons and thermal particles also produce radiation thorough bremsstrahlung. The loss rate due to bremsstrahlung is given approximately (e.g., Blumental & Gould 1970)

$$b_{\mathrm{brems}} \simeq 1.5 \times 10^{-16} n_e \gamma [\ln\gamma + 0.36] \qquad [\mathrm{s}^{-1}]. \tag{3.28}$$

We assume $B \simeq 0.1 - 1.0$ G for a blazar jet. U_{ph} is estimated roughly from the luminosity in the source frame, $L \sim 10^{40} - 10^{42}$ erg/s (e.g., Kubo et al. 1998). Assuming the source radius $R \sim 10^{16}$ cm, we obtain $U_{\mathrm{ph}} \sim 10^{-4} - 10^{-2}$ erg/cm^3. Although the thermal electron density in the blazar jet is completly unknown, we choose $n_e \sim 10^{-3} - 1$ cm^{-3}, which is appropriate for a typical intracluster medium and/or supernova remnants.

The results are summarized in Figure 3.3. One finds only two cooling processes, synchrotron cooling and inverse Comton scattering, can effectively influence the cooling
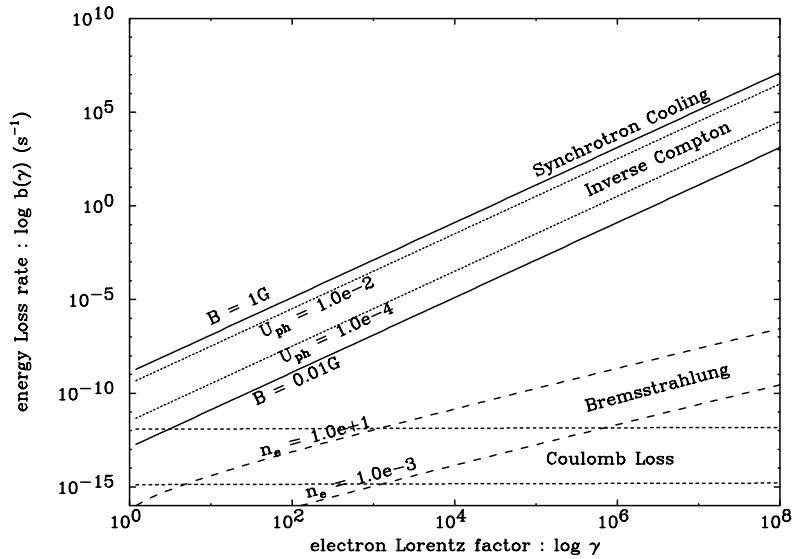
Figure 3.3: Energy loss rate $b(\gamma)$ from a single electron.

of the high-energy electrons. It should be noted that the result is essentially the same for any values of B, n_e and $U_{\rm ph}$ which are appropriate for blazars. Also note that the reduction of cross section in the Klein-Nishina regime would reduce the significance of inverse Compton losses at the high energy end ($\gamma \geq 10^5$; see, Figure 3.8), but that it is still more important than Coulomb and bremsstrahlung. Thus we conclude that the synchrotron radiation and the inverse Compton scattering are the dominant energy loss mechanisms to be further investigated.

3.3 Synchrotron Radiation

We first consider synchrotron radiation process. There exist numerous articles and reviews which have treated this process in detail (e.g., Blumenthal & Gould 1970; Rybicki & Lightman 1979). Here we merely collect the formulae which will be used in our calculations. We also describe the details for the synchrotron emission from a homogeneous self-absorbed (i.e., optically thick) source in § 11 and Appendix I.

3.3.1 Emission from a Single Electron

A relativistic electron in a magnetic field B will radiate fairly broad emission with a total emitted power per frequency,

$$P(\omega, \gamma) = \frac{\sqrt{3}e^3 B \sin\alpha}{2\pi m_e c^2} F(\frac{\omega}{\omega_c}), \qquad [\text{erg s}^{-1}\text{Hz}^{-1}] \qquad (3.29)$$

where e and m_e are the charge and mass of an electron, respectively. γ is the Lorentz factor of the electron, and α is the angle between the magnetic field and the electron velocity. $F(x)$ is defined as

$$F(x) \equiv x \int_x^\infty K_{5/3}(\eta)d\eta, \qquad (3.30)$$

where $K_{5/3}(x)$ is the modified Bessel functions of 5/3 order. ω_{c} is the critical frequency given as

$$\omega_{\mathrm{c}} = \frac{3\gamma^2 eB\sin\alpha}{2m_e c}. \qquad (3.31)$$
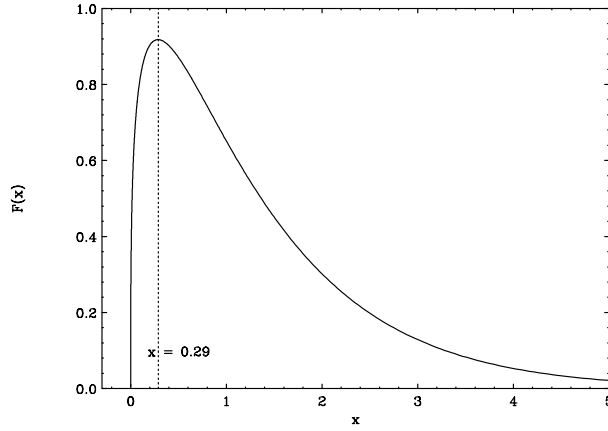
Figure 3.4: Synchrotron spectrum from a single electron as a function of $x \equiv \nu/\nu_{\mathrm{c}}$.

We show the function $F(x)$ in Figure 3.4. Since $F(x)$ peaks at $x \simeq 0.29$, the peak frequency of the synchrotron emission by an electron with Lorentz factor γ is expressed as

$$\nu_{\mathrm{p}} \simeq 1.2 \times 10^6 B\gamma^2 \sin\alpha. \qquad (3.32)$$

Similary, the synchrotron frequency *averaged* over the spectral shape for an electron of Lorentz factor γ is

$$\nu_{\mathrm{m}} \simeq 3.7 \times 10^6 B\gamma^2 \sin\alpha. \qquad (3.33)$$

An integration of equation (3.29) over the frequencies gives the cooling rate of a single electron by the synchrotron radiation

$$\dot{\gamma}_{\mathrm{sync}} = \frac{4\sigma_{\mathrm{T}}\gamma^2 U_B}{3m_e c}, \qquad (3.34)$$

where U_B is the magnetic field energy density and σ_{T} is the Thomson cross section.

3.3.2 Emission Coefficient : j_ν

Next we consider the synchrotron emission from electrons, whose number density per unit volume per unit energy is characterized by $N_e(\gamma)$. Electrons range from $\gamma_{\min}$ to $\gamma_{\max}$. The synchrotron emission coefficient $j_\nu(\nu)$ is derived straightforwardly from equation (3.29), noting that $\omega = 2\pi\nu$. We find the total emitted power per unit volume,

$$P_{tot}(\nu) = \int_{\gamma_{\min}}^{\gamma_{\max}} P(\nu, \gamma) N_e(\gamma) d\gamma. \tag{3.35}$$

For a distribution of randomly oriented emitters, we can write

$$j_\nu(\nu) = \frac{1}{4\pi} P_{tot}(\nu). \tag{3.36}$$

Thus we finally obtain

$$j_\nu(\nu) = c_2 B \int_{\gamma_{\min}}^{\gamma_{\max}} d\gamma N_e(\gamma) F(\frac{\nu}{c_1 B \gamma^2}), \tag{3.37}$$

where c_1 and c_2 are constants

$$c_1 = \frac{3e}{4\pi m_e c}, \qquad c_2 = \frac{\sqrt{3} e^3}{4\pi m_e c^2}. \tag{3.38}$$

We show examples of j_ν in Figure 3.5, for the magnetic field strength of 0.01 – 1.0 G. We assume a power law form for the electron population, $N(\gamma) = N_0 \gamma^{-2}$ ($1 < \gamma < 10^8$). Note that, at most the frequencies, j_ν is distributed as a power law, $j_\nu \propto \nu^{-p}$, where $p = 0.5$ (e.g., Rybicki & Lightman 1979).
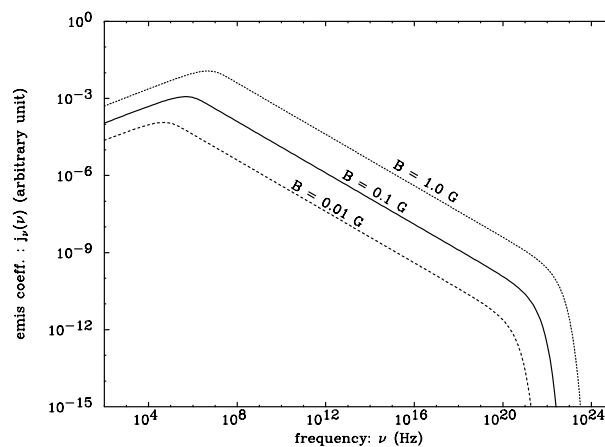
Figure 3.5: Emission coefficient j_ν of the synchrotron radiation for a power law electron population; $N(\gamma) = N_0 \gamma^{-2}$ ($1 < \gamma < 10^8$).

3.3.3   Absorption Coefficient : α_ν

Synchrotron emission is accompanied by absorption, in which a photon interacts with an electron, giving up its energy. In a classical scheme of electrodynamics, where the absorbed photon energy is much smaller than that of the electrons, one finds a simple formula for the self-absoption coefficient. We obtain

$$\alpha_\nu(\nu) = -\frac{1}{8\pi\nu^2 m_e}\int_{\gamma_{\min}}^{\gamma_{\max}} d\gamma P(\nu,\gamma)\gamma^2 \frac{\partial}{\partial\gamma}\left[\frac{N_e(\gamma)}{\gamma^2}\right]. \tag{3.39}$$

By replacing $P(\nu,\gamma)$ with equation (3.29), one finds

$$\alpha_\nu(\nu) = -\frac{c_3 B}{\nu^2}\int_{\gamma_{\min}}^{\gamma_{\max}} d\gamma\gamma^2 \frac{\partial}{\partial\gamma}\left[\frac{N_e(\gamma)}{\gamma^2}\right]F\left(\frac{\nu}{c_1 B\gamma^2}\right), \tag{3.40}$$

where c_3 is a constant

$$c_3 = \frac{\sqrt{3}e^3}{8\pi m_e^2 c^2}. \tag{3.41}$$

Figure 3.6 shows examples of α_ν, for the same population of electrons with Figure 3.5. Note that α_ν is strongly dependent on energy, such that $\alpha_\nu \propto \nu^{-3}$.
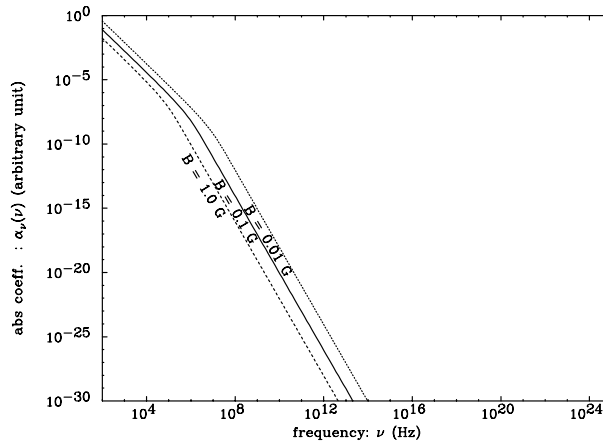
Figure 3.6: Absorption coefficient α_ν of the synchrotron radiation for a power law electron population; $N(\gamma) = N_0\gamma^{-2}$ $(1<\gamma<10^8)$.

3.4   Inverse Compton Radiation

In this section, we first consider the very simple case where a soft photon is scattered by a relativistic electron. Next we calculate the inverse Compton spectrum for arbitrary type of electron populations and photon spectra. We employ the formula derived by Jones (1968), which deals with the inverse Compton process more sophisticatedly, including the Klein-Nishina regime.

3.4.1 Scattering From a Single Electron

We start from the scattering event for a single electron and a single photon, which takes place in the Thomson regime. Geometries for inverse Compton scattering is given in Figure 3.7. We denote the electron energy γ, soft photon energy ϵ_0 and scattered photon energy ϵ, and express them in units of $m_e c^2$ (thus they are dimensionless values). We define the parameters with prime in the rest frame of the electron, while the parameters without prime are that in the observer's frame. From the Lorentz transformation and kinematics of Compton scattering, we have

$$\epsilon_0' = \epsilon_0 \gamma (1 - \beta \cos\theta_0), \tag{3.42}$$

$$\epsilon = \epsilon' \gamma (1 + \beta \cos\theta'), \tag{3.43}$$

where θ_0 and θ is the angles between the direction of motions of photons and electrons before/after the scattering, respectively. The scattering is well approximated as being elastic in the rest frame of electrons, such that $\epsilon_0' \simeq \epsilon$. Thus the energies of the photon before scattering, in the rest frame of the electron, and after scattering are in the ratios of

$$\epsilon_0 : \epsilon_0' : \epsilon \simeq 1 : \gamma : \gamma^2, \tag{3.44}$$

which implies a low-energy photon will be scattered up to higher energy by a factor of order γ^2.
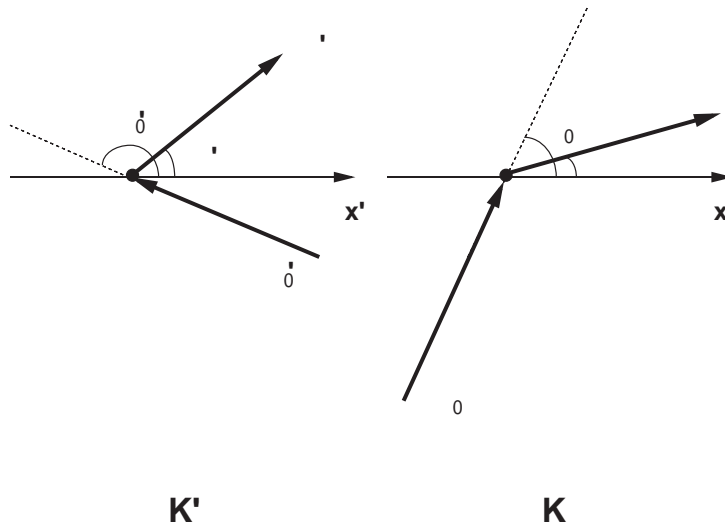
Figure 3.7: Geometries for inverse Compton scattering in the electron rest frame K (left) and the observer's frame K' (right).

Next we derive formulae for the case of an isotropic distributions of photons scattering off an isotropic distributions of electrons. This can be done by averaging equation (3.42) and (3.43) over angles. The total power emitted (scattered) from the electrons is

$$\frac{dE}{dt} = c\sigma_T\gamma^2 \int <(1-\beta\cos\theta)^2> \epsilon_0 n(\epsilon_0)d\epsilon_0 = c\sigma_T\gamma^2(1+\frac{1}{3}\beta^2)U_{\rm ph}, \qquad (3.45)$$

where $n(\epsilon_0)$ is the number density of photons per energy interval and $U_{\rm ph}$ is the soft photon energy density which is calculated from

$$U_{\rm ph} \equiv m_e c^2 \int \epsilon_0 n(\epsilon_0)d\epsilon_0. \qquad (3.46)$$

Thus the net power lost by an electron, subtracting the rate of decrease of the total initial soft photon energy $c\sigma_T U_{\rm ph}$, is

$$\dot{\gamma}_{\rm IC} = \frac{4\sigma_T\gamma^2 U_{\rm ph}}{3m_e c}. \qquad (3.47)$$

By comparing this with equation (3.34), we obtain an well-known relation between the energy loss rate of electrons and energy density of photons/magnetic field as

$$\frac{\dot{\gamma}_{\rm sync}}{\dot{\gamma}_{\rm IC}} = \frac{U_B}{U_{\rm ph}}. \qquad (3.48)$$

Note, however, that this relation only holds when the scattering takes place in the Thomson regime, in which $\gamma\epsilon_0 \ll 1$.

3.4.2   Inverse Compton Spectrum

To derive the inverse Compton spectrum for arbitrary distributions of electrons and soft photons, we introduce the formulae derived by Jones (1968). It is accurate in all soft photon energy ranges for both Thomson and Klein-Nishina regimes, as long as the photon and electron distributions are isotropic, and the electrons are ultra-relativistic ($\gamma \gg 1$). The differential photon production rate by inverse Compton scattering $q(\epsilon)$ is

$$q(\epsilon) = \int d\epsilon_0 n(\epsilon_0) \int d\gamma N(\gamma)C(\epsilon,\gamma,\epsilon_0), \qquad (3.49)$$

where $n(\epsilon_0)$ is the number density of soft photons per energy interval, and $C(\epsilon,\gamma,\epsilon_0)$ is the Compton kernel of Jones (1968)

$$C(\epsilon,\gamma,\epsilon_0) = \frac{2\pi r_e^2 c}{\gamma^2\epsilon_0}[2\kappa ln\kappa + (1+2\kappa)(1-\kappa) + \frac{(4\epsilon_0\gamma\kappa)^2}{2(1+4\epsilon_0\gamma\kappa)}(1-\kappa)], \qquad (3.50)$$

where

$$\kappa = \frac{\epsilon}{4\epsilon_0\gamma(\gamma-\epsilon)}. \qquad (3.51)$$

r_e is the classical electron radius, $r_e \equiv 2.82 \times 10^{-13}$ cm. For a given ϵ_0 and γ, the integration (3.49) can be performed under the range for ϵ

$$\epsilon_0 \leq \epsilon \leq \gamma \frac{4\epsilon_0 \gamma}{1 + 4\epsilon_0 \gamma}, \tag{3.52}$$

from the kinematics of electron-photon scattering.

This production rate $q(\epsilon)$ is converted to emission coefficient $j_\nu^{\rm IC}$ by the relation

$$j_\nu^{\rm IC} = \frac{h\epsilon}{4\pi} q(\epsilon), \tag{3.53}$$

where $h\nu = \epsilon m_e c^2$ and h is the Planck constant.

The energy loss rate per single electron $\dot{\gamma}_{\rm IC}$ in the Klein-Nishina regime is quite uncertain, because electrons do *not* lose their energy continuously, but only by a single encounter with a soft photon. Even in this case, we can estimate the average cooling rate of electrons by considering the energy conservation between electrons and up-scattered photons. From equation (3.49), we find the relation,

$$\dot{\gamma}_{\rm IC} = \int \epsilon d\epsilon \int d\epsilon_0 n(\epsilon_0, t) C(\epsilon, \gamma, \epsilon_0). \tag{3.54}$$

This should coincide with equation (3.47) in the Thomson limit. Figure 3.8 shows the change in the ratio, $\dot{\gamma}_{\rm IC}/\dot{\gamma}_{\rm sync}$, derived from equation (3.34) and (3.54) for various electron Lorentz factors. We assumed the electron population $N(\gamma) \propto \gamma^{-2}$, and changed the $\gamma_{\rm max}$ from 10^4 to 10^6. Note that for $\gamma_{\rm max} \leq 10^4$, this ratio is what is expected from the Thomson limit (i.e., equation (3.48)), but $\dot{\gamma}_{\rm IC}$ is strongly suppressed for larger values of $\gamma_{\rm max}$ ($\gamma_{\rm max} \geq 10^5$).

3.5 Particle Escape and Adiabatic Expansion

We assume 'fresh' electrons are injected continuously in the radiating region, while they can escape from this region after the typical time scale $t_{\rm esc}(\gamma)$. After the escape, electrons no longer radiate. Such a situation is also expected if the energy loss by the adiabatic expansion limits the accumulation of relativistic electrons within the photon emitting region. Since the low energy electrons do *not* cool effectively by both synchrotron and inverse Compton losses, the steady state will be achieved by the balance of the escape and the injection rates. For electrons with higher energies ($\gamma \sim \gamma_{\rm max}$), however, the escape is not important because the life time of electrons by radiative cooling may be much shorter than $t_{\rm esc}(\gamma)$. In general, electrons are randomly moving in the emitting region, so that the typical time scale of $t_{\rm esc}$, as well as its energy dependence are completely unknown. Although somewhat arbitrary, there is a good observational reason to believe that escape,
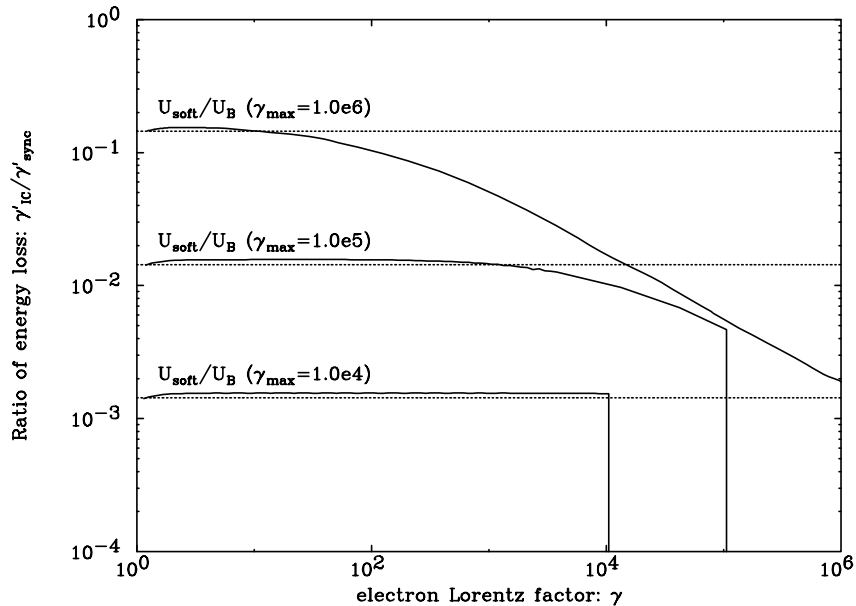
Figure 3.8: Ratio of electron cooling rate by synchrotron/Inverse Compton radiation. We assume $N(\gamma) = N_0\gamma^{-2}$ ($1 < \gamma < \gamma_{\max}$), where we set the normalization, $N_0 = 10.0$. The source radius is assumed to be $R = 10^{16}$ cm and magnetic field is $B = 0.1$ G, typical values for blazar emission. As $\gamma_{\max}$ increased from 10^4 to 10^6, inverse Compton cooling process becomes inefficient due to the reduction of cross section in the Klein-Nishina regime.

or, equivalently, sudden energy loss by adiabatic expansion, should be important (e.g., § 10.2.6). In this thesis, we will assume the most simple case where $t_{\rm esc}$ has no dependence on energy (a constant value). We see in § 10.6.1 that $t_{\rm esc}$ can be estimated from the turn-over frequency in the multi-wavelength spectra of blazars, where the cooling time and escape time of electrons are expected to be balanced.

3.6   Electron Kinetic Equation

In this section, kinetic equation is introduced to study the characteristic variabilities in the electron/photon spectra of blazars. This approach is well known as a leaky box model of the propagation of high energy cosmic-ray electrons in the inter-stellar medium (e.g., Kardashev 1962).

The time evolution of the high-energy electrons in the magnetic field and the photon field is described by the following kinetic equation:

$$\frac{\partial N_e(\gamma,t)}{\partial t} = \frac{\partial}{\partial \gamma}[g(\gamma,t)N_e(\gamma,t)] + Q(\gamma,t) - \frac{N_e(\gamma,t)}{t_{\rm esc}(\gamma)}, \qquad (3.55)$$

where $g(\gamma, t)$ represents the arbitrary types of energy loss and/or gain functions for a single electron. $Q(\gamma, t)$ represents the injection rate of the 'fresh' electrons, and $t_{\mathrm{esc}}(\gamma)$ is the escape time of the electrons.

For example, the loss function of synchrotron cooling process is given in equation (3.34),

$$g_{\mathrm{sync}}(\gamma) = \dot{\gamma}_{\mathrm{sync}} \propto \gamma^2. \tag{3.56}$$

and the loss function for inverse Compton process is that in equation (3.54)

$$g_{\mathrm{IC}}(\gamma, t) = \dot{\gamma}_{\mathrm{IC}}. \tag{3.57}$$

If the scattering takes place in the Thomson regime, the simpler equation (3.47) ($\propto \gamma^2$) would be applied.

The energy gain by the acceleration process is expressed by the acceleration rate $r_{\mathrm{acc}}(\gamma)$, which is defined in equation (3.14)

$$g_{\mathrm{acc}}(\gamma) = r_{\mathrm{acc}}\gamma \propto \gamma^{1-\xi}, \tag{3.58}$$

where ξ is the energy dependence of the diffusion coefficient on energy (see, equation (3.16)).

The general solution of equation (3.55) for arbitrary function $g(\gamma)$ was first given by Makino (1998), yielding

$$N_e = \frac{g(K)}{g(\gamma)}\exp(-\int_0^t \frac{dt'}{t_{\mathrm{esc}}(K')})N_{e0}(K) + \int_0^t \frac{g(K')}{g(\gamma)}\exp(-\int_0^{t-t'} \frac{dt''}{t_{\mathrm{esc}}(K'')})Q(K', t')dt', \tag{3.59}$$

where

$$y \equiv -\int \frac{d\gamma}{g(\gamma)}, \tag{3.60}$$

$$\gamma = \gamma(y), \tag{3.61}$$

$$K \equiv \gamma(t - \int \frac{d\gamma}{g(\gamma)}), \tag{3.62}$$

$$K' \equiv \gamma(t - t' - \int \frac{d\gamma}{g(\gamma)}), \tag{3.63}$$

$$K'' \equiv \gamma(t - t' - t'' - \int \frac{d\gamma}{g(\gamma)}). \tag{3.64}$$

In general, because of the high non-linearity of the processes involved, the numerical approach is necessary, in particular, when the inverse Compton scattering may occur in the Klein-Nishina regime. We will discuss this more in § 11.

3.7   Relativistic Beaming in Blazar Jets

Assume that there is an emission blob which radiates isotropically in the rest frame K'. In the observer's frame K, the blob is moving with relativistic speed $\beta=v/c$ (~1), and the radiation is strongly anisotropic. Three important effects are expected as follows.

3.7.1   Aberration of Light

Simple Lorentz transformation shows that the directions of the velocities of light in the two frames (K, K') are related by the formula,

$$\tan\theta = \frac{\sin\theta'}{\Gamma(\cos\theta' + v/c)}, \tag{3.65}$$

$$\cos\theta = \frac{\cos\theta' + v/c}{1 + (v/c)\cos\theta'}, \tag{3.66}$$

where Γ is the Lorentz factor of the blob and given $\Gamma \equiv [1 - \beta^2]^{-1/2}$. Considering the spatial case of $\theta' = \pi/2$, we obtain

$$\tan\theta = \frac{c}{\Gamma v} \qquad \sin\theta = \frac{1}{\Gamma} \tag{3.67}$$

This means that in the frame K, half of the photons are concentrated in a narrow cone of half angle $\theta\sim1/\Gamma$.

3.7.2   Time Dilation

The emission and arrival time intervals are different. The difference of arrival time Δt_a is expressed by the difference of the emission time Δt_e as

$$\Delta t_a = \Delta t_e(1 - \beta\cos\theta), \tag{3.68}$$

while $\Delta t'_e$ is related with Δt_e

$$\Delta t_e = \Gamma\Delta t'_e, \tag{3.69}$$

leading to

$$\Delta t_a = \Gamma(1 - \beta\cos\theta)\Delta t'_e \equiv \Delta t'_e/\delta. \tag{3.70}$$

This is a convenient derivation of the *beaming factor* δ ($= [\Gamma(1-\beta\cos\theta)]^{-1}$). As we see in Figure 3.9, the beaming factor exceeds unity if viewing angles are small. Note that, when the observer is located perpendicular to the moving direction (i.e., $\theta' = \pi/2$) in the source frame, $\delta \simeq \Gamma$ because $\sin\theta \simeq 1/\Gamma$.

3.7.3 Blue Shift of Frequencies and the Luminosity Enhancement

Since frequencies are the inverse of times, we have a simple relation,

$$\nu = \delta\nu'. \tag{3.71}$$

The specific intensity $I(\nu)$ divided by the cube of the frequency is Lorentz invariant (e.g., Rybicki & Lightman 1979). Thus we have

$$I(\nu) = \delta^3 I'(\nu') = \delta^3 I'(\nu/\delta). \tag{3.72}$$

Integration of $I(\nu)$ over the frequencies yields

$$I \equiv \int I(\nu)d\nu = \delta^4 \int I'(\nu')d\nu' = \delta^4 I'. \tag{3.73}$$

Assuming isotropy of the emission, the corresponding transformation for luminosity is

$$L_{\mathrm{obs}} = \delta^4 L'_{\mathrm{src}}. \tag{3.74}$$

Because of this factor δ^4, blazars, whose jet emissions are pointing closely to the observer, are strongly enhanced in brightness.
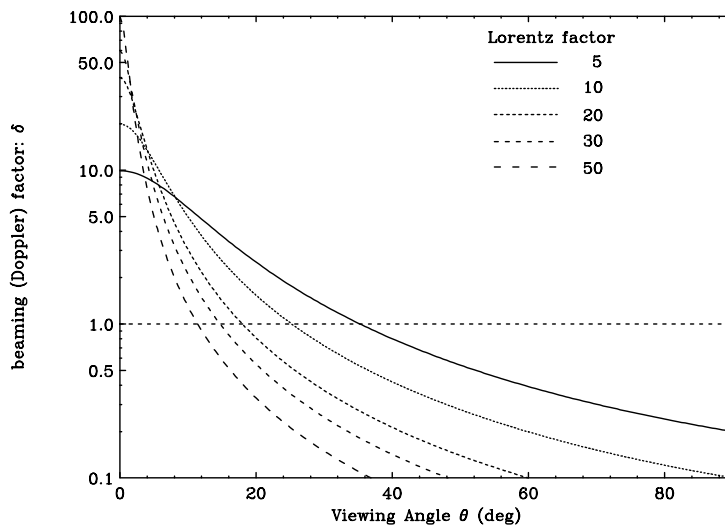
Figure 3.9: Beaming (Doppler) boosting factor δ as a function of viewing angle θ. Results for Lorentz factor, $\Gamma = 5$, 10, 20, 30 and 50 are shown respectively. Note that $\delta = 2\Gamma$ for $\theta = 0$, and $\delta = \Gamma$ for $\theta = 1/\Gamma$.

Chapter 4

Instruments on-board *ASCA*

4.1 *ASCA* Satellite

ASCA (Advanced Satellite for Cosmology and Astrophysics) satellite (Tanaka et al. 1994) is the fifteenth scientific satellite of Institute of Space and Astronautical Science (ISAS). *ASCA* is the fourth Japanese X-ray observatory succeeding *HAKUCHOU*, *TEMMA*, and *GINGA* satellites. It was launched by the M-3SII rocket on February 20, 1993 (JST) from Kagoshima Space Center (KSC) in Kagoshima, Japan. *ASCA* orbits on a nearly circular orbit with its height about 520 km at its perigee and about 620 km at its apogee. It weighs about 420 kg and the length of an extensible optical bench (EOB) is about 4.7 m. Figure 4.1 shows a schematic view of *ASCA* satellite in orbit.

Figure 4.1: Schematic drawing of *ASCA* satellite.

ASCA features imaging and spectroscopic capabilities with a large effective area and the highest energy resolution ever achieved in a wide energy band, which ranges from

0.5 keV to 10 keV. It carries four X-ray telescope (XRT), equipped with two X-ray CCD cameras (Solid state Imaging Spectrometer; SIS) and two gas scintillation imaging proportional counters (Gas Imaging Spectrometer; GIS) at their focal plane. The arrangement of these instruments is shown in Figure 4.2. These two types of detectors have complementary properties; the SIS has finer position and better energy resolution than GIS, while the GIS has faster time resolution and wider dynamic range in source intensity. We briefly describe the XRT, SIS, and GIS in the following sections.

Figure 4.2: Arrangement of instruments on *ASCA* satellite.

4.2   XRT

The *ASCA* XRT(X-ray telescope) consists of a large number of conical thin-foil reflectors to fill its aperture nested with their surface seen almost edge-on (Figure 4.2). It aims to achieve a large effective area and high throughput over a broad energy band up to 10 keV. Four XRT's on-board *ASCA* satellite are placed at the top of EOB. They were produced cooperatively by Nagoya University, NASA Goddard Space Flight Center (NASA/GSFC), and Institute of Space and Astronautical Science (ISAS).

X-rays from celestial sources are reflected by XRT only when its incident angle is smaller than the critical angle of 1°. To achieve a large effective area, over a hundred nested thin foils are used for *ASCA* XRT. Since it is difficult to shape a thin foil into a paraboloid and a hyperboloid, a conical surface is used as an approximation. Although this approximation reduces the image quality, the roughness of the reflectors' surface mainly contributes to the point spread function, whose half power diameter of 3 arc-minutes. Design parameters and performance of XRT are shown in Table 4.1.

Table 4.1: Design parameters and performance of *ASCA* XRT

Mirror substrate	127μm
Mirror surface	Acrylic lacquer 10μm + Au (500 øA)
Mirror length	100mm
Number of mirrors	120 foils
Inner (outer) diameter	120 (345) mm
Focal length	3500 mm
Incident angle	$0.24° \sim 0.7°$
Total weight[a]	~ 40 kg
Geometrical area	558 cm^2/telescope
Field of view	24 arcmin. (FWHM @ 1 keV)
	16 arcmin. (FWHM @ 1 keV)
Energy range	≤ 10 keV
Effective area[a] (4 XRTs)	~ 1300cm^2 (1 keV)
	~ 600cm^2 (7 keV)
Half power diameter	~ 3 arcmin.

4.3 SIS

The *ASCA* SIS is an X-ray sensitive CCD camera, and features high energy resolution and fine positional resolution. The details of the design and In-orbit performance is given in Burke et al. (1991) and Yamashita et al. (1997). Two SIS detectors (hereafter SIS0 and SIS1) are placed in the focal planes of two of the four XRT's. They were developed by the Massachusetts Institute of Technology (MIT), Osaka University, and Institute of Space and Astronautical Science (ISAS).

4.3.1 System Description

The SIS consists of four X-ray CCDs (Charge Coupled Device), analog electronics (SIS-AE), and digital electronics (SIS-DE). As shown in Figure 4.3, the four CCD chips are aligned in a square with narrow gaps. Each CCD chip has 422 × 420 pixels. The dimensions of the CCD chip are 11mm × 11mm which covers 11' × 11' in the sky. Design parameters and performance of SIS are summarized in Table 4.2.

The SIS is a frame transfer type CCD, whose detection part is made of an Si p-n junctions. An insulator layer made of SiO$_2$ is attached on the front surface of the n-type Si. The electrodes are built on both the front and the back of the device. By supplying specific patterns of voltages on the electrodes, charges in a pixel are transfered from one pixel to the next. A depletion layer is developed in the device by supplying a bias voltage

Figure 4.3: Alignment of the four CCD chips in SIS.

Table 4.2: Design parameters and performance of *ASCA* SIS

Irradiation Method	Front irradiation
Charge Transfer Method	Frame Transfer
Clock	3-phase drive
Number of pixels in Image Region	420 pixels × 422 lines per chip
Pixel Size	27 μm
Area	11×11 mm^2 per chip
Field of View	11×11 square arc minutes per chip
Thickness of Depletion Layer	$\sim 40\mu$m
Drive temperature	$\sim -62°$C
Energy Band	0.4-12 keV
Quantum Efficiency	80% at 6 keV
Energy Resolution	2% at 5.9 keV (FWHM)

between the electrodes on the front and on the back. The CCD chips are cooled down to $-62°$C with a thermo-electric cooler (TEC) from the back to reduce the thermal noise.

Two SIS-AE's are on-board corresponding to SIS0 and SIS1 respectively. Electric signals from SIS are fed into SIS-AE and their pulse heights are converted into digital signals with analog-to-digital converters (ADC). SIS-AE also generates driving clocks for the CCD chips and monitors and controls the temperature of the CCD chips. SIS-DE picks up X-ray events in the digital signals from SIS-AE with two digital signal processors (DSP) and sends them to a data processor (DP).

4.3.2 On-Board Data Processing

The observation modes are designed for scientific observations and consists of *faint* mode, *bright* mode, and *fast* mode. In the observation modes, the data are processed every four seconds independent of the bit rate (High/Medium/Low). The order of reading of the CCD chips can be changed in accordance with the aim of observation (CCD mode). Three CCD modes are designed for standard observations: 1-CCD mode, 2-CCD mode, and 4-CCD mode. The number preceding "CCD" in mode name is the number of chips to be read out.

In *faint* mode and *bright* mode X-ray images and spectra are simultaneously obtained with poor time resolution of 4 sec at most. Information on detected X-rays is acquired almost in the same way in both modes, except that the information is compressed in *bright* mode. 1-, 2-, and 4-CCD modes are available in faint and *bright* modes.

In the *bright mode* DP classifies an event by assigning a "grade". The grade ranges from 0 to 7 depending on the pattern of the pixel levels of neighboring pixels whose pixel levels exceed a split threshold. Definitions of grades are shown in Figure 4.4. DP also sums pixel levels which exceed the split threshold and are not of detached corner pixels, and compresses the summed pixel level with 12 bits length into 11 bit data.

In Table 4.3 operation mode of SIS are summarized. Most of the observations in this thesis were performed in normal 1-CCD *faint* mode for bit-High and normal 1-CCD *bright* mode for bit-Medium (§ 6.1). The telemetry limit is 64 cts/s/SIS for the former, while 32 cts/s/SIS for the latter. During the observation of Mrk 421 in 1998, SIS count rate exceeds this telemetry limit thus we perform careful data reduction to eliminate the effect of telemetry saturation (see, § 7.1.1).

Table 4.3: Summary of observation modes in SIS

	Faint	Bright	Fast
Time Resolution	4/8/16 sec	4/8/16 sec	16 ms
	(1/2/4CCD mode)		(1CCD mode)
Event Trans. Rate	128/16/4	512/64/16	1024/128/32
(cts/sec/2 sensors)	(High/Medium/Low bit rate)		
Data size per event	128 bits	32 bits	16 bits
CCD ID	2 bits	—	—
Pixel level	12 bits $\times 9$	11 bits	11 bits
Event position	9 bits $\times 2$	9 bits $\times 2$	1 bit
Time stamp	—	—	3 bits
Grade	—	3 bits	1 bits

Figure 4.4: Definitions of grades of events.

4.3.3 Reduction of the SIS data

Hot and Flickering Pixels

A pixel creating events but *no* incident particle is called a "hot pixel" or a "flickering pixel". These erroneous pixels are mainly due to a large dark current, caused by lattice defects on the insulator layer under electrodes of the CCD. Assuming the Poisson distribution, we regarded a pixel, whose number of events largely exceeds the average among surrounding pixels, as a flickering pixel. In a standard analysis the average is calculated from 5×5 pixels centering a pixel of interest. The threshold probability is set to $10^{-5.25}$, which corresponds to a probability that one out of all the pixels in a chip (422×420 pixels in total) exceeds the threshold by chance, namely, $1/(420 \times 422)$.

Echo

A pixel level suffers an artificial increase by an "echo" phenomenon, which originates from a transitional property of SIS-AE. In SIS-AE an analog signal from the CCD leaves an extra signal after the main signal as a result of a "ringing" effect. A significant pulse height remains even at a time when the signal from a next pixel is processed.

In the analysis, the *faint* mode data can be corrected to remove the echo phenomenon by subtracting pixel levels of the center pixel from that of right-hand pixels by the echo fraction for an observation period. In *bright* mode data, however, only summed pixel levels are obtained so that no correction to the data can be performed. In this case one should use a better subtraction technique of the echo phenomenon thorough calculating the response matrix.

Dark Frame Error (DFE)

A dark frame error (hereafter DFE) is a residual dark level causing pixel levels to be shifted by a constant amount, depending on the SIS condition during the observation. The DFE arises from incomplete estimation of dark levels in calculating pixel levels in SIS-DE. The dark level is calculated as an average of raw PH data which distributes asymmetrically around the true dark level.

The DFE is mainly due to light input in an optical band. The distribution of pixel levels at corner pixels are accumulated for each short time interval, each 64 sec usually, and compared with a template by cross-correlating them. This estimation is repeated throughout an observation period, and the time history of DFE values are obtained. For *faint* mode data the estimated DFE are subtracted from pixel levels of all the pixels sent to the ground. Since no DFE correction can be made for *bright* and *fast* mode data,

the effect of DFE on a spectral analysis are eliminated by using an appropriate response matrix.

Charge Transfer Inefficiency (CTI)

Charge transfer inefficiency (CTI) is defined as the probability that an electron in a charge cloud is not transfered from one pixel to the next. The CTI is caused by charge traps by lattice defects in channels of electrons in the CCD chips. Since such lattice defects are created by charged particles in orbit, CTI increases gradually.

CTI can be corrected, except for *fast* mode data. The method of the correction is straightforward – reading a CTI table to obtain CTI at an observation period, calculating a reduction factor of energy scale for each event by multiplying CTI by the number of transfers of electrons of the event, and dividing the pixel level of the event by the reduction factor.

4.4   GIS

ASCA GIS is a gas scintillation imaging proportional counter. It features high time resolution and high detection efficiency for hard X-ray photons. The detail description on the detector design and pre-flight calibrations are given in Ohashi et al. (1996). Two GISs (hereafter GIS2 and GIS3) are on-board the *ASCA* satellite and placed on focal planes of another two of the four XRT's. They were produced by University of Tokyo and Institute of Space and Astronautical Science (ISAS).

4.4.1   System Description

GIS consists of a gas cell, a position sensitive photo-multiplier (Imaging Photo-Multiplier Tube; IPMT), a high voltage unit, a housing, and electronics (GIS-E).

The gas cell has a cylindrical shape with $\sim$ 60mm diameter and $\sim$ 25mm height. A schematic view of the cross section of a gas cell and a position sensitive photo-multiplier tube of GIS are shown in Figure 4.5. The field of view of GIS is circular with 50' diameter in the sky. Xe gas (96%) and He gas (4%) are filled in the gas cell. In front of the gas cell, a plasma shield is placed to protect GIS from radiation damage. The gas cell is divided into two regions: a drift region and a scintillation region. IPMT is attached below the gas cell as shown in Figure 4.5. These cells are optically connected with each other through a quartz window at the bottom of the gas cell and a bialkali photo-electrode at the top of IPMT. Design parameters and performance of GIS are summarized in Table 4.4.

Figure 4.5: Cross sectional view of a gas cell and a position sensitive photo-multiplier tube of GIS. The voltage of each part of the detector supplied by a high voltage unit is shown at the right of the figure for reference. A schematic drawing of an X-ray detection is also shown.

Table 4.4: Design parameters and performance of GIS

Energy Band	0.7-15 keV
Energy Resolution	8% at 5.9 keV (FWHM)
Effective Area	50 mm diameter
Positional Resolution	0.5 mm (FWHM)
Time Resolution	$\sim$ 61 μsec (Minimum in PH mode)
	1.95 ms (Minimum in MPC mode)

The high voltage unit supplies appropriate voltages to the gas cell and IPMT as shown at the right in Figure 4.5. A bleeder is placed below IPMT and supplies voltages to a dynode and to the anodes of IPMT by dividing a high voltage from the high voltage unit. At the end of GIS2, a radiation belt monitor (RBM) is attached to monitor the flux of charged particles.

One GIS-E is on-board the satellite and processes signals from GIS2 and GIS3. GIS-E converts analog signals from two GIS's into digital signals with two 12 bits ADC and

four 8 bits flash ADC. The CPU in GIS-E collects and edits this information and sends it through a FIFO (First-In First-Out logic) to the DP of the satellite, which commonly edits SIS data and GIS data into a telemetry format. GIS-E also supplies power to two GIS's and RBM, controls the high voltage unit and the preamplifier to operate GIS, and handles the RBM flag to prevent the detectors from radiation damage.

4.4.2   On-Board Data Processing

The observation modes are designed for scientific observations and consists of PH normal mode (PH mode in short), PH $PCAL$ mode ($PCAL$ mode in short), and MPC mode. In the PH mode, X-ray images and spectra are both obtained with high time resolution up to $61\mu s$.

Arrival times of X-rays are measured with scalers, which count the system clock of the satellite. The frequency of the system clock depends on the bit rate: it is 16384 Hz for high bit rate, 2048 Hz for medium bit rate, and 512 Hz for low bit rate. Table 4.5 shows the clock speed relating to time assignment of GIS(2+3) with maximum counting rates observable with GIS. We find that for the high bit rate, telemetry limit is 128 cts/s/GIS while 16 cts/s/GIS for the medium bit rate. For Mrk 421 observation in 1998, the source was very bright and the telemetry was strongly saturated when the data was taken at medium bit-rate (§ 7.1.1). For the data taken at bit-High rate, dead-time of the detector is about 3 % for a bright source of 30 cts/s/GIS (Makishima et al. 1996).

Table 4.5: Clock speed relating to time assignment of GISs

| Bit Rate | Time stamp | | Telemetry output | | Maximum |
	Frequency	Period	Frequency	Period	Counting Rate
High	16384 Hz	~ 61 μs	256 Hz	~ 4 ms	256 c/s
Med	2048 Hz	~ 488 μs	32 Hz	31.25 ms	32 c/s
Low	512 Hz	~ 1.95 ms	4 Hz	125 ms	8 c/s

4.4.3   Reduction of the GIS data

Gain Correction

The gain of GIS mainly depends on the temperature of the gas cell and the position at which an X-ray is detected. The temperature dependence is due to characteristics of Xe gas in the gas cell. The positional dependence is caused by the positional dependence of the sensitivity of IPMT. On the surfaces of both GIS2 and GIS3, radioactive isotopes

^{55}Fe are mounted near the rim of their apertures. ^{55}Fe emits fluorescent X-rays of energy 5.895 keV. This X-ray line is used to measure the instantaneous gain number of GIS. The imaging capability of GIS enables us to extract only events from the isotopes and events from the isotopes do not contaminate X-rays from celestial sources.

The gain correction for GIS events is divided into two steps. First, a pulse height of an event is corrected taking the gain map into account. After this correction the corrected gain number should be constant over the surface of the detector. Second, the resultant pulse height is further corrected so that the X-rays from ^{55}Fe has a constant value. This cancels the temperature dependence of the gain number and the corrected pulse height is independent of the observation conditions, called a pulse height invariant (PI). According to pre-flight and in-flight calibrations, the uncertainty in the GIS gain is known to be 1%.

Background Rejection

Over 90% of background events can be rejected by means of evaluating a pulse height, a rise time, and the spread of the event. Sources of GIS background events are divided into two types.(a) X-rays absorbed at abnormal positions in the gas cell and (b) charged particles or high energy γ-rays. Only events with rise times between 159 and 218 (rise time window) are collected in the on-board data processing and are sent to the ground station. 92% of background events are rejected by filtering events with a narrower rise time window in the data analyses. Different rise time windows are set for events with different pulse heights. A table of rise time windows for various pulse heights is called an "RT mask". The spread discrimination rejects 60% of background events not rejected by the rise time discrimination. Only events in a certain range of spread patterns are collected in the on-board data processing and are sent to the ground station.

4.5 Alignment of the Detectors

The optical axes of the four XRT's point to slightly different positions on the sky. Also, the centers of the two SIS's and two GIS's correspond to different positions on the sky. This gives different effective areas to different detectors. The relations between these positions are measured by the *ASCA* calibration team and are used to evaluate the detector's response in analyses. The alignment of each detector is shown in Figure 4.6. The positions of the optical axes and detector centers in reference to the center of SIS0 are projected on the focal plane in the figure. The figure also shows "nominal positions" for various observation modes, where an image of the target of an observation is planned to be placed. In 1-CCD mode, for example, the satellite's attitude is controlled so that an image of the

target centers on the 1-CCD nominal position on the detectors.

Figure 4.6: Alignment of the detectors. The optical axes and detector centers of SIS0, SIS1, GIS2, and GIS3 are shown. Nominal positions for various observation modes are also plotted in the figure.

Chapter 5

Instruments on-board *RXTE*

Since our main goal is to understand variability and spectral behaviour of all TeV blazars, we need X-ray data taken at various states of source activity. For this purpose, we conducted several *RXTE* (Rossi X-ray Timing Explorer) observations as a guest observer. We also analyzed the archival data taken from 1996 April to 1998 January, to have more complete sample. We mainly analyze PCA data in $2.5-20$ keV range where the detector is well calibrated and the best noise-to-signal ratio is obtained.

5.1   *RXTE* Satellite

RXTE is a X-ray mission which was launched on December 30, 1995. The spacecraft was designed and built by the Goddard Space Flight Center (GSFC). It was launched by a Delta II rocket that put *RXTE* into a low-earth circular orbit whose apogee and perigee are 580 and 560 km, corresponding to an orbital period of about 90 minutes, at an inclination of 23 degrees.

RXTE carries two pointed instruments, the Proportional Counter Array (PCA) developed by GSFC and the High Energy X-ray Timing Experiment (HEXTE) developed by University of California at San Diego (UCSD). PCA covers the lower part of the energy range ($2 - 60$ keV), while the HEXTE covers a higher energy range, from 20 keV to more than 100 keV. These instruments are equipped with collimators yielding an angular resolution of 1 degree. In addition, *RXTE* carries an All-Sky monitor (ASM) from Massachusetts Institute of Technology (MIT), that scans about 80 % of the sky on every orbit. ASM allows constant monitoring of the sky at time scales of 90 minutes or longer. Figure 5.1 shows a schematic view of *RXTE* satellite in orbit.

RXTE is designed to facilitate the study of time variability in the emission of celestial X-ray sources with moderate spectral resolution. Time scales from microseconds to
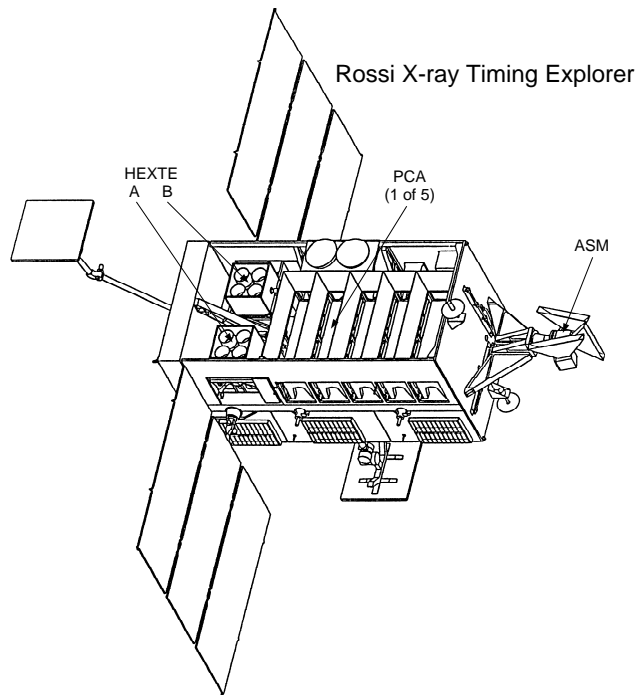
Figure 5.1: Schematic drawing of *RXTE* satellite. Three kinds of instruments, PCA, HEXTE and ASM are carried on the spacecraft.

months are covered in an instantaneous spectral range from 2 to 100 keV. It is designed for a required lifetime of two years, with a goal of five years.

5.2   PCA

5.2.1   System Description

The *RXTE* PCA (Proportional Counter Array) consists of five large proportional counters (PCUs) with anti-coincidence (hereafter "veto") features which provide a very low background. A mechanical hexagonal collimator is carried on each proportional counter, which provides an angular resolution of 1 degree (FWHM). Because of the large effective area, sources as faint as 1 mCrab can be detected only in a few seconds. The detailed description on the PCA design, as well as the orbit performances are given in Jahoda et al. (1996; 1999).

The total area of 5 PCUs is 6250 cm^2. The schematic view of an assembly of five units and each proportional counter are given in Figure 5.2. We summarize the design parameters and performance of PCA in Table 5.1. The PCA is effective over the energy

range $2 - 60$ keV with 18 % energy resolution at 6 keV. PCA units are filled with Xe gas and achieve low background through efficient veto schemes including side and rear chambers and a propane top layer.

The 1 degree FOV (FWHM) of the tubular (hexagonal) collimations yields a source confusion limit at ~ 0.1 mCrab. The Crab nebula will yield 8700 cts/s ($2 - 10$ keV) and 1200 cts/s (10 - 30 keV) in the PCA. The background in these two bands are 20 and 24 cts/s, respectively. With these backgrounds, an AGN source of intensity 1.3 mCrab and energy index 0.7 will be detected at ≥ 2 σ in only 1 sec at $2 - 10$ keV and at 3 σ in 10 sec at $10 - 30$ keV. Monitored veto rates will provide a measure of the background to at least 10 % of its value.
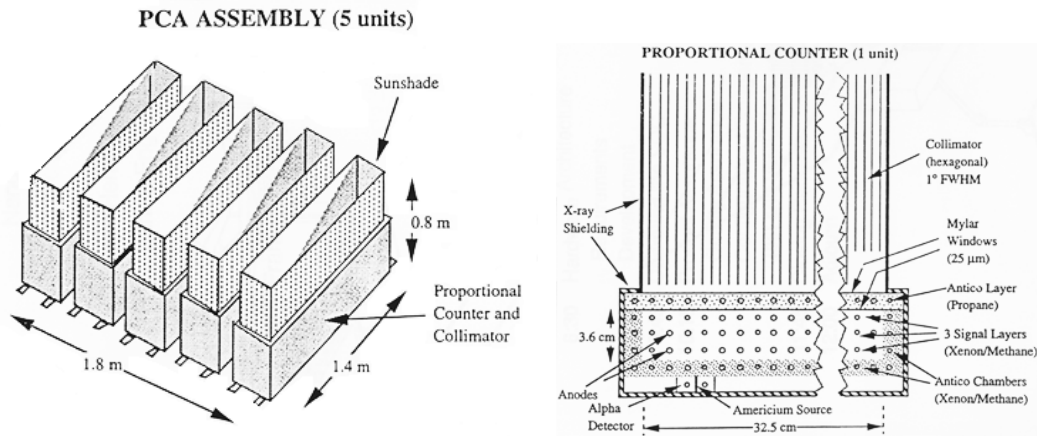
Figure 5.2: $left$: Assembly of 5 PCA counters with total area of 6250 cm^2. $right$: Schematic view of one PCA unit.

Table 5.1: Design parameters and performance of $RXTE$ PCA

Energy Band	$2 - 60$ keV
Energy Resolution	$\leq 18\%$ at 6 keV (FWHM)
Time Resolution	1 μ sec
Angular Resolution	1 degree (FWHM)
Detectors	5 proportional counters
Collecting Area	6500 cm^2
Net Area	3000 cm^2 (at 3 keV) and 6000 cm^2 (at 10 keV)
Layers	1 Propane veto, 3 Xe, 1 Xe veto layer
Sensitivity	0.1 mCrab ($2 - 10$ keV in minutes)
Background	2 mCrab
Telemetry	18 kb/s

5.2.2   On-Board Data Processing

The system will process count rates from the PCA up to 5×10^5 cts/s (only 6 % deadtime for the Crab) and will be able to determine photon arrival time with an accuracy of $\sim 1 \ \mu$sec. The PCA data stream can be binned and telemetered in 6 different modes simultaneously by 6 independent Event Analyzers (EA) which operate in parallel, each analyzing the total PCA data stream. Two other EAs will process the ASM data and control its rotation.

Two of the 6 PCA EAs are intended to be reserved for two standard PCA modes with timing and spectral parameters that will remain unchanged throughout the mission to provide a uniform mission data bank. For the remaining 4 PCA EAs, however, processing modes are flexibly selected by guest observers to accommodate the scientific requirements. The standard modes consists of *Standard*-1 and *Standard*-2. *Standard*-1 contains 8 rates sampled at 0.125 sec; the total good event rate from each individual counter, propane event rates summed over the PCA, and the rate of oll other events. *Standard*-1 also contains calibration spectra which are stored and telemeterd separately for each detector and each layer once every 128 seconds. *Standard*-2 contains 129 channel pulse height spectra for each signal layer of each detector, 33 channel propane layer spectra for each detector, and 29 rates of various combinations of combinations of coincidences for each detector read out every 16 seconds.

5.2.3   Reduction of PCA data

Energy Response

As we have seen in Figure 5.2, each PCU detector, from the top, consists of a thermal shield, a collimator, an aluminized mylar window, a propane volumes, and a detector body. The low energy threshold of the PCA is determined by the transmission of the mylar windows (1 mm each) and the propane volume. For generating the response matrix, the important quantity is the photo-electric stopping power of each layer and all exterior layers.

The gain of the counter is monitored continuously with an ^{241}Am radioactive source for which detection of the α particle identifies the calibration X-rays. Additional information about the energy scale has been obtained from measurements of the iron line in the super nova remnant Cassiopeia A, and the Xe-L escape peak which is collected in a special mode that keeps all events with a calibration flag.

PCA response matrices map 900 energies from 0.023 to 100 keV to 256 PHA channels. Half of the energy channels are equally spaced below 10 keV, except that the three channels

which include one of the Xe-L edges are split into two channels with channel boundary matching the atomic edge. The remaining channels are also equally divided except that the channel including the Xe-K edge is again split into two channels.

Background

The detector background mainly consists of two components – the diffuse sky background which enters through the collimator as X-rays, and the internal background which arises from interactions between radiation or particles in orbital environment with the detector or spacecraft. Since PCA does *not* produce continuous measurements of the background, it relies on a model background.

Figure 5.3 shows the total background summed over all 5 PCU detectors during the observation of Mrk 501 in 1998 May (§ 8). The upper line includes photon counts from the source, for comparison. Line features are present due to Xe-L escape photons, copper fluorescence (primarily from the backplane, and concentrated in the third layer), unflagged calibration events, and a contribution which appears to come from residual activity in the collimator. The background typically varies between $18-24$ cts/s/PCU. In practice, the most significant contributions to the background are dependent on the local particle environment of the satellite and the recent history of passage through SAA ; the presence of background components after passage through the SAA indicates that some of the detector or spacecraft becomes activated.
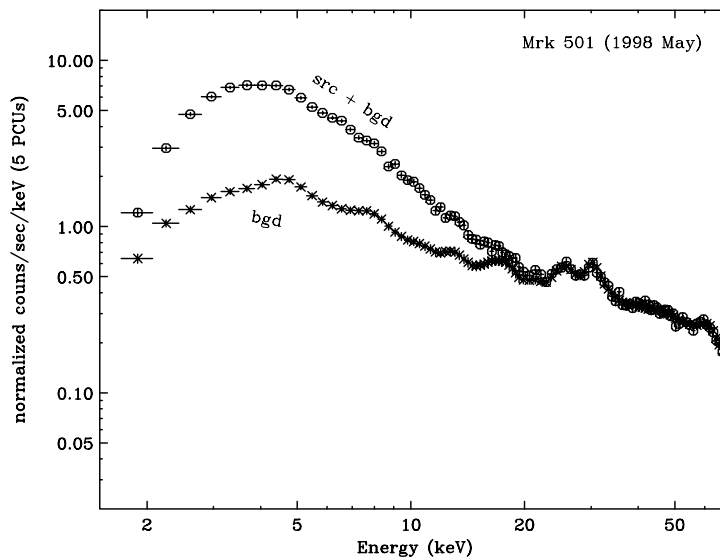
Figure 5.3: The PCA background versus source photon counts from Mrk 501 (from 1998 May observation). The count rate of 5 PCUs are summed.

To model the background, it is assumed that the internal background varies on a time scale which is long compared to the natural time-scale of the PCA *Standard*-2 data (16 sec). The design is such that the model can be evaluated once every 16 seconds, and that the equivalent of a *Standard*-2 data file can be created with separate information for each detector and each anode chain.

The modeled background spectrum can be based on parameters measured at the time of the observation, parameters describing the condition and position of the spacecraft, and parameters describing the evolution of the spacecraft. PCA background models based on these parameters have been constructed in two ways: using data from blank-sky observations and using data from periods of Earth occultation. The models based on the local particle parameters are constructed using data from only those spacecraft orbits in which the SAA-induced activation is small. Some of these data are still significantly contaminated by SAA-induced activation but this contamination can be later removed by an appropriately constructed model of the activation component of the background.

Electron Contamination

The background models are parameterized in terms of particle rate. In addition to the high energy protons and ions, low energy electrons may also lose their energy within the detector. Electrons with several 10s of keV may come through the collimator and stop in the first Xe layer. The rate of propane plus first layer coincidences measures such a population, and while these events are vetoed, the rate can be used to screen periods when there could be increased background, for instance due to the same electrons fluorescing the collimator. For the reliable data reduction, we screen the data when the electron rate is significantly high.

5.3 HEXTE

The HEXTE (High Energy X-ray Timing Experiment) features a large area and low background with a 1 degree field of view coaligned with the PCA field of view. Eight "Phoswich(NaI+CsI)" detectors are arranged in two clusters, each of which rocks on and off the source. This and automatic gain control for each of the eight detectors together yield a well determined background which permits the spectral measurements of a faint source (1 mCrab) at 100 keV in about 1 day. We summarize the design parameters and performance of HEXTE in Table 5.2.

In this thesis, however, we do not use HEXTE data for several reasons. Firstly, a lot of calibration problems still remain and make the analysis results quite uncertain. Secondly,

the typical exposure for *RXTE* observation ($\sim$ 1 ksec) was too short to yield the hard X-ray spectrum at > 20 keV. Thirdly, X-ray spectra of TeV blazars evolve significantly during the observation. Hence we cannot sum over the photons obtained in different epochs. To see this more clearly, one example of the HEXTE spectrum derived from 60 ksec integration of data is given in Figure F.1.

Table 5.2: Design parameters and performance of *RXTE* HEXTE

Energy Band	20 - 200 keV
Energy Resolution	$\leq$ 18% at 60 keV (FWHM)
Time Resolution	10 μ sec
Angular Resolution	1 degree (FWHM)
Detectors	2 clusters of NaI(Tl) and CsI(Na) phoswich units (4)
Collecting Area	1600 cm^2
Net Area	1200 cm^2 (at 50 keV) and 300 cm^2 (at 200 keV)
Sensitivity	1 mCrab (90-110 keV; 3 σ for 10^5 sec pointing)
Background	100 mCrab
Telemetry	5 kb/s

5.4   ASM

The ASM (All Sky Monitor) is the watchdog that alerts XTE to flares and changes of state in X-ray sources. It consists of three rotating Scanning Shadow Cameras (SSC) that can scan about 80 % of the sky in 90 minutes. The camera is sensitive to $2-10$ keV X-rays and have three energy channels. The cameras provide measurements of intensities of about 75 known celestial sources in a day and can measure the position of a previously unknown source with a precision of about 3'.

5.4.1   System Description

The ASM consists of three Scanning Shadow Cameras (SSC) on one rotating boom with a total net effective area of 90 cm^2 (180 cm^2 without masks). Figure 5.4 shows schematic view of the assembly of shadow cameras and their scan directions. The design parameters and performance of ASM are summarized in Table 5.3.

Each SSC is a one-dimensional "Dicke camera" consisting of a 1-dimensional mask and a 1-dimensional position-sensitive proportional counter (Figure 5.4). Because of the mask ('slit') above the proportional counter, the X-rays coming from different directions

should make different images on anodes, which is the principle of the Shadow Camera. The gross field of view of a single SSC is 6° × 90° FWHM, and the angular resolution in the narrow (imaging) direction is 0.2 degree.

A motorized drive will rotate the three SSCs from field to field in 6° steps. At each resting position, a ∼ 100 sec exposure of the X-ray sky will be made; a complete rotation is thus completed in 90 minutes. Since the 'crossed-field detectors' are stepped by only the 6° FWHM angle, each source is viewed twice. In this manner, each source gives rise to the entire mask pattern in the accumulated data, thus minimizing aliasing and side bands in the deconvolved results. During each rotation, ∼ 80 % of the sky will be surveyed to a depth of ∼ 20 mCrab (about 50 sources). Frequent spacecraft maneuvers will make it likely that 100 % of the sky is surveyed each day. In one day, the limiting sensitivity becomes ≤ 10 mCrab (∼ 75 sources).
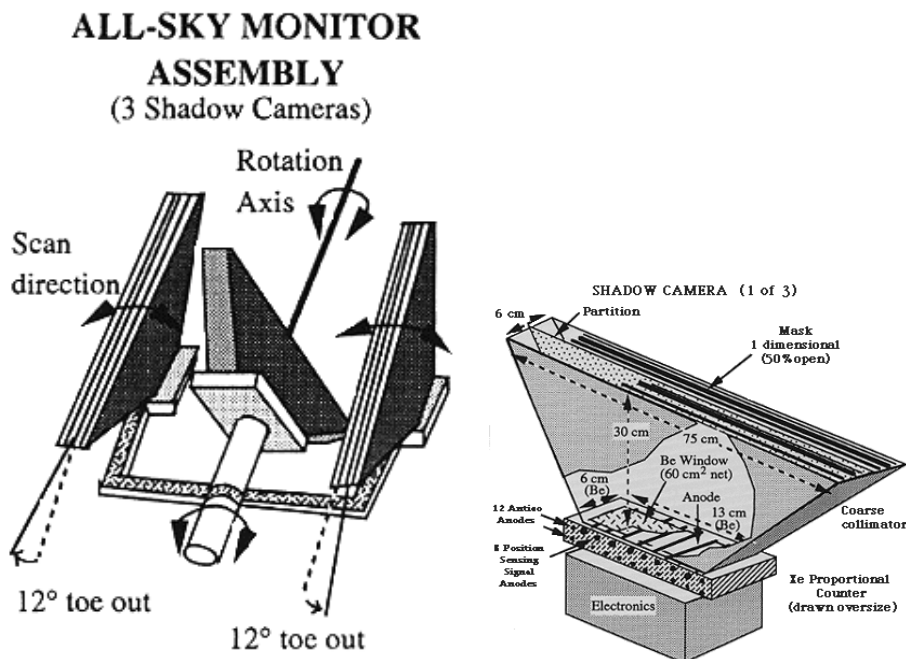
Figure 5.4: *left* : All-Sky Monitor assembly of 3 Shadow Cameras. ASM scans 80 % of the sky every 90 minutes to monitor the intensity of the brightest 75 X-ray sources and to provide an alert if a source changes state or brightness suddenly. This allows the spacecraft to be maneuvered to observe with more powerful PCA/HEXTE systems. *right* : Shadow Camera (1 of 3) of All Sky Monitor. Each SSC is a sealed proportional counter filled to 1.2 atm with $Xe-CO_2$, and sensitive depth of 13 mm.

Table 5.3: Design parameters and performance of *RXTE* ASM

Energy Band	$2 - 10$ keV
Energy Resolution	$\sim$20% in $2 - 10$ keV (3 energy channels)
Scan Time	90 min: 80 % of the sky per orbit
Angular Resolution	0.2 degree
Positional Resolution	3' $\times$ 15'
Detectors	3 Scanning Shadow Cameras
Collecting Area	180 cm^2 (without masks)
Net Area	90 cm^2 (3 detectors)
Sensitivity	20 mCrab in 90min; $\leq$ 10 mCrab in a day
Telemetry	3 kb/s

5.4.2 Reduction of ASM data

The position histograms are analyzed in near-real time in the Science Operations Facility at GSFC. The data is first fit with the model responses of each SSC to the catalogued bright X-ray sources within the field of view. A linear least squares calculation yields the strengths of each of these sources. Next, the fit residuals are examined via a cross-correlation technique for evidence of previously unknown or unexpectedly bright sources. When a new source is found, its coordinates are entered into the source catalogue. For quick-look analysis, the data will be performed on a dwell-by-dwell and SSC-by-SSC basis. For the definitive analysis, the analysis will be performed simultaneously on data from neighboring dwells and from multiple cameras. The resultant ASM light curves are open to public and one can obtain the data via online service for 75 sources (http://space.mit.edu/XTE/asmlc/ASM.html).

Chapter 6

Observation

6.1   X-ray Observations with *ASCA*

We analyzed data from 37 *ASCA* observations of four TeV blazars as listed in Table 6.1. The total net exposure amounts to 540 ksec for Mrk 421, 100 ksec for Mrk 501, 210 ksec for PKS 2155−304, and 60 ksec for 1ES 2344+514. The observational log for *ASCA* observations are shown in Table 6.2−6.5. Observation epoch of four TeV blazars are schematically shown in Figure 6.1.

The data we analyzed in this thesis consists of the data taken according to our proposal, and the data taken during the Performance Verification (PV) phase. For all observations, the SIS was operated in the *faint* mode for bit-High and *bright* mode for bit-Medium (see also § 4). In all observations, except for those taken in the PV phase, source positions were placed in the nominal position of 1-CCD mode at chip 1 and chip 3 of SIS0 and SIS1, respectively (Figure 4.6). The GIS was operated in *PH* mode with standard bit assignment for all observations. For the observations in the PV phase (1993), the SIS was operated in 4-CCD mode, and the GIS was operated in *PH* mode.

Most of *ASCA* observations listed in Table 6.2−6.5 are conducted simultaneously with the EGRET detector on-board the *CGRO* satellite and/or *Whipple* ground-based Atmospheric Cherenkov Telescope. *CGRO* observations lasts typically two weeks and the observations by *Whipple* lasts several hours per night. Observations with Cherenkov Telescope were performed in clear nights without bright moon. To cover the same time duration with γ-ray detectors in the X-ray band, *ASCA* observations were usually divided into several short time intervals ($\sim$ 10 ksec) during the multi-frequency observations, except for the 'big' campaign of Mrk 421 conducted in 1998.

Table 6.1: TeV blazars observed with *ASCA* & *RXTE*

Source	Other Name	Position RA	(J2000) DEC	(Galactic l	Co-ord) b	z [a] $[d_L]$ [b]	N_H^{Gal} [c]	class [d]
1101+384	Mrk 421	166.1138	38.2088	179.832	65.032	0.031 [3.853]	1.45	HBL
1652+398	Mrk 501	253.4676	39.7602	63.600	38.859	0.034 [4.229]	1.73	HBL
2155−304	PKS	329.7169	−30.2256	17.730	−52.246	0.117 [14.72]	1.77	HBL
2344+514	1ES	356.7702	51.7050	112.891	−9.908	0.044 [5.487]	16.0	HBL

[a] redshift of the source.

[b] luminosity distance in the units of 10^{26} cm. The Hubble constant is assumed to be $H_0 = 75$ km s^{-1} Mpc^{-1}.

[c] Galactic column density in the units of 10^{20} cm^{-2}. Elvis et al. (1989) for Mrk 421 and Mrk 501, Stark et al. (1992) for PKS 2155−304 and 1ES 2344+514.

[d] HBL: high-frequency-peaked BL Lac objects. For more detail, see § 2.
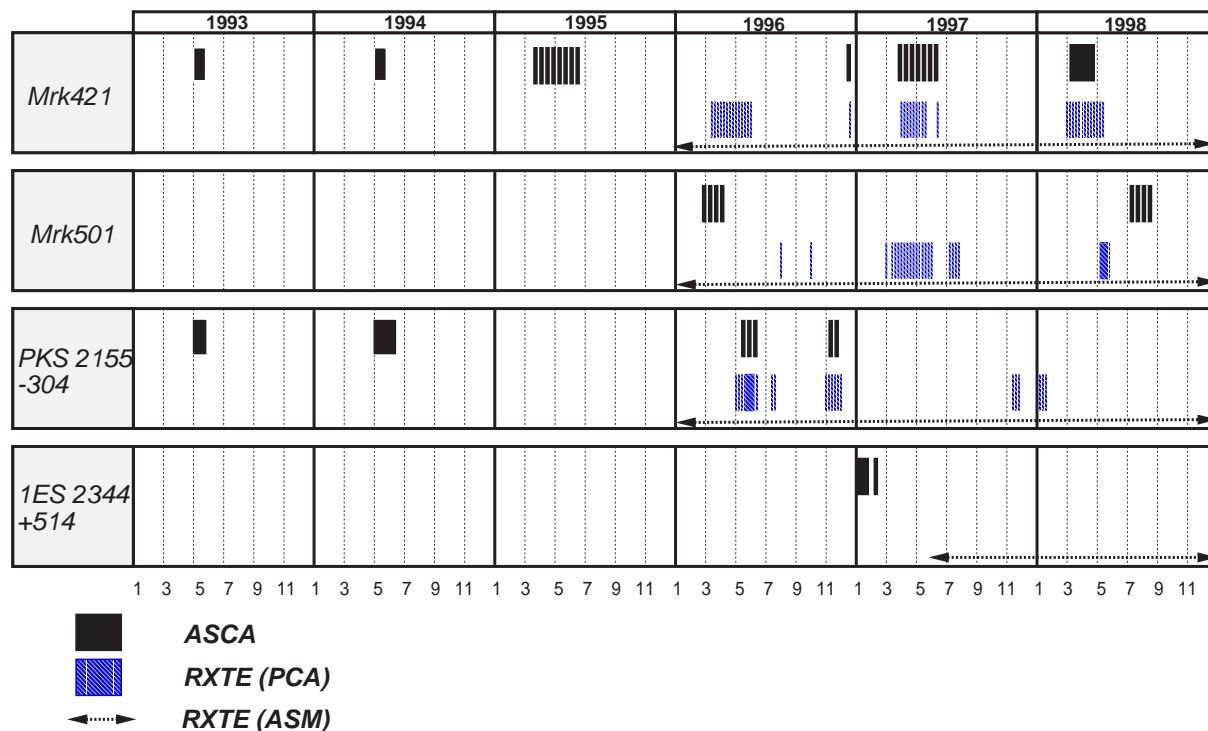
Figure 6.1: Observations of four TeV blazars with *ASCA* & *RXTE* . *black*: *ASCA* observations. *gray*: *RXTE* (PCA) observations. *Arrows* : *RXTE* (ASM) observations.

Table 6.2: *ASCA* observation log of Mrk 421

Source Name	Start (UT)	End (UT)	Exp. SIS	(ksec) GIS	SIS mode [a] bit-H/M	CCD mode [b]
Mrk 421	1993.05.10 03:22	1993.05.11 03:17	38.8	42.8	F/B	0123/2301
	1994.05.16 10:04	1994.05.17 08:06	29.5	38.9	F/B	1111/3333
	1995.04.25 19:16	1995.04.26 03:01	9.3	11.1	F/B	1111/3333
	1995.04.28 06:18	1995.04.28 13:51	8.4	9.3	F/B	1111/3333
	1995.04.29 11:23	1995.04.29 18:36	11.6	12.1	F/B	1111/3333
	1995.05.01 07:46	1995.05.01 15:32	9.9	10.3	F/B	1111/3333
	1995.05.03 11:12	1995.05.03 18:45	11.4	11.5	F/B	1111/3333
	1995.05.05 15:52	1995.05.05 23:51	11.2	11.5	F/B	1111/3333
	1995.05.06 19:05	1995.05.07 03:01	11.4	13.0	F/B	1111/3333
	1995.05.08 06:07	1995.05.08 13:27	11.5	12.4	F/B	1111/3333
	1996.12.15 18:37	1996.12.16 00:51	10.2	11.5	F/B	1111/3333
	1997.04.29 01:45	1997.04.29 08:00	10.1	12.3	F/B	1111/3333
	1997.04.30 01:35	1997.04.30 07:51	9.7	11.7	F/B	1111/3333
	1997.05.01 20:34	1997.05.02 04:06	11.6	13.3	F/B	1111/3333
	1997.05.03 03:23	1997.05.03 10:36	9.5	10.4	F/B	1111/3333
	1997.05.04 04:15	1997.05.04 11:56	10.3	10.9	F/B	1111/3333
	1997.05.06 01:37	1997.05.06 08:32	10.5	11.6	F/B	1111/3333
	1997.06.03 00:12	1997.06.03 06:51	10.2	11.1	F/B	1111/3333
	1998.04.23 23:08	1998.04.30 19:32	257.4	280.6	F/B	1111/3333

[a] F: *Faint* mode, B: *Bright* mode.

[b] CCD chip ID for SIS0/1. '1111/3333' represents nominal 1-CCD mode, while '0123/2301' is nominal 4-CCD mode.

Table 6.3: *ASCA* observation log of Mrk 501

Source Name	Start (UT)	End (UT)	Exp. SIS	(ksec) GIS	SIS mode bit-H/M	CCD mode
Mrk 501	1996.03.21 06:07	1996.03.21 12:01	10.6	11.5	F/B	1111/3333
	1996.03.26 02:57	1996.03.26 10:01	10.8	12.0	F/B	1111/3333
	1996.03.27 16:52	1996.03.27 22:41	10.6	11.5	F/B	1111/3333
	1996.04.02 16:35	1996.04.02 22:21	11.5	12.3	F/B	1111/3333
	1998.07.18 17:52	1998.07.19 04:11	16.1	17.9	F/B	1111/3333
	1998.07.20 19:14	1998.07.21 04:40	15.4	17.0	F/B	1111/3333
	1998.07.21 20:45	1998.07.22 05:21	13.4	15.6	F/B	1111/3333
	1998.07.23 21:47	1998.07.24 06:43	14.6	17.0	F/B	1111/3333

6.2 X-ray Observations with *RXTE*

We analyzed data from 287 *RXTE* observations of three TeV blazars as listed in Table 6.1 (no observation for 1ES 2344+514). The total net exposure was 185 ksec for Mrk

Table 6.4: *ASCA* observation log of PKS 2155−304

Source Name	Start (UT)	End (UT)	Exp. SIS	(ksec) GIS	SIS mode bit-H/M	CCD mode
PKS 2155−304	1993.05.03 20:56	1993.05.04 23:54	34.8	37.3	F/B	0123/2301
	1994.05.19 04:38	1994.05.21 07:56	84.8	96.1	F/B	1111/3333
	1996.05.22 03:14	1996.05.22 06:20	4.3	5.2	F/B	1111/3333
	1996.05.24 04:15	1996.05.24 09:40	9.5	11.0	F/B	1111/3333
	1996.05.26 16:31	1996.05.26 22:07	10.9	11.7	F/B	1111/3333
	1996.11.14 08:46	1996.11.14 20:20	18.2	20.6	F/B	1111/3333
	1996.11.15 09:23	1996.11.15 20:41	18.6	20.9	F/B	1111/3333

Table 6.5: *ASCA* observation log of 1ES 2344+514

Source Name	Start (UT)	End (UT)	Exp. SIS	(ksec) GIS	SIS mode bit-H/M	CCD mode
1ES 2344+514	1997.01.10 15:31	1997.01.11 15:10	36.0	39.8	F/B	1111/3333
	1997.01.23 05:09	1997.01.23 09:30	11.4	11.6	F/B	1111/3333
	1997.12.20 23:22	1997.12.21 05:41	11.3	12.8	F/B	1111/3333

421, 231 ksec for Mrk 501, and 255 ksec for PKS 2155−304. The detail log of *RXTE* observations is given in Appendix A (Table A.1−A.3; Mrk 421, A.4−A.5; Mrk 501, and A.6−A.8; PKS 2155−304). The large effective area of the PCA enables us to obtain high quality spectrum with relatively short observation time (see § 5). Typical exposure for one pointing is ∼ 1 ksec, and 20 ksec at the longest. Thus the pointing direction can be changed frequently even within a day.

In this thesis, we analyzed data taken according to our proposal and data sets from the *RXTE* public archive. We carried out 11 observations of Mrk 501 in 1998 May (net exposure time of 60 ksec). For the archival data, we used the data obtained from April 1996 to January 1998. We did not use the data before April 1996, because the reliable background model has not been available for this period
(for more detail, see, http://heasarc.gsfc.nasa.gov/docs/xte/pca_news.html).

In addition to the data taken with the PCA and HEXTE, the ASM data are also used. ASM scans 80 % of the sky in every 90 minutes to monitor the intensity of the brightest 75 X-ray sources. Four TeV blazars are included in the list and constantly monitored for more than 3 years (only 2 years data are available for 1ES 2344+514). Although ASM data is available with a time resolution of 90 minutes, we binned the data into one-day because of the low photon statistics.

All the PCA data analyzed in this thesis were taken by the combination of *standard*-1 mode, *standard*-2 mode, *GoodXenon*1-16*s* mode and *GoodXenon*2-16*s* mode. In this combination, the data extracted from *standard*-2 mode, which has a time resolution of 16 sec, are sufficient for the temporal and spectral analysis presented in this thesis. We also note that we do not use the HEXTE data for the analysis, as we mentioned in § 5.3.

6.3   Individual Targets

Mrk 421

Since the launch of *ASCA* in 1993, we have performed extensive observations of Mrk 421. It spanned more than five years from 1993 to 1998 (Takahashi et al. 1994; 1995; 1998), while observations spanned two years (1996−1997) for *RXTE* .

Our observations are based on two different strategies. First approach is the *continuous* observations for more than 1 day, which enables us uninterrupted monitoring of time evolution of blazars (1993, 1994 and 1998 observations; Table 6.2). In particular, we conducted intensive world-wide campaign in 1998 from radio to TeV. During this campaign, EGRET instrument could not obtain the data due to the deterioration of the detector. Unprecedented continuous coverage in the X-ray band with *ASCA* started from 1998 April 23 to April 30 UT, yielding a net exposure of 280 ksec.

Second approach is the short observations of 8−10 ksec which are spaced between 1 to 3 days apart, such that it covered the GeV/TeV γ-ray observations. Main purpose of this approach was to monitor long term stability, rather than the short term behaviour (1995, 1997 observations with *ASCA* and all *RXTE* observations; Table A.1−A.3). With this approach, we succeeded to have 11 simultaneous observations in keV X-ray and TeV γ-ray bands (see, Table 6.7).

Mrk 501

Observation in 1996 were divided into four short intervals of ∼ 10 ksec. One of four observations was done simultaneously with EGRET and *Whipple* (see below) and the observation in 1998 was done simultaneously with the *HEGRA* Cherenkov telescope.

To investigate the rapid time variability for this source, we conducted 2-day continuous observation in 1998 May by *RXTE* . This is probably the longest continuous observation for this source in the X-ray energy band (Table A.5). In order to increase data samples, we extracted data sets from public archive for 1996−1998 observations. This includes the *RXTE* data during the historical highest state in 1997 April to July, as well as the quies-

cent and the intermediate state before/after the flare. Most of the *RXTE* observations of Mrk 501 have exposures of ~ 1 ksec. These observations were separated about one day. 19 observations were conducted *truly* simultaneously in keV X-ray and TeV γ-ray bands.

PKS 2155−304

We analyzed the X-ray data of PKS 2155−304 from 1993 to 1998 observations. We observed the source three times with *ASCA* . *ASCA* observation in 1994 was conducted as a part of multi-frequency campaign (Urry et al. 1997). The *ASCA* observation continued for 2 days (Table 6.4; Kataoka et al. 2000). The observation in 1993 was continuous for one day, but the source was extremely bright that a part of the data is not available because of the saturation of the detectors. In order to monitor the long term variability of the source, the observation in 1996 was divided into 5 short intervals (~ 10 ksec).

For *RXTE* observations, we used archival data. The *RXTE* observation conducted in 1996 May was a part of multi-frequency campaign. During the campaign, *RXTE* continuously monitored the source for two weeks (Table A.6). 1997 observations were short in time (~ 1 ksec), but recorded highest flux ever observed for this source. 1997 November observations are partly overlapped with the GeV (EGRET) and TeV (*Durham Mark* 6 Cherenkov telescope) γ-ray observations.

1ES 2344+514

We conducted three *ASCA* observations of 1ES 2344+514 in 1997. One of which was the observation lasted one day and the others are 10 ksec short observations (Table 6.5). No *RXTE* observations have been conducted for this source so far, except for daily monitoring by the All Sky Monitor.

6.4 Simultaneous Observations

6.4.1 X-ray and GeV γ-ray (EGRET) observations

The log of multi-frequency campaigns with EGRET instrument is summarized in Table 6.6. Because of the relatively weak emission of HBLs in the GeV energy band, the sources could not be detected with high significancies ($\geq 4\ \sigma$) in several observation periods. However, Mrk 421, Mrk 501 and PKS 2155−304 were detected at least once, during the multi-wavelength observations presented in this thesis.

Table 6.6: List of simultaneous X-ray/GeV (EGRET) observations

Source Name	Viewing Period (VP)	EGRET Start (UT) [yymmdd]	End (UT) [yymmdd]	Detection? [a]	ASCA [yymmdd]	RXTE [yymmdd]
Mrk 421	326.0	940510	940517	YES	940516	—
	418.0	950425	950509	NO	950425	—
					∼ 950508	
Mrk 501	516.5	960321	960403	YES	960321	—
					∼ 960402	
	617.8	970409	970415	NO	—	970409
						∼ 970415
PKS 2155 −304	520.4	960521	960528	NO	960522 ∼ 960526	960521 ∼ 960528
	702.0	971118	971125	YES	—	971120 ∼ 971122
	709.1	980106	980113	NO	—	980109 ∼ 980113

[a] YES: GeV γ-rays are detected at $\geq 4\,\sigma$ level. NO : GeV γ-rays are not detected during the observation.

6.4.2 X-ray and TeV γ-ray (*Whipple*) observations

The X-ray observations listed in Table 6.7 were conducted simultaneously with TeV observations with the *Whipple* Cherenkov telescope. For the big campaign, we conducted in April 1998, we obtained additional data from other two TeV Cherenkov telescopes, *HEGRA* and *CAT*. No simultaneous X-ray/TeV observation has been performed for PKS 2155−304 and 1ES 2344+514.

Table 6.7: List of simultaneous X-ray/TeV (*Whipple*) observations

Source Name	TeV(*Whipple*) observation Start Time [MJD]	End Time [MJD]	significance σ	*ASCA* Start (UT) yymmdd	*RXTE* yymmdd [OBS-ID]
Mrk 421	50567.15	50567.25	—	970429	970429 [P20341-01-04-00]
	50568.15	50568.25	—	970430	970430 [P20341-01-04-01]
	50570.15	50570.25	—	970502	970502 [P20341-01-05-00]
	50571.15	50571.25	—	970503	970503 [P20341-01-05-01]
	50574.15	50574.25	—	970506	970506 [P20341-01-05-05]
	50927.13	50927.29	—	980424	(980424)[†]
	50928.22	50930.24	—	980425	(980425)[†]
	50930.14	50930.28	—	980427	(980427)[†]
	50931.14	50931.28	—	980428	(980428)[†]
	50932.19	50932.28	—	980429	(980429)[†]
	50933.22	50932.27	—	980430	(980430)[†]
Mrk 501	50168.38	50168.48	0.94	960326	—-
	50545.36	50545.46	10.32	—	970407 [P20340-04-09/10-00]
	50546.20	50545.30	11.85	—	970408 [P20340-04-11/12-00]
	50547.37	50547.47	7.88	—	970409 [P20340-04-13/14-00]
	50550.33	50550.43	16.32	—	970412 [P20340-04-19/20-00]
	50551.35	50551.45	32.06	—	970413 [P20340-04-21/22-00]
	50552.37	50551.47	22.46	—	970414 [P20340-04-23/24-00]
	50553.37	50553.47	19.83	—	970415 [P20340-04-25/26-00]
	50554.38	50554.48	27.24	—	970416 [P20340-04-27/28-00]
	50570.29	50570.39	7.01	—	970502 [P20340-01-02/03-00]
	50573.31	50573.41	17.80	—	970505 [P20340-01-07/08-00]
	50574.34	50574.44	14.52	—	970506 [P20340-01-09/10-00]
	50575.23	50575.33	12.01	—	970507 [P20340-01-11/12-00]
	50576.30	50576.40	27.50	—	970508 [P20340-01-13/14-00]
	50577.28	50577.38	40.54	—	970509 [P20340-01-15/16-00]
	50582.27	50582.37	8.62	—	970514 [P20340-01-25/26-00]
	50959.29	50959.39	2.86	—	980526 [P30249-01-01-04]
	50960.29	50960.39	3.98	—	970527 [P30249-01-01-06]
	51013.17	51013.27	3.11	980719	—

[†]: *RXTE* observations were conducted, but data are not in archive. These results are not shown in this thesis.

Chapter 7

Analysis and Results of *ASCA* Observations

7.1 Analysis

7.1.1 Data Reduction

We reduced the data using the analysis softwares supplied by the *ASCA* Guest Observer Facility at the NASA Goddard Space Flight Center (GSFC) and the Institute of Space and Astronautical Science (ISAS). We first selected the data by the orbital conditions of the satellite. The minimum elevation angle from the Earth's limb is 10 and 5 degrees for the SIS and the GIS, respectively. The minimum cutoff rigidity is 6 GeV/c. We excluded the data obtained during the passage through the South Atlantic Anomaly. For the SIS data, we selected the data based on the criterion that the angle between the target and the illuminated Earth's limb is larger than 20 degree, to avoid the contamination by radiation from the Earth's atmosphere.

We next reduced the data by taking the detector performance and stability of satellite attitude into account. Since the attitude of satellite is not stable just after changing the pointing direction, we excluded the data obtained when the difference between the actual Euler angle and scheduled angle is larger than ~ 1 arcmin. We reduced the background in the GIS data by using the information of rise time discrimination (see § 4.4.3). We excluded hot pixels and flickering pixels of the SIS (§ 4.3.3) and selected the normal SIS events with grades 0, 2, 3 and 4 (see, Figure 4.4). The latter selection can effectively reduce background events mainly by charged particles. These criteria for data reduction are summarized in Table 7.1.

For the SIS data, we converted *faint* data to *bright* data and combined all data as

75

bright data. Since the echo and dark frame errors (§ 4.3.3; 4.3.3) cannot be corrected in *bright* format, we estimated the dark frame errors using *faint* data. The correction of dark frame errors and echo were incorporated in the detector response of the SIS for the spectral analysis.

Table 7.1: Screening criteria for *ASCA* analysis

Screening Item	Screening	Criteria
	SIS 0/1	GIS 2/3
Elevation [a]	10.0	5.0
Cutoff Rigidity [b]	6.0	6.0
SAA Cut [c]	YES	YES
Bright Earth [d]	20.0	—
Maneuver [e]	YES	YES
Grade (SIS only) [f]	0,2,3,4	—
Hot Pixel (SIS only) [g]	YES	—
Rise Time (GIS only) [h]	—	YES

[a] The minimum elevation angle above the Earth's limb
[b] The minimum cutoff rigidity
[c] 'YES' if the data in SAA are excluded
[d] The minimum angle between the target and the illuminated Earth's limb
[e] 'YES' if the data when the attitude of satellite was unstable were eliminated
[f] SIS grade selection (see, Figure 4.4) used in the analysis
[g] 'YES' if the hot pixels and flickering pixels are removed
[h] 'YES' if the rise time discriminator are used to reduce background

7.1.2   Background Subtraction

After the screening processes were done, we separated the source and background photons using the images on the SIS and the GIS. We extracted the source counts from a circular region centered on a target with a radius of 3 arcmin for the SIS (1-CCD mode). This is because the half power diameter of the XRT is 3 arcmin (see, §4.2) and more than 50 % photons are included within a radius of 3 arcmin. For the SIS (4-CCD mode) and the GIS, larger region were selected with a radius of 6 arcmin. The radius used to extract source photons is given in Table 7.2 for each observation.

Most of the TeV blazars analyzed in this thesis are bright, in the sense that the background becomes comparable with source photons only at ≥ 8 keV. In this case, the Cosmic X-ray Background and its fluctuations are negligible compared with the count rate from the source ($\leq 1\%$). However, to measure the flux and spectral form of the faint sources, it is important to subtract both the internal and external background accurately (§ 4.3.3;

4.4.3). In our observations, 1ES 2344+514 is the faintest and needs background subtraction. We also subtracted the background for an observation of Mrk 421 in 1993, because the source was relatively faint during the observation. We performed no background subtraction for other observations (§ 6), to avoid any instrumental artifacts.

Since the background of the SIS detectors is flat on the chip, we estimate the background from the entire chip after subtracting the target region. For the GIS, we estimated the background from the region at the same off-axis angle as the source position. This is because the intrinsic (detector) background is dependent on the distance from the optical axis (e.g., Makishima et al. 1996).

Table 7.2: Image region for source and background spectrum

Source Name	Start Date (UT)	Source radius (arcmin) S0/S1/G2/G3	Background radius (arcmin) S0/S1/G2/G3	Local BGD
Mrk 421	1993.05.10	6/6/6/6	6/6/6/6	L[a]
	1994.05.16	3/3/6/6	—	—[b]
	1995.04.25	3/3/6/6	—	—
	∼ 1995.05.08	3/3/6/6	—	—
	1996.12.15	3/3/6/6	—	—
	∼ 1997.06.02	3/3/6/6	—	—
	1998.04.23	1/2.6/6/6 [c]	—	—
Mrk 501	1996.03.21	3/3/6/6	—	—
	∼ 1996.04.02	3/3/6/6	—	—
	1998.07.18	3/3/6/6	—	—
	∼ 1998.07.23	3/3/6/6	—	—
PKS 2155	1993.05.03	6/6/6/6 [d]	—	—
− 304	1994.05.19	3/3/6/6	—	—
	1996.05.22	3/3/6/6	—	—
	∼ 1996.05.26	3/3/6/6	—	—
	1996.11.14	3/3/6/6	—	—
	∼ 1996.11.15	3/3/6/6	—	—
1ES 2344	1997.01.10	3/3/6/6	3/3/6/6	L
+514	1997.01.23	3/3/6/6	3/3/6/6	L
	1997.12.20	3/3/6/6	3/3/6/6	L

[a] L: local background is subtracted.

[b] Background was not subtracted, because the source was very bright.

[c] Image region of the SIS is small to avoid the effects from the telemetry saturation (see § 7.1.3 for more detail). The GIS light curves were approximately calculated from the count rate on the Lower Discriminator (LD).

[d] Data taken at medium bit rate were not used because the telemetry was strongly saturated.

7.1.3   Treatment of the Telemetry Saturation

In two observations of PKS 2155−304 (1993) and Mrk 421 (1998) (Table 7.2), sources were extremely bright and telemetry was partly saturated. When the telemetry is saturated, the part of of the data are lost before transmitting to the ground station.

The saturation limit is 16 cts/s for the GIS data taken at the medium bit rate (§ 4.4.2). For Mrk 421 observation in 1998, the GIS count rates exceed this limit, hence we approximately estimate the count rate from the hit rate of the Lower Discriminator (LD). We also extracted the data from the period in which effects of the saturation are negligible. For PKS 2155−304 (1993), the GIS was not saturated through the observation.

The saturation limit for the SIS *bright* mode is 32 cts/s when the data are taken at a medium bit rate (1-CCD mode; § 4.3.2). Since the nominal source position is close to the readout gate on the CCD chip, the X-ray events closer to the center of image are read out earlier. Saturated portion on the chip can be eliminated by selecting the narrower source region than usual (3 arcmin). For the Mrk 421 observation in 1998, we found that the effects of saturation is negligibly small when we choose the source radius at 1.0 arcmin for the SIS0, while 2.6 arcmin for the SIS1 (Figure 7.1).

We note that the calibration of the SIS is done assuming the source radius of 3 arcmin. We thus verify that the analysis results do not change even if we choose narrower source region (1 arcmin) than usual. For PKS 2155−304 observation in 1993, all regions on the chips are heavily affected by telemetry saturation, thus we did not use the data taken at medium bit rate (about 60 % in total) because it is very difficult to estimate the flux of the source.

7.2   Results from Temporal Studies

7.2.1   Time Variability

As described in § 2, time variability is one of the marked features of blazars. Four TeV blazars were observed repeatedly with *ASCA* since the launch in 1993 (§ 6). We investigate both the long-term (weeks to years) and the short-term (hours to weeks) variability. We used the GIS data to compare the source count rate, because the GIS has wider field of view than the SIS (§ 4.4.1) and is less affected by the attitude of the satellite and position of the source on the detector.

In the following analysis, the source counts are extracted from a circular region centered on a target with a radius of 6 arcmin for the GIS. The binning time is 1024 sec and the count rate of the GIS2 and the GIS3 are summed in the energy band 0.7−7.5 keV.
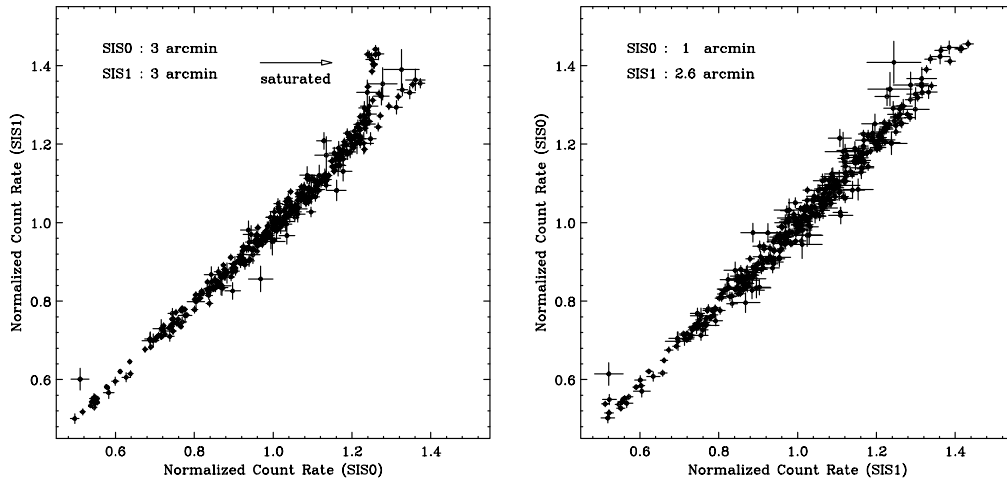
Figure 7.1: Relation of the normalized SIS0 count rate versus normalized SIS1 count rate, during Mrk 421 observation in 1998. *left*; the source radii are 3 arcmin for both the SIS0 and SIS1. Count rates are normalized to their mean values; 20.5 cts/s for the SIS0 and 16.7 cts/s for the SIS1. The SIS0 light curve is saturated when the source was in the brightest state and the data were taken at the medium bit-rate. The effect is indicated by an arrow. *right*; the source radii are 1 arcmin for the SIS0 and 2.6 min for the SIS1. Count rates are normalized to their mean values; 8.2 cts/s for the SIS0 and 15.5 cts/s for the SIS1. The effect of telemetry saturation has disappeared.

Mrk 421

As we see in Figure 7.2, the source was the faintest in 1993 ($2-5$ cts/s for the GIS) and the brightest in 1998 ($10-40$ cts/s for the GIS). In addition to this large-amplitude variability on time scales from weeks to years, rapid variability is clearly seen during the observations in 1993 and 1994. Count rate varied by a factor of 2 during a half day period. A small but rapid variability on time-scales of hours to days is also seen in the 1995 and 1997 data. The source intensity varied 40 % or less during 8 hours. In the 1998 observation, the source was extremely bright and the occurrence of day-by-day flare was clearly detected. The subsequent analysis revealed that Mrk 421 was in the historical high state during our observation in 1998 (see, § 7.3).

Mrk 501

The light curves of Mrk 501 are shown in Figure 7.3. To carry out simultaneous monitoring of the source with the γ-ray detectors, we divided our observations into short time intervals (~ 10 ksec). For the 1996 observations, the flux decreased gradually by a factor of 2 (6 $-$ 3 cts/s for the GIS) on a time scale of two weeks. In 1998, the source was brighter (7 cts/s for the GIS) than 1996 observations. A small flux variation of 30 % was observed
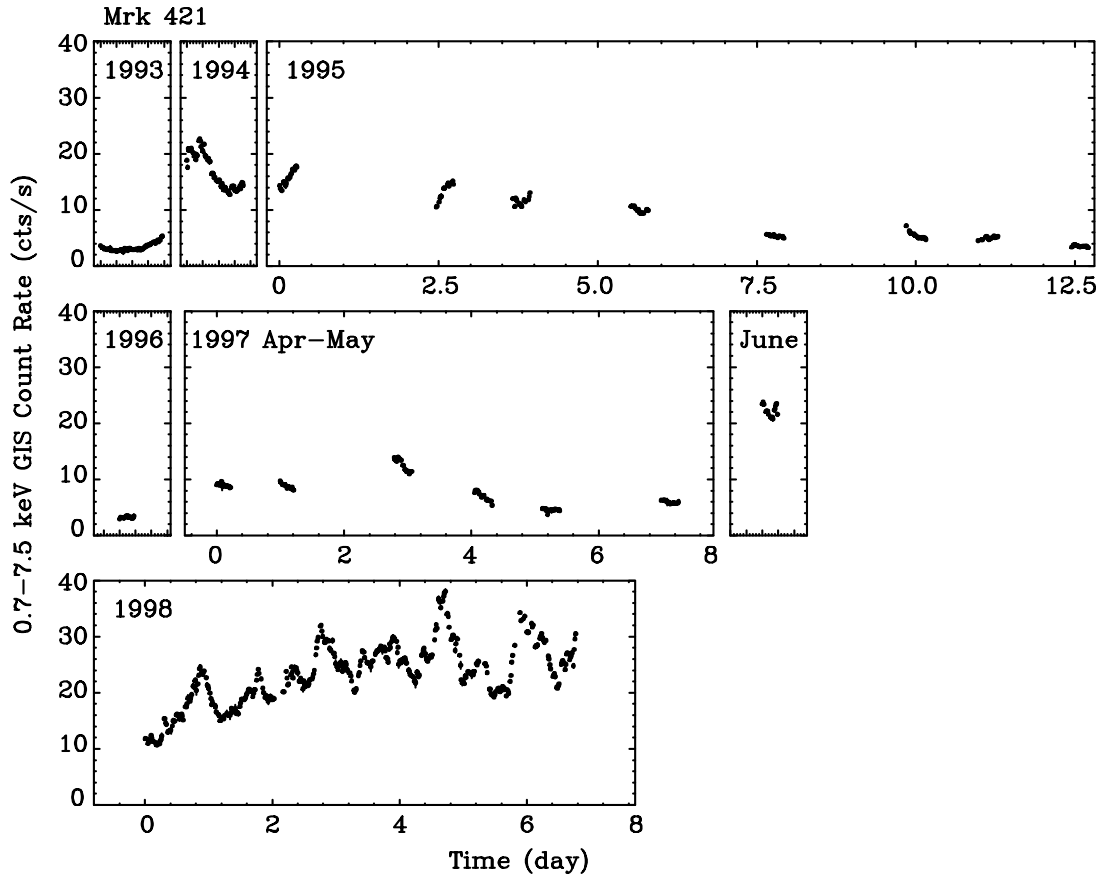
Figure 7.2: The GIS light curves of Mrk 421 from 1993 to 1998 *ASCA* observations. The source counts are extracted from a circular region centered on the target with a radius of 6 arcmin for the GIS. The binning time is 1024 sec. Energy band is 0.7−7.5 keV. The count rate of the GIS2 and the GIS3 are summed. We estimate the GIS count rate from the LD hit rate for 1998 observation, because the source was very bright and the telemetry was partly saturated.

during one-week observation. Contrary to Mrk 421, no significant variability as short as hours is seen in the light curve; a constant fit of the data for each observation (~ 10 ksec) does not indicate any rapid time variability in the sense that $P(\chi^2) < 1\%$.

PKS 2155−304

The light curves of PKS 2155−304 are shown in Figure 7.4. The source was brightest in 1993 (15−23 cts/s for the GIS) and the faintest in 1996 (3−4 cts/s for the GIS), which indicates the changes of more than factor 5 in the flux. Similar to Mrk 421, PKS 2155−304 also shows time variability on time scales as short as hours. The 1993 observation caught a brightening phase. The source varied by 60 % during one day. In 1994, PKS 2155−304 was continuously observed for two days. At the beginning of the 1994 observation, we
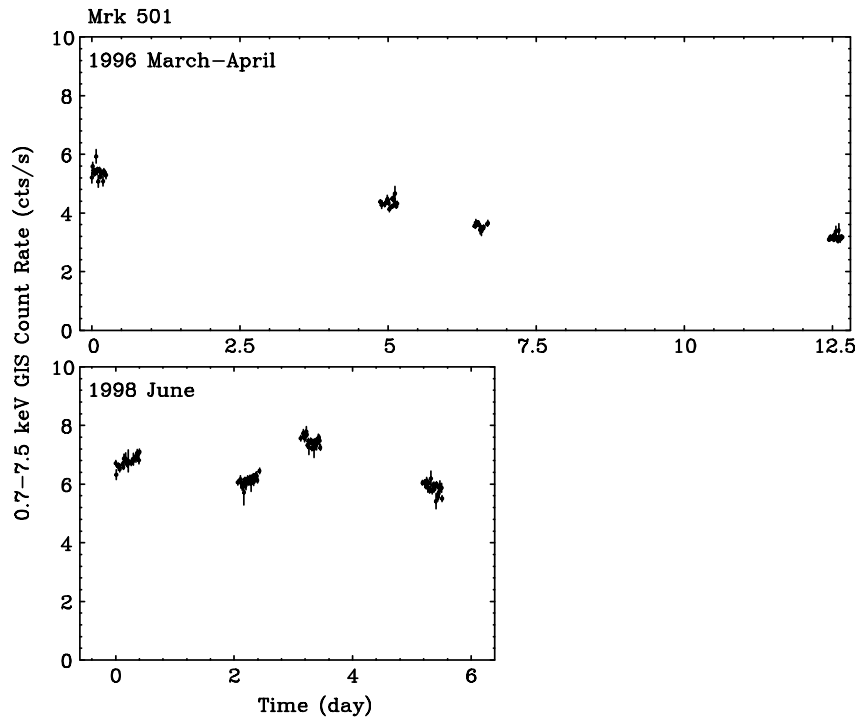
Figure 7.3: The GIS light curves of Mrk 501 from 1996 to 1998 *ASCA* observations. The source counts are extracted from a circular region centered on a target with a radius of 6 arcmin for the GIS. The binning time is 1024 sec. Energy band is 0.7−7.5 keV. The count rate of the GIS2 and the GIS3 are summed.

detected a large flare, where the source intensity varied by a factor of 2 in 8 hours. After the flare, the flux became quite stable but fluctuated with the amplitude of 20 %. In 1996 May observations, the source intensity varied by about 50 % in 4 days, but only 10 % fluctuation during each observation period (4 hours). Two observations in 1996 November showed no significant variabilities or flares.

1ES 2344+514

The light curves of 1ES 2344+514 are shown in Figure 7.5. The source was brightest in January 1997 (0.8 cts/s for the GIS) and faintest in December 1997 (0.5 cts/s for the GIS), which indicates the changes by a factor of ~ 2 in flux. No time variability as rapid as hours was detected during the observations ($P(\chi^2) > 1$ % for a constant fit).
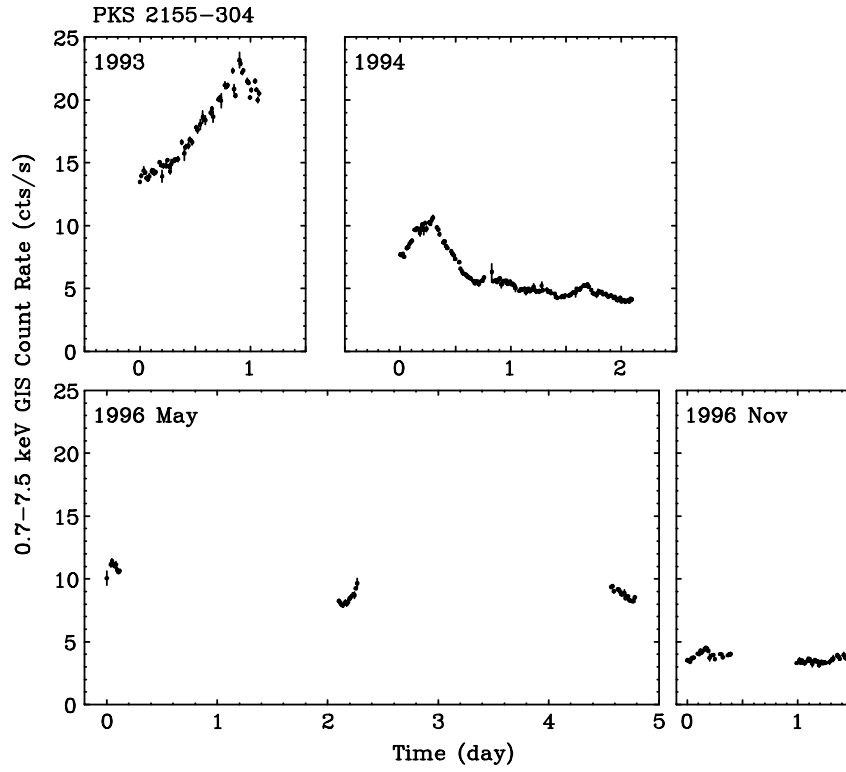
Figure 7.4: The GIS light curves of PKS 2155−304 from 1993 to 1996 *ASCA* observations. The source counts are extracted from a circular region centered on a target with a radius of 6 arcmin for the GIS. The binning time is 1024 sec. Energy band is 0.7−7.5 keV. The count rate of the GIS2 and the GIS3 are summed.

7.2.2   Energy Dependence of Variability

Variability Amplitude

In order to quantify the variability properties, we first introduce the general definition of the fractional *rms* variability parameter (e.g., Rodriguez-Pascual et al. 1997; Zhang et al. 1999). The *rms* variability characterizes the mean variability of the source during the observation. The parameter is defined as follows.

We assume there are data series (a light curve) $F_i(t)$, where i is the ID of the data number $(1 \leq i \leq N)$ and t is the time. The standard deviation for this time series is

$$\sigma_F^2 = \frac{1}{N-1} \sum_{i=1}^{N} (F_i(t) - F_{\mathrm{mean}})^2, \tag{7.1}$$

where F_{mean} is the mean count rate. We define the *random variance*, due to random errors $\sigma_i(t)$ associated with $F_i(t)$ as

$$\Delta_F^2 = \frac{1}{N} \sum_{i=1}^{N} \sigma_i(t)^2. \tag{7.2}$$
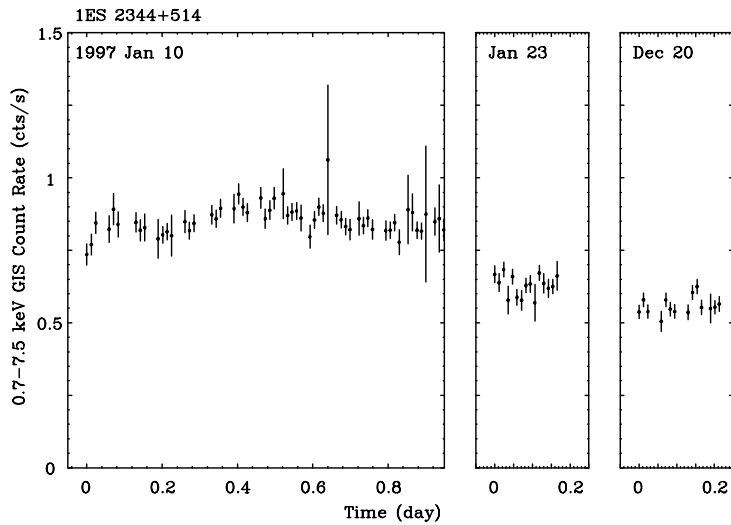
Figure 7.5: The GIS light curves of 1ES 2344+514 in 1997 *ASCA* observations. The source counts are extracted from a circular region centered on a target with a radius of 6 arcmin for the GIS. The binning time is 1024 sec. Energy band is 0.7−7.5 keV. The count rate of the GIS2 and the GIS3 are summed.

The excess variance, σ_{exc}, is then defined as the difference between the standard deviation σ_F^2 and the random variance Δ_F^2.

$$\sigma_{\mathrm{exc}}^2 = \sigma_F^2 - \Delta_F^2. \tag{7.3}$$

Finally, we define the fractional *rms* variability parameter as

$$F_{\mathrm{var}} = \sigma_{\mathrm{exc}}/F_{\mathrm{mean}}. \tag{7.4}$$

Long-Term Trend of Variability

We calculate the F_{var} of four TeV blazars using the GIS light curves shown in Figure 7.2−7.5. To investigate the long-term trend of variability in various energy bands, we divided the GIS light curves into five energy bands; 0.7−1.0 keV, 1.0−1.5 keV, 1.5−2.0 keV, 2.0−3.0 keV and 3.0−7.5 keV.

The results are summarized in Figure 7.6. From the figure, one can find a clear trend such that the amplitude of variability becomes larger as the photon energy increases for all objects studied here. For Mrk 421 data, however, we do not include the 1998 data because we cannot estimate the light curves separated by energy only from the LD count rate. F_{var} was calculated using the data from 1993 to 1997. We calculate the F_{var} of Mrk 421 observation in 1998 using the SIS light curves in the next section.
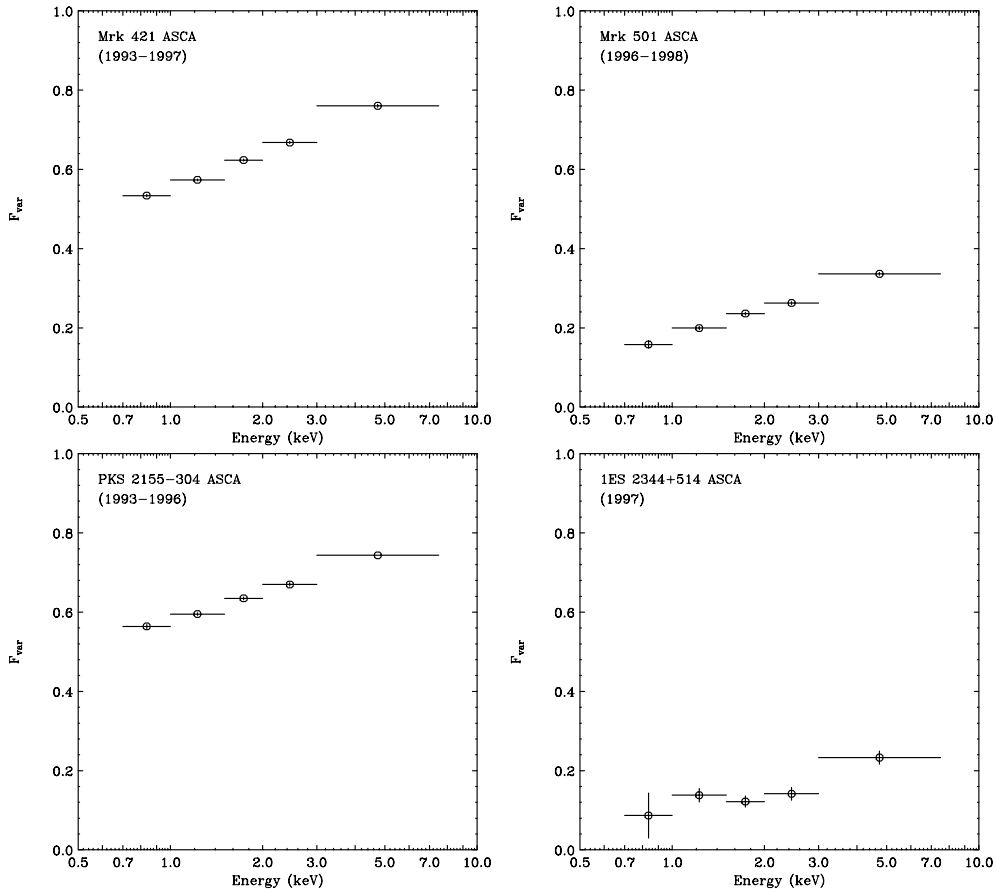
Figure 7.6: Energy dependence of variability of four TeV blazars. The variability parameter was calculated in 0.7−1.0 keV, 1.0−1.5 keV, 1.5−2.0 keV, 2.0−3.0 keV and 3.0−7.5 keV, respectively. For the light curves in total *ASCA* bandpass (0.7−7.5 keV), see Figure 7.2−7.5. *top left*: Mrk 421, *top right*: Mrk 501, *bottom left*: PKS 2155−304, and *bottom right*: 1ES 2344+514. For Mrk 421, we do not include the data in 1998.

Variability of Day-by-Day Flares (Mrk 421 1998)

In order to study the variability of Mrk 421 during the 1998 observation, we use the SIS data binned at 1024 sec. Count rates from the SIS0 and the SIS1 are summed. First, variability was calculated for the total exposure (7 days) in five energy bands, corresponding to 0.5−1.0 keV, 1.0−1.5 keV, 1.5−2.0 keV, 2.0−3.0 keV and 3.0−7.5 keV, respectively. As shown in Figure 7.7, the energy dependence of the variability for Mrk 421 in 1998 is similar to that obtained in 1993−1997 (Figure 7.6).

Since the observation in 1998 continued for 7 days and included ∼10 day-by-day flares (Figure 7.2), we also assess the variability behavior for *each* flare event. For this purpose, we divided the total exposure into 10 segments as shown in Figure 7.8. Except for the first (#1) and the last interval (#10), each segment typically involves one flare event.
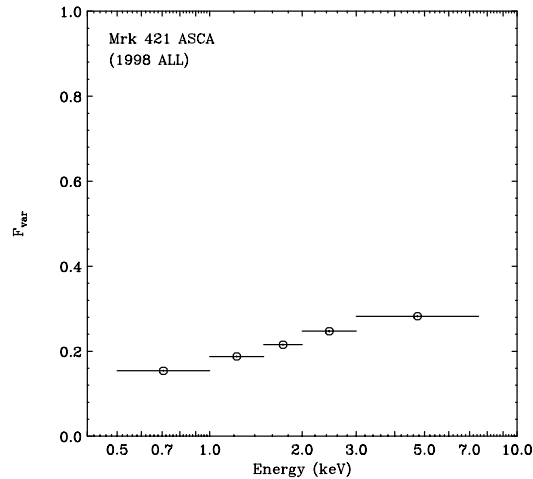
Figure 7.7: Energy dependence of variability of Mrk 421 in 1998. The variability parameter was calculated for the total exposure in five energy bands (0.5−1.0 keV, 1.0−1.5 keV, 1.5−2.0 keV, 2.0−3.0 keV and 3.0−7.5 keV). We used the SIS data binned at 1024 sec, because the GIS light curves are strongly saturated.

We calculate the variability parameter F_{var} from time-segments #2 to 9. The energy dependence of variability of individual flares are shown in Figure 7.9, respectively.
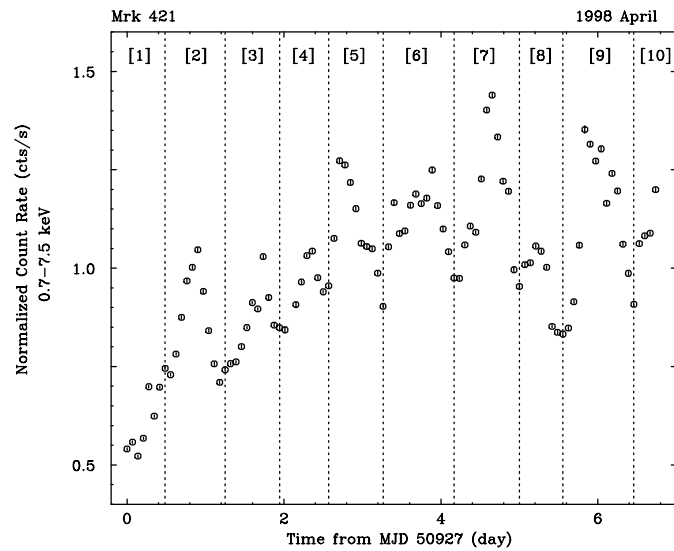
Figure 7.8: The SIS light curve of Mrk 421 obtained in 1998 observation and the division of time interval in 10 separate segments. Each point represents 6 ksec integration of the data.

Four flares exhibit a similar trend to Figure 7.7, such that the variability becomes larger as the photon energy increases (segments # 2,5,7,9), while the energy dependence of variability is flat and not as clear for the flares involved in segments # 3,4,6 and 8. These

results indicate important features for the variability of TeV blazars; on a longer time-scale, variability amplitude becomes larger as increasing photon energy, but for individual flares (or shorter time-scale), the energy dependence of variability changes *flare-by-flare*.
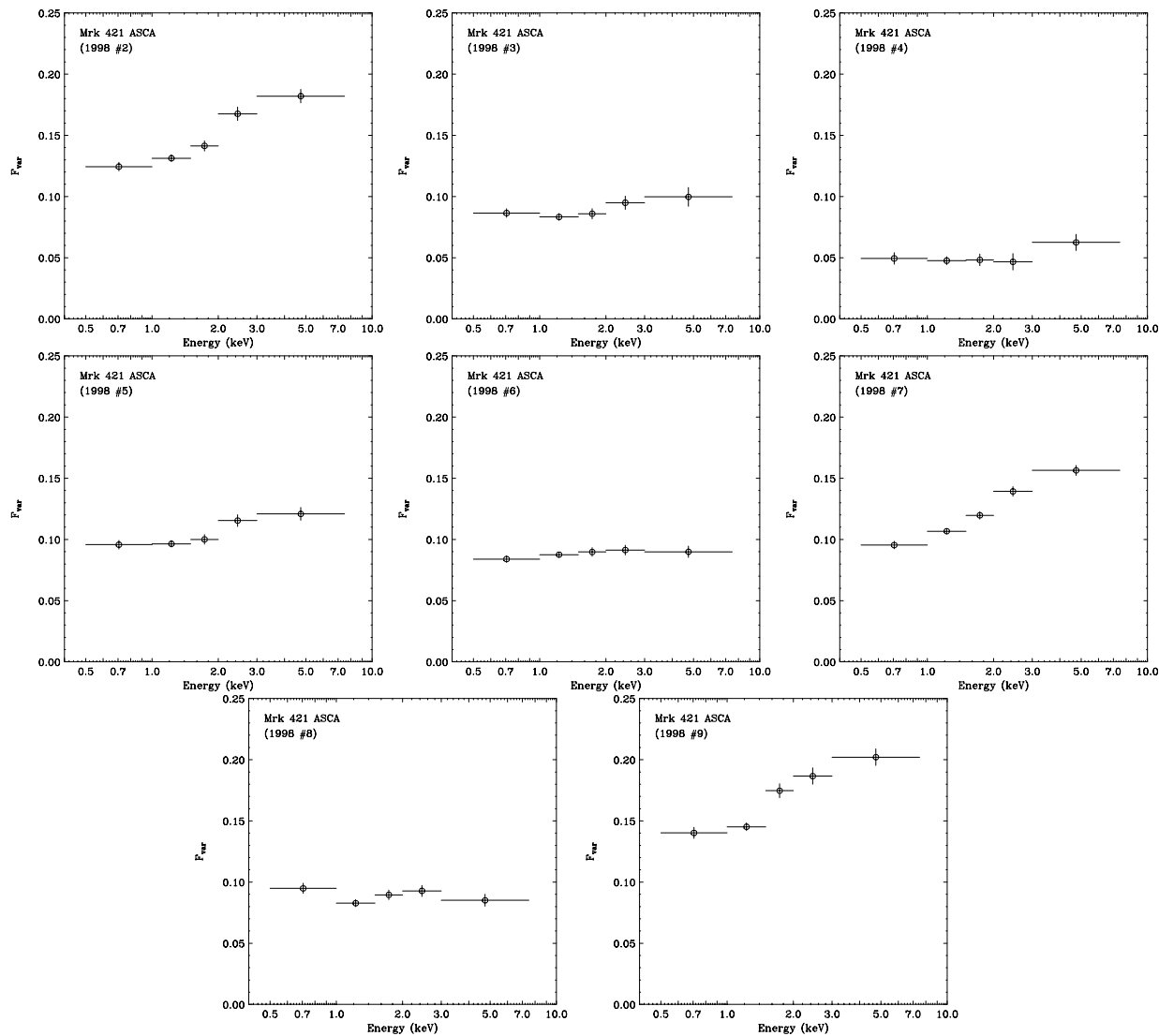
Figure 7.9: Energy dependence of variability of Mrk 421 in 1998 observations. Variability for individual flares is separately shown. Time segments are defined in Figure 7.8. The combined SIS data were used.

7.2.3 Structure Function

In 1998 observation of Mrk 421, we detected day-by-day flares as shown in Figure 7.2. This naturally leads us to an idea that there exists some *preferred* time scale for the rapid variability of blazars. Variability parameter, F_{var}, is a measure of the *mean* variability of the source. Since it averages over all the variability during the observation, the more detailed analysis of the time-scale and the time-profile of the variability requires a more sophisticated technique than the F_{var} - type analysis. To quantify the characteristic time scale of the variability and investigate its physical origin, we use a numerical technique called the Structure Function (hereafter the SF).

The definition of the SF and their properties are given by Simonetti et al. (1985). It provides a measure of the mean difference in the flux densities as a function of the separation in the sampling interval. The first order SF is defined as

$$\text{SF}(\tau) = \frac{1}{N} \sum [a(t) - a(t + \tau)]^2, \tag{7.5}$$

where $a(t)$ is a point of the time series $\{a\}$ and summation is made over all pairs, whose separation times are equal to τ. N is the number of such pairs.

The SF analysis gives information similar to power spectrum analysis, but the SF has advantages when examining non-periodic data. In particular, the SF is free from the DC component in the time series, whereas other methods such as Auto Correlation Function (ACF) are not. Furthermore, Hughes et al. (1992) argue that the SF technique provides a method of quantifying time variability without the problems of windowing, and aliasing, which are encountered in the traditional power spectrum analysis techniques.

The SF is closely related to the power spectrum density distribution. If the $\text{SF}(\tau) \propto \tau^\beta$ ($\beta > 0$), then the power spectrum has the distribution $P(f) \propto f^{-(\beta+1)}$, where f is frequency (e.g., Paltani et al. 1997; Figure 7.11). Importantly, when the significant time variability does *not* exist below $\tau_{\min}$ and $a(t)$ is approximately linear in τ, the SF will be $\propto \tau^2$ in the range $\tau \leq \tau_{\min}$.

The SF for a typical measured process consists of three different parts, as schematically shown in Figure 7.10; (i) for the shortest separation times, plateau appears with an amplitude which is just the twice of the variance of the measurement noise ($2\ \sigma_{\text{noise}}^2$), (ii) for τ longer than the longest variability time scale, there is a plateau (roll-over) with an amplitude equal to twice the variance of the fluctuation ($2\ \sigma_{\text{signal}}^2$), (iii) these regions are linked by a curve whose slope depends on the nature of the intrinsic variation of the source (e.g., red noise, flickering noise, etc). Time scale at which plateau (roll-over; t_{var} in Figure 7.10) appears, is thought to be the *characteristic* time scale of the measured time variability.
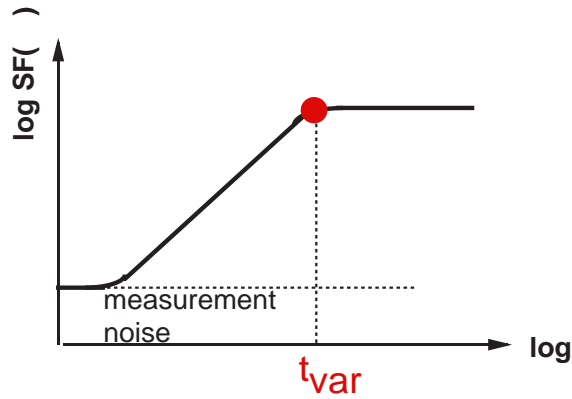
Figure 7.10: Schematic drawing of the 'typical' structure function for a measured time series.

In order to investigate possible systematic errors on the SF analysis, the 1st order SF was calculated for the simulated light curves, whose power spectrum densities are expressed as $P(f) \propto f^{-\alpha}$. We assumed $\alpha = 2.2$ in the following analysis. The length of simulated data was set to 6.7 day, which is similar to the actual observation of Mrk 421 in 1998 (Figure 7.2). To generate the time series, we simply superimposed sine functions with random phases from 0 to 2π, with the constraint that the power in each frequency bin decreases as specified by the power spectrum density. We then extracted the light curve from the simulated data with the actual window for Mrk 421 (1998) observation. The SFs were calculated from thousand sets of simulated light curves prepared with different seeds for the random number generator. Finally, we made the histograms of the SF(τ) for each τ to estimate the systematic errors on the SF.

Simulated SFs are shown in Figure 7.11 with the range of the deviation. The solid line is the ensemble averages of the simulated SFs, while the two dotted lines show the 1 $\sigma\ rms$. One finds that the uncertainty of the calculated SF(τ) becomes larger at larger values of τ. It is less than 20 % for $\tau \leq 0.1$ day, while about a factor of 10 for $\tau \geq 5$ day. An oscillation and large errors of the latter is due to insufficient sampling of the data at long time-scale. We should note that in the time region $\tau \geq 0.3 \times$ [Maximum Sampling Interval] (≥ 2 day for this particular data sets), the calculated SFs have an uncertainty of more than factor 2.

We calculate the SFs for the observations whose net exposure times were longer than 40 ksec (§ 6). The results are summarized in Figure 7.12. We mark a time scale by an arrow above which the calculated SF contains large uncertainty of more than factor 2.
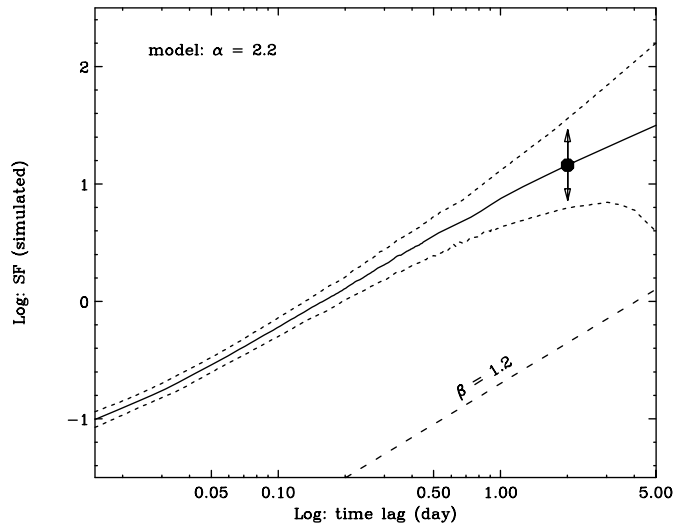
Figure 7.11: Simulated structure function for $P(f) \propto f^{-\alpha}$ ($\alpha = 2.2$). Assumed data length is 6.7 day, which coincides with the Mrk 421 observation in 1998. Solid line is the ensemble average of the SFs produced by the Monte Calro simulations described in the text. Dotted lines are 1 σ *rms* for the simulated SFs. Large dash is a line corresponding to $\beta = 1.2$ (SF $\propto \tau^{\beta}$), drawn to guide an eye. Arrow plotted at $\tau = 2$ (day) indicates that the SF contains the uncertainty of factor 2 at this point.

Mrk 421

The 1st order SFs are separately shown for the 1993 observation (*upper left*), 1994 observation (*upper right*) and the 1998 observation (*middle left*). The SIS data, binned at 1024 sec were used for the calculation. We fitted SF(τ) by a power law $\propto \tau^{\beta}$ in the time domain $0 < \tau/$day < 0.3. The best fit slopes were $\beta = 1.5 \pm 0.1$ (1993), $\beta = 1.7 \pm 0.1$, and $\beta = 1.2 \pm 0.1$ (1998). For the 1998 data, we clearly detect a roll-over around the time scale $\tau \simeq 0.5$, which corresponds to the typical time scale for an individual flare event. Both 1993 and 1994 observations are too short to identify the same roll-over due to the large errors in the SF.

PKS 2155−304

The SFs of 1993 and 1994 observations are separately shown in Figure 7.12 (*middle right* and *lower left*). Power law slopes of the SFs are $\beta = 2.0 \pm 0.2$ (1993) and $\beta = 1.4 \pm 0.1$ (1994) in $0 < \tau/$day < 0.3, respectively. For the 1994 data, we see a roll-over around 0.3 day, which corresponds to the rise/decay-time of the large flare event (see, Figure 7.4).

1ES 2344+514 (1997)

The SF for 1ES 2344+514 observation in 1997 are given in Figure 7.12 (*lower right*). The best fit power law index is $\beta = 2.3 \pm 1.1$ for $0 < \tau/\text{day} < 0.3$.

Analysis of Time Asymmetry

It is very intriguing to characterize the shape of the flares seen in the light curves (e.g., § 7.2). Structure function is also viable to test the asymmetry of the light curves. We adopt a convenient approach suggested by Kawaguchi et al. (1998). We separate $\text{SF}(\tau)$ into two parts, SF_+ and SF_-, depending on the sign of $a(t) - a(t+\tau)$;

$$\text{SF}_+(\tau) = \frac{1}{N_+} \sum [a(t) - a(t+\tau)]^2 \quad (\text{for} \quad a(t) - a(t+\tau) < 0), \tag{7.6}$$

$$\text{SF}_-(\tau) = \frac{1}{N_-} \sum [a(t) - a(t+\tau)]^2 \quad (\text{for} \quad a(t) - a(t+\tau) > 0). \tag{7.7}$$

The summation in SF_+ (or SF_-) is made only for pairs that have plus (or minus) signs of $a(t) - a(t+\tau)$, and N_+ (or N_-) are the numbers of such pairs.

The negative sign of $a(t) - a(t+\tau)$ represents the increasing luminosity with time; thus SF_+ approximately indicates the structure function of brightening phases, and similarly, SF_- represents the decaying phases. If the studied light curve is symmetric in time, $\text{SF}_+(\tau)$ and $\text{SF}_-(\tau)$ are expected to coincide with $\text{SF}(\tau)$. On the other hand, if the light curve is characterized with rapid rise and gradual decay, a relation becomes $\text{SF}_+(\tau) > \text{SF}_-(\tau)$.

We calculate $\text{SF}_+(\tau)$ and $\text{SF}_-(\tau)$ for Mrk 421 data obtained in 1998. Since we conducted simultaneous EUV (extreme ultraviolet; $60-90$ Å) observation with the *EUVE* during this campaign (§ 9), we also plot the SF for the *EUVE* light curve (see, Figure 9.2). Results are separately shown in Figure 7.13 for *EUVE*, $0.5-2.0$ keV, $2.0-4.0$ keV and $4.0-7.5$ keV data. Upper panels show SF_+, SF_- and usual SF, respectively, while lower panels are the differences between SF_+ and SF_-, normalized by SF. We define the *symmetrical parameter* $\text{Sy}(\tau)$ as

$$\text{Sy}(\tau) = \frac{\text{SF}_+(\tau) - \text{SF}_-(\tau)}{\text{SF}(\tau)}. \tag{7.8}$$

Since we are interested in the symmetry of a single flare event, $\text{Sy}(\tau)$ was calculated in the time region $0 \le \tau \le 0.5$ (day), where 0.5 day is the characteristic time scale of Mrk 421 (Figure 7.12). We averaged over $\text{Sy}(\tau)$ in the time domain $0 \le \tau \le 0.5$ day, and plot them against the photon energy. The results are shown in Figure 7.14. The figure indicates two important results;

(1) Sy(τ) is always larger than zero, which indicates the time profile of day-by-day flares of Mrk 421 favours 'rise-time < decay-time'.

(2) Deviations of Sy(τ) from zero become smaller as photon energy increases, which indicates that the light curves are more symmetric at higher energies.

Since the light curve of Mrk 421 in 1998 includes many of the flare events and they are superposed on each other, we also applied the same analysis for the light curves after subtraction of the general trend in the light curves. We first fitted the light curves with a quadratic function, then subtracted the best fit function as a 'trend'. We confirmed that the result presented in this section is not affected by the *pileup* of flares. Full details are given in Appendix C.
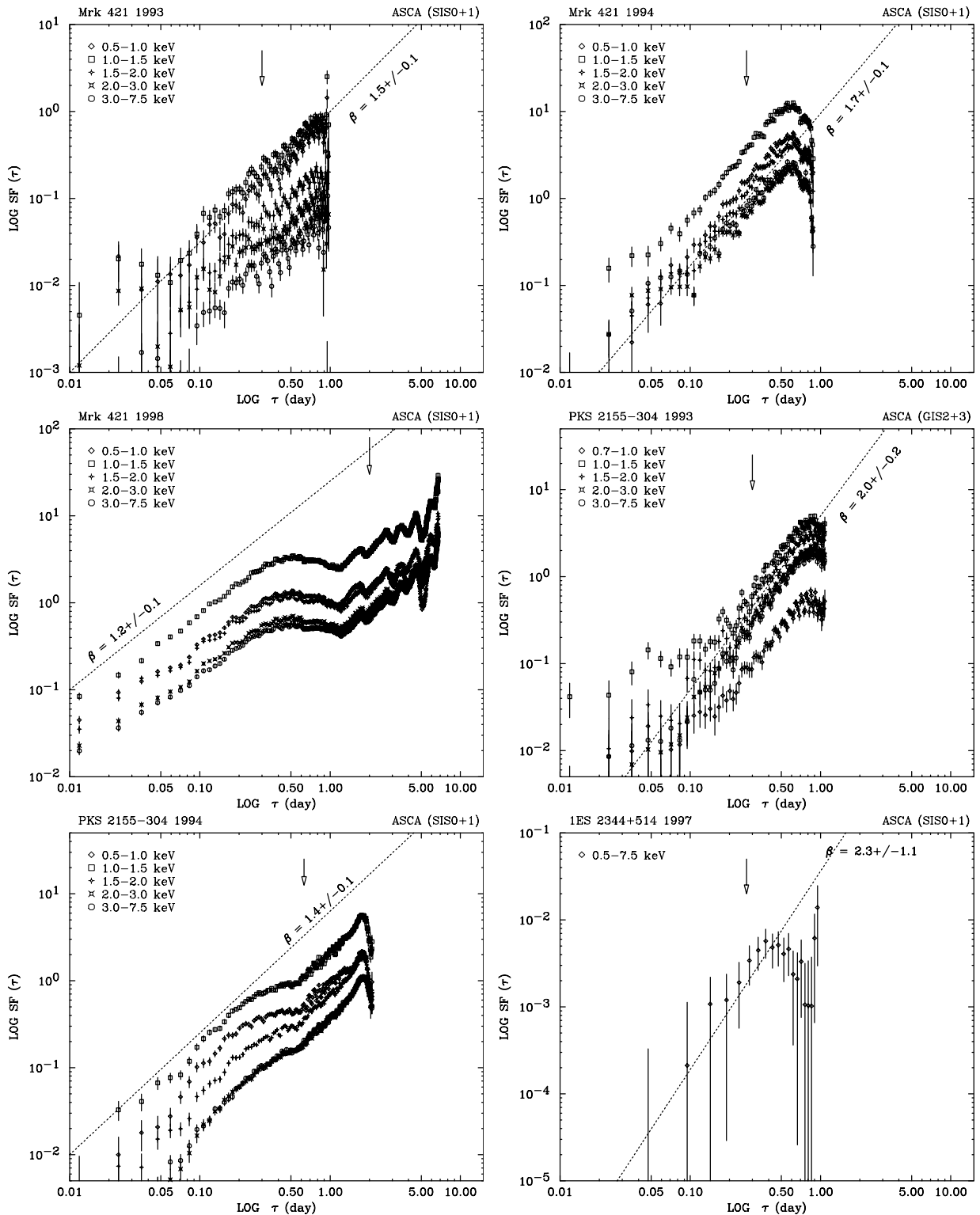
Figure 7.12: 1st order structure function of Mrk 421 (1993; 1994; 1998), PKS 2155−304 (1993; 1994) and 1ES 2344+514. The SFs of various energy bands are shown separately. SF(τ) was fitted by a power law $\propto \tau^\beta$ in the time domain $0 < \tau/\text{day} < 0.3$. The best fit index is given in each panel. Arrows indicate the points above which SF values contain uncertainties of more than factor 2. The SIS data were used, except for the PKS 2155−304 observation in 1993.
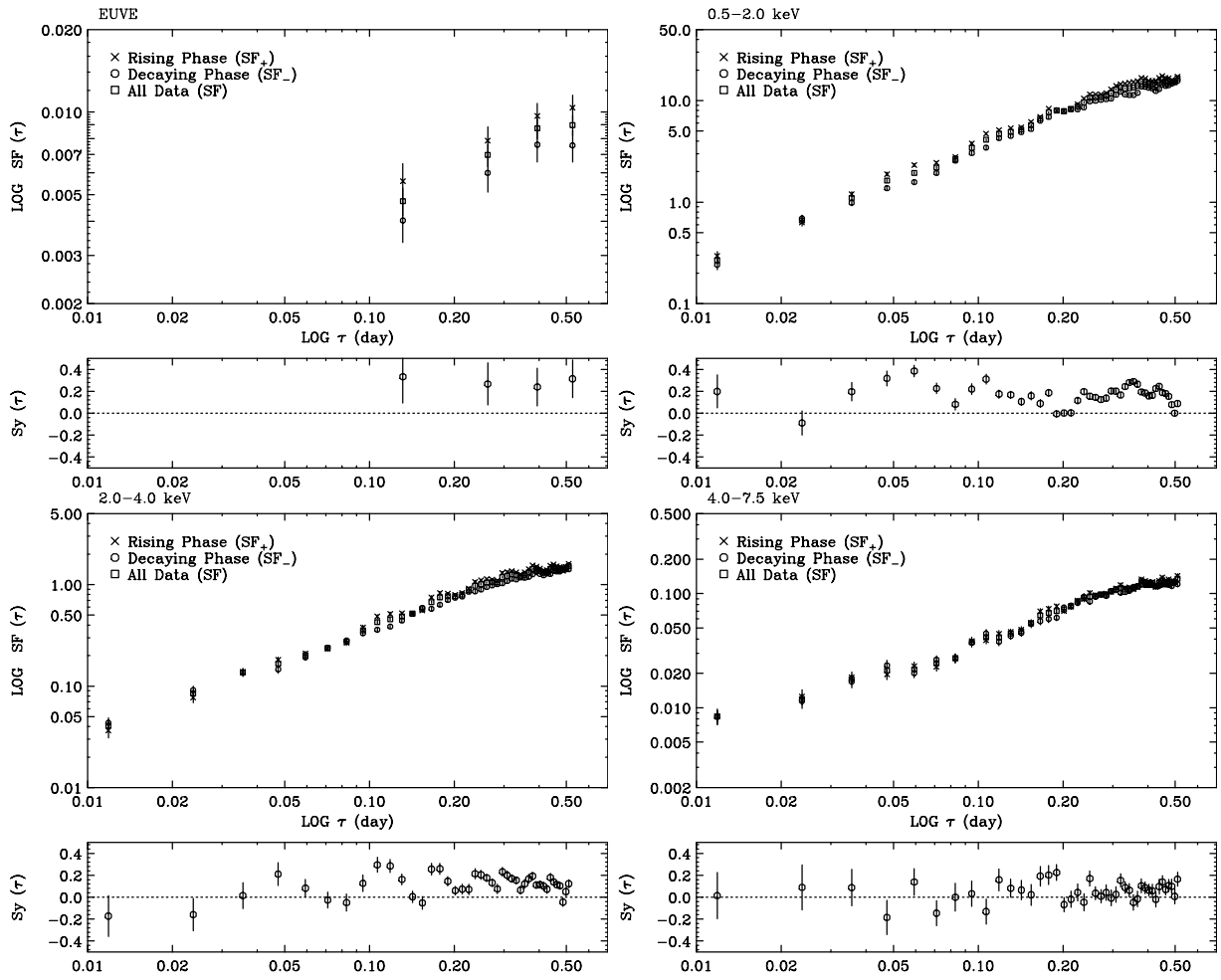
Figure 7.13: Symmetry of the light curves of Mrk 421 (1998) in various energy bands. *top*; 1st order structure function. The data from rising phase (SF$_+$) and decaying phase (SF$_-$) are separately shown (see, text). *bottom*; *symmetry* parameter which is defined as [SF$_+$−SF$_-$]/SF.
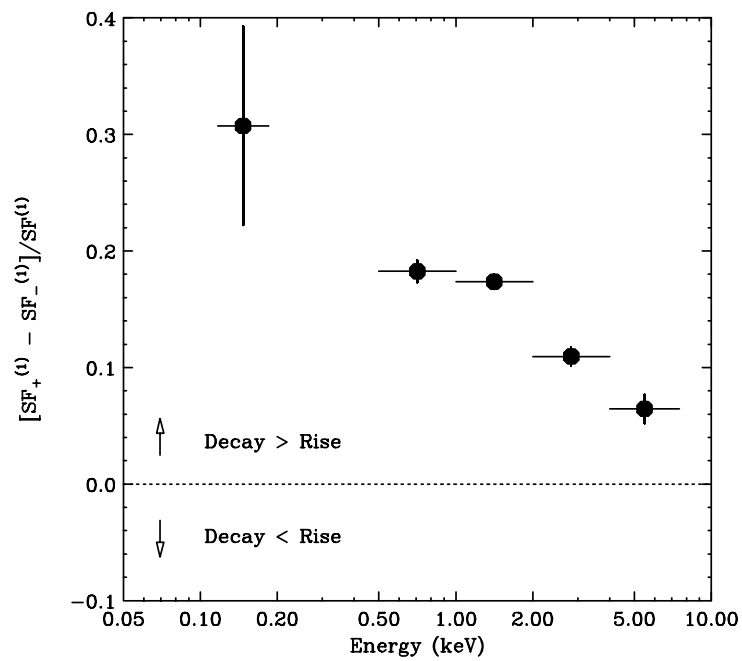
Figure 7.14: Energy dependence of the averaged symmetry parameter $\mathrm{Sy}(\tau) = [\mathrm{SF}_+ - \mathrm{SF}_-]/\mathrm{SF}$ for Mrk 421 observation in 1998. $\mathrm{Sy}(\tau)$ was averaged over the time lags smaller than 0.5 day. Light curves are almost symmetric, i.e., $[\mathrm{SF}_+ - \mathrm{SF}_-]/\mathrm{SF} \sim 0$ at higher energy band, but at lower energies, the symmetry tends to break down. Corresponding structure functions are given in Figure 7.13.

7.2.4 Spectral Evolutions

In the previous section § 7.2.2, we found that variability amplitude generally becomes larger at increasing photon energy, but on shorter time scales, variety exists as shown in Figure 7.9. Such flare-by-flare behavior may be associated with different spectral evolution of each flare event. Actually, when the variability is larger in a higher energy band, the photon spectra become harder during the flare.

To characterize the spectral evolution of TeV blazars, we investigate the correlation between the count rates (0.7−7.5 keV) and the hardness ratio. We define the hardness ratio as the photon counts in higher energy band (2−7.5 keV) to those in lower energy band (0.7−2 keV). In this expression of the intensity versus hardness, we can also investigate the presence of characteristic hysteresis associated with the 'time-lags' in various energy bands (§ 2.2.3).

We concentrate on the spectral evolution during the continuous observations whose net exposure times were longer than 40 ksec (§ 6). The GIS count rates are used except for the Mrk 421 observation in 1998. In the subsequent analysis, in order to reduce errors and present the time evolution of hardness ratios more clearly, we rebinned the light curves at 6 ksec (12 ksec for 1ES 2344+514 to reduce errors).

Mrk 421

The relations between brightness (count rate) and the hardness ratio for 1993 and 1994 observations are shown in Figure 7.15. In both cases, the general trend is that the spectrum becomes steeper (i.e., relatively less photons in the high energy band) in the declining phase and harder in the brightening phase. Mrk 421 observation in 1994 (§ 7.2) shows the 'clockwise' hysteresis as reported by Takahashi et al. (1996; Figure 2.6). However, the re-analysis of 1993 observation shows a hint of the reverse '*anti*-clockwise' hysteresis, which will be discussed later (§ 7.2.5).

For the 7-day observation in 1998, the spectral evolution in time-segments #2−9 (Figure 7.8) is shown in the separate panels of Figure 7.16. Note that the hardness ratio increased significantly during four of the flares (segments #2, 5, 7, 9) while in others, it did not (segments #3, 4, 6, 8). These results are consistent with what is expected from the energy dependence of the variability amplitude (Figure 7.9).

Strikingly, the spectral evolutions show a complex mixture of the 'clockwise' motions (segments #2, 4), '*anti*-clockwise' motions (segments #3, 6, 8), and 'no significant hysteresis' (segments #5, 7, 9). This clearly indicates that not only the variability amplitudes but also the time-lags may vary flare-by-flare.
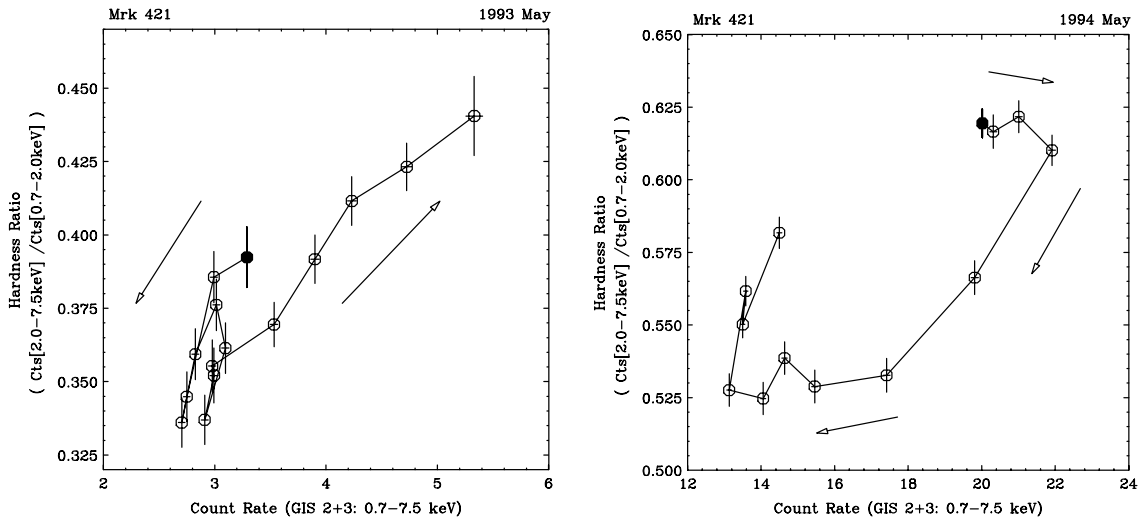
Figure 7.15: The GIS 2+3 count rate (0.7−7.5 keV) versus hardness ratio for Mrk 421 1993 (*left*) and 1994 observations (*right*). Each point represents 6 ksec integration. The large filled circle represents the start point of the observation.

PKS 2155−304

The relation of brightness (count rate) and the hardness ratio for 1993 and 1994 observations of PKS 2155−304 is shown in Figure 7.17. In both cases, the general trend is that the spectrum becomes steeper in the declining phase and harder in the brightening phase, similar to the case for Mrk 421. The figure of 1994 observation shows a clear 'clockwise' hysteresis during the first large-flare (Kataoka et al. 2000), while 1993 observation shows no significant hysteresis. For this particular source, Sembay et al. (1993) has reported both 'clockwise' and the '*anti*-clockwise' patterns using the *GINGA* data.

1ES 2344−514

The relation of brightness (count rate) and the hardness ratio for 1997 observation of 1ES 2344+514 is shown in Figure 7.18. Unfortunately, variability trend is not clear because the source was faint and less variable during the observation.

7.2.5   Search for Time Lags and Time Leads

In the previous section, we found a hint of energy dependent 'time-lags' via the analysis of variability of energy-binned light curves, which causes the diversity in the observed spectral evolution. Importantly, the clockwise hysteresis is expected when the time variations in the low energy band lag behind those in the high energy band, while *anti*-clockwise
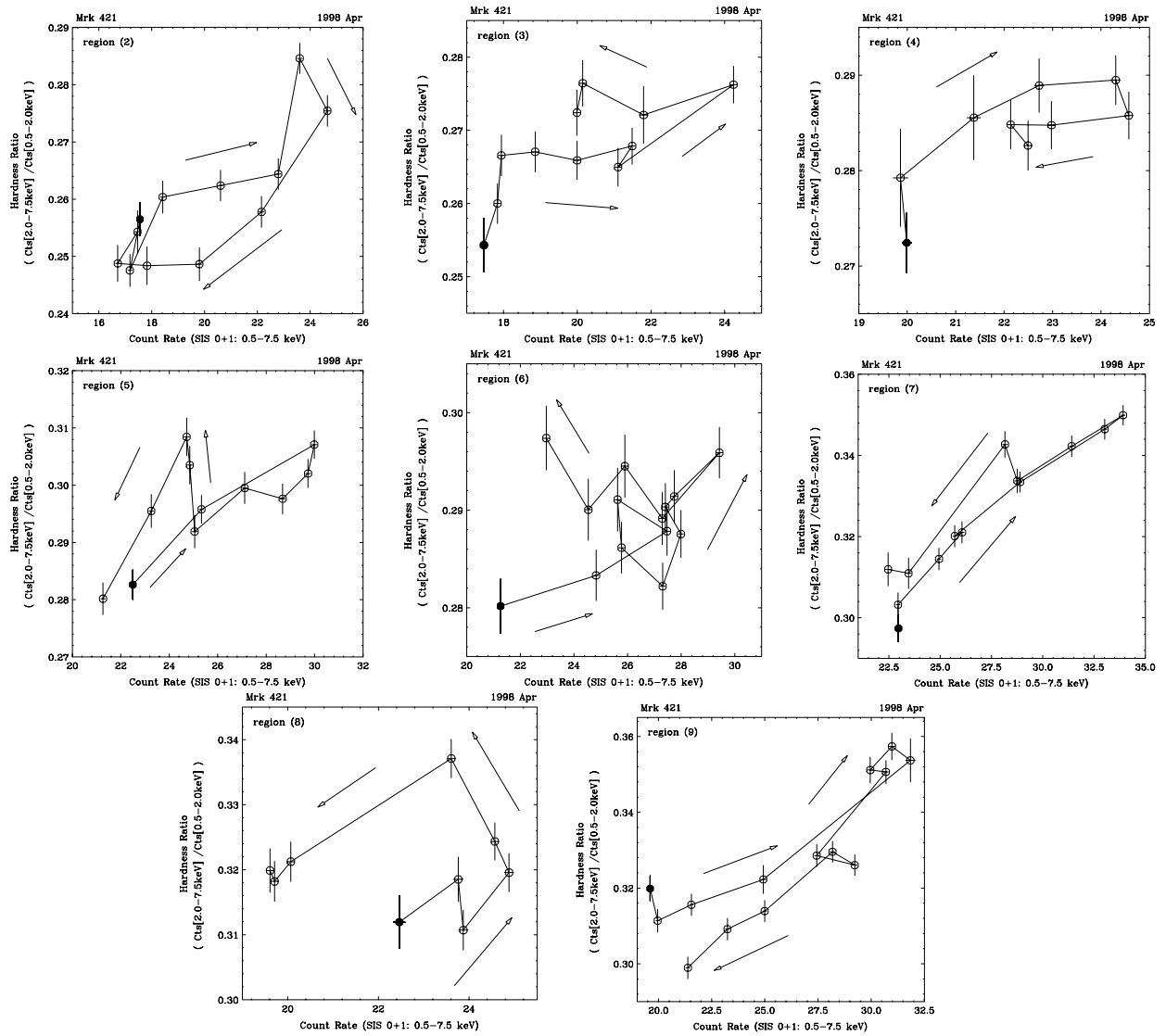
Figure 7.16: Spectral Evolutions of Mrk 421 in 1998 observation. Evolutions in 8 time-segments (#2–9), which were defined in Figure 7.8, are separately shown. Arrows indicates the direction of evolution in the count rate versus hardness ratio plane.

motion is expected in the opposite case (Kirk, Rieger & Mastichiadis 1998; see also § 2.2.3). In this section, we evaluate the time lags more quantitatively in various energy bands.

Discrete Correlation Function (DCF)

In order to study the time series in various energy bands quantitatively, we apply the discrete correlation function given by Edelson & Krolik (1988). This technique was specifically designed to analyze unevenly sampled data sets. The first step is to calculate the
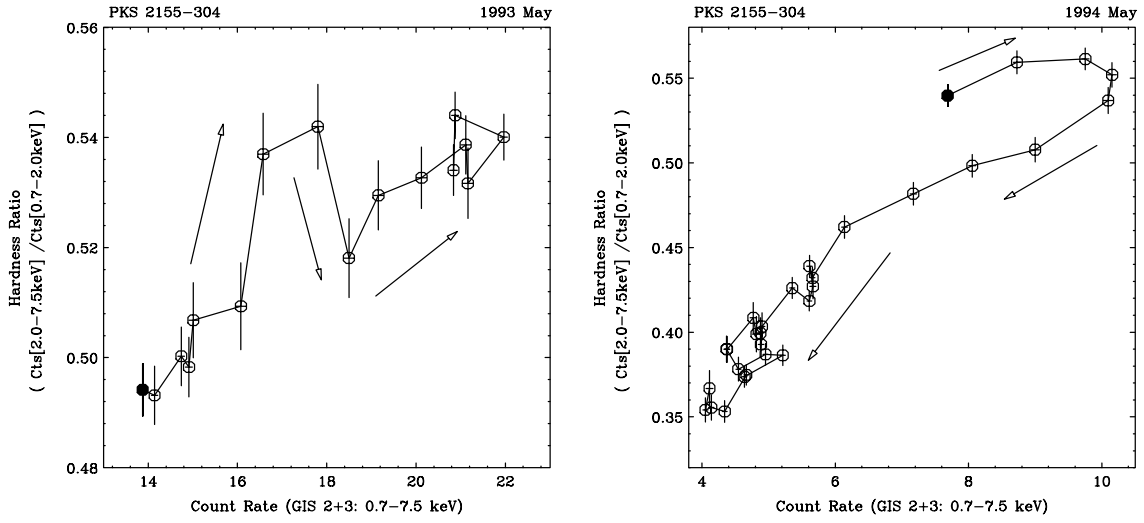
Figure 7.17: The GIS 2+3 count rate (0.7−7.5 keV) versus hardness ratio of PKS 2155−304. *left*: 1993 observation and *right*: 1994 observation. Each point represents 6 ksec integration. The large filled circle is the start point of the observation.
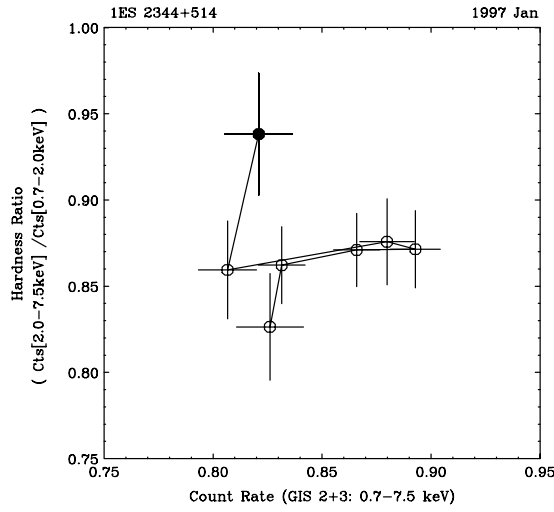
Figure 7.18: The GIS 2+3 count rate (0.7−7.5 keV) versus hardness ratio for 1ES 2344+514 observation. Each point represents 6 ksec integration. The large filled circle is the start point of the observation.

set of unbinned discrete correlation functions (UDCF) between each data point in the two data streams. This is defined in the time domain as

$$\mathrm{UDCF}_{ij} = \frac{(a_i - \bar{a})(b_j - \bar{b})}{\sqrt{\sigma_a^2 \sigma_b^2}}, \qquad (7.9)$$

where a_i and b_j are points of the data set $\{a\}$ and $\{b\}$, $\bar{a}$ and $\bar{b}$ are the means of the data sets, and σ_a and σ_b are the standard deviation of each data set. The discrete correlation

function (DCF) for each time lag τ is defined as an average of the UDCF that have the separation time of $\tau - \Delta\tau/2 \leq \Delta t_{ij} \leq \tau + \Delta\tau/2$,

$$\mathrm{DCF}(\tau) = \frac{1}{M} \sum \mathrm{UDCF}_{ij}(\tau), \tag{7.10}$$

where M is the number of pairs in the bin.

The advantage of the DCF lies in the fact that it uses all the data points available, does not introduce new errors through interpolation, and calculates a meaningful error estimates. The standard error for each bin is calculated as

$$\sigma_{\mathrm{DCF}} = \frac{1}{M-1} (\sum [\mathrm{UDCF}_{ij} - \mathrm{DCF}(\tau)]^2)^{1/2}. \tag{7.11}$$

In the following, we calculated the time lags of flux variations in four energy bands ($0.5-1.0$ keV, $1.0-1.5$ keV, $1.5-2.0$ keV, and $2.0-3.0$ keV) as compared to that in the $3.0-7.5$ keV band, using the DCF technique. Both the SIS and the GIS light curves were used for the analysis. The error on the lag was determined from the uncertainty ($1~\sigma$ error) of the peak parameter obtained by the minimum χ^2 fitting of the DCF distribution to a Gaussian. We also evaluate the errors on the lag using the Monte Calro simulation taking the uncertainties in fluxes into account. We found that both estimates of errors are exactly consistent as described in Appendix C.

Mrk 421 (1993)

The result of Mrk 421 observation in 1993 is shown in Figure 7.19. As indicated from the *anti*-clockwise motion shown in Figure 7.15, one finds that the soft X-ray variability *leads* that in hard X-rays by 5 ksec.

Mrk 421 (1994)

For the Mrk 421 observation in 1994, we see a canonical 'soft-lag' as shown in Figure 7.20. We find that the soft X-ray variation lags behind that in the harder ($3.0-7.5$ keV) X-ray band by 6 ksec, which is consistent with the results reported in Takahashi et al. (1996).

PKS 2155−304 (1993)

The DCF distributions for PKS 2155−304 observation in 1993 are shown in Figure 7.21. As indicated from no significant hysteresis (Figure 7.17), no significant time lags are found between the hard X-rays and the soft X-rays.
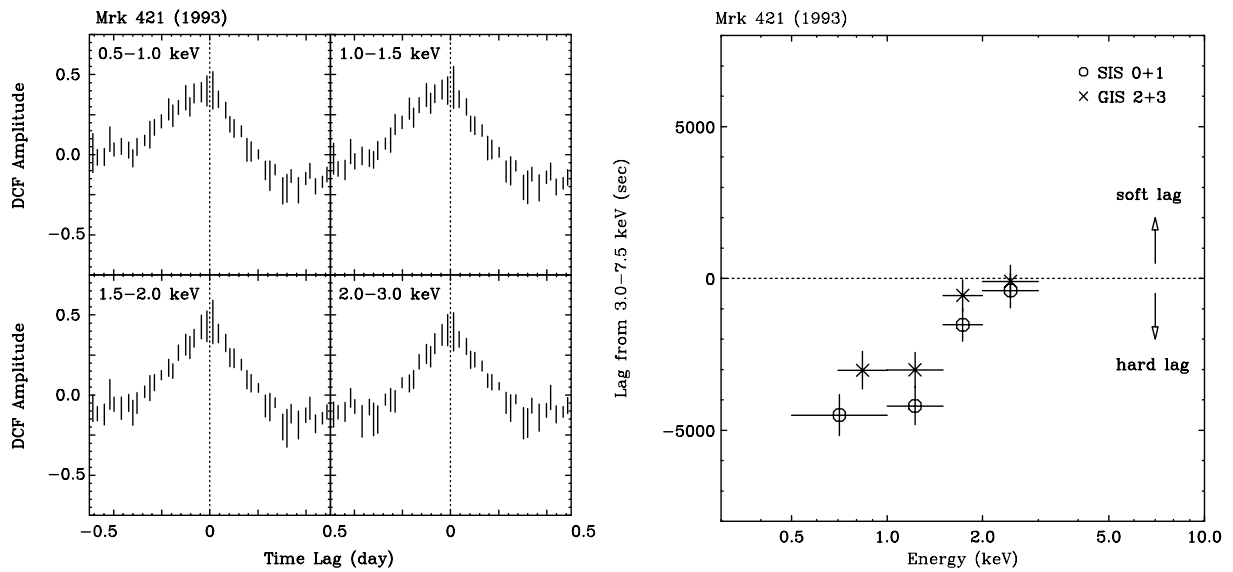
Figure 7.19: *left*; Discrete correlation function of Mrk 421 in 1993. *right*; Time lag of Mrk 421 in 1993.
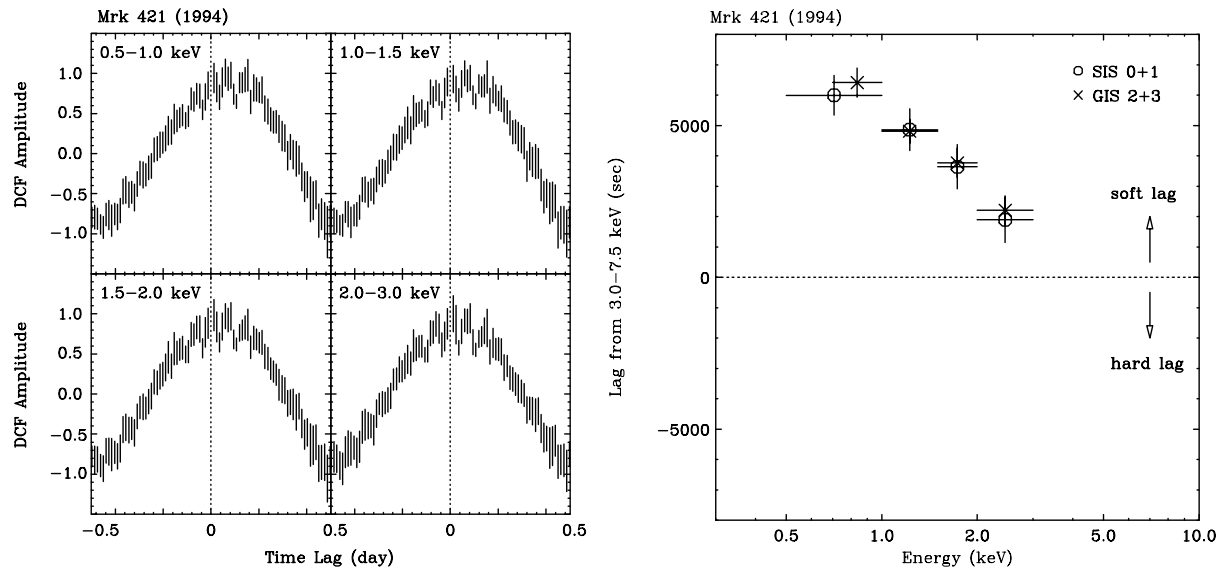
Figure 7.20: *left*; Discrete correlation function of Mrk 421 in 1994. *right*; Time lags of Mrk 421 in 1994.

PKS 2155−304 (1994)

The results for PKS 2155−304 observation in 1994 are shown in Figure 7.22. Although the rising portion of the flare has not been observed, this provides a well-defined and well-sampled light curve for an isolated large flare (see also § 10.2). We found that the
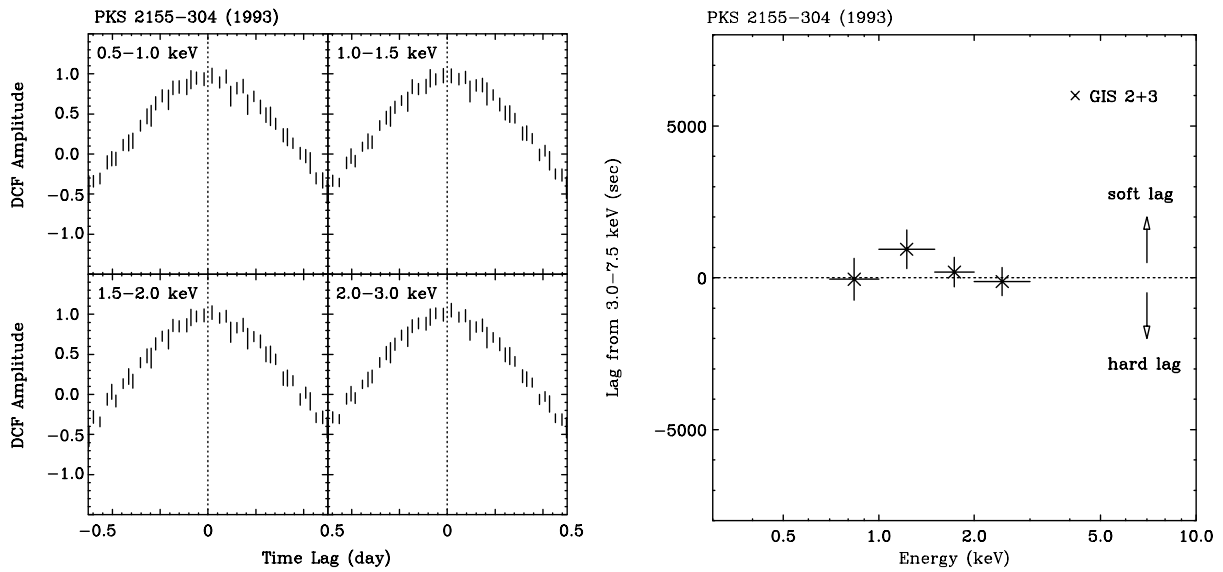
Figure 7.21: *left*; Discrete correlation function of PKS 2155−304 in 1993. *right*; Time lags of PKS 2155−304 in 1993.

soft X-ray variability lags behind that in harder X-rays by 4 ksec (Kataoka et al. 2000).
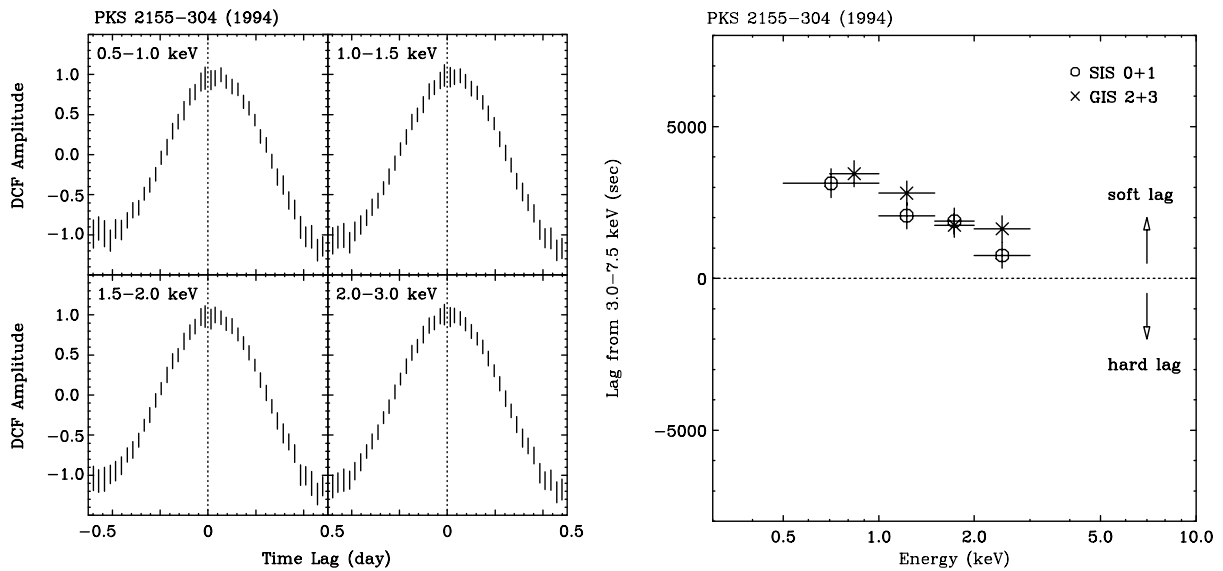
Figure 7.22: *left*; Discrete correlation function of PKS 2155−304 in 1994. *right*; Time lags of PKS 2155−304 in 1994.

Mrk 421 (1998)

For the Mrk 421 data obtained in 1998, we separately calculated the DCFs for eight time-segments (#2−9) defined in Figure 7.8. The DCF distributions for individual time segments are given in Appendix B. Calculated time-lags in four energy bands as compared to 3.0−7.5 keV band are summarized in Figure 7.23. For time segments #2 and 3, we also calculate the time lags using the GIS data, because the source was in a relatively low state and the telemetry was not saturated (§ 7.1.1). The GIS results are consistent with the SIS data.
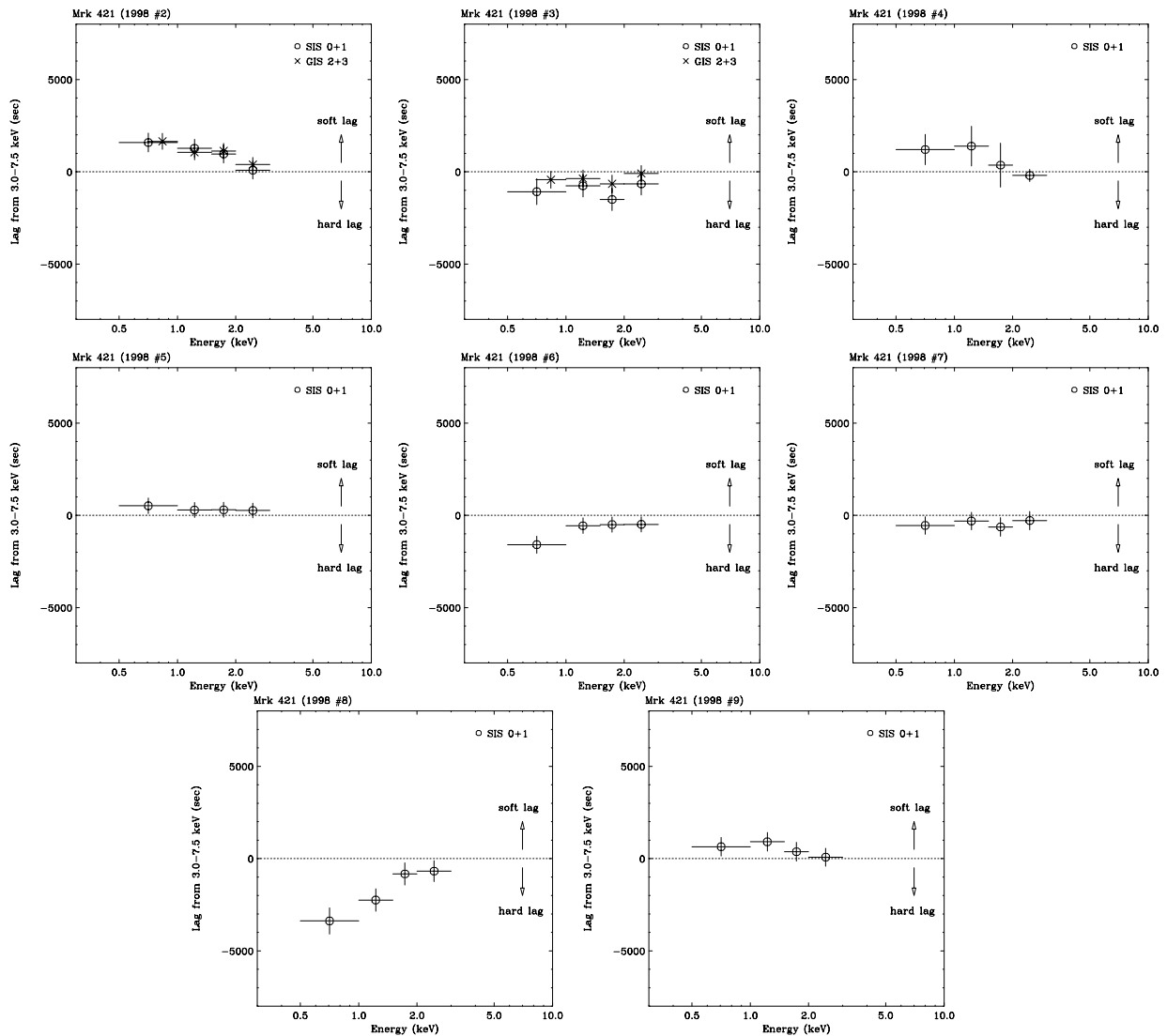
Figure 7.23: Time lags of Mrk 421 in 1998. Time lags in eight time segments (#2-9) defined in Figure 7.8 are separately shown. The DCF distributions for corresponding time segments are given in Appendix B.

We detected the complicated mixture of 'soft lag' (segments #2, 4) and 'hard lag' (segments #3, 6, 8), with several segments showing no apparent time-lag (segments #5, 7, 9). These results are in agreement with the implications from loopwise patterns (Figure 7.16).

We also applied the same analysis for the light curves after subtraction of the general trend in the light curves. We confirmed that the result presented in this section is not affected by the *pileup* of flares. Full details are given in Appendix C.

Combining the above findings with the results shown in § 7.2.2, we notice that the 'hard-lag' flares (region #3, 6, 8) may be associated with the flares whose variabilities have less dependence on energy (Figure 7.9). To see this more clearly, we plot the time-lags versus variability ratio in two energy bands, $F_{\mathrm{var}}(3.0-7.5 \mathrm{\ keV})/F_{\mathrm{var}}(0.5-1.0 \mathrm{\ keV})$ in Figure 7.24. Interestingly, an apparent correlation can be seen (the correlation coefficient is 0.7), but more data are necessary to deduce further conclusions.
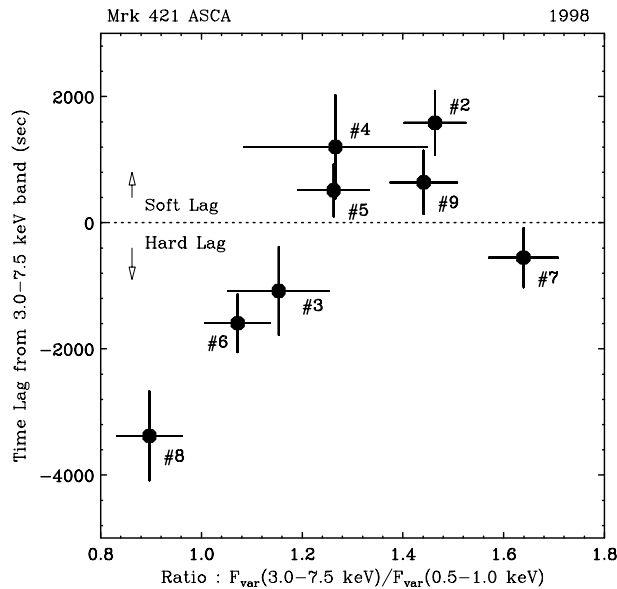
Figure 7.24: Ratio of variabilities in low energy band and high energy band, $F_{\mathrm{var}}(3.0\text{-}7.5 \mathrm{\ keV})/F_{\mathrm{var}}(0.5\text{-}1.0 \mathrm{\ keV})$, versus time lags calculated from the DCF. Data from Mrk 421 observation in 1998.

# 7.3	Results from Spectral Studies

We performed model fitting to evaluate the photon spectra of blazars. We made the source spectra for the image regions shown in Table 7.2 for observations listed in Table 6.2−6.5. The SIS and the GIS spectra after the background subtraction are shown in Appendix D. All spectra were fitted with the XSPEC version 10.00 provided by NASA/GSFC. The detector response of the SIS is generated from *sisrmg* version 4.2. We use the response version 4.0 for the GIS and 2.10 for the XRT.

## 7.3.1	Fit with a Power Law Function plus Absorption

We first fitted the spectrum with a power law function plus absorption arising from neutral material. The model function gives

$$\frac{dN}{dE} = N_0 \times \exp(-N_{\rm H} \times \sigma(E)) \times E^{-\Gamma}, \tag{7.12}$$

where N_0 is the normalization in unit of photons/cm^2/s/keV, Γ is the photon spectral index, and $\sigma(E)$ is the cross section for photo-electric absorption with solar abundances taken from Morrison & McCammon (1983). The absorbing column was parameterized in terms of the equivalent Hydrogen column density $N_{\rm H}$ (Table 6.1).

As the first step, we fixed the column density at the Galactic column density. The results are listed in the Table 7.3. Formally, none of the fits are acceptable, meaning that the probability $P(\chi^2) < 1\%$. One can imagine three reasons for this: (i) photon spectra are not well expressed by a power law form; (ii) photon spectra evolve significantly during the observation; and (iii) consistency between the SIS and the GIS detectors is not good at the lowest energy band ($E < 1$ keV; see below).

In the second step, we fitted the spectrum with the column density $N_{\rm H}$ allowed to be free. We are aware that this is an unphysical model in the sense that the $N_{\rm H}$ can vary with the spectral form, which is unlikely. However, when the spectrum is gradually bending at higher energy bands from a power law form, this can be a convenient expression of the data. The results are also shown in Table 7.3. The fits are significantly improved over those obtained for a fixed $N_{\rm H}$. The best fit values of absorption much larger than the Galactic means that the spectra are convex (i.e., gradually steepening toward higher energy). In order to see the convex spectra of TeV blazar, we fit the data below 1 keV with a power law function plus Galactic absorption (Figure 7.25). large residuals in the ratio of the model to the data above 2 keV are clearly present (*top* and *middle*). The data were taken from the Mrk 421 observation in 1998. We also show the residuals to the power law function with free absorption, where the entire energy bandpass was used

Table 7.3: Fit results of *ASCA* spectra with a power law function plus absorption

Source Name	Start Date	N_H $10^{20}/cm^2$	Photon Index	Flux (2-10keV) 10^{-12} erg/cm^2/s	χ^2 (d.o.f)	N_H $10^{20}/cm^2$	Photon Index	χ^2 (d.o.f)
Mrk421	1993.05.10$^\sharp$	$9.38^{+0.29}_{-0.29}$	$2.97^{+0.01}_{-0.01}$	24.3 ± 0.1	2.43(1203)	1.45fix	$2.79^{+0.00}_{-0.00}$	3.10(1204)
	1994.05.16$^\sharp$	$9.91^{+0.15}_{-0.15}$	$2.37^{+0.00}_{-0.00}$	256 ± 0.5	2.70(1605)	1.45fix	$2.22^{+0.00}_{-0.00}$	4.81(1606)
	1995.04.25$^\sharp$	$13.55^{+0.30}_{-0.30}$	$2.48^{+0.01}_{-0.01}$	221 ± 0.9	1.35(1369)	1.45fix	$2.26^{+0.00}_{-0.00}$	2.69(1370)
	1995.04.28$^\sharp$	$11.49^{+0.36}_{-0.36}$	$2.44^{+0.01}_{-0.01}$	194 ± 0.9	1.88(1268)	1.45fix	$2.25^{+0.00}_{-0.00}$	2.55(1269)
	1995.04.29$^\sharp$	$12.13^{+0.32}_{-0.32}$	$2.58^{+0.01}_{-0.01}$	152 ± 0.7	1.47(1268)	1.45fix	$2.37^{+0.00}_{-0.00}$	2.42(1269)
	1995.05.01$^\sharp$	$12.21^{+0.37}_{-0.37}$	$2.58^{+0.01}_{-0.01}$	124 ± 0.7	1.36(1159)	1.45fix	$2.42^{+0.00}_{-0.00}$	2.16(1160)
	1995.05.03$^\sharp$	$11.65^{+0.46}_{-0.47}$	$2.71^{+0.01}_{-0.01}$	63.2 ± 0.7	1.19(1001)	1.45fix	$2.49^{+0.01}_{-0.01}$	1.71(1002)
	1995.05.05$^\sharp$	$12.63^{+0.46}_{-0.45}$	$2.77^{+0.02}_{-0.02}$	62.2 ± 0.4	1.19(998)	1.45fix	$2.54^{+0.01}_{-0.01}$	1.99(999)
	1995.05.06$^\sharp$	$12.25^{+0.48}_{-0.47}$	$2.83^{+0.01}_{-0.01}$	52.7 ± 0.4	1.10(965)	1.45fix	$2.60^{+0.01}_{-0.01}$	1.68(966)
	1995.05.08$^\sharp$	$9.89^{+0.55}_{-0.54}$	$2.67^{+0.01}_{-0.01}$	42.1 ± 0.3	1.20(916)	1.45fix	$2.50^{+0.01}_{-0.01}$	1.48(917)
	1996.12.15$^\sharp$	$15.10^{+0.63}_{-0.62}$	$3.06^{+0.02}_{-0.02}$	28.5 ± 0.3	1.36(772)	1.45fix	$2.75^{+0.01}_{-0.01}$	2.05(773)
	1997.04.29$^\sharp$	$17.15^{+0.39}_{-0.38}$	$2.72^{+0.01}_{-0.01}$	108 ± 0.6	1.58(1169)	1.45fix	$2.41^{+0.00}_{-0.00}$	3.20(1170)
	1997.04.30$^\sharp$	$16.83^{+0.40}_{-0.39}$	$2.77^{+0.01}_{-0.01}$	102 ± 0.6	1.61(1125)	1.45fix	$2.46^{+0.00}_{-0.00}$	3.12(1126)
	1997.05.01$^\sharp$	$16.77^{+0.30}_{-0.30}$	$2.72^{+0.01}_{-0.01}$	150 ± 0.6	1.76(1283)	1.45fix	$2.42^{+0.00}_{-0.00}$	4.05(1284)
	1997.05.03$^\sharp$	$15.71^{+0.45}_{-0.44}$	$2.81^{+0.01}_{-0.01}$	76.5 ± 0.5	1.47(1030)	1.45fix	$2.51^{+0.00}_{-0.00}$	2.58(1031)
	1997.05.04	$14.84^{+0.54}_{-0.54}$	$3.00^{+0.01}_{-0.02}$	43.2 ± 0.4	1.23(850)	1.45fix	$2.70^{+0.01}_{-0.01}$	2.02(851)
	1997.05.06$^\sharp$	$15.33^{+0.46}_{-0.45}$	$2.86^{+0.01}_{-0.01}$	63.3 ± 0.4	1.41(992)	1.45fix	$2.57^{+0.01}_{-0.00}$	2.45(993)
	1997.06.02$^\sharp$	$18.21^{+0.25}_{-0.24}$	$2.53^{+0.00}_{-0.00}$	317 ± 0.9	2.86(1444)	1.45fix	$2.22^{+0.01}_{-0.01}$	6.67(1445)
	1998.04.23$^\sharp$	$17.03^{+0.64}_{-0.59}$	$2.53^{+0.00}_{-0.00}$	325 ± 0.3	18.5(1609)	1.45fix	$2.27^{+0.00}_{-0.00}$	64.8(1610)
Mrk501	1996.03.21	$11.25^{+0.49}_{-0.49}$	$2.17^{+0.01}_{-0.01}$	98.2 ± 1.0	1.25(1186)	1.73fix	$2.00^{+0.01}_{-0.01}$	1.60(1187)
	1996.03.26	$11.77^{+0.54}_{-0.53}$	$2.23^{+0.01}_{-0.01}$	74.9 ± 0.5	1.16(1106)	1.73fix	$2.06^{+0.01}_{-0.01}$	1.51(1107)
	1996.03.27	$12.16^{+0.61}_{-0.61}$	$2.36^{+0.01}_{-0.01}$	55.1 ± 0.4	1.14(958)	1.73fix	$2.17^{+0.01}_{-0.01}$	1.47(959)
	1996.04.02	$13.09^{+0.61}_{-0.60}$	$2.45^{+0.01}_{-0.01}$	46.0 ± 0.4	1.11(948)	1.73fix	$2.23^{+0.01}_{-0.01}$	1.52(949)
	1998.07.18$^\sharp$	$13.90^{+0.40}_{-0.40}$	$2.00^{+0.01}_{-0.01}$	129 ± 0.7	1.33(1406)	1.73fix	$1.82^{+0.00}_{-0.00}$	2.06(1407)
	1998.07.20	$13.28^{+0.43}_{-0.43}$	$2.02^{+0.01}_{-0.01}$	114 ± 0.6	1.21(1360)	1.73fix	$1.84^{+0.00}_{-0.00}$	1.79(1361)
	1998.07.21	$13.77^{+0.41}_{-0.41}$	$1.99^{+0.01}_{-0.01}$	144 ± 0.8	1.21(1407)	1.73fix	$1.80^{+0.00}_{-0.00}$	2.01(1408)
	1998.07.23	$12.98^{+0.45}_{-0.45}$	$2.08^{+0.01}_{-0.01}$	110 ± 0.7	1.24(1317)	1.73fix	$1.90^{+0.00}_{-0.00}$	1.77(1318)
PKS2155 −304	†1993.05.03$^\sharp$	$7.18^{+0.23}_{-0.23}$	$2.44^{+0.00}_{-0.01}$	252 ± 0.8	1.95(1459)	1.77fix	$2.34^{+0.00}_{-0.00}$	2.34(1460)
	1994.05.19$^\sharp$	$9.45^{+0.16}_{-0.16}$	$2.68^{+0.00}_{-0.00}$	72.4 ± 0.2	2.96(1560)	1.77fix	$2.53^{+0.00}_{-0.00}$	4.57(1561)
	1996.05.22$^\sharp$	$17.56^{+0.54}_{-0.54}$	$2.47^{+0.01}_{-0.01}$	155 ± 1.0	1.76(1063)	1.77fix	$2.18^{+0.01}_{-0.01}$	2.66(1064)
	1996.05.24$^\sharp$	$16.90^{+0.48}_{-0.48}$	$2.72^{+0.01}_{-0.01}$	99.4 ± 0.6	1.78(1036)	1.77fix	$2.42^{+0.01}_{-0.01}$	2.86(1037)
	1996.05.26$^\sharp$	$14.44^{+0.38}_{-0.37}$	$2.48^{+0.01}_{-0.01}$	122 ± 0.5	2.11(1251)	1.77fix	$2.24^{+0.01}_{-0.01}$	3.12(1252)
	1996.11.14$^\sharp$	$12.57^{+0.44}_{-0.43}$	$2.79^{+0.01}_{-0.01}$	43.4 ± 0.3	1.66(1023)	1.77fix	$2.56^{+0.01}_{-0.01}$	2.32(1024)
	1996.11.15$^\sharp$	$10.05^{+0.44}_{-0.43}$	$2.67^{+0.01}_{-0.01}$	41.2 ± 0.3	1.45(1070)	1.77fix	$2.49^{+0.00}_{-0.01}$	1.81(1071)
1ES2344 +514	1997.01.10	$27.65^{+0.86}_{-0.85}$	$2.13^{+0.02}_{-0.02}$	16.0 ± 0.1	1.17(1038)	16.0fix	$1.95^{+0.01}_{-0.01}$	1.37(1039)
	1997.01.23	$30.43^{+1.88}_{-1.85}$	$2.42^{+0.04}_{-0.04}$	9.74 ± 0.2	1.02(435)	16.0fix	$2.18^{+0.02}_{-0.02}$	1.17(436)
	1997.12.20	$26.00^{+2.01}_{-1.88}$	$2.21^{+0.04}_{-0.04}$	9.46 ± 0.2	1.08(441)	16.0fix	$2.05^{+0.02}_{-0.02}$	1.14(442)

† : Both the SIS and the GIS data were used, but the data taken at medium bit rate were not used because of the strong telemetry saturation.

$^\sharp$: The source was variable during the observation. Probability for constant fit of the light curve was $P(\chi^2) < 1$ %.

All errors are 1 σ.

(Figure 7.25 (*bottom*)).

However, we must note that most of the fit are still unacceptable. As suggested by the rapid time variability and the changes in the hardness ratio (§ 7.2.4), the X-ray spectra

Figure 7.25: *ASCA* SIS0 spectrum fitted to a power law function. *top*; The SIS0 data for Mrk 421 obtained from 1998 04/24 00:48:20 to 04/24 01:45:00, fitted to a power law function with Galactic absorption. Only the data below 1.0 keV was used for the fit. *center*; residuals to a power law function with Galactic absorption. *bottom*; residuals to a power law function with free absorption, where the entire SIS0 bandpass was used.

of the TeV blazars evolve significantly during the observation. Thus in the third step, we divided the observation into short time intervals not to be affected by variations of photon spectra. We cut the exposure into 5 ksec segments for each and fitted the photon spectra for individual time segments. In this case, acceptable fits were obtained ($P(\chi^2) >$ 1%) except for some of the data obtained in 1997/1998 observations (Mrk 421 and Mrk 501; see § 6).

For these recent observations, we have to consider effects caused by the degradation of the on-board detectors more carefully, in particular the SIS. Lower energy region (E < 1 keV) is reported to be affected by the SIS degradation. According to Yamashita et al. (1999) and Dotani et al. (1999; private communication), the SIS data shows 'flatter' spectrum than the real spectrum. The discrepancy between the SIS and the GIS spectra might be explained by this effect. In this case, we also test the case where only $1.0 - 7.5$ keV photons are used for the fit. We obtained satisfactory fits in those cases.

The results of combined fit of the SIS/GIS spectra taken from 1998 observation of Mrk 421 are listed in Table 7.4. We selected the time region from 1998 04/24 00:48:20 to 04/24 01:45:00, because these intervals are exactly overlapped with *BeppoSAX* ob-

servation, hence the cross-check of the results is possible. We also note that during this interval, the source counts are relatively low and we can use the GIS data as well (§ 7.1.3). The best fit parameters determined respectively by fitting the SIS0, SIS1, GIS2 and GIS3 data are also shown in this Table 7.4. Confidence contour plots of spectral fits are given in Figure 7.26, where contour levels of 1 σ, 90 % and 99 % are shown.

Table 7.4: Results of spectral fitting of Mrk 421 with a power law function plus absorption.

Mission	Detector	$N_{\rm H}$	Photon	Flux (2-10keV)	χ^2
		$10^{20}/{\rm cm}^2$	Index	10^{-12} erg/cm^2/s	(d.o.f)
ASCA	SIS0	$13.80^{+1.90}_{-1.87}$	$2.66^{+0.05}_{-0.05}$	145 ± 4.4	$1.18(98)$
	SIS1	$19.05^{+2.25}_{-2.19}$	$2.79^{+0.06}_{-0.06}$	132 ± 4.7	$1.10(111)$
	GIS2	$5.41^{+3.12}_{-3.04}$	$2.62^{+0.06}_{-0.05}$	149 ± 4.1	$0.79(189)$
	GIS3	$5.61^{+2.75}_{-2.68}$	$2.65^{+0.05}_{-0.05}$	155 ± 3.8	$0.94(205)$
	combine (0.7-7.5 keV)	$16.13^{+1.12}_{-1.10}$	$2.72^{+0.03}_{-0.03}$	146 ± 2.1	$1.17(611)$
	combine (1.0-7.5 keV)	$16.90^{+2.40}_{-2.35}$	$2.72^{+0.03}_{-0.03}$	146 ± 2.1	$1.08(544)$

Data from 1998 04/24 00:48:20 to 04/24 01:45:00 were used for the fit, when *ASCA* and *BeppoSAX* observed Mrk 421 contemporaneously. Fitting model is a power law function plus free absorption. the *ASCA* energy band. All errors are 1 σ.
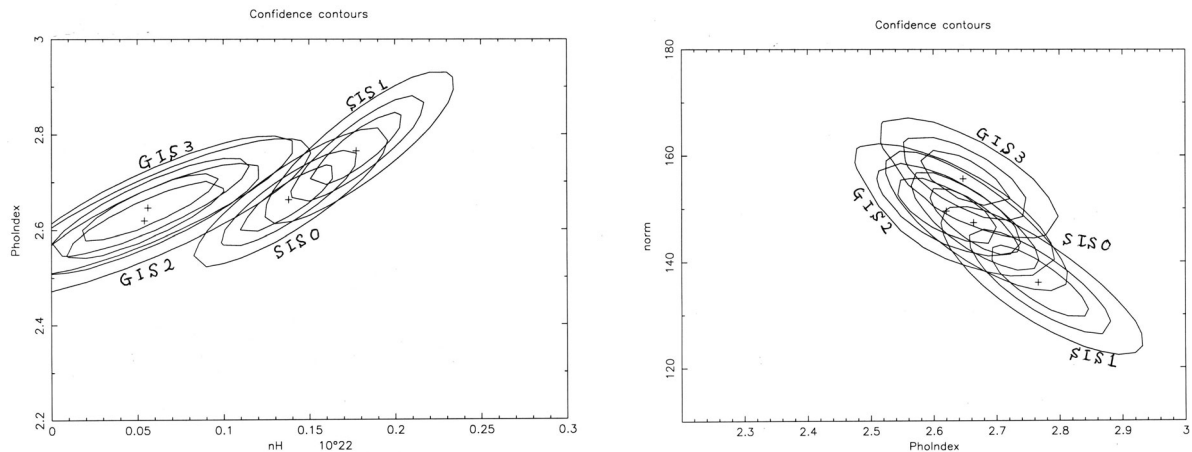
Figure 7.26: Confidence contour plots of spectral fitting for Mrk 421 observation in 1998. Data from 1998 04/24 00:48:20 to 04/24 01:45:00 were used, when *ASCA* and *BeppoSAX* observed Mrk 421 contemporaneously. Three contour levels for 1 σ, 90 % and 99 % errors are shown separately. The result are summarized in Table 7.4.

Results of fitting of all photon spectra of TeV blazars with a power law function plus free absorption, are summarized in Figure 7.27. This figure shows the distribution of luminosity and photon indices, where luminosity is simply calculated from the $2-10$ keV

flux multiplied by $4\pi d_{\rm L}^2$ (see, Table 6.1). One finds two clear trends from this figure; (i) the photon spectra are steeper for high luminosity sources, (ii) the spectra tend to be harder when the source becomes brighter. The latter corresponds to the general trend found in § 7.2.2 that the variability amplitude becomes larger at increasing photon energy. However, broad distribution of fluxes versus photon indices implies that a variety exists for individual flares, as was implied by the day-by-day flares observed in Mrk 421 (Figure 7.7).
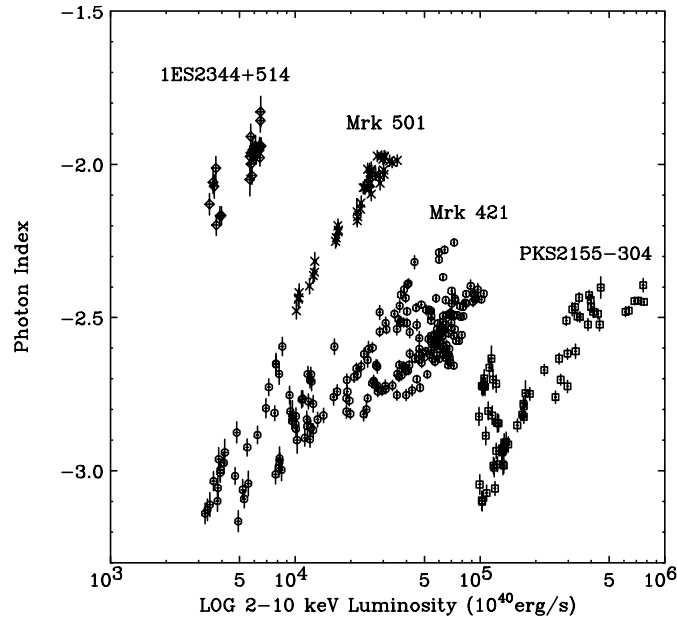
Figure 7.27: Distribution of luminosity and photon indices for all observations with *ASCA* . Mrk 421; from 1993 to 1998 data, Mrk 501; from 1996 to 1998 data, PKS 2155−304; from 1993 to 1996 data, 1ES 2344+514; from 1997 data. Fluxes are simply converted to luminosities by multiplying $4\pi d_{\rm L}^2$, where $d_{\rm L}$ is the luminosity distance.

7.3.2 Fit with a Cutoff Power Law Function

Since the photon spectra of TeV blazars show convex shape, we use another model which is expected to fit the spectrum

$$\frac{dN}{dE} = N_0 \times \exp(-N_{\mathrm{H}}^{\mathrm{Gal}} \times \sigma(E)) \times E^{-\Gamma} \times \exp(-E_{\mathrm{c}}/E), \qquad (7.13)$$

where Γ is the photon index and E_{c} is the cutoff energy, respectively. This model has two advantages. First, one does not need the Hydrogen column density to vary, which is more physical. Second, the function has a simpler form. One can differentiate the function analytically.

An intrinsic photon spectrum (Galactic absorption corrected) in νF_ν space (e.g., § 2) is expressed as

$$E^2 \frac{dN}{dE} = N_0 \times E^{2-\Gamma} \times \exp(-E_{\mathrm{c}}/E). \qquad (7.14)$$

The peak energy E_{p} and an associated error on E_{p} are given,

$$E_{\mathrm{p}} = \frac{E_{\mathrm{c}}}{\Gamma - 2} \quad (\Gamma > 2), \qquad \sigma_{E_{\mathrm{p}}} = \sqrt{\frac{1}{(\Gamma-2)^2}\sigma_{E_{\mathrm{c}}}^2 + \frac{E_{\mathrm{c}}^2}{(\Gamma-2)^4}\sigma_\Gamma^2}, \qquad (7.15)$$

where $\sigma_{E_{\mathrm{c}}}$ and σ_Γ are errors on E_{c} and Γ, respectively. One cannot determine E_{p} for $\Gamma \leq 2$, because in such cases, the spectra are monotonously rising in the total energy band.

The results are listed in Table 7.5. As were done for the free absorption model in § 7.3.1, we divided the observations into 5 ksec exposure segments and fitted the photon spectra for individual segments. In this case, statistically acceptable fit $(P(\chi^2) > 1\%)$ were obtained for all sources.

Figure 7.28 shows an example of the SIS0 spectrum fitted by the cutoff power law function and its residuals. Data are same as Figure 7.25, but the fitting model is the cutoff power law function. The result of combined fit of the SIS/GIS spectra taken from 1998 observation of Mrk 421 are listed in Table 7.6. Goodness of fit is almost equal to that for the free absorption model (Table 7.4).

Results from fitting all the photon spectra of TeV blazars with cutoff power law function are summarized in Figure 7.29. The distribution of peak luminosity L_{p} versus peak energy E_{p} is shown. The peak luminosity is simply calculated from the luminosity at $E = E_{\mathrm{p}}$. Four TeV blazars observed with *ASCA* have their peaks in the X-ray energy band; $0.5-2$ keV for Mrk 421, $1-4$ keV for Mrk 501, $0.5-1.6$ keV for PKS 2155$-$304 and $1.5-3$ keV for 1ES 2344+514.

One finds a clear correlation between the E_{p} and the L_{p} for both Mrk 421 and Mrk 501, while the correlation is not clear for PKS 2155$-$304. Correlations found for Mrk 421 and Mrk 501 are quite different; a luminosity change of an order of magnitude would

Table 7.5: Fit result of *ASCA* spectra with a cutoff power law function

Source Name	Start Date	N_{H} $10^{20}/\mathrm{cm}^2$	E_{c} keV	Photon Index	Flux (2-10keV) $10^{-12}\ \mathrm{erg/cm^2/s}$	χ^2 (d.o.f)
Mrk 421	1993.05.10$^\sharp$	1.45fix	$0.65^{+0.02}_{-0.02}$	$3.19^{+0.01}_{-0.01}$	24.0 ± 0.2	2.36(1203)
	1994.05.16$^\sharp$	1.45fix	$0.62^{+0.01}_{-0.01}$	$2.56^{+0.01}_{-0.01}$	253 ± 0.9	2.76(1605)
	1995.04.25$^\sharp$	1.45fix	$0.90^{+0.02}_{-0.02}$	$2.76^{+0.01}_{-0.01}$	217 ± 1.5	1.29(1369)
	1995.04.28$^\sharp$	1.45fix	$0.74^{+0.03}_{-0.03}$	$2.67^{+0.01}_{-0.02}$	192 ± 1.6	1.87(1268)
	1995.04.29$^\sharp$	1.45fix	$0.80^{+0.02}_{-0.02}$	$2.83^{+0.01}_{-0.01}$	150 ± 1.1	1.46(1268)
	1995.05.01$^\sharp$	1.45fix	$0.82^{+0.03}_{-0.03}$	$2.90^{+0.02}_{-0.02}$	122 ± 1.1	1.33(1159)
	1995.05.03$^\sharp$	1.45fix	$0.77^{+0.04}_{-0.04}$	$2.95^{+0.02}_{-0.02}$	62.4 ± 0.7	1.20(1001)
	1995.05.05$^\sharp$	1.45fix	$0.86^{+0.03}_{-0.03}$	$3.05^{+0.02}_{-0.02}$	61.4 ± 0.7	1.29(998)
	1995.05.06$^\sharp$	1.45fix	$0.83^{+0.04}_{-0.04}$	$3.09^{+0.02}_{-0.02}$	52.1 ± 0.6	1.09(965)
	1995.05.08$^\sharp$	1.45fix	$0.63^{+0.04}_{-0.04}$	$2.87^{+0.03}_{-0.02}$	41.7 ± 0.5	1.20(916)
	1996.12.15$^\sharp$	1.45fix	$1.05^{+0.05}_{-0.05}$	$3.40^{+0.03}_{-0.03}$	28.1 ± 0.5	1.38(772)
	1997.04.29$^\sharp$	1.45fix	$1.18^{+0.03}_{-0.03}$	$3.09^{+0.02}_{-0.02}$	106 ± 1.2	1.54(1169)
	1997.04.30$^\sharp$	1.45fix	$1.17^{+0.03}_{-0.03}$	$3.14^{+0.02}_{-0.02}$	100 ± 1.1	1.55(1125)
	1997.05.01$^\sharp$	1.45fix	$1.16^{+0.02}_{-0.02}$	$3.09^{+0.01}_{-0.01}$	144 ± 1.2	1.71(1283)
	1997.05.03$^\sharp$	1.45fix	$1.08^{+0.03}_{-0.03}$	$3.15^{+0.02}_{-0.02}$	75.3 ± 0.9	1.46(1030)
	1997.05.04	1.45fix	$1.02^{+0.04}_{-0.04}$	$3.32^{+0.03}_{-0.03}$	42.7 ± 0.7	1.24(850)
	1997.05.06$^\sharp$	1.45fix	$1.06^{+0.03}_{-0.03}$	$3.20^{+0.02}_{-0.02}$	62.4 ± 0.8	1.40(992)
	1997.06.02$^\sharp$	1.45fix	$1.24^{+0.02}_{-0.02}$	$2.91^{+0.01}_{-0.01}$	310 ± 2.1	2.79(1444)
	1998.04.23$^\sharp$	1.45fix	$1.10^{+0.00}_{-0.00}$	$2.85^{+0.00}_{-0.00}$	320 ± 0.6	19.5(1609)
Mrk 501	1996.03.21	1.73fix	$0.67^{+0.03}_{-0.03}$	$2.37^{+0.02}_{-0.02}$	97.0 ± 0.9	1.26(1186)
	1996.03.26	1.73fix	$0.7^{+0.04}_{-0.04}$	$2.45^{+0.02}_{-0.02}$	74.0 ± 0.8	1.17(1106)
	1996.03.27	1.73fix	$0.75^{+0.04}_{-0.04}$	$2.59^{+0.03}_{-0.03}$	54.3 ± 0.72	1.15(958)
	1996.04.02	1.73fix	$0.82^{+0.04}_{-0.04}$	$2.70^{+0.03}_{-0.03}$	45.4 ± 0.6	1.12(948)
	1998.07.18$^\sharp$	1.73fix	$0.85^{+0.03}_{-0.03}$	$2.25^{+0.01}_{-0.01}$	127 ± 1.1	1.32(1406)
	1998.07.20	1.73fix	$0.80^{+0.03}_{-0.03}$	$2.26^{+0.02}_{-0.02}$	112 ± 1.1	1.21(1360)
	1998.07.21	1.73fix	$0.82^{+0.03}_{-0.03}$	$2.22^{+0.01}_{-0.02}$	141 ± 1.2	1.35(1407)
	1998.07.23	1.73fix	$0.77^{+0.03}_{-0.03}$	$2.30^{+0.02}_{-0.02}$	108 ± 1.1	1.26(1317)
PKS 2155 −304	†1993.05.03$^\sharp$	1.77fix	$0.43^{+0.02}_{-0.02}$	$2.58^{+0.01}_{-0.01}$	249 ± 1.2	1.88(1459)
	1994.05.19$^\sharp$	1.77fix	$0.57^{+0.01}_{-0.01}$	$2.86^{+0.01}_{-0.01}$	71.8 ± 0.3	2.99(1560)
	1996.05.22$^\sharp$	1.77fix	$1.14^{+0.04}_{-0.04}$	$2.82^{+0.02}_{-0.02}$	152 ± 2.0	1.77(1063)
	1996.05.24$^\sharp$	1.77fix	$1.13^{+0.04}_{-0.04}$	$3.08^{+0.02}_{-0.02}$	97.7 ± 1.3	1.78(1036)
	1996.05.26$^\sharp$	1.77fix	$0.92^{+0.03}_{-0.03}$	$2.76^{+0.02}_{-0.02}$	120 ± 1.1	2.14(1251)
	1996.11.14$^\sharp$	1.77fix	$0.82^{+0.03}_{-0.03}$	$3.05^{+0.02}_{-0.02}$	42.9 ± 0.5	1.66(1023)
	1996.11.15$^\sharp$	1.77fix	$0.61^{+0.03}_{-0.03}$	$2.85^{+0.02}_{-0.02}$	40.8 ± 0.4	1.47(1070)
GIS he 1ES 2344 +514	1997.01.10	16.0fix	$0.79^{+0.06}_{-0.06}$	$2.36^{+0.03}_{-0.03}$	15.7 ± 0.3	1.17(1038)
	1997.01.23	16.0fix	$1.04^{+0.13}_{-0.13}$	$2.73^{+0.07}_{-0.07}$	9.55 ± 0.4	1.02(435)
	1997.12.20	16.0fix	$0.70^{+0.14}_{-0.14}$	$2.42^{+0.08}_{-0.07}$	9.33 ± 0.4	1.08(441)

† : Data from both SISs were used, but the data taken at medium bit rate were not used because of the strong telemetry saturation.

$^\sharp$: The source was variable during the observation. Probability for constant fit of the light curve was $\mathrm{P}(\chi^2) < 1\ \%$.

All errors are 1 σ.

cause only factor 2 change in the peak position for Mrk 421, while it makes more than factor 40 change for the case of Mrk 501.
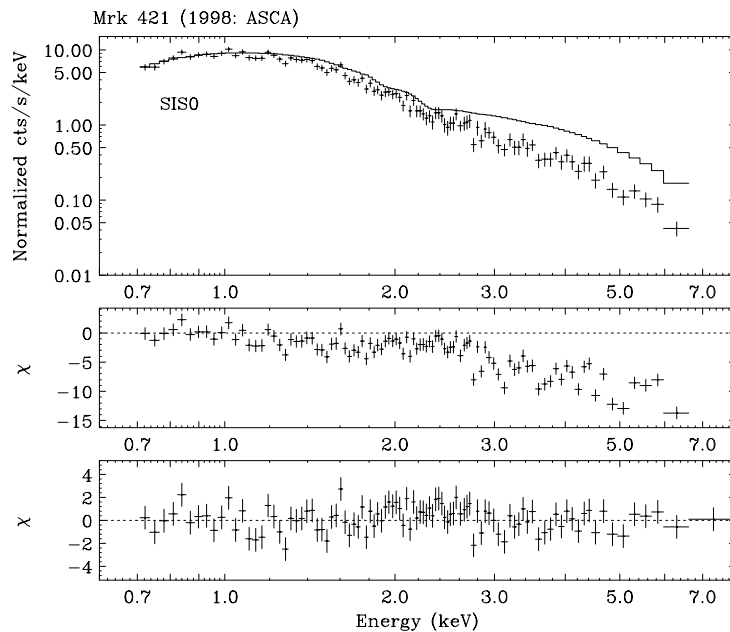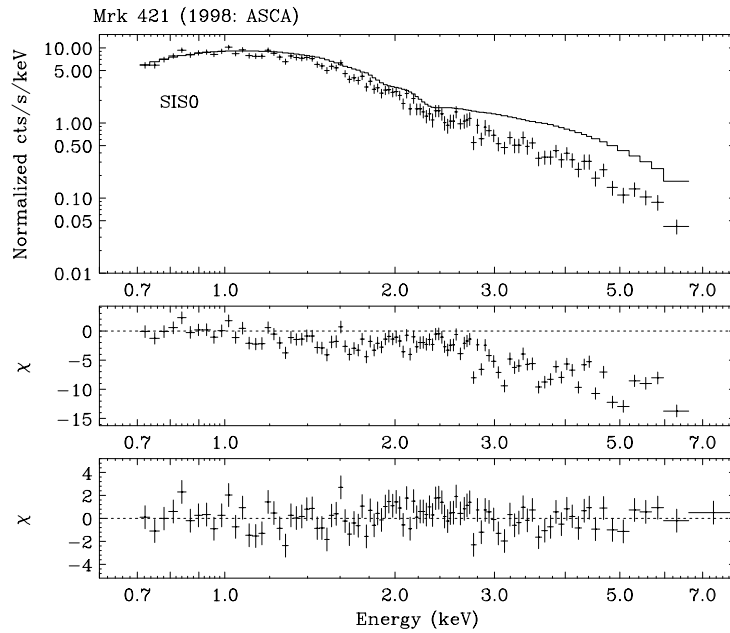
Figure 7.28: *ASCA* SIS0 spectrum fitted to a cutoff power law function. *top*; The SIS0 data for Mrk 421 obtained from 1998 04:24:00:48:20 to 04/24 01:45:00, fitted to a power law function with Galactic absorption. Only the data below 1.0 keV were used for the fit. *center*; residuals to a power law function with Galactic absorption. *bottom*; residuals to a cutoff power law function with Galactic absorption, where the entire SIS0 bandpass were used.

Table 7.6: Results of spectral fitting of Mrk 421 with a cutoff power law function.

Mission	Detector	E_c (keV)	Photon Index	Flux (2-10keV) 10^{-12} erg/cm^2/s	χ^2 (d.o.f)
ASCA	SIS0	$1.00^{+0.15}_{-0.15}$	$3.00^{+0.09}_{-0.09}$	142±7.3	1.14(98)
	SIS1	$1.40^{+0.18}_{-0.17}$	$3.25^{+0.11}_{-0.11}$	129±9.3	1.07(111)
	GIS2	$0.31^{+0.21}_{-0.21}$	$2.72^{+0.11}_{-0.11}$	148±8.5	0.79(189)
	GIS3	$0.31^{+0.19}_{-0.18}$	$2.74^{+0.10}_{-0.10}$	154±7.9	0.94(205)
combine (0.7-7.5 keV)		$1.11^{+0.08}_{-0.08}$	$3.07^{+0.05}_{-0.05}$	143±2.1	1.16(611)
combine (1.0-7.5 keV)		$0.99^{+0.14}_{-0.14}$	$3.01^{+0.07}_{-0.07}$	144±7.4	1.06(544)

Data from 1998 04:24:00:48:20 to 04/24 01:45:00 were used for the fit, when *ASCA* and *BeppoSAX* observed Mrk 421 contemporaneously. Fitting model is a power law function plus exponential cutoff. The absorption is fixed to the Galactic value. the *ASCA* energy band. All errors are 1 σ.

7.3.3 Shift of the Synchrotron Peak

As shown in Figure 7.29, the peaks of νF_ν spectra are found in the X-ray energy band for the four TeV blazars studied by us. Considering the convex curvature of the X-ray photon spectra, this is likely to be because the peak of the synchrotron (LE) component
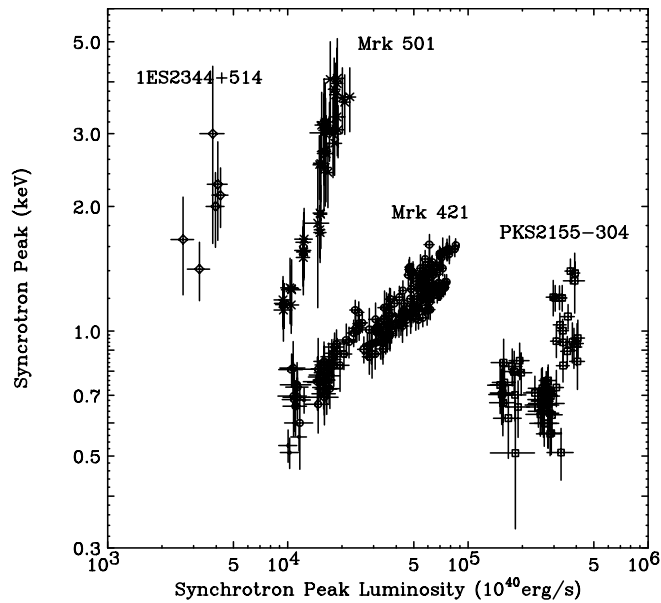
Figure 7.29: Distribution of peak luminosity L_p versus peak energy energy E_p as described in the text.

is located in the X-ray band (see § 2).

To see the time evolution of the photon spectra more clearly, we show the photon spectra in νF_ν space (Figure 7.30). The SIS spectra were convolved from the cutoff power law function. We divided the total *ASCA* bandpass (0.7−7.5 keV) into 22 logarithmic-equal energy bands to reduce errors. Figure 7.30 shows the combined results from different observations. The spectral evolutions during individual observations are summarized in Appendix E (Figure E.1−E.2).

Mrk 421

Mrk 421 shows very modest shifts in the peak position. In 1993 observation, when the source was the faintest, the peak was located below 0.7 keV. For 1994−1997 observations, we detected the peak around 1 keV. When the source was the brightest in 1998, flux increased more than a factor of 30 than that in 1993 and the peak was detected at ~ 2 keV. A correlation between peak energy E_p and peak luminosity L_p is expressed as $E_p \propto L_p^{0.36}$ (see, Figure 7.29).

Mrk 501

In 1996 April observation when Mrk 501 was in the faintest state, the synchrotron peak was detected at 1 keV. For 1998 observations, the peak was shifted to a significantly higher energy (4 keV) although an increase in flux was relatively small (factor of 2). For

this source, a clear correlation between the peak energy and the peak luminosity can be expressed as $E_p \propto L_p^{1.6}$ (see, Figure 7.29).

PKS 2155−304

PKS 2155−304 was brightest in 1993, while it was the faintest in 1996. Interestingly, however, synchrotron peak exists below 0.7 keV during 1993 observation, but around 1 keV during 1996 observation. The spectra in the lowest state of 1994 observation are very similar to that in the 1993 observation, but the flux is lower by a factor of 4. There seems no clear correlation between E_p and L_p, as was suggested from Figure 7.29.

1ES 2344+514

1ES 2344+514 was brightest in January 10 (1997), while it was the faintest in December 20 (1997). Synchrotron peak seems to be shifted from 1 keV to 4 keV corresponding to the factor 2 increase in the flux. This suggest that the spectral evolution of 1ES 2344+514 is similar to that for Mrk 501, but not conclusive because of the low photon statistics, and because there are relatively few *ASCA* observations. .
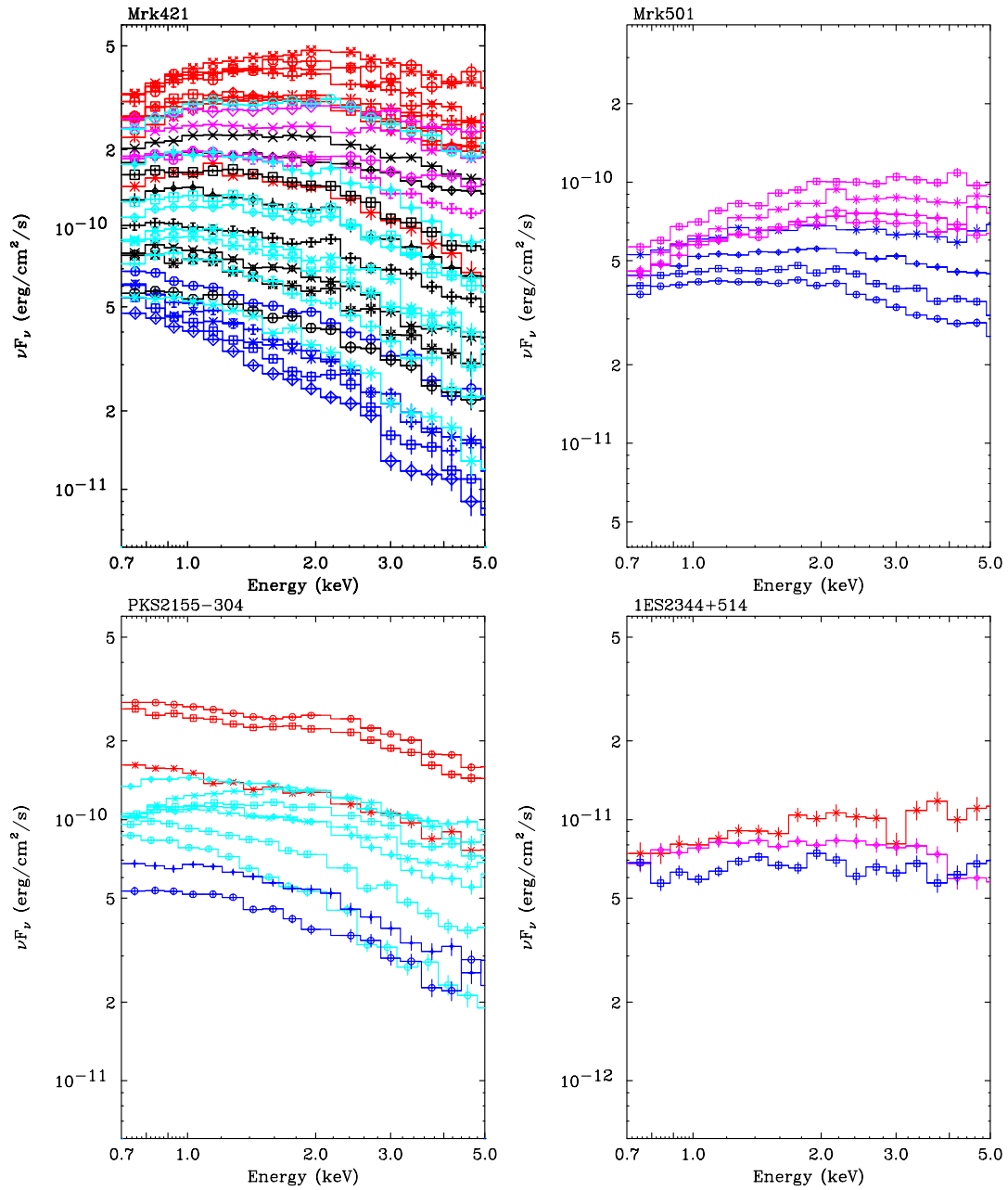
Figure 7.30: Synchrotron peak shifts of four TeV blazars. *top left*: Mrk 421, *top right*: Mrk 501, *bottom left*: PKS 2155−304 and *bottom right*: 1ES 2344+514.

Chapter 8

Analysis and Results of *RXTE* Observations

8.1 Analysis

8.1.1 Data Reduction

To reduce the PCA data, we first selected the data by orbital conditions and pointing stability. The minimum elevation angle from the Earth's limb was set to be 10 degrees. We excluded the data obtained during the passage through the South Atlantic Anomaly (SAA). Since the PCA detector is activated during the SAA and the background increases significantly just after the passage, we only use the data when the background goes back to the quiescent level and becomes quite stable, which is typically 30 minutes after the SAA passage. Since the attitude of satellite is not stable just after changing the pointing direction, we excluded the data obtained when the difference between the actual pointing direction and scheduled direction is larger than 1.2 arcmin.

Next we eliminated the data which includes significant electron contamination. Electrons creates background components by interaction with spacecraft or detector body. To analyze the faint sources, the PCA team recommends filtering out time when electron rate is larger than 0.1, which is the criterion used in this thesis. Additional data selections had been done from various operational reasons.

In March 1996, PCU3 and PCU4 began to experience occasional breakdowns. Since then, these two PCUs, individually or together, are occasionally turned off to prevent further damage. We thus used the data only from 3 PCUs (PCU0/1/2) whose exposure times are much larger and uninterrupted than those for PCU3 and PCU4. The PCUs have three xenon layers (X1, X2, X3) each consisting of two anodes chains (Left, Right). The

top layer detects roughly 90 % of the cosmic photons and 50 % of the internal instrumental background. Thus the best signal-to-noise for weak sources are achieved by selecting only events from the top layer (X1) and excluding events from the mid and bottom layers (X2 and X3). These criteria for data reduction are summarized in Table 8.1.

Table 8.1: Screening criteria for *RXTE* analysis

Screening Item	Screening Criteria
Elevation [a]	< 10.0
Att. Stability[b]	< 1.2 arcmin
Time since SAA[c]	> 30 min
Electron Rate[d]	< 0.1
PCU_ON[e]	PCU_0, 1, 2 (PCU_3, 4 were not used)
Layer[f]	X1 only (X2, X3 were not used)

[a] The minimum elevation angle above the Earth's limb

[b] The maximum fluctuation in the pointing direction

[c] The minimum time since the SAA passage

[d] The maximum rate for electron background

[e] ID of PCUs used in the analysis

[f] ID of PCU layers used in the analysis

8.1.2   Background Subtraction

After the screening processes were done, we estimated the PCA background for each observation. Since the PCA is not an imaging detector, the modeled background has to be subtracted from the source data. The PCA background consists of two components (see, § 5.2.3). One is the diffuse sky background which enters through the collimator as X-rays, and the other is the internal background which arises from interactions between radiation or particles in orbital environment with the detector or spacecraft. While the sky background is assumed to be constant at any one pointing position, the internal background may vary as the detectors move through different ambient conditions. The estimation of background is based on the detailed modeling of activation, especially during the SAA passage and instantaneous particle flux coming into the detector.

To estimate the background, we use the latest version of *pcabackest* (Version 2.1b) supplied from *RXTE* Observer Facility at the NASA GSFC. It is assumed that the internal background varies on a time scale long compared to 16 seconds, the natural time scale of the PCA *Standard*-2 data (see § 5). The background model was evaluated once

every 16 seconds, and the equivalent of a *Standard*-2 data file was created with separate information for each detector and each anode chain. We applied all of the good time intervals to the output files from *pcabackest* exactly as we did to the *Standard*-2 data.

8.2 Results from Temporal Studies

8.2.1 Time Variability

We first study the time variability for each source, by means of PCA count rates during the observations. Count rates are extracted from the sum of the PCU 0, 1 and 2 data. To obtain the best signal-to-noise ratio, only the data for the PHA channels from 6 (2.5 keV) to 53 (20 keV) were used in the following analysis.

Mrk 421

The light curves of Mrk 421 from 1996 to 1997 observations are shown in Figure 8.1. The source was the faintest in 1996 December ($4-5$ cts/s for PCA) and the brightest in 1996 May ($20-152$ cts/s for PCA), which was the change of more than factor of 30. Note that the amplitude of variation is larger than that observed with *ASCA* in lower X-ray energy bands (Figure 7.2). In addition to this large-amplitude, long term variability, the data reveal very rapid variability, on time scales as short as hours to days. In particular, flux variations in 1996 May (Figure 8.1 (b)) are remarkable, where the flux increased and decreased by a factor of 6 within a day. The occurrence of day-by-day flares is implied from the figure, as was clearly detected during the 1998 observation with *ASCA* (Figure 7.2).

Mrk 501

The light curves of Mrk 501 are summarized in Figure 8.2. The source was the faintest in 1998 May ($26-34$ cts/s for PCA) and the brightest in 1997 Apr$-$July ($68-201$ cts/s for PCA), which was a change of a factor $\sim$10. Subsequent analysis revealed that the fluxes observed in 1997 Apr/July are the historical record for this source (Figure 8.2 (d)(f)). In 1998 May, we monitored the source almost continuously for two days to search for the rapid time variability (fig 8.2 (g)). About 30 % fluctuation in the flux was detected, but the source did not show any significant variations as short as hours.

PKS 2155$-$304

The light curves of PKS 2155$-$304 from 1996 to 1998 observations are shown in Figure 8.3. The source was the faintest in 1998 January ($4-13$ cts/s for PCA; (e)) and the brightest
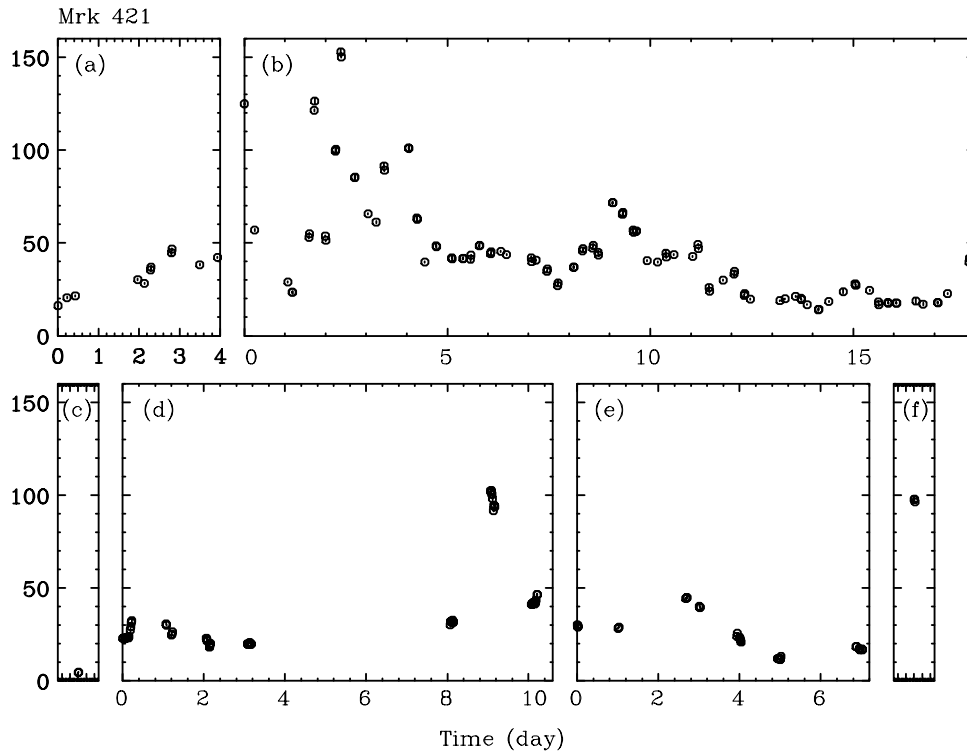
Figure 8.1: PCA light curves of Mrk 421 from 1996 to 1997 *RXTE* observations. The source counts are extracted from PCU 0, 1 and 2. The binning time is 1024 sec. Energy band is $2.5-20$ keV. Each panel corresponds to the data: (a) $96/4/19 - 4/23$, (b)$96/5/3 - 5/21$, (c) $96/12/10$, (d) $97/4/2 - 4/12$, (e) : $97/4/29 - 5/6$, (f) : $97/6/3$.

in 1997 November ($41-56$ cts/s for PCA; (d)), which was the change of a factor $\sim$10. Observations in 1996 May was conducted almost continuously (Figure 8.3 (a)), providing the longest uninterrupted X-ray data of the source for 12 days. During the May 1996 campaign, the source was highly variable and occurrence of $\sim$ 10 day-by-day flares is clearly seen.

All Sky Monitor

Figure 8.4 shows the variation of the ASM count rates from 1996 to 1999 for four TeV blazars. In the figure, we binned the data into 10-day to reduce the errors on fluxes.

Mrk 421 showed the flux variation of a more than factor 10, and the highest flux was observed in April 1998. This was the epoch when the *ASCA* satellite also observed Mrk 421 for 7 days and found that the source was in the historical high state (Takahashi et al. 1998; Figure 7.2). Mrk 501 also showed large amplitude variability. The highest state was observed in 1997 April to July (see, Figure 8.2). PKS $2155-304$ and 1ES 2344+514 seem less variable on time scales of longer than 10 days, but the changes in flux by an
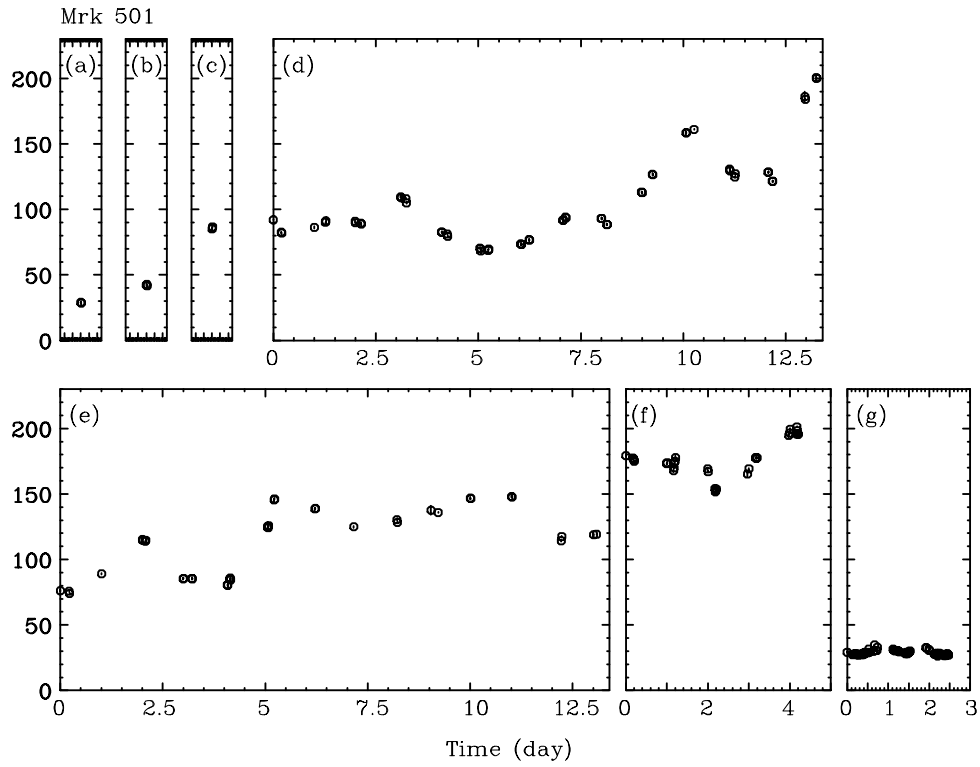
Figure 8.2: PCA light curves of Mrk 501 from 1996 to 1998 *RXTE* observations. The source counts are extracted from PCU 0, 1 and 2. The binning time is 1024 sec. Energy band is $2.5-20$ keV. Each panel corresponds to the data: (a) 96/8/1, (b)96/10/22, (c) 97/3/18, (d) $97/4/3 - 4/16$, (e) : $97/5/2 - 5/15$, (f) : $97/7/11 - 7/16$, (g) : $98/5/25 - 5/27$.

order of magnitude are seen in the figure.
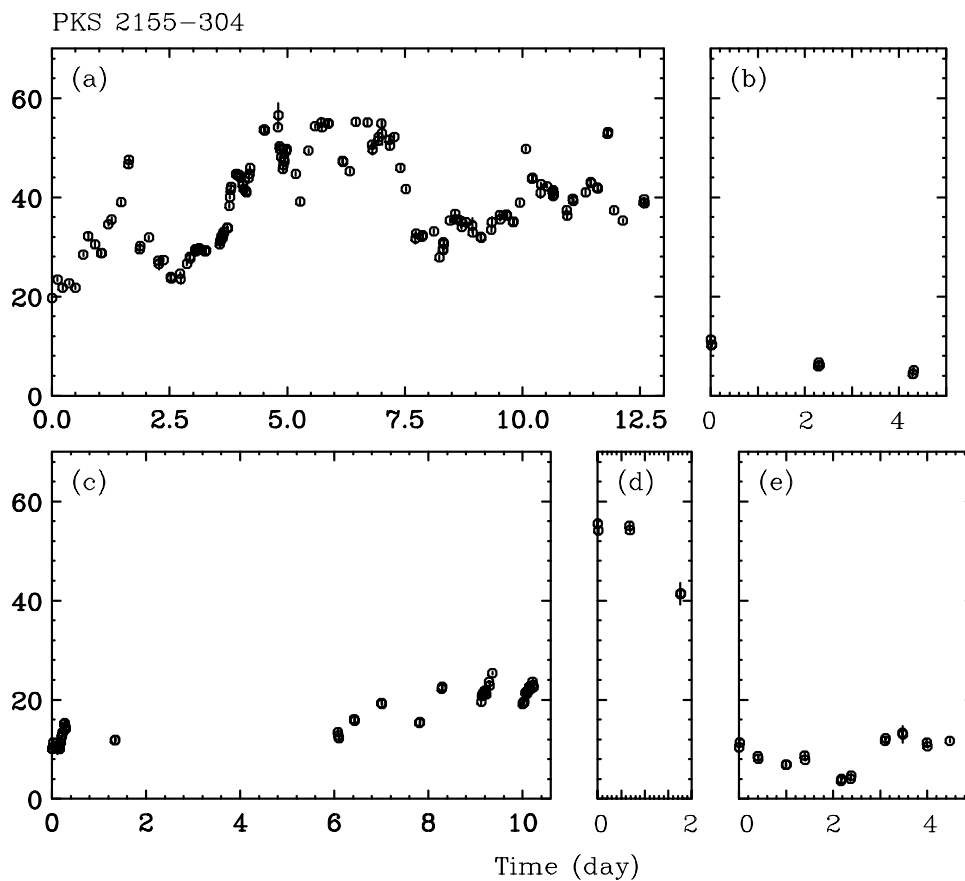
Figure 8.3: PCA light curves of PKS 2155−304 from 1996 to 1998 *RXTE* observations. The source counts are extracted from PCU 0, 1 and 2. The binning time is 1024 sec. Energy band is 2.5−20 keV. Each panel corresponds to the data: (a) 96/5/16 − 5/28, (b)96/7/23 − 7/27, (c) 96/11/14 − 11/24, (d) 97/11/20 − 11/22, (e) : 98/1/9 − 1/13.
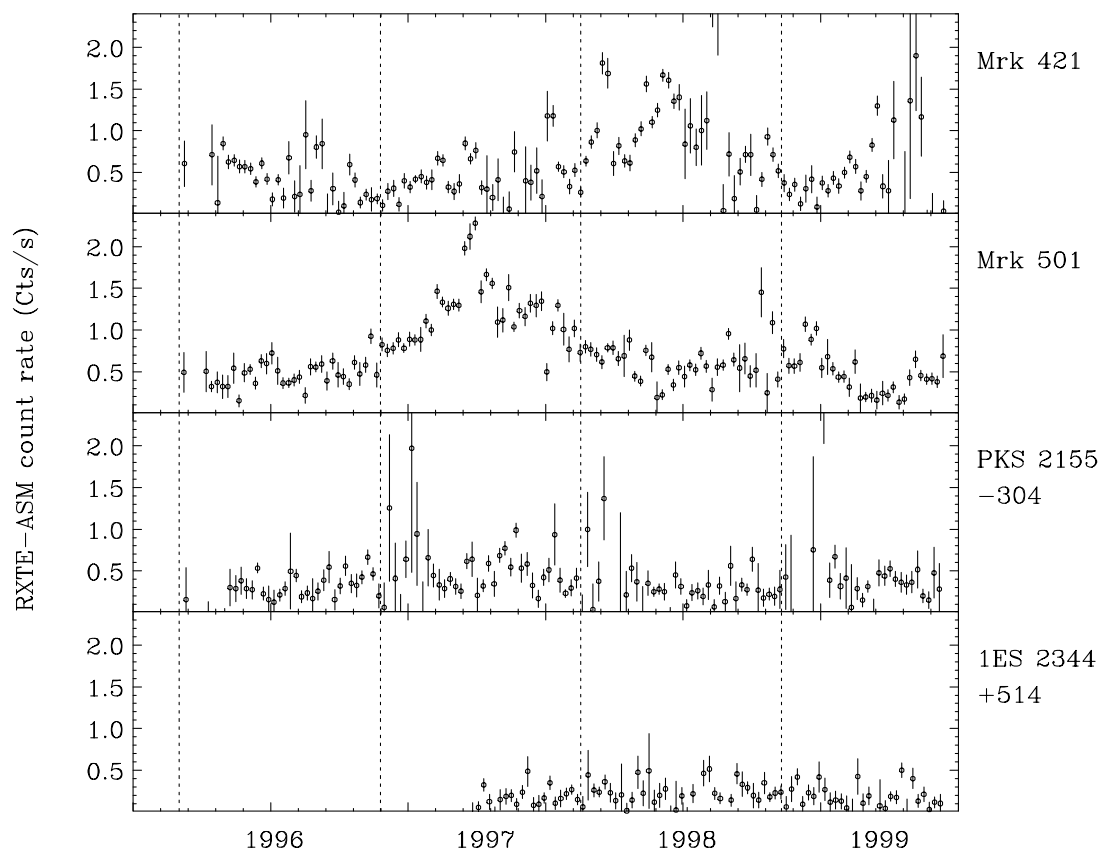
Figure 8.4: *RXTE* ASM Light Curve for TeV blazars. *top*: Mrk 421, *second*: Mrk 501, *third*: PKS 2155−304, and *bottom*: 1ES 2344+514. To reduce errors, the count rates are binned at 10 days.

8.2.2   Energy Dependence of Variability

Long-Term Trend of Variability

We calculate the fractional *rms* variability parameter F_{var} using the PCA light curves shown in Figure 8.1−8.3. To investigate the long-term trend of variability in various energy bands, we divided the PCA light curves into four energy bands; 2.5−5 keV, 5−7.5 keV, 7.5−10 keV and 10−20 keV. The results are summarized in Figure 7.6. From the figure, one can find a clear trend that the amplitude of variability becomes larger as photon energy increases for Mrk 421, Mrk 501 and PKS 2155−304. The energy dependence of variability is similar to that obtained from *ASCA* data for three TeV blazars (§ 7.6). This clearly indicates that the variability amplitude becomes larger for higher energy photons, in the very wide energy range from soft X-rays (0.5 keV) to hard X-rays (20 keV).
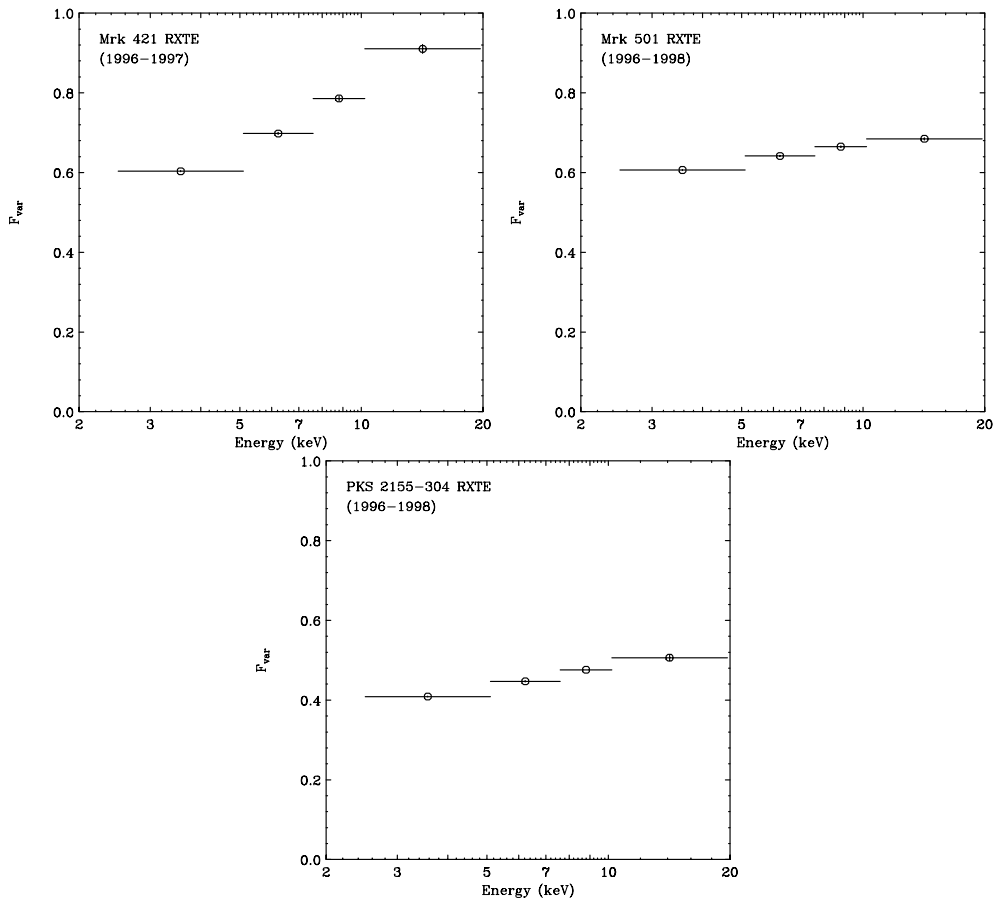
Figure 8.5: Energy dependence of variability of three TeV blazars. The variability parameter was calculated in 2.5−5 keV, 5−7.5 keV, 7.5−10 keV and 10−20 keV, respectively. For the light curves in total *RXTE* bandpass (2.5−20 keV), see Figure 8.1− 8.3. *top left*: Mrk 421, *top right*: Mrk 501, and *bottom*: PKS 2155−304.

Variability of Day-by-Day Flares (PKS 2155−304 1996 May)

In order to study the short-term variability of PKS 2155−304 during the 1996 May observation, we use the PCA data binned at 1024 sec. Variability was calculated for the total exposure (12-days) in four energy bands 2.5−5 keV, 5−7.5 keV, 7.5−10 keV and 10−20 keV, respectively. As shown in Figure 8.6, variability amplitude becomes larger as the photon energy increases (see also Figure 8.5).
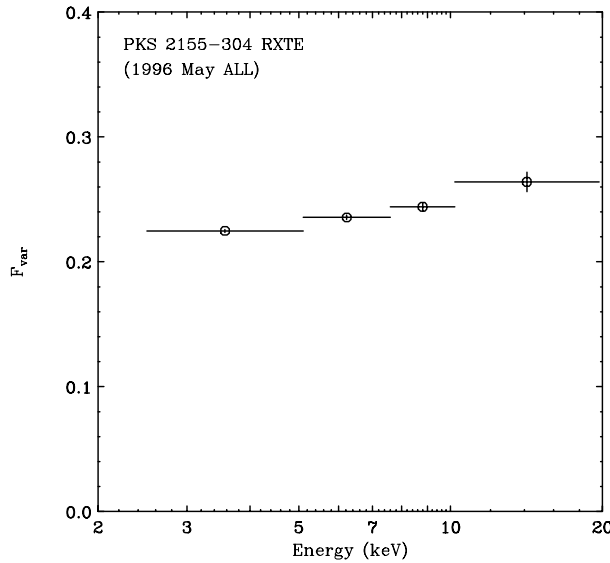
Figure 8.6: Energy dependence of variability of PKS 2155−304 in 1996 May. The variability parameter was calculated for the total 12-day observation in four energy bands (2.5−5 keV, 5−7.5 keV, 7.5−10 keV and 10−20 keV). We used the PCA data binned at 1024 sec.

In order to study the variability behavior for *each* flare event, we divided the total exposure into 9 segments as shown in Figure 8.7. Each segment typically contains one flare. We calculate the variability parameter F_{var} from time-segment #1 to #9. The energy dependencies of variability for individual flares are shown in Figure 8.8.

In five of the flares (# 1, 2, 6, 8, 9), the variability amplitudes becomes larger in higher energy bands, while the trend is not clear for the reminder. Such behavior is very similar to what has been observed for Mrk 421 with *ASCA* (Figure 7.9). These results support the fact that on longer time scales, the variability amplitude becomes larger at increasing photon energy, but for individual flares (or in shorter time-scale), energy dependence of variability changes *flare-by-flare*.
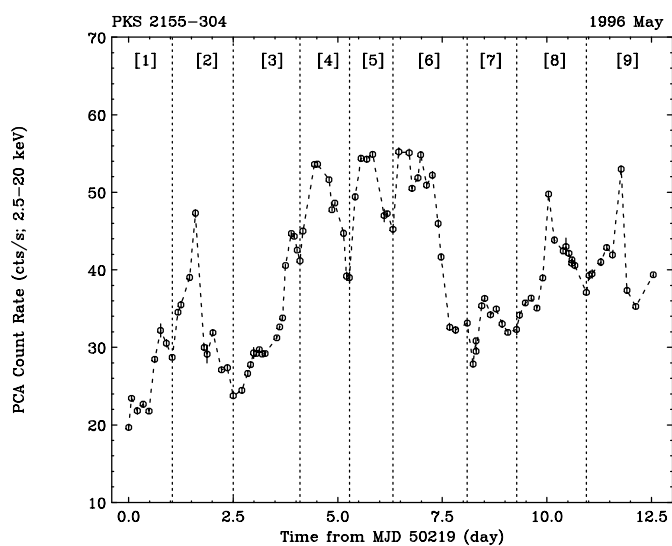
Figure 8.7: PCA light curve of PKS 2155−304 obtained in 1996 May and the division of time interval into 9 separate segments. Data points are joined to guide the eye. Each point represents 1 ksec integration of the PCA data.
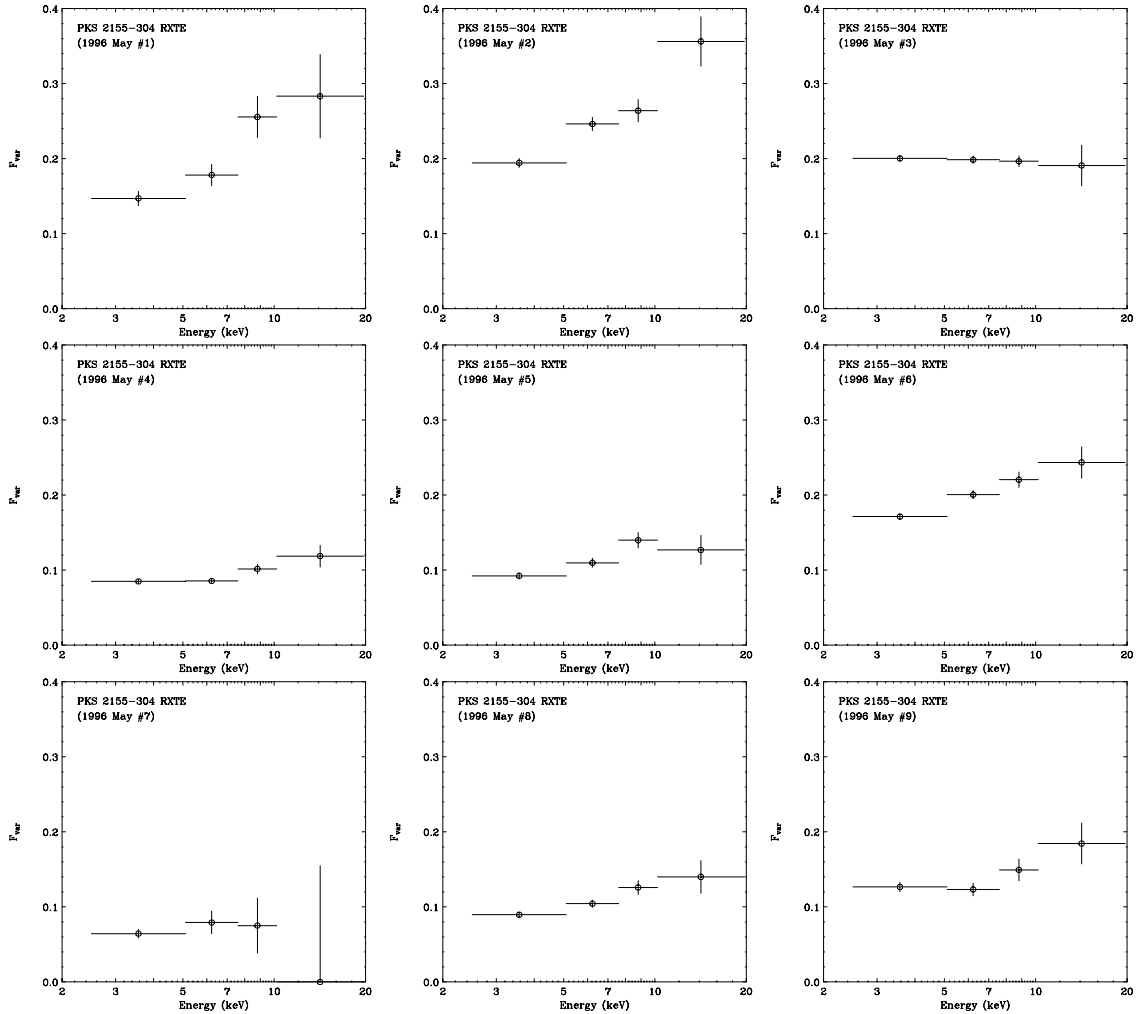
Figure 8.8: Energy dependence of variability of PKS 2155−304 in 1996 May *RXTE* observations. Variabilities for individual flare events are separately shown. Time segments are defined in Figure 8.7. The PCA data were used.

8.2.3   Structure Function

PCA and ASM Data

In this section, we calculate the Structure Function (SF) using the PCA and ASM data. The results are summarized in Figure 8.9.

For Mrk 421 (*top*), we use the PCA data obtained in 1996 May (Figure 8.1(b)). Although data were sampled rather sparsely, we see a hint of a roll-over at ~ 0.5 day, which is consistent with the *ASCA* results (§ 7.2.3). On longer time scales (of $\tau > 1$ day), both the PCA and the ASM data show a flat slope of $\beta \simeq 0.3$.

We plot the SFs of Mrk 501 (*middle*) for 1997 April and 1998 May (Figure 8.2 (d)(g)). For 1998 May data, we divided the total exposure into three parts according to the gaps in the pointing (see Figure 8.2), and calculate the average SF of the three parts. Slope of the SF is steep, such that $\beta \simeq 2.0$ for the PCA data. A roll-over is marginally detected at ~ 1 day. On time scale longer than 1 day, the ASM data shows flatter slope of $\beta \sim 0.5$ than the slope below the roll-over.

For PKS 2155−304 (*bottom*), we calculate the SF for the 12-day observation in 1996 May (Figure 8.3 (a)). The SF gradually rolls around $\tau \sim 0.3$ day, which is consistent with the *ASCA* results (§ 7.2.3). In shorter time scale than 0.3 day, slope of the SF is $\beta \simeq 1.5$, while in longer time scale ($\tau > 1$ day), both the PCA and the ASM data shows flatter slopes of $\beta \sim 0.7$. Close look at the ASM data indicates a sign of appearance of another plateau at ~ 100 day. Such a *second* roll-over cannot be seen both for Mrk 421 and Mrk 501.

Analysis of Time Asymmetry

We calculate the asymmetry of the light curve for PKS 2155−304 based on 12-day uninterrupted data. We measure the time asymmetry of the light curves by the same procedure discussed in § 7.2.3. We first calculate the SF_+ and SF_- using the light curves in the energy range 2.5−5 keV, 5−7.5 keV, 7.5−10 keV, 10−15 keV and 15−20 keV, respectively. Next, *symmetrical parameter* $Sy(\tau)$ was calculated as the difference of SF_+ and SF_- normalized by an original structure function. We calculate the ensemble average of $Sy(\tau)$ in time region $0 \le \tau \le 1$ (day).

Results are summarized in Figure 8.10. This result is consistent with what was found for Mrk 421 data in 1998 (Figure 7.13). We find that the light curves of PKS 2155−304 favors 'rise-time < decay-time' and that the light curves become more symmetric at higher energies. In fact, $Sy(\tau)$ is consistent with zero at the highest energy bands.

Combined *RXTE* and *ASCA* Data

When the *ASCA* and *RXTE* results are combined, we can obtain the variability information of four TeV blazars in the very wide time-domain from 10^3 to 10^7 sec. To compare the light curves from four different detectors (*ASCA* SIS/GIS, *RXTE* PCA and ASM), we normalized the light curves by their average values. The results are summarized in Figure 8.11. In these figures, we do not plot the data above the point where the SF values are affected by insufficient long sampling (see § 7.2.3).

As seen in the figure, the SFs of four TeV blazars are well represented by a broken power-law form. We find a break (roll-over) at $\tau = 0.5$ day for Mrk 421, $\simeq 1$ day for Mrk 501, 0.3 day for PKS 2155−304 and 1−10 day for 1ES 2344+514. Importantly, below the break, the SFs have very steep slopes; $\beta \simeq 1.2$ for Mrk 421, 2.0 for Mrk 501, 1.5 for PKS 2155−304 and 2.3 for 1ES 2344+514. This indicates that the rapid time variability of TeV blazars has a strong red-noise character and/or is well approximated by a simple linear trend (see, § 7.2.3). Above the break, the SF slopes flatten to $0 < \beta < 1$ and similar to flickering noise.
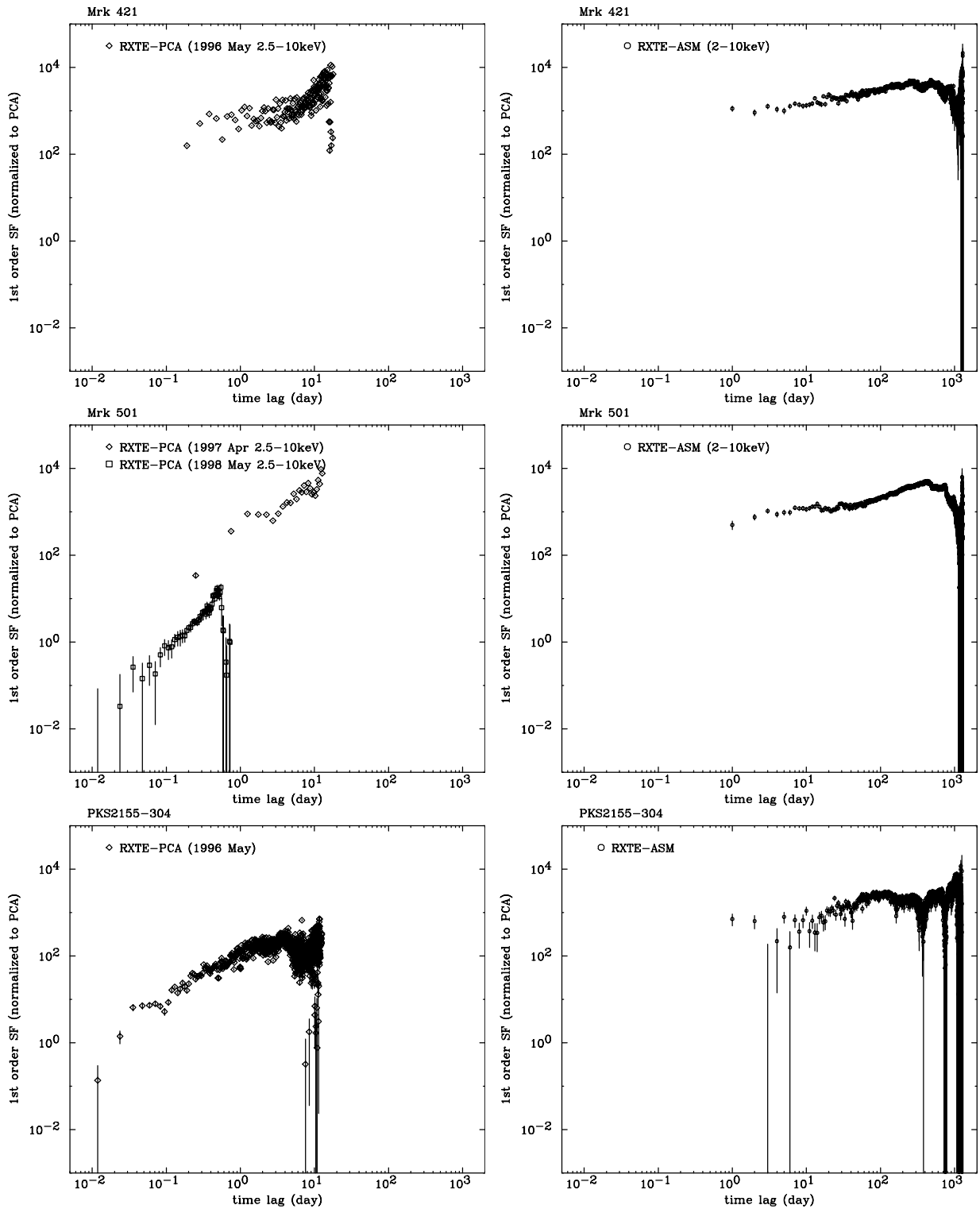
Figure 8.9: 1st order structure function (SF) of three TeV blazars observed with *RXTE* . *top left*: Mrk 421 (1996 May; Figure 8.1(b)), *top right*: Mrk 421 (ASM; Figure 8.4), *middle left*: Mrk 501 (1997 April and 1998 May ; Figure 8.2(d)(g)), *middle right*: Mrk 501 (ASM; Figure 8.4), *bottom left*: PKS 2155−304 (1996 May; Figure 8.3(a)), and *bottom right*: PKS 2155−304 (ASM; Figure 8.4). The PCA light curves from 2.5 keV to 10 keV were used and count rates are normalized to the PCA values.
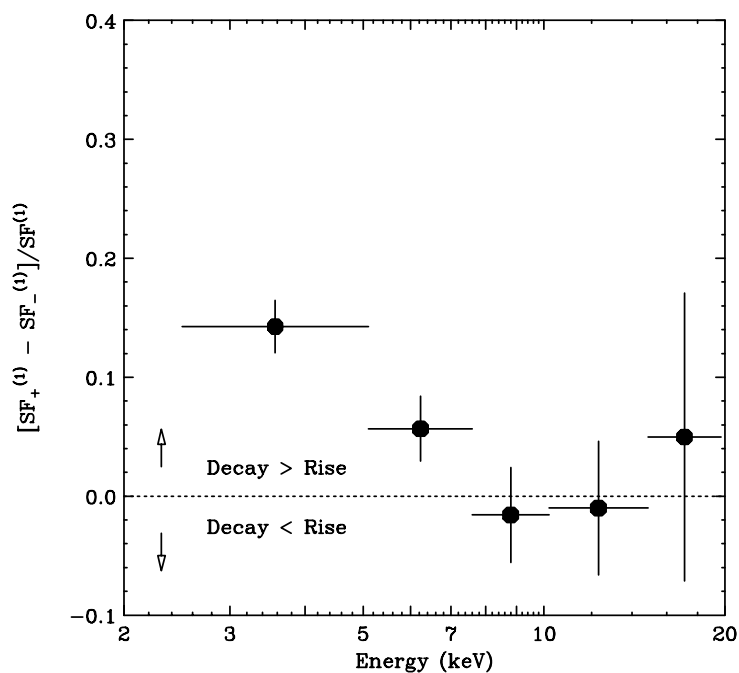
Figure 8.10: Energy dependence of the symmetry parameter $\mathrm{Sy}(\tau) = [\mathrm{SF}_+ - \mathrm{SF}_-]/\mathrm{SF}$ for PKS 2155−304 observed in 1996 May. $\mathrm{Sy}(\tau)$ was averaged over the time lags smaller than one day. Light curves are almost symmetric, i.e., $[\mathrm{SF}_+ - \mathrm{SF}_-]/\mathrm{SF} \sim 0$ at higher energy band, but at lower energies, the symmetry tends to break down.
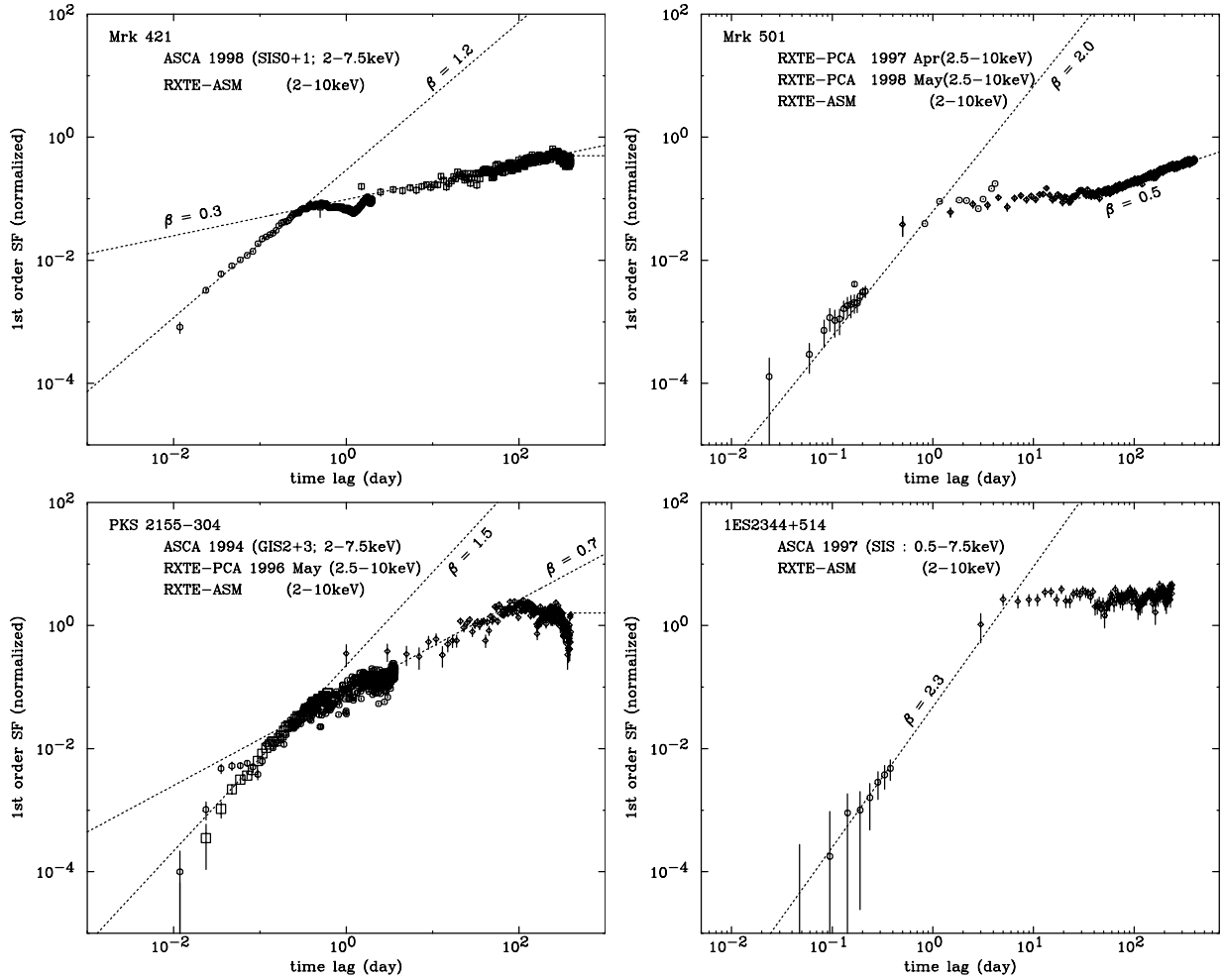
Figure 8.11: Structure functions of TeV blazars (*ASCA* and *RXTE* combined). *top left*: the combined SF of Mrk 421 using the *ASCA* (1998) and the *RXTE* ASM data. *top right*: the combined SF of Mrk 501 using the *RXTE* PCA (1997 April; 1998 May) and the ASM data. *bottom left*: the combined SF of PKS 2155−304 using the *ASCA* (1994), the *RXTE* PCA (1996 May) and the ASM data. *bottom right*: the combined SF of 1ES 2344+514 using the *ASCA* (1997) and the *RXTE* ASM data. Dotted lines are the best fit power-laws.

8.2.4   Spectral Evolutions

We investigate the correlation between the count rate $(2.5-20$ keV$)$ and the hardness ratio as we did for the *ASCA* data (§ 7.2.4). For the *RXTE* data, we define the hardness ratio as the photon counts in $7.5-20$ keV to those in $2.5-7.5$ keV. We concentrate on the spectral evolution of PKS $2155-304$ during the 12-day observation, because it is best suited to study the time evolution of the spectrum.

PKS 2155−304

We divided data into nine time segments as described in § 8.7. The spectral evolution is shown in the correlation between the intensity versus hardness (Figure 8.12). The general trend of the spectral evolution is that hardness increases when the intensity increases, as is also indicated from the changes in amplitude of variability (Figure 8.8).

In time segments #2 and 3, we can see 'clockwise' hysteresis, as seen in the data obtained with *ASCA* (§ 7.2.4). Reverse motion (*anti*-clockwise) is also detected for region #4 and 8. In other time segments (# 1, 5, 6, 7, 9), loopwise motion is not clear. This complicated 'flare-by-flare' behavior is very similar to that observed for Mrk 421 in 1998 (Figure 7.16).

We do not calculate the time-lags for the PCA data, because in most cases, observations are separated by more than 5 ksec and too sparse to calculate the time-lags.
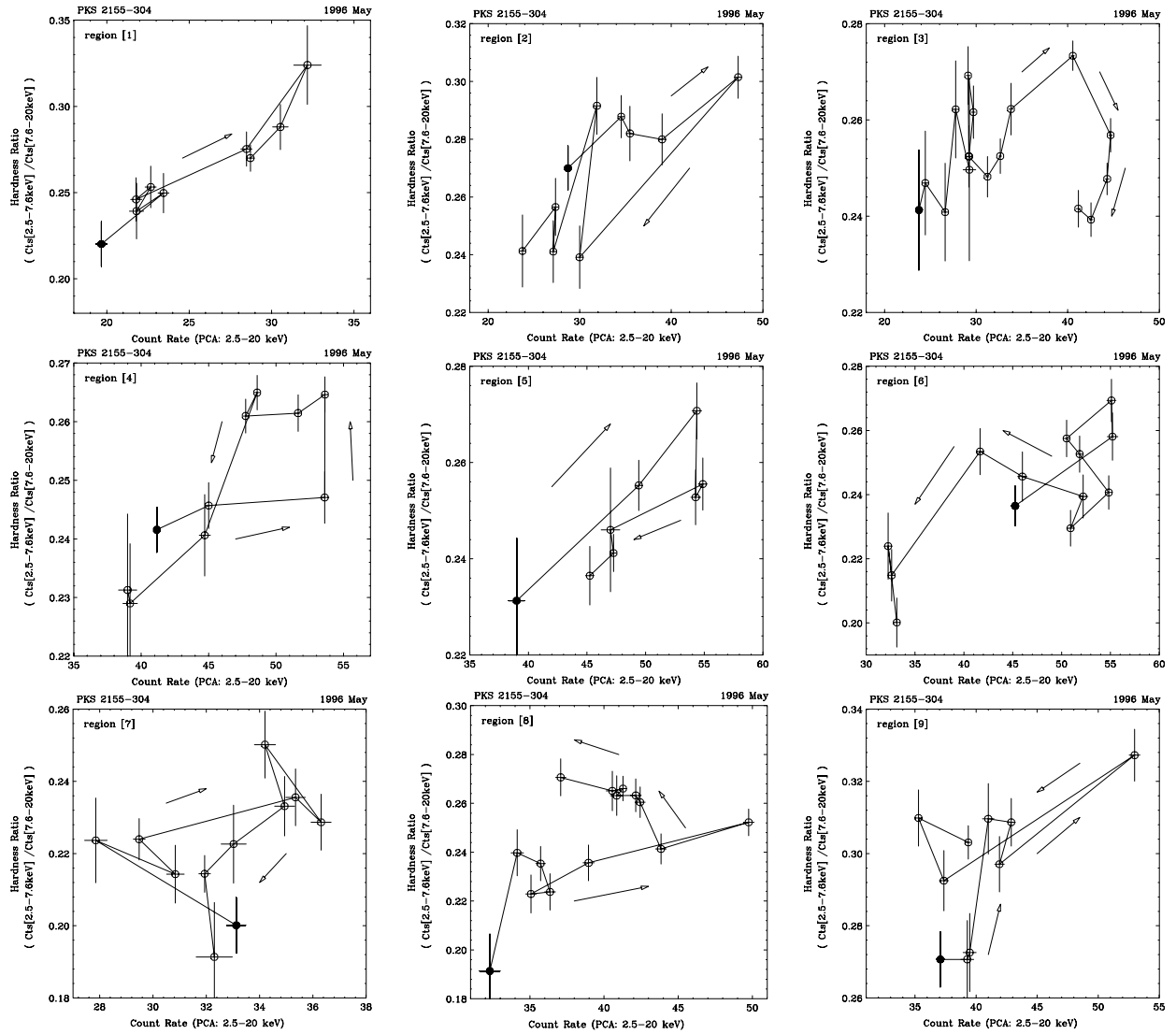
Figure 8.12: Variability patterns for 9 separated segments which are defined in Figure 8.7. Arrows indicate the direction of spectral evolution. The filled circle is the start point of each time segment.

8.3   Results from Spectral Studies

We extracted the energy spectra of PCA for all observations listed in Table A.1−A.8. We use the same analysis procedure as that for the *ASCA* data (§ 7.3). All spectra were fitted with the XSPEC version 10.00. The detector response of PCA are generated from *pcarsp* version 2.37. Although PCA has sensitivity in the 2.5−60 keV (§ 5.2), we only used data from 2.5 keV to 20 keV because each observation was too short to yield enough photon statistics above 20 keV.

8.3.1   Fit with a Power Law Function

We fitted the spectrum with a power law function plus Galactic absorption arising from neutral materials (§ 7.3.1). Since the TeV blazars are highly variable and their spectra evolve on a time scale of hours, we separated the observations into ∼ 1 ksec intervals if the exposure is longer than 1 ksec. We found that the simple power law function gives a good representation for most of the PCA data. When a power law function is not adequate, we introduce an additional exponential cutoff to the power law function as described in § 7.3.2. The gradual steepening of spectra found in *ASCA* data (Figure 7.25), is also seen in the energy band covered by *RXTE* .

As an example, we show the spectrum of Mrk 501 taken in 1997 July in Figure 8.13. The best-fit parameters for the model are summarized in Table 8.2. In this case, photon spectrum is gradually steepening to higher energies, thus the fit with a power law function is statistically unacceptable. However, one can see that the fit is improved by using a cutoff power law function.

The results of spectral fitting for all *RXTE* observations of TeV blazars are summarized in Appendix G (Table G.1 – G.10). Examples of *RXTE* spectra for each TeV blazar are given in Figure H.1 (Mrk 421), Figure H.2 (Mrk 501), Figure H.3 and Figure H.4 (PKS 2155−304).

Table 8.2: An example of spectral fitting of Mrk 501

Mission	Detector	N_{H}	E_c	Photon	Flux (2-10 keV)	χ^2
		$(10^{20}/\mathrm{cm}^2)$	(keV)	Index	$(10^{-12}\ \mathrm{erg/cm}^2/\mathrm{s})$	(d.o.f)
I. *RXTE*	PCA	1.73 (fix)	—	$1.95^{+0.01}_{-0.01}$	618±1.6	2.65(45)
II.		1.73 (fix)	$1.11^{+0.13}_{-0.13}$	$2.15^{+0.02}_{-0.02}$	610±19	1.10(44)

Mrk 501 data from 1997 07/12 03:36:51 to 07/12 03:58:27 were used for the fit. Fitting functions are [I] a power law function plus free absorption, [II] a cutoff power law function. The data in the energy band 2.5−20 keV were used. All errors are 1 σ.
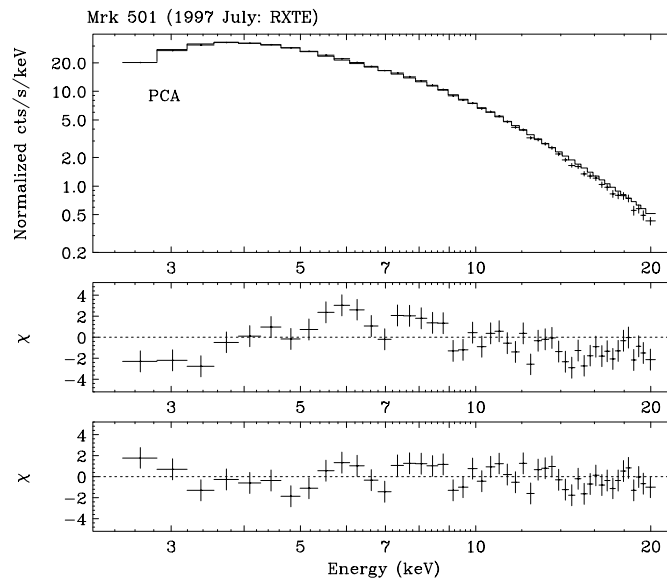
Figure 8.13: The *RXTE* PCA spectra and the best fit power law function. *top*; PCA data for Mrk 501 obtained from 1997 07/12:03:36:51 to 07/12 03:58:27, fitted to a power law function with Galactic absorption. *center*; residuals to a power law function with Galactic absorption. *bottom*; residuals to a cutoff power law function.

Correlations between the isotropic luminosities and photon indices 421, Mrk 501 and PKS 2155−304 are summarized in Figure 8.14. Corresponding figure for *ASCA* observations is Figure 7.27. Photon spectral indices distributed in a wide range from −3.2 to −2.2 for Mrk 421, −2.5 to −1.7 for Mrk 501 and −3.3 to −2.3 for PKS 2155−304. One finds that the spectra tend to be harder when the source becomes brighter, as was indicated in § 8.2.2

8.3.2   Comparison between *ASCA* and *RXTE*

Observations listed in Table 8.3 were conducted simultaneously with *RXTE* and *ASCA* . Therefore, these data enable us to test the consistency between the instruments on-board *ASCA* and *RXTE* . In order to use the energy range covered by two satellites, we selected the data from 2.5 keV to 7.5 keV. Results of the fit with a power law function plus Galactic absorption are shown in Figure 8.15. One can see that the fluxes determined by *RXTE* observations are systematically higher than those determined by *ASCA* by about 15 %. Also note that the photon indices of *RXTE* spectra are systematically stepper than that for *ASCA* results about 0.1. This trend is not improved even if we use the all energy bands, 0.7−7.5 keV for *ASCA* and 2.5−20 keV for *RXTE* .

There are several reasons which may account for these discrepancies. Most serious
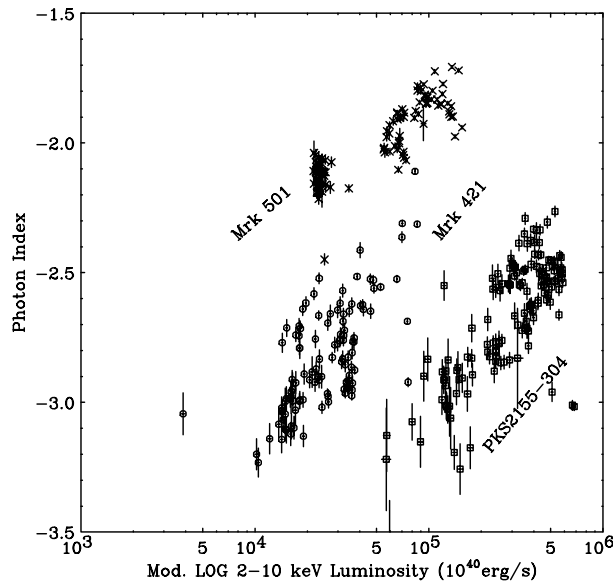
Figure 8.14: Distribution of luminosities and photon indices for all observations with *RXTE* . Mrk 421; from 1996 to 1997 data, Mrk 501; from 1996 to 1998 data, PKS 2155−304; from 1996 to 1998 data. Fluxes are simply converted to the isotropic luminosities by multiplying $4\pi d_L^2$, where d_L is the luminosity distance.

issue would be imprecise cross-calibration between *ASCA* and *RXTE* . Response matrix of *ASCA* is made, based on both the pre-flight data and in-flight calibration against the Crab. The *standard* value of the Crab spectrum in literature is used for the in-flight calibration (2.1; e.g., Toor & Seward. 1974). On the other hand, the response matrix of *RXTE* PCA is mainly based on the pre-flight calibration. Their observational results for the Crab are slightly different than the value mentioned above. The difference in the spectrum of the Crab ($\Delta \Gamma \sim 0.1$) is consistent with the difference seen in Figure 8.15. Also note that the systematic differences of the background subtraction methods between imaging (*ASCA*) and collimating (*RXTE*) instruments would produce the difference in the estimated fluxes.

Table 8.3: List of simultaneous X-ray observations by *ASCA* and *RXTE*

Source	Start	End	*ASCA*		*RXTE*	
			Photon	Flux (2-10keV)	Photon	Flux (2-10keV)
Name	[MJD]	[MJD]	Index	10^{-12} erg/cm^2/s	Index	10^{-12} erg/cm^2/s
Mrk 421	50567.21	50567.27	2.73±0.04	102.0±1.1	2.97±0.03	129.5±1.2
	50568.21	50568.27	2.75±0.04	98.4±1.1	2.85±0.04	122.8±1.2
	50569.89	50569.94	2.73±0.05	161.4±1.9	2.85±0.04	193.7±2.1
	50571.15	50571.21	2.72±0.06	88.1±1.3	2.87±0.04	110.2±1.3
	50571.21	50571.27	2.77±0.06	85.0±1.4	2.94±0.04	96.1±1.0
	50572.21	50572.27	3.03±0.09	44.8±1.0	3.25±0.07	56.0±1.0
	50574.08	50574.14	2.91±0.05	65.5±0.9	2.93±0.06	80.8±1.3
	50574.14	50574.19	2.86±0.06	63.7±1.0	2.98±0.05	76.2±1.1
	50574.19	50574.25	2.83±0.07	61.0±1.1	3.00±0.06	76.0±1.2
	50602.24	50602.26	2.48±0.03	340.6±2.6	2.61±0.02	402.0±1.8
PKS 2155	50225.18	50225.24	2.42±0.04	156.5±1.6	2.50±0.02	186.5±1.0
−304	50227.24	50227.29	2.58±0.05	91.7±1.2	2.68±0.07	114.0±2.2
	50227.29	50227.35	2.68±0.04	97.5±1.1	2.70±0.03	119.3±0.9
	50227.35	50227.40	2.63±0.05	105.5±1.4	2.69±0.04	126.0±1.4
	50401.41	50401.47	2.85±0.07	36.1±0.7	2.90±0.07	46.1±0.8
	50401.47	50401.53	2.74±0.07	40.5±0.8	2.93±0.06	52.9±0.8
	50401.53	50401.59	2.63±0.07	44.0±0.9	2.78±0.05	56.9±1.1
	50401.59	50401.65	2.83±0.07	45.5±0.8	2.89±0.05	61.2±0.8
	50402.64	50402.69	2.64±0.07	37.1±0.7	2.73±0.08	44.8±0.9

List of simultaneous X-ray observations by *ASCA* and *RXTE*. Fitting model is Galactic absorption plus a power law function. Data from 2.5 keV to 7.5 keV were used for the fit.
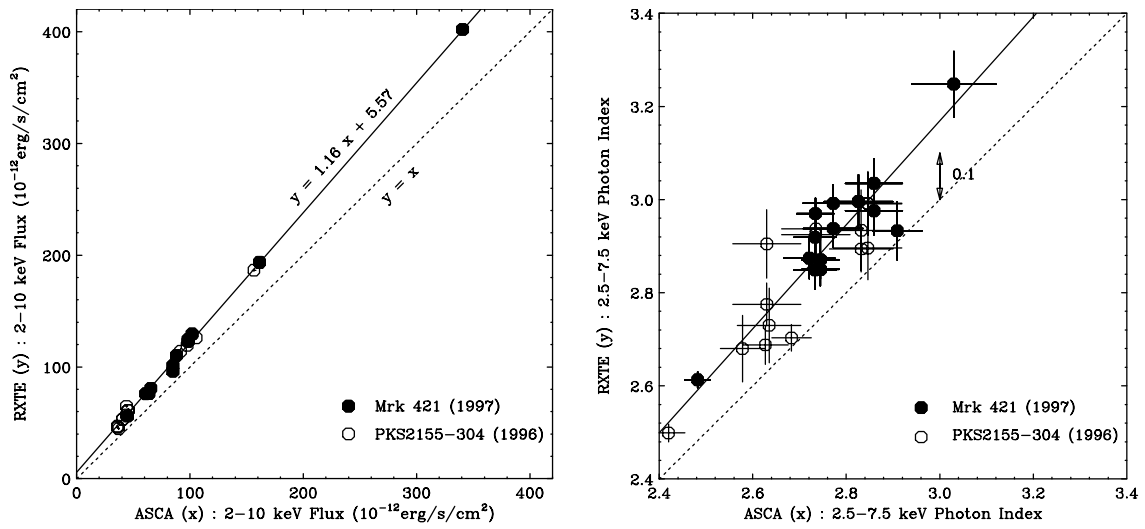
Figure 8.15: Comparison between *ASCA* and *RXTE* . Data from simultaneous observation of Mrk 421 and PKS 2155−304 are used. In order to use the energy range covered by different instruments, we selected the data from 2.5 keV to 7.5 keV. *left* : distribution of *ASCA* flux (2−10 keV) versus *RXTE* flux (2−10keV). *right* : distribution of *ASCA* photon index versus *RXTE* photon index.

8.3.3   Shift of the Synchrotron Peak

To study the time evolution of photon spectra in various states of the source activity, we describe the photon spectra for each TeV blazar in νF_ν space. The PCA spectra were convolved with the best-fit functions (either a power law function or a cutoff power law function). We binned the total PCA bandpass ($2.5-20$ keV) into 20 energy bands to reduce errors.

The evolution of photon spectra of four TeV blazars are shown in Figure $8.16-8.18$. We can clearly see different characteristics of each source.

Mrk 421

Evolution of νF_ν spectra of Mrk 421 in different observations is summarized in Figure 8.16. Contrary to the *ASCA* result, one cannot identify the synchrotron peak in the PCA energy band ($2.5-20$ keV). However, when the source was in the brightest state (#1), the spectrum is very flat, which indicates that the synchrotron peak is present close to 2.5 keV. This result is consistent with what expected from the *ASCA* data, where synchrotron peak is around 2 keV, when the source was in the brightest state.
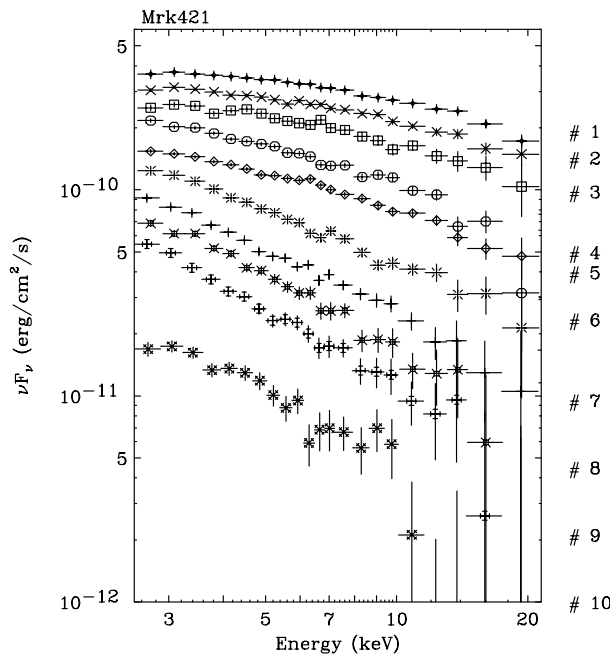
Figure 8.16: Synchrotron peak shifts of Mrk 421 observed with *RXTE* . Data are from #1: MJD 50208.56, #2: MJD 50207.90, #3: MJD 50208.43, #4: MJD 50215.25, #5: MJD 50208.17, #6: MJD 50213.64, #7: MJD 50571.23 #8: MJD 50222.25,#9: MJD 50572.23, #10: MJD 50427.89. For more detail, see Table G.1 − G.3.

Mrk 501

The changes of νF_ν spectra of Mrk 501 are shown in Figure 8.17. When the source was the faintest (#8), energy spectrum was steepest (photon index 2.5) and the synchrotron peak was well below 2.5 keV. However, during the flare, the spectrum largely flattened (photon index 1.7) and the synchrotron peak moved to above 20 keV (#1) – the largest shift ever observed in blazars (Pian et al. 1998; Kataoka et al. 1999a,b). Extrapolating the relation between the peak luminosity L_p and the peak energy E_p found in the *ASCA* results ($E_\mathrm{p} \propto L_\mathrm{p}^{1.6}$), we expect that the synchrotron peak reaches to ~ 100 keV in the highest state. Note that the amplitude of flux variation is much smaller than that of Mrk 421, but showed dramatical change in the synchrotron peak position.
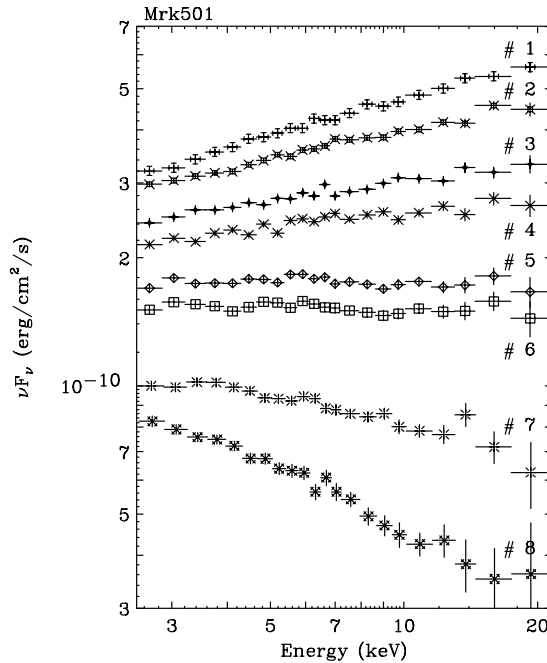
Figure 8.17: Synchrotron peak shifts of Mrk 501 observed with *RXTE* . Data are from #1: MJD 50554.17, #2: MJD 50551.46, #3: MJD 50550.45, #4: MJD 50544.31, #5: MJD 50545.44, #6: MJD 50546.25, #7: MJD 50378.51 #8: MJD 50296.57. For more detail, see Table G.4 – G.6.

PKS 2155−304

We show the changes of νF_ν spectra of PKS 2155−304 in Figure 8.18. There seems to be no clear trend between the flux and spectral shape – in fact, when the source was in the brightest state (#1), spectrum was very *steep*, indicating that synchrotron peak exists at an energy much lower than 2.5 keV. On the other hand, some observations showed very

flat spectra, although luminosity was relatively low (#3, #4). Such a lack of a clear trend has also been implied from the *ASCA* data (Figure 7.30).
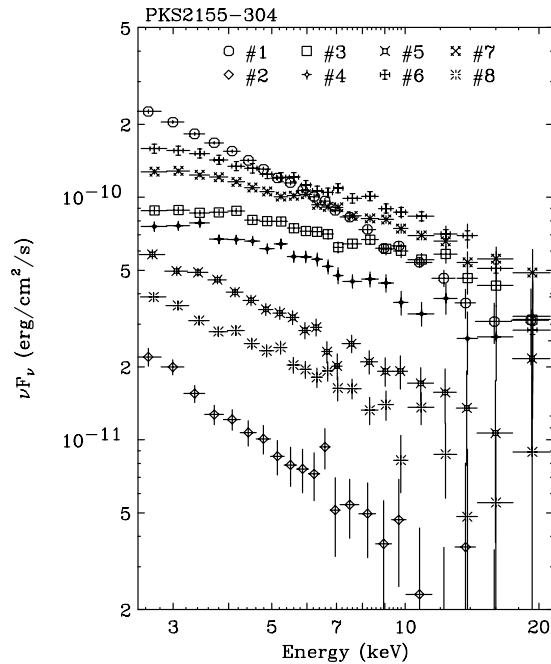
Figure 8.18: Synchrotron peak shifts of PKS 2155−304 observed with *RXTE* . Data are from #1: MJD 50772.96, #2: MJD 50824.40, #3: 50220.23, #4: MJD 50221.90, #5: MJD 50409.13, #6: MJD 50224.91, #7: MJD 50223.95 #8: MJD 50287.38. For more detail, see Table G.7 − G.10.

Combined *ASCA* and *RXTE* Results

By combining with the *ASCA* and *RXTE* results, we can study the X-ray spectral evolution of TeV blazars in different phases of source activity, using more complete data samples.

Figure 8.19 shows the distribution of peak luminosity $L_{\rm p}$ versus peak energy $E_{\rm p}$, compiled from Figure 7.30 from the *ASCA* and Figure 8.16−8.18 from the *RXTE* results. For Mrk 421 and PKS 2155−304, we have seen that all *RXTE* spectra are located above the synchrotron peak energy, and thus we only plot the *ASCA* results. For Mrk 501, some *RXTE* observations revealed relatively flat energy spectra whose photon indices were close to $\Gamma \sim 2.0$. This means that the synchrotron peak exists in the *RXTE* energy band. When the source was in a brighter phase, the photon spectra are harder (~ 1.7) and the peak is thought to be shifted to higher energy than the PCA bandpass.

In Figure 8.19, we added the *RXTE* results of Mrk 501 as a 'box' region and a lower limit to compare the *ASCA* results. In this, we took the systematic differences between

ASCA and *RXTE* into account (§ 8.3.2); when the photon index of a cutoff power law function (§ 7.3.2) gives $\Gamma \leq 2.1$, the spectra is monotonously rising in PCA bandpass, hence E_p is located above 20 keV (equation (7.15)). When Γ is larger than 2.1 and E_p is measured to be in the PCA bandpass, the peak is likely existing in the energy range of the PCA. One can see that the *RXTE* results are exactly on a line which is expected from the *ASCA* results.
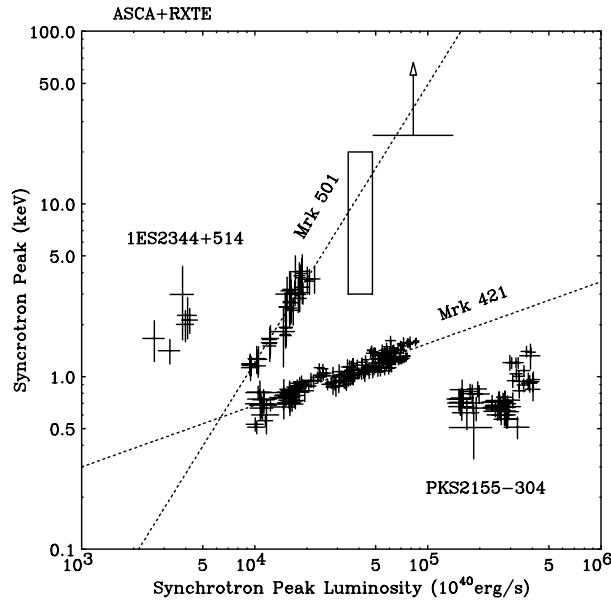
Figure 8.19: Distribution of peak luminosity L_p versus peak energy energy E_p from combined *ASCA* and *RXTE* results.

Chapter 9

Multi-wavelength Properties of TeV Blazars

In previous sections, we have investigated the rapid variability and spectral evolution of TeV blazars, highlighting the X-ray observations by *ASCA* and *RXTE* . However, the overall spectral energy distribution of blazars generally ranges over a very wide range – from radio to TeV γ-ray bands – and such spectra are one of the most important features allowing us to understand these sources. To reveal the multi-frequency properties of TeV blazars, we have to carry out multi-frequency monitoring campaigns of the source in various states of activity.

Results from previous campaigns strongly suggest correlated variations in X-ray and TeV γ-ray fluxes, while variability is much less pronounced in other energy bands (e.g., Macomb et al. 1995; Buckley et al. 1996). However, a problem remains that most of the data are taken either *non*-simultaneously (but contemporaneous within a week; e.g., Macomb et al. 1995) or are very sparsely sampled (e.g., Buckley et al. 1996).

From the X-ray studies of rapid variability, we now know that the characteristic variability time scale of TeV blazars are very short, ranging from 0.3 day to $\sim$ 1 day (§ 8.2.3). TeV flux variations are sometimes faster – rapid variability as short as an hour had been reported (Gaidos et al. 1996). Thus the discussion based on those *quasi*-simultaneous data may be incomplete. We need *exactly* simultaneous monitoring, especially in the X-ray and TeV energy bands, to correctly understand the sources. In the following, we summarize the results from *truly* simultaneous campaigns of TeV blazars conducted from 1996 to 1998. Observations logs are given in § 6.4.

9.1   Mrk 421

X-ray/TeV γ-ray correlation

Figure 9.1 shows the long term variability of Mrk 421 in X-ray and TeV γ-ray energy bands. Two remarkable flares were observed in TeV energy band in 1996 May, where flux reached up to ~ 10 Crab and rapidly decreased to the quiescent level on time scale as short as an hour (Gaidos et al. 1996; indicated by an arrow in Figure 9.1). Importantly, *RXTE* observations also revealed that Mrk 421 was very bright and extremely active during 1996 May observations (e.g., § 8.1).
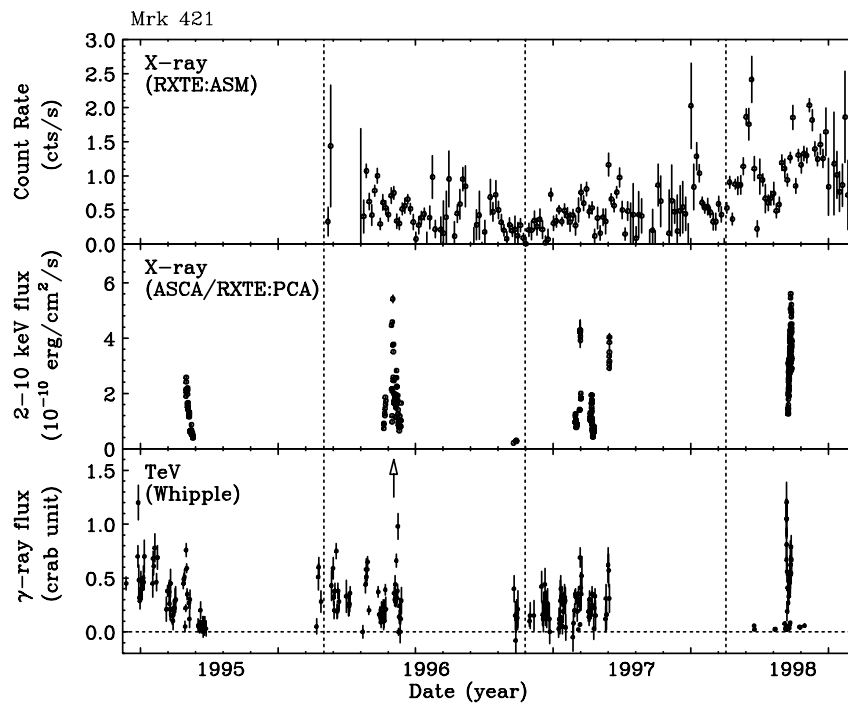
Figure 9.1: X-ray and TeV γ-ray flux variation from 1995 to 1998. *top* and *middle* : X-ray flux $(2-10$ keV; this work), *bottom* : TeV γ-ray flux above 350 GeV (roughly estimated from McEnery et al. 1997 and private communication with M.Catanese). TeV γ-ray flux are given in unit of Crab flux. TeV data from May 7, 1996 (6.2 Crab) is suppressed and represented here by an arrow.

During 1998 April observation, *ASCA* recorded a higher flux than that observed in 1996 May – to our knowledge, this is the record high flux ever observed for this source in the X-ray band. The campaign started from a pronounced high amplitude flare recorded by *BeppoSAX* and *Whipple* (Maraschi et al. 1999b), and high activity of the source continues during the whole campaign both in X-ray and TeV γ-ray.

Simultaneous observations by TeV telescopes revealed that the TeV flux was also in a high state, although extremely rapid variability as short as an hour was not observed

during this campaign. Such a correlation is more clearly seen in multiband light curves taken at April 1998 (Figure 9.2). This figure combines the results from TeV telescopes (*Whipple* , *HEGRA* and *CAT*), X-ray observations (*ASCA* , *BeppoSAX* and *RXTE*) and *EUVE*. Light curves are normalized by their average values. It should be noted that the rapid flares observed in the X-ray energy band were also detected at TeV energies (e.g., flares at MJD 50924.5 and 50928.0). During this campaign, the X-ray flux was gradually increasing on a time scale of ~ 10 days, which is the same trend as that observed in TeV flux variation.
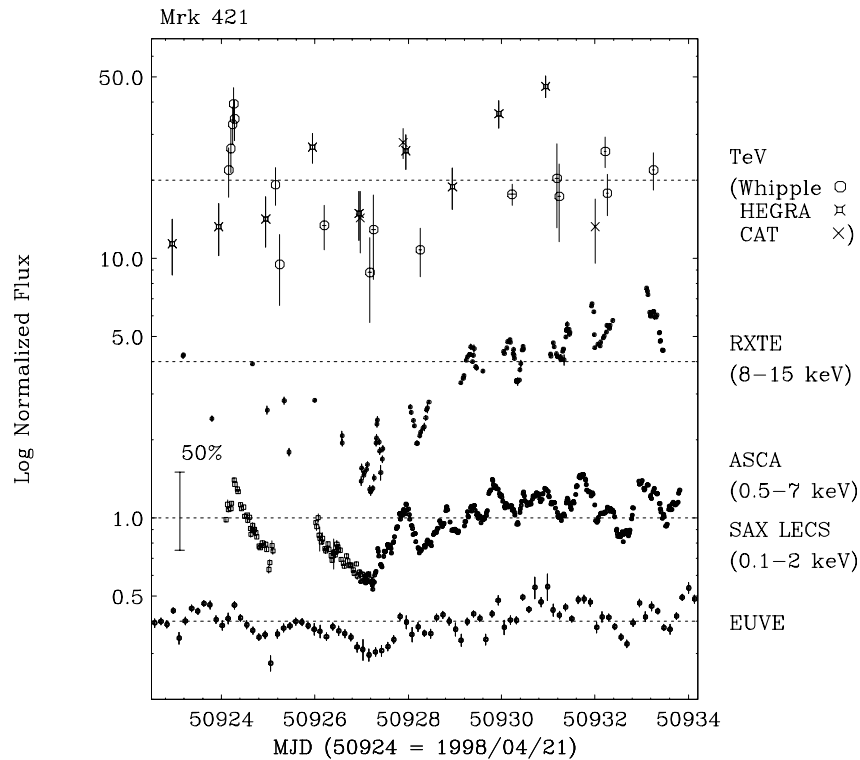
Figure 9.2: Multiband flux variations of Mrk 421 during 1998 campaign. TeV data: *Whipple* , *HEGRA* , and *CAT*. X-ray data: ASCA, *RXTE* , and *BeppoSAX*. UV data : *EUVE*. All light curves are normalized by their average values. Figure adopted from Takahashi et al (1999; in preparation).

In Figure 9.3, we plot the keV X-ray flux ($2-10$ keV) versus TeV γ-ray flux (in Crab units) obtained from observations in 1997 and 1998. In the plot, each point is calculated from the period when both *ASCA* and *Whipple* observed the source simultaneously. A clear correlation was found for the first time, where [TeV γ-ray flux] $\propto$ [X-ray flux]$^{0.92\pm0.12}$. We also plot in Figure 9.4 the flux correlation between UV and TeV data. Since the UV flux variation is small compared to the X-ray variation, correlation slope is steeper, where [TeV γ-ray flux] $\propto$ [UV flux]$^{2.71\pm0.67}$.
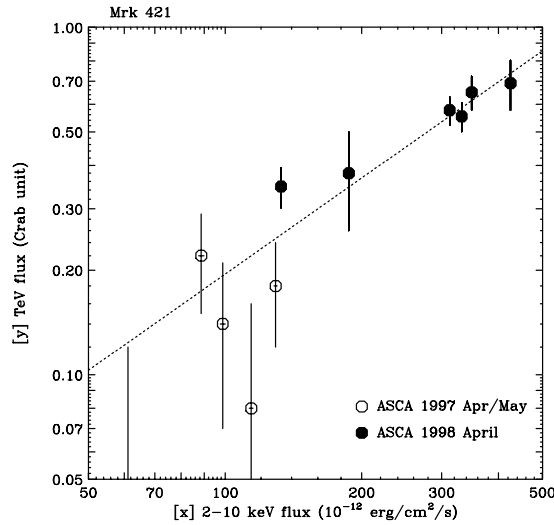
Figure 9.3: Correlation between X-ray flux (2−10 keV) and TeV γ-ray flux (> 350 GeV). X-ray flux measurements come from *ASCA* data, while TeV fluxes are *Whipple* data. TeV fluxes are given in unit of Crab flux. Dashed line shows the best-fit line of [TeV flux] ∝ [keV flux]$^{0.92}$.
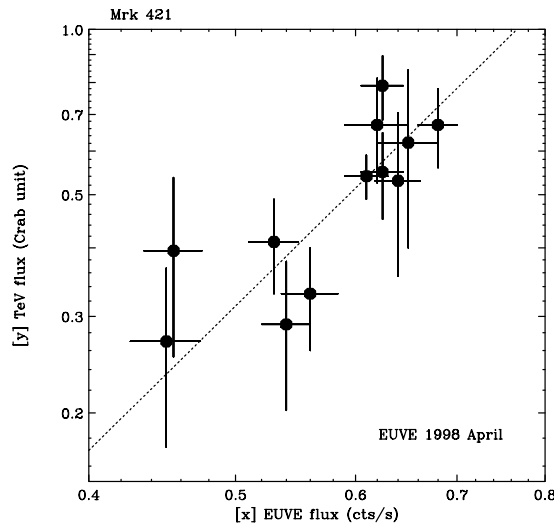
Figure 9.4: Correlation between *EUVE* count rate and TeV γ-ray flux (> 350 GeV). TeV fluxes are given in unit of Crab flux. Dashed line shows the best-fit line of [TeV flux] ∝ [keV flux]$^{2.7}$.

Evolution of Multi-frequency Spectrum

Evolution of multi-frequency spectrum of Mrk 421 is given in Figure 9.5. Open circles come from Macomb et al (1995), while other symbols (#1−4) represent our new results taken exactly simultaneously in X-ray (also *EUVE*) and TeV γ-ray bands.

Several important features are seen in the figure. First, the slope of X-ray photon

spectra ($\Gamma_{\mathrm{X-ray}} \sim 3$; see § 7.3) are steep, and very similar to those in the TeV energy band ($\Gamma_{\mathrm{TeV}} \sim 3$; Aharonian et al.1999b). Second, the amplitude of TeV flux variation is less or almost comparable with that in the X-ray energy bands (see also Figure 9.3). Third, although X-ray flux changed dramatically in various seasons, only small changes are implied in the synchrotron peak position, as we have quantitatively discussed in § 7.3.3.
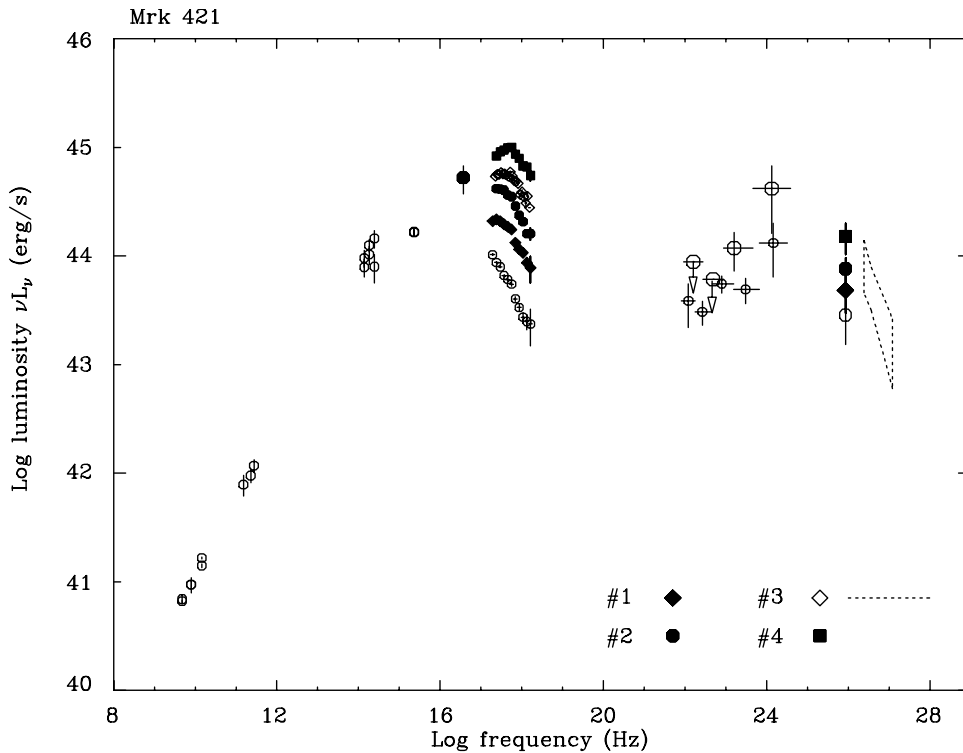
Figure 9.5: Multi-frequency spectra of Mrk 421 in various source activities. Truly simultaneous data for *EUVE*, X-ray and TeV γ-ray bands were plotted with non-simultaneous archival data. #1 : data from MJD 50571.15 to MJD 50571.20 (May 3, 1997; this work), #2 : data from MJD 50927.13 to MJD 50927.29 (Apr 24, 1998; this work), #3 : data from MJD 50927.84 to MJD 50927.90 (Apr 24, 1998; this work), #4 : data from MJD 50933.22 to MJD 50933.27 (Apr 30, 1998; this work). Open circles are published data from Macomb et al (1995). For #1−4, TeV data are provided by *Whipple* Cherenkov observatory (private communication with M.Catanese), while TeV data (*HEGRA*) for #4 come from Aharonian et al (1999b).

9.2   Mrk 501

X-ray/TeV γ-ray correlation

Figure 9.6 shows a long term variability of Mrk 501 comparing the X-ray and TeV γ-ray energy bands. One finds that the source was in a historically high state during the 1997 pointings. This clearly suggests that the flux variation in both X-ray and TeV γ-ray energy bands is well correlated on time scales of months to years. During the flare in 1997 April/May, flux reached $\sim$ 4 Crab in the TeV energy bands (Catanese et al. 1997), which was the factor 40 increase of flux compared to that reported in the quiescent state (Quinn et al. 1995; 1999).
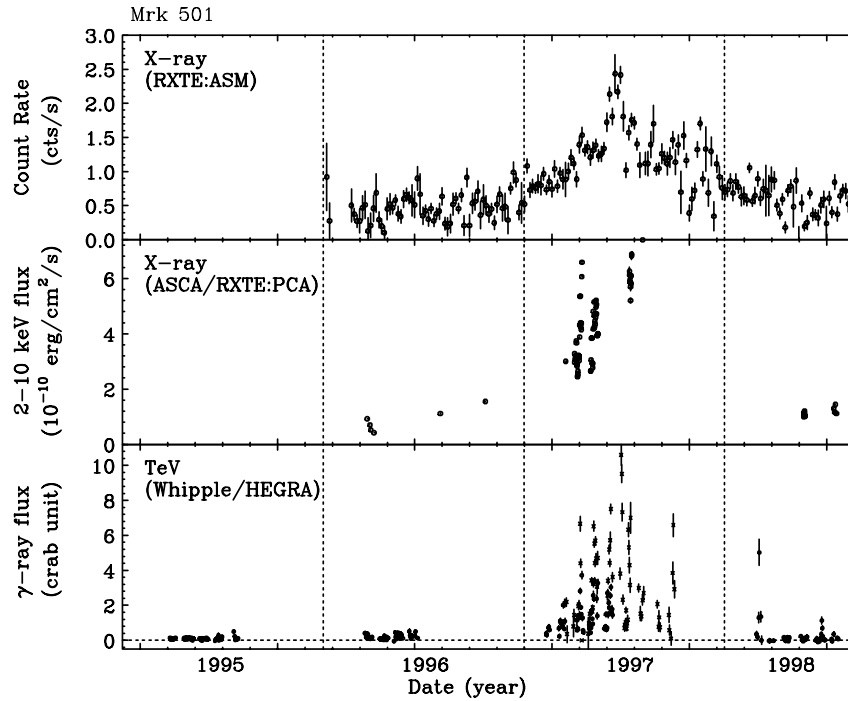
Figure 9.6: X-ray and TeV γ-ray flux variation from 1995 to 1998. *top* and *middle* : X-ray flux (2−10 keV; this work), *bottom* : TeV γ-ray flux above 350 GeV (Quinn et al .1999) and Aharonian et al (1999a; above 1 TeV). TeV γ-ray flux are given in unit of Crab flux.

The light curves during the first multi-wavelength campaign conducted in 1996, which included γ-ray detectors, are shown in Figure 9.7. These observations have two important results. Firstly, EGRET detected GeV γ-ray emission for the first time at 3.5 σ level, which was also confirmed by the follow up observations in 1996 April/May (Table 9.1; Kataoka et al. 1999). Secondly, since the observations were conducted when the source was relatively low emission state, this establish the 'baseline' spectral energy distribution of Mrk 501 compared to the high state emission in 1997.
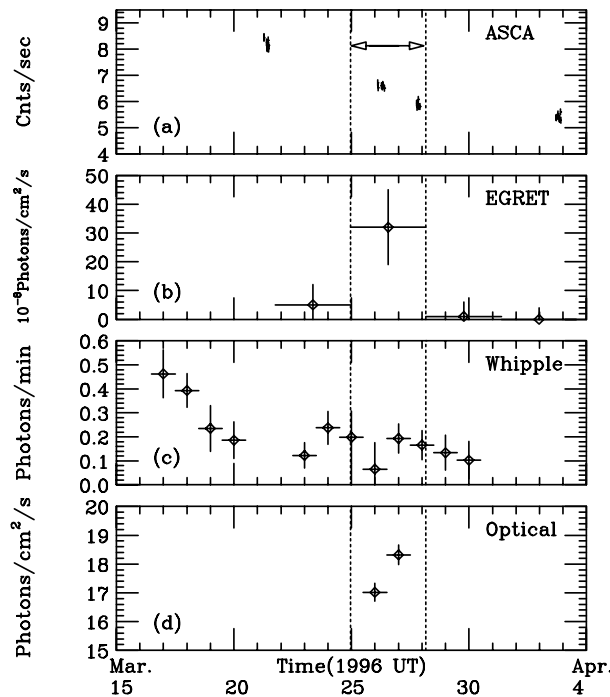
Figure 9.7: Time history of Mrk 501 during the March 1996 campaign. (a): X–ray (*ASCA*: 0.7 − 10 keV), (b): GeV (*EGRET*: 100 MeV − 10 GeV), (c): TeV (*Whipple*: above 350 GeV) and (d): Optical (R − band: 650 nm). The *ASCA* count rates are from the summed SIS0 and SIS1 data, extracted from a circular region centered on the target with a radius of 3 arcmin. The time interval marked with arrows is when EGRET detected Mrk 501 at 3.5 σ significance for the first time. All errors are 1 σ. Figure from Kataoka et al (1999).

Multi-wavelength observations of Mrk 501 during the high state in 1997 demonstrated a clear correlation of fluxes in the X-ray band and TeV γ-ray bands (Catanese et al. 1997). Large amplitude flux change as well as spectral evolution were reported in the X-ray energy band by *BeppoSAX* observations (Pian et al. 1998). Based on three ToO observations conducted in Apr 7, 11 and 16 with *BeppoSAX* , they presented that (1) 2−10 keV flux increased to more than 5×10^{-10} (erg/cm^2/s) and (2) synchrotron peak shifted to higher energies $\sim$ 100 keV, both of which are consistent with our results (§ 8.3.3).

ASCA and *RXTE* observations reported in this thesis were based on much larger samples, which were taken at various phases of source activity. Figure 9.8 shows the flux variations of X-ray and TeV γ-ray bands taken at April/May 1997, when the source was in a very high state. One finds a clear correlation in both energy bands on a time scale of a day, as well as on longer time scales.

X-ray and TeV γ-ray fluxes are plotted in Figure 9.9, based on *truly* simultaneous

Table 9.1: EGRET results for Mrk 501

EGRET VP [a]	Interval	Aspect [b]	Exposure [c]	Significance (σ)	Flux [d]
9.5	12-Sep-1991 — 19-Sep-1991	3.3°	2.28	0.5	< 11
201.0	17-Nov-1992 — 24-Nov-1992	2.5°	1.12	1.7	9±6
202.0	24-Nov-1992 — 01-Dec-1992	5.8°	1.06	1.1	8±7
516.5	21-Mar-1996 — 03-Apr-1996	3.1°	1.47	2.1	10±5
	(25-Mar-1996 — 28-Mar-1996)		0.46	3.5	32±13
519.0	23-Apr-1996 — 07-May-1996	1.2°	2.10	4.0	18±5
	(E>500 MeV)		2.97	5.2	[e]6±2
617.8	04-Apr-1997 — 15-Apr-1997	3.0°	0.82	1.5	9±7

a: EGRET Viewing Period

b: Angle between the source and the EGRET instrument

c: Exposure in unit of 10^8 cm^2 s

d: Flux (E>100 MeV) in units of 10^{-8} cm^{-2}s^{-1}

e: Flux (E>500 MeV) in units of 10^{-8} cm^{-2}s^{-1}

The error is 1 σ.
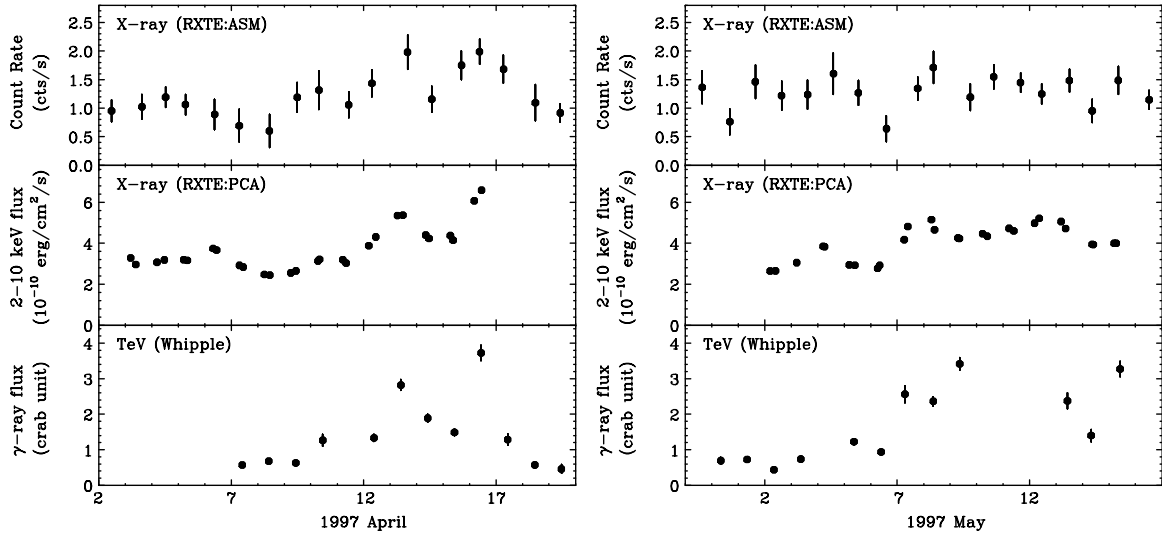
Figure 9.8: X-ray and TeV γ-ray flux variation in 1997. *left* : April 1997, *right* : May 1997. *top* and *middle* : X-ray flux (2−10 keV; this work), *bottom* : TeV γ-ray flux above 350 GeV (Quinn et al .1999). TeV γ-ray fluxes are given in unit of Crab flux.

data. One finds a clear correlation, but different from that found in Mrk 421. For Mrk 501, we obtained a quadratic relation, where [TeV γ-ray flux] $\propto$ [X-ray flux]$^{1.96\pm0.07}$.
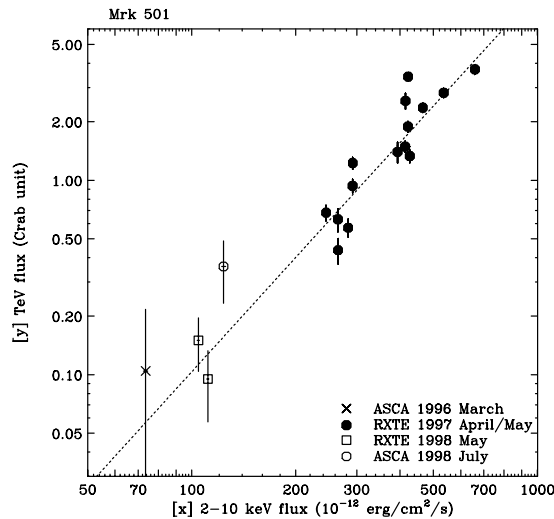
Figure 9.9: Correlation between X-ray flux (2−10 keV) and TeV γ-ray flux (> 350 GeV). X-ray fluxes come from *ASCA* and *RXTE* data, while TeV fluxes are *Whipple* data. TeV fluxes are given in unit of Crab flux. Dashed line shows the best-fit line of [TeV flux] $\propto$ [keV flux]$^{1.96}$.

Evolution of Multi-frequency Spectrum

Evolution of the multi-frequency spectrum of Mrk 501 is shown in Figure 9.10. Open circles are data from public archive (taken from Kataoka et al. 1999), while other symbols represent our new results derived from simultaneous monitoring in the X-ray and TeV γ-ray bands. For the data obtained in March 1996, we also plot the EGRET and optical data.

Compared to the results for Mrk 421, some significant differences are implied in the multiband specta. First, the changes in X-ray flux are accompanied by large shift in the position of the synchrotron peak, as shown in § 7.3.3 and 8.3.3. Second, the slope of X-ray spectra varies widely, ranging from $\Gamma_{X-ray} \sim 1.7$ to 2.5 (see § 7.3, 8.3), while the photon index in the TeV energy band is almost unchanged and steeper; $\Gamma_{TeV} \sim 2.5$ (e.g, Petry et al. 1997; Aharonian et al. 1999a). Third, amplitude of TeV flux variation is much larger than that in the X-ray energy band (see also Figure 9.9).
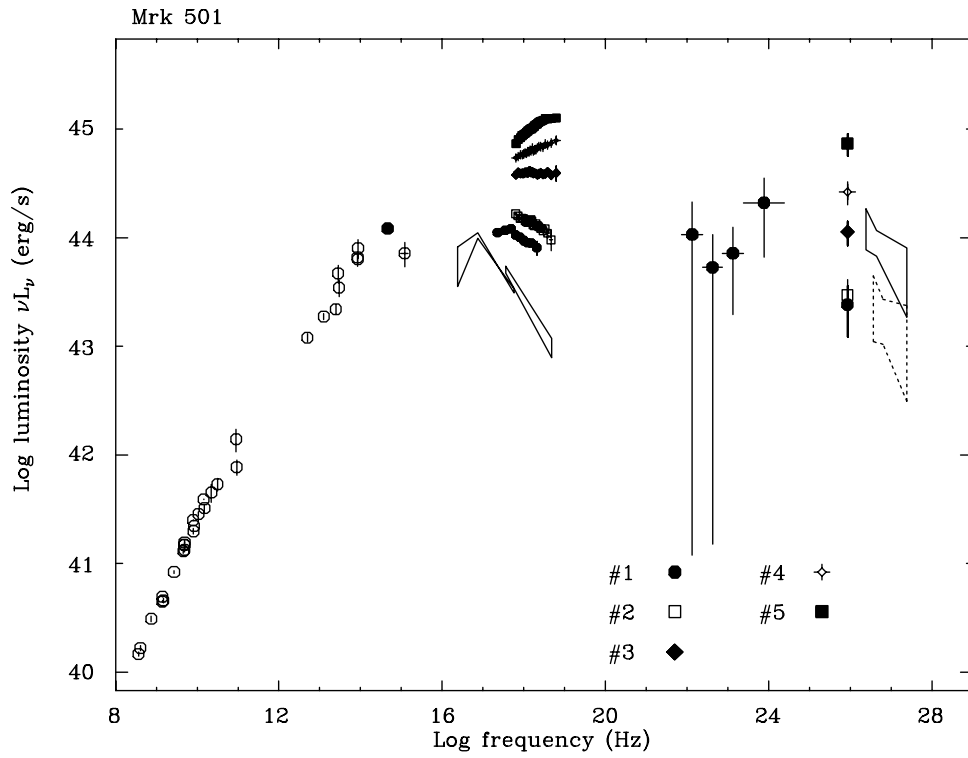
Figure 9.10: Multi-frequency spectra for Mrk 501 in various source activities. Truly simultaneous data in optical, X-ray, GeV γ-ray and TeV γ-ray bands were plotted with non-simultaneous archival data. #1 : data from MJD 50166.96 to MJD 50170.17 (Mar 25-28, 1996; Kataoka et al. 1999a), #2 : data from MJD 50960.29 to MJD 50960.39 (May 27, 1998; this work), #3 : data from MJD 50545.36 to MJD 50545.46 (Apr 7, 1997; this work), #4 : data from MJD 50550.33 to MJD 50550.43 (Apr 12, 1997; this work), #5 : data from MJD 50554.38 to MJD 50554.48 (Apr 16, 1997; this work). Open circles : NASA/IPAC Extragalactic data base (NED). Solid figure : *ROSAT* (Comastri et al. 1997), *GINGA* (Makino et al. 1991), *HEGRA* (Aharonian et al. 1997). Dashed figure : *HEGRA* (Bradbury et al. 1997).

9.3 PKS 2155−304

Flux Variation

Figure 9.11 shows the long term variability of PKS 2155−304 in X-ray and TeV γ-ray energy bands. The detection of the TeV γ-ray emission was reported only recently by Chadwick et al (1999). When the highest TeV emission was detected in 1997 November, *RXTE* observation also recorded the highest X-ray flux ever observed (§ 8.3). At the same epoch, the EGRET observed the source and found that GeV γ-ray flux increased by factor 3 compared to that in the 1996 observation (Sreekumar & Vestrand 1997). This probably implies the correlation of emission in various energy bands, but needs further study.
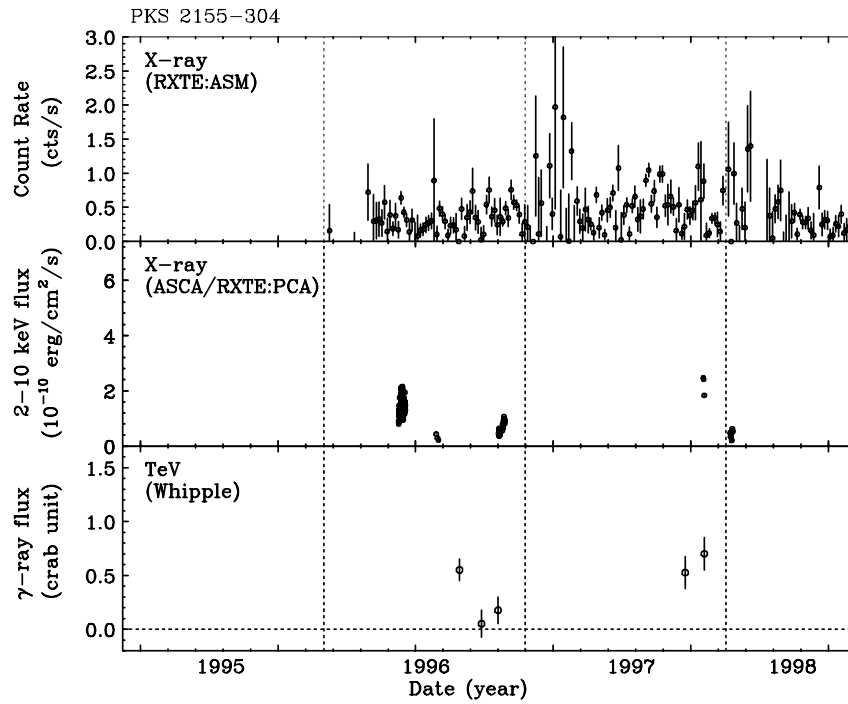
Figure 9.11: X-ray and TeV γ-ray flux variation from 1995 to 1998. *top* and *middle* : X-ray flux (2−10 keV; this work), *bottom* : TeV γ-ray flux above 300 GeV (roughly estimated from Chadwick et al. 1999). Note that the TeV γ-ray emission was detected only recently. TeV γ-ray flux are given in unit of Crab flux.

Evolution of Multi-frequency Spectrum

Evolution of multi-frequency spectra of PKS 2155−304 is given in Figure 9.12. Open circles are data from archive. In this figure, TeV flux is given as an averaged flux from all

observations, including 1997 November (Chadwick et al. 1999). We also plot the EGRET spectrum estimated from the flux in Sreekumar & Vestrand (1997), assuming a spectral form reported in Vestrand et al (1995).

In contrast to the sparse sampling of γ-ray observations, lower energy band data are even better sampled than other TeV blazars. Filled circles are simultaneous data from optical to X-ray obtained in 1994 May campaign (Urry et al. 1997; Kataoka et al. 2000). Compared to Mrk 421 and Mrk 501, X-ray flux variation seems to be rather *chaotic*; when the source was in the brightest state (1997 November; #2), the spectrum was very steep, suggesting that synchrotron peak exists at much lower energies than X-ray energy band. However, for 1994 May data when the source was rather fainter, synchrotron peak existed at ∼ 1 keV (§ 7.3.3, 8.3.3).
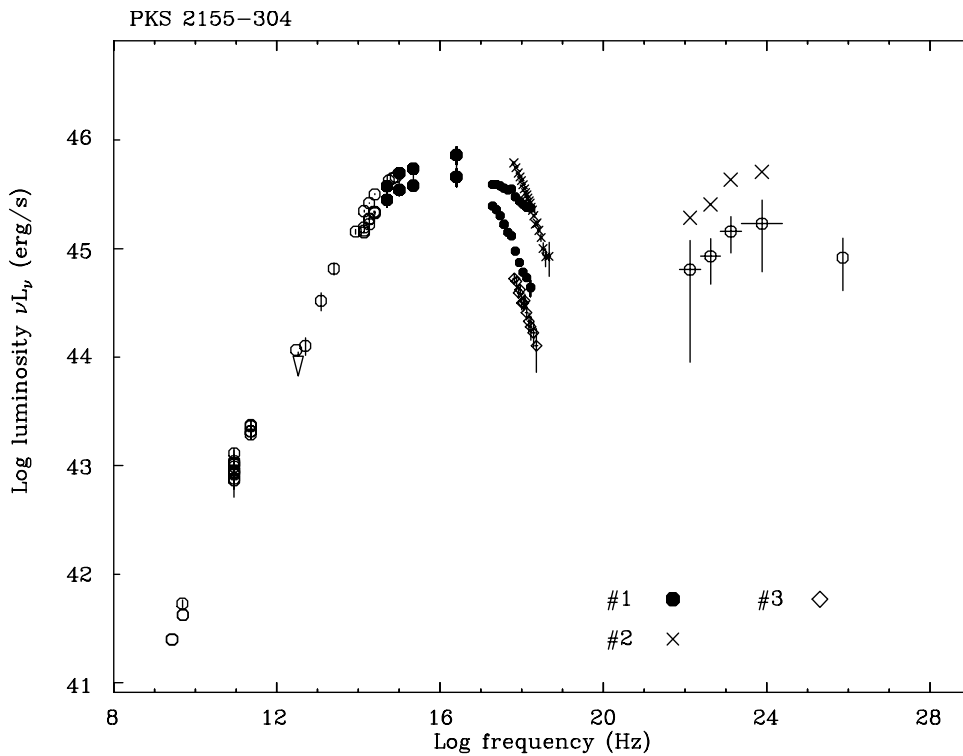
Figure 9.12: Multi-frequency spectra for PKS 2155−304 in various states of source activity. Truly simultaneous data in *IUE*, *EUVE*, X-ray bands were plotted with non-simultaneous archival data. #1 : data from MJD 49491.23 to MJD 49493.33 (Mar 19-21, 1994; Urry et al. 1997; Kataoka et al. 2000), #2 : data from MJD 50772.96 to MJD 50772.97 (Nov 20, 1997; this work), #3 : data from MJD 50291.66 to MJD 50291.68 (July 27, 1996; this work). Open circles : NED data base. Lower EGRET data are from Vestrand, Stacy & Sreekumar (1995), while upper EGRET data are estimated from Sreekumar & Vestrand (1997). TeV γ-ray data come from Chadwick et al. (1999). #2 is when the source was the brightest, while #3 is when the source was the faintest in the X-ray energy band.

9.4   1ES 2344+514

Flux Variation

Figure 9.13 shows the long term variability of 1ES 2344+514 in X-ray and TeV γ-ray energy bands. Only a very few observations had been conducted before the detection of TeV γ-rays as the third TeV blazar (Catanese et al. 1998). Unfortunately, no X-ray observations had been conducted when the *Whipple* telescope detected TeV γ-rays (1995 December 20); no *RXTE* ASM data are available on this source before 1997. More data are required to test a correlated variability in various energy bands.
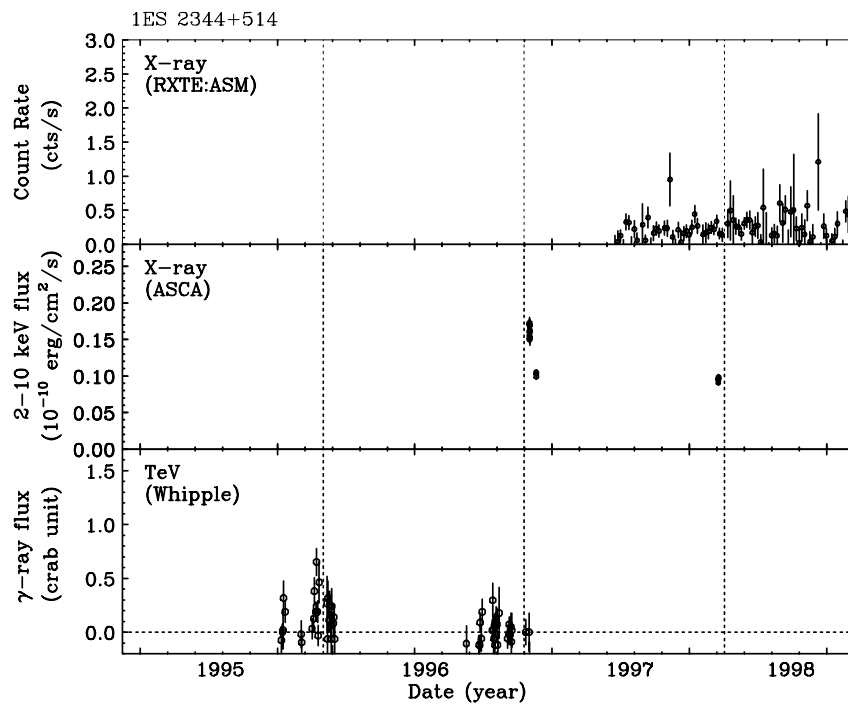
Figure 9.13: X-ray and TeV γ-ray flux variation from 1995 to 1998. *top* and *middle* : X-ray flux (2−10 keV; this work), *bottom* : TeV γ-ray flux above 350 GeV, from Catanese et al. 1998. Note that, TeV γ-rays were not detected above 2 σ level for 1996/97 observational seasons.

Evolution of Multi-frequency Spectrum

Evolution of multi-frequency spectrum of 1ES 2344+514 is given in Figure 9.14. Open circles are data from the public archive. Three TeV points are from Dec. 20 1995 (highest flux), averaged flux from 1995 to 1996, and upper limit from 1996 and 1997 observations. No EGRET detection has been reported for this source.

1ES 2344+514 is also the faintest TeV blazar in the X-ray energy band. However,

spectral evolution correlated with a flux change, similar to that for Mrk 501, is suggested as shown in Figure 9.14. When the source was in a quiescent state, it showed a steep spectrum with photon index of $\Gamma_{X-ray} \sim 2.3$. It hardened to ~ 1.8 when the source becomes brighter (Giommi et al. 1999; § 8.3). This supports an idea that the synchrotron peak largely moves with the flux change as that were observed in Mrk 501 (§ 7.3.3). Further observations are necessary for confirmation.
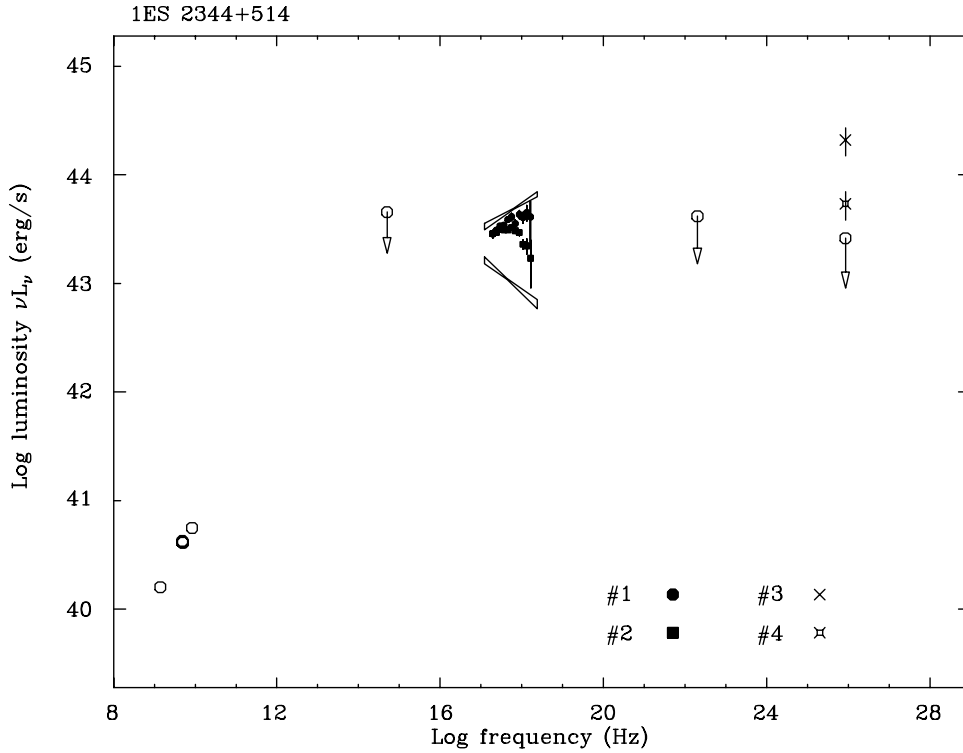
Figure 9.14: Multi-frequency spectra for 1ES 2344+514 in various source activities. No simultaneous data with X-ray observations has been available. #1 : data from MJD 50458.68 to MJD 50458.84 (Jan 10, 1997; this work), #2 : data from MJD 50471.23 to MJD 50471.40 (Jan 23, 1997; this work), #3 : TeV data on 1995 Dec 20 (TeV flare; Catanese et al. 1998), #4 : TeV average flux from 1995 to 1996 (Catanese et al. 1998). Open circles : Perlman et al. 1996; Patnaik et al. 1992; Gregory & Condon 1991. Solid figure: *BeppoSAX* (Giommi et al. 1999). Upper limit for TeV emission was derived from 1996/1997 observations (Catanese et al. 1998).

Chapter 10

Discussion

10.1 Summary of Results

We have observed 4 TeV blazars with X-ray satellites *ASCA* and *RXTE* . These observations provide the highest quality spectral and timing information over a very wide energy range of $0.7-20$ keV. It is noted that 30 X-ray observations were conducted simultaneously with *Whipple* Cherenkov telescopes (TeV), and 7 observations are also contemporaneous with EGRET on-board *CGRO* (GeV). To our knowledge, our current work is based on the largest sample of X-ray/GeV/TeV γ-ray data for TeV blazars, obtained in various states of source activities. In the following, we briefly summarize major results contained in this thesis.

X-ray Time Variability

Unprecedented big campaigns for Mrk 421 (1998; 7days) and PKS $2155-304$ (1996; 12 days) revealed more than 10 flares with time scales of about a day which occured during the observations, indicating that variabilities in TeV blazars are more dynamic and complicated than we had imagined. Successive occurrence of flare events had been proposed by previous observations (e.g., Buckley et al. 1996), but data were too short and/or too undersampled to study in detail the time profile. We thus confirmed for the first time that rapid flares repeat day-by-day in those TeV blazars.

This naturally leads us to an idea that there exists some *prefered* time scale for variability of blazars. Structure function of TeV blazar variability showed a roll-over around 1 day, which we interpret as the characteristic time scale of rapid variability in blazars. Time scale was ~ 0.5 day for Mrk 421, 0.3 day for PKS $2155-304$ and ~ 1 day for Mrk 501. Notably, these time scales reflect the typical rise/decay time of individual flare events.
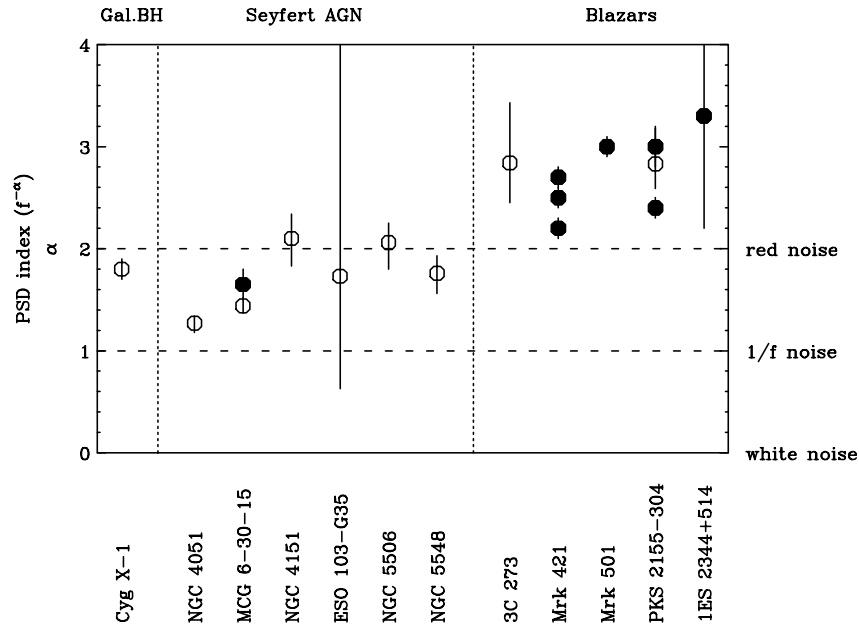
Figure 10.1: Comparison of PSD slopes for various black hole systems. *Open cicle* : Hayashida et al (1998). *Filled cicle* : Estimated from Structure Function analysis (this work). The power law indices for PSD (α for $f^{-\alpha}$) are simply estimated from SF index (β) as $\alpha = \beta + 1$.

On a shorter time scale (≤ 0.3 day), slopes of SFs (β) are quite steep, ranging from 1.2 to 2.3 for all TeV blazars (this corresponds to the PSD index where $f^{-\alpha}$ of $\alpha = 2 \sim 3$). This clearly indicates that the physical processes operating in TeV blazars are strong red-noise type ($\beta \sim 1$) or actually no significant process exits ($\beta \sim 2$) up to the characteristic time scale described above (~ 1 day). As we can see in Figure 10.1, this is very different from other types of mass-accreting black hole systems, whose variabilities are well characterized by a fractal, flickering noise ($0 < \beta < 1$).

It is also remarked that the most of the flare events were characterized by nearly equal rise-time and decay-time, thus forming a quasi-symmetric time profile. To evaluate the time asymmetry of the light curves in various energy bands, we used an applied technique introduced by Kawaguchi et al. (1998). We discovered that the symmetry of the time profile tends to break down at lower X-ray energies both for Mrk 421 (Figure 7.14) and PKS 2155−304 (Figure 8.10).

Another important discovery is the detection of 'hard-lag' flares. Such an *unusual* behaviour was first implied for PKS 2155−304 (Sembay et al. 1993), but was not confirmed due to limited photon statistics and short coverage of previous observations. We confirmed that the *paradigm* that the soft X-ray variations always lag behind the hard X-ray variations ('soft lag') was *not* generally true − in fact, we detected complicated

mixture of 'soft lag' and 'hard lag' during the 7-day observation of Mrk 421 in 1998. As many authors have suggested, variability amplitude tends to become larger as photon energy increases, but some clear exceptions were found, which may possibly related to the hard-lag behaviours (Figure 7.24).

X-ray Spectral Evolution

In the X-ray band, photon spectra of those TeV blazars are well represented by a power law form, but smoothly steepening to higher energies. Using 5-year complete samples of *ASCA* and *RXTE* data, we confirmed a general trend that the spectra tend to steepen when the sources become fainter (e.g., Giommi et al. 1990). It is also noted that low luminosity TeV blazars tend to have flatter spectrum (Figure 7.27), possibly indicating a smooth connection to other types of blazar classes, such as LBLs and QHBs (see Figure 2.11; Ghisellini et al. 1998; Kubo et al. 1998).

The peak of the synchrotron component (LE component) was detected with *ASCA* (in conjunction with the data in other wavelengths) for all TeV blazars. More remarkably, we found that the position of the peak shifts from lower to higher energy when the source becomes brighter. We showed that the spectral evolution of Mrk 421 indicates very little change in the peak position ($0.5 - 2$ keV), while Mrk 501 records largest shift ever observed ($1 - 100$ keV; Catanese et al. 1997 and Pian et al. 1998). For the first time, we succeeded to quantify the correlation between the peak luminosity (L_p) and the peak energy (E_p) (Figure 8.19). We found $E_p \propto L_p^{0.4}$ for Mrk 421 and $E_p \propto L_p^{1.6}$ for Mrk 501. This naturally indicates that the origin of the flare may be quite different in those two objects.

Inter-band Variability

The results from several previous campaigns had suggested that the variability in blazars correlates in multi-frequency bands (e.g., Macomb et al. 1995; Buckley et al. 1996). However, non-simultaneity of observations and/or rather sparse sampling prevented us from concluding the inter-band variability. In the present work, Mrk 421 and Mrk 501 were intensively monitored in both X-ray and TeV γ-ray bands, providing *exactly* simultaneous X-ray and TeV flux information in various phases of source activity. We found that variations in keV and TeV bands are well correlated on time scale of a day to years. We found that the amplitude of variation is comparable in both energy bands for Mrk 421 ([X-ray flux] $\propto$ [TeV flux]; see, Figure 9.3), while quadratic for Mrk 501 ([X-ray flux]^2 $\propto$ [TeV flux]; see, Figure 9.9).

10.2   Dynamics of Rapid Variability

In the following, we discuss dynamical time scales which characterize the rapid variability in blazars. For simplicity, we will consider the synchrotron process as the dominant cooling process for high energy electrons, ignoring the inverse Compton cooling. This approximation is valid for TeV blazars because (1) the synchrotron luminosity is generally greater than the Compton luminosity, and (2) the reduction of the cross section in the Klein-Nishina regime significantly decreases the Compton scattering efficiency. More detailed discussion will be given in § 10.6.

10.2.1   Synchrotron Cooling

The non-thermal emission of the low energy (LE) component is most likely produced by synchrotron emission from high energy electrons (see, § 2, § 3). X-ray energy band is considered to be the highest part of LE component for TeV blazars. Cooling rate of a single electron by synchrotron radiation is given in equation (3.34). Thus the time t_{cool} when an an electron loses half of its energy would roughly be (in the observer's frame)

$$t_{\mathrm{cool}}(\gamma) \simeq 5 \times 10^8 B^{-2} \gamma^{-1} \delta^{-1} (\mathrm{sec}), \tag{10.1}$$

where γ is the electron Lorentz factor. Since the peak observed frequency of the synchrotron emission is related to γ by equation (3.32), we found a simple relation,

$$t_{\mathrm{cool}}(E_{\mathrm{keV}}) \simeq 1.2 \times 10^3 B^{-3/2} E_{\mathrm{keV}}^{-1/2} \delta^{-1/2} (\mathrm{sec}), \tag{10.2}$$

where E_{keV} is the observed photon energy in keV and δ is a beaming factor (Takahashi et al. 1996). Since the cooling time is proportional to γ^{-1}, higher energy electrons cool much faster than lower energy electrons, which may account for the 'soft-lag' behaviour often observed in TeV blazars.

By calculating the Discrete Correlation Function (DCF) in various photon energies, Takahashi et al. (1996) found that the soft X-ray ($E < 1$ keV) variability lagged behind that for hard X-ray band ($E > 2$ keV) by 4×10^3 sec, consistent with our present analysis (Figure 7.20). They associated the soft-lag with the difference of cooling time with respect to the energy and derived a magnetic field $B \sim 0.2\,(\delta/5)^{-1/3}$ (G). Importantly, this was the first case where the magnetic field was calculated only from the observed X-ray variability.

Similar approach was adopted by Kataoka et al. (2000) for the PKS 2155−304 flare in 1994 (§ 7.2.5). Since the X–ray light curve during the flare was very symmetric, they evaluated the time lags in various energy bands with more direct method than the DCF, and compared the results with those obtained from DCF. They fitted the light curves to

a Gaussian and searched for the time shift of the peak of the flare. In this model, the photon count rate at an arbitrary time t is expressed as: $f(t) = C_0 + C_1 \times \exp\left[-(t - t_p)^2/2\sigma^2\right]$, where C_0 is a constant offset, C_1 is the amplitude of the flare component, t_p is the peaking time, and σ is the duration of the flare, respectively. The light curves were divided into 10 logarithmic-equal energy bands from 0.5 keV to 7.5 keV (for the SIS data) and 0.7 keV to 7.5 keV (for the GIS data; 9 bands). A Gaussian provides a sufficient fit of the resultant energy-binned light curves; the χ^2 probability of the fit was $P(\chi^2) \geq 0.1$ for 12 of 19 light curves. Note here that there was not any systematic (preferential) trend for the data whose probability $P(\chi^2)$ are less than 0.1. In Figure 10.2, we show examples of the Gaussian fit, which turned out to be a good representation of the data.
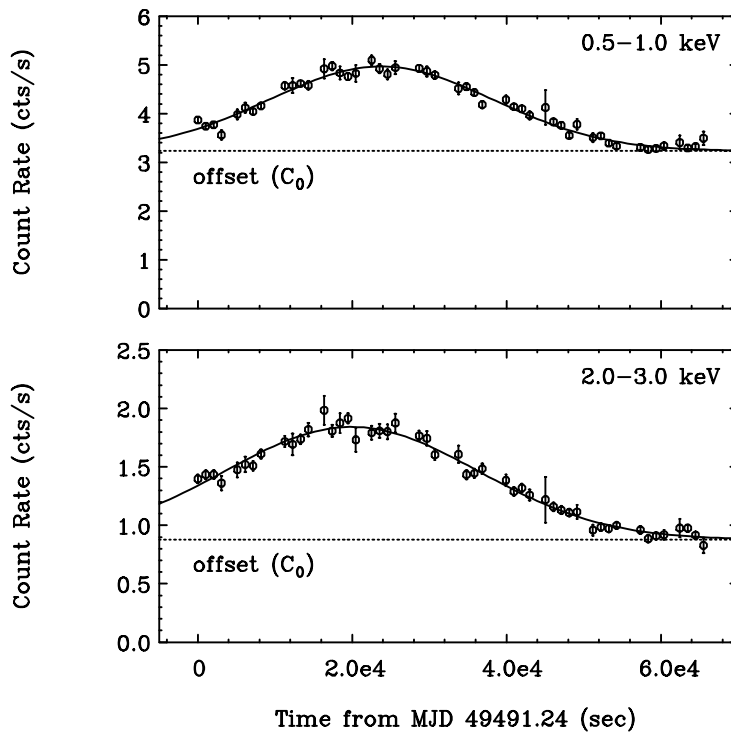
Figure 10.2: A Gaussian fit to the time profile of PKS 2155−304 during the flare in 1994. The count rates of both SIS detectors are summed. The solid line corresponds to the best fit with a Gaussian function given in the text. Upper Panel: Light curve in the 0.5 − 1.0 keV band; $\chi^2_{\rm red} = 1.5$ for 49 dof. Lower Panel: Light curve in the 2.0 − 3.0 keV band; $\chi^2_{\rm red} = 1.1$ for 49 dof (figure from Kataoka et al. 2000).

Figure 10.3 (a) shows the dependence on energy of the flare duration derived from fitting the energy-binned light curves. This result is consistent with a constant fit of σ = 1.5 × 10^4 sec. Figure 10.3 (b) shows the energy dependence of the flare amplitude, defined as the ratio of the normalization of the flare to the constant offset: $Ap \equiv C_1/C_0$.

The flare amplitude becomes larger as the photon energy increases. This is mostly due to the decrease in the constant offset (C_0) at higher energies. In other words, the spectrum during the flare is harder than that in the quiescent state. Figure 10.3 (c) is the lag of the peak time, calculated from the difference of t_p of the Gaussian, as compared to that measured in the $3.0-7.5$ keV band. As shown in the figure, the hard X–ray ($3.0-7.5$ keV) variability leads the soft X–rays ($0.5-1.0$ keV) by ~ 4 ksec. Finally, Figure 10.3 (d) shows the time lag measured from DCF technique, as was the case for the Mrk 421 (Takahashi et al. 1996). Lag is consistent with that estimated from the Gaussian fitting.
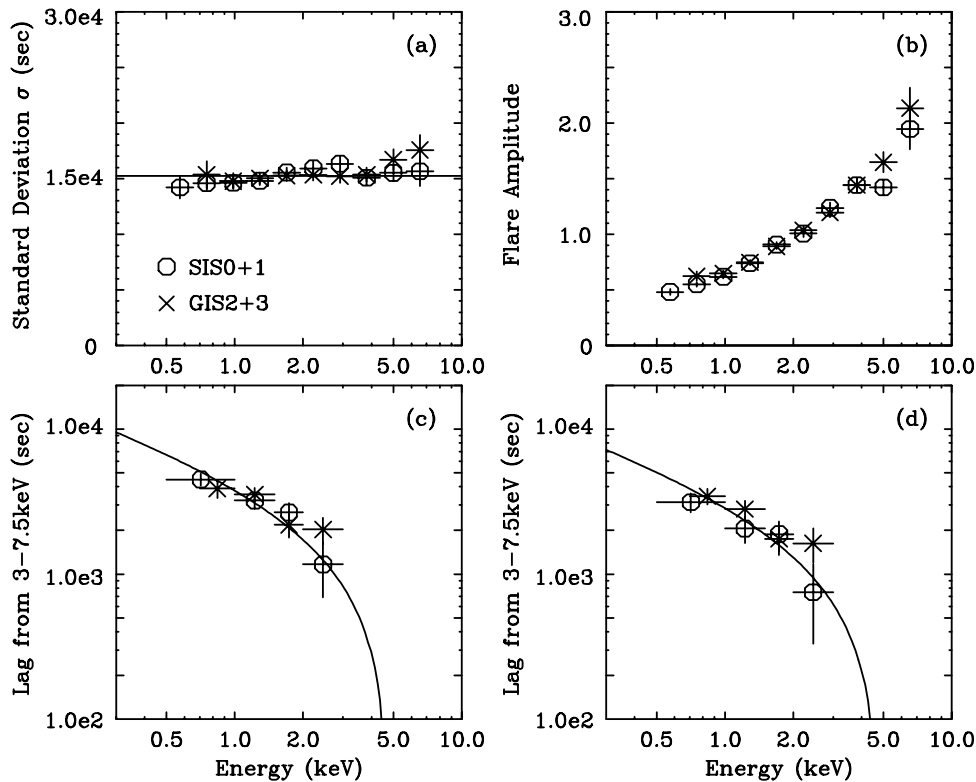
Figure 10.3: Measurement of the parameters describing the 1994 May flare of PKS 2155−304. The circles are combined SIS data, while the crosses are combined GIS data. (a): The flare duration, estimated by the standard deviation, σ, of the Gaussian fits at various X–ray energies. The solid line is a constant fit ($\sigma = 1.5 \times 10^4$ sec). (b): The flare amplitude ($Ap \equiv C_1/C_0$) at various X–ray energies, determined by a Gaussian fit. (c): Time lag of photons of various X–ray energies versus the $3.0-7.5$ keV band photons, calculated from the peaking time determined by a Gaussian fit. The solid line is the best fit with a function (10.2). The best fit parameter is $B = 0.11$ G for $\delta = 25$. (d): Time lag of photons of various X–ray energies versus the $3.0-7.5$ keV band photons, calculated using the discrete correlation function (DCF). The solid line is the best fit with a function (10.2). The best fit parameter is $B = 0.13$ G for $\delta = 25$ (figure from Kataoka et al. 2000).

Importantly, two methods mentioned above yielded consistent values for B. They

found the magnetic field for PKS 2155$-$304 to be $B = (0.12 \pm 0.02)(\delta/25)^{-1/3}$ (G).

10.2.2 Smoothing by Light Travel Time

From results of Mrk 421 and PKS 2155$-$304, one can approximate the typical values of the magnetic field B of Mrk 421 and PKS 2155$-$304 as $B \sim 0.1 - 0.2$ (G), when a beaming factor is $\delta \simeq 10$. In order to derive the magnetic field from the time lag, we need a complete sample of flares. Unfortunately, we do not have any samples of 'complete flares' for Mrk 501 and 1ES2344+514. With the magnetic field of $B \sim 0.1$ (G), we can estimate the cooling times of electrons which emit photons of various energies from equation (10.2); $t_{\rm cool}(0.1$ keV; UV$) \simeq 4 \times 10^4$ (sec), $t_{\rm cool}(1$ keV; soft X-ray$) \simeq 1 \times 10^4$ (sec) and $t_{\rm cool}(10$ keV; hard X-ray$) \simeq 4 \times 10^3$ (sec). In the X-ray band, cooling time is much *shorter* than the decay time of an each flare event. As is clearly seen in the light curves of Mrk 421 (e.g., Figure 7.2; see also Figure 10.4) and PKS 2155$-$304 (Figure 10.2), typical time scale of the decay in a flare is 0.3$-$0.5 day for these sources. It should be also noted that the time scale of the rise in a flare is also 0.3$-$0.5 day (see also, § 7.2.3; 8.2.3).

This clearly indicates that a mechanism other than synchrotron cooling, actually determines the decay-time of each flare. The most natural interpretation is the *smoothing* of rapid variabilities by source light travel time (e.g., Chiaberge & Ghisellini. 1999; Kataoka et al. 2000). Rapid variability on time scale shorter than R/c, where R is the emission region size, cannot be observed, because of the relaxation (smoothing) by the light travel effects over the source on a light-crossing time scale. The observational fact that rise and decay time-scales of the short term flares are nearly comparable, bears important consequences (Figure 10.2). In fact, it is highly unlikely that these time scales are directly associated with the particle acceleration and cooling time scales, since a priori there is no reason for them to be equal, and observed equality would be accidental (Ghisellini et al. 1997).

This simple idea was confirmed by a detection of energy-dependence of time-asymmetry of the light curves (Figure 7.14, 8.10). We found two important properties in the light curves ; (i) time profiles of TeV blazars are almost symmetric, but in the strict sense, they are characterized by the 'rapid rise and gradual decay', and (ii) the symmetry of the time profile more strongly breaks down at lower energies (§ 7.2.3; 8.2.3). It should be noted that both of these are most naturally interpreted by the balance of cooling time ($t_{\rm cool}$) and light travel time ($t_{\rm crs} = R/c$). Since cooling time becomes comparable with the source light travel time only at lower energy bands, smoothing of rapid time variability should be more important at high energy X-ray band, forming a symmetric time profile. We show an example of time profile of a flare in Figure 10.4 (Mrk 421 in 1998; time-region

#2) which clearly demonstrates the fact that the hard X-rays decayed more rapidly than the soft X-rays and UV photons.
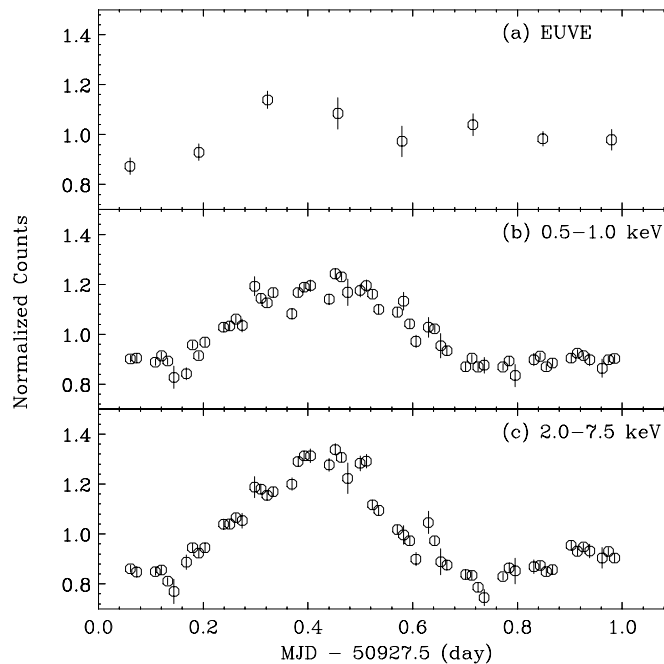
Figure 10.4: Time profiles of a flare of Mrk 421 observed in 1998 (time-region # 2). *top* (a): *EUVE* (∼0.1 keV), *middle* (b): *ASCA* SIS (0.5−1.0 keV), *bottom*(c): *ASCA* SIS 3.0−7.5 keV. Note that time profile of the flare becomes more symmetric at higher energy bands and amplitude of variability is larger as increasing photon energy.

We also note that the importance of light travel time (t_{crs}) is implied from another reason. In Figure 10.5, we show the time profiles of different types of flares observed for Mrk 421 in 1998. For the flare in time-region #2 (see, Figure 7.8), we can see a symmetric triangular shape whose rise-time and decay-time are nearly equal. However, for the flare in time-region #9, we can see a plateau in the light curve. For this particular flare (#9), after the flux reached the maximum, it remained almost constant for 0.4 day (Figure 10.5). This indicates that, for the flare in time-region #9, the electron and photon distributions would have enough time to reach a 'new' equilibrium state, and form a *plateau* in the light curve (e.g., Mastichiadis & Kirk 1997; Chiaberge & Ghisellini 1999; see also § 11).

Assume that the flares are explained by a shock front propagating through the emission region, supplying freshly accelerated electrons only in the front's vicinity (Kirk, Rieger & Mastichiadis 1998). A plateau in the light curve appears only when the duration of a change in electron injection (t_{inj}) is larger than t_{crs}. This corresponds to a physical condition in which shock velocity is much slower than the speed of light, because the injection process take R/V_s to influence the whole region, where V_s is the shock velocity.

In this case, newly accelerated electrons are injected to the emission region for $t_{\text{inj}} > t_{\text{crs}}$. On the other hand, a symmetric triangular shape of the light curve corresponds to a highly relativistic shock, $V_s \sim c$. In any case, present observational data indicate that the balance of duration of an injection event t_{inj} and source light travel time t_{crs} is important to describe the rapid variability in blazars.
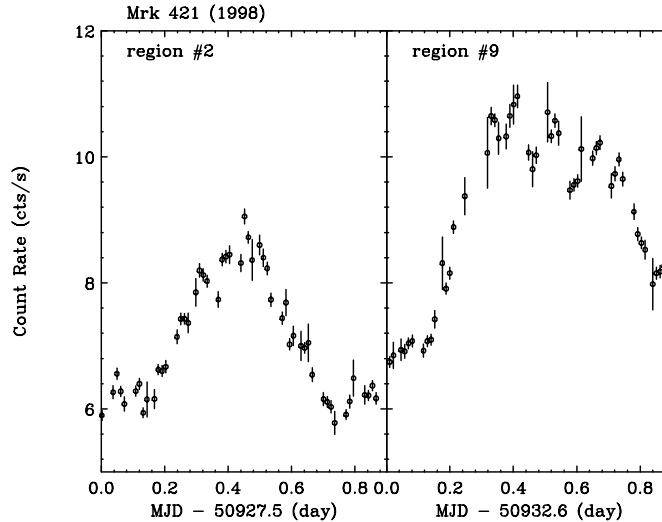
Figure 10.5: Time profiles of two different flares of Mrk 421 observed in 1998. SIS light curves of energy band 1.0−1.5 keV are plotted. *left* : time-region #2, *right* : time-region #9 (see, § Figure 7.8). Note that a plateau appears in the light curve of #9, whose duration of flare is longer than that of #2.

10.2.3 Acceleration of Electrons

As we have seen in previous sections, electrons with higher energy cool faster than electrons with lower energy ($t_{\text{cool}} \propto \gamma^{-1}$). Thus if the nature of rapid variability of the system (*flare*) is controlled by *instantaneous* injection of electrons up to γ_{max} and energy loss by radiative cooling, soft X-ray variations should *always* lag behind those in the hard X-ray band. However, we are aware that there were observations in which no time-lags or opposite sign of lags were reported (e.g., Sembay et al. 1993; Figure 7.19; Figure 7.21). Curiously, such observations were only little studied or forgotten in previous works, probably because it cannot be understood by a simple synchrotron cooling scenario. Another reason might be that observations were too short to cover the whole flare duration, thus reducing a motivation for strongly arguing the presence of such *unusual* behaviour.

Uninterrupted observation of Mrk 421 in 1998 revealed that the actual situation is much complex than we had expected. Sign of lags had changed flare by flare (Figure 7.23). In some flares, we actually detected completely opposite behaviour, where the soft X-ray

variations *preceded* that in the hard X-rays ('hard lag'; see, Figure 10.6). It is clearly shown that the time variation in lower energy band lags behind that in the higher energy band. Mechanism other than the synchrotron cooling is necessary to account for the *slower* response for higher energy electrons.
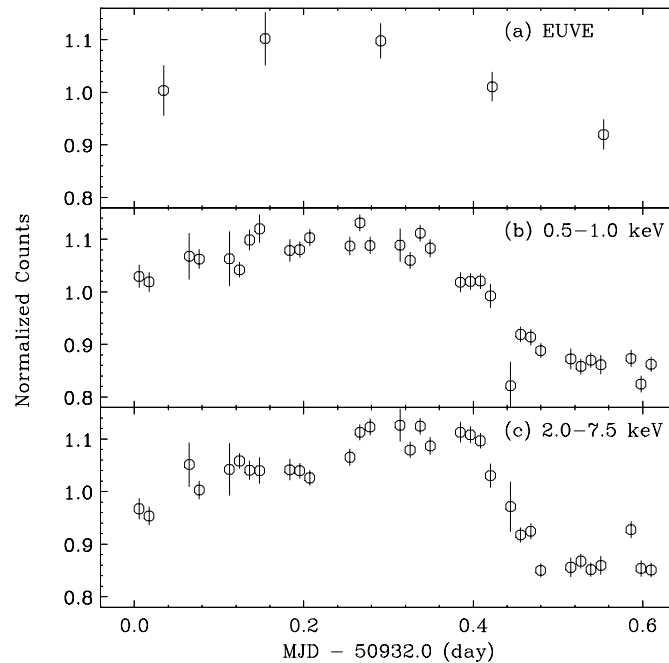
Figure 10.6: Time profiles of a flare of Mrk 421 observed in 1998 (time-region # 8). *top* (a): *EUVE* (~ 0.1 keV), *middle* (b): *ASCA* SIS (0.5−1.0 keV), *bottom*(c): *ASCA* SIS 3.0−7.5 keV. Note that the time variation in higher energy band lags behind that in the lower energy band (*hard lag*), and variability amplitude is almost equal through *EUVE* to *ASCA* .

Since the cooling time of electrons is a function of B and δ (equation (10.1)), it might be expected that the magnetic filed and/or beaming factor changed flare by flare. However, this is not plausible for two reasons. First, even if the magnetic field is variable, one cannot account for the hard lag ('zero-lag' at most; see equation 10.2). Second, since the synchrotron emissivity is proportional to B^2 (e.g., equation (3.34)), changes in magnetic field inevitably would cause a large-amplitude variations also in the lowest energy bands (e.g., radio/optical) as well as X-ray bands. This has not been observed. Optical flux (R band) for Mrk 421 during the 1998 ASCA observation (24−30 April) showed only small fluctuation within 12.6±0.1 (fag) (Mattox 1999, private communication). Changes of beaming factor, e.g., due to the bending of jet (Wagner et al. 1993) might explain the changes of cooling time. However, it is not plausible because the fluctuation of beaming factor produce completely *coherent* variations in energy (see, also § 11.7). Such coherent variability have never been observed for Mrk 421, although this might had been the case

for a particular flare of 2155−304 observed in 1991 (see, Edelson et al. 1995).

In TeV blazars, we believe that most natural interpretation of 'hard lag' behaviour is based on the acceleration of electrons at shock front postulated to exist in blazar jets. Such a shock is expected to be produced by several different ways, for examples, by a collision of emission blob with surrounding materials in the vicinity of the jet (e.g., BLR; see, § 2) and/or by a collision of blobs moving with different bulk Lorentz factors (*internal shock* scenario; e.g., Ghisellini 1999; see also the discussion below). As we described in § 3.1, when the low energy electrons are injected into the shock front, they are gradually accelerated to higher energies up to the maximum Lorentz factor γ_{max}, where radiative loss and energy gain are equally balanced. The efficiency of acceleration is expressed by the *acceleration time scale*, t_{acc} (see, § 3.1.4). In practice, t_{acc} would be dependent on the electron energy in accordance with shock acceleration process. For example, t_{acc} (γ) $\propto \gamma$ for diffusive acceleration with a 'gyro-Bohm' process (e.g., Inoue & Takahara. 1996) and $\propto \gamma^{1/3}$ for fully developed Kolmogorov turbulence. Although we assume t_{acc} to be constant for simplicity, the following discussion can be applied for the case that the acceleration time has some dependences on energy (see, § 3.1.3).

10.2.4 Application of Acceleration/Cooling Model to Data

Let's assume a simple case where electrons with mono-energetic Lorentz factor γ_0 ($\ll \gamma_{max}$) are picked up (injected) into the acceleration process at a shock front, and subsequently drift away from into the downstream flow. Drifted electrons will be cooled by synchrotron process in a homogeneous magnetic field B, in which electrons emit most of the radiation (emission region). We define the magnetic field strength around the shock front B_s ($\neq B$ in general) and the shock velocity V_s. We note that t_{acc} and γ_{max} would be a function of B_s and V_s, but a detailed description is beyond the scope of this thesis (e.g., $t_{acc} \propto B_s^{-1}V_s^{-2}$ and $\gamma_{max} \propto B_s^{-1/2}V_s$ for diffusive acceleration with a 'gyro-Bohm' process; Inoue & Takahara. 1996).

From the equation (3.21), we obtain an upper limit on the electron energy which can be accelerated at time t,

$$\gamma(t) = (\frac{1}{\gamma_{max}} + [\frac{1}{\gamma_0} - \frac{1}{\gamma_{max}}]\exp(-t/t_{acc}))^{-1}. \tag{10.3}$$

What is important is that the higher energy electrons require *longer time to be accelerated*, which produces opposite sign of time-lag expected from the synchrotron cooling process. 'Hard lag' thus appears as a delay in the start time of the flare for higher X-rays. When the variation at observed photon energy E_1 is found to be lagged behind the variation at

energy E_0 ($E_0 < E_1$) for Δ t (sec), one finds a simple relation,

$$\Delta t \simeq \frac{t_{\mathrm{acc}}}{2} \delta^{-1} \ln(\frac{E_1}{E_0}). \tag{10.4}$$

The combination of 'soft-lag' by radiative cooling in the emission region, and 'hard-lag' by acceleration process (equation (10.2) and (10.4)) can be applied for the explanation of the observed behaviour of flare-by-flare changes in sign of the time-lag. If we take the acceleration process into account, the time lag can be expressed as,

$$\Delta t(E_0, E_1) \simeq 1.2 \times 10^3 B^{-3/2} \delta^{-1/2} (E_0^{-1/2} - E_1^{-1/2}) - \frac{t_{\mathrm{acc}}}{2} \delta^{-1} \ln(\frac{E_1}{E_0}) \quad (\mathrm{sec}), \tag{10.5}$$

where $\Delta t(E_0, E_1)$ is the time lag of the light curves at observed photon energy E_0 from that at the energy E_1 (in unit of keV; $E_0 < E_1$).

We applied this simple model to Mrk 421 data obtained in 1998. We fixed the magnetic field in the emission region and beaming factor to $B = 0.2$ (G) and $\delta = 10$, as calculated from the time-lag for 1994 data (Takahashi et al. 1996). Regarding this point, we note that the time-lag for Mrk 421 in 1994 is well represented by synchrotron cooling term only, because the energy dependence of the cooling time derived from the time lag is consistent with the synchrotron cooling process. We do not need to introduce an additional acceleration term. This corresponds the physical case in which the electron populations are rapidly ($t_{\mathrm{acc}} \simeq 0$) accelerated from γ_0 to γ_{max}.

Since flare-by-flare changes of B are unlikely (see above), we fixed the magnetic field to 0.2 G and fit the 1998 data with only one free parameter, t_{acc}. Figure 10.7 shows the model fit to the time-lag for time-region #2−9 (see, Figure 7.8). Best fit models are given as a solid line. Upper panel shows the case where the magnetic field was larger/smaller by factor of 2 than the assumed value (0.2 G), but t_{acc} is fixed at the best fit value. The lower panel corresponds to the case when the acceleration time changed by factor of 2, but B is fixed to 0.2 G.

One finds that all the data are consistent with this simple model ($P(\chi^2) > 0.1$) and that parameters (B and t_{acc}) are well constrained within a factor of 2. The calculated acceleration time ranges from 1×10^3 sec to 6×10^3 sec in observer's frame. Since the cooling time of electrons which emit X-ray photons at 1 keV is $t_{\mathrm{cool}} \simeq 5 \times 10^3$ (sec) for $B = 0.2$ (G) and $\delta = 10$, the derived acceleration time is nearly equal to the cooling time. We should note that if $B_{\mathrm{s}} \simeq B$, the acceleration time (t_{acc}) and cooling time (t_{cool}) are expected to be balanced for electrons that emit photons in the X-ray energy bands. The steep X-ray photon spectra of TeV blazars ($\Gamma_{\mathrm{X-ray}} > 2$; Figure 7.27 and 8.14) imply that the X-ray band corresponds to the highest part of the LE component, thus reflecting the electron population close to the γ_{max}. However, if the magnetic field is compressed around

the shock, i.e. $B_s \gg B$, acceleration time can be much shorter than the cooling time, even in the X-ray energy bands.

Variability or flaring behaviour can arise from a number of reasons. When the shock front overruns a region of the jet in which the local electron density is enhanced, the number of electrons picked up and injected into the acceleration process is expected to increase (Kirk, Rieger & Mastichiadis 1998). In this case, we do not expect any changes in acceleration time, thus variations of observed time-lags for each flare event cannot be explained. On the other hand, if the density change is associated with a change in the magnetic field in the shocked region (B_s) or changes in the shock velocity (V_s), acceleration time *can* also vary. In such situation, time-lags may also vary, corresponding to the balance of the acceleration time and the cooling time, as was the case for Mrk 421 flares in 1998.

Although the full description of the shock process is necessary to deepen the current discussion, a simple model in which electrons are accelerated in the 'accelerated region' and injected to a 'emitting region' for the radiation can qualitatively explain properties of the complicated time profiles observed in Mrk 421. Present results, which indicate $t_{cool}(\text{X-ray}) \geq t_{acc}$, might indicate the tangled magnetic field around the shock (B_s) is enhanced as compared to that in the emitting region (B).

As a summary, our current discussions assumed a single emitting region associated with a single shock front (one-zone homogeneous model). The structure of jet is assumed to be globally smooth, but locally the jet may include tangled regions, e.g., with enhanced plasma density. Various types of flares can be produced when the shock overruns such a tangled region. We found that this picture qualitatively accounts for the observed properties of TeV blazars.

10.2.5   Comment on Multiple Emission Models

Instead of assuming a single emission region, one might expect multiple emission regions and shock fronts in the jet, all of which are characterized by different physical quantities (e.g., region size and magnetic field density). These quantity may vary independently. Complex features observed from Mrk 421 in 1998 could be generated by the superpositions of flares originating in different emitting regions. When a flare arises in a blob with strong magnetic field, the observed lag becomes small, while larger lag would be observed when the magnetic field is relatively small.

Such a situation seems to be realistic in some sense, however, we prefer one-zone model for several reasons; (1) rapid variability in TeV blazars is well correlated in the X-ray and TeV γ-ray bands, suggesting that same spatial region and same population of relativistic

electrons dominated the emission (Figure 9.3; 9.6). (2) clear correlation between the flux and the photon index, as well as shift of the synchrotron peak (e.g., Figure 8.19) rules out superpositions of photon spectra which are produced in different emission region characterized by different physical parameters. (3) spectral energy distribution of TeV blazars is well represented by one-zone homogeneous model (see also, § 11)

Also note that our discussion based on one-zone model is not affected as long as individual emitting region is concerned. Balance of 4 time scales, $t_{\rm cool}$, $t_{\rm acc}$, $t_{\rm crs}$ and $t_{\rm inj}$ must be held even when we assume a complicated multiple emission region model.

10.2.6   Cooling Time vs Escape Time

In the previous sections, we considered four timescales which characterize the rapid variability in blazars. We would like to comment here on another dynamical time scale; $t_{\rm esc}$. Many authors have assumed that the relativistic electrons are injected into the emission region with a specified distribution and escape on a timescale $t_{\rm esc}$ (e.g., Inoue & Takahara. 1996). After particles escape from the emission region, these particles no longer radiate. For low-energy electrons whose cooling time is longer than $t_{\rm esc}$, they cannot cool completely before leaving the source, thus the spectral form becomes similar to that of the injection. However, for the high energy electrons of $t_{\rm cool} < t_{\rm esc}$, they lose most of the energy before leaving the source. If the electron injection spectrum is a power law form of $\propto \gamma^{-s}$, it breaks by one power in the index ($\propto \gamma^{-s-1}$) for $\gamma > \gamma_{\rm br}$, where $\gamma_{\rm br}$ is the electron Lorentz factor which satisfies $t_{\rm cool}(\gamma_{\rm br}) = t_{\rm esc}$.

There is a good observational reason to believe that escape, or equivalently, sudden energy loss by adiabatic expansion is important. In fact, the photon spectral index starts to deviate from that in the radio (millimeter) band by ~ 0.5 around IR/optical band for TeV blazars (e.g., § 9). Thus the electron loss by escape, rather than cooling, is more important for low energy electrons which emit photons from radio to optical band. In the X-ray energy band, cooling time is expected to be much shorter than $t_{\rm esc}$. Since we are dealing with the rapid variability observed in the X-ray energy band, $t_{\rm esc}$ is not crucial. But $t_{\rm esc}$ could be important when the cooling time is longer than $t_{\rm esc}$ (see also, § 10.6).
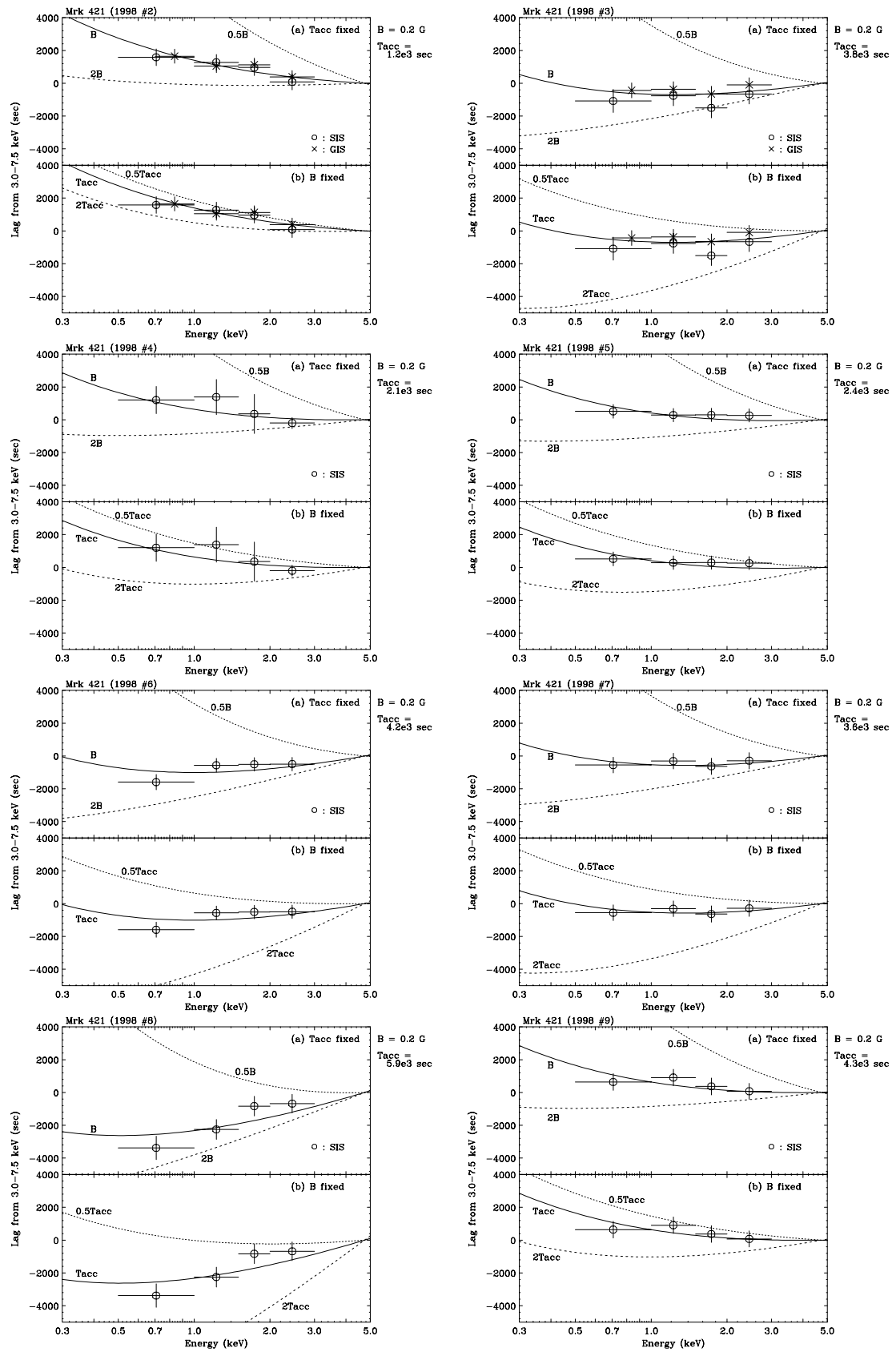
Figure 10.7: Fit with acceleration plus cooling model. Data from 1998 observation of 421. Acceleration time is given in observer's frame (assuming $\delta = 10$).

10.3 Properties of Short-Time Variability in Blazars

As we have seen in Figure 10.1, rapid time variability of TeV blazars is clearly different from that of Galactic black holes and galaxies. This is most probably due to different physical origins and/or locations where the X-ray photons are produced, and hence, different time variability is observed. In fact, X-ray photons are considered to be emitted almost isotropically from the most inner part of the accretion disk for Galactic black holes and Seyfert galaxies (see, e.g., Tanaka et al. 1995; Dotani et al. 1997), while non-thermal emission from relativistic electrons in the relativistic jet is thought to be the origin of X-ray photons for blazars (see, § 2).

For TeV blazars, we showed that time variability shows strong red-noise type behaviour, and variability shorter than *characteristic* time scale is strongly suppressed. This is more clearly seen in Figure 10.8, in which variability of different time scales are separately shown. For the case of Cyg X−1 (*left*), similar time variability is seen in various time scales. Existence of time variability in the shortest time scale well explains an observed flat PSD index of Cyg X−1 (1.7−1.8; Figure 10.1). For the case of Mrk 421 (*right*), however, time variability changes dramatically in various time scales. On the shortest time scales (< 0.2 day), time variability seems to be absent and the light curve is almost constant. On longer time scales (< 2.0 day), variability which is often called a 'flare' appears. Rise-time and decay-time of a flare are what we have derived as the *characteristic* time scale using SF analysis. Although the last panel is somewhat undersampled, large amplitude variations are clearly seen, which are similar to that in the middle panel.

Despite the long history of X-ray astronomy, the physical processes which may account for the *canonical* (quasi-fractal) time variability of Galactic black holes and Seyfert galaxies are still under debate. The situation is more severe for blazars, where only few studies have been performed to investigate the nature of rapid variability in blazars. In the X-ray band, Tagliaferri et al. (1991) have studied $EXOSAT$ observations of PKS 2155−304 (exposure of about 1 day), and found that the power spectrum follows a power-law with an index −2.5±0.2, which is exactly consistent with our SF analysis. Hayashida et al. (1998) also found very steep power spectra for both PKS 2155−304 and 3C 273 as were given in Figure 10.1. In the optical band, Paltani et al. (1997) studied the time variability based on 15 nights data. They also reported that the PSD is well described by a power-law with an index −2.4, comparable with the index found in the X-ray domain. No PSD studies had been reported for variabilities in Mrk 421, Mrk 501 and 1ES 2344+514 prior to this thesis.
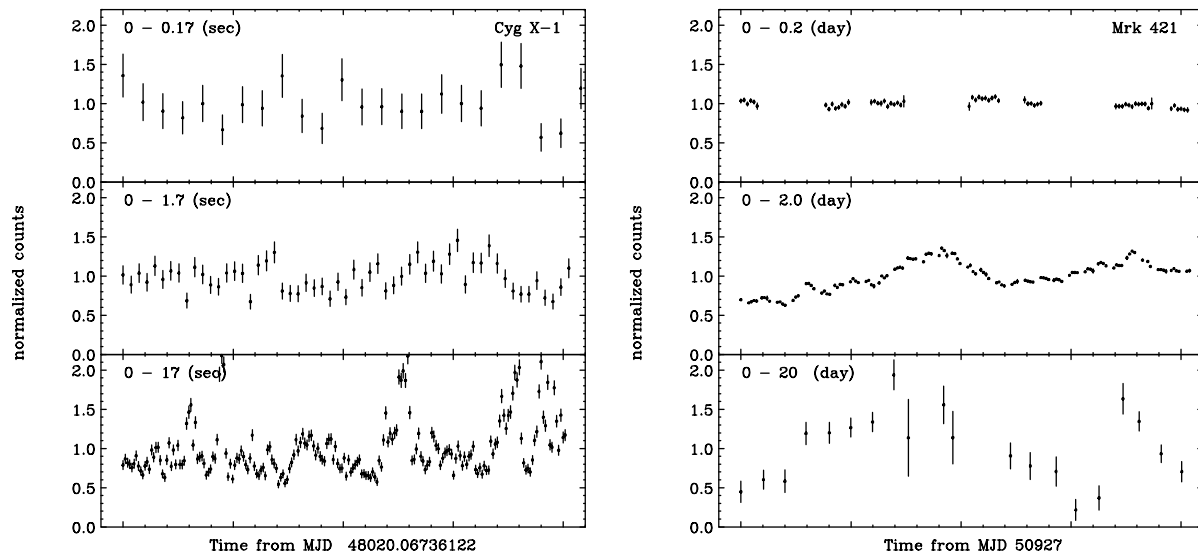
Figure 10.8: Self-similarity of rapid variabilities in Cyg X−1 and Mrk 421. Variabilities of different time scales are separately shown. *left* : time variability in Cyg X−1. Data come from Hayashida et al (1998). *top*; 0−0.17 (sec), *middle*; 0−1.7 (sec), and *bottom*; 0−17 (sec). Start time is MJD 48020.06736122 (1990/05/09). *right* : time variability in Mrk 421. *top*; 0−0.2 (day), *middle*; 0−2 (day), and *bottom*; 0−20 day. Start time is MJD 50927.0 (1998/04/23).

The absence or suppression of rapid time variability (≤ 1 day) in blazars implies that there exists a *prefered location* in which X-ray photons are produced. Characteristic time scale of each flare event, $t_{\rm obs} \sim 1$ day, indicates that the size of the emission region is $\sim 10^{16}$ cm in the source frame, if the emitting blob is moving with the Lorentz factor of $\Gamma \sim 10$. Since the jet is collimated within a narrow cone with angle $\theta \simeq 1/\Gamma$, one finds that the X-ray emission site is $D \sim 10^{17}$ cm from the base of the jet. Absence of rapid variability shorter than ~ 1 day rules out the X-ray emission inside of this. Similarly, more distant region, as expected from radio emitting region (which is ≥ 1 pc; see also § 10.4), is also ruled out because it cannot explain the rapid time variability as short as 1 day.

There are several reasons which may account for this 'critical' distance $D \sim 10^{17}$ cm. First, even if the X-rays are actually produced at the base of the jet, and hence close to the accretion disk, the produced X-rays should be inevitably absorbed by photon-photon interactions, with associated pair production. A simple calculation reveals that the optical depth to pair production for X-ray and γ-ray photons well exceeds unity at the base of the jet ($\tau_{\gamma-\gamma} \geq 100$), thus we cannot observe both emissions in this region. Second, the shock fronts themselves may be absent at the base of the jet, and high energy electrons which are fully accelerated to emit X-rays, would be absent for distance closer than $D \sim$

10^{17} cm. In the following, we suggest a possible interpretation which may account for this preferred location of the shock fronts. This is called *internal shock scenario* and first introduced in the field of modeling γ-ray bursts. Very recently, Ghisellini (1999) pointed that this idea successfully explains some of observed characteristics in blazars.

Let's assume a central engine is not working continuously, but produces different blobs of material moving with different bulk Lorentz factors. For simplicity, we consider two relativistic blobs. blob-1: Lorentz factor is Γ_1 and emitted at $t = 0$, blob-2: Lorentz factor is Γ_2 ($\Gamma_2 = a\Gamma_1$; $a > 1$) and emitted at $t = \tau$. Assuming that blobs are initially separated by a few Schwarzschild radii ($\sim 3R_g$), blob-2 cathes up the blob-1 at a distance of

$$D = c\tau\Gamma_1^2(\frac{2a^2}{a^2 - 1}) \sim 10R_g\Gamma_1^2. \tag{10.6}$$

Despite the uncertainties in parameters a and τ, a distance at which two blobs collide is roughly estimated as $\sim 10~R_g~\Gamma_1^2$.

A radial distance of the jet at D is

$$R = D\sin\theta \simeq D\theta \simeq D/\Gamma_1. \tag{10.7}$$

Observed time scale is shortened by $\simeq 1/\Gamma_1$, because of the beaming effect (§ 3.7). Thus we obtain the observed time scale for blazars,

$$t_{\mathrm{obs}} \sim D/(c\Gamma_1^2) \sim 10R_g/c. \tag{10.8}$$

In this scenario, we expect that *no* significant time variabitility would be observed for distance closer than D, because blobs are smoothly moving in the jets and shock fronts are absent in this region. Thus it is natural that rapid time variability shorter than $D/(c~\Gamma_1^2)$ is strongly suppressed, as was indicated from temporal studies of X-ray light curves of TeV blazars.

Based on the discussion above, it is intriguing to estimate the mass of central black holes in TeV blazars. Since the Schwarzschild radius is expressed as

$$R_g/c \simeq 1.1 \times 10^{-10}(\frac{M}{M_\odot}) \quad (\text{day}), \tag{10.9}$$

we obtain $M \sim 5 \times 10^8~M_\odot$ for $t_{\mathrm{obs}} = 0.5$ (day). Interestingly, this result is also consistent with the typical mass of central black holes postulated to exist in active galactic nuclei (e.g., Hayashida et al. 1998).

10.4 X-ray Flares and Implications on the Jet Structure

In § 7.3.3 and 8.3.3, we found that the position of the synchrotron peak shifts from lower to higher energy when the source becomes brighter. The correlation was most clear for Mrk 421 ($E_{\mathrm{p}} \propto L_{\mathrm{p}}^{0.4}$) and Mrk 501 ($E_{\mathrm{p}} \propto L_{\mathrm{p}}^{1.6}$), where L_{p} is the peak luminosity and E_{p} is the peak energy (§ 7.3.3; 8.3.3). The difference of spectral evolution in both objects implies that quite different mechanisms were at work when the sources went into the flaring states.

Since the peak luminosity is proportional to the number of photons at peak ($n_{\mathrm{ph}}(E_{\mathrm{p}})$) multiplied by the peak energy, a simple relation can be found:

$$L_{\mathrm{p}} \propto E_{\mathrm{p}} n_{\mathrm{ph}}(E_{\mathrm{p}}) \propto \gamma_{\mathrm{p}}^2 n_{\mathrm{e}}(\gamma_{\mathrm{p}}), \tag{10.10}$$

where γ_{p} is the Lorentz factor of electron which emits photon of energy E_{p} and $n_{\mathrm{e}}(\gamma_{\mathrm{p}})$ is the number of electrons at γ_{p}. We thus find the relations,

$$n_{\mathrm{e}}(\gamma_{\mathrm{p}}) \propto \gamma_{\mathrm{p}}^{3.6} \quad (\mathrm{Mrk421}), \tag{10.11}$$

$$n_{\mathrm{e}}(\gamma_{\mathrm{p}}) \propto \gamma_{\mathrm{p}}^{-0.8} \quad (\mathrm{Mrk501}). \tag{10.12}$$

This implies that for the case of Mrk 421, increase of γ_{p} by a factor of 2 requires more than factor 10 *increase* in number of electrons at peak energy. On the other hand, the same amount of increase of γ_{p} requires *decreases* in number of electrons by a factor of 2 for the case of Mrk 501. Such variations in spectral behaviors may be associated with the difference of physical conditions in relativistic jets, which is discussed below.

Assume that a substantial amount of gas (e.g., in a form of clouds) is distributed in the jet. In these clouds, density of low-energy electrons is enhanced as compared to the ambient, but other physical quantities such as magnetic field strength are unchanged. Those clouds essentially provide a plentiful source of low-energy electrons for the shock front. When a shock front overruns one of such clouds, fresh electrons are successively injected and assumed to undergo continuous acceleration by repeatedly crossing and recrossing the shock front, as well as simultaneously cooling by synchrotron radiation (e.g., Kirk, Rieger & Mastichiadis 1998). In this scenario, number of electrons increases significantly, but only small changes are implied for the maximum Lorentz factor as were observed in Mrk 421.

On the other hand, when clouds are absent or very sparsely distributed in the jet, flares may be produced in several diffent manners. For an example, if the shock overruns the enhanced tangled-magnetic field region, this may cause changes in acceleration time

of electrons, and hence increase the maximum Lorentz factor (see also, § 10.2.4). Importantly, regardless of detailed models for flaring behaviour, total number of electrons is *conserved* in this case. During the flare, acceleration can be assumed to be more efficient than radiative cooling, thus the present electron population as a whole will be accelerated to higher energies, but no additional electrons are supplied into the shock.

In latter case, numbers of electrons at the peak ($n_e(\gamma_p)$) will *decrease*, reflecting the power-law shape of an electron population. If the differential number density of electrons is expressed as $N_e \propto \gamma^{-2}$ (standard shock; § 3.1.5), electron number decreases as $n_e(\gamma_p) \propto \gamma_p N_e(\gamma_p) \propto \gamma_p^{-1}$. Importantly, this relation is very close to the case we have observed in Mrk 501 (equation (10.12)).

Present discussion based on the X-ray spectral evolution suggests very important implications for internal jet structures of Mrk 421 and Mrk 501. Only a small shift of synchrotron peak observed in Mrk 421 may be associated with electron clouds *filling* the jet, while the jet of Mrk 501 seems to be relatively empty. During the flare of Mrk 421, kinetic power of the shock is equally distributed to large number of low-energy electrons newly injected into the shock, thus increasing the number of high energy electrons. Large shifts of synchrotron peak observed in Mrk 501, on the other hand, is possible only when the internal jet is rather sparse and transparent to the shock propagation. Kinetic power of the shock is spent to *increase* the energies of individual electrons and hence *number-conservative.*

It may thus be worthwhile to compare our X-ray implications to the VLBI results. Accurate measurements of changes in the parsec-scale jet structure imaged with VLBI provide constraints on the jet kinematics and geometry. When combined with estimates of the Doppler beaming factor (determined, for example, from the X-ray time variability), the apparent motion of the jet components can be used to constrain the Lorentz factor of the jet and the angle of the jet to the line-of-sight. Although VLBI observations do not yet have an enough resolution to image the region production of the X-ray/γ-rays (~ 0.01 pc), they provide the highest resolution structual information available, and can image the region immediately downstream.

VLBI maps of Mrk 421 and Mrk 501 at 18 cm are separately shown in Figure 10.9. Both objects are observed in a space VLBI project using the $HALCA$ satellite and 12 ground stations (Giovannini et al. 1998). It is interesting that the subparsec- and parsec-scale jets of Mrk 421 and Mrk 501 appear to be weak relative to those of other blazars (Marscher et al. 1999). Most importantly, superluminal motions have been detected only for Mrk 501 ($v = 6.7\ c$; Giovannini et al. 1998), while subluminal motions were implied for Mrk 421 ($v \simeq 0.3\ c$; Piner et al. 1999). An apparent velocity of Mrk 501 implies that
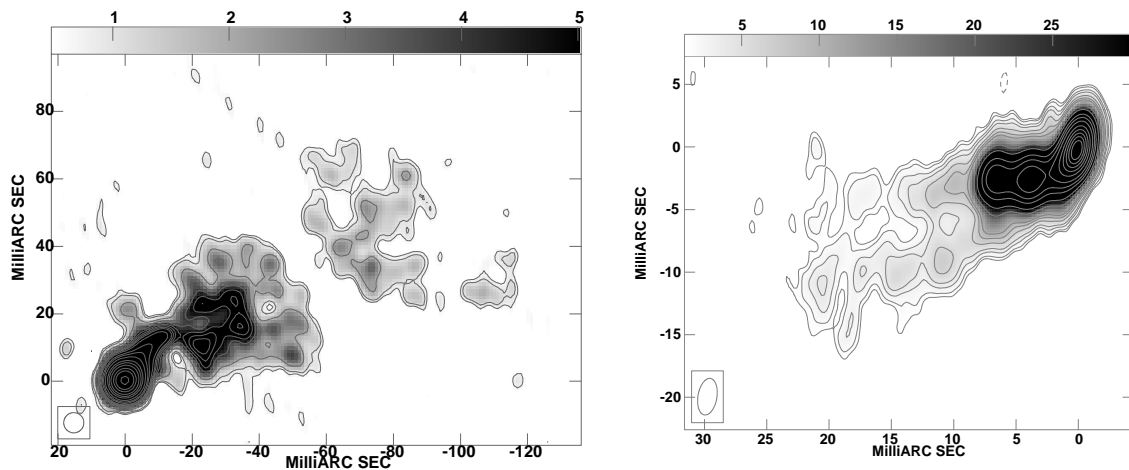
Figure 10.9: Global Space VLBI map of Mrk 421 (*left*) and Mrk 501 (*right*). In these figures, 1 mas corresponds to 0.9 pc. Superluminal motions were detected only for Mrk 501 ($v \sim 6.7\ c$). Figures from Giovannini et al (1998).

the real jet velocity has to be $\geq 0.989\ c$ and the jet has to be oriented at an angle smaller than 17 deg (Giovannini et al. 1998). By assuming that the bulk and pattern jet velocity are comparable, Giovannini et al (1998) derive that the beaming factor of Mrk 501 as $\delta \sim 1.3-5.6$. For the case of Mrk 421, the results are consistent with *no-beaming*.

In any case, the estimated beaming factors for both sources are relatively low compared with the lower limits derived from time variabilities in other wavebands; for examples, Takahashi et al. (1996) derived $\delta \geq 5$ for Mrk 421 and Kataoka et al. (1999) derived $\delta \geq 6$ for Mrk 501 using the X-ray/TeV γ-ray time variability (see also, § 10.6). Marscher (1999) disscussed that rather low superluminal apparent speeds and lackluster variability properties of the radio jets evidences that the bulk flow of the jets *decelerates* from X-ray/TeV γ-ray emitting section (~ 0.01 pc) to the radio emitting region (~ 1 pc). The weak subparsec- and parsec-scale jets of those objects are readily understood as the consequence of heavy energy and monmentum loss in the upstream of the jet where most of the energy and momtentum of the relativistic electrons are transfered to the radiation in the X-ray and TeV γ-rays.

Remarkably, very different manners of X-ray spectral evolutions of Mrk 421 and Mrk 501 presented in this thesis is exactly consistent with those VLBI observations. Our X-ray observations predict that relativisitc outflows of Mrk 421 will be decelerated faster than that for Mrk 501, because the jet of Mrk 421 is filled with low-energy materials and kinetic

energy of outflows are more efficiently dissipated during the propagation. The absence of superluminal motion of Mrk 421 in radio bands thus indicates that the high energy outflow has been sufficiently decelerated when it reaches to more distant, radio emitting region.

10.5 Implications from Inter-band Correlation

From the *truly* simultaneous observations of Mrk 421 and Mrk 501, we found that the flux variations in the X-ray and TeV γ-ray bands are well correlated on time scale of *hours to years*. These results imply that the same spatial region and the same population of relativistic electrons are responsible for the emission, as is predicted from the simple synchrotron self-Compton (SSC) scenario. The amplitude of variation was comparable in both enengy bands for Mrk 421 ([TeV flux] $\propto$ [X-ray flux]$^{0.92\pm0.12}$), while quadratic for Mrk 501 ([TeV flux] $\propto$ [X-ray flux]$^{1.96\pm0.07}$). In this section, we briefly discuss inter-band correlations expected from the simple SSC model and interpret the difference of Mrk 421 and Mrk 501.

Consider the electron population whose number density is given by $N_{\rm e}$. Since energy loss rate of a single electron is proportional to the magnetic field density U_B (equation (3.34)), one finds a simple relation between the observed synchrotron luminosity and physical quantities as

$$L_{\rm sync} \propto \delta^4 N_{\rm e} B^2, \tag{10.13}$$

where δ is the beaming factor of emission blob. If the emission is taking place in the Thomson regime ($\gamma h\nu \ll m_{\rm e}c^2\delta$), similar relation for the SSC flux is simply given by

$$L_{\rm SSC} \propto N_{\rm e} L_{\rm sync} \propto \delta^4 N_{\rm e}^2 B^2. \tag{10.14}$$

When the scattering takes place in the Klein-Nishina regime ($\gamma h\nu > m_{\rm e}c^2\delta$), the situation is more complicated because the cross-section for the inverse Compton process reduces significantly. Corresponding relation for SSC luminosity in the Klein-Nishina regime is

$$L_{\rm SSC}^{\rm KN} \propto N_{\rm e} L_{\rm sync}^{\rm eff} \propto \delta^4 N_{\rm e} N_{\rm e}^{\rm eff} B^2, \tag{10.15}$$

where $L_{\rm e}^{\rm eff}$ and $N_{\rm e}^{\rm eff}$, respectively, are the synchrotron luminosity and electron energy density *effectively* involved in the inverse Compton process.

In previous sections, we concluded that the variability of Mrk 421 is most probably due to the changes in number of electrons ($N_{\rm e}$), rather than changes in δ or B. Above relations thus predict $L_{\rm SSC} \propto L_{\rm sync}^2$ for Thomson scattering, while $L_{\rm SSC} \propto N_{\rm e}^{\rm eff} L_{\rm sync}$ for Klein-Nishina regime. Observational results imply that the X-ray spectrum and TeV γ-ray spectrum have similar slopes, whose differential photon indices are ~ 3.0. This indicates that the both emissions come from the *same*, high energy end of the electron distribution. Thus the above prediction can be directly compared with the observed relation of Mrk 421. From simultaneous observations in X-ray and TeV γ-ray bands, we found a relation [TeV

flux] $\propto$ [X-ray flux]. This suggests that the SSC process are operating in the Klein-Nishina regime, keeping $N_{\mathrm{e}}^{\mathrm{eff}}$ almost constant.

This prediction is plausible because the seed photons that are Comptonized to produce TeV flux are *not* X-ray photons (Takahashi et al. 1996; Ghisellini & Maraschi 1996). Assuming a typical value for B of $0.1-0.2$ G and δ of 10, we expect that the Lorentz factor of electrons which emit X-ray photons is $\gamma \sim 10^5$ (equation (3.32)). We thus expect γ $h\nu_{\mathrm{X-ray}} \sim 10 \ m_{\mathrm{e}}c^2\delta$, which implies the scattering takes place in the Klein-Nishina regime. Seed photons for TeV γ-ray production are more likely to be optical/UV photons:

$$\nu_{\mathrm{seed}} \simeq m_{\mathrm{e}}c^2\delta/h\gamma \sim 10^{15-16}(\mathrm{Hz}), \tag{10.16}$$

where h is the Planck constant. In this energy band, variability is small compared to that in the X-ray band (e.g., Buckley et al. 1996; Figure 9.2) and we can approximate $N_{\mathrm{e}}^{\mathrm{eff}}$ to be constant. Thus X-ray and TeV γ-ray correlation of Mrk 421, [TeV flux] $\propto$ [X-ray flux], is accurately consistent with the SSC scenario operating in the Klein-Nishina regime.

For the case of Mrk 501, however, quadratic relation of [TeV flux] $\propto$ [X-ray flux]^2 does *not* simply mean that the SSC process is operating in the Thomson regime. There are two reasons to explain this relation; (1) spectral evolution of Mrk 501 implies that large changes in γ_{max} (§ 10.4), (2) X-ray spectrum of Mrk 501 is flatter ($1.7-2.5$ in photon index) than that in the TeV γ-rays (~ 2.5 in photon index), suggesting that electrons responsible for emission in both bands are different in energy. For the latter point, we should note that the correlation of fluxes between UV (not X-ray) and TeV energy bands for Mrk421 is [TeV flux] $\propto$ [UV flux]$^{2.7\pm0.7}$, which is similar to the relation found for Mrk 501 (Figure 9.4).

When the γ_{max} varies significantly during the flare, evolution of synchrotron/self-Compton luminosity cannot be simply written as equation $(10.13)-(10.15)$, because the observed energy range is only limited in X-ray and TeV γ-ray bands. To evaluate the effects of the reduction of cross section in the Klein-Nishina regime, we approximate the spectral energy distribution (SED) of Mrk 501 as two broken power-laws (Figure 10.10). Lower component is synchrotron radiation, while upper is SSC radiation. For simplicity, we assume both components are *self-similar* and spectral index (in νF_ν space) is α ($>$ 0) below the break and β (< 0) above the break, respectively.

We assume a flare in which γ_{max} increased by factor ξ (> 1). We denote initial X-ray/TeV γ-ray fluxes as F_{s} and F_{c}, respectively. Initial break (*peaks*) in the synchrotron component is ν_{s}, while it is ν_{c} for the SSC component. Since the synchrotron frequency is $\propto \gamma^2$, ν_{s} increases by factor ξ^2 during the flare. In the Thomson regime, we expect ν_{c} to increase by factor ξ^4, because $\nu_{\mathrm{c}} \propto \gamma^2 \ \nu_{\mathrm{s}}$ (equation (3.44)). Thus for the case of
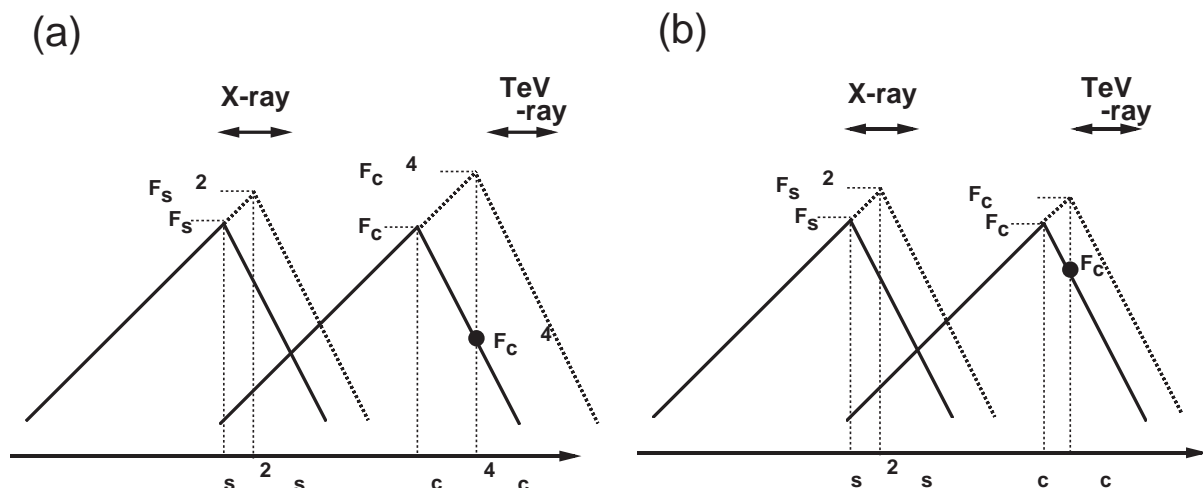
Figure 10.10: Schematic view of spectral evolution of Mrk 501. (a) : spectral evolution in Thomson regime, (b) : spectral evolution in Klein-Nishina regime. For Mrk 501, appropriate values for α and β are 0.2 and -0.5, respectively.

Mrk 501, the X-ray flux during the flare is roughly be $F_s \, \xi^{2\alpha}$ and TeV γ-ray flux is F_c $\xi^{4\alpha}$ (Figure 10.10), compared with the initial values of F_s and $F_c \, \xi^{4\beta}$. Thus the index of correlation k_{TM} between X-ray and TeV γ-ray flux is ([TeV flux] $\propto$ [X-ray flux]$^{k_{\mathrm{TM}}}$)

$$k_{\mathrm{TM}} \simeq \frac{4(\alpha - \beta)}{2\alpha}. \qquad (10.17)$$

Selecting the appropriate values of α and β ($\alpha \sim 0.2$ and $\beta \sim -0.5$ for Mrk 501), we finally obtain $k_{\mathrm{TM}}(\mathrm{Mrk}\ 501) \sim 7$. This is much larger than the observed relation.

In the Klein-Nishina regime, we expect ν_c increased by factor ξ, because the maximum energy of Comtpon scattered photon is limited to $\gamma_{\mathrm{max}} \, m_e c^2$. The X-ray flux during the flare is roughly be $F_s \, \xi^{2\alpha}$ while TeV γ-ray flux is $F_c \, \xi^{\alpha}$, compared with the initial values of F_s and $F_c \, \xi^{\beta}$. Thus the index of correlation k_{KN} between X-ray and TeV γ-ray flux is ([TeV flux] $\propto$ [X-ray flux]$^{k_{\mathrm{KN}}}$)

$$k_{\mathrm{KN}} \simeq \frac{\alpha - \beta}{2\alpha}. \qquad (10.18)$$

Selecting the appropriate values of α and β ($\alpha \sim 0.2$ and $\beta \sim -0.5$ for Mrk 501), we obtain $k_{\mathrm{KN}}(\mathrm{Mrk}\ 501) \sim 2$. This value is exactly consistent with the observed relation.

In summary, different correlations between X-ray/TeV γ-ray fluxes found in Mrk 421 and Mrk 501 are due to the different origins of the spectral evolution – number of electrons increased for Mrk 421, while maximum Lorentz factor increased for Mrk 501. Importantly, both observed relations are consistent if the Synchrotron self-Compton scattering takes place in the Klein-Nishina regime.

10.6   Constraints on the Physical Parameters

In § 10.2, we derived the magnetic field strength B by comparing observed time lags in various X-ray energy bands. The magnetic field of Mrk 421 and PKS 2155−304 were successfully determined to be $B \simeq 0.1$−0.2 G, assuming the beaming factor δ of 10. However, we should note that these constraints had been obtained only from the time-variability. Several important physical quantities are still unknown. Even in the one-zone SSC scenario, we need 7 parameters to specify the model, which cannot be determined only from the time variability constraints. In the following, we consider the constraints that can be derived from the multi-frequency spectra and compared with the limit obtained from 'time-lags' in the X-ray light curves.

One can find similar discussions in Bednarek & Protheroe (1997; 1999), Tavecchio, Maraschi & Ghisellini (1998) and Kataoka et al (1999). Following approach has two advantages compared to the previous works – (1) multi-frequency spectra taken at various states of activities are evaluated by polynomial fits for each TeV blazar, and (2) our discussion is more flexible and less affected by the uncertainties in the observational data.

10.6.1   Allowed Parameter Region

To specify the spectral energy distribution, we need the magnetic field B, region size R, beaming factor δ, escape time t_{esc}, and the electron injection spectrum as input parameters (§ 3; see, also § 11). We adopt a specific form for the injected electron spectrum, $Q(\gamma) = q_{\mathrm{e}} \, \gamma^{-s} \exp(-\gamma/\gamma_{\mathrm{max}})$, where γ_{max} is the maximum Lorentz factor of electrons. Seven free parameters listed here are required to specify the model.

Importantly, all these parameters can be calculated from seven observables: synchrotron maximum frequency, $\nu_{\mathrm{s}}^{\mathrm{max}}$; Compton maximum frequency, $\nu_{\mathrm{C}}^{\mathrm{max}}$; synchrotron break frequency, $\nu_{\mathrm{s}}^{\mathrm{br}}$; variability time scale, t_{var}; synchrotron luminosity, $L_{\mathrm{s}}^{\mathrm{tot}}$; Compton luminosity, $L_{\mathrm{C}}^{\mathrm{tot}}$; and radio (millimeter) spectral index, α. The slope of injected electrons is simply related with α as $s = 2\alpha + 1$ (e.g., Blumenthal & Gould. 1970; § 3.3.2). Since the radio (millimeter) band is thought to be the uncooled portion of the electron distribution (§ 10.2.6, see also below), $\nu_{\mathrm{s}}^{\mathrm{br}}$ is the frequncy where the spectral index starts to deviate from that in the radio (millimeter) band.

Despite the equal numbers of observables and parameters (7 observables for 7 parameters), the model cannot be specified uniquely. The reasons are; (1) the region size is described by an inequality $R \leq ct_{\mathrm{var}}\delta$ (2) most of the present data are not well sampled and not obtained simultaneously, (3) multi-frequency spectra of blazars track smooth curves, hence we cannot clearly define the accurate positions of 'maximum frequency'

or 'break frequncy', (4) Klein-Nishina effects probably reduce the Compton flux signifi-
cantly at TeV energy band, which may cause the underestimate of the seed photon (i.e.,
synchrotron photon) density.
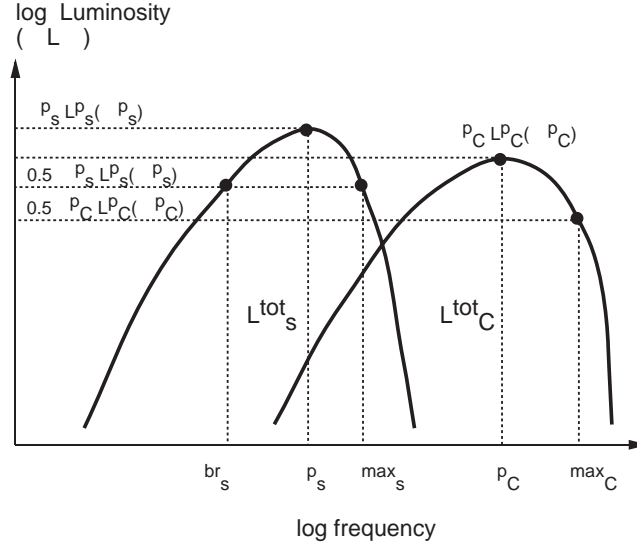
Figure 10.11: Definition of parameters from polynomial (cubic) fit. Spectral energy distribution of a TeV blazar is schematically shown. Horizontal axis is 'log frequency', while vertical axis is 'log νL_ν luminosity'.

To constrain the physical paramters, we first need to determine 7 observables. For this purpose, the multi-frequency spectrum of each TeV blazar was fitted with polynomial function of a form; $\log(\nu L_\nu) = a + b \log\nu + c (\log\nu)^2 + d (\log\nu)^3$, where a, b, c, d are the constants (Comastri et al. 1995). Since there are at least two components in the multi-frequency spectrum, we fitted the lower component (LE component; radio to X-rays) and the higher component (HE component; γ-rays) with separate polynomial functions. We determined 'observables' from the best fit cubic functions, which are schematically shown in Figure 10.11.

A relation $R \leq ct_{\mathrm{var}}\delta$ gives only an upper limit on the dimension of the source. But if we choose very small number for R, extremely high Doppler factor is required from the transparency condition (see below). Following Tavecchio, Maraschi & Ghisellini (1998), we limit ourselves in the range, $R = \xi ct_{\mathrm{var}}\delta$ $(1/3 < \xi < 1)$. The escape time of electrons, t_{esc}, is also quite uncertain, but it needs to be longer than light travel time over the source (R/c). It is, however, not plausible that t_{esc} is much larger than R/c. If so, no break (ν_s^{br}) would be observed in the spectral energy distribution up to ν_s^{max}, which contradicts the obserations. We thus adopt a limit to t_{esc} as $t_{\mathrm{esc}} = \eta\, R/c$ $(1 < \eta < 10)$.

First constraint on parameters is derived as follows. The maximum Lorentz factor of

electrons is approximately related to the observable $\nu_{\mathrm{s}}^{\mathrm{max}}$,

$$\gamma_{\mathrm{max}} \simeq [\frac{\nu_{\mathrm{s}}^{\mathrm{max}}}{3.7 \times 10^6 B \delta}]^{1/2}, \qquad (10.19)$$

where the electron pitch angle with respect to the magnetic field was set to be $\pi/2$ (equation 3.33). Since the Compton-scattered spectrum extends up to $\nu_{\mathrm{C}}^{\mathrm{max}}$, the maximum electron energy must be larger $h\nu_{\mathrm{C}}^{\mathrm{max}}$ in the source frame. We thus obtain the first constraint,

$$h\nu_{\mathrm{C}}^{\mathrm{max}} \leq \gamma_{\mathrm{max}} m_{\mathrm{e}} c^2 \delta \simeq [\frac{\nu_{\mathrm{s}}^{\mathrm{max}}}{3.7 \times 10^6 B}]^{1/2} m_{\mathrm{e}} c^2 \delta^{1/2}. \qquad (10.20)$$

The second relation can be derived using the ratio of *total* luminosities of the synchrotron radiation and the total luminosity of the self-Compton radiation. As we have seen in equation (3.48), this ratio is directly related to the ratio between the radiation and the magnetic field densities inside the source as,

$$\frac{L_{\mathrm{C}}^{\mathrm{tot}}}{L_{\mathrm{s}}^{\mathrm{tot}}} = \frac{U_{\mathrm{s}}^{\mathrm{avail}}}{U_B}, \qquad (10.21)$$

where $U_{\mathrm{s}}^{\mathrm{avail}}$ indicates the synchrotron photons which can effectively involved in the inverse-Compton scattering, below the Klein-Nishina limit. We conveniently express $U_{\mathrm{s}}^{\mathrm{avail}}$ as $U_{\mathrm{s}}^{\mathrm{avail}} = (1/\kappa) \, U_{\mathrm{s}}$, where U_{s} is the *total* soft photon density and $\kappa > 1$. If the scattering takes place purely in the Thomson regime, κ is equal to 1. Since U_{s} is related to $L_{\mathrm{s}}^{\mathrm{tot}}$ as

$$U_{\mathrm{s}} = \frac{L_{\mathrm{s}}^{\mathrm{tot}}}{4\pi R^2 c \delta^4}, \qquad (10.22)$$

we find a relation

$$U_B = \frac{1}{\kappa} U_{\mathrm{s}} \frac{L_{\mathrm{s}}^{\mathrm{tot}}}{L_{\mathrm{C}}^{\mathrm{tot}}} = \frac{1}{4\pi R^2 c \delta^4 \kappa} (\frac{L_{\mathrm{s}}^{\mathrm{tot}\,2}}{L_{\mathrm{C}}^{\mathrm{tot}}}). \qquad (10.23)$$

Considering the reduction of cross section in the Klein-Nishina regime, we assume $1 < \kappa < 10$ in the following. This range of κ is valid as long as γ_{max} is not too large (e.g., $\gamma_{\mathrm{max}} \leq 10^6$; Figure 3.8). Thus we finally obtain the second constraint

$$\frac{1}{4\pi R^2 c \delta^4} (\frac{L_{\mathrm{s}}^{\mathrm{tot}\,2}}{L_{\mathrm{C}}^{\mathrm{tot}}})(\frac{1}{10}) < U_B < \frac{1}{4\pi R^2 c \delta^4} (\frac{L_{\mathrm{s}}^{\mathrm{tot}\,2}}{L_{\mathrm{C}}^{\mathrm{tot}}}). \qquad (10.24)$$

The third constraint is derived from the balance between cooling and electron-escape time scale (e.g., Sikora, Begelman & Rees 1994; Inoue & Takahara 1996). An injection of a power-law energy distribution of electrons up to a certain maximum energy (as expected from shock acceleration) into the radiating region should yield a steady-state electron distribution with a break in its index at a characteristic energy γ_{br}. γ_{br} is estimated from a similar relation with equation (10.19),

$$\gamma_{\mathrm{br}} \simeq [\frac{\nu_{\mathrm{s}}^{\mathrm{br}}}{3.7 \times 10^6 B \delta}]^{1/2}. \qquad (10.25)$$

By equating the cooling time of electrons at γ_{br} with electron escape time, we obtain

$$t_{cool}(\gamma_{br}) = \frac{3m_e c^2}{4(U_B + U_s^{avail})\sigma_T \gamma_{br} c} = t_{esc}, \tag{10.26}$$

where σ_T is the Thomson cross section (see, equation (3.34), (3.47)). Combining with equation (10.21) and $t_{esc} = \eta \ R/c$ (1< η < 10), we finally obtain the third constraint,

$$\frac{3m_e c^2}{4U_B \sigma_T \gamma_{br} R}\left(\frac{1}{10}\right) < \frac{L_C^{tot}}{L_s^{tot}} + 1 < \frac{3m_e c^2}{4U_B \sigma_T \gamma_{br} R}. \tag{10.27}$$

An additional constraint is derived from the condition of transparency of γ-rays to pair production absorption. Importantly, the transparency condition does not depend on the specific emission mechanisms, therefore it can place a strong and *independent* constraint on the minimum value of the Doppler factor in the SSC model. Following Dondi & Ghisellini (1995) and Tavecchio, Maraschi & Ghisellini (1998), conditions can be written

$$\delta > \left[\frac{\sigma_T d_L^2}{5hc^2}\frac{F(\nu_{tgt})}{t_{var}}\right]^{\frac{1}{4+2\beta}}, \tag{10.28}$$

where ν_{tgt} is the frequency of *target* photons for pair production, related with γ-ray photons ν_γ as $1.6 \times 10^{40}/\nu_\gamma$. β is the spectral energy index of target photons, $F(\nu_{tgt})$ is the flux density of target photons per frequency, and d_L is the luminosity distance, respectively.

All of above four conditions (equation (10.20), (10.24), (10.27) and (10.28)) are written in terms of two physical parameters: the magnetic field and the beaming factor. Each constraint then corresponds to an allowed region in the (δ, B) plane. On the other hand, the X-ray observation of 'time-lags' strongly limit B and δ along a narrow line $B \propto \delta^{-1/3}$ (e.g., equation (10.2)). Thus this provides a crucial test to examine whether the limits from spectral energy distribution and time-variability are mutually consistent. In the next section, we evaluate the allowed parameter space (δ, B) for each TeV blazar.

10.6.2 Individual Target

To evaluate the SED for each TeV blazar, we collected the non-simultaneous data from the literature and combined with our simultaneous X-ray/TeV γ-ray data (see § 9). Since the constraints described above basically assume a *steady state* emission, lowest fluxes in the literature were plotted as an approximate *quiescent* state. Balance of cooling time and escape time ($t_{cool}(\gamma_{br}) = t_{esc}$) is only expected when the electron population has enough time to reach an equilibrium state. Similarly, the ratio between the radiation and the magnetic field densities (equation 10.21) holds when the photon distribution is in an equipartition (e.g., § 11). In the following, however, we also use simultaneous data in

various flaring states to check the consistency of parameters derived from the spectra in the quiescent state.

The results of polynomial fit are summarized in Table 10.1. We define ν_s^{br} as the frequency where synchrotron luminosity reaches a half of its peak value $(\nu_s^p L_\nu(\nu_s^p))$, while ν_s^{max} is the frequency where the synchrotron luminosity decreased to a half of the peak (Figure 10.11). Since 1ES 2344+514 has not been detected by EGRET (Figure 9.14), we conveniently assume a best-fit polynominal function of Mrk 501 for the Compton radiation of 1ES 2344+514.

It should be noted that for Mrk 421 and PKS 2155−304, the total synchrotron lu- minotisy L_s^{tot} is larger than the total Compton luminosity L_C^{tot} by a factor of 2−3, while nearly equal for the case of Mrk 501. Also note that the maximum synchrotron frequency becomes larger for fainter sources (see, also Figure 7.27).

Table 10.1: Results of polynonimal (cubic) fit

source	α	ν_s^{br} (Hz)	ν_s^p (Hz)	ν_s^{max} (Hz)	$\nu_s^p L_s(\nu_s^p)$ (erg/s)	L_s^{tot} (erg/s)	ν_C^p (Hz)	ν_C^{max} (Hz)	$\nu_C^p L_C(\nu_C^p)$ (erg/s)	L_C^{tot} (erg/s)
Mrk 421	0.3	14.4	15.8	17.2	44.3	45.2	24.2	25.7	44.0	44.8
Mrk 501	0.4	13.8	15.7	17.6	44.0	44.9	23.0	24.8	44.1	45.0
PKS 2155 −304	0.2	14.6	16.0	17.3	45.7	46.5	24.2	25.7	45.3	46.2
1ES 2344 +514	0.5	14.1	16.0	17.9	43.3	44.2	23.0	24.8	43.4	44.3

Frequencies and luminosities are all given in *log*.

radio (millimeter) spectral index, α ; synchrotron break frequency, ν_s^{br} ; synchrotron peak frequency, ν_s^p ; synchrotron maximum frequency, ν_s^{max} ; synchrotron peak luminosity, $\nu_s^p L_s(\nu_s^p)$; total synchrotron luminosity, L_s^{tot} ; SSC peak frequency, ν_C^p ; SSC maximum frequency, ν_C^{max} ; SSC peak luminosity, $\nu_C^p L_C(\nu_C^p)$; total SSC luminosity, L_C^{tot} ;

The 7 input observables for the allowed parameter space are summarized in Table 10.2. t_{var} was determined from the characteristic time scale of the X-ray time variability found in this thesis (§ 8.2.3). We assume $t_{var} = 1$ day for 1ES 2344+514, because its variability time scale is completely unknown, but longer than ~ 0.5 day (Figure 8.11). Other input quantities are same as Table 10.1, except for additional errors in the values of ν_C^{max} and L_C^{tot}. We add systematic errors of factor 3 and factor 2 in the values of ν_C^{max} and L_C^{tot}, respectively. This is because the Compton component is evaluated only from GeV/TeV γ-ray data, thus quite uncertain. On the other hand, the quality of the

synchrotron spectrum is much better than the Compton specturm, so we can neglect the errors on ν_s^{max} and L_s^{tot}.

Table 10.2: Input observables for individual TeV blazars

source	α	ν_s^{br} (Hz)	ν_s^{max} (Hz)	L_s^{tot} (erg/s)	$\nu_C^{max\dagger}$ (Hz)	$L_C^{tot\dagger}$ (erg/s)	t_{var} (sec)
Mrk 421	0.3	14.4	17.2	45.2	$25.7^{+0.5}_{-0.5}$	$44.8^{+0.3}_{-0.3}$	4.3×10^4
Mrk 501	0.4	13.8	17.6	44.9	$24.8^{+0.5}_{-0.5}$	$45.0^{+0.3}_{-0.3}$	1.0×10^5
PKS 2155 -304	0.2	14.6	17.3	46.5	$25.7^{+0.5}_{-0.5}$	$46.2^{+0.3}_{-0.3}$	3.0×10^4
1ES 2344 $+514$	0.5	14.1	17.9	44.2	$24.8^{+0.5\ddagger}_{-0.5}$	$44.3^{+0.3}_{-0.3}$	$1.0 \times 10^{5\ddagger}$

Frequencies and luminosities are all given in *log*.

radio (millimeter) spectral index, α ; synchrotron break frequency, ν_s^{br} ; synchrotron maximum frequency, ν_s^{max} ; total synchrotron luminosity, L_s^{tot} ; SSC maximum frequency, ν_C^{max} ; total SSC luminosity, L_C^{tot} ; variability time scale, t_{var} ;

† Uncertainties of factor 3 in the value of ν_C^{max} and factor 2 in the value of L_C^{tot} are taken into account.

‡ : assumed to be equal to Mrk 501, because EGRET detection has not been reported.

Mrk 421

In Figure 10.12, we show the parameter space for Mrk 421 (*right*). Thin region is the allowed space derived from the *quiescent* SED of Mrk 421 (Table 10.2 and Figure 10.12 (*left*)). Uncertainties of factor 3 in the value of R, factor 10 in t_{esc} and the reduction of Compton flux in the Klein-Nishina regime (up to factor 10) are considered. We also investigate the allowed parameter space for various flaring states plotted in Figure 9.5. Filled area is the overlapped region. The solid vertical line is the lower limit from the transparency condition derived from TeV γ-ray/optical correlation in time variability (Buckley et al. 1996; equation (10.28)).

We also plot the equipartition condition for the magnetic field density and synchrotron photon density, $U_B = U_s^{avail}$. Dashed line with a label 'TM' is the case when all the scattering takes place in the Thomson regime, although this is unlikely for the TeV blazars (see the discussion in § 10.5). A line with a label 'KN' is the case when the scattering takes place in the Klein-Nishina regime, reducing the effective seed photon density by a factor of $\kappa = 10$. Both lines assume $R = c\, t_{var}\, \delta$ for simplicity.

Importantly, this equipartition line divides the *synchrotron cooling dominant* region and *Compton cooling dominant* region in the $\delta - B$ plane. Synchrotron cooling approximation (see, § 10.2.1) is only valid in the right of this line, while in the left, Compton

cooling is more effective. Thus current allowed region for Mrk 421 indicates that the syn-
chrotron cooling is more dominant than Compton cooling process, even in the Thomson
scattering limit. This is consistent with the fact that $L_\mathrm{s}^\mathrm{tot}$ is larger by factor ~ 3 than $L_\mathrm{C}^\mathrm{tot}$
(Figure 9.5).

Finally, we superpose a constraint from the observed time-lags in various X-ray energy
band (Takahashi et al. 1996). Synchrotron cooling is assumed to be dominant cooling
process. The line is appeared as a flat solid line ($B \propto \delta^{-1/3}$) with measurement errors
on the lag (dotted lines). It is extremely important that this line, which is completely
independent of the spectral constraints, is nicely in agreement with the parameter region
allowed by those constraints.
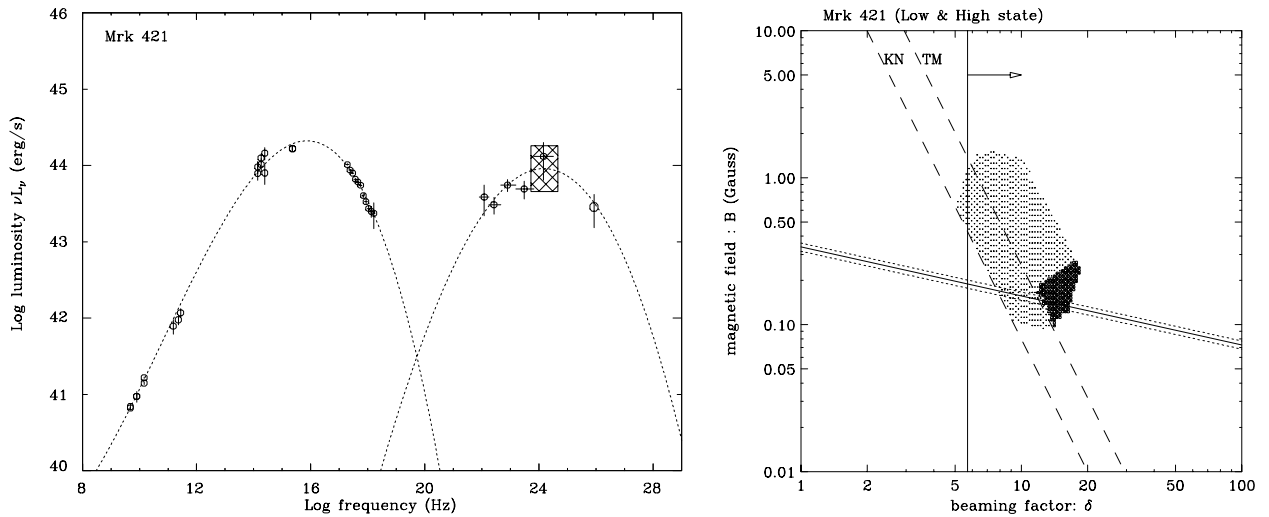
Figure 10.12: *left*: polynomial (cubic) fit of νF_ν spectrum of Mrk 421. Hatched region is the uncer-
tainty associated with the estimates of $\nu_\mathrm{C}^\mathrm{p}$ (factor 3) and L_C^p (factor 2). *right* : the parameter space (δ,
B) allowed by the one-zone SSC model for Mrk 421 data. Thin region is the allowed space using only
SED data for quiescent state (*left*), while thick region is the overlapped region for various source activ-
ities (Figure 9.5). Solid line put in dashed lines is a limit derived from X-ray observation of 'time-lags',
assuming the synchrotron cooling process. Vertical line is the limit from TeV γ-ray/optical transparency
condition. Dashed lines show the equipartition between U_B and $U_\mathrm{s}^\mathrm{avail}$, which divides the dominance of
synchrotron/Compton cooling processes. Lines for Thomson limit and Klein-Nishina limit are separately
shown.

Mrk 501

Figure 10.13 shows the parameter space for Mrk 501 (*right*). Thin region is the allowed
space derived from the *quiescent* SED of Mrk 501 (Table 10.2 and Figure 10.13 (*left*)).
Uncertainties in parameters are same as that for Mrk 421. Filled area is the overlapped

region with those derived for various flaring states (Figure 9.10). The solid vertical line is the lower limit from the transparency condition derived from TeV γ-ray/optical correlation in time variability (Catanese et al. 1997; equation (10.28)).

The equipartition condition for magnetic field density U_B and synchrotron density U_s^{avail} is shown as dashed lines. A line for pure Thomson limit and Klein-Nishina limit (κ = 10) are separately shown. One finds that synchrotron cooling is dominant as long as scattering takes place in the Klein-Nishina regime. Unfortunately, no X-ray observation of 'time-lags' are reported, hence only spectral constraints are shown in the figure.
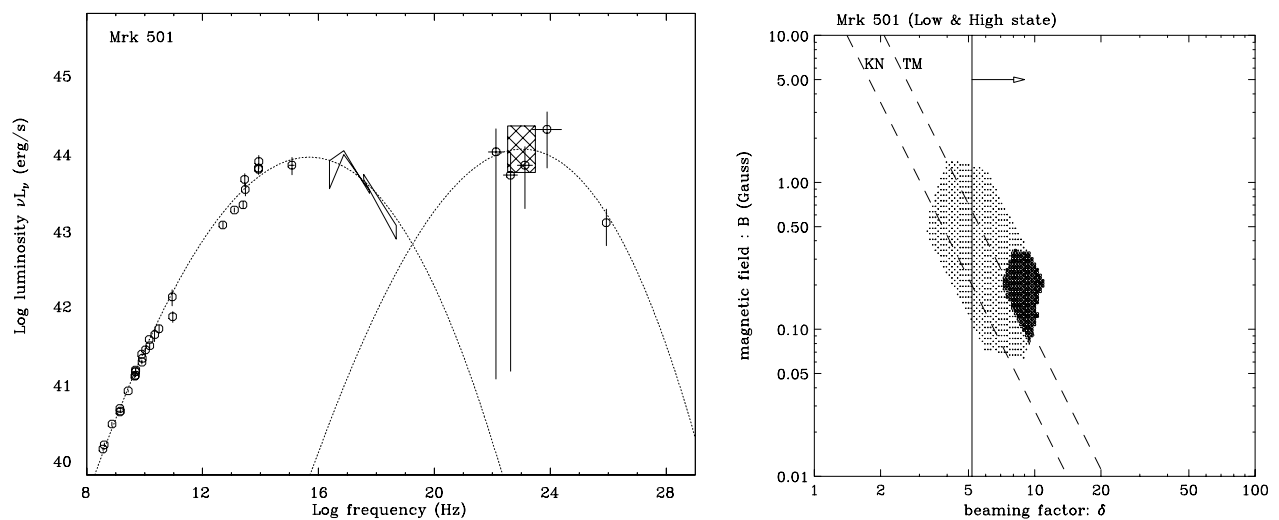
Figure 10.13: *left*: polynomial (cubic) fit of νF_ν spectrum of Mrk 501. Hatched region is the uncertainty associated with the estimates of ν_C^p (factor 3) and L_C^p (factor 2). *right*: the parameter space (δ, B) allowed by the one-zone SSC model for Mrk 501 data. Thin region is the allowed space using only SED data for quiescent state (*left*), while thick region is the overlapped region for various source activities (Figure 9.10). Vertical line is the limit from TeV γ-ray/optical transparency condition. Dashed line shows the equipartition between U_B and U_s^{avail}, which divides the dominance of synchrotron/Compton cooling processes. Lines for Thomson limit and Klein-Nishina limit are separately shown.

PKS 2155−304

Figure 10.14 shows the parameter space for PKS 2155−304 (*right*). Thin region is the allowed space derived from the *quiescent* SED of PKS 2155−304 (Table 10.2 and Figure 10.14 (*left*)). Uncertainties in parameters are assumed to be same as that for Mrk 421. Filled area is the overlapped region for those derived from *non*-simultaneous EGRET observations (see Figure 9.12). Transparency conditions cannot be calculated because no correlation of variability have been reported between synchrotron and Compton components.

Equipartition condition for U_B and U_s^{avail} are given as dashed lines, both for Thomson and Klein-Nishina case ($\kappa = 10$). Synchrotron cooling approximation is valid as long as scattering takes place in the Klein-Nishina regime. Also note that L_s^{tot} is larger by factor $\simeq$ 2 than L_C^{tot}, which implies that synchrotron cooling dominates in this source (Figure 9.12). Another constraint from the observed time-lags in various X-ray energy bands (Kataoka et al. 2000) is given in narrow solid-dotted lines ($B \propto \delta^{-1/3}$). Similar to the case of Mrk 421, this line is exactly consistent with the parameter region *independently* determined from the spectral constraints.
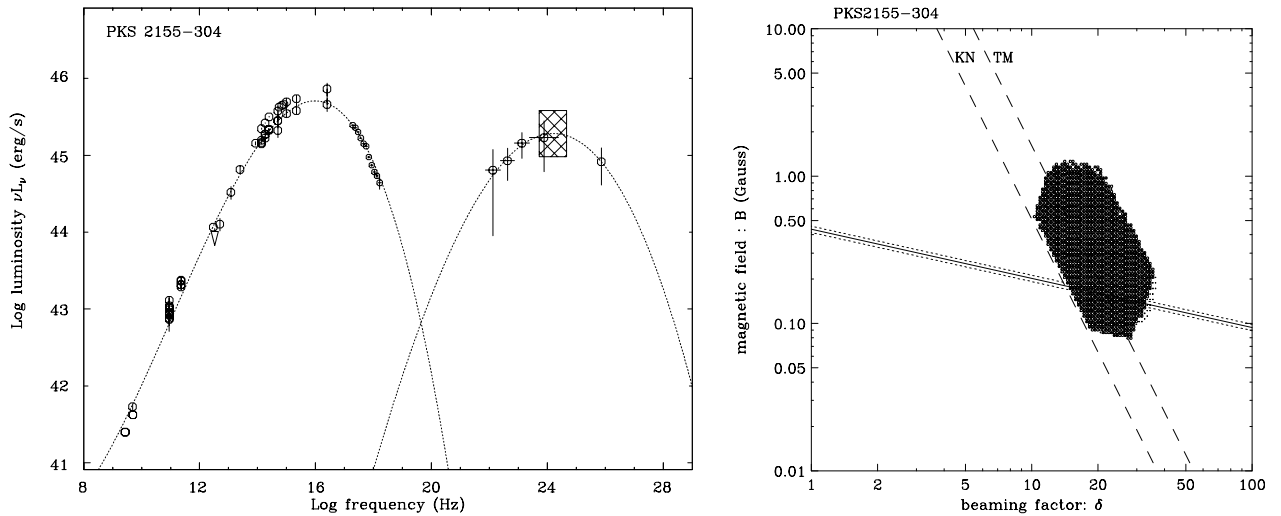
Figure 10.14: *left*: polynomial (cubic) fit of νF_ν spectrum of PKS 2155−304. Hatched region is the uncertainty associated with the estimates of ν_C^{p} (factor 3) and L_C^{p} (factor 2). *right* : the parameter space (δ, B) allowed by the one-zone SSC model for PKS 2155−304 data. Thin region is the allowed space using only SED data for quiescent state (*left*), while thick region is the overlapped region with a higher state (Figure 9.12). Solid line put in dashed lines is a limit derived from X-ray observation of 'time-lags', assuming the synchrotron cooling process. Dashed lines show the equipartition between U_B and U_s^{avail}, which divides the dominance of synchrotron/Compton cooling processes. Lines for Thomson limit and Klein-Nishina limit are separately shown.

1ES 2344+514

Figure 10.15 shows the parameter space for 1ES 2344+514 (*right*). Thin region is the allowed parameter space derived from the *quiescent* SED of 1ES 2344+514 (Table 10.2 and Figure 10.15 (*left*). Since the data are too sparse especially in the γ-ray (EGRET) range, we conveniently assumed a polynomial function of Mrk 501, just by changing the normalization. Luminosity ratio, $L_s^{\text{tot}}/L_C^{\text{tot}}$, is assumed to be equal in these two sources. Thus following 'allowed region' may be fault if the Compton spectrum of 1ES 2344+514

is completely different from the Mrk 501. Transparency conditions cannot be calculated because any correlations of time variability has not been reported.

The equipartition condition for magnetic field density U_B and synchrotron density U_s^{avail} is shown as dashed lines. Line for pure Thomson limit and Klein-Nishina limit (κ = 10) are separately shown. One finds that synchrotron cooling is dominant as long as scattering takes place in the Klein-Nishina regime. More observations in various energy bands are awaited for this source.
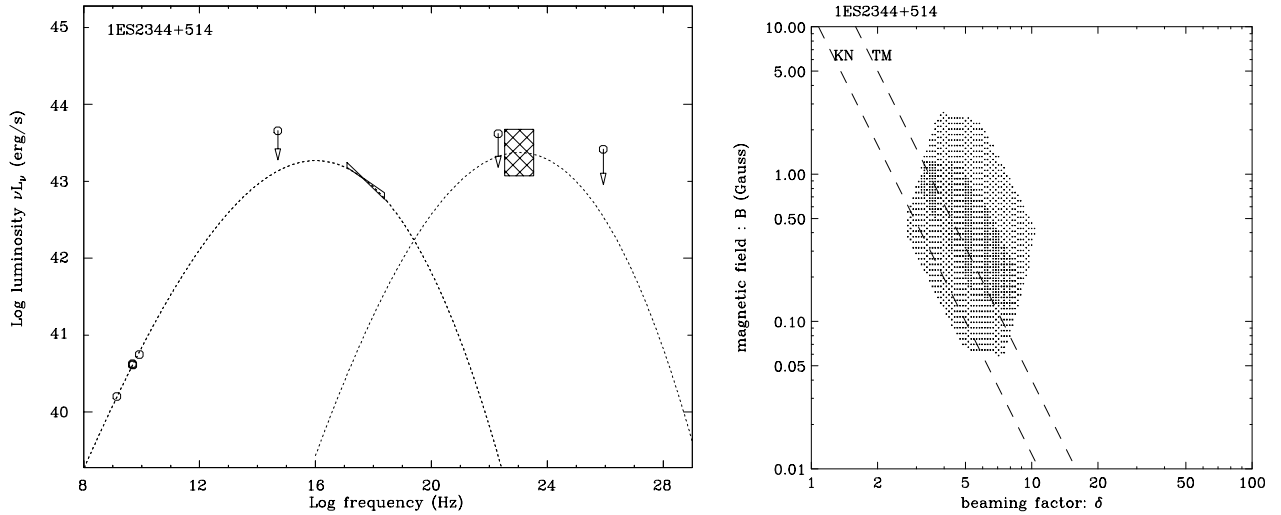
Figure 10.15: *left*: polynomial (cubic) fit of νF_ν spectrum of 1 2344+514. Hatched region is the uncertainty associated with the estimates of ν_C^{p} (factor 3) and L_C^{p} (factor 2). *right* : the parameter space (δ, B) allowed by the one-zone SSC model for 1ES 2344+514 data. Thin region is the allowed space using only SED data for quiescent state (*left*), while thick region is the overlapped region for various source activities (Figure 9.14). Dashed line shows the equipartition between U_B and U_s^{avail}, which divides the dominance of synchrotron/Compton cooling processes. Lines for Thomson limit and Klein-Nishina limit are separately shown.

Summary

In summary, the calculated physical quantities for TeV blazars are shown in Table 10.3 (5 of 7 parameters). We assumed parameters in the overlapped region of (δ, B) space, although these might be over-constraints if the photon distributions are far from equipartition in the flaring states. The limits listed here are only from the spectral constraints and additional constraints from observed 'time-lags' are not taken into account. Allowed space would be more tightly constrained for Mrk 421 and PKS 2155−304, if those limits are combined ($B \simeq 0.1-0.2$ G). Remaining two physical quantities are easily derived from these 5 parameters. The range of t_{esc} is just $R/c-10R/c$. Normalization of input electrons

q_e can be determined *uniquely* to agree with observed L_s^{tot}, but it is difficult to express it in an analytical form.

Importantly, our derived parameter (Table 10.3) indicates that the magnetic field strength B and the maximum Lorentz factor γ_{max} of TeV blazars are very similar in the quiescent state. Since we assumed parameters in the overlapped region of (δ, B) space, these two parameters are not changed even in the flaring states. On the other hand, γ_{max} and q_e can vary in various states of source activity, as suggested from the different way of spectral evolution observed in Mrk 421 and Mrk 501 (§ 9). For an example, we expect that the γ_{max} of Mrk 501 increased to $\sim 5 \times 10^6$ when the source was in the high state, while B and δ stayed constant (see, § 11.7).

Table 10.3: Output physical quantities for individual TeV blazars

source	s	δ	B (G)	$R^{\dagger}$ (pc)	γ_{max}
Mrk 421	1.6	12−18	0.1−0.3	$(1.6−7.4) \times 10^{-3}$	$(0.9−1.8) \times 10^5$
Mrk 501	1.8	7−11	0.1−0.4	$(1.9−10) \times 10^{-3}$	$(1.9−3.8) \times 10^5$
PKS 2155 −304	1.4	10−36	0.08−1.2	$(1.0−10) \times 10^{-3}$	$(0.5−1.6) \times 10^5$
1ES 2344 +514	1.9	3−10	0.06−2.5	$(0.8−8.4) \times 10^{-3}$	$(1.3−7.1) \times 10^5$

Resultant allowed parameter regions determined from the quiescent spectral energy distributions. Limits from observed 'time-lags' are not taken into account. Allowed space would be more tightly constrained for Mrk 421 and 2155−304, if 'time-lags' are considered ($B \simeq 0.1−0.2$ G). electron injection spectral index, s; beaming factor, δ; magnetic field strength, B; emission region size, R; maximum Lorentz factor of electron, γ_{max}.
$\dagger$: Uncertainties of factor 3 in the value of R is taken into account.

10.7   Motivation to develop a 'NEW' theoretical model

From detailed discussion in this chapter, we found that the spectral and temporal behaviour of TeV blazars is well explained by a simple one-zone SSC scenario. One of the most important discoveries is that the rapid X-ray time variability in blazars are probably characterized by 4 dynamical time scales; acceleration time t_{acc}, cooling time t_{cool} and source light travel time t_{crs} and injection time t_{inj}. It is, however, unfortunate that the most of the previous models consider *steady state* emission only, in spite of rapid variability which is often seen in blazars.

Very recently, several authors have started to develop *time-dependent* SSC model to

interpret the rapid variabilities and spectral evolutions of blazars. Mastichiadis & Kirk (1997) and Dermer (1998) considered time-dependent SSC models where the variability is on time scales longer than R/c (see, also § 2.3.2). However, our current results strongly predicts that the cooling time of the highest electrons is much shorter than t_{crs}, thus rapid variability could be relaxed (smoothed) by light travel time effects over the source. Chiaberge & Ghisellini (1999) and Kataoka et al. (2000) took this relaxation effect into account, but their models neglected the time scale for electrons to be accelerated (t_{acc}).

Kirk & Mastichiadis (1998) considered more sophisticated scenario where a thin shock front propagates through the emission region with a finite velocity V_s, supplying freshly accelerated electrons only in the front's vicinity. They argued that the balance of acceleration and cooling processes plays an important role to characterize blazar's variability, in particular at $\gamma \sim \gamma_{max}$. However, their model neglects the effects of smoothing of rapid variability by light-crossing time scale.

As a consequence, a time-dependent model which considers 4 dynamical time scales properly, has not been developed so far. To confirm many ideas discussed in this thesis and investigate the relative importance of those dynamical time scales, we developed a *new* time-dependent SSC code. This model is an improved version of a model presented in Kataoka et al. (2000). We introduced an acceleration term in the time dependent particle kinetic equation in the model. Thus all the relevant time scales, t_{acc}, t_{cool}, t_{crs} and t_{inj}, are accurately considered in the code.

Since our code follows the full time evolution of electrons and photons in the source, we can study both the spectral evolution and temporal variability in blazars. For example, clockwise and anti-clockwise loop pattern can be simulated for various types of flares. Those results will be directly compared with the observational data (e.g., Figure 7.16). Our SSC code is also viable to predict possible variability patterns which may be observed in future, with a variety of balances of 4 dynamical time scales.

In § 10.6, we have investigated the allowed regions and successfully put constraints in the parameter space. In the next chapter, we will apply these *self-consistent* solutions to the observational data. We will also discuss the effects of cross section reduction in the Klein-Nishina regime, as well as relative importance of synchrotron/Compton cooling process in the next chapter.

Chapter 11

Time-Dependent SSC Model

11.1 One-zone Homogeneous SSC Model

We derive the standard solution for the one-zone homogeneous SSC model, assuming a *spherical geometry* of radius R.

For a general source at a distance $d_{\rm L}$ from the observer, the spectral energy flux $F(\nu)$ is determined by the photon emission coefficient j_ν and the absorption coefficient α_ν by

$$F(\nu) = \frac{1}{4\pi d_{\rm L}^2} \int d^3\vec{r} \ [4\pi j_\nu(\vec{r})\exp(-\int \alpha_\nu(\vec{r'})ds')]. \tag{11.1}$$

This is an integral over the volume of the source with an exponential absorption factor involving a line integral from the source point $(\vec{r})$ through to the exterior of the source in the direction of the observer. For the synchrotron case, j_ν and α_ν are respectively given in equation (3.37) and (3.40).

Gould (1979) applied the solution for the synchrotron emission from a homogeneous sphere for which j_ν and α_ν are constants over the volume. The integration is trivial (see, Appendix I), yielding the synchrotron luminosity $L_{\rm sync}(\nu)$ $(\equiv 4\pi d_{\rm L}^2 F_{\rm sync}(\nu))$

$$L_{\rm sync}(\nu) = 4\pi^2 R^2 \frac{j_\nu}{\alpha_\nu}(1 - \frac{2}{\tau_\nu{}^2}[1 - e^{-\tau_\nu}(\tau_\nu + 1)]), \tag{11.2}$$

where τ_ν is the optical depth in the blob along the line of sight and expressed as $\tau_\nu = 2\alpha_\nu R$. The electron pitch angle with respect to the magnetic field is set to $\alpha = \pi/2$.

We calculate the inverse Compton emission incorporating the effects of cross section reduction in the Klein-Nishina regime. The differential photon production rate, $q(\epsilon)$, is calculated from equation (3.49). Note that for the SSC model, $n(\epsilon_0)$ is the number density of *synchrotron photons produced by the same electrons*, per energy interval. To be exact, $n(\epsilon_0)$ varies depending on the position in the emission blob and we have to take this effect

195

into account (Gould 1979). Approximately, we calculated $n(\epsilon_0)$ at the center of the blob with the correction factor $C_{\mathrm{corr}} = 0.75$ (see Appendix I). Thus we have

$$n(\epsilon_0) = \frac{4\pi}{hc\epsilon_0} C_{\mathrm{corr}} \frac{j_\nu}{\alpha_\nu} (1 - e^{-\alpha_\nu R}). \tag{11.3}$$

The Compton luminosity is obtained from the integration of equation (11.1) for the case of the SSC radiation

$$L_{\mathrm{SSC}}(\nu, t) = 4\pi^2 R^2 \frac{j_\nu^{\mathrm{SSC}}}{\alpha_\nu^{\mathrm{SSC}}} (1 - \frac{2}{\tau_\nu^{\mathrm{SSC}2}} [1 - e^{-\tau_\nu^{\mathrm{SSC}}} (\tau_\nu^{\mathrm{SSC}} + 1)]), \tag{11.4}$$

where j_ν^{SSC} is the emission coefficient of the Compton emission given in equation (3.53) and $\alpha_\nu^{\mathrm{SSC}}$ is the absorption coefficient of the Compton emission, respectively. Since the optical depth for the self absorption, τ_ν^{SSC}, is negligibly small for the Compton emission, we approximated it as zero;

$$L_{\mathrm{SSC}}(\nu, t) \simeq \frac{16}{3} \pi^2 R^3 j_\nu^{\mathrm{SSC}}. \tag{11.5}$$

11.2   Application to the Time-Dependent Model

11.2.1   Assumptions

Our kinetic code was developed as an application of a homogeneous SSC model for the steady state, which represents spectra of TeV blazars in the quiescent state. In the code, we assume a model in which electrons are accelerated at a shock front and cool by synchrotron and inverse Compton radiation in the homogeneous magnetic field behind it. Similar to Kirk, Rieger & Mastichiadis (1998), we treat two spatial zones; one around the shock front, in which the particles are continuously accelerated (acceleration region), and one downstream of the shock front, in which the electrons emit most of the radiation (emission region). The emission region has a spherical volume of radius R. We assume both regions are connected closely in space. The electrons in the shock's vicinity will escape from the acceleration region at a constant rate r_{esc}, and are *uniformly* injected into the emission region. Thus the injection rate of electrons into the emission region is exactly the same as the escape rate from the acceleration region. The shematic view of our modeling is given in Figure 11.1.

Thus we need two kinetic equations of electrons corresponding to each region. For the acceleration region, we have

$$\frac{\partial N_{\mathrm{s}}(\gamma, t)}{\partial t} = \frac{\partial}{\partial \gamma} [(\beta_{\mathrm{s}} \gamma^2 - \frac{1}{t_{\mathrm{acc,s}}} \gamma) N_{\mathrm{s}}(\gamma, t)] + q_{\mathrm{s}} \delta(\gamma - \gamma_0) - \frac{N_{\mathrm{s}}(\gamma, t)}{t_{\mathrm{esc,s}}}, \tag{11.6}$$
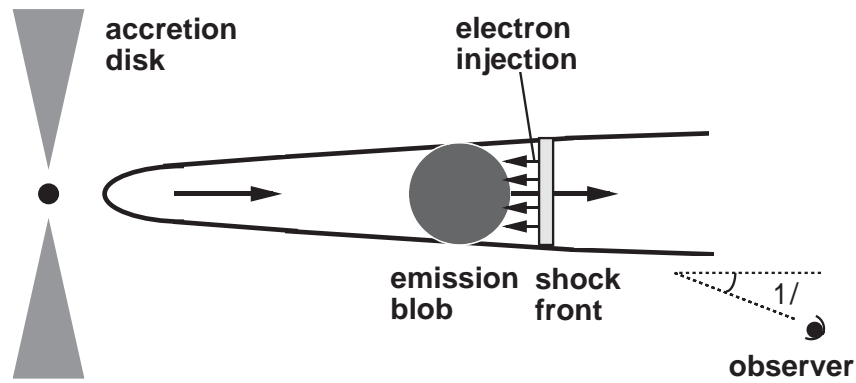
Figure 11.1: Schematic view of the model adopted in this thesis. The electrons are accelerated only in the shock's vicinity and escape at a constant rate. All of them are injected into the emission blob where they radiate.

and for the emission region,

$$\frac{\partial N_e(\gamma, t)}{\partial t} = \frac{\partial}{\partial \gamma}[(\dot{\gamma}_{\rm sync} + \dot{\gamma}_{\rm SSC})N_e(\gamma, t)] + Q(\gamma, t) - \frac{N_e(\gamma, t)}{t_{\rm esc}}, \qquad (11.7)$$

where $N_{\rm s}$ and $N_{\rm e}$ is the number density of electrons per unit energy (see, § 3.6). The suffix s indicates the quantities in the acceleration region, while others are those in the emitting region. For simplicity, we approximate $\beta_{\rm s}$ as a constant value. For acceleration region, we assume low energy electrons are injected only at γ_0 ($\simeq 1$), and gradually accelerated to higer energies in a time scale characterized by $t_{\rm acc,s}$. The maximum energy to which the electrons can be accelerated is determined by the balance of cooling and acceralation efficiency; $\beta_{\rm s}\gamma_{\rm max}^2 = \gamma_{\rm max}/t_{\rm acc,s}$.

11.2.2 Connection between Acceleration Region and Emission Region

The kinetic equation for the shock region (11.6) can be solved analytically, if we assume $\beta_{\rm s}$ and $t_{\rm acc,s}$ has no dependence on energy. This corresponds to the case of $\xi = 0$ for equation (3.16). The solution is expressed as (see, § 3.1.5 or Kirk, Rieger, & Mastichiadis 1998)

$$N_{\rm s}(\gamma, t) = \frac{A}{\gamma^2}\left(\frac{1}{\gamma} - \frac{1}{\gamma_{\rm max}}\right)^{\frac{t_{\rm acc,s} - t_{\rm esc,s}}{t_{\rm esc,s}}} \qquad (\gamma_0 < \gamma < \gamma_1(t)), \qquad (11.8)$$

where

$$A = q_{\rm s}t_{\rm acc,s}\gamma_0^{t_{\rm acc,s}/t_{\rm esc,s}}\left(1 - \frac{\gamma_0}{\gamma_{\rm max}}\right)^{-t_{\rm acc,s}/t_{\rm esc,s}}, \qquad (11.9)$$

$$\gamma_{\rm max} = (\beta_{\rm s}t_{\rm acc,s})^{-1}, \qquad (11.10)$$

$$\gamma_1(t) = (\frac{1}{\gamma_{\mathrm{max}}} + [\frac{1}{\gamma_0} - \frac{1}{\gamma_{\mathrm{max}}}]\exp(-t/t_{\mathrm{acc,s}}))^{-1},\tag{11.11}$$

As a result, the spectrum of accelerated electrons is well approximated by a power law up to a cut-off at the energy at which radiative losses balance energy gains:

$$N_{\mathrm{s}}(\gamma, t) \simeq q_{\mathrm{s}} t_{\mathrm{acc,s}} \gamma^{-(1+\frac{t_{\mathrm{acc,s}}}{t_{\mathrm{esc,s}}})}.\tag{11.12}$$

Assume that the electron injection function $Q(\gamma, t)$ for the emission region is characterized by a power law in the same energy range ($\gamma_0 < \gamma < \gamma_{\mathrm{max}}$),

$$Q(\gamma, t) \simeq q_{\mathrm{e}} \gamma^{-s}.\tag{11.13}$$

Since the electrons escape from the acceleration region in a time scale $t_{\mathrm{esc,s}}$, and are injected into the emitting region, we have relations which connect the quantities in these two regions,

$$q_e \simeq q_{\mathrm{s}} \frac{t_{\mathrm{acc,s}}}{t_{\mathrm{esc,s}}},\tag{11.14}$$

$$s \simeq 1 + \frac{t_{\mathrm{acc,s}}}{t_{\mathrm{esc,s}}},\tag{11.15}$$

$$\gamma_{\mathrm{max}} \simeq (\beta_{\mathrm{s}} t_{\mathrm{acc,s}})^{-1}.\tag{11.16}$$

11.2.3   Numerical Approach

In order to follow the time evolution of the radiation from the emission region, we have to solve a differential equation (11.7). Since we do not have analytical solution for this equation, due to the high non-linearity of the process involved, we have to solve the equation numerically.

Consider a well-defined electron population in the emission region, characterized by $N_e(\gamma, t)$. Given the electron population, the synchrotron emission including the self-absorption can be calculated using the spherical solution for the radiative transfer equation (11.2). The inverse Compton emission incorporating the effects of cross section reduction in the Klein-Nishina regime is calculated by equation (11.4).

The right-hand side of the equation (11.7) is now described by the quantities at time t, and solved numerically to obtain the electron population at time $t+\Delta t$. We adopted an implicit difference scheme by Chang & Cooper (1970), with some modifications for our purposes, since we are dealing with a kinetic equation with injection/escape terms and no diffusion term. This scheme is suitable for finding non-negative and particle number conserving solutions. Details of the techniques in calculations are given in Appendix J.

11.2.4 Light Travel Time Effects

In order to incorporate the light-travel time effects properly in the calculation, we divide the source into $(2t_{\mathrm{crs}}/\Delta t)$ slices of ΔR thickness for each, where t_{crs} $(= R/c)$ is the source light-crossing time and Δt is a time-step of the calculation. The interval Δt must be shorter than the shortest relevant time scale, e.g., radiative cooling times or acceleration time scale. We define $\Delta R \equiv c\Delta t$. The schematic view of this division of the emission blob into slices is given in Figure 11.2.
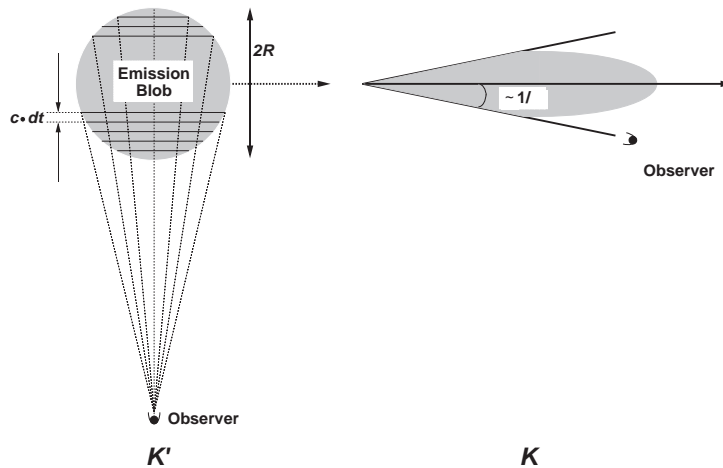
Figure 11.2: The schematic view of the division of the emission blob into 'slices'. Left Panel: Source frame (K'). Right Panel: Observer's frame (K). The emission blob is first cut into slices in the source frame and contributions from each shell are summed. In the observer's frame, the radiation is concentrated in a narrow cone with a half angle $\theta \simeq 1/\Gamma$.

We first consider the slices in the source frame K', with line of sight placed at 90° with respect to the surface of the slices. In the observer's frame K, emission will be concentrated in the forward direction within a narrow cone of half-angle $1/\Gamma$ (§ 3), if the blob moves with a Lorentz factor Γ ($\simeq \delta$ for our case). Volume of each slice is expressed as

$$\Delta V(k) = \pi(R - k)(R + k)\Delta R, \tag{11.17}$$

where k is the distance of the slice from the center of the sphere. Thus the 'weight' function normalized to the spherical volume $V_0 = 4\pi R^3/3$ is

$$w(k) = \frac{3(R - k)(R + k)\Delta R}{4R^3}, \tag{11.18}$$

This function is illustrated in Figure 11.3. The observer will see, at any given time, photons produced in different parts of the source, characterized by an electron distribution
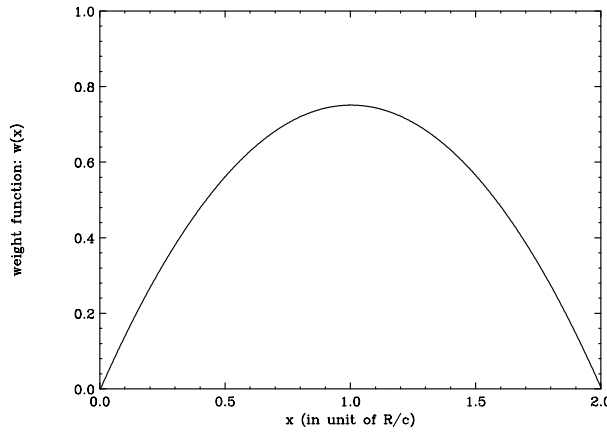
Figure 11.3: Weight funcition of 'slices' for spherical geometry. An integration of $w(x)$ from 0 to $2R/c$ is normlized to 1.

of a different age. This is expressed as

$$L_{\mathrm{mod}}(t) = L(t) \times w(R) + L(t - \Delta t) \times w(R - c\Delta t)..... + L(t - 2R/c) \times w(R). \quad (11.19)$$

where $L(t)$ is the total luminosity emitted from the blob at time t and $L_{\mathrm{mod}}(t)$ is the *observed* luminosity at time t. Thus the observed spectra is a sum of different spectra, emitted from different slices at different times.

11.3   Acceleration of Electrons

11.3.1   Electron Injection at γ_0

We discuss the time evolution of electron spectrum in the acceleration region, based on the discussion in the previous section. The analytic solution (11.8) predicts a very sharp cut-off in the electron distribution at $\gamma = \gamma_1(t)$, which is reflected to the sharp cut-off in the synchrotron spectrum. However, observed photon spectra of blazars show very smooth curvature even in the X-ray band (e.g., § 9). This indicates that, in reality the broad cut-off in the electron spectrum. Such a smooth cut-off might be explained if we incorporate more realistic geometry and/or inhomogeneousness of the source. To mimic the observational photon spectra with 'broad' cut-off, we approximate the solution (11.8) in a simpler form with an exponential cut-off at $\gamma = \gamma_1(t)$. We thus obtain the approximate expressions for equations (11.8) – (11.11), holding the relations (11.14) – (11.16).

$$N_{\mathrm{s}}(\gamma, t) \simeq q_{\mathrm{s}} t_{\mathrm{acc,s}} \gamma^{-(1 + \frac{t_{\mathrm{acc,s}}}{t_{\mathrm{esc,s}}})} \exp(\gamma / \gamma_1(t)), \qquad (11.20)$$

$$\gamma_1(t) = (\frac{1}{\gamma_{\mathrm{max}}} + [\frac{1}{\gamma_0} - \frac{1}{\gamma_{\mathrm{max}}}]\exp(-t/t_{\mathrm{acc,s}}))^{-1}, \tag{11.21}$$

$$\gamma_{\mathrm{max}} = (\beta_{\mathrm{s}} t_{\mathrm{acc,s}})^{-1}. \tag{11.22}$$

In Figure 11.4, we show the time evolution of $N_{\mathrm{s}}(\gamma, t)$ at $t = 0$, t_{acc}, $4t_{\mathrm{acc}}$, $8t_{\mathrm{acc}}$ and 14 t_{acc}. We assume here $t_{\mathrm{acc,s}} = 10^5$ sec, $t_{\mathrm{esc,s}} = 2.5\ t_{\mathrm{acc,s}}$ and $\gamma_{\mathrm{max}} = 10^5$. For time $t \gg t_{\mathrm{acc}}$, the electron population does not change because $\gamma_1(t) \simeq \gamma_{\mathrm{max}}$. We divided $N_s(\gamma, \infty)$ by the escape time $t_{\mathrm{esc,s}}$ to obtain the injection function $Q(\gamma)$ for the emitting region at the steady state (see, § 11.2.2).
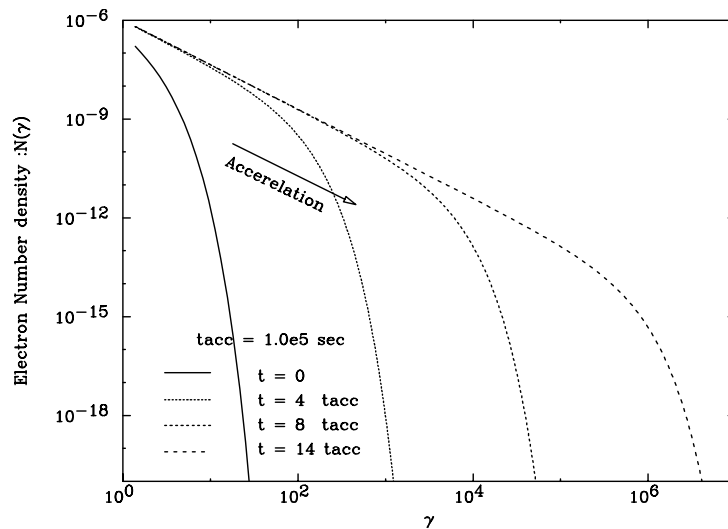
Figure 11.4: Evolution of the electron distribution which are constantly accelerated at rate $(t_{\mathrm{acc}})^{-1}$. Mono-energetic electrons ($\gamma = \gamma_0 \simeq 1$) are assumed to be injected into the acceleration region.

11.3.2 Evolution of Electron Distribution after Stopping the Injection

Assume that the 'fresh' electrons are injected only for $0 < t < t_{\mathrm{inj}}$, and injection stops after that ($t > t_{\mathrm{inj}}$). This may be one of the simplest models of flares in blazars. From the general solution of kinetic equation (3.59) with $Q(\gamma, t) \equiv 0$, one finds

$$N_{\mathrm{s}}(\gamma, t) = \frac{K/t_{\mathrm{acc,s}} - \beta_{\mathrm{s}} K^2}{\gamma/t_{\mathrm{acc,s}} - \beta_{\mathrm{s}}\gamma^2} \exp(-t/t_{\mathrm{esc,s}}) N_{\mathrm{s},0}(K), \tag{11.23}$$

where

$$K = [t_{\mathrm{acc,s}}\exp(t/t_{\mathrm{acc,s}})(\frac{1}{t_{\mathrm{acc,s}}\gamma} - \beta_{\mathrm{s}}) + \beta_{\mathrm{s}}]^{-1}. \tag{11.24}$$

$N_{\mathrm{s},0}$ is the electron population at $t = t_{\mathrm{inj}}$.

Note that the electron population $N_{\mathrm{s},0}(K)$ has low-energy cut-off at $K = \gamma_0$, and high-energy cut-off at $K = \gamma_1(t_{\mathrm{inj}})$. From equation (11.24), we can calculate the shift of those cut-offs in time,

$$\gamma_0'(t) = [t_{\mathrm{acc,s}}(\beta_{\mathrm{s}} + \frac{1/t_{\mathrm{acc,s}} - \beta_{\mathrm{s}}\gamma_0}{\gamma_0 \exp(\frac{t-t_{\mathrm{inj}}}{t_{\mathrm{acc,s}}})})]^{-1}, \tag{11.25}$$

$$\gamma_1'(t) = [t_{\mathrm{acc,s}}(\beta_{\mathrm{s}} + \frac{1/t_{\mathrm{acc,s}} - \beta_{\mathrm{s}}\gamma_1(t_{\mathrm{inj}})}{\gamma_1(t_{\mathrm{inj}}) \exp(\frac{t-t_{\mathrm{inj}}}{t_{\mathrm{acc,s}}})})]^{-1} \qquad (t > t_{\mathrm{inj}}). \tag{11.26}$$

The electron population at time $t(> t_{\mathrm{inj}})$ is well approximated by a simple function

$$N_{\mathrm{s}}(\gamma, t) \simeq q_{\mathrm{s}} t_{\mathrm{acc,s}} \gamma^{-s}[\exp(-\gamma/\gamma_1'(t)) - \exp(\gamma/\gamma_0'(t))]. \tag{11.27}$$
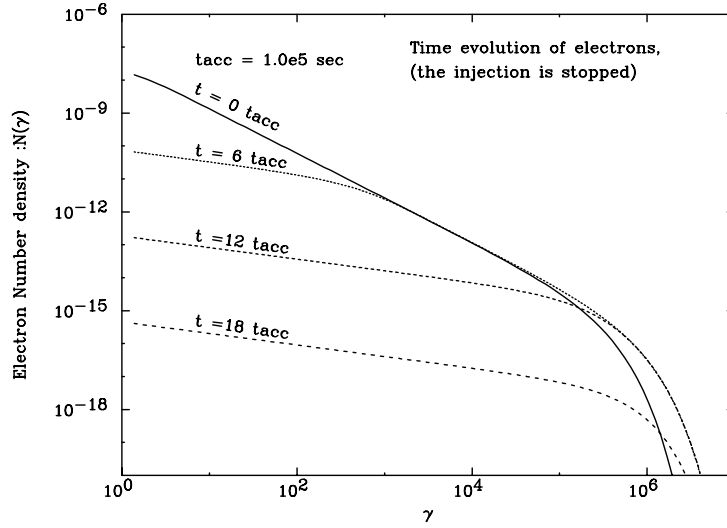
Figure 11.5: Evolution of the electron distribution after the injection has been stopped. In this particular case, the number of electrons reduces significantly at low energy, while highest energy electrons still be accelerated $(\gamma_1(t_{\mathrm{inj}}) < \gamma_{\mathrm{max}})$.

In Figure 11.5, we show an example of time evolution of electrons after the injection is stopped. We set $t_{\mathrm{acc,s}} = 10^5$ sec, $t_{\mathrm{inj}} = 10t_{\mathrm{acc,s}}$, $\beta_{\mathrm{s}} = 10^{-10}$, and $\gamma_0 = 1$. One finds that the maximum energy of electrons increases even after the stop of the injection, because in this particular case, $\gamma_1(t_{\mathrm{inj}}) < \gamma_{\mathrm{max}}$. Also note that the electron number density decreases significantly from low energy to higher energy.

11.4   Examples [I] – Steady State Emission

To verify the SSC code developed in this thesis, we show examples of the calculation. Further detailed modeling will be shown in the last part of this chapter, with application

to the observational data.

11.4.1   SSC Spectrum and Higher Order Comptonization

In order to follow the time evolution of the SSC spectrum, we start from the steady state solution of the Synchrotron self-Compton (SSC) model.

In Figure 11.6, we compute a SSC spectrum using our numerical code, with the same parameter set of Figure 5*a* in Band & Grindlay (1985). In the calculation, the electron population has a power law form $N_e(\gamma) = 4\times10^6 \ \gamma^{-3}$, in a range $1 < \gamma < 10^3$. Source radius is $R = 2 \times 10^{14}$ cm. Our result agrees perfectly with their result. We also calculate the second order Comptonization spectrum for comparison, using the same formula (3.49). In the calculation, the incident photon density is now the photons from the first order inverse Compton scattering. Note, however, that these Componized spectra have slightly different slopes than those in Band & Grindlay (1985), especially in the lowest energy band ($\leq 10^{11}$ Hz). This is because we have neglected the self-absorption of Comptonized spectrum for simplicity. Strictly speaking, self-Compton photons are also absorbed by the electrons, although this effect is negligiblly small because the Compton flux is much lower than the synchrotron flux in this energy band.
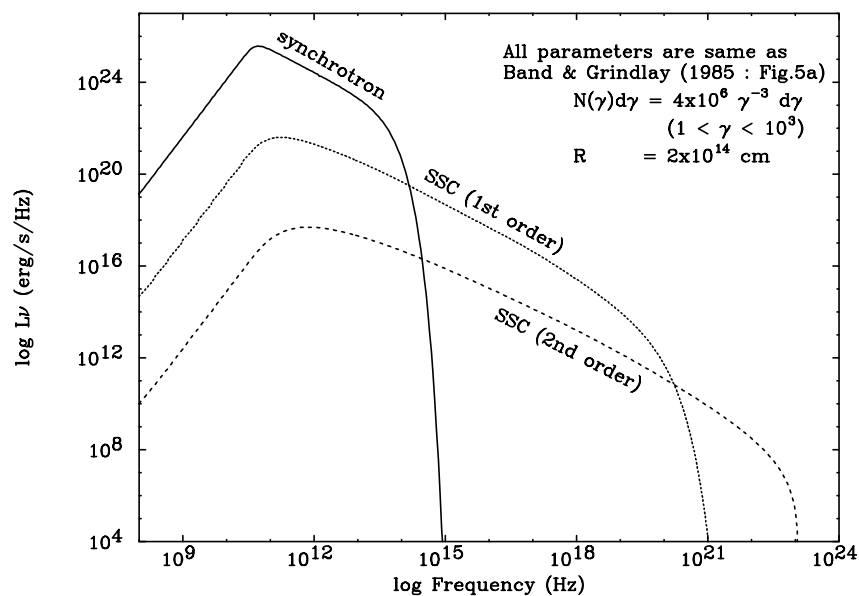
Figure 11.6: An example of synchrotron self-Compton spectrum calculated with our numerical code. All parameters are same as Figure 5*a* in Band & Grindlay (1985). We assume power law electron distribution of $N_e(\gamma)\mathrm{d}\gamma = 4\times10^6\gamma^{-3}\mathrm{d}\gamma$ for $1<\gamma<10^3$ in a spherical source of $R = 2\times10^{14}$ cm.

11.4.2   Effects of the Changes in Parameters

In order to study the variety of spectral behavious observed from TeV blazars, it is important to investigate how the physical quantities in the emission region or parameters for the injected electron spectrum effects the photon spectrum. To highlight the effects caused by the changes of individual parameters, we have changed only one parameter with other parameters fixed. As a *baseline* of the spectral energy distribution, we choose magnetic field $B = 0.1$ G, region size $R = 1.0 \times 10^{16}$ cm, beaming factor $\delta = 10$, and the redshift $z = 0.1$, which are suggested from the observation (e.g., § 10). We adopt a specific form for the electron distribution from $\gamma_{\min}$ to $\gamma_{\max}$, $N(\gamma) = N_0 \gamma^{-s} \exp(-\gamma/\gamma_{\max})$, where $\gamma_{\min}$ and $\gamma_{\max}$ is the minimum/maximum Lorentz factor of electrons, respectively. We choose $\gamma_{\min} = 1$, $\gamma_{\max} = 10^5$, $N_0 = 100.0$ (/cm^3) and $s = 2$ as a baseline.

Figure 11.7(a) shows the changes in SSC spectrum by varying the magnetic field B from 0.01 G to 1.0 G. Since the synchortron emission from a single electron is proportional to B^2 (e.g., equation (3.34)), flux becomes higher when B increases, while the ratio of synchrotron and Compton components does not vary. Also note that the peak frequency of synchrotron component increases as $\propto B$ (see, equation (3.32)).

Figure 11.7(b) is the change caused by the region size R. The flux increases as $\propto R^3$, because the total number of electrons is proportional to the volume of the emission region.

Figure 11.7(c) is the case of the change in beaming factor δ from 10 to 50. The change in the flux in a manner $\propto \delta^4$ and the blue shift of the frequency $\propto \delta$ are clearly seen (see, equation (3.71) and (3.74))

Figure 11.7(d) shows the changes in the redshift z of the source from 0.01 to 1.0. Because of the $d_{\rm L}^{-2}$ dependence of the flux, where $d_{\rm L}$ is the distance from the source, the flux changes roughly in a manner $\propto z^{-2}$ if the source redshift is changed (valid for $z \leq 1$).

Figure 11.7(e) is the changes due to the normalization of electrons N_0 and the flux changes just as $\propto N_0$.

Figure 11.7(f) shows the changes in the maximum electron Lorentz factor $\gamma_{\max}$ from 10^4 to 10^6. The synchrotron peak shifts as $\propto \gamma_{\max}^2$ (see, equation (3.32)), while the shift of the Compton peak at $\gamma_{\max} = 10^6$ is rather small. This is because the scattering takes place in the Klein-Nishina regime (see, § 3.4.2).

Figure 11.7(g) is the change due to the minimum electron Lorentz factor $\gamma_{\min}$. This does not affect the photon spectrum very much if $1 < \gamma_{\min} < 100$, while makes sharp cut-off in low-energy photon spectrum if $\gamma_{\min} > 100$.

Finally, Figure 11.7(h) shows the changes in the spectral index of electrons s from 1.5

to 2.5. This is reflected to the photon spectral index p as $p \propto (s-1)/2$ (e.g., Rybicki & Lightman. 1979), but the spectral shape is not changed for the low-energy photons for which self-absoption is dominant.
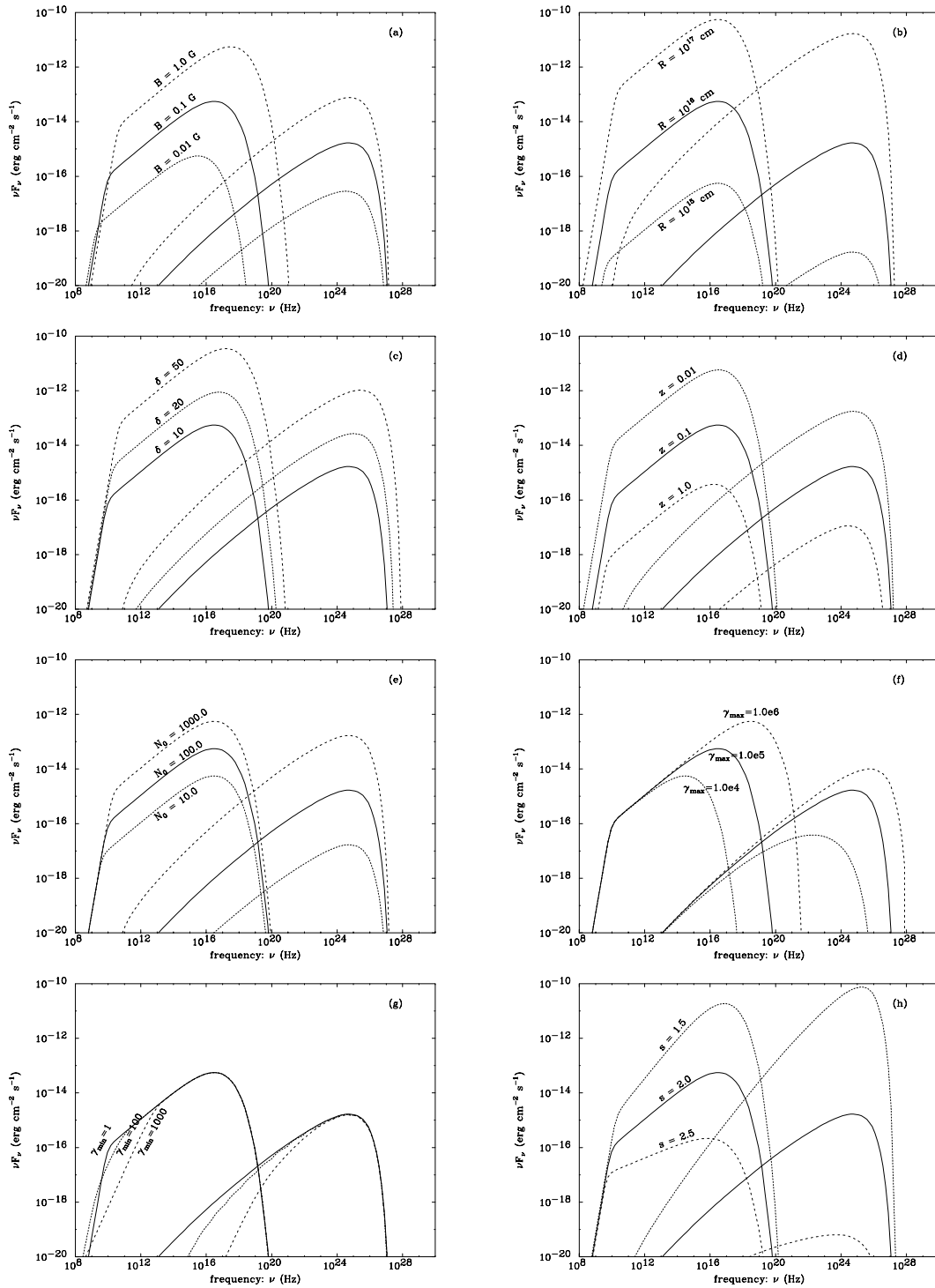
Figure 11.7: Synchortron self-Compton spectra for various parameter changes; (a) magnetic field B, (b) region size R, (c) beaming factor δ, (d) redshift z, (e) electron normalization N_0, (f) electron maximum Lorentz factor γ_{max}, (g) electron minimum Lorentz factor γ_{min}, and (h) electron spectral index s.

11.5 Examples [II] – Time Evolution

11.5.1 Synchrotron Cooling Model

We compare the time evolution of the electron spectrum derived from our code with the analytic solutions given by Kardashev (1962) and Makino (1998) for verification. In the calculation, we assume that electrons lose their energy only by synchrotron radiation, but not by the inverse Compon process. We also assume electron number is conserved, such that the injection rate $Q(\gamma) \equiv 0$ and the escape rate $N(\gamma)/t_{\rm esc} \equiv 0$. In this simplest case, the kinetic equation is given by

$$\frac{\partial N_e(\gamma, t)}{\partial t} = A \frac{\partial}{\partial \gamma} [\gamma^2 N_e(\gamma, t)], \qquad (11.28)$$

where A is a constant

$$A \equiv \frac{4\sigma_{\rm T} U_B}{3 m_e c}. \qquad (11.29)$$
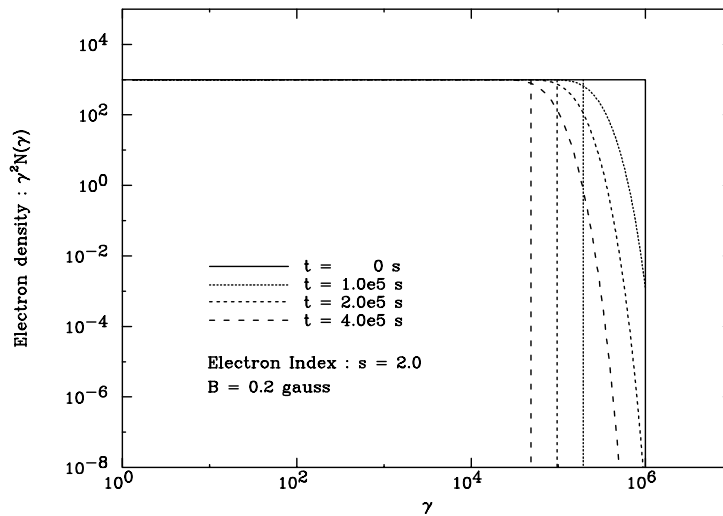
Figure 11.8: Time evolution of the electron spectrum by the synchrotron cooling process. We assume power law electron distribution of $N_e(\gamma) = N_0 \gamma^{-2}$ ($1 < \gamma < 10^6$). The magnetic field is 0.2 G and inverse Compton losses are not taken into account. Electron spectra with sharp edges represent analytical solutions given by Kardashev (1962), while others (dull edge) are from the numerical calculation.

For the initial condition of $N_e(\gamma, 0) = N_0 \gamma^{-s}$ at time $t = 0$, the analytic solution of equation (11.28) is given by

$$N_e(\gamma, t) = N_0 \gamma^{-s} (1 - At\gamma)^{s-2}, \qquad (\gamma A t < 1) \qquad (11.30)$$

and $N_e(\gamma,t) = 0$ otherwise (e.g., Kardashev 1962). In Figure 11.8, we show the time evolution of electron energy spectrum for $s = 2$ and $B = 0.2$ G calculated from our numerical code. The results obtained from analytical solutions are also given shown in the figure. Note that for all γ, analytic solution shows a sharp cut-off at $\gamma_c = 1/At$. Numerical calculation also shows cut-off at $\gamma_c = 1/At$, but rather smooth than the analytic solution.

11.5.2   Time Evolution of the SSC Spectrum and Light Curves

Once we have a numerical code that computes time evolution of the spectrum, we can simulate spectral evolution during a *flare* observed from TeV blazars. At the same time, we extract light curves by taking the light travel time effects into account.

It is very interesting to know the response to the flare-like injection of electrons in the emission region. We concentrate on a specific case defined as follows. First, no electron population exists at time $t = 0$, i.e. $N_e(\gamma, 0) = 0$. The mono-energetic electrons ($\gamma = \gamma_{in}$) are injected for $0 < t < R/c$ and injection goes back to zero after R/c. For simplicity, we consider neither escape nor the acceleration of electrons. In this case, the electron population injected into the emission region is expressed by the delta-function, $Q(\gamma) = Q_0\delta\,(\gamma-\gamma_{in})$, where Q_0 is a constant. Here we choose $\gamma_{in} = 10^5$. The physical quantities in the emission region are assumed to be; $B = 0.1$ G, $R = 1.0\times10^{16}$ cm, $\delta = 10$ and $z = 0.1$.
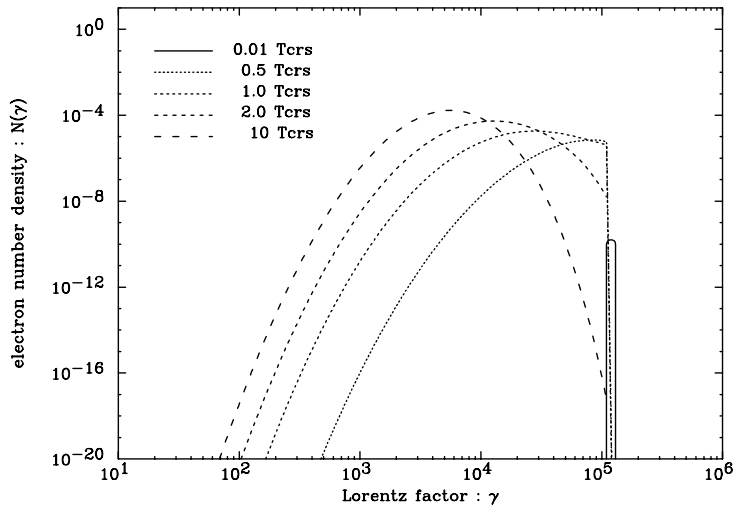
Figure 11.9: The spectral evolution of electrons at different times. We assume the mono-energetic electrons ($\gamma_{in} = 10^5$) are injected only for $0<t<R/c$ ($= t_{crs}$). The electron spectra at $t = 0$, $0.5t_{crs}$, t_{crs}, $2t_{crs}$ and $10t_{crs}$ are shown respectively.
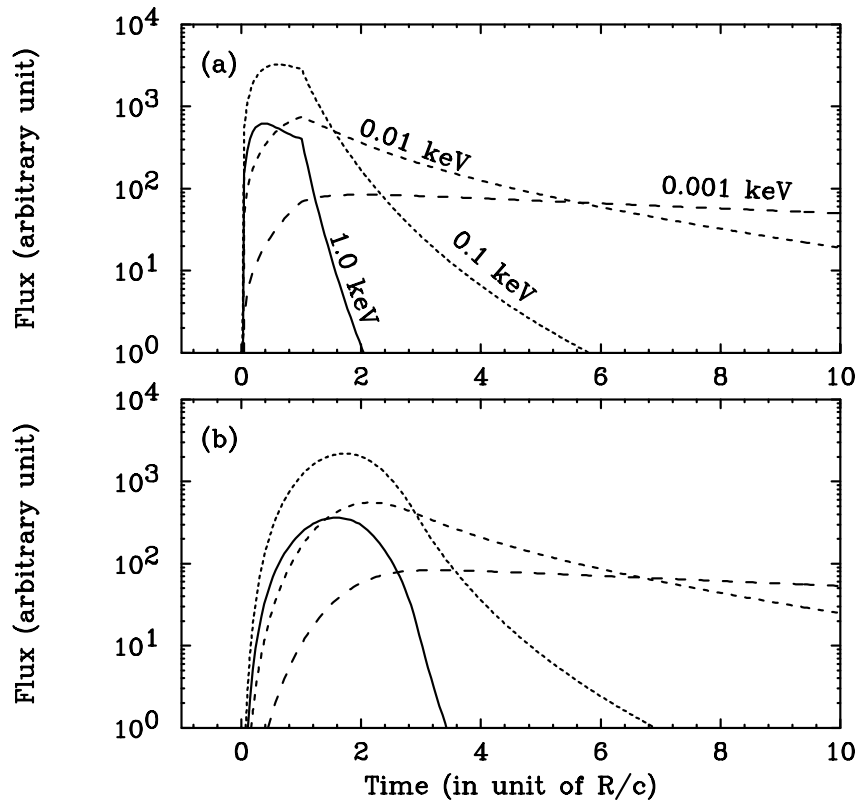
Figure 11.10: Light curves of the flux at different energy bands from 0.001 keV to 1.0 keV, in observer's frame. The upper panel (a) shows the case of ignoring the light travel time effects, while the lower panel (b) taking into account.

The time evolution of electrons is shown in Figure 11.9. For $0 < t < R/c$, accumulation of fresh electrons and the energy loss by synchrotron radiation occur at the same time, enhancing low-energy population in the number density distribution of electrons. It should be noted that the high energy end of electron distribution reaches the equilibrium state in a very short time ($\leq 0.5\ t_{\rm crs}$) and does not vary for the rest of the injection time. After $t > R/c$, total number of electrons becomes constant, but the peak of the distribution moves to lower energy, by the radiative cooling.

Figure 11.10 shows the corresponding light curves of synchrotron fluxes at various energy bands. The upper panel shows the light curves when the light travel time effects are not taken into account. Since we assume an instantaneous and uniform injection throughout the source, the rise time of the flux is much shorter than R/c, especially at $\gamma \sim \gamma_{\rm in}$. The *plateau*-like structure can be seen in the light curve, especially energy above 0.1 keV. Although the rise time varies in different energy bands, peaking time is roughly $\sim R/c$ for all energy bands. The lower panel shows the light curves, when the light travel
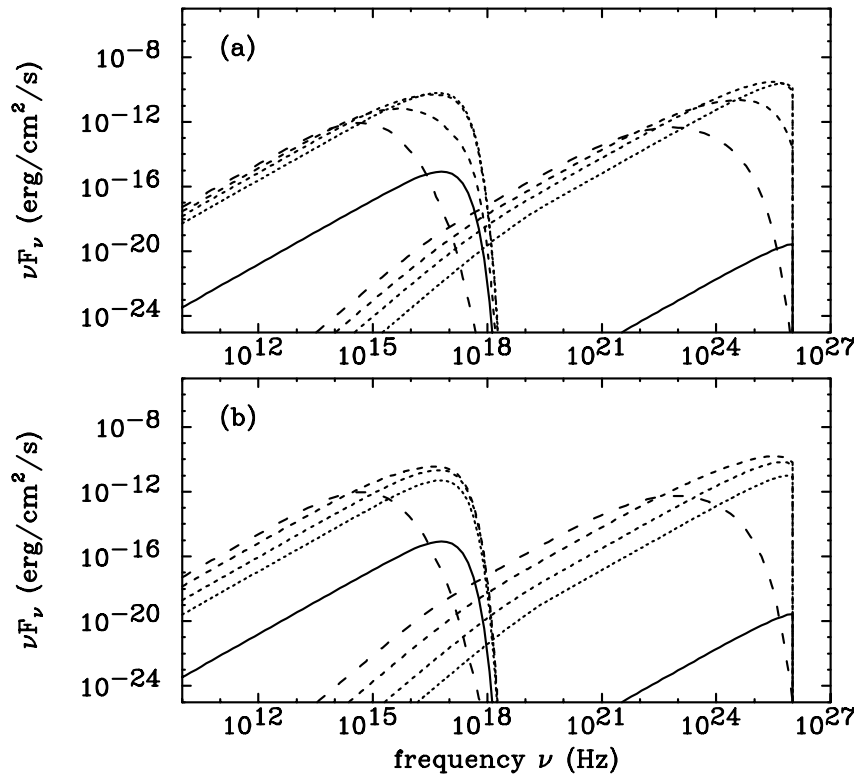
Figure 11.11: Evolution of synchrotron self-Compton spectra at different times. The dashes and solid line show the photon spectra at $t = 0$, $0.5t_{crs}$, t_{crs}, $2t_{crs}$ and $10t_{crs}$. Notation of lines are same as Figure 11.9.

time effects are properly taken into account. In this case, the light curve at high energy band (1.0 keV) has symmetric shape and very similar to the weight function $w(x)$, in Figure 11.3. This symmetry is broken for lower-energy light curves, which have longer decay times than R/c. In the low-energy band, time constant for the decay is dominated by the cooling effect. It should be noted that the peaking time in Figure 11.10(b) is energy dependent, such that the lower energy peaks lag behind the high energy peaks (see also, Chiaberge & Ghisellini 1999).

Finally, we show the time evolution of both the synchrotron spectra and the self-Compton spectra in Figure 11.11. The upper panel (a) shows the evolution ignoring light travel time effects, while the lower panel (b) considers smoothing by the source light-crossing time scale. It is clearly seen that the multi-frequency spectra evolves more slowly if the light travel time effect is taken into account.

11.6 Comments on the Time-Dependent Model

11.6.1 Emission from the Acceleration Region

In the previous sections, we have considered two spatial zones which are closely connected in space. One is around the shock front, in which particles are continuously accelerated, and the other is the downstream of it in which electrons emit most of the radiation (see, Figure 11.1). In our current modeling, we considered the radiation only from the latter, however, one may consider it inappropriate, because the acceleration region also has the magnetic field B_s thus can radiate. In the following, we will roughly estimate the synchrotron emission from the accelerating region (L_s), as compared to the radiation from the emitting region (L_e).

Let's denote the acceleration region size R_s and emitting region size R. Physically, R_s may corresponds to the boundary distance where inside of it, the particle effectively return to the shock front (see, § 3.1.4). Escape times from both regions are quite uncertain, however, one can envision that those values are order of region size divided by the light velocity (e.g., equation (3.14)). We then have approximate relations

$$t_{\mathrm{esc,s}} \sim R_s/c, \quad t_{\mathrm{esc}} \sim R/c. \tag{11.31}$$

The ratio of both region sizes is given

$$\frac{R_s}{R} \sim \frac{t_{\mathrm{esc,s}}}{t_{\mathrm{esc}}}. \tag{11.32}$$

Since the maximum Lorentz factor γ_{max} is determined by the balance between the acceleration and cooling around the shock front (equation (11.16)), the magnetic field strength B_s can be written

$$B_s = (C_s \gamma_{\mathrm{max}} t_{\mathrm{acc,s}})^{-1/2}, \tag{11.33}$$

where C_s is a constant

$$C_s = \frac{4}{3} \frac{\sigma_{\mathrm{T}}}{m_{\mathrm{e}}c} \frac{1}{8\pi}. \tag{11.34}$$

From the equation (11.12), the ratio of number density of electrons in both regions is given

$$\frac{n_s}{n_{\mathrm{e}}} \simeq \frac{N_s(\gamma_{\mathrm{min}})}{N_{\mathrm{e}}(\gamma_{\mathrm{min}})} = \frac{q_s t_{\mathrm{acc,s}}}{q_{\mathrm{e}} t_{\mathrm{esc}}} = \frac{t_{\mathrm{esc,s}}}{t_{\mathrm{esc}}}, \tag{11.35}$$

where we use the relations (11.12) and (11.14).

Since the synchrotron luminosity is proportional to $B^2 R^3 n$, the ratio of synchrotron luminosities in both regions is calculated to be

$$\frac{L_s}{L_e} \simeq \frac{B_s^2 R_s^3 n_s}{B^2 R^3 n_{\mathrm{e}}} = \frac{1}{B^2 C_s \gamma_{\mathrm{max}} t_{\mathrm{acc,s}}} \left(\frac{t_{\mathrm{esc,s}}}{t_{\mathrm{esc}}}\right)^4, \tag{11.36}$$

where we use the equation (11.32), (11.33) and (11.35). From the equation (11.15), we finally obtain,

$$\frac{L_{\mathrm{s}}}{L_{\mathrm{e}}} = \frac{1}{B^2 C_{\mathrm{s}} \gamma_{\max} t_{\mathrm{acc,s}}} \left(\frac{1}{s-1} \frac{t_{\mathrm{acc,s}}}{t_{\mathrm{esc}}} \right)^4 . \tag{11.37}$$

For example, if $B = 0.1$ G, $\gamma_{\max} = 10^5$, $t_{\mathrm{esc}} = 10^6$ s, $t_{\mathrm{acc,s}} = 10^5$ s and $s = 2$, which are typical for blazars (e.g., Table 10.3), one finds that $L_{\mathrm{s}}/L_{\mathrm{e}} \sim 10^{-2}$. This value is probably the upper limit which corresponds to the case of $B_{\mathrm{s}} \simeq B$. Note that for more shorter acceleration time $t_{\mathrm{acc,s}}$ and stronger magnetic field B, this ratio becomes much smaller than 10^{-2}. We thus conclude that the radiation from the acceleration region is negligible compared to that in the emission region.

11.6.2   Scope for Improvement

We proceed under the assumption that electrons are injected uniformly throughout a homogeneous emission region. Such a description may be adequate as long as the injection time-scale is longer than R/c (Dermer 1998), but is unphysical for shorter time-scales since the particle injection process itself should take (at least) $\sim R/c$ to influence the whole region. In a more realistic picture, a thin shock front may propagate through the emission region with a finite velocity v_{s}, supplying freshly accelerated electrons only in the front's vicinity (Kirk, Rieger & Mastichiadis 1998). However, such a detailed calculation necessarily involves some additional, uncertain parameters, not to mention the assumption of a particular geometry. Instead, we will choose the injection to be uniform and instantaneous over the emission volume. Such a choice, albeit unrealistic, will allow us to clarify the role of light travel time effects on blazar variability (Below, however, we will also consider the duration of the injection to be comparable to R/c).

In our current assumption, synchrotron cooling process occurs uniformly and instantaneously over the emission region because (1) electrons are injected uniformly over the emission region and (2) the magnetic field strength is uniform throughout the blob. For the Compton scattering process, however, each electron should experience the changes in the photon field with some 'delay', which depends on the position in the emission blob. In other words, the synchrotron photons require the time $\sim R/c$ to fill up the blob to be scattered. This will cause additional delay for the response of Compton photon spectrum. However, for TeV blazars dealt in this thesis, the synchrotron cooling process must be dominant and the effects caused by Compton cooling process is small because (1) the synchrotron luminosity is greater or nearly equal to the Compton luminosity, and (2) the reduction of the cross section in the Klein-Nishina regime will significantly affect the Compton scattering efficiency. For these reasons, we approximate here that the

synchrotron radiation (i.e., the soft photons for the inverse Compton scattering) instantaneously fills the whole of the emission region, just to reduce the computational time (see also Chiaberge & Ghisellini 1999).

11.7 Application to the Observational Data

11.7.1 Steady State Emission

In § 10.6.1, we successfully constrained the allowed regions for physical quantities of TeV blazars, assuming the relations expected by the homogeneous SSC scenario. In the following, we practically fit the multi-frequency spectra of TeV blazars using the one-zone SSC solution for a spherical geometry. 7 parameters for the model were determined to be consistent with the parameter regions we have constrained. For Mrk 421 and PKS 2155−304, the tightest constraint from the X-ray observations of 'time-lags' are considered as well as the spectral constraints. We summarize the 7 parameters for the SSC model in Table 11.1. Although there still remains flexibility in selected values of parameters, we note that our derived parameters are not affected by more than a factor of 2 even if taking the uncertainty of the observables into account (see, Table 10.3).

Table 11.1: Input model parameters for TeV blazars

source	s	δ	B (G)	R (pc)	γ_{max}	t_{esc} (in R/c)	q_{e} (cm^{-3}s^{-1})
Mrk 421	1.6	14	0.13	$5.9{\times}10^{-3}$	$1.6{\times}10^{5}$	8	$7.4{\times}10^{-6}$
Mrk 501	1.8	9	0.13	$9.6{\times}10^{-3}$	$3.1{\times}10^{5}$	8	$3.8{\times}10^{-5}$
PKS 2155 −304	1.4	28	0.14	$7.7{\times}10^{-3}$	$8.3{\times}10^{4}$	10	$6.1{\times}10^{-7}$
1ES 2344 +514	1.9	7	0.18	$3.2{\times}10^{-3}$	$4.4{\times}10^{5}$	6	$3.2{\times}10^{-3}$

electron injection spectral index, s; beaming factor, δ; magnetic field strength, B; emission region size, R; maximum Lorentz factor of electron, γ_{max}; electron escape time, t_{esc}; electron normalization, q_{e}. We adopted a cutoff power law for the injected electron population : $Q(\gamma) = q_e \ \gamma^{-s} \ \exp(-\gamma/\gamma_{\mathrm{max}})$. We set the minimum Lorentz factor of the electrons, $\gamma_{\mathrm{min}} = 1$, for simplicity.

The input parameters for our SSC model are determined almost at the *center* of the allowed parameter region for different constraints discussed in § 10.6. To obtain the steady state solution for electron and photon spectra based on the parameters listed in Table 11.1,

we start from the initial condition $N_e(\gamma, 0) = Q(\gamma)$ and calculate the time evolution of the spectra to more than $t > 30\ t_{\mathrm{crs}}$, assuming constant injection and escape. We adopted a cutoff power law for the injected electron population: $Q(\gamma) = q_e\ \gamma^{-s}\ \exp(-\gamma/\gamma_{\max})$.

In Figure 11.12−11.15 (*left* panel), we show the synchrotron self-Compton model spectra at the *steady state*, superposed on the multi-frequency spectra for Mrk 421, Mrk 501, PKS 2155−304 and 1ES 2344+514. One can see that our SSC model lines are nicely consistent with the observational data, except for the discrepancy in the radio band. The discrepancy in the radio band can be an effect of the emission arising from larger distances than the location of the X-ray/γ-ray emitting region (e.g., Marscher 1980). In fact, VLBI observations of these objects have reveled that the radio emission comes from a very large region than that expected from the rapid X-ray/γ-ray time variability (≥ 10 pc; see, Figure 10.9).

Right panel of each figure (Figure 11.12− 11.15) shows the ratio of electron cooling rate by synchrotron/inverse Compton radiation for the steady state. Horizontal line shows the electron Lorentz factor, while the vertical line shows the energy loss rate of an electron ($\dot{\gamma}_{\mathrm{sync,SSC}}$; equation (3.34), equation (3.54)) multiplied by γ^{-2}. Those values are constant for synchrotron loss ($\dot{\gamma}_{\mathrm{sync}} \propto \gamma^2$), hence normalized to a unity. Corresponding *ASCA* energy band is shown as dashed lines (0.7−10 keV; equation (3.33)). Importantly the ratio $\dot{\gamma}_{\mathrm{SSC}}/\dot{\gamma}_{\mathrm{sync}}$ exactly coincides with U_{sync}/U_B for low-energy electrons, while Compton scattering efficiency reduces significantly for the high energy electrons due to the cross section reduction in the Klein-Nishina regime. One finds that synchrotron cooling is more dominant in the X-ray band, which is in fact consistent with our previous assumption (§ 10.6).

Table 11.2 shows the energy densities of photons, magnetic field and electrons derived from the SSC fit of each source. *Effective* synchrotron photon density, $U_{\mathrm{sync}}^{\mathrm{avail}}$, was calculated simply from equation (10.21). One finds that for these TeV blazars, there exists an approximate equality between U_B and U_{sync}, however, Klein-Nishina effect reduces the soft photon density which are effectively involved in the self-Compton scattering process ($U_{\mathrm{sync}}^{\mathrm{avail}}$) by a factor of several. This also confirms our previous assumption of $1 < \kappa < 10$ to be valid (§ 10.6).

More importantly, electron energy density U_e is larger than U_B and U_{sync} by a factor of ~ 10. This indicates that the relativistic jets are particle dominated. Even when we take ambiguities in selected input parameters into account, this conclusion does not be affected. An implication that the particle energy dominates over magnetic energy density may pose an interesting issue on the jet formation mechanism. Most of the models of bulk acceleration of jets relied on some roles of magnetic field dominated situation. The
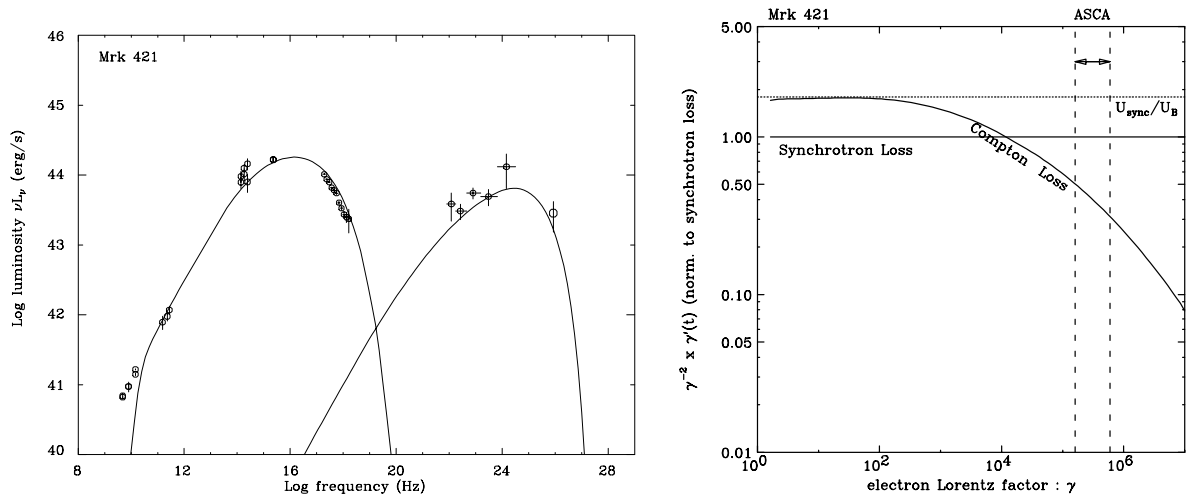
Figure 11.12: *left* : One-zone SSC model fit for the steady state emission of Mrk 421. Model parameters are given in Table 11.1. *right* : Ratio of electron cooling rate by synchrotron/inverse Compton radiation for the steady state of Mrk 421.
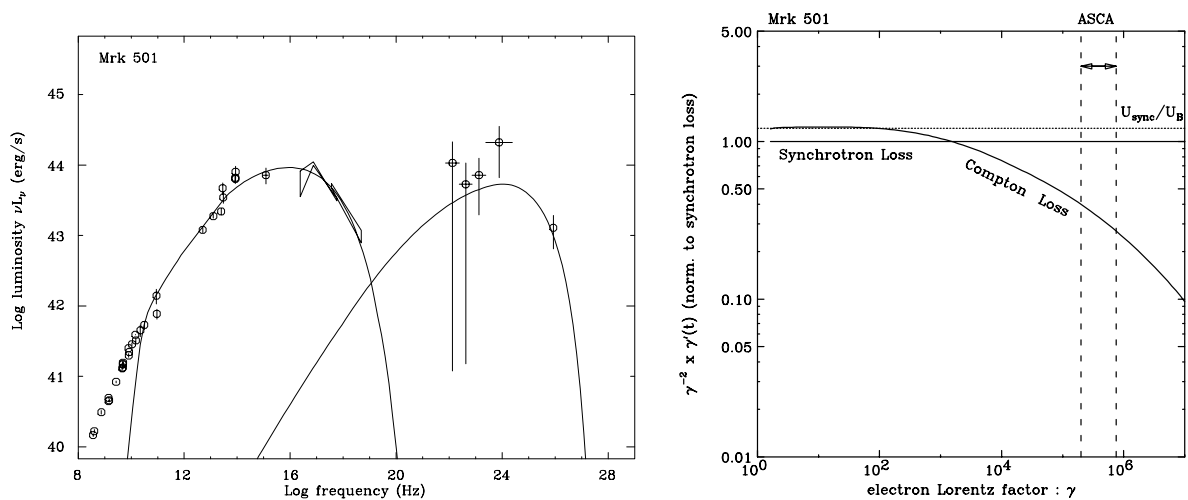
Figure 11.13: *left* : One-zone SSC model fit for the steady state emission of Mrk 501. Model parameters are given in Table 11.1. *right* : Ratio of electron cooling rate by synchrotron/inverse Compton radiation for the steady state of Mrk 501.

present results seems to argue against such 'magnetic driven jet' formation. An alternative mechanism for jet formation is necessary to account for this.
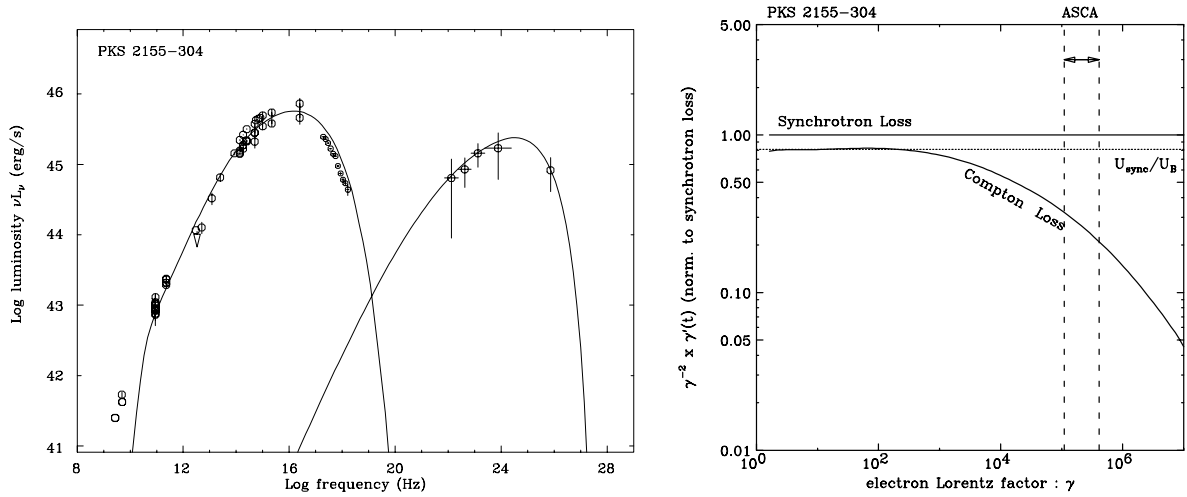
Figure 11.14: *left* : One-zone SSC model fit for the steady state emission of PKS 2155−304. Model parameters are given in Table 11.1. *right* : Ratio of electron cooling rate by synchrotron/inverse Compton radiation for the steady state of PKS 2155−304.
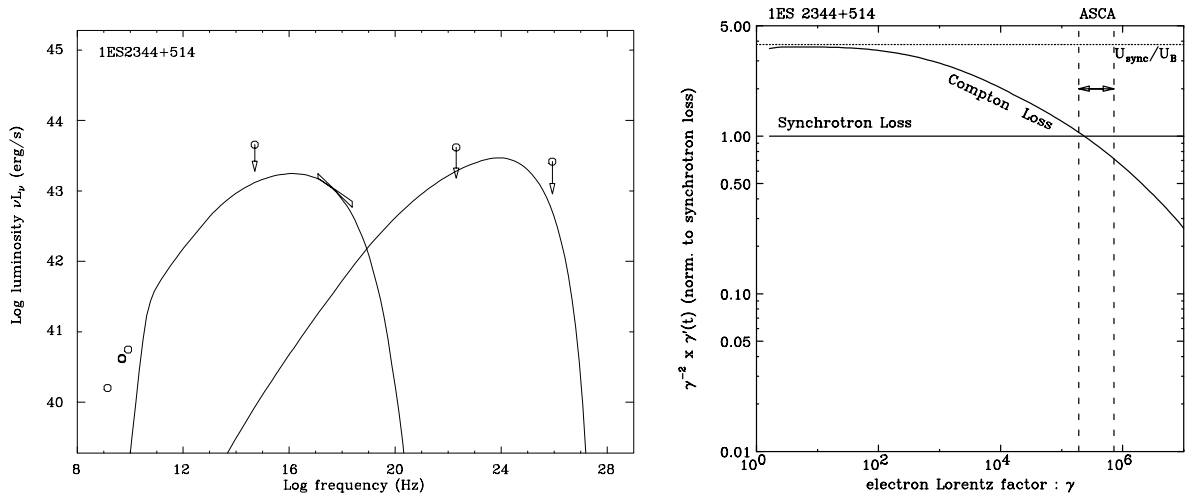
Figure 11.15: *left* : One-zone SSC model fit for the steady state emission of 1ES 2344+514. Model parameters are given in Table 11.1. *right* : Ratio of electron cooling rate by synchrotron/inverse Compton radiation for the steady state of 1ES 2344+514.

11.7.2   Modeling PKS 2155−304 Flare in 1994

Based on the physical parameters selected above, and the resultant 'steady state' spectrum as an initial condition, we model the X–ray flare of PKS 2155−304 in 1994 May. This particular flare was selected because (1) the flare was isolated, excluding the effects caused by the superposition of many flare events, (2) amplitude of flare was large, and (3) 'time-lags' are observed in the various X-ray energy bands (Figure 10.2; 10.3).   Since PKS

Table 11.2: Energy density of photons, magnetic field and electrons

source	U_B (erg/cm^3)	U_{sync} (erg/cm^3)	$U_{\mathrm{sync}}^{\mathrm{avail}}$ (erg/cm^3)	U_{SSC} (erg/cm^3)	n_{e} (/cm^3)	U_{e} (erg/cm^3)	U_{e}/U_B
Mrk 421	$7.1{\times}10^{-4}$	$5.7{\times}10^{-4}$	$2.4{\times}10^{-4}$	$2.0{\times}10^{-4}$	$7.0{\times}10^{1}$	$3.3{\times}10^{-3}$	4.6
Mrk 501	$6.6{\times}10^{-4}$	$8.0{\times}10^{-4}$	$3.7{\times}10^{-4}$	$4.4{\times}10^{-4}$	$4.8{\times}10^{2}$	$6.2{\times}10^{-3}$	9.3
PKS 2155 $-$304	$8.2{\times}10^{-4}$	$6.6{\times}10^{-4}$	$3.5{\times}10^{-4}$	$2.8{\times}10^{-4}$	$1.6{\times}10^{1}$	$2.9{\times}10^{-3}$	3.5
1ES 2344 $+$514	$1.3{\times}10^{-3}$	$4.9{\times}10^{-3}$	$2.0{\times}10^{-3}$	$7.6{\times}10^{-3}$	$9.4{\times}10^{3}$	$7.3{\times}10^{-2}$	56

Energy density of photons, magnetic field and electrons derived from the steady state SSC model fit. Parameters are given in Table 11.1. magnetic field; U_B, total synchrotron photon density; U_{sync}, *effective* synchrotron photon density; $U_{\mathrm{sync}}^{\mathrm{avail}}$, self-Compton photon density; U_{SSC}, number density of electrons; n_{e}, energy density of electrons; U_{e}, ratio of electron energy density and magnetic field density; U_{e}/U_B. Minimum Lorentz factor of electrons is assumed to be $\gamma_{\mathrm{min}} = 1$.

2155$-$304 did not show any clear trends between the peak synchrotron luminosity and peak energy (Figure 8.19), an origin of the flare is not as clear as that for Mrk 421 and Mrk 501 (§ 10.4). Various types of flaring behavior were thus investigated by changing the parameters for the injected electron spectrum and/or the physical quantities in the emission region.

In the following, we simulated the light curves, as well as the time evolution of spectra, when γ_{max} increased by a factor of 1.6 during one t_{crs} interval from the start of the flare. For this particular case, a model fit of the time-lags (§ 10.2.4) revealed that t_{acc} is consistent with zero, which corresponds to the rapid electron injection up to γ_{max}. We thus assume $t_{\mathrm{acc}} \simeq 0$ and γ_{max} changed *instantaneously* during the flare for the present case.

We varied the injected electron spectrum as $Q_e(\gamma) = q_e\ \gamma^{-s}\ \exp(-\gamma/1.6\gamma_{\mathrm{max}})$ for $0 \leq t \leq t_{\mathrm{crs}}$ and $Q_e(\gamma) = q_e\ \gamma^{-s}\ \exp(-\gamma/\gamma_{\mathrm{max}})$ otherwise. After the calculation was performed in the source frame, it was transformed into the observer's frame for comparison with the observational data. We take the time-step to be $\Delta t = 2000$ sec throughout the calculation. This corresponds to $\Delta t < 100$ sec in the observer's frame, much shorter than the variability time scales, such as the synchrotron cooling time.

In Figure 11.16, we show the calculated light curves from *EUVE* to *ASCA* energies. The flux was normalized to that for the steady state ($t = 0$), and the time axis was normalized to the source light-crossing time-scale (R/c). The symmetric light curve during the flare is reproduced quite well. Notably, the peaking time of the flare at lower energies lags behind that for higher energies, and the amplitude of the flare becomes larger as

the photon energy increases,which agree qualitatively with the observational data (Figure 10.2).
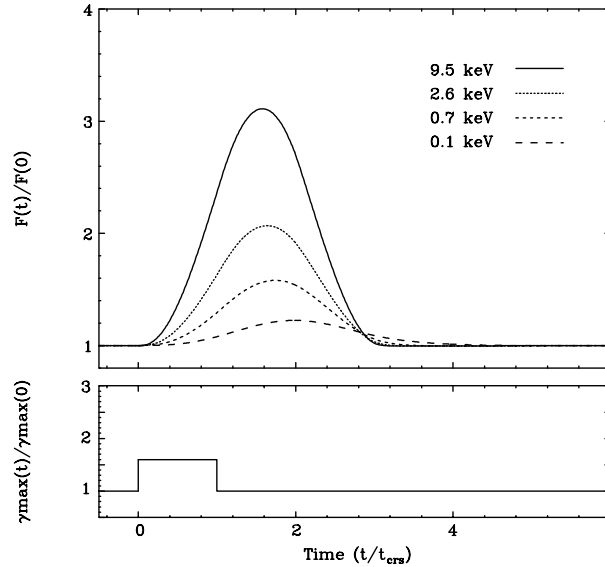
Figure 11.16: Upper Panel: Simulated light curves at different UV/X–ray energies, reproducing the rapid flare of PKS 2155−304 in 1994 May. We plotted the time evolution of the fluxes at different frequencies, normalized to the initial ($t = 0$) value. The quasi-symmetric shape of the high energy light curves and the increasing time lag of the peak with decreasing energy is clearly seen. Lower Panel: Assumed change of γ_{max} during the flare. The γ_{max} is assumed to increase by a factor of 1.6 from the initial value for $0 \leq t \leq t_{\mathrm{crs}}$. Time-axes of both panels are in units of the source light-crossing time (t_{crs}). In the observer's frame, t_{crs} corresponds to 0.3 day. Figure from Kataoka et al (2000).

Importantly, the position of the peak time is determined by the balance of slices in which the emitted flux is increasing and slices in which the decaying phase has already started. For example, at the highest X–ray energy band which corresponds to $\gamma \sim \gamma_{\mathrm{max}}$, the peak of the light curve will occur at a time t, where $t_{\mathrm{crs}} < t < 2t_{\mathrm{crs}}$. This is because these electrons in the slices cool much faster than t_{crs} and the volume which contains the flare information is maximum at the center of the sphere, which can be observed after t_{crs} from the start of the flare (see Figure 11.2). The whole emission region requires $2\,t_{\mathrm{crs}}$ to be completely visible to the observer. This will cause a decaying of the flux (foreside slices) and an increasing of the flux (backside slices) at the same time. However, in the lower energy band where $t_{\mathrm{cool}} \gg t_{\mathrm{crs}}$, the electrons do *not* cool effectively. The emitted flux will continue to increase even after $2\,t_{\mathrm{crs}}$. This combination of the increasing/decreasing phase of slices can cause a time lag in the position of the peak as can be seen in Figure 11.16.

The dashed lines in Figure 11.17 (a) and (b) show the spectral evolution calculated from the adopted model. The $2 - 10$ keV flux was obtained by integration of the calculated spectrum in the $2 - 10$ keV band, so it can be readily compared with the observational data. The photon spectral index was simply determined from the ratio of the fluxes at 0.7 keV to 7.5 keV. Since the *ASCA* observation started after the onset of the flare, we shifted our simulated light curves in the time-axis for comparison. The fact that the peaking time of the photon index leads that for the flux is quite well reproduced. This can be also seen in Figure 11.18, where the 'clockwise' hysteresis in the flux $(2 - 10$ keV) versus photon index $(0.7 - 7.5$ keV) plane can be clearly seen.
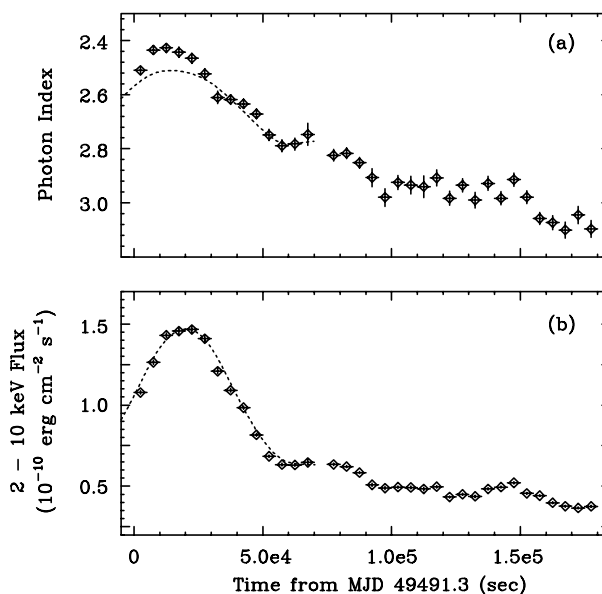
Figure 11.17: Detailed time history of PKS 2155$-$304 during the 1994 May campaign. Each data point corresponds to an equal 5 ksec interval and all SIS/GIS data are combined for the fit. The model is a power law with free absorption. (a): Variation of the differential photon index in the 0.7$-$ 7.5 keV band. The dashed line is a model prediction as described in § 3. (b): Variation of the 2 - 10 keV flux in units of 10^{-10} erg cm^{-2} s^{-1}. The dashed line is a model prediction using our time-dependent code. Figure from Kataoka et al (2000).

To make a quantitative comparison of the observed and modeled light curves in different energy bands, we analyzed the light curves in the same way as that for the observational data (for comparison, see Figure 10.3). The dashed lines in Figure 11.19 (a)$-$(c) were calculated from a Gaussian fit of the simulated light curves, and converted to the observer's frame. Figure 11.19 (a) shows the duration of the flare, determined from the standard deviation (σ) of the Gaussian. This stays nearly constant at $\sim 1.5 \times 10^4$ sec, but the model shows a sign of increase at lower X–ray energies – σ for 0.5 keV is 8 %
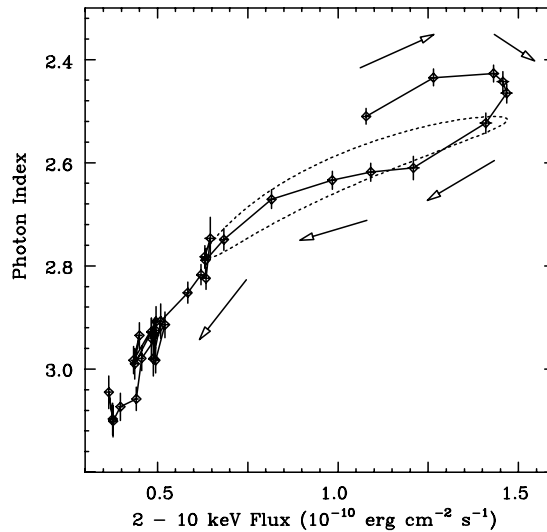
Figure 11.18: Evolution of the X–ray spectrum of PKS 2155−304, in the flux versus photon index plane. The solid line connects the observational data, while the dashed line is the model prediction from our time-dependent code. Figure from Kataoka et al (2000).

longer than that for 5.0 keV. Although we do not detect any such increase (broadening) in the observed X-ray light curves, flares observed by *EUVE* and *IUE* showed considerably longer time scales than that in the *ASCA* band (Urry et al. 1997). This may suggest that the duration of the flare actually increases at lower energies, if both flares have the same origin. Also note that the Gaussian fit of the simulated light curves could make systematic errors on σ, if the symmetry of the light curves is broken only in the lowest X-ray energy bands.

The amplitude of the flare ($Ap \equiv C_1/C_0$) was calculated to be 0.5 for 0.5 keV and 1.6 for 5 keV – precisely in agreement with the observational data (Figure 11.19 (b)). We compared the light curves at 5 keV to those for the lower energies, and found a 'soft-lag' where the $0.5 - 1$ keV photons lag behind 5 keV photons about 4 ksec, quantitatively in agreement with the observational data (Figure 11.19 (c)). Importantly, this result implies that the observed time lag is well represented by the difference of the synchrotron cooling time scales.

We also computed the discrete correlation function for the model light curves. The result is given in Figure 11.19 (d). Again, we obtained a similar result as with Gaussian fits, and verified a 'soft-lag' where the $0.5 - 1$ keV photons lag behind 5 keV photons about ~ 4 ksec.

Finally, in Figure 11.20 we show the time evolution of the multi-wavelength synchrotron self-Compton spectra after the start of the flare, at $t/t_{\rm crs} = 1.0$, 1.6 and 2.4 (for
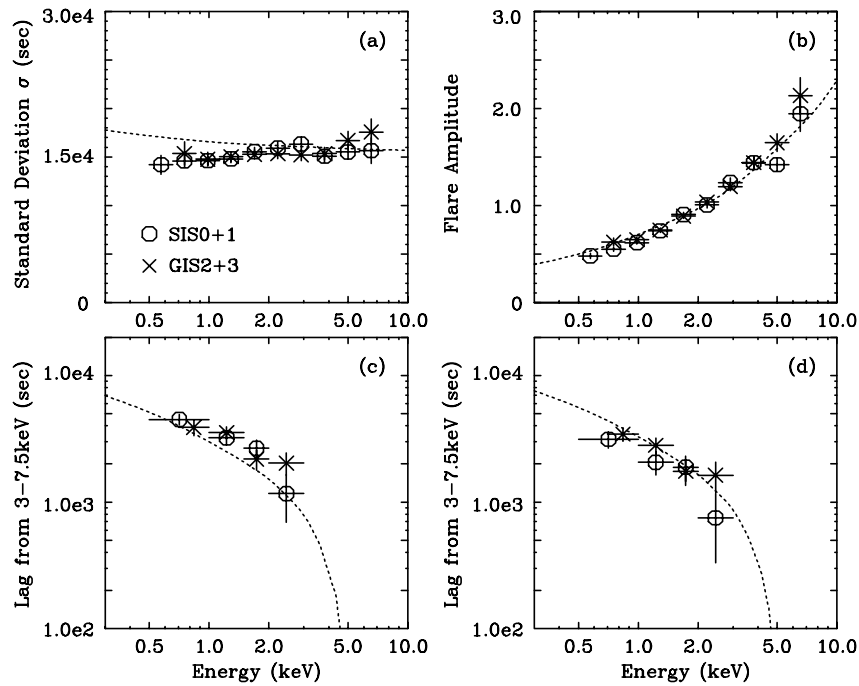
Figure 11.19: Measurement of the parameters describing the 1994 May flare of PKS 2155−304. Observational data are same as Figure 10.3, but model lines (dotted lines) are calculated using our time-dependent code.

comparison, see also Figure 11.16). The X–ray spectrum clearly becomes harder when the flux increases. Also note that the flux variation of the Compton spectrum is smaller than that for synchrotron spectrum. This is because the reduction of Compton cross section in the Klein-Nishina regime strongly suppresses the increase of the flux at the highest photon energies ($\sim h\nu_{\rm c}^{\rm max}$).

We also investigated other scenarios for the flare, such as increasing the normalization of the injected electrons (q_e) or the magnetic field strength (B), but these did not give good representations of the data. In a more realistic situation, all of these parameters probably vary simultaneously, but our modeling implies that the most essential parameter during this particular flare is $\gamma_{\rm max}$.

11.7.3 Modeling Mrk 421 Flare

Next we consider variability patterns and spectral evolutions of Mrk 421. In the following, we will discuss *general* behaviours which are expected in various types of flares, rather than focusing on some particular flares which have been observed. In the subsequent analysis, we will consider a single, isolated, large amplitude variability for various changes
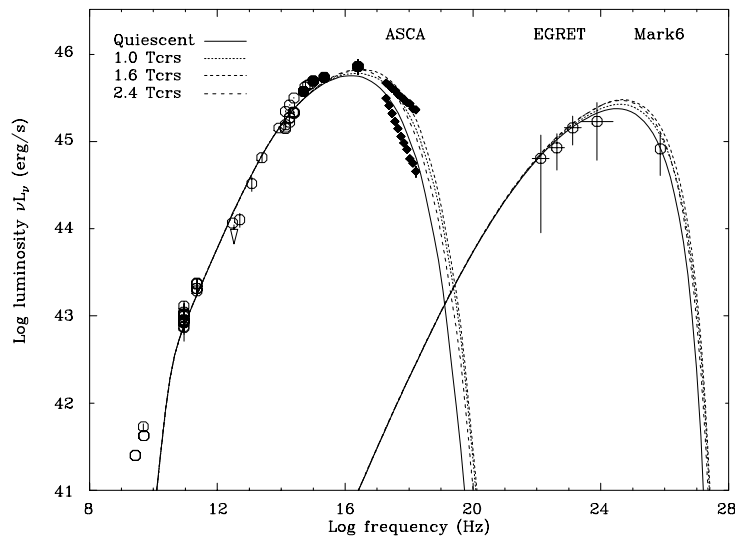
Figure 11.20: Multi-band spectrum of PKS 2155−304. The filled circles are the nearly simultaneous *IUE* and *EUVE* data reported in Urry et al. (1997). The filled squares are the X–ray data obtained with *ASCA* (this work). The solid line and dashed lines represent the time evolution of the photon spectra calculated from the time-dependent SSC model. The multi-frequency spectra at $t/t_{\mathrm{crs}} = 0$, 1.0, 1.6 and 2.4 are shown respectively. Figure from Kataoka et al (2000).

in physical parameters. More complicated situation (e.g., Figure 7.8), however, could be easily understood as a superposition of variety of such flare events. We assume that the duration of the change is impulsive, and continues $\Delta t = t_{\mathrm{crs}}$ for simplicity. One can find a similar discussion, although including less variety, in Mastichiadis & Kirk (1997) in which variability is assumed to continue until both electron/photon distributions reach to the 'new' equilibrium state.

Flares due to Changes in δ

We first consider the case where the beaming factor δ changes impulsively by a factor of 2 (Figure 11.21). The symmetric time profile of the flare, whose rise-time and decay-time are characterized with t_{crs}, are clearly seen. Since the beaming factor is defined as $\delta = [\Gamma(1 - \beta)\cos \theta]^{-1}$ (§ 3.7.2), such situation is physically possible if the trajectory of the emitting blob is curved (e.g., local spatial bending of the jet; e.g., Wagner et al. 1993) or Lorentz factor Γ itself has been changed. In any case, Figure 11.21 shows that the resultant variability should be *coherent* in energy, which strongly contradicts to the observation. No time lags will be observed for time variability in various energy bands.
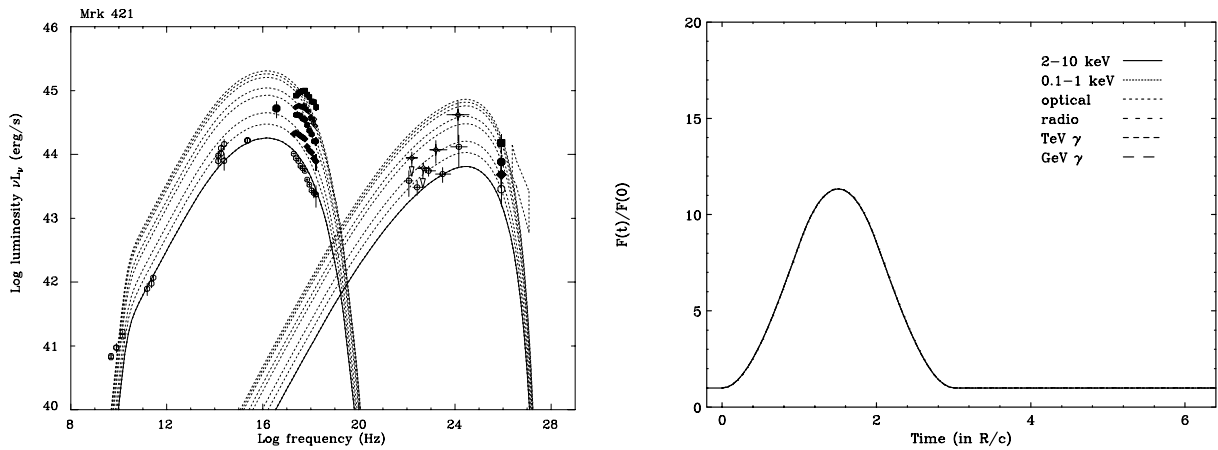
Figure 11.21: *left* : Evolution of the multi-frequency spectra of Mrk 421 in the case where the beaming factor (δ) changes impulsively by a factor of 2. Duration of the change is assumed to be t_{crs}. *right* : Plot of the flux at various frequencies (normalized to its queiscent value) for the flare that corresponds to a change in δ by a factor of 2.

Flares due to Changes in B

Next case is a flare due to the impulsive change in magnetic field strength B by factor of 5 (Figure 11.22). In this case, the whole synchrotron spectrum is blue-shifted ($\nu \propto B$) and boosted in intensity ($L_{\mathrm{sync}} \propto B^2$) although the observed amplitude becomes smaller because (1) flare duration is too short to reach a new equilibrium state and (2) strong cooling reduces the variability amplitude for the high energy electrons. Light travel time effect also reduces the amplitude because slices of increasing B and decreasing B are summed up at the same time.

It is reamarkable that the self-Compton flux, on the other hand, reduces significantly from its original value. This result is consistent with that discussed in Mastichiadis & Kirk (1997) and apparently contradicts the case we have shown in Figure 11.7 (a), in which the total electron distribution was held to be constant. Although such curious behaviour during a flare have never been observed, this case is interesting from the standpoint of the energetics in the jet.

In current case, we keep the electron injection rate $Q(\gamma)$ to be constant. Thus the electron kinetic energy input to the emission region per unit time per unit volume is

$$P_{\mathrm{e}} = m_{\mathrm{e}} c^2 \int_{\gamma_{\mathrm{min}}}^{\infty} (\gamma - 1) Q_{\mathrm{e}} d\gamma. \tag{11.38}$$

For the high energy electrons, the sum of the synchrotron and inverse Compton energy loss (equation (3.34); 3.54) would be balanced with P_{e}, to reach a 'new' equilibrium state. In the situation where P_{e} is constant during the flare, increasing synchrotron luminosity

thus inevitably will cause the decrease in self-Compton luminosity.
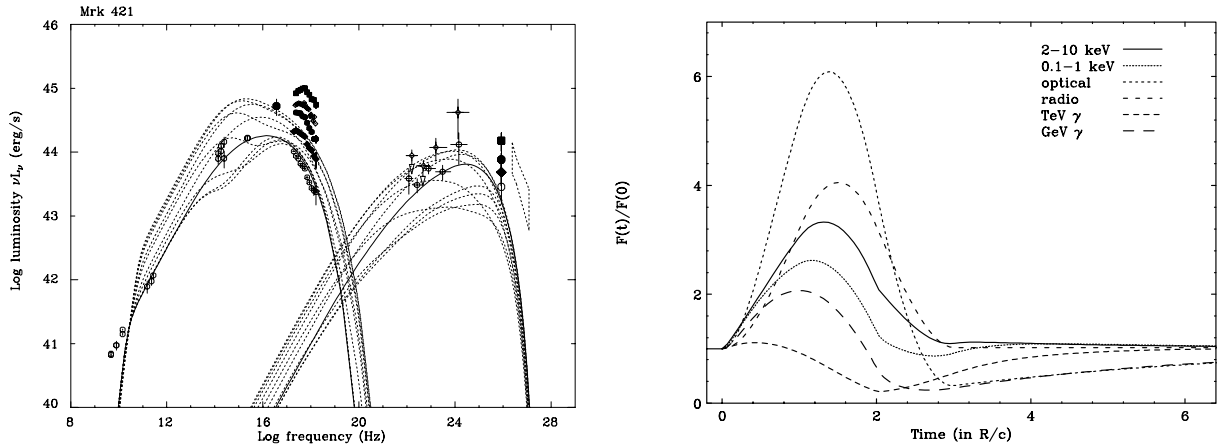
Figure 11.22: *left* : Evolution of the multi-frequency spectra of Mrk 421 in the case where the magnetic field strength B changes impulsively by a factor of 5. Duration of the change is assumed to be t_{crs}. *right* : Plot of the flux at various frequencies (normalized to its quiescent value) for the flare that corresponds to a change in B by a factor of 5.

Flares due to Changes in γ_{max}

The third case is a flare due to changes in the maximum Lorentz factor of electrons γ_{max} (Figure 11.23). γ_{max} was assumed to be changed instantaneously by factor of 5 for t_{crs}. This case of flare was good representation of the data for a particular flare observed for PKS 2155$-$304 (see § 11.7.2).

The result seems to describe adequately the variability of the self-Compton flux, however, X-ray spectrum becomes too flat compared to its relatively small changes in peak luminosity (Figure 11.23). Also note that the variability amplitude in the X-ray band is a factor 2 larger than that in the TeV energy band (*right* panel), which does not agree with the observational results where [X-ray flux] $\propto$ [TeV γ-ray flux] (see, Figure 9.3).

In this thesis, we found that the peak energy of the synchrotron component for Mrk 421 *did* shift during the flare, but the change was very small ($\sim 0.5 - 2$ keV) compared to the large amplitude variations in flux. We thus expect that the factor of ~ 2 changes practically expected in γ_{max}, but the *main* cause of the flux variation must be other than the changes in γ_{max}.

In this case, time lags will be observed in various energy bands. Observed lag will be consistent with that expected from the synchrotron cooling time scale in the X-ray energy band, because the synchrotron cooling is more dominant than Compton cooling

process (Figure 11.12). Amplitude becomes larger as the photon energy increases, which qualitatively agrees with the observational data (§ 7.2.2).
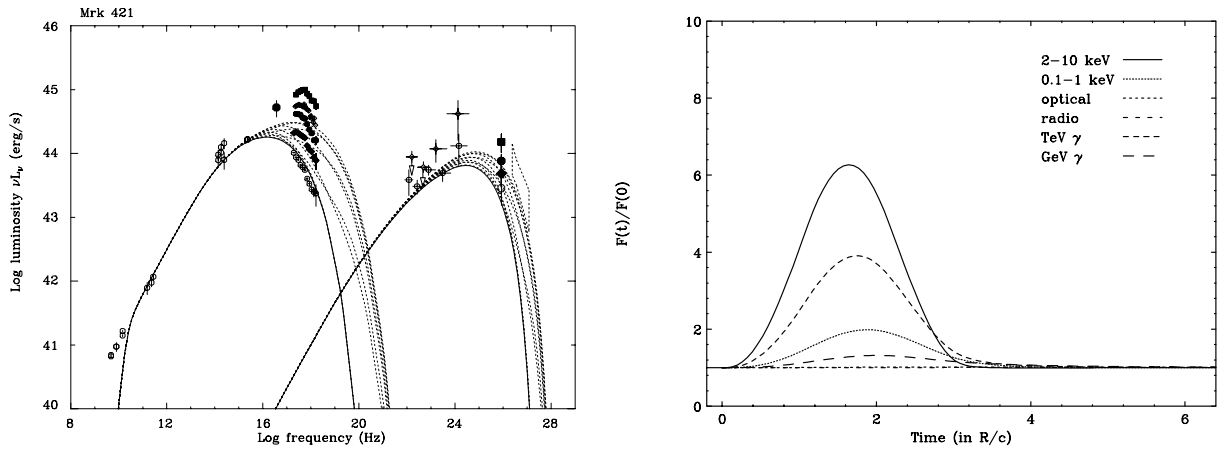
Figure 11.23: *left* : Evolution of the multi-frequency spectra of Mrk 421 in the case where the maximum Lorentz factor of electron (γ_{max}) changes impulsively by a factor of 5. Duration of the change is assumed to be t_{crs}. *right* : Plot of the flux at various frequencies (normalized to its quiescent value) for the flare that corresponds to a change in γ_{max} by a factor of 5.

Flares due to Changes in q_{e}

Finally, we simulate a flare due to the impulsive change in electron injection normalization q_{e} by a factor of 10. In this case, the model fit seems to be better than all of the previous cases from radio to γ-ray bands. Amplitude of variability becomes larger as the photon energy increases, but energy dependence is smaller than a case of the flare due to γ_{max}. Only discrepancy is the fact that the amplitude of variability in TeV band is larger than that in the X-ray band. The relation of variability amplitude in both energy bands is somewhat between the Thomson limit ([X-ray] $\propto$ [TeV γ-ray]^2) and the Klein-Nishina limit ([X-ray] $\propto$ [TeV γ-ray]) (see, § 10.5).

Time lags will be observed in various energy bands. Observed lag will be consistent with that expected from the synchrotron cooling time scale in the X-ray energy band, because the synchrotron cooling is more dominant than Compton cooling process (Figure 11.12). The symmetric time profile of the flare are only seen for high energy light curves (X-ray and TeV γ-ray). For radio$-$optical and GeV band, light curves are assymmetric whose rise time is characterized with t_{crs}, while decay-time is more longer cooling time (t_{cool}) or escape time (t_{esc}).

In summary, in the practical situation, we expect that both γ_{max} and q_{e} can vary during the flare of Mrk 421. However, large amplitude variations in flux are mostly due to the

increasing number of injected electrons (q_e). Linear correlation between the X-ray and TeV γ-ray flux can be also explained by the combination of these two types of variations. Time lags in various X-ray energy bands as well as the symmetric time profile are well represented by these simple models of the flare.
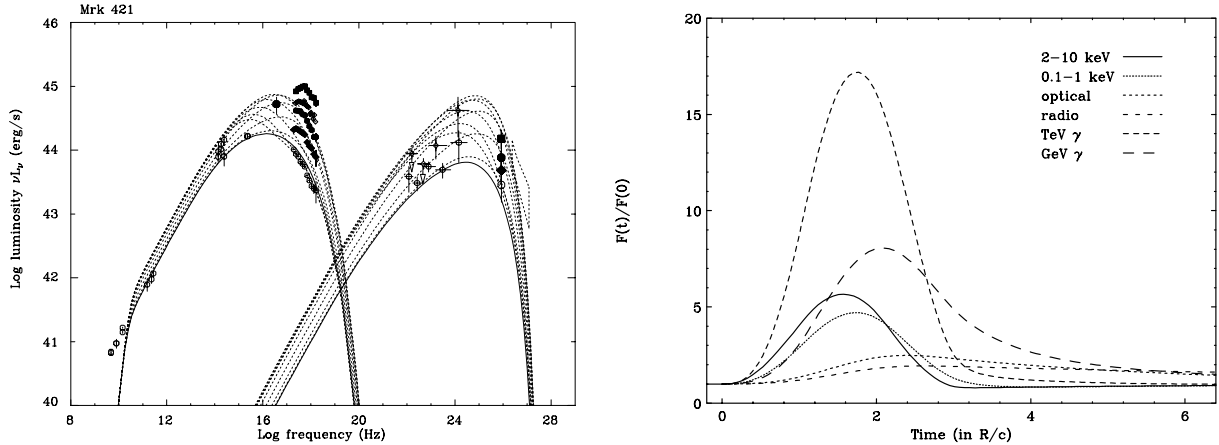
Figure 11.24: *left* : Evolution of the multi-frequency spectra of Mrk 421 in the case where the amplitude of electron injection (q_e) changes impulsively by a factor of 10. Duration of the change is assumed to be t_{crs}. *right* : Plot of the flux at various frequencies (normalized to its quiescent value) for the flare that corresponds to a change in q_e by a factor of 10.

11.7.4   Spectral Evolutions

In the previous section, we found that the flare of Mrk 421 is well explained by the changes in q_e and γ_{max}. Since for this particular source, the former is more important, we study the spectral behaviour during the flare in which q_e changes factor of 10 for t_{crs}.

Rapid Electron Injection up to γ_{max}

We first consider that fresh electrons are *instantaneously* injected into the emission region up to γ_{max}. Thus for all electron energy bands, the relation $t_{acc} \ll t_{cool}$ holds. Although this situation may seem to be somewhat unphysical, this may occur when the tangled magnetic field in the acceleration region B_s is much stronger than that in the emitting region (see § 10 for more detail).

   Figure 11.25 (*left*) shows the light curves of synchrotron component in various energy bands (the same situation as with Figure 11.24). One finds that (1) peak time of the flare lags in lower photon energy, and (2) light curves are symmetric for high energy band (t_{cool}

$\ll t_{\rm crs}$), while the symmetry breaks down in the lower energy ($t_{\rm cool} \geq t_{\rm crs}$), both of which are exactly consistent with the observational data (Figure 10.2, § 7.2.3; 8.2.3).

Spectral evolutions during the flare is most conveniently expressed as a track pattern in the flux versus photon index plane. This expression is equivalent to the patterns of the brightness versus hardness, which was introduced in § 7.2.4. Figure 11.25 (*right*) shows variability patterns in various X-ray energy bands. One can see the canonical clockwise-loop in all energy-bands.
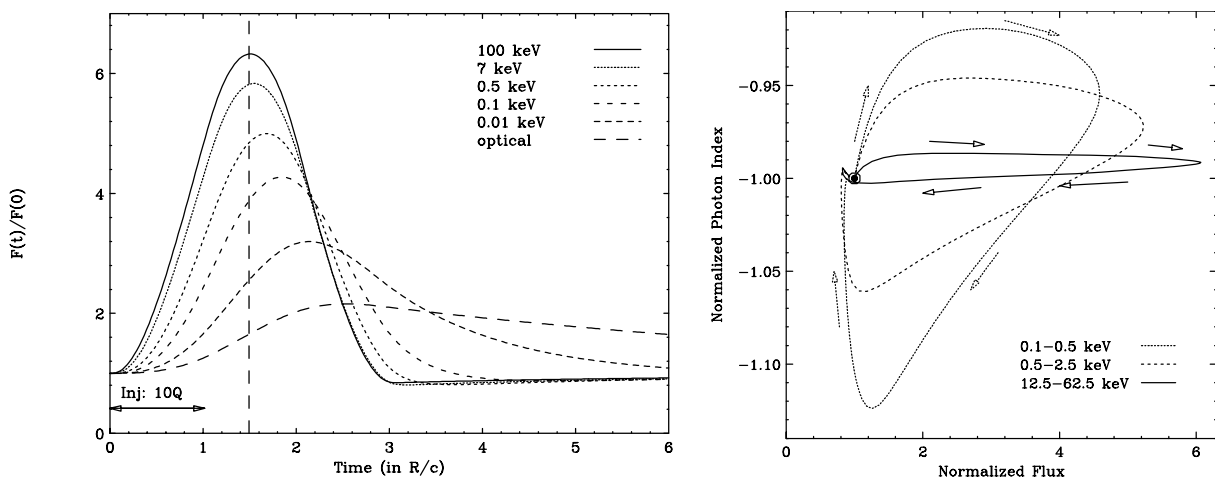
Figure 11.25: Simulation of a flare in which electron injection normalization changed by a factor of 10 for $t_{\rm crs}$. Electrons are assumed to be injected instantaneously up to $\gamma_{\rm max}$. *left* : Light curves of synchrotron component in various energy bands. *right* : Variability patterns in the flux versus photon index plane, which represents the spectral evolutions in various energy bands. One can see the canonical clockwise-loop in all energy-bands.

Acceleration of Electrons up to $\gamma_{\rm max}$

We next consider the case in which fresh electrons are mono-enegetically injected at $\gamma_{\rm min}$ for $0 < t < t_{\rm crs}$, and subsequently accelerated up to $\gamma_{\rm max}$. Acceleration time of the electrons are assumed to be $t_{\rm acc} = 8.0 \times 10^4$ (sec) in the source frame. For the SSC parameters of Mrk 421 assumed here (Table 11.1), current value of $t_{\rm acc}$ is roughly equal with the cooling time at ~ 1 keV. Thus this exmaple may correspond to the case in which the magnetic field in the accelerating region is almost eqaual to that in the emission region.

Figure 11.26 (*left*) shows the light curves of synchrotron component in various energy bands. Clear differences can be seen from the previous case; (1) start time of the flare is different in various energy bands, and (2) very little time-lags are observed in the X-ray energy bands. More precisely speaking, the peak time of the flare is fastest in the *ASCA*

energy band ($0.5-7$ keV), while in other wavelengths, peak-time will be lagged behind that in the *ASCA* band. Remarkably, hard X-ray (100 keV) variation also lags, showing the '*hard-lag*' behaviour.

This is more cleary seen in the flux versus photon index plane (Figure 11.26; *right*). In the hard X-ray energy bands, variability patterns track a loop in opposite direction, characterized with *anti*-clockwise motion. The possible patterns in 'clockwise' hysterisis were first discussed by Kirk, Rieger & Mastichiadis (1998). They argued that for the lower energy band where $t_{cool} \gg t_{acc}$, variability pattern is always a canonical clockwise loop, while around the maximum energy of electrons, *anti*-clockwise pattern could be observed because $t_{cool} \simeq t_{acc}$. Thus our simulation is consistent with their results. The balance of *soft-lag* due to the radiative cooling and *hard-lag* from the acceleration process determines whether clockwise or *anti*-clockwise loop is mainly observed.
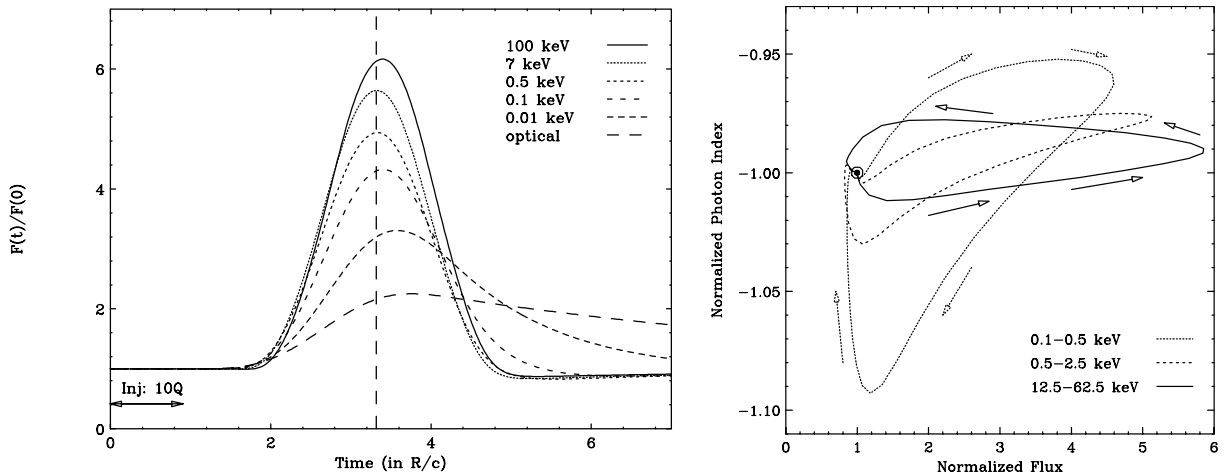
Figure 11.26: Simulation of a flare in which electron injection normalization changed by a factor of 10 for t_{crs}. Electrons are assumed to be injected at γ_{min}, and accelerated up to γ_{max} with a constant rate of $t_{acc} = 8.0 \times 10^4$ sec in the source flame. *left* : Light curves of synchrotron component in various energy bands. *right* : Variability patterns in the flux versus photon index plane, which represents the spectral evolutions in various energy bands. One can see the canonical clockwise-loop in low energy bands ($0.1-0.5$ keV and $0.5-2.5$ keV), while *unusual anti*-clockwise loop can be seen in the highest X-ray energy bands ($12.5-62.5$ keV).

Electron Injection Longer than t_{crs}

Final example is where the fresh electrons are instantaneously injected into the emission region up to γ_{max} for 3 t_{crs}. Only difference from the first case of Figure 11.25 is the duration of the flare, which was set to be t_{crs} in the previous case. Figure 11.27 (*left*)

shows the light curves of synchrotron component in various energy bands. One can see a *plateau* in the high energy light curves. In the low energy band (UV and optical), such structure in time profile is ambiguous, beause the rise-time of a flare itself is larger than 3 t_{crs}. Interestingly, such a *plateau*, although not as common, has been observed for Mrk 421 during 1998 campaign (see, § 10.2; Figure 10.5). A plateau appears only when the duration of a change in electron injection (t_{inj}) is larger than t_{crs}, thus enough time is allowed for electrons/photons to reach a new equilibrium state.

Spectral evolution during the flare is most conveniently expressed as a track pattern in the flux versus photon index plane (Figure 11.27). As was the previous case of $t_{inj} = t_{crs}$, canonical clockwise-loops can be seen in all energy-bands.
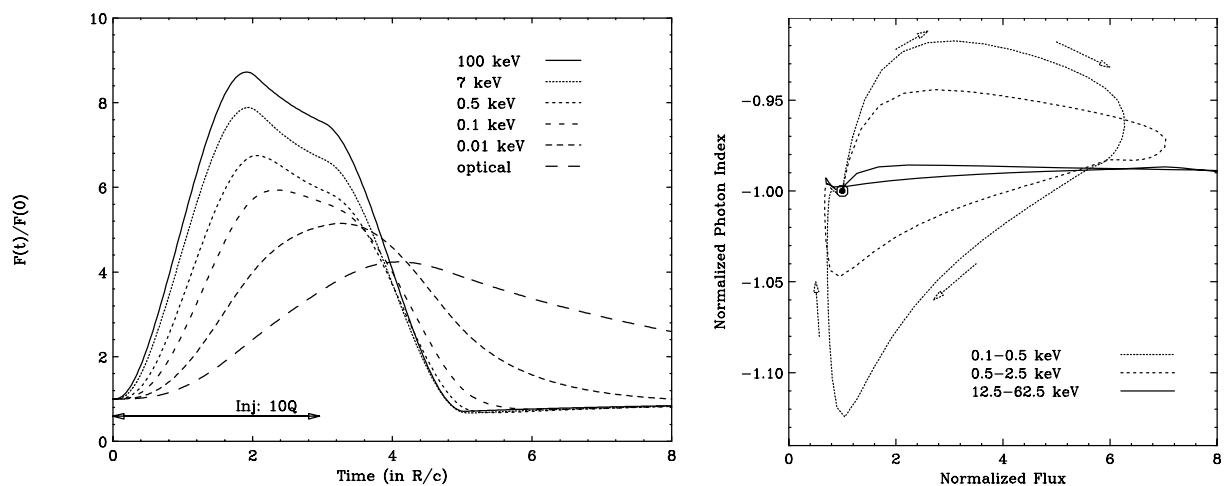
Figure 11.27: Simulation of a flare in which electron injection normalization changed by a factor of 10 for 3 t_{crs}. Electrons are instantaneously injected at γ_{min}. *left*: Light curves of synchrotron component in various energy bands. *right*: Variability patterns in the flux versus photon index plane, which represents the spectral evolution in various energy bands. One can see the canonical clockwise-loop in all energy bands (0.1−0.5 keV and 0.5−2.5 keV).

11.7.5 Modeling Mrk 501 Flare

Next we model the flaring behaviours in Mrk 501. In similarity to the case of Mrk 421, we considered various types of flares, rather than focusing on some particular flares which have been observed. Our previous discussion suggest that the flare of Mrk 501 is mostly due to the changes in γ_{max} as well as the spectral hardening during the flare (see, § 10.4).

In Figure 11.28 (*left*), we show the time evolution of Mrk 501 multi-frequncy spectrum during a single flare event. We assume γ_{max} changed by factor 20 ($\gamma_{max} = 6{\times}10^{6}$) from the quiescent state and the electron injection spectrum hardens from $s = 1.8$ to 1.2. The

amplitudes of variation in various energy bands are qualitatively in agreement with the observation.
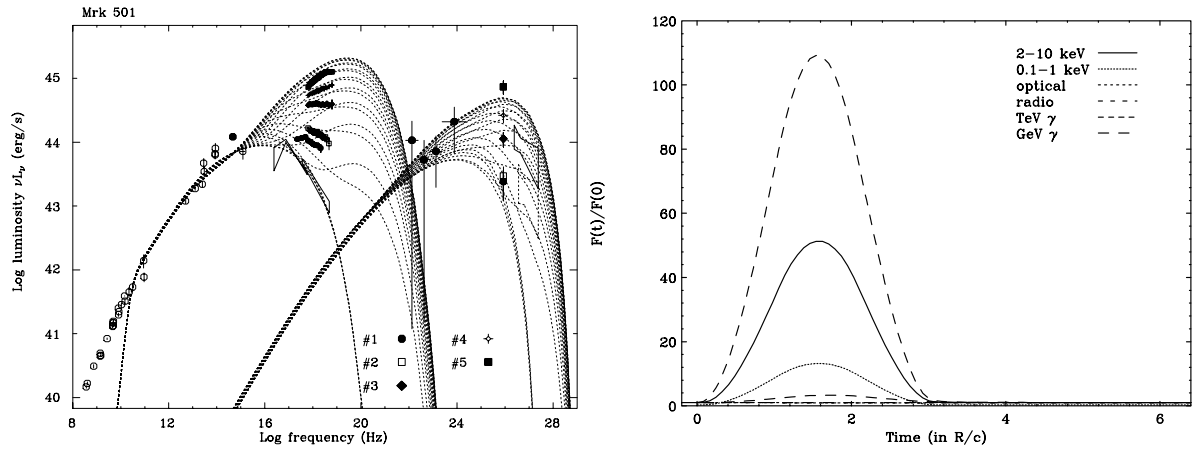
Figure 11.28: *left*: Evolution of the multi-frequency spectra of Mrk 501 in the flaring states. *right*: Plot of the flux at various frequencies (normalized to its quiescent value) for the Mrk 501 flare. During the flare, hard electron population ($s = 1.2$) with the maximum Lorentz factror of $\gamma_{\mathrm{max}} = 6 \times 10^6$ are injected for $t_{\mathrm{inj}} = t_{\mathrm{crs}}$.

11.7.6   Unified Picture of Rapid Variability in TeV Blazars

From the X-ray observations of TeV blazars, we have suggested in § 10 that the rapid variability events observed in blazars are well characterized by 4 dynamical scales; acceleration time: t_{acc}, cooling time: t_{cool}, source light travel time: t_{crs}, and electron injection time: t_{inj}. In this chapter, we have confirmed this scenario based on a newly developed time-dependent SSC model. Although the real situation may be much more complicated than we have imagined, those dynamical time scales should play important roles to specify time vaiability in blazars. We assumed here that the electron escape time (t_{esc}) is always longer than t_{cool}. Note, however, that if this relation is not correct, i.e., $t_{\mathrm{cool}} > t_{\mathrm{esc}}$, we have to replace t_{cool} to t_{esc} because escape is more efficient than cooling process.

As a summary, we give a unified picture of rapid variability considering the balance of 4 dynamical time scales. Possible 24 (4!) patterns are reduced to 12 patterns by two physical constraints; (i) t_{acc} must be shorter than t_{cool} because magnetic field strength in the shocked region would be stronger or equal to that in the emitting region ($B \le B_{\mathrm{s}}$), (ii) t_{inj} must be longer than source light travel time because the particle injection process itself should take (at least) $\sim R/c$ to influence the whole emission region.

In Figure 11.29 and 11.30, we illustrate the *allowed* time profiles which can be observed

in blazars. For simplicity, we assume a 'box-shaped' (step-function like) injection profile which lasts t_{inj}. Of course, the injection profile itself may vary in time; however, this approximation is correct as long as $t_{\mathrm{inj}} \simeq t_{\mathrm{crs}}$, since more rapid changes in injection ($< t_{\mathrm{crs}}$) are unplausible from causality. Thus results presented here will be affected only when t_{inj} is much larger than t_{crs} and variable on longer time scale.

For examples, 'soft lag' flares observed for PKS 2155−304 in 1994 May (§ Figure 10.2) correspond to the case (7), because the flare was very symmetric and peak time of the flare shows the 'soft-lag' behaviour. A *plateau*-like flare observed for Mrk 421 in 1998 (Figure 10.5) is the case (12), while hard lag flare corresponds to (6). Variability patterns which are listed here but have not been observed, remaines as a 'homework' in the future observations. Interestingly, we predict all types of the flares are characterized by rapid-rise and gradual-decay, or nearly equal rise and decay. Flares in opposite sense, i.e., gradual rise and rapid decay, will be possible only when the duration of the flare is much larger than t_{crs} and injection event itself has such peculiar time profile.

(1) $t_{acc} \sim t_{cool} \gtrsim t_{inj} \gtrsim t_{crs}$

     triangle
     symmetric
     hard lag

(2) $t_{cool} > t_{acc} \gtrsim t_{inj} \gtrsim t_{crs}$

     triangle
     asymmetric
     soft lag

(3) $t_{cool} > t_{crs} \sim t_{inj} > t_{acc}$

     triangle
     asymmetric
     soft lag

(4) $t_{cool} > t_{inj} > t_{acc} > t_{crs}$

     plateau
     asymmetric
     soft lag

(5) $t_{cool} > t_{inj} > t_{crs} > t_{acc}$

     plateau
     asymmetric
     soft lag

(6) $t_{crs} \sim t_{inj} > t_{acc} \sim t_{cool}$

     triangle
     symmetric
     hard lag

Figure 11.29:

(7) $t_{crs} \sim t_{inj} \gtrsim t_{cool} > t_{acc}$

triangle
symmetric
soft lag

(8) $t_{inj} > t_{acc} \sim t_{cool} \gtrsim t_{crs}$

plateau
symmetric
hard lag

(9) $t_{inj} > t_{cool} > t_{acc} > t_{crs}$

plateau
asymmetric
soft lag

(10) $t_{inj} > t_{cool} > t_{crs} > t_{acc}$

plateau
asymmetric
soft lag

(11) $t_{inj} > t_{crs} > t_{acc} \sim t_{cool}$

plateau
symmetric
hard lag

(12) $t_{inj} > t_{crs} > t_{cool} > t_{acc}$

plateau
symmetric
soft lag

Figure 11.30: Unified picture of rapid variability in blazars. All the variability patterns are well explained by the combination of 4 dynamical time scales. These are; acceleration time : t_{acc}, cooling time : t_{cool}, source light travel time : t_{crs}, and electron injection time : t_{inj}. For simplicity, we assumed here that the electron escape time (t_{esc}) is always longer than t_{cool}. Note however that, if the relation is not correct, i.e., $t_{cool} > t_{esc}$, we have to replace t_{cool} in the figure to t_{esc} because escape is more efficient than cooling process.

Chapter 12

Conclusion

We studied the rapid variability and spectral evolution of four TeV blazars observed with the *ASCA* and *RXTE* satellites. These observations provide the highest quality spectral information as well as light curves in the X-ray energy range of $0.7-20$ keV. Since the spectral energy distribution spanning over a very wide energy range and large-amplitude time variability are marked features of blazars, these sources were contemporaneously observed in various energies, including UV, X-ray, GeV and TeV γ-ray bands. We conducted a number of multi-frequency campaigns for the TeV blazars. In particular, our observations of Mrk 421 and Mrk 501 in both X-ray and TeV γ-ray bands provide the first truly simultaneous data in various phases of source activity. From the study of the time-dependent spectral evolution based on the largest samples of X-ray/GeV/TeV γ-ray data, we discovered following major results:

(1) The overall spectra of all TeV blazars form two distinct peaks in the $\nu L(\nu)$ representation. We detected and determined the position of the peak of the lower energy synchrotron component in the X-ray energy band for all TeV blazars: this position is clearly time-variable. Clear correlations were found between peak energy ($E_{\rm p}$) and peak luminosity ($L_{\rm p}$) for both Mrk 421 and Mrk 501. The relations are $E_{\rm p} \propto L_{\rm p}^{0.4}$ for Mrk 421 and $E_{\rm p} \propto L_{\rm p}^{1.6}$ for Mrk 501. Mrk 421 showed very small changes in the peak position, while Mrk 501 showed the largest shift ever observed in blazars.

(2) From the truly simultaneous data, we found that variability in the X-ray and TeV γ-ray bands is well correlated on time scale of a day to years, indicating that the same spatial region and the same population of relativistic electrons are responsible for the emission in both bands. The amplitude of flux variability was comparable in X-ray and TeV γ-ray bands for Mrk 421 ([X-ray flux] $\propto$ [TeV flux]), while quadratic for Mrk 501 ([X-ray flux]^2 $\propto$ [TeV flux]).

Clear correlation of E_{p} with L_{p}, found in Mrk 421 and Mrk 501, suggests that general characteristics of the flaring behavior are repeatable in these objects. We argue that the different properties of spectral evolution observed in Mrk 421 and Mrk 501 are due to a variety of changes in physical quantities during the flare. Data for Mrk 421 indicate that the flux variability is associated with an increase in the number of electrons, while only small changes are implied in maximum Lorentz factor of electrons (γ_{max}). On the other hand, the flare of Mrk 501 is mostly due to the large changes in γ_{max} while keeping the electron number almost conservative. Although different origins of flares produce quite diffent spectral behavior, in both cases, the data are consistent with the synchrotron self-Compton (SSC) scenario operating close to the Klein-Nishina regime.

Our analysis, based on the X-ray spectral evolution suggests very important implications for internal jet structure of Mrk 421 and Mrk 501. According to the recent VLBI observations, superluminal motions have been detected only for Mrk 501, while subluminal motions were implied for Mrk 421. Only a small shift of the synchrotron peak observed in Mrk 421 indicates that electron clouds *fill* the jet, while the filling factor of the clouds in the jet of Mrk 501 appears to be much lower. During the flare of Mrk 421, kinetic power of the shock (which is presumably responsible for the acceleration of the radiating particles) causes roughly equal distribution of energy to large number of low-energy electrons newly injected into the shock: this increases the number of high energy electrons. Large shifts of the synchrotron peak observed in Mrk 501, on the other hand, are possible only when the internal jet encounters a medium that is rather sparse and transparent to the shock propagation. Kinetic power of the shock is spent to *increase* the energies of individual electrons and hence *number-conservative*. The absence of superluminal motion of Mrk 421 in the radio band indicates that the high energy outflow has been sufficiently decelerated when it reaches to more distant, radio emitting region.

From the study of time variability in the X-ray band, we found following major results:

(3) Unprecedented long observations of Mrk 421 and PKS 2155−304 revealed day-by-day flares from UV to hard X-rays, and TeV γ-ray bands. Structure function of the X-ray time series in TeV blazars showed a roll-over at $\sim$ 1 day, which is interpreted as a characteristic time scale of a single flare event. On a shorter time scales, rapid variability is strongly suppressed, implying 'strong red-noise' power spectrum density ($\propto f^{-2} \sim f^{-3}$). This is clearly different from the results obtained in Seyfert galaxies or Galactic Black Hole systems whose rapid time variability is well represented by a fractal, flickering noise ($\propto f^{-1} \sim f^{-2}$).

(4) 7-day uniterrupted observation of Mrk 421 revealed that the lags of time variability

in various X-ray energy bands were relatively small compared to those found in previous observations. Detailed temporal analysis showed that time-lags changed flare by flare. Importantly, we found a signature of 'hard-lag' behavior, where soft X-ray variations *preceded* those in the hard X-ray band.

(5) We detected a general trend that the amplitude of variability became larger at increasing photon energy. However in some flares, variability in lower energy band was larger or comparable to that in the higher energy band.

(6) Time profiles of individual flare events were almost symmetric, which is characterized by a nearly equal rise-time and decay-time. Importantly, this time-scale was longer than the synchrotron cooling time for X-ray emitting electrons. From the detailed analysis, we discovered that the symmetry of the time profile tends to break down at lower energies.

The absence of rapid variability on time scales shorter than ≤ 1 day implies that the X-ray emission site is located $\sim 10^{17-18}$ cm ($\sim 100~R_g$) from the base of the jet. In this region, high energy electrons lose their energy by radiative (synchrotron/inverse Compton) cooling processes, but the current paradigm is insufficient to understand all observational properties obtained in this thesis. Our results on different sign of lags in the light curve of Mrk 421 can be explained if we take the effect of electron acceleration into account. We confirmed that *usual* 'soft-lag' pattern is observed when the acceleration time of electrons is much shorter than the cooling time, while 'hard-lag' can be detected when the acceleration time of electrons is almost equal to their cooling time. Such opposite sense of lag is expected only if the electron energy is close to γ_{max}, which corresponds to the X-ray energy band in the photon space.

Symmetry of the time profiles tends to break down in the lower energy bands because cooling time becomes longer than the light travel time across the source. This results in an asymmetrical time profile where the decay-time is longer than the rise-time. We argue that 4 dynamical time scales must be considered properly. These are (i) acceleration time (t_{acc}), (ii) cooling time (t_{cool}), (iii) source light travel time (t_{crs}), and (iv) electron injection time (t_{inj}). We suggest that all the variability patterns currently known for blazars are well understood by the balance of these dynamical time scales.

By considering both the spectral energy distribution and the limits from X-ray time variability, we successfully place constraints on the physical quantities relevant for the overall electromagnetic emission from TeV blazars. Based on the synchrotron self-Compton (SSC) scenario, we found that the physical parameters are similar among those objects, where the magnetic field strength $B = 0.1-0.4$ Gauss, beaming factor $\delta = 10-40$, region

size $R = 10^{-3}-10^{-2}$ pc, and maximum Lorentz factor of electrons $\gamma_{\max} = 5 \times 10^4 - 4 \times 10^5$ for the quiescent state.

To confirm our knowledge of spectral evolution and rapid variability in blazars more *quantitatively*, we have developed a new time-dependent SSC model, incorporating the radiative cooling and acceleration process, as well as light travel time effects properly. We successfully modeled rapid variability and spectral evolution of TeV blazars assuming the physical parameters derived above.

Our present work places a number of *new* observational constraints on the rapid time variability, internal jet structure, and origin of the flare mechanism for TeV γ-ray emitting blazars. However, physical links to other blazar classes, such as LBLs and OVV quasars, still remain unsolved. We need better quality, contemporaneous data over a wide range of observational baands, especially in the hard X–ray and γ–ray regimes, to better understand dynamics operating in all blazar classes. Observations with the next generation of satellites, featuring improved sensitivity at hard X–ray/γ–ray energies, are expected to bring valuable information.

Appendix A

RXTE Observation Log of TeV Blazars

Table A.1: *RXTE* observation log of Mrk 421 (1)

Source Name	OBS-ID [a]	Start (UT)	End (UT)	Exp. (ksec)	Data Mode [b]
Mrk 421	P10345-01-35-00	1996.04.19 02:00	1996.04.19 02:11	0.608	S1/S2/GX1/GX2
	P10345-01-36-00	1996.04.19 07:27	1996.04.19 08:06	2.304	S1/S2/GX1/GX2
	P10345-01-37-00	1996.04.19 12:24	1996.04.19 12:56	1.904	S1/S2/GX1/GX2
	P10345-01-38-00	1996.04.19 16:35	1996.04.19 16:46	0.624	S1/S2/GX1/GX2
	P10345-01-39-00	1996.04.19 19:51	1996.04.19 20:01	0.544	S1/S2/GX1/GX2
	P10345-01-40-00	1996.04.21 01:16	1996.04.21 01:43	1.568	S1/S2/GX1/GX2
	P10345-01-41-00	1996.04.21 05:16	1996.04.21 05:28	0.672	S1/S2/GX1/GX2
	P10345-01-42-00	1996.04.21 09:06	1996.04.21 09:45	2.304	S1/S2/GX1/GX2
	P10345-01-43-00	1996.04.21 14:58	1996.04.21 15:08	0.56	S1/S2/GX1/GX2
	P10345-01-44-00	1996.04.21 21:25	1996.04.21 21:35	0.576	S1/S2/GX1/GX2
	P10345-01-46-00	1996.04.22 14:02	1996.04.22 14:48	2.736	S1/S2/GX1/GX2
	P10345-01-47-00	1996.04.22 18:13	1996.04.22 18:24	0.64	S1/S2/GX1/GX2
	P10345-01-48-00	1996.04.23 00:27	1996.04.23 00:38	0.624	S1/S2/GX1/GX2
	P10345-01-49-00	1996.05.03 04:13	1996.05.03 04:37	1.408	S1/S2/GX1/GX2
	P10345-01-50-00	1996.05.03 10:06	1996.05.03 10:17	0.656	S1/S2/GX1/GX2
	P10345-01-51-00	1996.05.03 13:19	1996.05.03 13:29	0.576	S1/S2/GX1/GX2
	P10345-01-52-00	1996.05.04 00:50	1996.05.04 01:16	1.536	S1/S2/GX1/GX2
	P10345-01-53-00	1996.05.04 05:58	1996.05.04 06:31	1.984	S1/S2/GX1/GX2
	P10345-01-54-00	1996.05.04 08:32	1996.05.04 08:42	0.576	S1/S2/GX1/GX2
	P10345-01-55-00	1996.05.04 18:32	1996.05.04 18:42	0.56	S1/S2/GX1/GX2
	P10345-01-56-00	1996.05.04 21:38	1996.05.04 21:48	0.576	S1/S2/GX1/GX2
	P10345-01-57-00	1996.05.05 04:03	1996.05.05 04:40	2.192	S1/S2/GX1/GX2
	P10345-01-58-00	1996.05.05 10:08	1996.05.05 10:18	0.544	S1/S2/GX1/GX2
	P10345-01-59-00	1996.05.05 13:21	1996.05.05 13:41	1.2	S1/S2/GX1/GX2
	P10345-01-60-00	1996.05.05 21:33	1996.05.05 21:53	1.2	S1/S2/GX1/GX2
	P10345-01-61-00	1996.05.06 05:21	1996.05.06 05:30	0.544	S1/S2/GX1/GX2
	P10345-01-62-00	1996.05.06 10:08	1996.05.06 10:19	0.64	S1/S2/GX1/GX2
	P10345-01-63-00	1996.05.06 14:57	1996.05.06 15:07	0.608	S1/S2/GX1/GX2
	P10345-01-64-00	1996.05.06 23:13	1996.05.06 23:34	1.264	S1/S2/GX1/GX2
	P10345-01-65-00	1996.05.07 05:20	1996.05.07 05:31	0.672	S1/S2/GX1/GX2
	P10345-01-66-00	1996.05.07 10:03	1996.05.07 10:23	1.184	S1/S2/GX1/GX2
	P10345-01-67-00	1996.05.07 15:00	1996.05.07 15:09	0.528	S1/S2/GX1/GX2
	P10345-01-68-00	1996.05.07 21:33	1996.05.07 21:54	1.232	S1/S2/GX1/GX2
	P10345-01-69-00	1996.05.08 06:56	1996.05.08 07:07	0.64	S1/S2/GX1/GX2
	P10345-01-70-00	1996.05.08 13:31	1996.05.08 13:43	0.672	S1/S2/GX1/GX2
	P10345-01-71-00	1996.05.08 18:10	1996.05.08 18:23	0.752	S1/S2/GX1/GX2
	P10345-01-72-00	1996.05.08 23:09	1996.05.08 23:37	1.664	S1/S2/GX1/GX2
	P10345-01-73-00	1996.05.09 05:54	1996.05.09 06:20	1.552	S1/S2/GX1/GX2

Table A.2: *RXTE* observation log of Mrk 421 (2) *continued*

Source Name	OBS-ID [a]	Start (UT)	End (UT)	Exp. (ksec)	Data Mode [b]
Mrk 421	P10345-01-74-00	1996.05.09 11:50	1996.05.09 12:01	0.608	S1/S2/GX1/GX2
	P10345-01-75-00	1996.05.09 15:16	1996.05.09 15:28	0.688	S1/S2/GX1/GX2
	P10345-01-77-00	1996.05.10 06:00	1996.05.10 06:10	0.544	S1/S2/GX1/GX2
	P10345-01-78-00	1996.05.10 08:34	1996.05.10 08:44	0.544	S1/S2/GX1/GX2
	P10345-01-79-00	1996.05.10 15:20	1996.05.10 15:38	1.04	S1/S2/GX1/GX2
	P10345-01-80-00	1996.05.10 21:12	1996.05.10 21:55	2.528	S1/S2/GX1/GX2
	P10345-01-81-00	1996.05.11 06:59	1996.05.11 07:09	0.56	S1/S2/GX1/GX2
	P10345-01-82-00	1996.05.11 12:24	1996.05.11 12:34	0.544	S1/S2/GX1/GX2
	P10345-01-83-00	1996.05.11 18:20	1996.05.11 18:31	0.64	S1/S2/GX1/GX2
	P10345-01-84-00	1996.05.11 21:32	1996.05.11 22:01	1.696	S1/S2/GX1/GX2
	P10345-01-85-00	1996.05.12 06:00	1996.05.12 06:13	0.736	S1/S2/GX1/GX2
	P10345-01-86-00	1996.05.12 11:57	1996.05.12 12:07	0.592	S1/S2/GX1/GX2
	P10345-01-87-00	1996.05.12 18:19	1996.05.12 18:31	0.704	S1/S2/GX1/GX2
	P10345-01-88-00	1996.05.12 19:58	1996.05.12 20:18	1.168	S1/S2/GX1/GX2
	P10345-01-89-00	1996.05.13 02:21	1996.05.13 02:31	0.56	S1/S2/GX1/GX2
	P10345-01-90-00	1996.05.13 08:36	1996.05.13 08:46	0.608	S1/S2/GX1/GX2
	P10345-01-91-00	1996.05.13 13:40	1996.05.13 13:50	0.56	S1/S2/GX1/GX2
	P10345-01-92-00	1996.05.13 18:19	1996.05.13 18:35	0.944	S1/S2/GX1/GX2
	P10345-01-93-00	1996.05.14 05:25	1996.05.14 05:35	0.56	S1/S2/GX1/GX2
	P10345-01-94-00	1996.05.14 08:38	1996.05.14 08:48	0.576	S1/S2/GX1/GX2
	P10345-01-95-00	1996.05.14 15:16	1996.05.14 15:25	0.528	S1/S2/GX1/GX2
	P10345-01-96-00	1996.05.14 23:21	1996.05.14 23:43	1.312	S1/S2/GX1/GX2
	P10345-01-97-00	1996.05.15 06:03	1996.05.15 06:13	0.56	S1/S2/GX1/GX2
	P10345-01-98-00	1996.05.15 11:55	1996.05.15 12:09	0.8	S1/S2/GX1/GX2
	P10345-01-01-10	1996.05.15 15:34	1996.05.15 15:43	0.544	S1/S2/GX1/GX2
	P10345-01-02-10	1996.05.15 22:24	1996.05.15 22:34	0.56	S1/S2/GX1/GX2
	P10345-01-03-10	1996.05.16 08:54	1996.05.16 09:04	0.576	S1/S2/GX1/GX2
	P10345-01-04-10	1996.05.16 12:00	1996.05.16 12:10	0.56	S1/S2/GX1/GX2
	P10345-01-05-10	1996.05.16 18:17	1996.05.16 18:35	1.04	S1/S2/GX1/GX2
	P10345-01-06-10	1996.05.16 21:28	1996.05.16 21:57	1.712	S1/S2/GX1/GX2
	P10345-01-07-10	1996.05.17 01:03	1996.05.17 01:17	0.816	S1/S2/GX1/GX2
	P10345-01-08-10	1996.05.17 07:47	1996.05.17 07:57	0.544	S1/S2/GX1/GX2
	P10345-01-09-10	1996.05.17 13:55	1996.05.17 14:04	0.512	S1/S2/GX1/GX2
	P10345-01-10-10	1996.05.17 22:26	1996.05.17 22:36	0.544	S1/S2/GX1/GX2
	P10345-01-11-10	1996.05.18 05:39	1996.05.18 05:49	0.544	S1/S2/GX1/GX2
	P10345-01-12-10	1996.05.18 14:04	1996.05.18 14:14	0.544	S1/S2/GX1/GX2
	P10345-01-13-10	1996.05.18 19:05	1996.05.18 19:26	1.216	S1/S2/GX1/GX2
	P10345-01-15-10	1996.05.19 01:03	1996.05.19 01:17	0.8	S1/S2/GX1/GX2

Table A.3: *RXTE* observation log of Mrk 421 (3) *continued*

Source Name	OBS-ID [a]	Start (UT)	End (UT)	Exp. (ksec)	Data Mode [b]
Mrk 421	P10345-01-16-10	1996.05.19 05:52	1996.05.19 06:08	0.912	S1/S2/GX1/GX2
	P10345-01-17-10	1996.05.19 17:24	1996.05.19 17:34	0.544	S1/S2/GX1/GX2
	P10345-01-18-10	1996.05.19 21:49	1996.05.19 21:57	0.432	S1/S2/GX1/GX2
	P10345-01-19-10	1996.05.20 06:16	1996.05.20 06:27	0.608	S1/S2/GX1/GX2
	P10345-01-20-10	1996.05.20 12:05	1996.05.20 12:15	0.576	S1/S2/GX1/GX2
	P10345-01-21-10	1996.05.20 19:02	1996.05.20 19:15	0.752	S1/S2/GX1/GX2
	P10345-01-14-10	1996.05.21 01:08	1996.05.21 01:27	1.088	S1/S2/GX1/GX2
	P10341-02-02-00	1996.12.10 21:05	1996.12.10 21:44	2.336	S1/S2/GX1/GX2
	P20341-01-02-01	1997.04.02 03:30	1997.04.02 09:03	19.968	S1/S2/GX1/GX2
	P20341-01-02-00	1997.04.03 05:08	1997.04.03 09:04	14.144	S1/S2/GX1/GX2
	P20341-01-01-00	1997.04.04 05:15	1997.04.04 07:26	7.808	S1/S2/GX1/GX2
	P20341-01-01-01	1997.04.05 05:12	1997.04.05 06:19	4.0	S1/S2/GX1/GX2
	P20341-01-01-02	1997.04.05 06:48	1997.04.05 07:45	3.376	S1/S2/GX1/GX2
	P20341-01-01-03	1997.04.10 05:31	1997.04.10 06:13	2.512	S1/S2/GX1/GX2
	P20341-01-01-04	1997.04.10 06:55	1997.04.10 07:29	2.032	S1/S2/GX1/GX2
	P20341-01-03-00	1997.04.11 05:20	1997.04.11 07:46	8.752	S1/S2/GX1/GX2
	P20341-01-03-01	1997.04.12 05:21	1997.04.12 08:58	12.976	S1/S2/GX1/GX2
	P20341-01-04-00	1997.04.29 05:29	1997.04.29 05:51	1.28	S1/S2/GX1/GX2
	P20341-01-04-01	1997.04.30 05:29	1997.04.30 06:36	3.984	S1/S2/GX1/GX2
	P20341-01-04-02	1997.05.01 21:27	1997.05.01 22:06	2.336	S1/S2/GX1/GX2
	P20341-01-05-00	1997.05.02 05:30	1997.05.02 06:21	3.024	S1/S2/GX1/GX2
	P20341-01-05-01	1997.05.03 03:55	1997.05.03 04:10	0.896	S1/S2/GX1/GX2
	P20341-01-05-02	1997.05.03 05:29	1997.05.03 06:34	3.856	S1/S2/GX1/GX2
	P20341-01-05-03	1997.05.04 03:54	1997.05.04 04:12	1.024	S1/S2/GX1/GX2
	P20341-01-05-04	1997.05.04 05:30	1997.05.04 05:51	1.216	S1/S2/GX1/GX2
	P20341-01-05-05	1997.05.06 02:21	1997.05.06 05:15	10.416	S1/S2/GX1/GX2
	P20341-01-05-06	1997.05.06 05:39	1997.05.06 05:56	0.976	S1/S2/GX1/GX2
	P20341-01-06-00	1997.06.03 05:59	1997.06.03 06:34	2.096	S1/S2/GX1/GX2

Table A.4: *RXTE* observation log of Mrk 501 (1)

Source Name	OBS-ID	Start (UT)	End (UT)	Exp. (ksec)	Data Mode
Mrk 501	P10341-03-01-00	1996.08.01 13:26	1996.08.01 14:01	2.064	S1/S2/GX1/GX2
	P10341-03-02-00	1996.10.22 11:52	1996.10.22 12:26	2.032	S1/S2/GX1/GX2
	P20340-01-01-00	1997.03.18 02:03	1997.03.18 02:54	3.056	S1/S2/GX1/GX2
	P20340-04-01-00	1997.04.03 04:27	1997.04.03 04:55	1.632	S1/S2/GX1/GX2
	P20340-04-02-00	1997.04.03 09:17	1997.04.03 09:33	0.944	S1/S2/GX1/GX2
	P20340-04-03-00	1997.04.04 04:28	1997.04.04 04:44	0.944	S1/S2/GX1/GX2
	P20340-04-04-00	1997.04.04 11:09	1997.04.04 11:34	1.488	S1/S2/GX1/GX2
	P20340-04-05-00	1997.04.05 04:27	1997.04.05 04:59	1.872	S1/S2/GX1/GX2
	P20340-04-06-00	1997.04.05 07:58	1997.04.05 08:19	1.248	S1/S2/GX1/GX2
	P20340-04-07-00	1997.04.06 07:15	1997.04.06 07:31	0.928	S1/S2/GX1/GX2
	P20340-04-08-00	1997.04.06 10:27	1997.04.06 10:42	0.864	S1/S2/GX1/GX2
	P20340-04-09-00	1997.04.07 07:15	1997.04.07 07:30	0.864	S1/S2/GX1/GX2
	P20340-04-10-00	1997.04.07 10:36	1997.04.07 10:52	0.912	S1/S2/GX1/GX2
	P20340-04-11-00	1997.04.08 05:40	1997.04.08 06:08	1.648	S1/S2/GX1/GX2
	P20340-04-12-00	1997.04.08 10:37	1997.04.08 10:53	0.912	S1/S2/GX1/GX2
	P20340-04-13-00	1997.04.09 05:40	1997.04.09 06:08	1.648	S1/S2/GX1/GX2
	P20340-04-14-00	1997.04.09 10:28	1997.04.09 10:43	0.864	S1/S2/GX1/GX2
	P20340-04-15-00	1997.04.10 06:26	1997.04.10 06:42	0.944	S1/S2/GX1/GX2
	P20340-04-16-00	1997.04.10 07:42	1997.04.10 07:57	0.88	S1/S2/GX1/GX2
	P20340-04-17-00	1997.04.11 04:51	1997.04.11 05:07	0.912	S1/S2/GX1/GX2
	P20340-04-18-00	1997.04.11 07:59	1997.04.11 08:38	2.32	S1/S2/GX1/GX2
	P20340-04-19-00	1997.04.12 04:24	1997.04.12 04:39	0.88	S1/S2/GX1/GX2
	P20340-04-20-00	1997.04.12 10:45	1997.04.12 11:03	1.056	S1/S2/GX1/GX2
	P20340-04-21-00	1997.04.13 06:24	1997.04.13 06:53	1.728	S1/S2/GX1/GX2
	P20340-04-22-00	1997.04.13 11:01	1997.04.13 11:54	3.168	S1/S2/GX1/GX2
	P20340-04-23-00	1997.04.14 08:00	1997.04.14 08:16	0.912	S1/S2/GX1/GX2
	P20340-04-24-00	1997.04.14 10:58	1997.04.14 11:40	2.512	S1/S2/GX1/GX2
	P20340-04-25-00	1997.04.15 06:20	1997.04.15 06:41	1.216	S1/S2/GX1/GX2
	P20340-04-26-00	1997.04.15 08:56	1997.04.15 09:12	0.944	S1/S2/GX1/GX2
	P20340-04-27-00	1997.04.16 04:07	1997.04.16 04:25	1.056	S1/S2/GX1/GX2
	P20340-04-28-00	1997.04.16 10:39	1997.04.16 10:51	0.72	S1/S2/GX1/GX2
	P20340-01-02-00	1997.05.02 04:19	1997.05.02 05:18	3.536	S1/S2/GX1/GX2
	P20340-01-03-00	1997.05.02 09:24	1997.05.02 10:11	2.768	S1/S2/GX1/GX2
	P20340-01-04-00	1997.05.03 04:22	1997.05.03 05:17	3.264	S1/S2/GX1/GX2
	P20340-01-05-00	1997.05.04 04:24	1997.05.04 05:18	3.2	S1/S2/GX1/GX2
	P20340-01-06-00	1997.05.04 06:03	1997.05.04 06:25	1.28	S1/S2/GX1/GX2
	P20340-01-07-00	1997.05.05 04:15	1997.05.05 04:42	1.584	S1/S2/GX1/GX2
	P20340-01-08-00	1997.05.05 09:26	1997.05.05 10:12	2.736	S1/S2/GX1/GX2
	P20340-01-09-00	1997.05.06 06:08	1997.05.06 06:45	2.176	S1/S2/GX1/GX2
	P20340-01-10-00	1997.05.06 07:35	1997.05.06 08:36	3.616	S1/S2/GX1/GX2

Table A.5: *RXTE* observation log of Mrk 501 (2) *continued*

Source Name	OBS-ID	Start (UT)	End (UT)	Exp. (ksec)	Data Mode
Mrk 501	P20340-01-11-00	1997.05.07 05:49	1997.05.07 07:00	4.224	S1/S2/GX1/GX2
	P20340-01-12-00	1997.05.07 09:28	1997.05.07 09:50	1.28	S1/S2/GX1/GX2
	P20340-01-13-00	1997.05.08 06:53	1997.05.08 07:01	0.48	S1/S2/GX1/GX2
	P20340-01-14-00	1997.05.08 09:25	1997.05.08 10:17	3.104	S1/S2/GX1/GX2
	P20340-01-15-00	1997.05.09 06:53	1997.05.09 07:04	0.608	S1/S2/GX1/GX2
	P20340-01-16-00	1997.05.09 07:58	1997.05.09 08:40	2.528	S1/S2/GX1/GX2
	P20340-01-17-00	1997.05.10 05:14	1997.05.10 05:30	0.912	S1/S2/GX1/GX2
	P20340-01-18-00	1997.05.10 09:29	1997.05.10 09:59	1.744	S1/S2/GX1/GX2
	P20340-01-19-00	1997.05.11 05:13	1997.05.11 05:29	0.912	S1/S2/GX1/GX2
	P20340-01-20-00	1997.05.11 09:26	1997.05.11 09:42	0.912	S1/S2/GX1/GX2
	P20340-01-21-00	1997.05.12 04:22	1997.05.12 04:44	1.296	S1/S2/GX1/GX2
	P20340-01-22-00	1997.05.12 08:35	1997.05.12 08:45	0.608	S1/S2/GX1/GX2
	P20340-01-23-00	1997.05.13 04:32	1997.05.13 04:46	0.8	S1/S2/GX1/GX2
	P20340-01-24-00	1997.05.13 08:34	1997.05.13 08:46	0.72	S1/S2/GX1/GX2
	P20340-01-25-00	1997.05.14 08:32	1997.05.14 08:47	0.896	S1/S2/GX1/GX2
	P20340-01-26-00	1997.05.14 09:34	1997.05.14 09:51	0.976	S1/S2/GX1/GX2
	P20340-01-27-00	1997.05.15 04:26	1997.05.15 05:08	2.512	S1/S2/GX1/GX2
	P20340-01-28-00	1997.05.15 06:13	1997.05.15 06:49	2.128	S1/S2/GX1/GX2
	P20421-01-01-01	1997.07.11 23:23	1997.07.11 23:51	1.68	S1/S2/GX1/GX2
	P20421-01-01-00	1997.07.12 03:36	1997.07.12 05:09	5.536	S1/S2/GX1/GX2
	P20421-01-02-01	1997.07.12 23:22	1997.07.12 23:51	1.728	S1/S2/GX1/GX2
	P20421-01-02-00	1997.07.13 03:37	1997.07.13 05:09	5.472	S1/S2/GX1/GX2
	P20421-01-03-01	1997.07.13 23:21	1997.07.13 23:49	1.664	S1/S2/GX1/GX2
	P20421-01-03-00	1997.07.14 03:38	1997.07.14 04:48	4.16	S1/S2/GX1/GX2
	P20421-01-04-01	1997.07.14 22:50	1997.07.15 00:07	4.608	S1/S2/GX1/GX2
	P20421-01-04-00	1997.07.15 03:38	1997.07.15 04:55	4.624	S1/S2/GX1/GX2
	P20421-01-05-01	1997.07.15 22:51	1997.07.15 23:51	3.584	S1/S2/GX1/GX2
	P20421-01-05-00	1997.07.16 03:40	1997.07.16 04:55	4.512	S1/S2/GX1/GX2
	P30249-01-01-08	1998.05.25 03:46	1998.05.25 04:22	2.16	S1/S2/GX1/GX2
	P30249-01-01-00	1998.05.25 06:58	1998.05.25 11:08	14.992	S1/S2/GX1/GX2
	P30249-01-01-01	1998.05.25 12:44	1998.05.25 17:42	17.872	S1/S2/GX1/GX2
	P30249-01-01-02	1998.05.25 19:24	1998.05.25 20:11	2.816	S1/S2/GX1/GX2
	P30249-01-01-03	1998.05.25 21:04	1998.05.25 22:20	4.512	S1/S2/GX1/GX2
	P30249-01-01-04	1998.05.26 06:57	1998.05.26 11:08	15.056	S1/S2/GX1/GX2
	P30249-01-01-05	1998.05.26 14:23	1998.05.26 17:42	11.936	S1/S2/GX1/GX2
	P30249-01-01-09	1998.05.27 02:06	1998.05.27 02:36	1.808	S1/S2/GX1/GX2
	P30249-01-01-10	1998.05.27 03:45	1998.05.27 04:12	1.6	S1/S2/GX1/GX2
	P30249-01-01-06	1998.05.27 06:55	1998.05.27 11:08	15.168	S1/S2/GX1/GX2
	P30249-01-01-07	1998.05.27 12:44	1998.05.27 15:59	11.696	S1/S2/GX1/GX2

Table A.6: *RXTE* observation log of PKS 2155−304 (1)

Source Name	OBS-ID	Start (UT)	End (UT)	Exp. (ksec)	Data Mode
PKS 2155 −304	P10356-01-01-00	1996.05.16 00:40	1996.05.16 00:50	0.592	S1/S2/GX1/GX2
	P10356-01-02-00	1996.05.16 03:24	1996.05.16 03:47	1.36	S1/S2/GX1/GX2
	P10356-01-03-00	1996.05.16 06:15	1996.05.16 06:40	1.472	S1/S2/GX1/GX2
	P10356-01-04-00	1996.05.16 09:32	1996.05.16 09:42	0.544	S1/S2/GX1/GX2
	P10356-01-05-00	1996.05.16 12:38	1996.05.16 12:48	0.544	S1/S2/GX1/GX2
	P10356-01-06-00	1996.05.16 16:39	1996.05.16 17:09	1.76	S1/S2/GX1/GX2
	P10356-01-07-00	1996.05.16 19:03	1996.05.16 19:14	0.608	S1/S2/GX1/GX2
	P10356-01-08-00	1996.05.16 22:25	1996.05.16 22:41	0.912	S1/S2/GX1/GX2
	P10356-01-09-00	1996.05.17 01:45	1996.05.17 02:16	1.808	S1/S2/GX1/GX2
	P10356-01-10-00	1996.05.17 05:27	1996.05.17 05:49	1.296	S1/S2/GX1/GX2
	P10356-01-11-00	1996.05.17 07:09	1996.05.17 07:19	0.592	S1/S2/GX1/GX2
	P10356-01-12-00	1996.05.17 11:57	1996.05.17 12:14	0.976	S1/S2/GX1/GX2
	P10356-01-13-00	1996.05.17 15:51	1996.05.17 16:01	0.544	S1/S2/GX1/GX2
	P10356-01-14-00	1996.05.17 21:33	1996.05.17 21:58	1.472	S1/S2/GX1/GX2
	P10356-01-15-00	1996.05.18 02:16	1996.05.18 02:25	0.512	S1/S2/GX1/GX2
	P10356-01-16-00	1996.05.18 05:02	1996.05.18 05:11	0.528	S1/S2/GX1/GX2
	P10356-01-17-00	1996.05.18 07:10	1996.05.18 07:20	0.592	S1/S2/GX1/GX2
	P10356-01-18-00	1996.05.18 09:35	1996.05.18 09:45	0.56	S1/S2/GX1/GX2
	P10356-01-45-00	1996.05.18 13:28	1996.05.18 13:36	0.432	S1/S2/GX1/GX2
	P10356-01-20-00	1996.05.18 18:14	1996.05.18 18:37	1.344	S1/S2/GX1/GX2
	P10356-01-21-00	1996.05.18 21:33	1996.05.18 22:15	2.496	S1/S2/GX1/GX2
	P10356-01-19-00	1996.05.18 23:09	1996.05.18 23:55	2.736	S1/S2/GX1/GX2
	P10356-02-01-01	1996.05.19 01:45	1996.05.19 04:11	8.704	S1/S2/GX1/GX2
	P10356-02-01-00	1996.05.19 06:36	1996.05.19 07:31	3.248	S1/S2/GX1/GX2
	P10356-02-01-02	1996.05.19 14:30	1996.05.19 16:56	8.736	S1/S2/GX1/GX2
	P10356-02-01-03	1996.05.19 18:02	1996.05.19 20:34	9.072	S1/S2/GX1/GX2
	P10356-02-01-04	1996.05.19 22:26	1996.05.19 05:48	26.528	S1/S2/GX1/GX2
	P10356-02-01-07	1996.05.20 12:43	1996.05.20 13:45	3.664	S1/S2/GX1/GX2
	P10356-02-01-05	1996.05.20 19:55	1996.05.20 00:40	17.104	S1/S2/GX1/GX2
	P10356-01-23-00	1996.05.21 04:59	1996.05.21 05:07	0.48	S1/S2/GX1/GX2
	P10356-01-24-00	1996.05.21 07:15	1996.05.21 07:39	1.392	S1/S2/GX1/GX2
	P10356-01-25-00	1996.05.21 11:30	1996.05.21 11:44	0.8	S1/S2/GX1/GX2
	P10356-01-26-00	1996.05.21 14:59	1996.05.21 15:34	2.096	S1/S2/GX1/GX2
	P10356-01-27-00	1996.05.21 18:18	1996.05.21 18:55	2.176	S1/S2/GX1/GX2
	P10356-01-28-00	1996.05.21 21:37	1996.05.21 22:01	1.392	S1/S2/GX1/GX2
	P10356-01-29-00	1996.05.22 01:45	1996.05.22 01:55	0.56	S1/S2/GX1/GX2
	P10356-01-31-00	1996.05.22 04:58	1996.05.22 05:23	1.504	S1/S2/GX1/GX2
	P10356-01-30-00	1996.05.22 08:38	1996.05.22 08:48	0.576	S1/S2/GX1/GX2

Table A.7: *RXTE* observation log of PKS 2155−304 (2) *continued*

Source Name	OBS-ID	Start (UT)	End (UT)	Exp. (ksec)	Data Mode
PKS 2155 −304	P10356-01-33-00	1996.05.22 11:50	1996.05.22 12:29	2.32	S1/S2/GX1/GX2
	P10356-01-34-00	1996.05.22 17:35	1996.05.22 17:45	0.592	S1/S2/GX1/GX2
	P10356-01-35-00	1996.05.22 20:02	1996.05.22 20:25	1.376	S1/S2/GX1/GX2
	P10356-01-32-00	1996.05.22 23:15	1996.05.22 23:56	2.448	S1/S2/GX1/GX2
	P10356-01-36-00	1996.05.23 00:51	1996.05.23 01:33	2.512	S1/S2/GX1/GX2
	P10356-01-39-00	1996.05.23 04:56	1996.05.23 05:06	0.592	S1/S2/GX1/GX2
	P10356-01-38-00	1996.05.23 07:19	1996.05.23 07:42	1.344	S1/S2/GX1/GX2
	P10356-01-40-00	1996.05.23 10:31	1996.05.23 10:54	1.328	S1/S2/GX1/GX2
	P10356-01-41-00	1996.05.23 13:21	1996.05.23 13:37	0.928	S1/S2/GX1/GX2
	P10356-01-42-00	1996.05.23 18:21	1996.05.23 18:40	1.136	S1/S2/GX1/GX2
	P10356-01-43-00	1996.05.23 21:44	1996.05.23 22:05	1.216	S1/S2/GX1/GX2
	P10356-01-46-00	1996.05.24 03:32	1996.05.24 03:42	0.592	S1/S2/GX1/GX2
	P10356-01-47-00	1996.05.24 06:26	1996.05.24 06:36	0.56	S1/S2/GX1/GX2
	P10357-01-01-00	1996.05.24 08:02	1996.05.24 08:27	1.456	S1/S2/GX1/GX2
	P10356-01-48-00	1996.05.24 08:27	1996.05.24 08:39	0.72	S1/S2/GX1/GX2
	P10356-01-49-00	1996.05.24 11:44	1996.05.24 11:55	0.624	S1/S2/GX1/GX2
	P10356-01-50-00	1996.05.24 14:27	1996.05.24 14:37	0.544	S1/S2/GX1/GX2
	P10356-01-52-00	1996.05.24 17:39	1996.05.24 17:49	0.56	S1/S2/GX1/GX2
	P10356-01-51-00	1996.05.24 20:05	1996.05.24 20:29	1.408	S1/S2/GX1/GX2
	P10356-01-53-00	1996.05.24 23:18	1996.05.24 23:48	1.792	S1/S2/GX1/GX2
	P10356-01-54-00	1996.05.25 03:23	1996.05.25 03:47	1.424	S1/S2/GX1/GX2
	P10356-01-56-00	1996.05.25 08:55	1996.05.25 09:07	0.704	S1/S2/GX1/GX2
	P10356-01-57-00	1996.05.25 13:17	1996.05.25 13:56	2.32	S1/S2/GX1/GX2
	P10356-01-58-00	1996.05.25 16:41	1996.05.25 17:08	1.6	S1/S2/GX1/GX2
	P10356-01-59-00	1996.05.25 20:06	1996.05.25 20:28	1.312	S1/S2/GX1/GX2
	P10356-01-60-00	1996.05.25 23:20	1996.05.25 23:45	1.504	S1/S2/GX1/GX2
	P10356-01-61-00	1996.05.26 02:30	1996.05.26 02:42	0.72	S1/S2/GX1/GX2
	P10356-01-62-00	1996.05.26 05:43	1996.05.26 05:56	0.784	S1/S2/GX1/GX2
	P10356-01-63-00	1996.05.26 10:04	1996.05.26 10:16	0.704	S1/S2/GX1/GX2
	P10356-01-64-00	1996.05.26 13:16	1996.05.26 13:53	2.192	S1/S2/GX1/GX2
	P10356-01-66-00	1996.05.26 16:15	1996.05.26 16:23	0.464	S1/S2/GX1/GX2
	P10357-01-02-00	1996.05.26 16:23	1996.05.26 17:01	2.272	S1/S2/GX1/GX2
	P10356-01-68-00	1996.05.26 23:20	1996.05.26 23:43	1.376	S1/S2/GX1/GX2
	P10356-01-73-00	1996.05.27 02:33	1996.05.27 02:45	0.72	S1/S2/GX1/GX2
	P10356-01-69-00	1996.05.27 08:59	1996.05.27 09:09	0.592	S1/S2/GX1/GX2
	P10356-01-70-00	1996.05.27 11:38	1996.05.27 11:52	0.8	S1/S2/GX1/GX2
	P10356-01-71-00	1996.05.27 15:00	1996.05.27 15:19	1.104	S1/S2/GX1/GX2
	P10356-01-72-00	1996.05.27 20:09	1996.05.27 20:22	0.752	S1/S2/GX1/GX2
	P10356-01-74-00	1996.05.27 23:22	1996.05.27 23:41	1.136	S1/S2/GX1/GX2

Table A.8: *RXTE* observation log of PKS 2155−304 (3) *continued*

Source Name	OBS-ID	Start (UT)	End (UT)	Exp. (ksec)	Data Mode
PKS 2155 −304	P10356-01-75-00	1996.05.28 03:54	1996.05.28 04:06	0.704	S1/S2/GX1/GX2
	P10357-01-03-00	1996.05.28 14:43	1996.05.28 15:26	2.544	S1/S2/GX1/GX2
	P10357-01-04-00	1996.07.23 09:02	1996.07.23 09:34	1.904	S1/S2/GX1/GX2
	P10357-01-05-00	1996.07.25 15:55	1996.07.25 16:27	1.888	S1/S2/GX1/GX2
	P10357-01-06-00	1996.07.27 15:57	1996.07.27 16:23	1.504	S1/S2/GX1/GX2
	P10357-01-07-00	1996.11.14 07:39	1996.11.14 14:56	26.176	S1/S2/GX1/GX2
	P10357-01-07-01	1996.11.15 15:44	1996.11.15 16:02	1.088	S1/S2/GX1/GX2
	P10356-02-03-00	1996.11.20 09:33	1996.11.20 09:58	1.456	S1/S2/GX1/GX2
	P10356-02-04-00	1996.11.20 17:39	1996.11.20 17:58	1.104	S1/S2/GX1/GX2
	P10356-02-05-00	1996.11.21 07:37	1996.11.21 08:02	1.456	S1/S2/GX1/GX2
	P10356-02-06-00	1996.11.22 03:00	1996.11.22 03:16	0.912	S1/S2/GX1/GX2
	P10356-02-07-00	1996.11.22 14:17	1996.11.22 14:32	0.912	S1/S2/GX1/GX2
	P10356-02-02-00	1996.11.23 10:38	1996.11.23 16:24	20.768	S1/S2/GX1/GX2
	P10356-02-02-01	1996.11.24 07:38	1996.11.24 13:12	20.032	S1/S2/GX1/GX2
	P30253-01-42-00	1997.11.20 22:54	1997.11.20 23:25	1.808	S1/S2/GX1/GX2
	P30253-01-41-00	1997.11.21 15:21	1997.11.21 15:37	0.944	S1/S2/GX1/GX2
	P30253-01-40-00	1997.11.22 17:09	1997.11.22 17:24	0.88	S1/S2/GX1/GX2
	P30253-01-01-00	1998.01.09 03:07	1998.01.09 03:29	1.296	S1/S2/GX1/GX2
	P30253-01-02-00	1998.01.09 12:49	1998.01.09 13:05	0.912	S1/S2/GX1/GX2
	P30253-01-03-00	1998.01.10 03:09	1998.01.10 03:30	1.216	S1/S2/GX1/GX2
	P30253-01-04-00	1998.01.10 12:54	1998.01.10 13:09	0.88	S1/S2/GX1/GX2
	P30253-01-05-00	1998.01.11 07:24	1998.01.11 07:39	0.896	S1/S2/GX1/GX2
	P30253-01-06-00	1998.01.11 12:12	1998.01.11 12:24	0.72	S1/S2/GX1/GX2
	P30253-01-07-00	1998.01.12 05:51	1998.01.12 06:04	0.736	S1/S2/GX1/GX2
	P30253-01-08-00	1998.01.12 14:22	1998.01.12 14:46	1.408	S1/S2/GX1/GX2
	P30253-01-09-00	1998.01.13 03:12	1998.01.13 03:33	1.216	S1/S2/GX1/GX2
	P30253-01-10-00	1998.01.13 14:24	1998.01.13 14:46	1.28	S1/S2/GX1/GX2

[a] proposal ID and observation plan number.

[b] *RXTE* PCA data mode. S1: *standard*-1 mode, S2: *standard*-2 mode, GX1: *GoodXenon*1-16*s* mode, GX2: *GoodXenon*2-16*s* mode.

Appendix B

DCF Distributions of Mrk 421 during 1998 Campaign
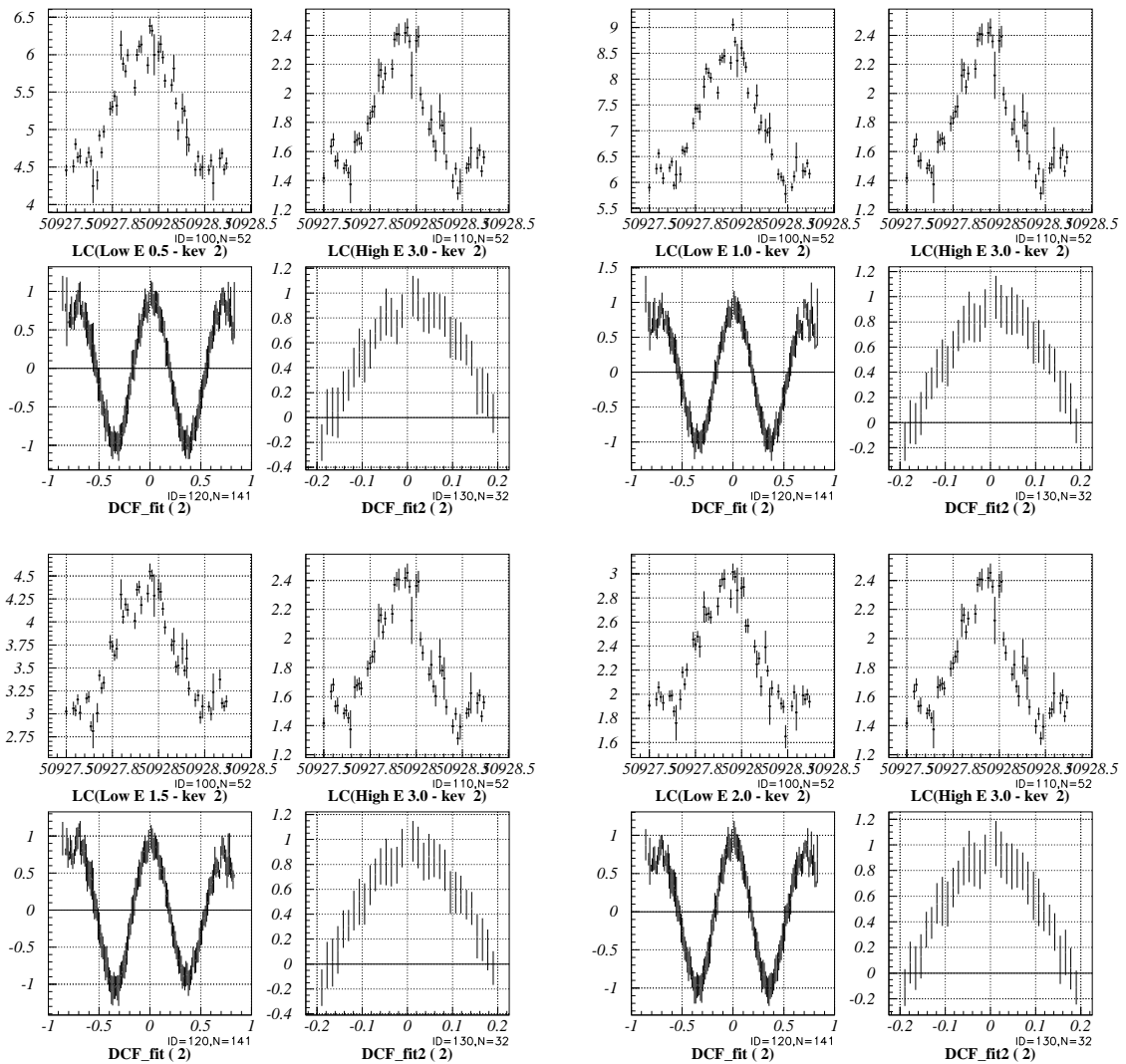
Figure B.1: DCF of time segment 2 for Mrk 421 in 1998.
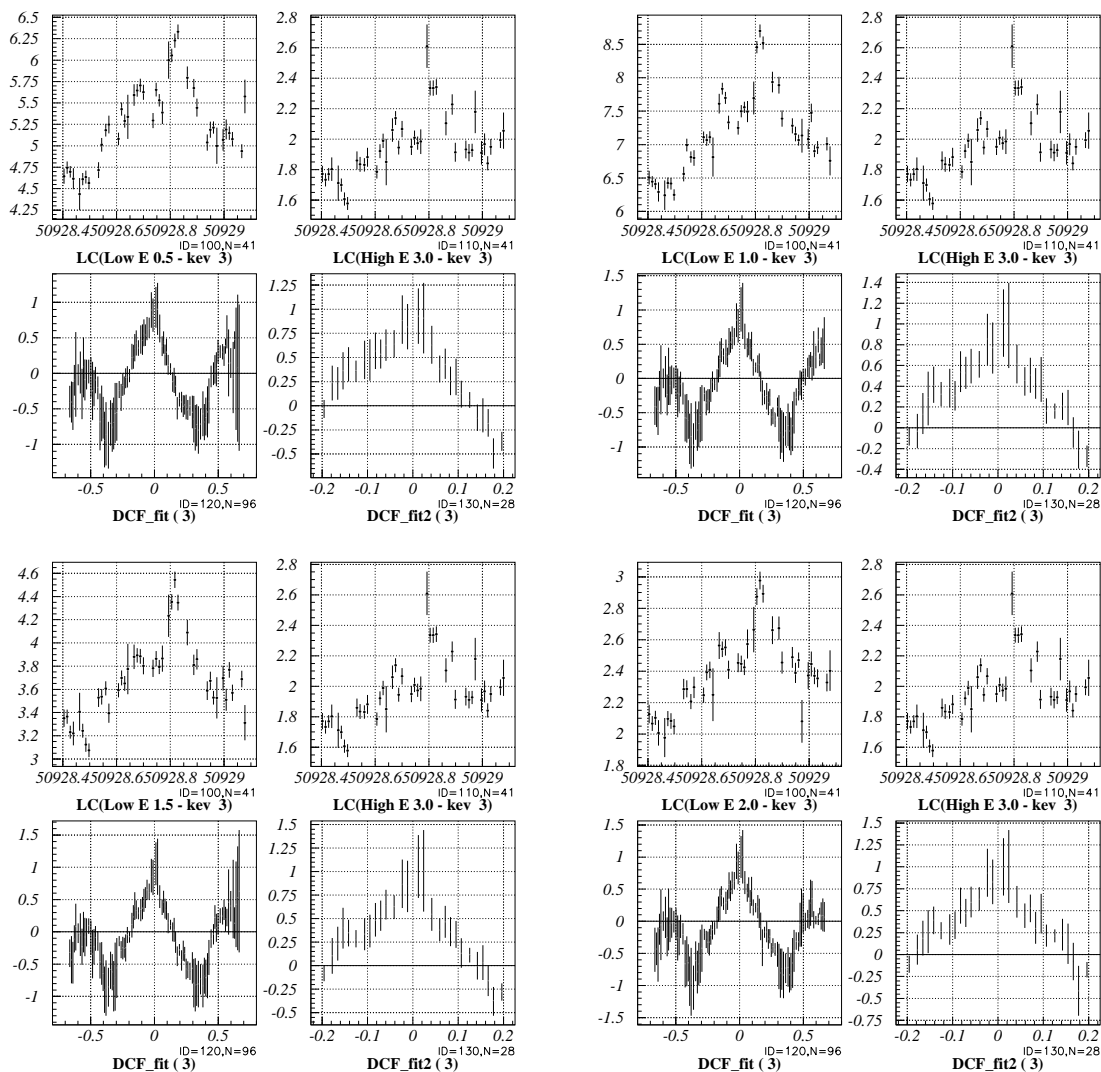
Figure B.2: DCF of time segment 3 for Mrk 421 in 1998.
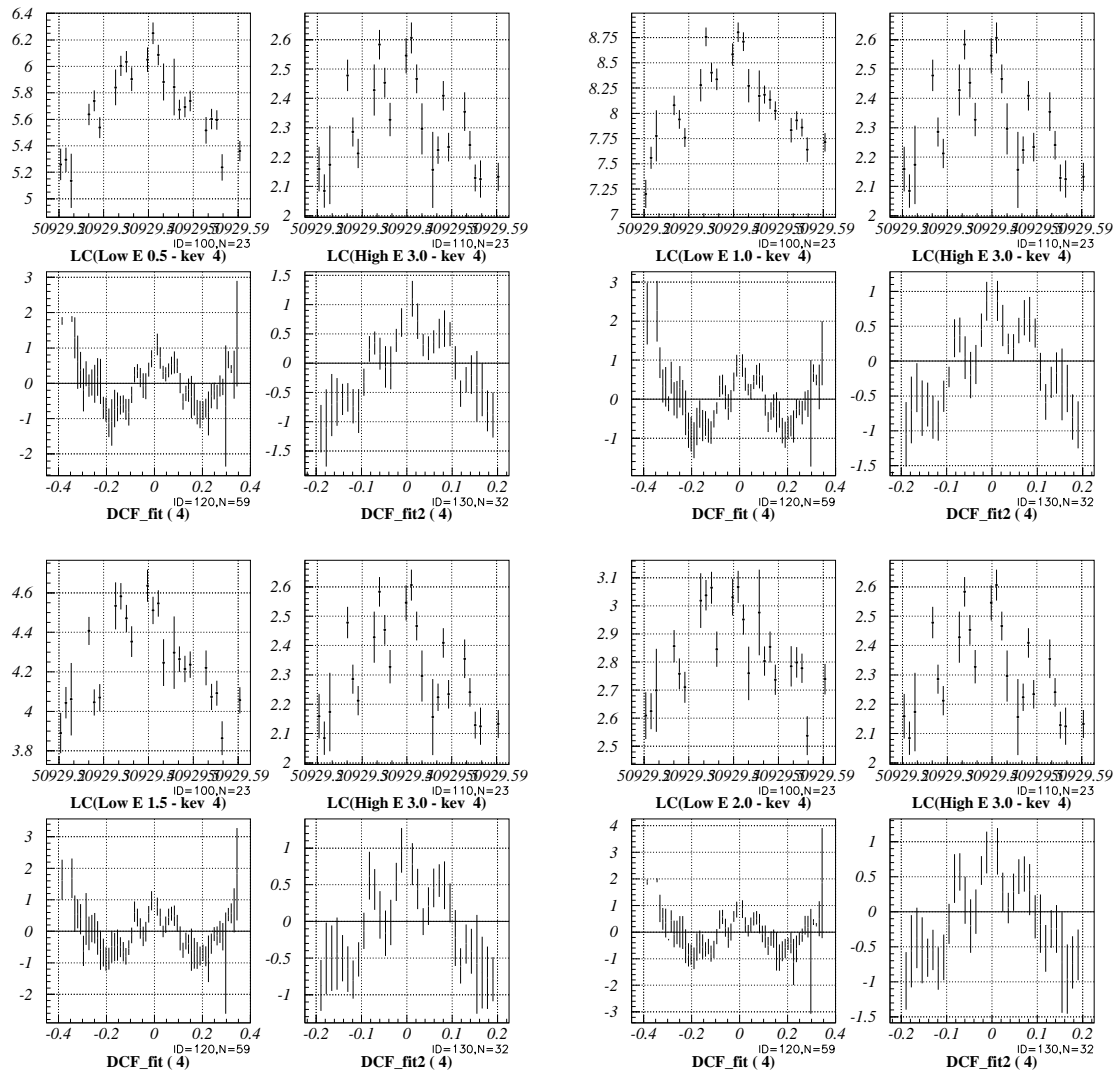
Figure B.3: DCF of time segment 4 for Mrk 421 in 1998.
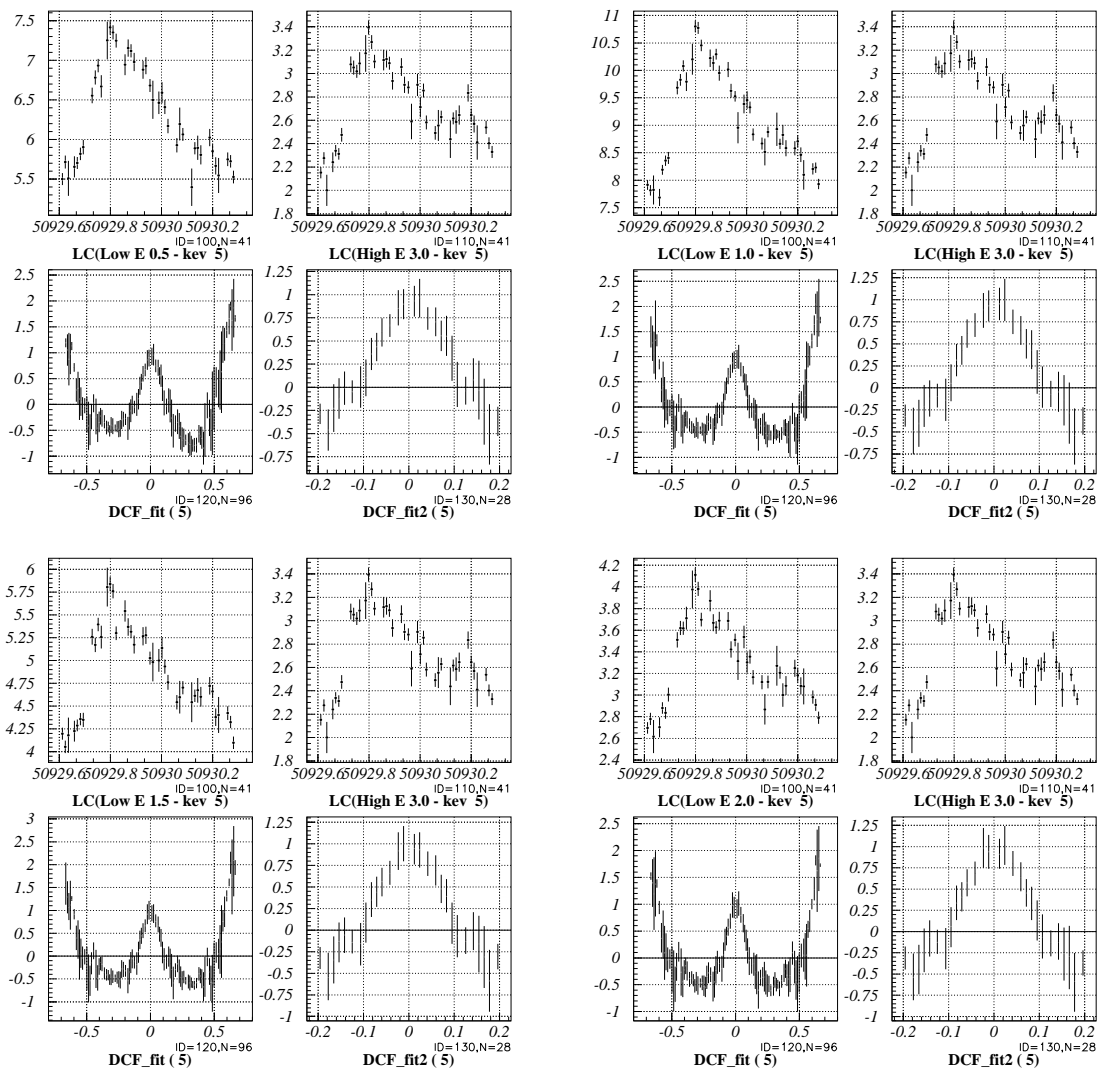
Figure B.4: DCF of time segment 5 for Mrk 421 in 1998.
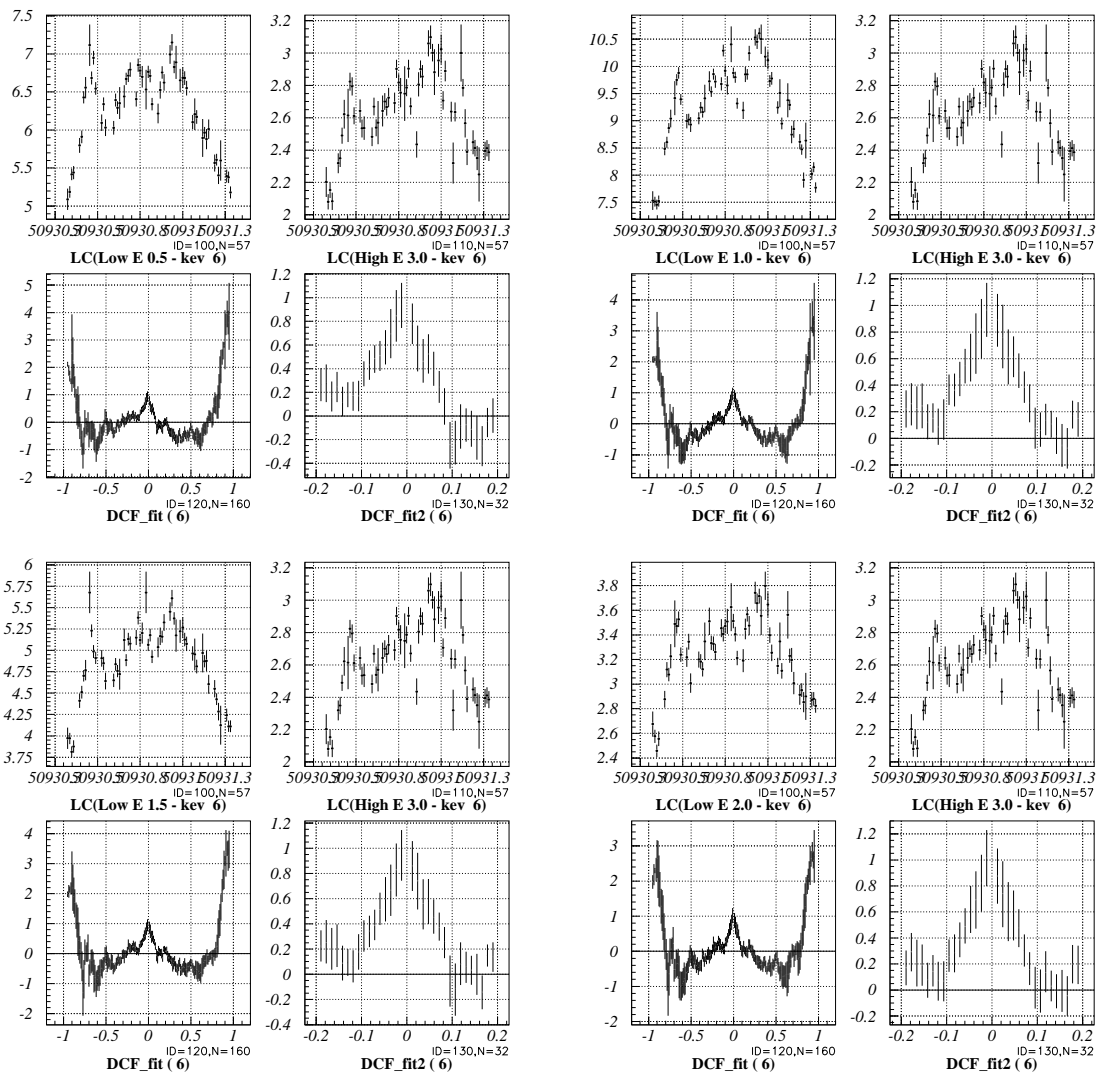
Figure B.5: DCF of time segment 6 for Mrk 421 in 1998.
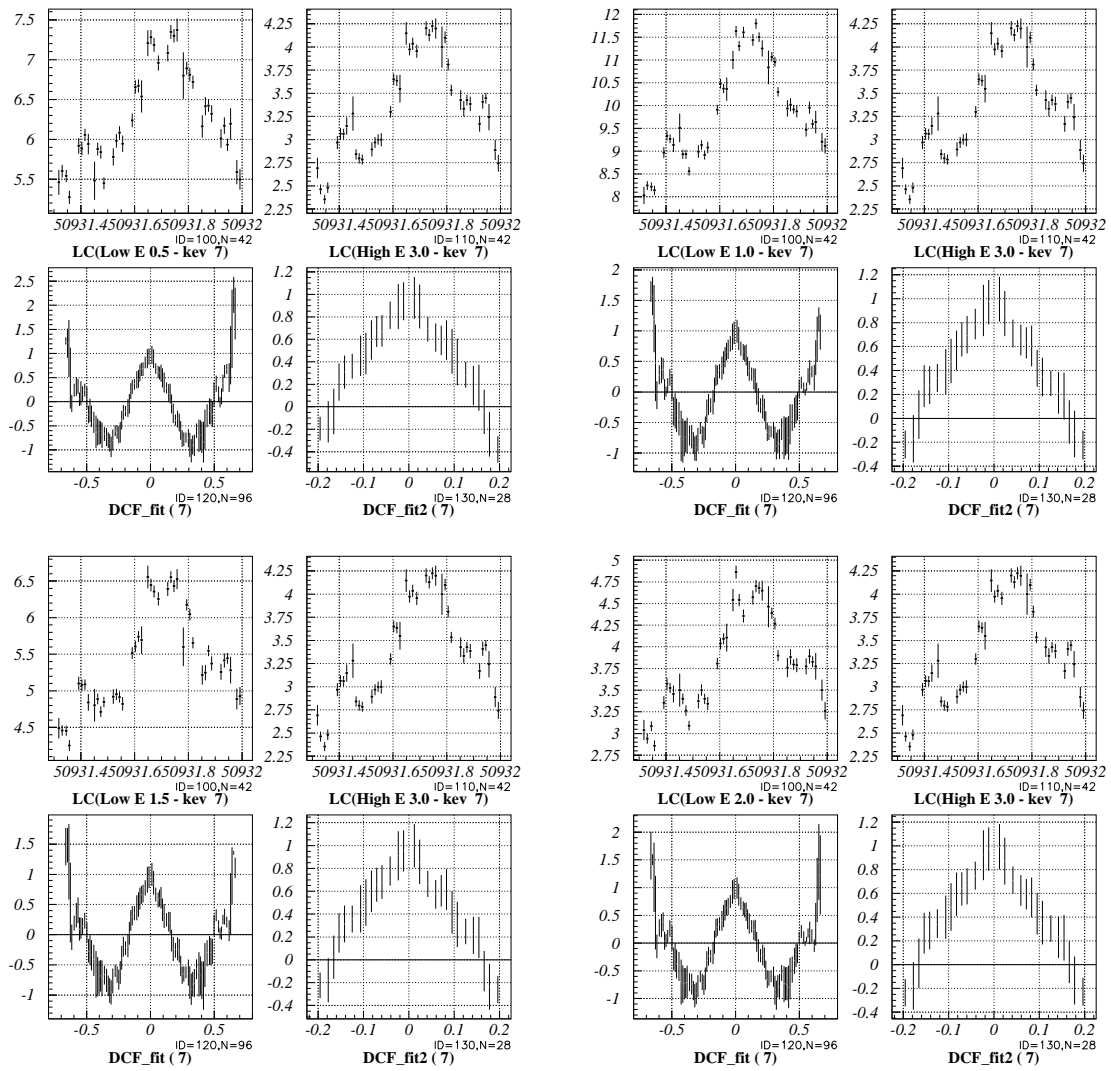
Figure B.6: DCF of time segment 7 for Mrk 421 in 1998.
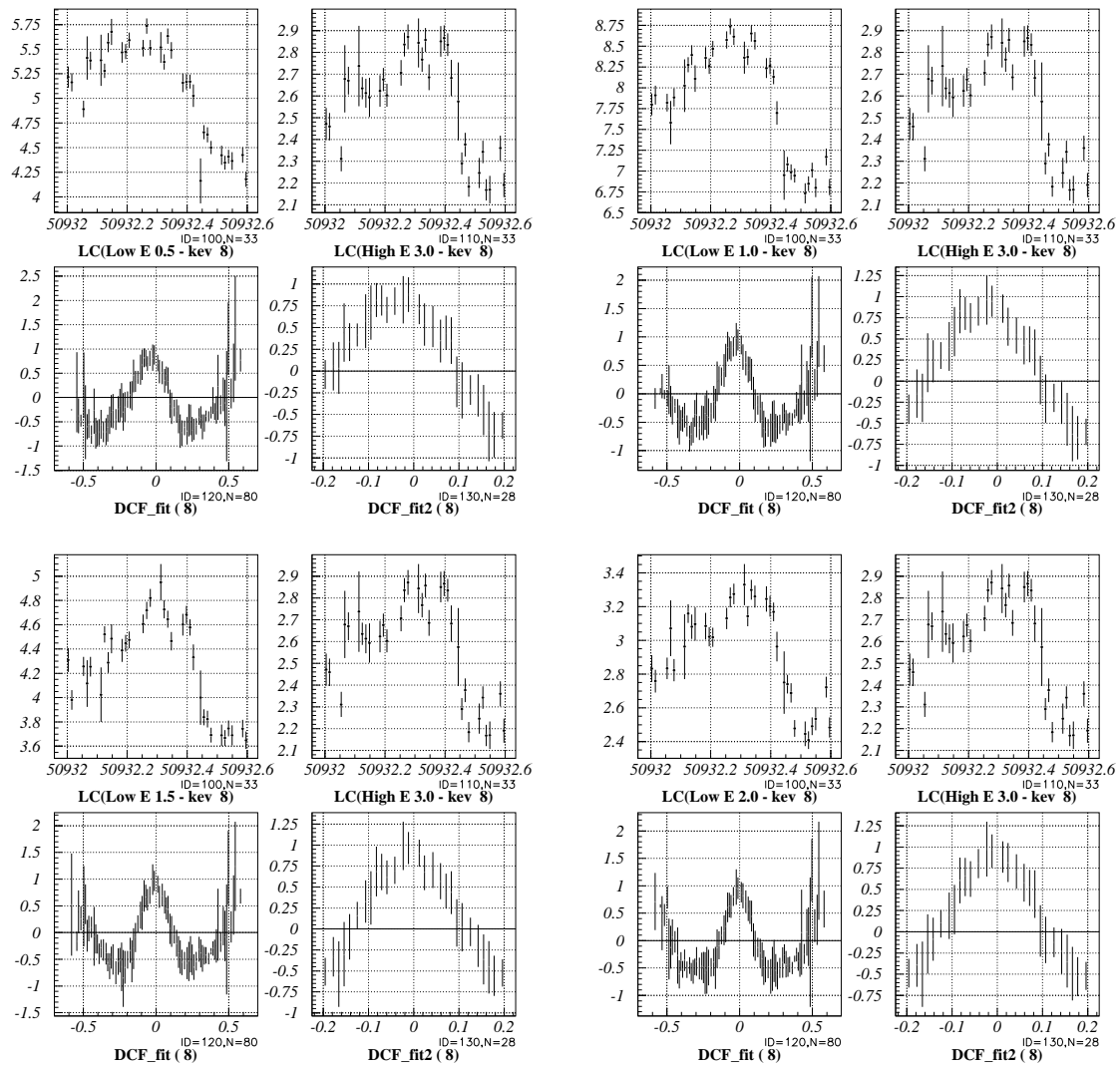
Figure B.7: DCF of time segment 8 for Mrk 421 in 1998.
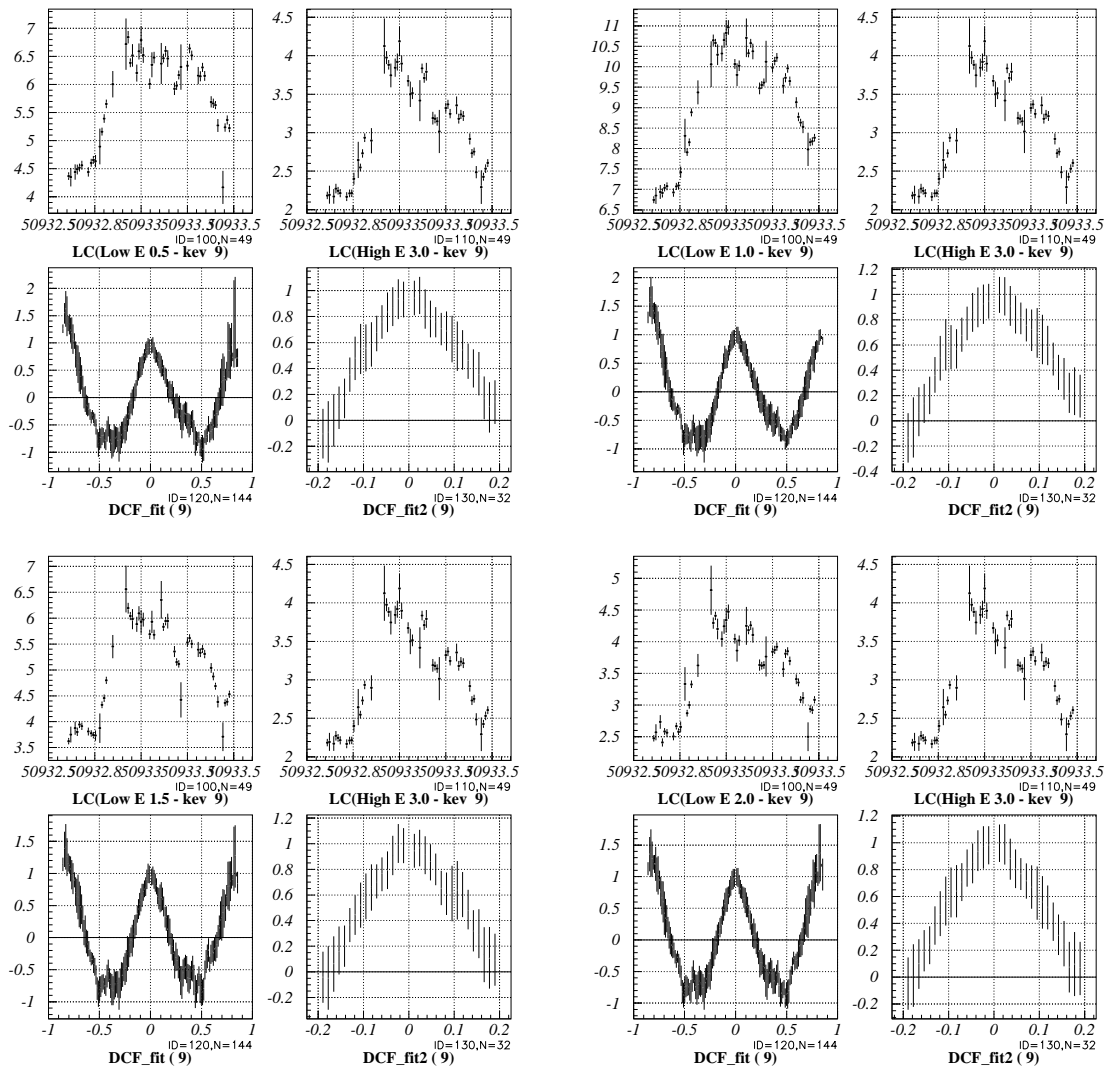
Figure B.8: DCF of time segment 9 for Mrk 421 in 1998.

Appendix C

Estimation of Errors in the Temporal Analysis

C.1   Errors on Lags Estimated from the Monte Calro Simulations

In § 7.2.5, the errors on the lags were simply determined from the uncertainty (1 σ error) of the peak parameter obtained by the minimum χ^2 fitting of the distribution DCF to a Gaussian. More accurately, errors on the lags should be determined by taking the flux uncertainties due to photon statistics into account. The statistical significance of the detection of a lag may not be assessed just by a cross-correlation analysis. In order to test the dependence of our DCF results on photon statistics and estimate the errors on the lags more properly, we apply Monte Calro simulation method which considers the flux randomization (e.g., Zhang et al. 1999).

We assumed that errors on fluxes resulting from the total photon number in a bin (more than a thousand in our case) are normally distributed. We modified each real flux at a certain time ($F(t)$) by adding a random Gaussian deviation based on the quoted error $\sigma_F(t)$ for each data point of the light curves. The modification of each data point is randomly determined from Monte Calro simulations, thus statistically independent of each other. We apply the DCF to each 'randomized' light curves and investigate the distribution of the 'time-lag'. This process was repeated for 2000 times to build up a cross-correlation peak distribution. We defined the errors on the 'lag' as the 68 % (i.e., 1 σ) of the time-lags are included in the range.

In Figure C.1, we show the results of Monte Calro simulation for two time segments of Mrk 421 observation in 1998. Time-region #2 is where the maximum 'soft-lag' was

observed and time-region #8 is the region of an opposite sense ('hard-lag'; Figure 7.23). One finds that errors on the lags determined from Monte Calro simulation are exactly consistent with the that determined from the uncertainties of the peak parameter in DCF distribution fitted to a Gaussian function. Thus we conclude that the statistical significance of detection of time-lags is not affected even if we take uncertainty in observed fluxes into account.
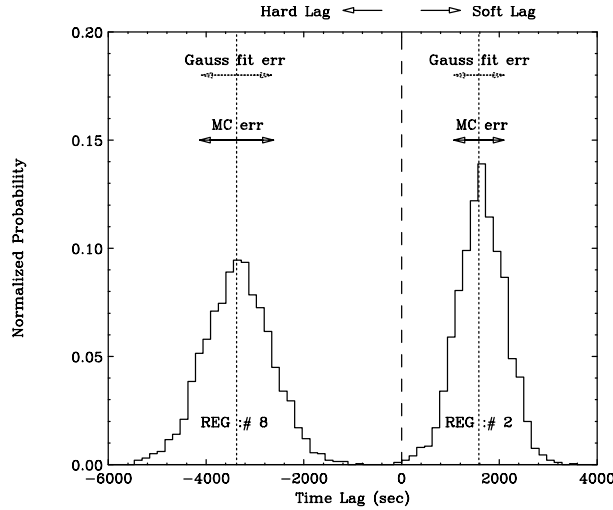
Figure C.1: Errors on time-lags determined from the Monte Calro Simulation (solid arrows). Two examples for Mrk 421 observation in 1998 are shown in the figure. Time-region #2, where the maximum 'soft-lag' was observed and time-region #8, where the maximum 'hard-lag' was observed (see, Figure 7.8, C.2). Lags are calculated for the light curve of 0.5-1.0 keV band as compared to that in 3.0-7.5 keV. Errors are exactly consistent with the previous estimation in which the error was determined from uncertainty of the peak parameter obtained by the minimum χ^2 fitting of the distribution of DCF to a Gaussian (dotted arrows).

C.2   Analysis of De-Trended Light Curves

During 7-day observation of Mrk 421 in 1998, successive occurrence of flares has been observed. These day-by-day flares are superposed on each other, forming an 'offset' in the light curves. Such an offset, or long-term trend, seems to become larger as photon energy increases (Figure 9.2). This is because the amplitude of a flare is larger at increasing photon energy (e.g., § 7.2.2). Thus it is important to verify that these energy-dependent 'offset' do not affect our analysis results. To evaluate the effect quantitatively, we fitted the light curves of Mrk 421 (1998) with a quadratic function, then subtracted the best fit function as a 'trend' (see, Figure C.2 (*left*)). Fittings were performed in various energy

bands from 0.5 keV to 7.5 keV.

Time Lags

Upper right panel of Figure C.2 shows a de-trended light curves in total *ASCA* band (0.5−7.5 keV). Bottom panel shows the time-lags for de-trended light curves in 0.5−1 keV band as compared to that in 3−7.5 keV. Corresponding figure for the original light curve (with 'offset') is Figure C.2 (*left*). One finds that results from de-trended light curves are exactly consistent with that calculated for the original light curves.
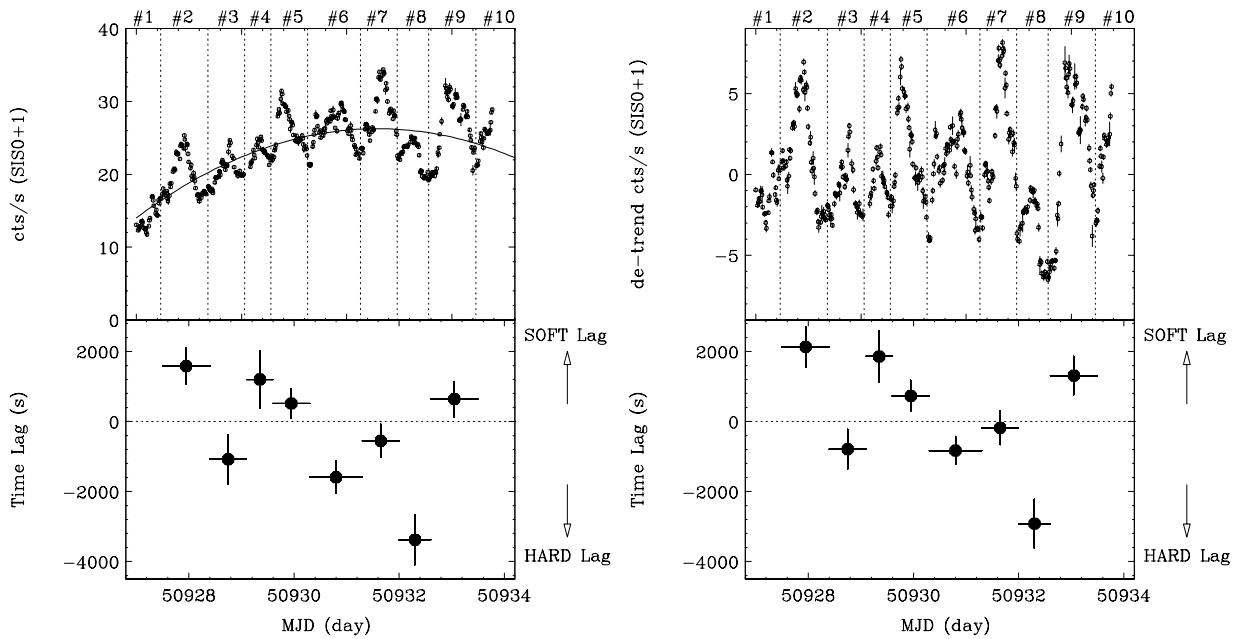
Figure C.2: Time lags of Mrk 421 during 1998 observation. *left* (*upper*); the SIS light curve for total *ASCA* bandpass (0.5−7.5 keV). The best fit quadratic function is shown as a solid line. *left* (*bottom*); time lags of 0.5-1.0 keV band as compared to that in 3.0−7.5 keV. *right* (*upper*); the SIS light curve after subtracting a quadratic trend. *right* (*bottom*); time lags of 0.5-1.0 keV band as compared to that in 3.0−7.5 keV. Results are exactly consistent with that in the left panel.

Time Asymmetry

We next calculate the structure function for these 'de-trended' light curves. For the structure function analysis, however, it is not evident that 'trend (offset)' should be removed or not. Some authors do this, while others argue strong objections (e.g., Smith et al. 1993). Remaining trend in the light curve may suppress the very features one is searching for, in particular, source has periodicity in short time scale. On the other hand, removal of the trend prevents us from investing time scales exceeding the length of the data run (Smith

et al. 1993). This should be carefully determined according to a purpose of the temporal study as well as the nature of time variability in the source.

In any case, we calculate the structure function using de-trended light curves in various energy bands. An example for SF is given in Figure C.3 (*left*). One can see that the slope of SF is unchanged in shorter time scale ($\tau < 1$ day; α 1.1−1.2).

We next measured time asymmetry of the light curve (Figure C.3 *right*). One can see a similar energy depencence with Figure 7.14, even if a quadratic trend is subtracted. We thus conclude that (1) rapid variability in TeV blazars is strong red noise type, and (2) time profile becomes more symmetric at higher energy bands regardless of 'trend' in the light curve.
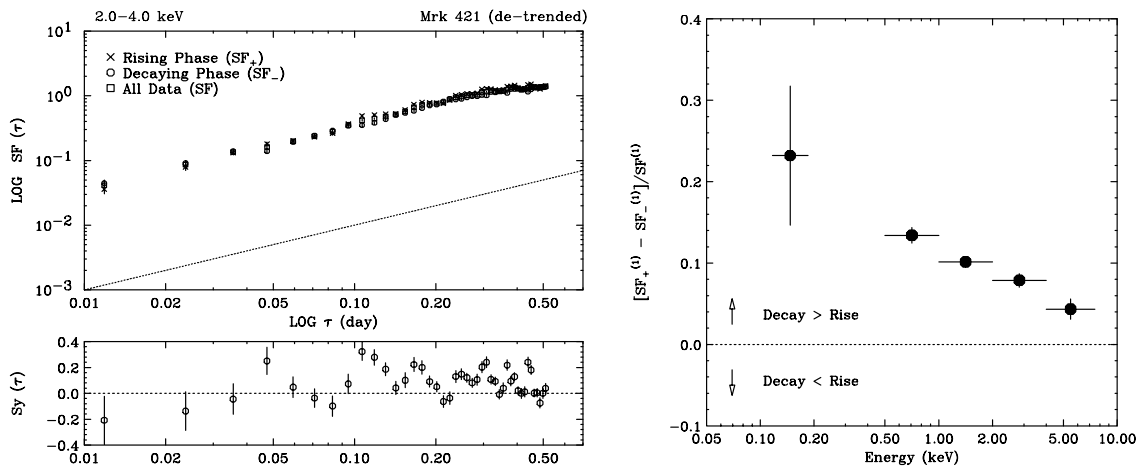
Figure C.3: *left*: Symmetry of the light curves for Mrk 421 in 2.0−4.0 keV. SF from rising phase and decaying phase are separately shown. Dotted line is SF(τ) ∝ τ to guide eyes. bottom panel shows the symmetry parameter. *right*: Energy dependence of the averaged symmetry parameter [SF$_+$ − SF$_-$]/SF, which was calculated for the time lags smaller than 0.5 day. We subtracted the best-fit quadratic function as a 'trend' from the original light curves. One can see that our results are not affected even if the 'trend' is subtracted (for comparison, see, Figure 7.14).

Appendix D

ASCA Spectra of TeV blazars
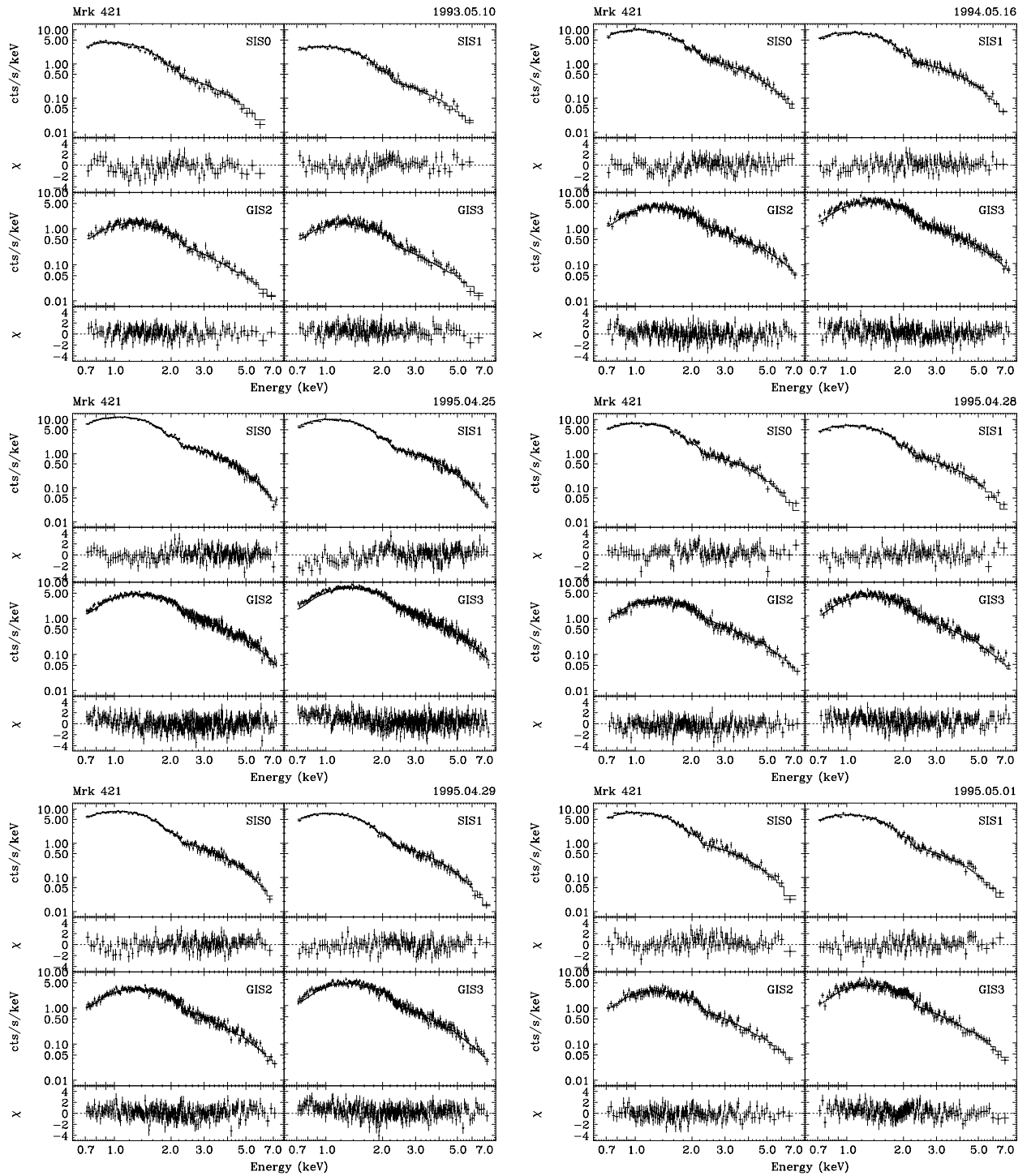
Figure D.1: Energy spectra of Mrk 421 (1).
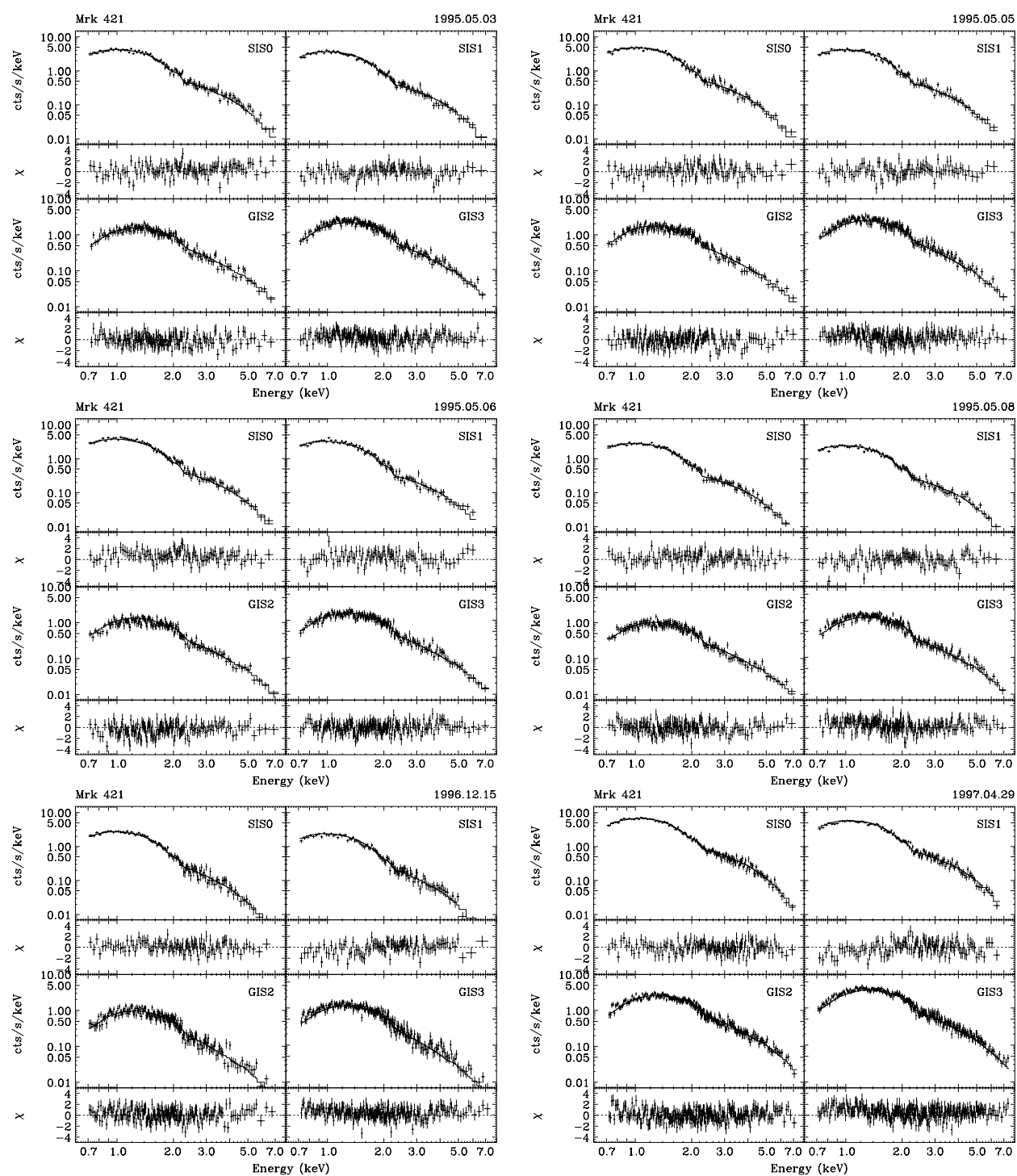
Figure D.2: Energy spectra of Mrk 421 (2).
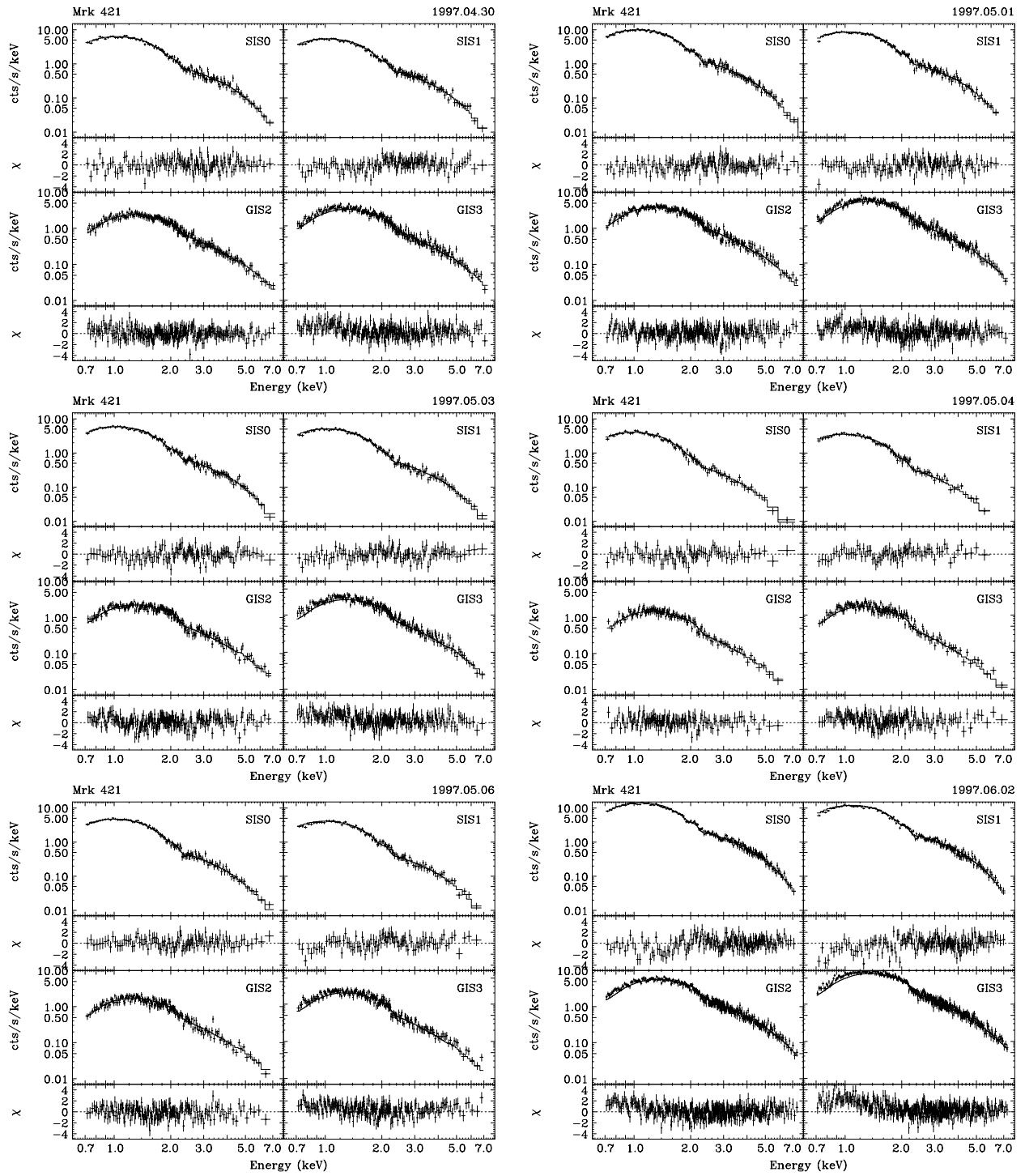
Figure D.3: Energy spectra of Mrk 421 (3).
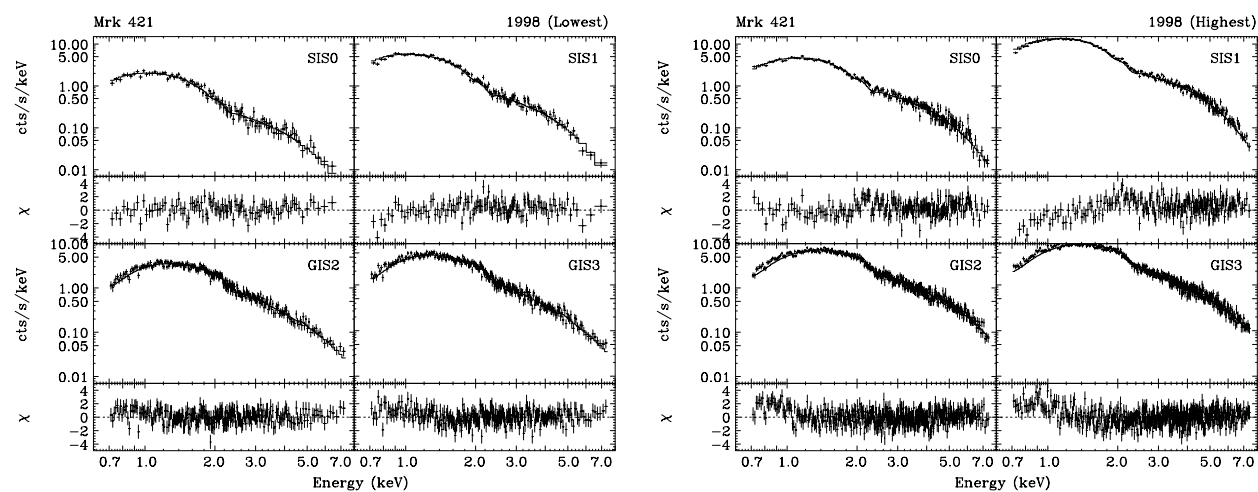
Figure D.4: *ASCA* energy spectra of Mrk 421 (4).
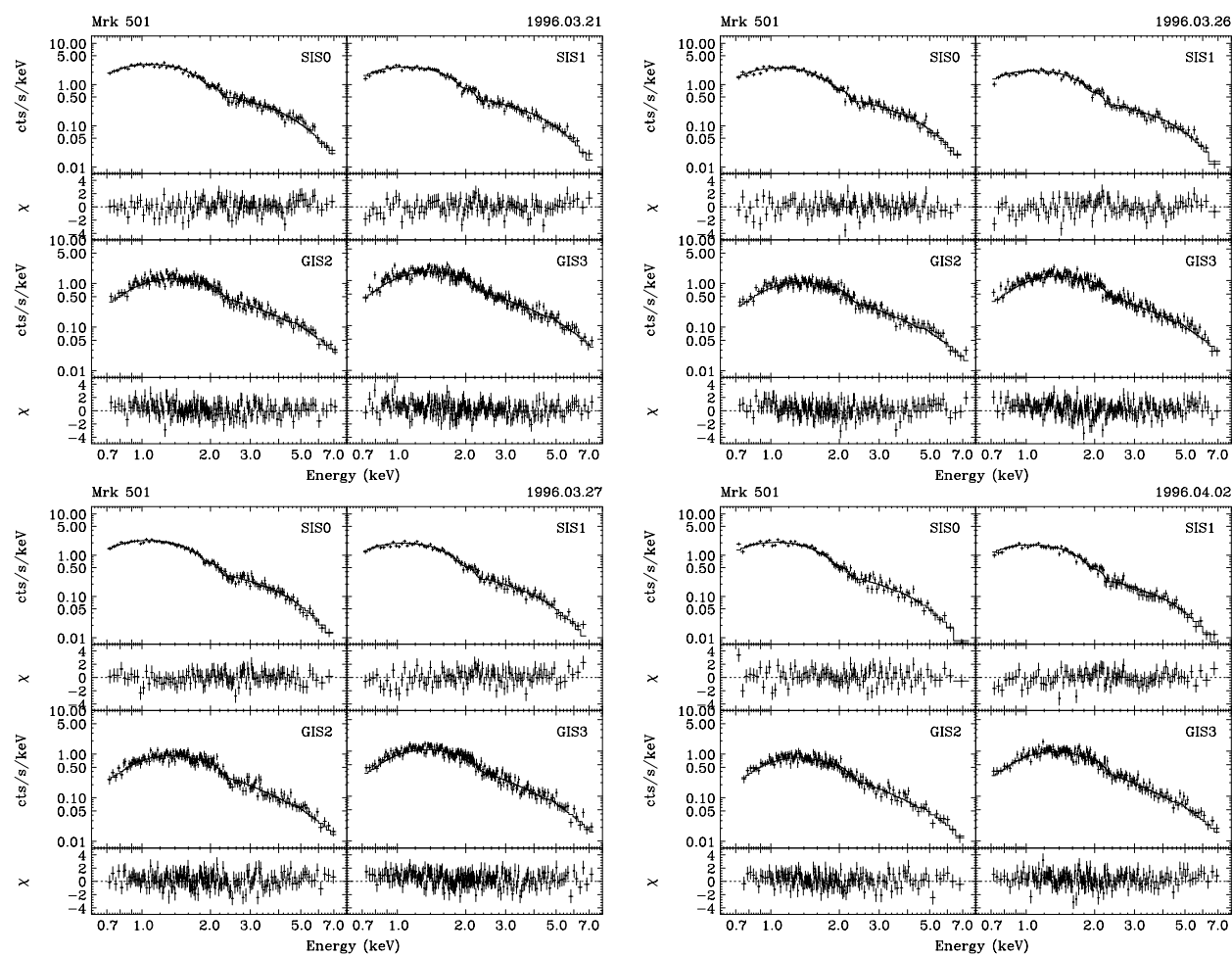
Figure D.5: *ASCA* energy spectra of Mrk 501 (1).
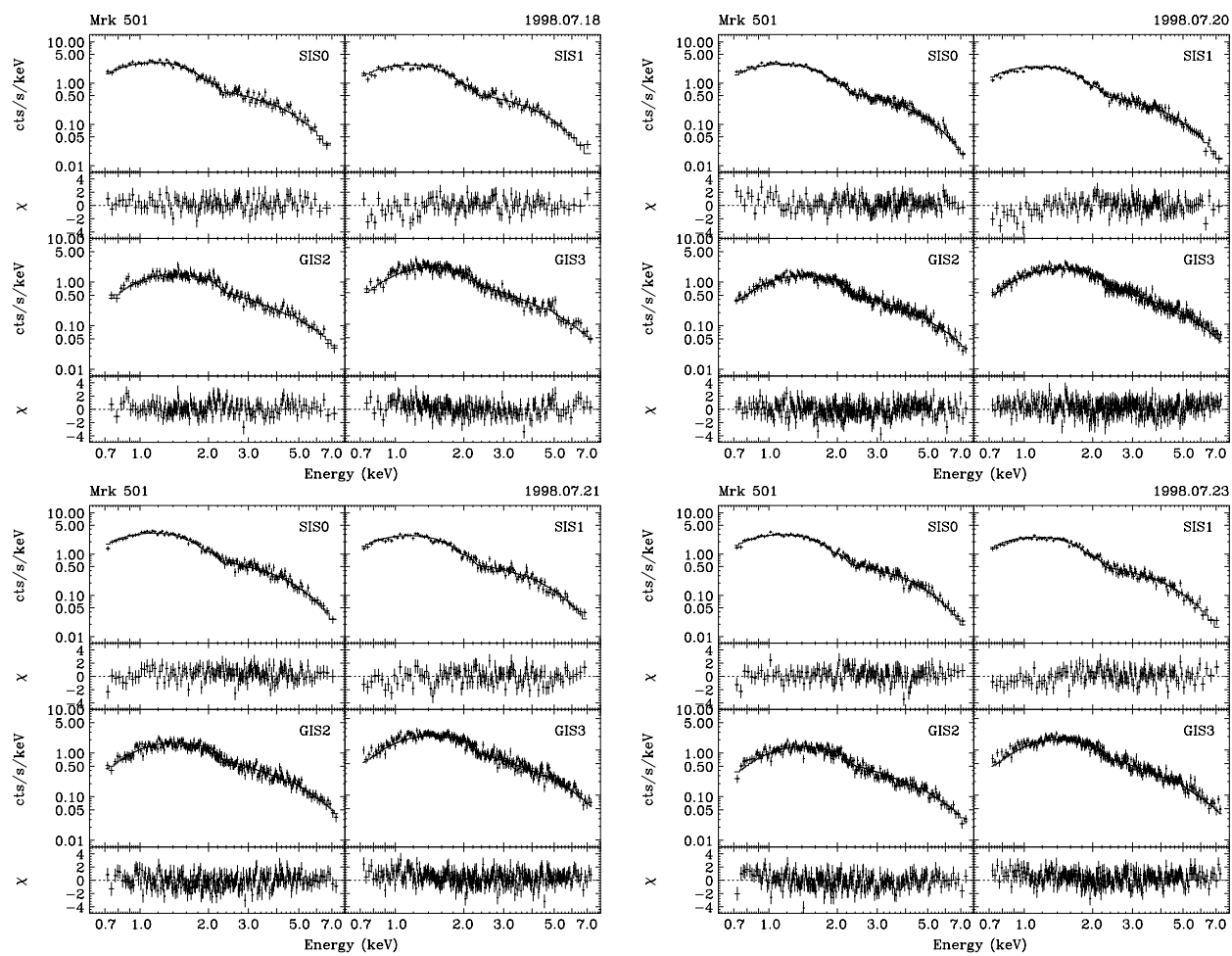
Figure D.6: *ASCA* energy spectra of Mrk 501 (2).
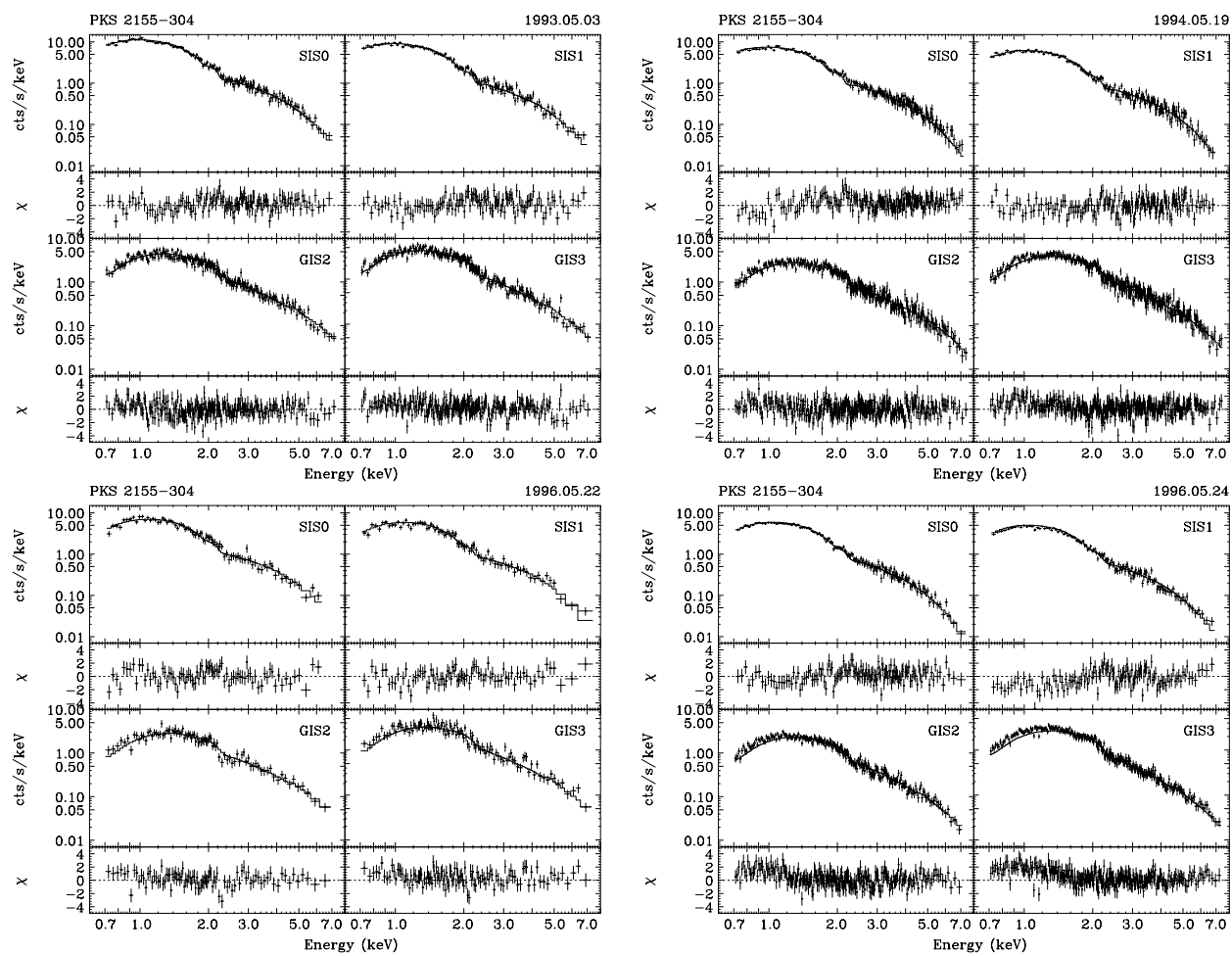
Figure D.7: *ASCA* energy spectra of PKS 2155−304 (1).
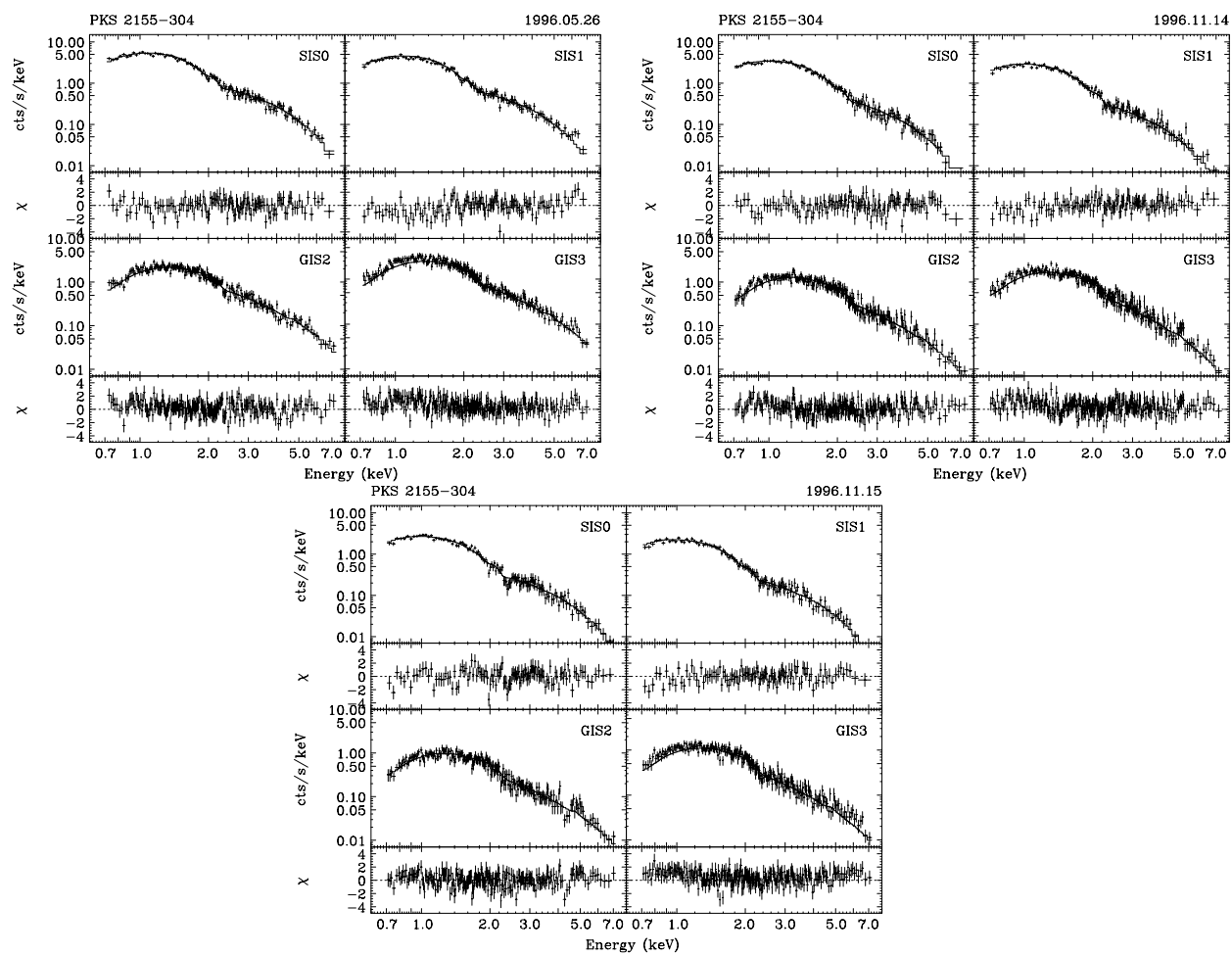
Figure D.8: *ASCA* energy spectra of PKS 2155−304 (2).
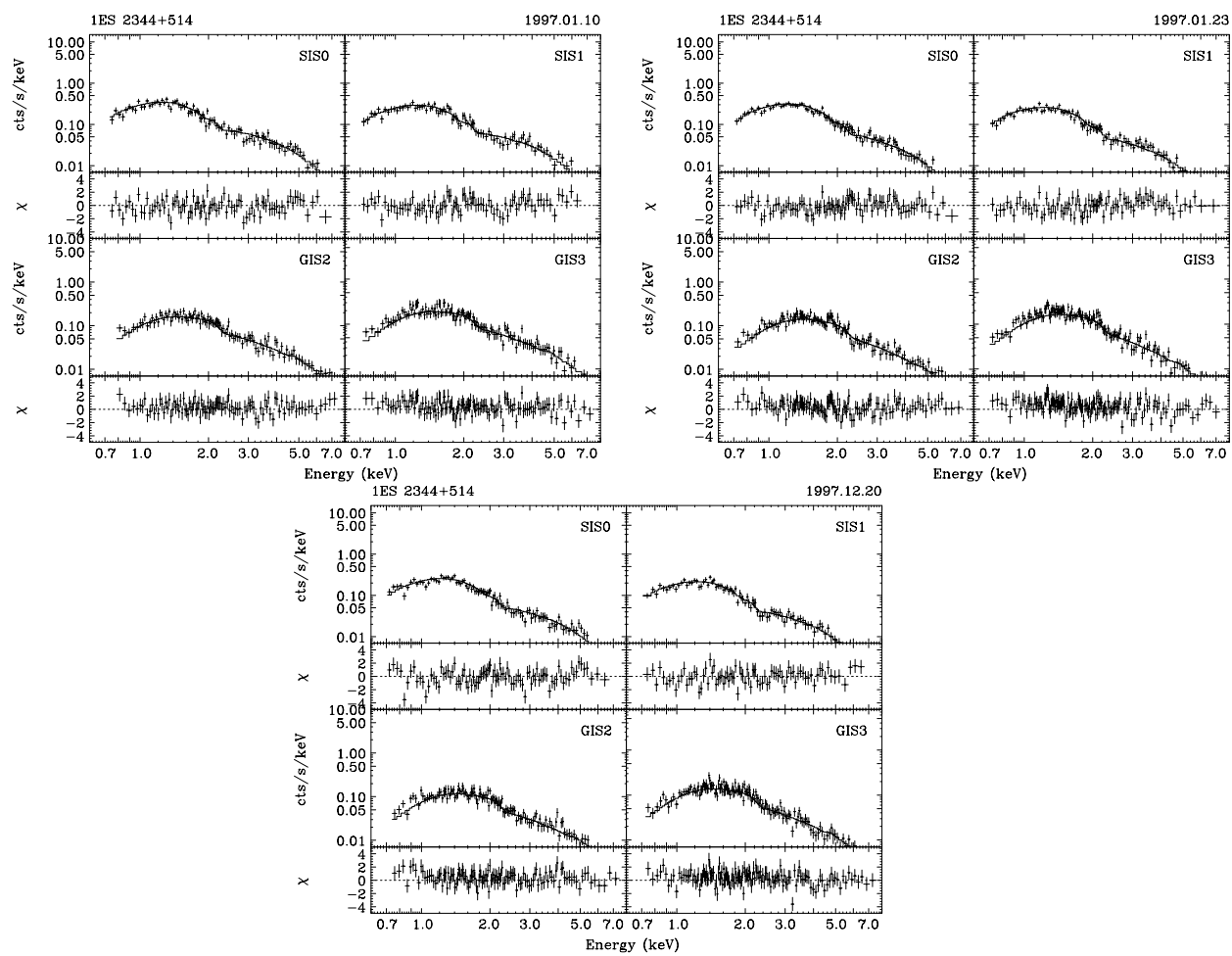
Figure D.9: *ASCA* energy spectra of 1ES 2344+514 (1).

Appendix E

Synchrotron Peak Shifts of TeV blazars
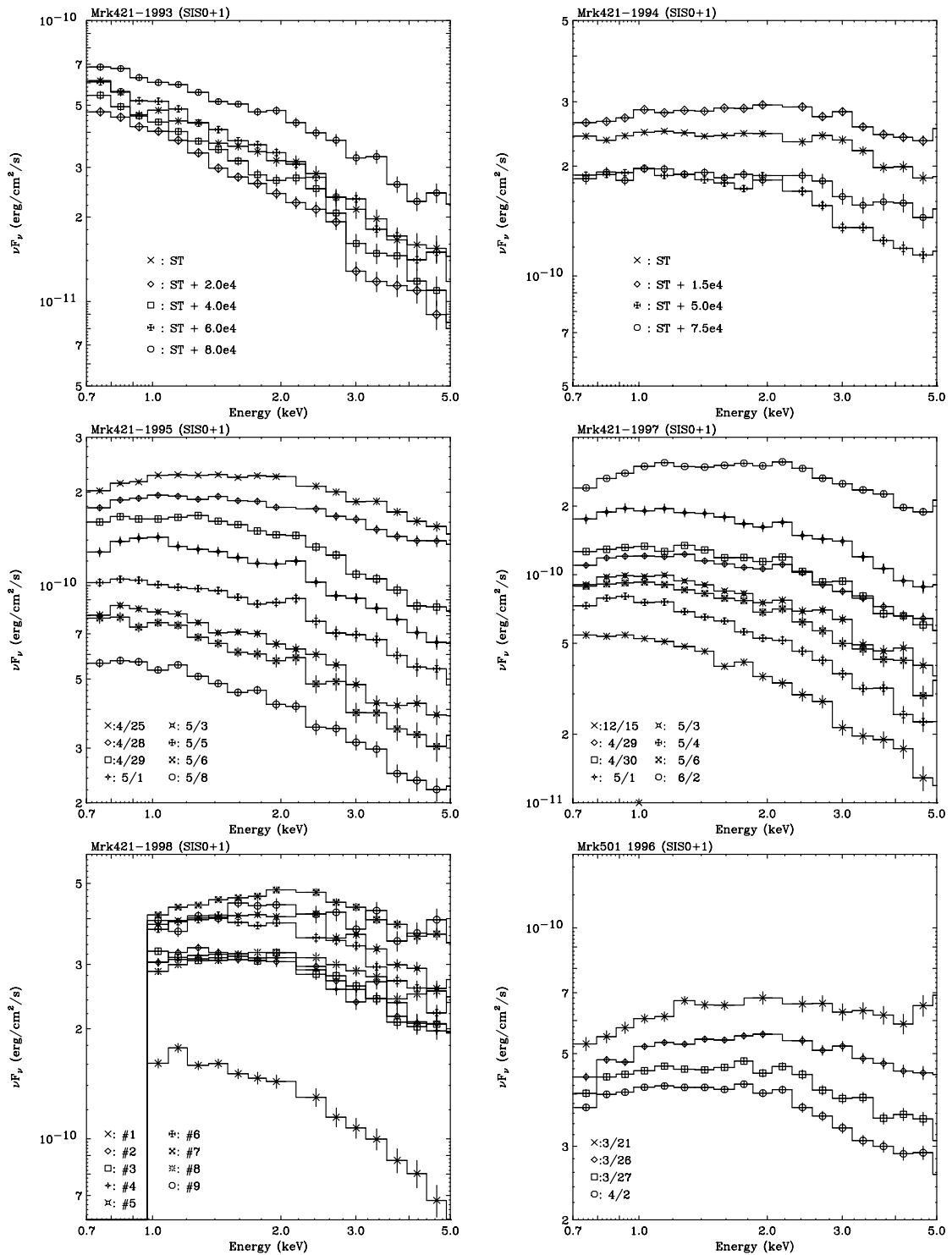
Figure E.1:
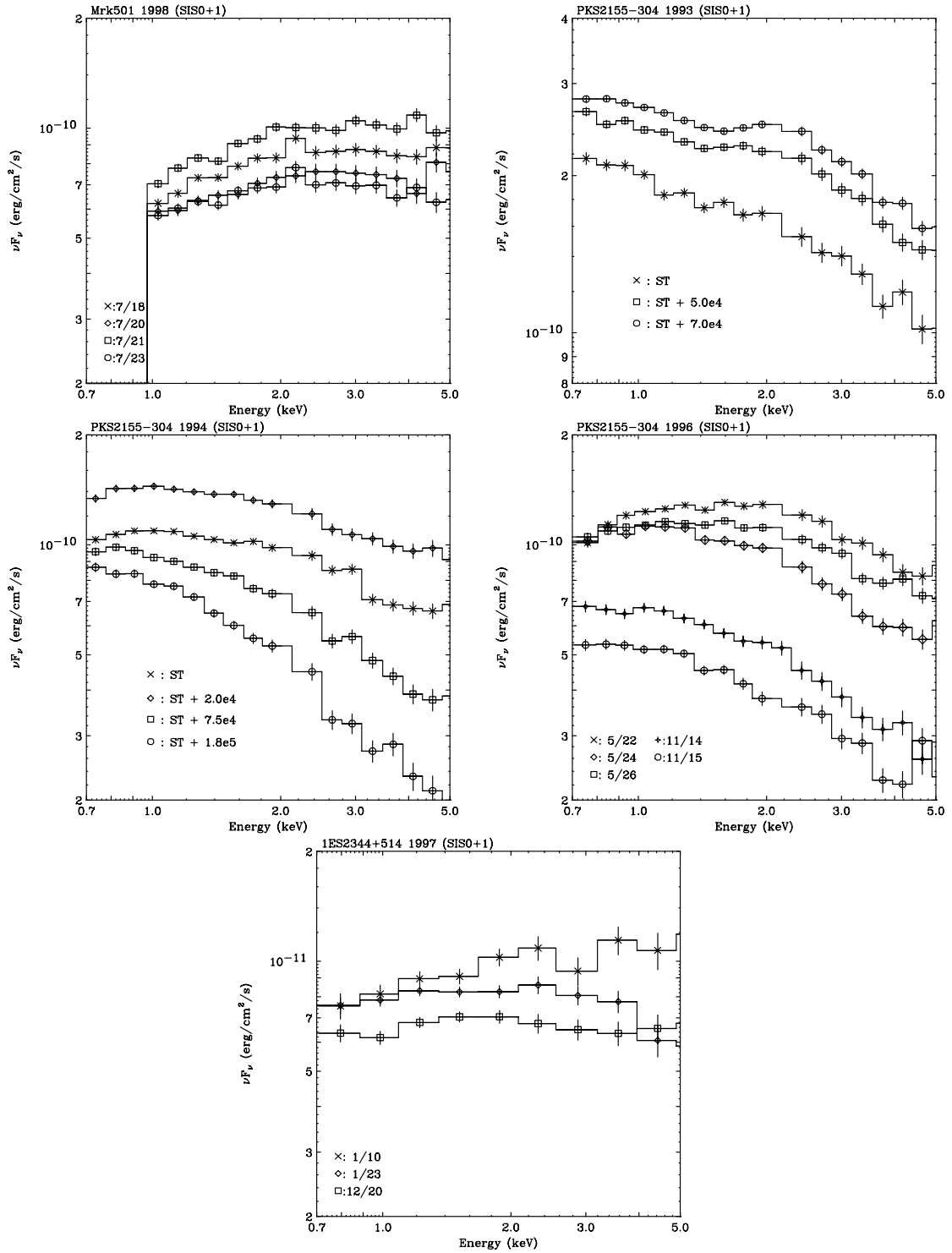
Figure E.2: Synchrotron peak shifts of Mrk 421, Mrk 501, PKS 2155−304 and 1ES 2344+514. Results from different observational seasons are separately shown. 'ST' is the start time of each observation as listed in § 6.1.

Appendix F

HEXTE spectra of Mrk 501 in 1998
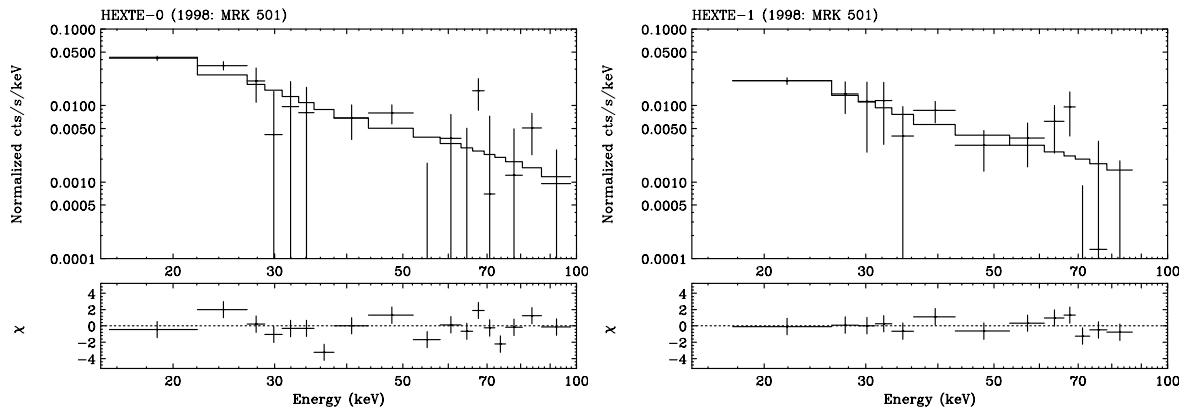
Figure F.1: *RXTE* HEXTE spectra for Mrk 501 obtained in 1998 May, fitted by a power law function. Data for total exposure (net 60 ksec) are summed. *left*: energy spectra for cluster-0, *right*: energy spectra for cluster-1.

Table F.1: Results of spectral fitting of HEXTE data

Detector	cluster	Photon Index	Flux (20-50keV) 10^{-12} erg/cm^2/s	χ^2 (d.o.f)
HEXTE	0	$2.17^{+0.25}_{-0.21}$	$23.6^{+26.7}_{-11.4}$	$1.95(16)$
HEXTE	1	$1.93^{+0.36}_{-0.29}$	$22.9^{+47.2}_{-14.0}$	$0.67(11)$

Data from 1998 05/25 to 05/27 were used for the fit (60 ksec in total). Fitting model is just a power law, because the Galactic absorption is negligibly small in this energy band. All errors are 1 σ.

Appendix G

Spectral Fit Results of *RXTE* Observations

Table G.1: Fit results of *RXTE* spectra of Mrk 421 (1)

Target	Start MJD	Stop MJD	Int.	N_H	Photon	Flux (2-10keV)	χ^2 (dof)
			time (ksec)	$10^{20}/cm^2$	Index	10^{-12} erg/cm^2/s	
Mrk 421	50192.084	50192.090	0.56	1.45fix	$3.08^{+0.05}_{-0.05}$	$73.38^{+1.27}_{-1.27}$	0.73(45)
	50192.315	50192.318	0.26	1.45fix	$2.95^{+0.06}_{-0.06}$	$88.21^{+1.96}_{-1.95}$	0.58(45)
	50192.516	50192.522	0.50	1.45fix	$2.92^{+0.04}_{-0.04}$	$92.03^{+1.42}_{-1.41}$	0.75(45)
	50194.053	50194.056	0.27	1.45fix	$2.90^{+0.04}_{-0.04}$	$129.30^{+2.09}_{-2.12}$	0.88(45)
	50194.219	50194.227	0.66	1.45fix	$2.87^{+0.03}_{-0.03}$	$120.30^{+1.32}_{-1.29}$	1.29(45)
	50194.381	50194.385	0.37	1.45fix	$2.66^{+0.03}_{-0.03}$	$145.50^{+1.88}_{-1.84}$	0.82(45)
	50194.892	50194.899	0.54	1.45fix	$2.65^{+0.02}_{-0.02}$	$187.00^{+1.59}_{-1.68}$	0.68(45)
	50195.584	50195.590	0.48	1.45fix	$2.77^{+0.03}_{-0.03}$	$159.80^{+1.66}_{-1.76}$	0.85(45)
	50196.019	50196.026	0.59	1.45fix	$2.74^{+0.02}_{-0.02}$	$173.70^{+1.58}_{-1.50}$	0.56(45)
	50206.176	50206.182	0.53	1.45fix	$2.11^{+0.01}_{-0.01}$	$445.70^{+2.15}_{-2.18}$	1.62(45)
	50206.425	50206.428	0.21	1.45fix	$2.41^{+0.03}_{-0.03}$	$215.60^{+2.69}_{-2.75}$	0.65(45)
	50207.248	50207.254	0.50	1.45fix	$2.76^{+0.03}_{-0.03}$	$119.10^{+1.47}_{-1.53}$	0.71(45)
	50207.356	50207.362	0.53	1.45fix	$2.79^{+0.04}_{-0.04}$	$97.01^{+1.41}_{-1.40}$	0.61(45)
	50207.772	50207.778	0.53	1.45fix	$2.63^{+0.02}_{-0.02}$	$216.40^{+1.75}_{-1.73}$	0.86(45)
	50207.901	50207.907	0.53	1.45fix	$2.31^{+0.01}_{-0.01}$	$458.10^{+2.25}_{-2.25}$	1.96(45)
	50208.169	50208.184	1.30	1.45fix	$2.52^{+0.01}_{-0.01}$	$206.90^{+1.11}_{-1.05}$	1.27(45)
	50208.426	50208.428	0.21	1.45fix	$2.36^{+0.02}_{-0.02}$	$375.00^{+3.45}_{-3.48}$	1.35(45)
	50208.556	50208.569	1.14	1.45fix	$2.27^{+0.01}_{-0.01}$	$556.40^{+1.65}_{-1.69}$	3.44(45)†
	50209.223	50209.228	0.46	1.45fix	$2.56^{+0.02}_{-0.02}$	$258.70^{+2.05}_{-1.96}$	0.78(45)
	50209.426	50209.429	0.24	1.45fix	$2.65^{+0.03}_{-0.03}$	$247.30^{+2.85}_{-2.84}$	0.78(45)
	50209.623	50209.629	0.51	1.45fix	$2.52^{+0.01}_{-0.01}$	$350.80^{+2.09}_{-2.13}$	1.09(45)
	50210.223	50210.229	0.50	1.45fix	$2.31^{+0.01}_{-0.01}$	$377.20^{+2.19}_{-2.14}$	1.34(45)
	50210.427	50210.432	0.42	1.45fix	$2.52^{+0.02}_{-0.02}$	$246.30^{+1.99}_{-2.08}$	0.96(45)
	50210.625	50210.630	0.50	1.45fix	$2.76^{+0.03}_{-0.03}$	$164.30^{+1.71}_{-1.61}$	0.84(45)
	50210.902	50210.906	0.32	1.45fix	$2.77^{+0.03}_{-0.03}$	$198.50^{+2.23}_{-2.22}$	0.53(45)
	50211.290	50211.296	0.46	1.45fix	$2.85^{+0.03}_{-0.03}$	$176.60^{+1.85}_{-1.81}$	0.72(45)
	50211.563	50211.571	0.64	1.45fix	$2.76^{+0.02}_{-0.02}$	$172.60^{+1.52}_{-1.44}$	1.06(45)
	50211.757	50211.765	0.69	1.45fix	$2.66^{+0.02}_{-0.02}$	$173.10^{+1.44}_{-1.43}$	0.91(45)
	50211.964	50211.972	0.64	1.45fix	$2.75^{+0.02}_{-0.02}$	$199.00^{+1.54}_{-1.59}$	0.99(45)
	50212.245	50212.258	1.09	1.45fix	$2.97^{+0.02}_{-0.02}$	$193.10^{+1.24}_{-1.26}$	1.09(45)
	50212.493	50212.500	0.56	1.45fix	$2.86^{+0.02}_{-0.02}$	$192.30^{+1.66}_{-1.71}$	0.65(45)

Table G.2: Fit results of Mrk 421 (2) – *continued*

Target	Start MJD	Stop MJD	Int. time (ksec)	$N_{\rm H}$ $10^{20}/{\rm cm}^2$	Photon Index	Flux (2-10keV) 10^{-12} erg/cm^2/s	χ^2 (dof)
Mrk 421	50212.636	50212.644	0.64	1.45fix	$2.90^{+0.02}_{-0.02}$	$186.40^{+1.54}_{-1.59}$	0.65(45)
	50213.250	50213.256	0.50	1.45fix	$2.84^{+0.03}_{-0.03}$	$169.00^{+1.73}_{-1.71}$	0.75(45)
	50213.358	50213.363	0.42	1.45fix	$2.83^{+0.03}_{-0.03}$	$171.20^{+1.91}_{-1.99}$	0.66(45)
	50213.639	50213.651	1.01	1.45fix	$2.83^{+0.02}_{-0.02}$	$149.10^{+1.11}_{-1.18}$	0.71(45)
	50213.892	50213.904	1.06	1.45fix	$2.88^{+0.06}_{-0.06}$	$114.10^{+2.54}_{-2.45}$	0.57(45)
	50214.292	50214.297	0.43	1.45fix	$2.78^{+0.03}_{-0.03}$	$153.70^{+1.80}_{-1.72}$	0.65(45)
	50214.517	50214.522	0.50	1.45fix	$2.81^{+0.02}_{-0.02}$	$193.80^{+1.80}_{-1.78}$	0.92(45)
	50214.764	50214.770	0.53	1.45fix	$2.77^{+0.02}_{-0.02}$	$195.40^{+1.75}_{-1.70}$	0.70(45)
	50214.897	50214.903	0.50	1.45fix	$2.83^{+0.02}_{-0.02}$	$184.20^{+1.74}_{-1.75}$	0.99(45)
	50215.250	50215.258	0.67	1.45fix	$2.56^{+0.01}_{-0.01}$	$282.80^{+1.75}_{-1.67}$	1.29(45)
	50215.498	50215.504	0.53	1.45fix	$2.53^{+0.02}_{-0.02}$	$256.90^{+1.86}_{-1.86}$	0.96(45)
	50215.763	50215.769	0.54	1.45fix	$2.62^{+0.02}_{-0.02}$	$222.80^{+1.74}_{-1.80}$	0.79(45)
	50215.832	50215.836	0.34	1.45fix	$2.64^{+0.02}_{-0.02}$	$225.50^{+2.25}_{-2.20}$	0.81(45)
	50216.098	50216.104	0.54	1.45fix	$2.74^{+0.03}_{-0.02}$	$166.40^{+1.61}_{-1.62}$	0.55(45)
	50216.360	50216.364	0.38	1.45fix	$2.64^{+0.03}_{-0.03}$	$160.10^{+1.89}_{-1.85}$	0.81(45)
	50216.569	50216.576	0.54	1.45fix	$2.69^{+0.02}_{-0.02}$	$172.20^{+1.63}_{-1.54}$	0.85(45)
	50216.763	50216.768	0.48	1.45fix	$2.57^{+0.03}_{-0.02}$	$171.20^{+1.70}_{-1.69}$	0.68(45)
	50217.227	50217.232	0.42	1.45fix	$2.72^{+0.03}_{-0.03}$	$175.10^{+1.85}_{-1.87}$	0.72(45)
	50217.361	50217.366	0.46	1.45fix	$2.62^{+0.02}_{-0.02}$	$193.00^{+1.80}_{-1.75}$	1.13(45)
	50217.972	50217.977	0.43	1.45fix	$2.83^{+0.04}_{-0.03}$	$125.80^{+1.70}_{-1.62}$	0.65(45)
	50218.252	50218.258	0.53	1.45fix	$2.69^{+0.03}_{-0.03}$	$140.70^{+1.55}_{-1.50}$	0.66(45)
	50218.497	50218.505	0.77	1.45fix	$2.99^{+0.03}_{-0.03}$	$96.96^{+1.17}_{-1.16}$	1.35(45)
	50218.648	50218.654	0.51	1.45fix	$3.09^{+0.05}_{-0.05}$	$86.68^{+1.45}_{-1.44}$	0.62(45)
	50219.371	50219.377	0.56	1.45fix	$3.12^{+0.04}_{-0.05}$	$85.98^{+1.34}_{-1.33}$	1.02(45)
	50219.500	50219.506	0.53	1.45fix	$3.10^{+0.04}_{-0.04}$	$89.69^{+1.38}_{-1.39}$	1.02(45)
	50219.763	50219.766	0.27	1.45fix	$3.03^{+0.06}_{-0.06}$	$91.51^{+1.93}_{-1.93}$	0.71(45)
	50219.897	50219.907	0.94	1.45fix	$2.98^{+0.04}_{-0.03}$	$85.59^{+1.04}_{-1.03}$	0.57(45)
	50220.044	50220.050	0.58	1.45fix	$3.14^{+0.05}_{-0.05}$	$76.40^{+1.32}_{-1.32}$	0.84(45)
	50220.324	50220.330	0.51	1.45fix	$3.14^{+0.06}_{-0.06}$	$65.07^{+1.30}_{-1.30}$	0.97(45)
	50220.580	50220.585	0.48	1.45fix	$3.00^{+0.05}_{-0.05}$	$80.02^{+1.42}_{-1.40}$	0.48(45)
	50221.236	50221.241	0.50	1.45fix	$2.92^{+0.04}_{-0.03}$	$118.50^{+1.57}_{-1.48}$	0.83(45)
	50221.586	50221.592	0.53	1.45fix	$2.89^{+0.04}_{-0.04}$	$102.90^{+1.47}_{-1.38}$	0.77(45)
	50221.800	50221.809	0.74	1.45fix	$3.04^{+0.04}_{-0.04}$	$79.83^{+1.16}_{-1.15}$	0.69(45)
	50222.044	50222.052	0.70	1.45fix	$3.10^{+0.04}_{-0.04}$	$80.06^{+1.19}_{-1.19}$	0.78(45)
	50222.244	50222.255	0.90	1.45fix	$3.07^{+0.04}_{-0.04}$	$77.83^{+1.03}_{-1.03}$	0.76(45)
	50223.261	50223.267	0.50	1.45fix	$3.11^{+0.05}_{-0.05}$	$81.07^{+1.40}_{-1.39}$	0.61(45)
	50223.503	50223.510	0.54	1.45fix	$3.13^{+0.04}_{-0.04}$	$101.70^{+1.42}_{-1.46}$	0.91(45)
	50224.047	50224.053	0.50	1.45fix	$2.62^{+0.03}_{-0.03}$	$165.60^{+1.65}_{-1.66}$	0.61(45)
	50427.884	50427.905	1.81	1.45fix	$3.04^{+0.08}_{-0.08}$	$20.73^{+0.54}_{-0.55}$	0.70(45)
	50540.147	50540.164	1.47	1.45fix	$2.79^{+0.03}_{-0.03}$	$96.46^{+0.93}_{-0.93}$	0.50(45)
	50540.214	50540.236	1.89	1.45fix	$2.74^{+0.02}_{-0.02}$	$96.22^{+0.81}_{-0.81}$	0.71(45)
	50540.281	50540.294	1.14	1.45fix	$2.71^{+0.03}_{-0.03}$	$97.67^{+1.04}_{-1.04}$	0.61(45)
	50540.294	50540.307	1.15	1.45fix	$2.71^{+0.03}_{-0.03}$	$95.90^{+1.03}_{-1.02}$	0.47(45)
	50540.348	50540.362	1.25	1.45fix	$2.58^{+0.02}_{-0.02}$	$117.20^{+1.00}_{-1.05}$	0.69(45)
	50540.362	50540.376	1.23	1.45fix	$2.52^{+0.02}_{-0.02}$	$125.40^{+0.99}_{-1.07}$	0.68(45)

Table G.3: Fit results of Mrk 421 (3) – *continued*

Target	Start MJD	Stop MJD	Int. time (ksec)	$N_{\rm H}$ $10^{20}/{\rm cm}^2$	Photon Index	Flux (2-10keV) 10^{-12} erg/cm^2/s	χ^2 (dof)
Mrk 421	50541.215	50541.236	1.79	1.45fix	$2.67^{+0.02}_{-0.02}$	$124.70^{+0.88}_{-0.89}$	0.87(45)
	50541.349	50541.363	1.22	1.45fix	$2.64^{+0.03}_{-0.03}$	$100.90^{+1.01}_{-0.97}$	0.73(45)
	50541.363	50541.377	1.22	1.45fix	$2.62^{+0.03}_{-0.02}$	$105.00^{+1.02}_{-0.98}$	0.58(45)
	50542.219	50542.237	1.58	1.45fix	$2.74^{+0.03}_{-0.03}$	$92.02^{+0.88}_{-0.87}$	0.59(45)
	50542.219	50542.237	1.58	1.45fix	$2.74^{+0.03}_{-0.03}$	$92.02^{+0.88}_{-0.87}$	0.59(45)
	50542.284	50542.296	1.09	1.45fix	$2.77^{+0.04}_{-0.04}$	$76.83^{+1.02}_{-1.02}$	0.45(45)
	50542.296	50542.309	1.09	1.45fix	$2.71^{+0.03}_{-0.03}$	$81.43^{+1.00}_{-1.00}$	0.61(45)
	50543.218	50543.238	1.71	1.45fix	$2.99^{+0.03}_{-0.03}$	$88.31^{+0.87}_{-0.88}$	0.58(45)
	50543.284	50543.297	1.06	1.45fix	$2.91^{+0.03}_{-0.03}$	$87.75^{+1.10}_{-1.09}$	0.61(45)
	50543.297	50543.309	1.07	1.45fix	$2.96^{+0.04}_{-0.04}$	$86.62^{+1.10}_{-1.08}$	0.57(45)
	50543.318	50543.322	0.32	1.45fix	$2.98^{+0.06}_{-0.06}$	$86.55^{+2.01}_{-1.99}$	0.52(45)
	50548.229	50548.242	1.09	1.45fix	$3.00^{+0.02}_{-0.02}$	$141.60^{+1.22}_{-1.31}$	1.05(45)
	50548.248	50548.258	0.85	1.45fix	$2.98^{+0.03}_{-0.03}$	$140.90^{+1.43}_{-1.43}$	0.63(45)
	50548.289	50548.311	1.92	1.45fix	$2.97^{+0.02}_{-0.02}$	$140.00^{+0.91}_{-0.98}$	0.78(45)
	50549.223	50549.236	1.14	1.45fix	$2.98^{+0.01}_{-0.01}$	$451.50^{+1.90}_{-1.99}$	2.13(45)†
	50549.236	50549.249	1.15	1.45fix	$2.96^{+0.02}_{-0.02}$	$450.70^{+1.90}_{-1.96}$	2.00(45)†
	50549.249	50549.262	1.15	1.45fix	$2.97^{+0.02}_{-0.02}$	$443.50^{+1.88}_{-1.94}$	2.27(45)†
	50549.289	50549.312	1.97	1.45fix	$2.92^{+0.01}_{-0.01}$	$410.90^{+1.43}_{-1.36}$	2.53(45)†
	50549.318	50549.323	0.45	1.45fix	$2.92^{+0.02}_{-0.02}$	$406.40^{+1.86}_{-1.78}$	0.69(45)
	50550.223	50550.245	1.89	1.45fix	$2.92^{+0.02}_{-0.01}$	$180.00^{+1.03}_{-1.03}$	0.97(45)
	50550.247	50550.263	1.38	1.45fix	$2.94^{+0.02}_{-0.02}$	$181.50^{+1.24}_{-1.19}$	0.87(45)
	50550.290	50550.302	1.04	1.45fix	$2.94^{+0.02}_{-0.02}$	$185.10^{+1.42}_{-1.40}$	1.03(45)
	50550.302	50550.314	1.07	1.45fix	$2.95^{+0.02}_{-0.02}$	$182.70^{+1.41}_{-1.37}$	0.80(45)
	50550.318	50550.329	0.99	1.45fix	$2.91^{+0.02}_{-0.02}$	$184.40^{+1.43}_{-1.44}$	0.94(45)
	50550.357	50550.373	1.41	1.45fix	$2.88^{+0.02}_{-0.02}$	$200.20^{+1.26}_{-1.19}$	1.03(45)
	50567.229	50567.243	1.25	1.45fix	$3.02^{+0.02}_{-0.02}$	$130.10^{+1.14}_{-1.16}$	0.74(45)
	50568.229	50568.242	1.15	1.45fix	$2.90^{+0.02}_{-0.02}$	$123.30^{+1.10}_{-1.18}$	0.99(45)
	50568.242	50568.257	1.25	1.45fix	$2.92^{+0.03}_{-0.03}$	$125.00^{+1.35}_{-1.35}$	0.55(45)
	50569.896	50569.901	0.46	1.45fix	$2.93^{+0.03}_{-0.03}$	$194.60^{+2.13}_{-2.14}$	0.77(45)
	50569.905	50569.920	1.26	1.45fix	$2.95^{+0.02}_{-0.02}$	$194.10^{+1.28}_{-1.33}$	0.65(45)
	50570.229	50570.243	1.20	1.45fix	$2.96^{+0.02}_{-0.02}$	$176.90^{+1.24}_{-1.34}$	1.21(45)
	50570.243	50570.258	1.30	1.45fix	$2.95^{+0.02}_{-0.02}$	$174.10^{+1.52}_{-1.47}$	0.79(45)
	50571.163	50571.173	0.86	1.45fix	$2.91^{+0.03}_{-0.03}$	$110.50^{+1.31}_{-1.26}$	0.64(45)
	50571.229	50571.244	1.30	1.45fix	$2.99^{+0.03}_{-0.03}$	$101.10^{+1.05}_{-1.05}$	0.54(45)
	50571.244	50571.259	1.31	1.45fix	$3.00^{+0.03}_{-0.03}$	$96.33^{+1.02}_{-1.02}$	0.78(45)
	50572.163	50572.174	0.99	1.45fix	$3.20^{+0.06}_{-0.06}$	$54.73^{+1.08}_{-1.07}$	0.63(45)
	50572.229	50572.243	1.17	1.45fix	$3.23^{+0.06}_{-0.05}$	$55.97^{+1.02}_{-1.01}$	0.57(45)
	50574.098	50574.106	0.69	1.45fix	$2.99^{+0.05}_{-0.05}$	$81.04^{+1.34}_{-1.32}$	0.46(45)
	50574.163	50574.177	1.15	1.45fix	$3.04^{+0.04}_{-0.04}$	$76.21^{+1.05}_{-1.04}$	0.42(45)
	50574.177	50574.190	1.15	1.45fix	$3.03^{+0.04}_{-0.04}$	$76.68^{+1.03}_{-1.04}$	0.60(45)
	50574.235	50574.247	0.96	1.45fix	$3.02^{+0.04}_{-0.04}$	$76.14^{+1.15}_{-1.15}$	0.58(45)
	50602.249	50602.261	1.02	1.45fix	$2.69^{+0.01}_{-0.01}$	$403.50^{+1.81}_{-1.85}$	1.53(45)
	50602.261	50602.273	1.02	1.45fix	$2.73^{+0.02}_{-0.02}$	$403.10^{+3.04}_{-2.95}$	2.05(45)†

† : Phton spectrum is not well represented by a power law function, however, the cutoff power law function is statistically acceptable as we see in Table G.11.

Table G.4: Fit results of *RXTE* spectra of Mrk 501 (1)

Target	Start MJD	Stop MJD	Int. time (ksec)	$N_{\rm H}$ $10^{20}/{\rm cm}^2$	Photon Index	Flux (2-10keV) 10^{-12} erg/cm^2/s	χ^2 (dof)
Mrk 501	50296.571	50296.583	1.07	1.73fix	$2.45^{+0.02}_{-0.02}$	$111.50^{+0.98}_{-0.93}$	0.81(45)
	50378.501	50378.517	1.42	1.73fix	$2.17^{+0.01}_{-0.01}$	$154.10^{+0.98}_{-0.88}$	0.86(45)
	50525.087	50525.089	0.19	1.73fix	$2.00^{+0.02}_{-0.02}$	$299.00^{+3.19}_{-3.20}$	0.78(45)
	50525.119	50525.120	0.13	1.73fix	$1.97^{+0.03}_{-0.03}$	$302.70^{+3.99}_{-3.89}$	0.66(45)
	50541.194	50541.204	0.85	1.73fix	$2.07^{+0.01}_{-0.01}$	$328.70^{+1.67}_{-1.58}$	0.74(45)
	50541.387	50541.397	0.91	1.73fix	$2.10^{+0.01}_{-0.01}$	$296.40^{+1.48}_{-1.52}$	0.88(45)
	50542.195	50542.197	0.16	1.73fix	$1.99^{+0.03}_{-0.03}$	$299.10^{+3.55}_{-3.58}$	0.56(45)
	50542.464	50542.474	0.82	1.73fix	$2.03^{+0.01}_{-0.01}$	$318.10^{+1.57}_{-1.64}$	0.84(45)
	50543.195	50543.207	1.04	1.73fix	$2.06^{+0.01}_{-0.01}$	$319.20^{+1.41}_{-1.50}$	1.00(45)
	50543.332	50543.341	0.77	1.73fix	$2.05^{+0.01}_{-0.01}$	$315.90^{+1.68}_{-1.67}$	1.13(45)
	50544.302	50544.311	0.75	1.73fix	$1.88^{+0.01}_{-0.01}$	$373.50^{+1.72}_{-1.77}$	1.10(45)
	50544.435	50544.445	0.83	1.73fix	$1.90^{+0.01}_{-0.01}$	$366.20^{+1.66}_{-1.64}$	0.98(45)
	50545.302	50545.311	0.78	1.73fix	$2.02^{+0.01}_{-0.01}$	$291.90^{+1.58}_{-1.59}$	0.86(45)
	50545.442	50545.452	0.86	1.73fix	$2.01^{+0.01}_{-0.01}$	$283.40^{+1.50}_{-1.47}$	0.71(45)
	50546.236	50546.240	0.38	1.73fix	$2.04^{+0.02}_{-0.02}$	$248.40^{+2.18}_{-2.09}$	0.64(45)
	50546.250	50546.255	0.45	1.73fix	$2.02^{+0.02}_{-0.02}$	$245.40^{+1.95}_{-1.98}$	0.62(45)
	50546.442	50546.452	0.86	1.73fix	$2.02^{+0.01}_{-0.01}$	$244.70^{+1.36}_{-1.46}$	0.82(45)
	50547.236	50547.241	0.45	1.73fix	$1.95^{+0.02}_{-0.02}$	$255.50^{+1.97}_{-1.96}$	0.66(45)
	50547.249	50547.255	0.51	1.73fix	$1.98^{+0.02}_{-0.02}$	$254.50^{+1.89}_{-1.81}$	0.70(45)
	50547.436	50547.446	0.82	1.73fix	$1.93^{+0.01}_{-0.01}$	$264.50^{+1.48}_{-1.46}$	0.62(45)
	50548.268	50548.275	0.62	1.73fix	$1.87^{+0.01}_{-0.01}$	$312.90^{+1.77}_{-1.78}$	1.27(45)
	50548.321	50548.330	0.85	1.73fix	$1.88^{+0.01}_{-0.01}$	$321.20^{+1.56}_{-1.54}$	0.81(45)
	50549.202	50549.208	0.54	1.73fix	$1.90^{+0.01}_{-0.01}$	$319.10^{+1.97}_{-1.89}$	0.78(45)
	50549.332	50549.342	0.82	1.73fix	$1.90^{+0.01}_{-0.01}$	$302.80^{+1.57}_{-1.54}$	0.77(45)
	50550.183	50550.193	0.85	1.73fix	$1.89^{+0.01}_{-0.01}$	$386.80^{+1.65}_{-1.70}$	0.92(45)
	50550.448	50550.451	0.26	1.73fix	$1.85^{+0.02}_{-0.02}$	$427.50^{+3.10}_{-3.19}$	1.47(45)
	50550.453	50550.460	0.54	1.73fix	$1.85^{+0.01}_{-0.01}$	$428.90^{+2.22}_{-2.27}$	1.00(45)
	50551.266	50551.276	0.82	1.73fix	$1.81^{+0.01}_{-0.01}$	$531.80^{+1.93}_{-1.96}$	1.11(45)
	50551.459	50551.469	0.90	1.73fix	$1.77^{+0.01}_{-0.01}$	$535.20^{+1.83}_{-1.88}$	1.13(45)
	50552.333	50552.342	0.78	1.73fix	$1.82^{+0.01}_{-0.01}$	$436.90^{+1.85}_{-1.76}$	1.18(45)
	50552.457	50552.469	1.02	1.73fix	$1.81^{+0.01}_{-0.01}$	$421.70^{+1.59}_{-1.54}$	0.81(45)
	50553.264	50553.276	1.06	1.73fix	$1.84^{+0.01}_{-0.01}$	$435.40^{+1.58}_{-1.54}$	0.91(45)
	50553.372	50553.382	0.88	1.73fix	$1.93^{+0.06}_{-0.06}$	$414.20^{+12.62}_{-12.65}$	1.08(45)
	50554.171	50554.183	1.02	1.73fix	$1.71^{+0.01}_{-0.01}$	$603.10^{+1.78}_{-1.81}$	1.25(45)
	50554.443	50554.451	0.66	1.73fix	$1.72^{+0.01}_{-0.01}$	$659.20^{+2.34}_{-2.31}$	1.15(45)
	50570.179	50570.182	0.27	1.73fix	$1.96^{+0.02}_{-0.02}$	$263.30^{+2.52}_{-2.60}$	0.89(45)
	50570.392	50570.402	0.85	1.73fix	$2.03^{+0.01}_{-0.01}$	$265.00^{+1.49}_{-1.48}$	0.57(45)
	50571.182	50571.188	0.50	1.73fix	$1.90^{+0.01}_{-0.01}$	$304.60^{+1.98}_{-2.00}$	0.83(45)
	50572.183	50572.188	0.40	1.73fix	$1.78^{+0.01}_{-0.01}$	$383.20^{+2.42}_{-2.35}$	0.90(45)
	50572.252	50572.260	0.67	1.73fix	$1.80^{+0.01}_{-0.01}$	$381.90^{+1.89}_{-1.81}$	0.86(45)

Table G.5: Fit results of Mrk 501 (2) – *continued*

Target	Start MJD	Stop MJD	Int. time (ksec)	N_{H} 10^{20}/cm^2	Photon Index	Flux (2-10keV) 10^{-12} erg/cm^2/s	χ^2 (dof)
Mrk 501	50573.177	50573.189	1.01	1.73fix	$1.91^{+0.01}_{-0.01}$	$293.70^{+1.38}_{-1.40}$	0.80(45)
	50573.393	50573.403	0.86	1.73fix	$1.89^{+0.01}_{-0.01}$	$292.10^{+1.47}_{-1.52}$	0.95(45)
	50574.256	50574.262	0.51	1.73fix	$1.92^{+0.02}_{-0.01}$	$276.60^{+1.89}_{-1.92}$	0.64(45)
	50574.316	50574.333	1.46	1.73fix	$1.88^{+0.01}_{-0.01}$	$291.80^{+1.18}_{-1.12}$	0.57(45)
	50575.244	50575.262	1.55	1.73fix	$1.77^{+0.01}_{-0.01}$	$415.30^{+1.28}_{-1.24}$	0.81(45)
	50575.394	50575.404	0.85	1.73fix	$1.72^{+0.01}_{-0.01}$	$480.70^{+1.75}_{-1.85}$	1.06(45)
	50576.392	50576.405	1.14	1.73fix	$1.80^{+0.01}_{-0.01}$	$465.90^{+1.56}_{-1.54}$	0.88(45)
	50577.332	50577.335	0.30	1.73fix	$1.82^{+0.01}_{-0.01}$	$422.50^{+2.94}_{-2.85}$	0.91(45)
	50578.395	50578.406	0.96	1.73fix	$1.82^{+0.01}_{-0.01}$	$433.00^{+1.62}_{-1.67}$	1.16(45)
	50579.393	50579.403	0.88	1.73fix	$1.83^{+0.01}_{-0.01}$	$459.30^{+1.74}_{-1.78}$	0.85(45)
	50580.183	50580.194	0.93	1.73fix	$1.83^{+0.01}_{-0.01}$	$495.10^{+1.74}_{-1.80}$	1.45(45)
	50581.189	50581.194	0.50	1.73fix	$1.86^{+0.01}_{-0.01}$	$503.50^{+2.43}_{-2.47}$	1.13(45)
	50582.399	50582.409	0.91	1.73fix	$1.84^{+0.01}_{-0.01}$	$393.70^{+1.62}_{-1.62}$	0.60(45)
	50583.187	50583.196	0.77	1.73fix	$1.79^{+0.01}_{-0.01}$	$397.50^{+1.73}_{-1.80}$	0.97(45)
	50583.259	50583.267	0.67	1.73fix	$1.80^{+0.01}_{-0.01}$	$399.30^{+1.92}_{-1.87}$	1.12(45)
	50640.982	50640.991	0.80	1.73fix	$1.98^{+0.01}_{-0.01}$	$628.50^{+2.22}_{-2.21}$	1.66(45)
	50641.151	50641.166	1.30	1.73fix	$1.96^{+0.01}_{-0.01}$	$619.90^{+1.65}_{-1.70}$	2.57(45)†
	50641.176	50641.191	1.28	1.73fix	$1.96^{+0.01}_{-0.01}$	$614.10^{+1.66}_{-1.70}$	2.44(45)†
	50641.982	50641.991	0.78	1.73fix	$1.90^{+0.01}_{-0.01}$	$596.70^{+2.10}_{-2.13}$	1.49(45)
	50642.151	50642.166	1.30	1.73fix	$1.88^{+0.01}_{-0.01}$	$581.60^{+1.57}_{-1.64}$	1.46(45)
	50642.175	50642.191	1.36	1.73fix	$1.86^{+0.01}_{-0.01}$	$597.10^{+1.56}_{-1.60}$	1.71(45)
	50642.982	50642.991	0.78	1.73fix	$1.85^{+0.01}_{-0.01}$	$569.60^{+2.03}_{-2.08}$	1.32(45)
	50643.152	50643.168	1.39	1.73fix	$1.85^{+0.01}_{-0.01}$	$521.70^{+1.42}_{-1.52}$	1.69(45)
	50643.175	50643.191	1.42	1.73fix	$1.85^{+0.01}_{-0.01}$	$521.10^{+1.49}_{-1.42}$	1.84(45)
	50643.982	50643.991	0.77	1.73fix	$1.89^{+0.01}_{-0.01}$	$582.80^{+2.15}_{-2.07}$	1.08(45)
	50644.152	50644.169	1.42	1.73fix	$1.90^{+0.01}_{-0.01}$	$611.80^{+1.55}_{-1.60}$	2.07(45)†
	50644.172	50644.192	1.66	1.73fix	$1.90^{+0.00}_{-0.01}$	$611.90^{+1.50}_{-1.41}$	1.56(45)
	50644.983	50644.992	0.75	1.73fix	$1.94^{+0.01}_{-0.01}$	$689.50^{+2.35}_{-2.26}$	1.51(45)
	50645.152	50645.171	1.60	1.73fix	$1.95^{+0.01}_{-0.01}$	$700.70^{+1.61}_{-1.56}$	3.53(45)†
	50645.173	50645.192	1.63	1.73fix	$1.96^{+0.01}_{-0.01}$	$686.00^{+1.53}_{-1.53}$	3.45(45)†
	50958.166	50958.173	0.58	1.73fix	$2.11^{+0.03}_{-0.03}$	$106.20^{+1.31}_{-1.40}$	0.63(45)
	50958.332	50958.351	1.62	1.73fix	$2.08^{+0.02}_{-0.02}$	$100.50^{+0.79}_{-0.76}$	0.69(45)
	50958.358	50958.372	1.25	1.73fix	$2.11^{+0.02}_{-0.02}$	$100.50^{+0.89}_{-0.88}$	0.77(45)
	50958.399	50958.411	1.02	1.73fix	$2.09^{+0.02}_{-0.02}$	$100.00^{+1.02}_{-0.95}$	0.49(45)
	50958.411	50958.423	1.01	1.73fix	$2.11^{+0.02}_{-0.02}$	$99.20^{+0.98}_{-0.98}$	0.54(45)
	50958.427	50958.439	1.07	1.73fix	$2.11^{+0.02}_{-0.02}$	$99.67^{+0.96}_{-0.95}$	0.57(45)
	50958.532	50958.545	1.09	1.73fix	$2.05^{+0.02}_{-0.02}$	$99.28^{+0.95}_{-0.94}$	0.99(45)
	50958.545	50958.558	1.10	1.73fix	$2.11^{+0.02}_{-0.02}$	$102.10^{+0.90}_{-0.97}$	0.66(45)
	50958.569	50958.573	0.29	1.73fix	$2.04^{+0.05}_{-0.05}$	$97.01^{+1.85}_{-1.85}$	0.70(45)
	50958.599	50958.612	1.15	1.73fix	$2.06^{+0.02}_{-0.02}$	$103.30^{+0.98}_{-0.88}$	0.90(45)

Table G.6: Fit results of Mrk 501 (3) – *continued*

Target	Start MJD	Stop MJD	Int. time (ksec)	N_{H} $10^{20}/\mathrm{cm}^2$	Photon Index	Flux (2-10keV) 10^{-12} erg/cm^2/s	χ^2 (dof)
Mrk 501	50958.612	50958.626	1.18	1.73 fix	$2.08^{+0.02}_{-0.02}$	$103.80^{+0.94}_{-0.89}$	0.71(45)
	50958.675	50958.696	1.81	1.73 fix	$2.06^{+0.02}_{-0.02}$	$108.10^{+0.73}_{-0.75}$	0.64(45)
	50958.704	50958.706	0.21	1.73 fix	$2.11^{+0.05}_{-0.05}$	$105.70^{+2.22}_{-2.23}$	0.52(45)
	50958.815	50958.827	1.04	1.73 fix	$2.08^{+0.02}_{-0.02}$	$107.80^{+0.99}_{-0.98}$	0.63(45)
	50958.827	50958.839	1.06	1.73 fix	$2.07^{+0.02}_{-0.02}$	$122.30^{+0.98}_{-1.06}$	0.94(45)
	50958.885	50958.906	1.79	1.73 fix	$2.07^{+0.02}_{-0.02}$	$112.50^{+0.74}_{-0.80}$	0.68(45)
	50959.291	50959.306	1.31	1.73 fix	$2.11^{+0.02}_{-0.02}$	$113.30^{+0.90}_{-0.89}$	0.47(45)
	50959.333	50959.354	1.81	1.73 fix	$2.11^{+0.02}_{-0.02}$	$111.30^{+0.79}_{-0.72}$	0.93(45)
	50959.356	50959.373	1.42	1.73 fix	$2.13^{+0.02}_{-0.02}$	$111.20^{+0.83}_{-0.88}$	0.61(45)
	50959.400	50959.423	1.97	1.73 fix	$2.11^{+0.02}_{-0.02}$	$110.10^{+0.76}_{-0.69}$	0.71(45)
	50959.427	50959.439	1.04	1.73 fix	$2.12^{+0.02}_{-0.02}$	$108.10^{+0.96}_{-1.04}$	0.64(45)
	50959.599	50959.613	1.18	1.73 fix	$2.14^{+0.02}_{-0.02}$	$105.70^{+0.94}_{-0.92}$	0.75(45)
	50959.613	50959.627	1.20	1.73 fix	$2.15^{+0.02}_{-0.02}$	$105.20^{+0.91}_{-0.91}$	0.93(45)
	50959.637	50959.639	0.21	1.73 fix	$2.15^{+0.05}_{-0.05}$	$103.40^{+2.25}_{-2.23}$	0.64(45)
	50959.675	50959.696	1.84	1.73 fix	$2.16^{+0.02}_{-0.02}$	$108.70^{+0.71}_{-0.79}$	0.87(45)
	50959.704	50959.706	0.14	1.73 fix	$2.19^{+0.06}_{-0.06}$	$108.00^{+2.69}_{-2.70}$	0.68(45)
	50960.096	50960.106	0.86	1.73 fix	$2.17^{+0.02}_{-0.02}$	$120.50^{+1.11}_{-1.20}$	0.95(45)
	50960.166	50960.172	0.58	1.73 fix	$2.16^{+0.03}_{-0.03}$	$113.50^{+1.34}_{-1.41}$	0.72(45)
	50960.289	50960.306	1.44	1.73 fix	$2.22^{+0.02}_{-0.02}$	$103.30^{+0.86}_{-0.83}$	0.54(45)
	50960.333	50960.353	1.78	1.73 fix	$2.18^{+0.02}_{-0.02}$	$104.50^{+0.74}_{-0.78}$	0.55(45)
	50960.356	50960.372	1.41	1.73 fix	$2.19^{+0.02}_{-0.02}$	$103.40^{+0.83}_{-0.87}$	0.60(45)
	50960.400	50960.422	1.87	1.73 fix	$2.16^{+0.02}_{-0.02}$	$103.20^{+0.74}_{-0.72}$	1.23(45)
	50960.427	50960.439	1.01	1.73 fix	$2.19^{+0.02}_{-0.02}$	$104.30^{+0.99}_{-1.04}$	0.68(45)
	50960.533	50960.546	1.12	1.73 fix	$2.19^{+0.02}_{-0.02}$	$100.90^{+0.91}_{-0.99}$	0.79(45)
	50960.546	50960.559	1.14	1.73 fix	$2.19^{+0.02}_{-0.02}$	$102.10^{+0.95}_{-0.92}$	0.62(45)
	50960.569	50960.572	0.27	1.73 fix	$2.16^{+0.05}_{-0.05}$	$97.14^{+1.94}_{-1.92}$	0.86(45)
	50960.599	50960.613	1.15	1.73 fix	$2.14^{+0.02}_{-0.02}$	$100.10^{+0.96}_{-0.89}$	0.69(45)
	50960.613	50960.627	1.18	1.73 fix	$2.19^{+0.02}_{-0.02}$	$103.50^{+0.93}_{-0.91}$	0.80(45)
	50960.636	50960.639	0.24	1.73 fix	$2.11^{+0.05}_{-0.05}$	$96.44^{+2.03}_{-2.02}$	0.65(45)

† : Phton spectrum is not well represented by a power law function, however, the cutoff power law function is statistically acceptable as we see in Table G.11.

Table G.7: Fit results of *RXTE* spectra of PKS 2155−304 (1)

Target	Start MJD	Stop MJD	Int. time (ksec)	$N_{\rm H}$ $10^{20}/{\rm cm}^2$	Photon Index	Flux (2-10keV) 10^{-12} erg/cm^2/s	χ^2 (dof)
PKS 2155	50219.027	50219.034	0.56	1.77fix	$2.68^{+0.04}_{-0.04}$	$79.96^{+1.27}_{-1.26}$	0.66(45)
−304	50219.150	50219.157	0.56	1.77fix	$2.50^{+0.04}_{-0.04}$	$91.32^{+1.28}_{-1.27}$	0.48(45)
	50219.260	50219.264	0.29	1.77fix	$2.52^{+0.05}_{-0.05}$	$85.06^{+1.71}_{-1.71}$	0.67(45)
	50219.397	50219.403	0.50	1.77fix	$2.56^{+0.04}_{-0.04}$	$88.86^{+1.32}_{-1.31}$	0.68(45)
	50219.527	50219.533	0.48	1.77fix	$2.56^{+0.04}_{-0.04}$	$85.71^{+1.33}_{-1.32}$	0.84(45)
	50219.694	50219.700	0.53	1.77fix	$2.44^{+0.03}_{-0.03}$	$108.50^{+1.36}_{-1.32}$	0.43(45)
	50219.940	50219.944	0.37	1.77fix	$2.83^{+0.20}_{-0.19}$	$118.60^{+8.60}_{-8.61}$	0.92(45)
	50220.080	50220.094	1.15	1.77fix	$2.46^{+0.02}_{-0.02}$	$110.50^{+1.06}_{-1.02}$	0.85(45)
	50220.227	50220.235	0.74	1.77fix	$2.35^{+0.02}_{-0.02}$	$129.90^{+1.14}_{-1.22}$	0.91(45)
	50220.298	50220.302	0.40	1.77fix	$2.39^{+0.03}_{-0.03}$	$134.70^{+1.65}_{-1.60}$	0.74(45)
	50220.498	50220.502	0.38	1.77fix	$2.38^{+0.03}_{-0.03}$	$148.40^{+1.72}_{-1.70}$	0.92(45)
	50220.661	50220.667	0.45	1.77fix	$2.31^{+0.02}_{-0.02}$	$176.10^{+1.69}_{-1.64}$	0.74(45)
	50220.898	50220.903	0.43	1.77fix	$2.50^{+0.03}_{-0.03}$	$116.90^{+1.51}_{-1.60}$	0.83(45)
	50221.094	50221.100	0.48	1.77fix	$2.39^{+0.03}_{-0.03}$	$120.60^{+1.48}_{-1.44}$	0.95(45)
	50221.298	50221.303	0.43	1.77fix	$2.54^{+0.04}_{-0.03}$	$107.30^{+1.51}_{-1.46}$	0.78(45)
	50221.399	50221.405	0.53	1.77fix	$2.55^{+0.03}_{-0.03}$	$107.20^{+1.39}_{-1.31}$	0.55(45)
	50221.561	50221.566	0.40	1.77fix	$2.57^{+0.04}_{-0.04}$	$94.03^{+1.48}_{-1.48}$	0.51(45)
	50221.760	50221.766	0.53	1.77fix	$2.54^{+0.04}_{-0.03}$	$96.19^{+1.30}_{-1.30}$	0.61(45)
	50221.898	50221.904	0.54	1.77fix	$2.54^{+0.03}_{-0.03}$	$105.30^{+1.37}_{-1.31}$	0.78(45)
	50221.964	50221.971	0.54	1.77fix	$2.48^{+0.03}_{-0.03}$	$107.40^{+1.38}_{-1.31}$	0.73(45)
	50222.081	50222.104	1.98	1.77fix	$2.51^{+0.02}_{-0.02}$	$114.00^{+0.68}_{-0.75}$	0.78(45)
	50222.151	50222.171	1.70	1.77fix	$2.48^{+0.02}_{-0.02}$	$115.00^{+0.75}_{-0.78}$	0.67(45)
	50222.275	50222.290	1.26	1.77fix	$2.47^{+0.02}_{-0.02}$	$112.20^{+0.88}_{-0.87}$	0.44(45)
	50222.290	50222.305	1.28	1.77fix	$2.48^{+0.02}_{-0.02}$	$113.50^{+0.83}_{-0.92}$	1.15(45)
	50222.604	50222.618	1.20	1.77fix	$2.55^{+0.02}_{-0.02}$	$121.40^{+0.96}_{-0.91}$	0.89(45)
	50222.618	50222.632	1.18	1.77fix	$2.55^{+0.02}_{-0.02}$	$123.20^{+1.00}_{-0.90}$	0.56(45)
	50222.663	50222.681	1.49	1.77fix	$2.54^{+0.02}_{-0.02}$	$126.30^{+0.82}_{-0.86}$	0.78(45)
	50222.681	50222.698	1.52	1.77fix	$2.49^{+0.02}_{-0.02}$	$128.40^{+0.86}_{-0.81}$	0.69(45)
	50222.752	50222.767	1.33	1.77fix	$2.49^{+0.02}_{-0.02}$	$131.00^{+0.95}_{-0.86}$	0.96(45)
	50222.801	50222.813	1.07	1.77fix	$2.43^{+0.02}_{-0.02}$	$148.80^{+1.05}_{-1.06}$	0.64(45)
	50222.813	50222.826	1.09	1.77fix	$2.43^{+0.02}_{-0.02}$	$156.50^{+1.33}_{-1.24}$	1.10(45)
	50222.826	50222.839	1.09	1.77fix	$2.43^{+0.02}_{-0.02}$	$161.50^{+1.06}_{-1.07}$	1.07(45)
	50222.941	50222.959	1.57	1.77fix	$2.48^{+0.02}_{-0.02}$	$173.70^{+1.15}_{-1.18}$	1.12(45)
	50222.959	50222.972	1.07	1.77fix	$2.52^{+0.02}_{-0.02}$	$174.20^{+1.11}_{-1.14}$	0.79(45)
	50223.012	50223.026	1.22	1.77fix	$2.53^{+0.02}_{-0.02}$	$174.70^{+1.23}_{-1.19}$	0.96(45)
	50223.026	50223.039	1.14	1.77fix	$2.52^{+0.02}_{-0.02}$	$173.30^{+1.10}_{-1.07}$	1.29(45)
	50223.082	50223.094	1.02	1.77fix	$2.55^{+0.02}_{-0.02}$	$167.60^{+1.14}_{-1.15}$	0.95(45)
	50223.094	50223.105	1.02	1.77fix	$2.58^{+0.02}_{-0.02}$	$169.30^{+1.14}_{-1.14}$	1.01(45)
	50223.152	50223.172	1.76	1.77fix	$2.55^{+0.01}_{-0.01}$	$162.50^{+0.82}_{-0.88}$	1.11(45)
	50223.222	50223.239	1.46	1.77fix	$2.54^{+0.01}_{-0.01}$	$177.00^{+0.94}_{-0.98}$	1.03(45)

Table G.8: Fit results of PKS 2155−304 (2) – *continued*

Target	Start MJD	Stop MJD	Int. time (ksec)	N_H $10^{20}/cm^2$	Photon Index	Flux (2-10keV) 10^{-12} erg/cm^2/s	χ^2 (dof)
PKS 2155	50223.531	50223.548	1.42	1.77fix	$2.51^{+0.01}_{-0.01}$	$209.50^{+1.06}_{-1.00}$	1.41(45)
−304	50223.548	50223.564	1.44	1.77fix	$2.49^{+0.01}_{-0.01}$	$206.80^{+1.04}_{-1.01}$	0.75(45)
	50223.829	50223.839	0.85	1.77fix	$2.48^{+0.02}_{-0.02}$	$210.10^{+1.34}_{-1.33}$	0.86(45)
	50223.872	50223.890	1.60	1.77fix	$2.49^{+0.01}_{-0.01}$	$193.10^{+1.11}_{-1.07}$	0.78(45)
	50223.890	50223.907	1.41	1.77fix	$2.48^{+0.01}_{-0.01}$	$188.40^{+1.00}_{-1.00}$	0.98(45)
	50223.942	50223.959	1.44	1.77fix	$2.45^{+0.02}_{-0.01}$	$179.20^{+1.06}_{-1.14}$	0.98(45)
	50223.959	50223.973	1.26	1.77fix	$2.45^{+0.01}_{-0.01}$	$183.90^{+1.06}_{-1.03}$	1.21(45)
	50224.012	50224.027	1.30	1.77fix	$2.46^{+0.02}_{-0.02}$	$192.50^{+1.56}_{-1.63}$	1.00(45)
	50224.207	50224.212	0.45	1.77fix	$2.59^{+0.02}_{-0.02}$	$178.20^{+1.70}_{-1.79}$	0.83(45)
	50224.302	50224.307	0.40	1.77fix	$2.61^{+0.03}_{-0.03}$	$155.80^{+1.76}_{-1.76}$	0.84(45)
	50224.479	50224.488	0.77	1.77fix	$2.53^{+0.02}_{-0.02}$	$192.60^{+1.43}_{-1.35}$	0.86(45)
	50224.624	50224.630	0.54	1.77fix	$2.43^{+0.02}_{-0.02}$	$207.40^{+1.68}_{-1.65}$	0.74(45)
	50224.763	50224.769	0.51	1.77fix	$2.52^{+0.02}_{-0.02}$	$213.30^{+1.70}_{-1.77}$	0.87(45)
	50224.901	50224.908	0.59	1.77fix	$2.50^{+0.02}_{-0.02}$	$214.30^{+1.61}_{-1.64}$	0.77(45)
	50225.207	50225.224	1.47	1.77fix	$2.56^{+0.01}_{-0.01}$	$186.40^{+0.94}_{-1.01}$	1.51(45)
	50225.359	50225.366	0.56	1.77fix	$2.56^{+0.02}_{-0.02}$	$179.20^{+1.56}_{-1.55}$	1.13(45)
	50225.493	50225.496	0.29	1.77fix	$2.49^{+0.03}_{-0.03}$	$213.60^{+2.31}_{-2.27}$	0.71(45)
	50225.734	50225.739	0.42	1.77fix	$2.44^{+0.02}_{-0.02}$	$211.50^{+1.93}_{-1.91}$	0.90(45)
	50225.834	50225.841	0.61	1.77fix	$2.46^{+0.02}_{-0.02}$	$194.40^{+1.55}_{-1.52}$	0.92(45)
	50225.968	50225.975	0.59	1.77fix	$2.52^{+0.02}_{-0.02}$	$203.40^{+1.62}_{-1.58}$	1.02(45)
	50226.035	50226.042	0.61	1.77fix	$2.54^{+0.02}_{-0.02}$	$215.70^{+1.65}_{-1.61}$	1.06(45)
	50226.205	50226.212	0.54	1.77fix	$2.66^{+0.02}_{-0.02}$	$205.10^{+1.68}_{-1.72}$	0.92(45)
	50226.305	50226.309	0.37	1.77fix	$2.56^{+0.02}_{-0.02}$	$205.10^{+2.04}_{-2.01}$	1.05(45)
	50226.438	50226.442	0.35	1.77fix	$2.61^{+0.03}_{-0.03}$	$182.70^{+1.98}_{-2.04}$	0.79(45)
	50226.556	50226.562	0.51	1.77fix	$2.54^{+0.02}_{-0.02}$	$162.60^{+1.58}_{-1.62}$	0.78(45)
	50226.764	50226.771	0.54	1.77fix	$2.69^{+0.03}_{-0.03}$	$132.80^{+1.46}_{-1.47}$	0.66(45)
	50226.906	50226.910	0.35	1.77fix	$2.66^{+0.04}_{-0.04}$	$130.10^{+1.77}_{-1.86}$	0.59(45)
	50227.147	50227.153	0.56	1.77fix	$2.78^{+0.03}_{-0.03}$	$137.10^{+1.50}_{-1.50}$	0.52(45)
	50227.269	50227.271	0.22	1.77fix	$2.67^{+0.05}_{-0.05}$	$113.90^{+2.21}_{-2.11}$	0.65(45)
	50227.336	50227.351	1.36	1.77fix	$2.70^{+0.02}_{-0.02}$	$119.30^{+0.91}_{-0.90}$	0.67(45)
	50227.353	50227.360	0.58	1.77fix	$2.72^{+0.03}_{-0.03}$	$125.90^{+1.42}_{-1.37}$	0.67(45)
	50227.489	50227.495	0.51	1.77fix	$2.63^{+0.03}_{-0.03}$	$141.30^{+1.49}_{-1.54}$	0.74(45)
	50227.603	50227.608	0.48	1.77fix	$2.65^{+0.03}_{-0.03}$	$145.50^{+1.63}_{-1.54}$	0.66(45)
	50227.736	50227.742	0.46	1.77fix	$2.57^{+0.03}_{-0.03}$	$134.10^{+1.56}_{-1.65}$	0.77(45)
	50227.837	50227.843	0.51	1.77fix	$2.63^{+0.03}_{-0.03}$	$139.10^{+1.56}_{-1.52}$	0.74(45)
	50227.974	50227.977	0.30	1.77fix	$2.71^{+0.04}_{-0.04}$	$134.10^{+1.96}_{-2.02}$	0.68(45)
	50228.141	50228.157	1.38	1.77fix	$2.71^{+0.02}_{-0.02}$	$130.40^{+0.88}_{-0.94}$	0.89(45)
	50228.371	50228.377	0.54	1.77fix	$2.73^{+0.03}_{-0.03}$	$136.70^{+1.54}_{-1.49}$	0.55(45)
	50228.553	50228.561	0.66	1.77fix	$2.62^{+0.02}_{-0.02}$	$142.10^{+1.34}_{-1.39}$	0.62(45)
	50228.695	50228.701	0.53	1.77fix	$2.67^{+0.03}_{-0.03}$	$146.70^{+1.54}_{-1.53}$	0.59(45)

Table G.9: Fit results of PKS 2155−304 (3) − *continued*

Target	Start MJD	Stop MJD	Int. time (ksec)	N_{H} $10^{20}/\mathrm{cm}^2$	Photon Index	Flux (2-10keV) 10^{-12} erg/cm^2/s	χ^2 (dof)
PKS 2155	50228.837	50228.843	0.54	1.77fix	$2.64^{+0.03}_{-0.03}$	$140.40^{+1.54}_{-1.45}$	1.20(45)
−304	50228.972	50228.978	0.53	1.77fix	$2.62^{+0.03}_{-0.03}$	$155.50^{+1.61}_{-1.52}$	0.63(45)
	50229.104	50229.111	0.66	1.77fix	$2.54^{+0.02}_{-0.02}$	$194.30^{+1.49}_{-1.49}$	0.84(45)
	50229.238	50229.245	0.61	1.77fix	$2.60^{+0.02}_{-0.02}$	$174.10^{+1.49}_{-1.52}$	0.56(45)
	50229.419	50229.427	0.66	1.77fix	$2.50^{+0.02}_{-0.02}$	$164.40^{+1.37}_{-1.40}$	0.70(45)
	50229.553	50229.560	0.64	1.77fix	$2.51^{+0.02}_{-0.02}$	$163.90^{+1.42}_{-1.39}$	0.66(45)
	50229.677	50229.682	0.45	1.77fix	$2.50^{+0.03}_{-0.03}$	$158.80^{+1.76}_{-1.66}$	0.71(45)
	50229.684	50229.702	1.57	1.77fix	$2.48^{+0.01}_{-0.01}$	$158.60^{+0.88}_{-0.90}$	0.50(45)
	50229.972	50229.979	0.59	1.77fix	$2.47^{+0.02}_{-0.02}$	$142.00^{+1.41}_{-1.38}$	0.67(45)
	50230.106	50230.112	0.53	1.77fix	$2.48^{+0.03}_{-0.02}$	$152.10^{+1.52}_{-1.51}$	0.57(45)
	50230.375	50230.379	0.34	1.77fix	$2.34^{+0.03}_{-0.03}$	$152.20^{+1.83}_{-1.90}$	0.91(45)
	50230.485	50230.493	0.70	1.77fix	$2.33^{+0.02}_{-0.02}$	$159.40^{+1.32}_{-1.31}$	0.50(45)
	50230.625	50230.631	0.50	1.77fix	$2.38^{+0.02}_{-0.02}$	$158.30^{+1.59}_{-1.51}$	0.79(45)
	50230.839	50230.845	0.45	1.77fix	$2.26^{+0.02}_{-0.02}$	$194.50^{+1.74}_{-1.77}$	0.47(45)
	50230.973	50230.979	0.51	1.77fix	$2.38^{+0.03}_{-0.03}$	$140.80^{+1.45}_{-1.50}$	0.52(45)
	50231.162	50231.170	0.66	1.77fix	$2.29^{+0.02}_{-0.02}$	$131.00^{+1.27}_{-1.21}$	0.75(45)
	50231.613	50231.632	1.58	1.77fix	$2.33^{+0.01}_{-0.01}$	$146.60^{+0.82}_{-0.86}$	0.66(45)
	50287.376	50287.393	1.42	1.77fix	$2.88^{+0.05}_{-0.05}$	$43.82^{+0.69}_{-0.68}$	0.61(45)
	50289.663	50289.680	1.49	1.77fix	$3.08^{+0.07}_{-0.07}$	$29.40^{+0.66}_{-0.66}$	0.45(45)
	50291.665	50291.681	1.42	1.77fix	$3.13^{+0.14}_{-0.14}$	$21.01^{+0.91}_{-0.91}$	0.45(45)
	50401.319	50401.332	1.10	1.77fix	$2.99^{+0.06}_{-0.06}$	$43.68^{+0.81}_{-0.81}$	0.50(45)
	50401.338	50401.343	0.40	1.77fix	$2.84^{+0.08}_{-0.08}$	$47.32^{+1.33}_{-1.32}$	0.37(45)
	50401.372	50401.385	1.09	1.77fix	$3.02^{+0.05}_{-0.05}$	$46.47^{+0.82}_{-0.81}$	0.51(45)
	50401.385	50401.398	1.10	1.77fix	$2.91^{+0.05}_{-0.05}$	$44.68^{+0.80}_{-0.80}$	0.58(45)
	50401.398	50401.411	1.12	1.77fix	$2.94^{+0.05}_{-0.05}$	$45.68^{+0.80}_{-0.80}$	0.52(45)
	50401.439	50401.452	1.10	1.77fix	$3.01^{+0.05}_{-0.05}$	$46.18^{+0.81}_{-0.81}$	0.69(45)
	50401.452	50401.464	1.10	1.77fix	$2.88^{+0.05}_{-0.05}$	$46.01^{+0.81}_{-0.80}$	0.48(45)
	50401.464	50401.477	1.10	1.77fix	$3.03^{+0.05}_{-0.05}$	$46.99^{+0.82}_{-0.82}$	0.60(45)
	50401.506	50401.520	1.22	1.77fix	$2.97^{+0.04}_{-0.04}$	$52.92^{+0.78}_{-0.79}$	0.48(45)
	50401.520	50401.534	1.22	1.77fix	$2.88^{+0.04}_{-0.04}$	$53.11^{+0.79}_{-0.79}$	0.71(45)
	50401.537	50401.544	0.62	1.77fix	$2.91^{+0.06}_{-0.06}$	$56.98^{+1.11}_{-1.12}$	0.60(45)
	50401.572	50401.587	1.28	1.77fix	$2.83^{+0.03}_{-0.03}$	$64.66^{+0.78}_{-0.79}$	0.70(45)
	50401.587	50401.602	1.28	1.77fix	$2.83^{+0.04}_{-0.04}$	$61.19^{+0.79}_{-0.79}$	0.76(45)
	50401.606	50401.611	0.40	1.77fix	$2.97^{+0.07}_{-0.07}$	$61.17^{+1.41}_{-1.41}$	0.59(45)
	50402.657	50402.667	0.86	1.77fix	$2.55^{+0.06}_{-0.06}$	$44.94^{+0.89}_{-0.88}$	0.93(45)
	50407.398	50407.413	1.30	1.77fix	$2.91^{+0.04}_{-0.04}$	$54.67^{+0.76}_{-0.77}$	0.56(45)
	50407.741	50407.746	0.50	1.77fix	$2.71^{+0.05}_{-0.05}$	$64.80^{+1.25}_{-1.25}$	0.82(45)
	50408.317	50408.334	1.42	1.77fix	$2.81^{+0.03}_{-0.03}$	$79.85^{+0.80}_{-0.80}$	0.78(45)
	50409.125	50409.135	0.88	1.77fix	$2.89^{+0.04}_{-0.04}$	$65.19^{+0.97}_{-0.98}$	0.55(45)

Table G.10: Fit results of PKS 2155$-$304 (4) $-$ *continued*

Target	Start MJD	Stop MJD	Int. time (ksec)	N_H 10^{20}/cm^2	Photon Index	Flux (2-10keV) 10^{-12} erg/cm^2/s	χ^2 (dof)
PKS 2155	50409.601	50409.605	0.34	1.77fix	$2.77^{+0.05}_{-0.05}$	$92.78^{+1.69}_{-1.68}$	0.47(45)
-304	50410.443	50410.448	0.50	1.77fix	$2.88^{+0.05}_{-0.04}$	$87.17^{+1.38}_{-1.38}$	0.64(45)
	50410.452	50410.467	1.23	1.77fix	$2.77^{+0.03}_{-0.03}$	$86.01^{+0.88}_{-0.87}$	0.54(45)
	50410.467	50410.481	1.23	1.77fix	$2.84^{+0.03}_{-0.03}$	$88.73^{+0.88}_{-0.87}$	0.39(45)
	50410.531	50410.548	1.42	1.77fix	$2.80^{+0.02}_{-0.03}$	$89.04^{+0.81}_{-0.80}$	0.66(45)
	50410.601	50410.614	1.12	1.77fix	$2.85^{+0.03}_{-0.03}$	$98.98^{+0.94}_{-0.94}$	0.70(45)
	50410.672	50410.681	0.82	1.77fix	$2.84^{+0.03}_{-0.03}$	$106.80^{+1.19}_{-1.09}$	0.74(45)
	50411.318	50411.333	1.30	1.77fix	$2.78^{+0.03}_{-0.03}$	$79.42^{+0.83}_{-0.84}$	0.81(45)
	50411.333	50411.348	1.31	1.77fix	$2.82^{+0.03}_{-0.03}$	$82.02^{+0.83}_{-0.83}$	0.44(45)
	50411.376	50411.389	1.10	1.77fix	$2.81^{+0.03}_{-0.03}$	$89.27^{+0.94}_{-0.93}$	0.61(45)
	50411.389	50411.402	1.09	1.77fix	$2.77^{+0.03}_{-0.03}$	$88.75^{+0.95}_{-0.94}$	0.58(45)
	50411.402	50411.414	1.10	1.77fix	$2.82^{+0.03}_{-0.03}$	$89.72^{+0.92}_{-0.93}$	0.76(45)
	50411.454	50411.467	1.20	1.77fix	$2.77^{+0.03}_{-0.03}$	$92.74^{+0.91}_{-0.90}$	0.59(45)
	50411.467	50411.481	1.20	1.77fix	$2.85^{+0.03}_{-0.03}$	$95.06^{+0.90}_{-0.90}$	0.87(45)
	50411.532	50411.548	1.42	1.77fix	$2.76^{+0.02}_{-0.02}$	$96.35^{+0.83}_{-0.82}$	0.90(45)
	50772.955	50772.969	1.25	1.77fix	$3.02^{+0.01}_{-0.02}$	$247.00^{+1.43}_{-1.51}$	1.09(45)
	50773.639	50773.650	0.91	1.77fix	$3.01^{+0.02}_{-0.02}$	$241.10^{+1.77}_{-1.67}$	0.56(45)
	50774.721	50774.724	0.30	1.77fix	$2.96^{+0.04}_{-0.04}$	$183.90^{+2.64}_{-2.55}$	0.79(45)
	50822.130	50822.133	0.32	1.77fix	$3.02^{+0.12}_{-0.11}$	$47.28^{+1.81}_{-1.79}$	0.36(45)
	50822.137	50822.141	0.29	1.77fix	$3.06^{+0.12}_{-0.12}$	$48.06^{+1.91}_{-1.88}$	0.66(45)
	50822.534	50822.544	0.88	1.77fix	$2.83^{+0.08}_{-0.08}$	$35.45^{+0.98}_{-0.96}$	0.63(45)
	50823.131	50823.142	0.88	1.77fix	$3.15^{+0.10}_{-0.10}$	$32.22^{+1.03}_{-1.02}$	0.42(45)
	50823.537	50823.546	0.74	1.77fix	$2.90^{+0.10}_{-0.09}$	$33.68^{+1.06}_{-1.04}$	0.56(45)
	50824.308	50824.318	0.86	1.77fix	$3.55^{+0.18}_{-0.17}$	$21.38^{+1.08}_{-1.06}$	0.61(45)
	50824.508	50824.514	0.50	1.77fix	$3.22^{+0.20}_{-0.19}$	$20.48^{+1.27}_{-1.24}$	0.41(45)
	50825.244	50825.252	0.70	1.77fix	$2.87^{+0.06}_{-0.06}$	$52.84^{+1.15}_{-1.14}$	0.83(45)
	50825.608	50825.613	0.40	1.77fix	$3.17^{+0.08}_{-0.08}$	$62.33^{+1.71}_{-1.70}$	0.69(45)
	50826.133	50826.144	0.88	1.77fix	$3.19^{+0.07}_{-0.06}$	$50.46^{+1.12}_{-1.11}$	0.86(45)
	50826.609	50826.613	0.40	1.77fix	$3.26^{+0.10}_{-0.10}$	$54.50^{+1.73}_{-1.70}$	0.62(45)

Table G.11: Fit results of TeV blazars with a cutoff power law function

| Target	Start MJD	Stop MJD	Int. time (ksec)	N_H 10^{20}/cm^2	E_c (keV)	Photon Index	Flux (2-10keV) 10^{-12} erg/cm^2/s	χ^2 (dof)
Mrk 421	50208.556	50208.569	1.14	1.45fix	$1.86^{+0.17}_{-0.17}$	$2.62^{+0.03}_{-0.03}$	$541.80^{+24.6}_{-23.2}$	0.63(44)
	50549.223	50549.236	1.14	1.45fix	$2.23^{+0.30}_{-0.29}$	$3.42^{+0.06}_{-0.06}$	$428.80^{+38.8}_{-34.6}$	0.76(44)
	50549.236	50549.249	1.15	1.45fix	$2.11^{+0.29}_{-0.29}$	$3.37^{+0.06}_{-0.06}$	$429.23^{+37.4}_{-34.1}$	0.74(44)
	50549.249	50549.262	1.15	1.45fix	$2.25^{+0.29}_{-0.29}$	$3.42^{+0.06}_{-0.06}$	$421.07^{+37.8}_{-33.9}$	0.87(44)
	50549.289	50549.312	1.97	1.45fix	$2.06^{+0.23}_{-0.23}$	$3.33^{+0.05}_{-0.05}$	$392.05^{+27.0}_{-25.1}$	0.65(44)
	50602.261	50602.273	1.02	1.45fix	$2.20^{+0.30}_{-0.30}$	$3.15^{+0.06}_{-0.06}$	$384.60^{+33.8}_{-30.9}$	0.78(44)
Mrk 501	50641.151	50641.166	1.30	1.73fix	$1.29^{+0.16}_{-0.16}$	$2.18^{+0.03}_{-0.03}$	$607.38^{+23.3}_{-22.1}$	1.01(44)
	50641.176	50641.191	1.28	1.73fix	$1.20^{+0.16}_{-0.16}$	$2.16^{+0.03}_{-0.03}$	$602.35^{+23.1}_{-22.1}$	1.10(44)
	50644.152	50644.169	1.42	1.73fix	$0.94^{+0.15}_{-0.15}$	$2.06^{+0.03}_{-0.03}$	$602.70^{+21.3}_{-20.4}$	1.11(44)
	50645.152	50645.171	1.60	1.73fix	$1.29^{+0.13}_{-0.13}$	$2.17^{+0.03}_{-0.03}$	$686.61^{+21.8}_{-20.9}$	1.26(44)
	50645.173	50645.192	1.63	1.73fix	$1.32^{+0.13}_{-0.13}$	$2.18^{+0.02}_{-0.02}$	$671.81^{+21.5}_{-20.5}$	1.02(44)

Appendix H

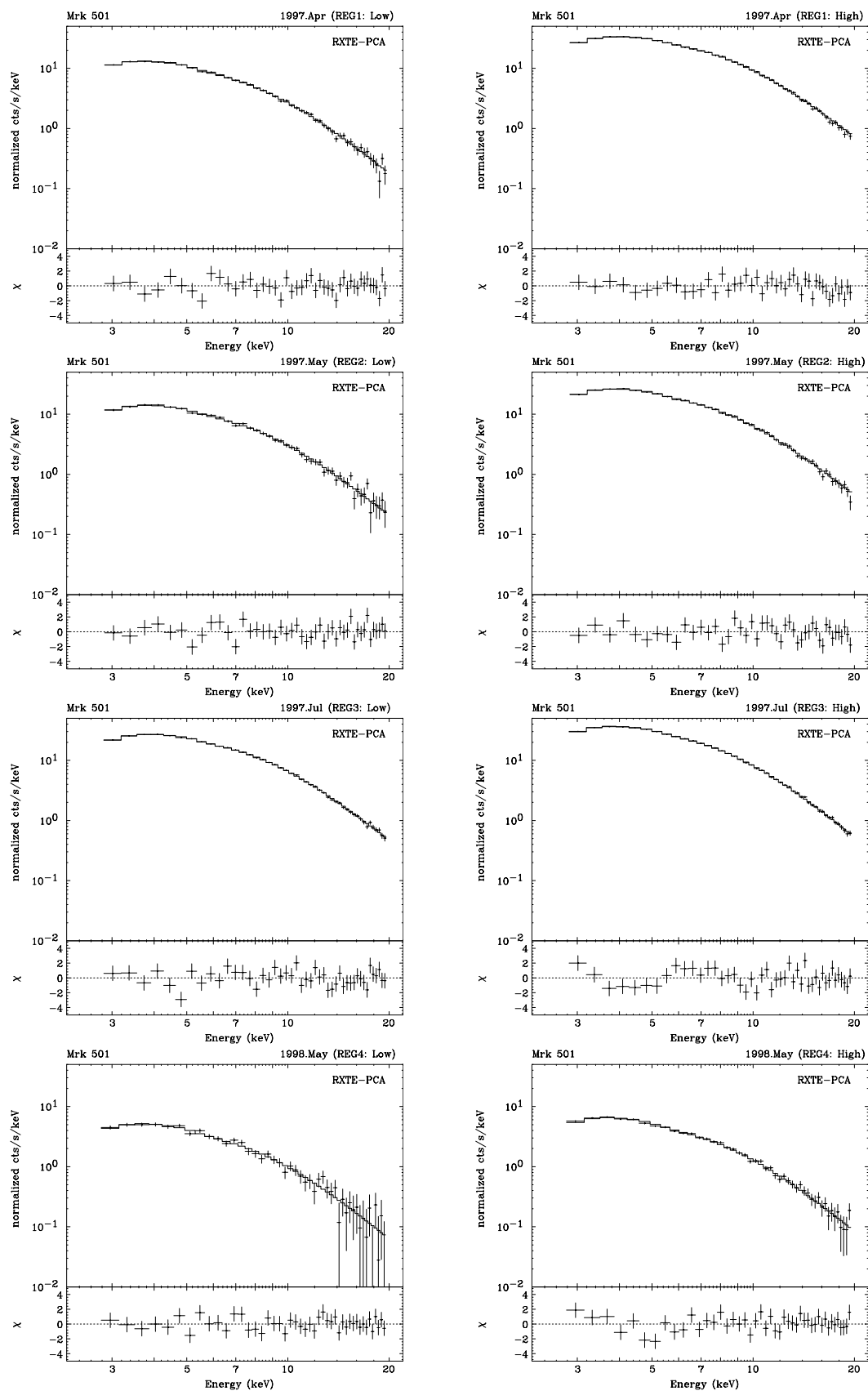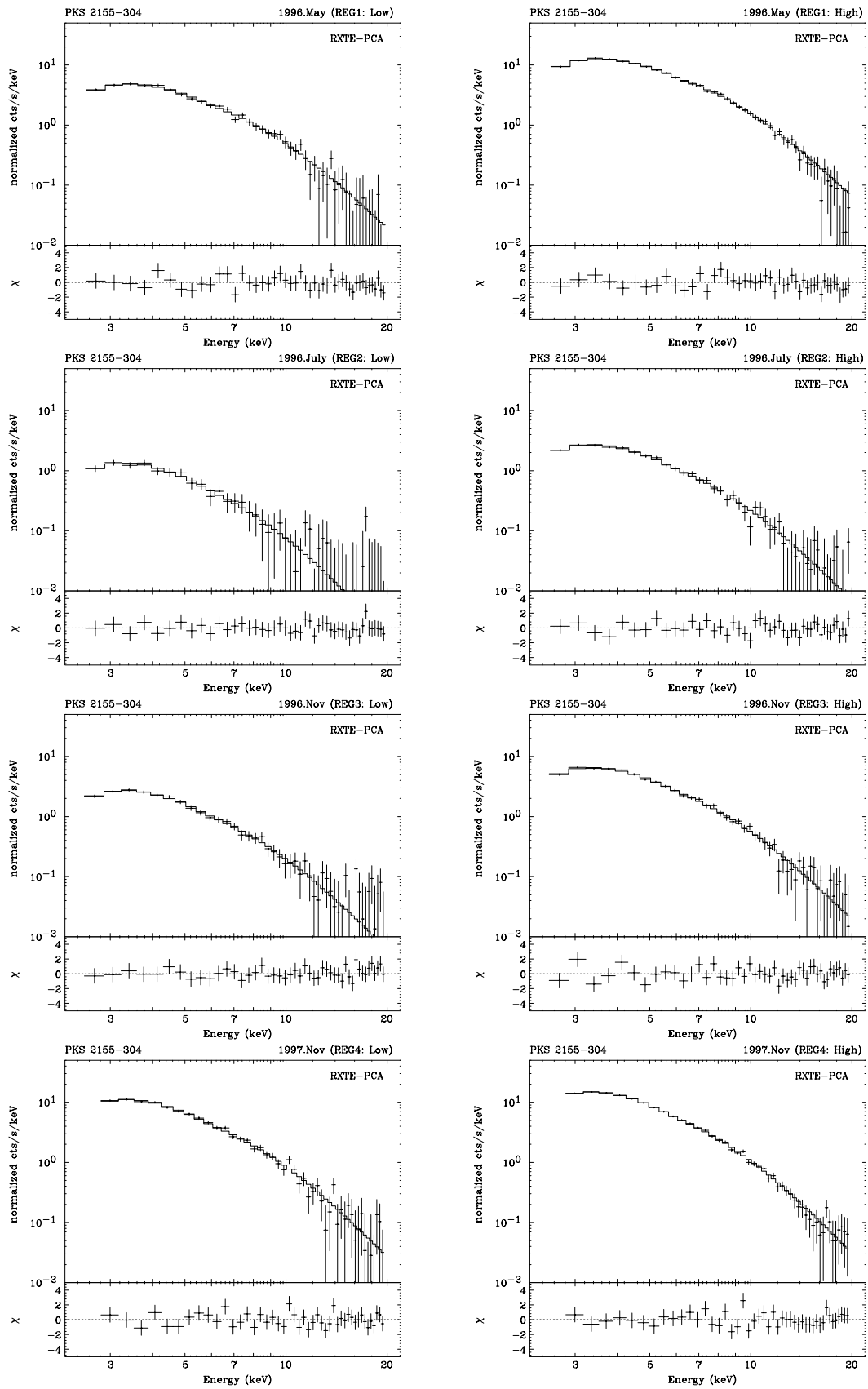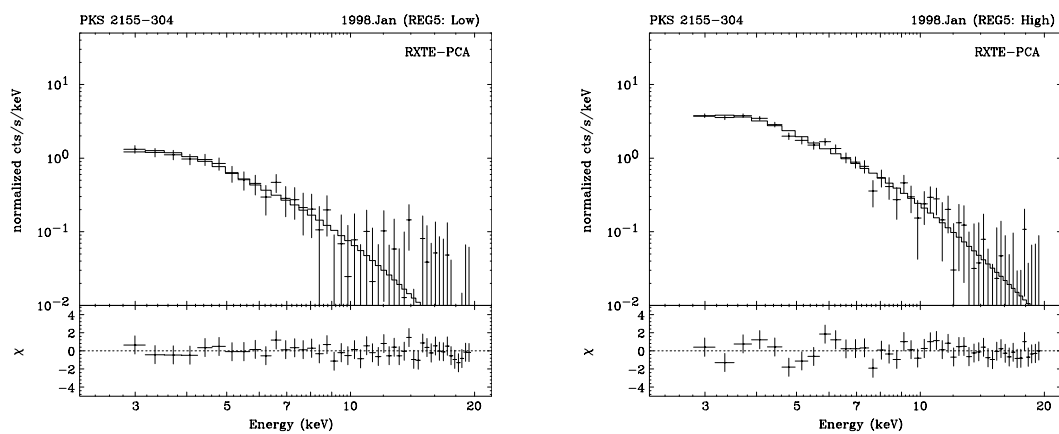# *RXTE* Spectra of TeV Blazars
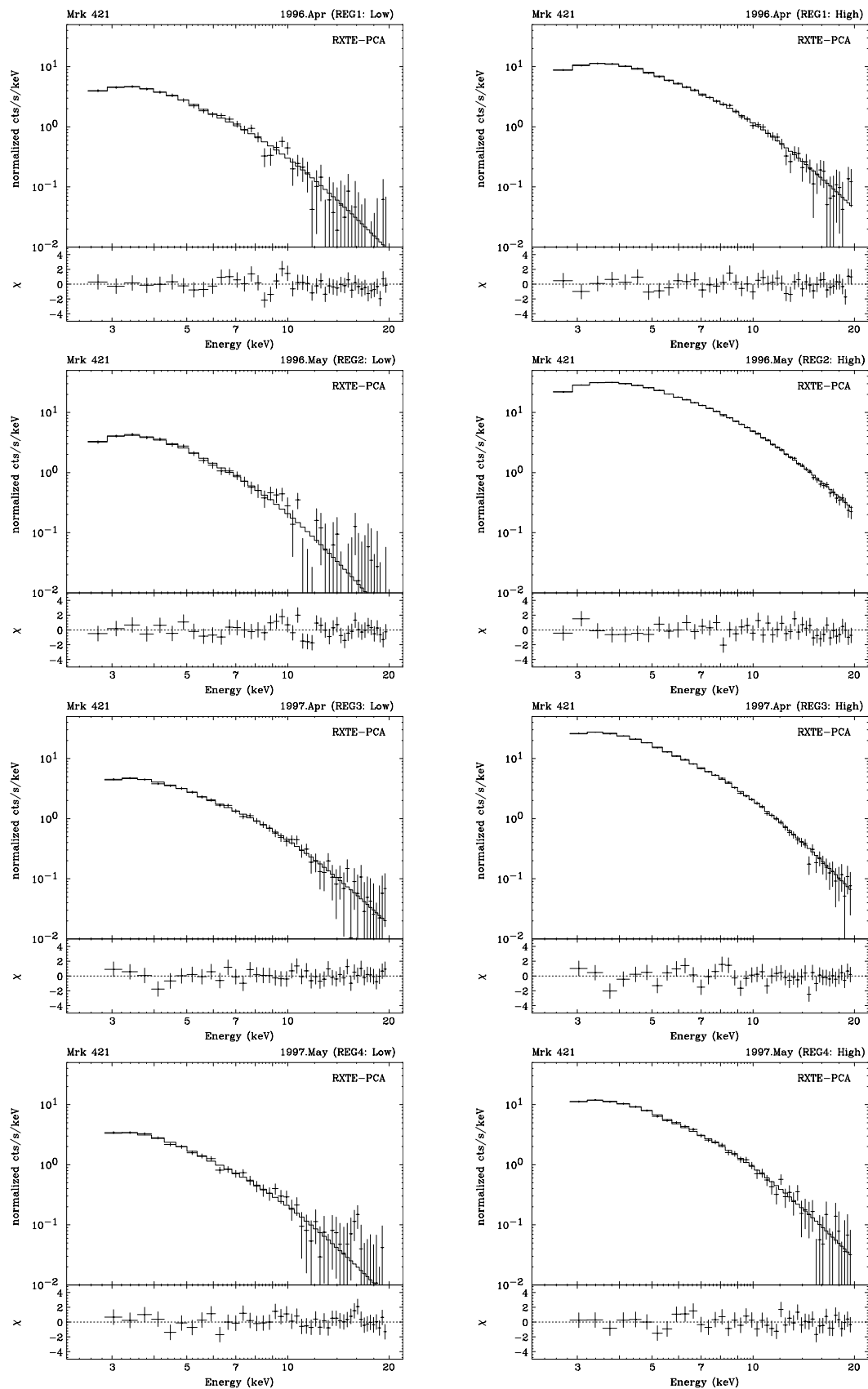
Figure H.1:

Figure H.2:

Figure H.3:

Figure H.4:

Appendix I

Homogeneous SSC model

I.1 Solution for a Spherical Geometry

We start from the equation (11.1)

$$F(\nu) = \frac{1}{4\pi d_{\mathrm{L}}^2} \int d^3\vec{r} \ [4\pi j_\nu(\vec{r})\exp(- \int \alpha_\nu(\vec{r'})ds')], \tag{I.1}$$

where j_ν and α_ν are emission and absorption coefficients respectively. For the synchrotron case, they are given in (3.37) and (3.40). We consider here the spherical source of radius R. The sphere can be divided into the sum of cylindrical shells, whose center-lines are aligned to the z axis. Each shell is very thin, having equal thickness dx. Those shells can be further cut into rings, which are aligned in parallel to xy-plane. Each ring has an equal width in height (dl) in the z direction. We first consider the emission from the each 'ring', summing up to a single 'cylinder' next, and finally all the contribution from cylindrical shells are added to calculate the emission from the entire sphere. The schematic view of the cross section of the homogeneous sphere is given in Figure I.1.

We start from the relations

$$r(\alpha)\sin\alpha = R\sin\theta, \tag{I.2}$$

$$dl = r(\alpha)\cos\alpha - r(\alpha + d\alpha)\cos(\alpha + d\alpha). \tag{I.3}$$

Both equations yield,

$$dl = \frac{R\sin\theta}{\sin^2\alpha}d\alpha. \tag{I.4}$$

Similarly, dx is simply given by

$$dx = R\sin(\theta + d\theta) - R\sin\theta = R\cos\theta d\theta. \tag{I.5}$$

observer
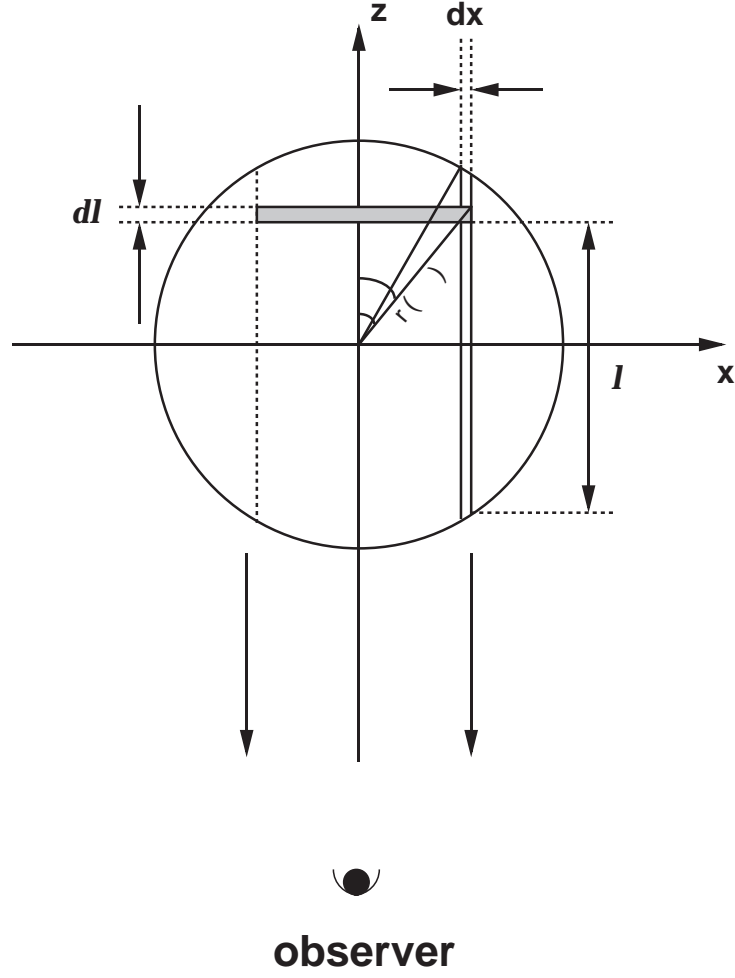
Figure I.1: Schematic view of the cross section of a homogeneous sphere. The shaded part represent a 'ring'.

We obtain the ring volume dV

$$dV = 2\pi R\sin\theta dxdl = 2\pi R^3\sin^2\theta\cos\theta d\theta\frac{d\alpha}{\sin^2\alpha}. \tag{I.6}$$

The photon flux emitted from this ring will be absorbed by a factor $\exp(-\alpha_\nu l)$ before escaping from the sphere. Assuming that only photons emitted in the solid angle $\Omega \sim \Omega + d\Omega$ can be observed, we can calculate the luminosity from the ring in $d\Omega$

$$dS_\nu(\alpha, \theta, d\Omega) = j_\nu d\Omega h\nu dV \exp(-\alpha_\nu l) = G(\theta)\frac{d\alpha}{\sin^2\alpha}\exp[-\alpha_\nu K(\alpha)], \tag{I.7}$$

where

$$G(\theta) \equiv j_\nu d\Omega h\nu 2\pi R^3\sin^2\theta\cos\theta d\theta\exp[-\alpha_\nu R\cos\theta], \tag{I.8}$$

$$K(\alpha) = \frac{\cos\alpha}{\sin\alpha} R\sin\theta. \tag{I.9}$$

Note that, there is a relation

$$\frac{d}{d\alpha}[\exp(-\alpha_\nu K(\alpha))] = \alpha_\nu R \frac{\sin\theta}{\sin^2\alpha}\exp[-\alpha_\nu K(\alpha)]. \tag{I.10}$$

Next we consider the emission from a single cylindrical shell. Integral of $dS_\nu(\alpha, \theta, d\Omega)$ over α yields the solution

$$dS_\nu(\theta, d\Omega) = \int_\theta^{\pi-\theta} \frac{G(\theta)}{\alpha_\nu R\sin\theta} \frac{d}{d\alpha}[\exp(-\alpha_\nu K(\alpha))]d\alpha = CJ(\theta), \tag{I.11}$$

where

$$C = \frac{1}{\alpha_\nu R} j_\nu d\Omega h\nu 2\pi R^3, \tag{I.12}$$

$$J(\theta) = \sin\theta\cos\theta d\theta[1 - \exp(-2\alpha_\nu R\cos\theta)]. \tag{I.13}$$

Finally, contributions from each cylindrical shell are summed up, and integrated over the solid angle. We have the total luminosity from the sphere S_ν,

$$S_\nu = 4\pi \int_0^{\pi/2} dS_\nu(\theta) = \frac{8\pi^2 j_\nu h\nu R^2}{\alpha_\nu} \int_0^1 t[1 - \exp(-2\alpha_\nu Rt)]dt \tag{I.14}$$

This yields straightforwardly the observed flux at distance d_{L}

$$L(\nu) = \frac{S_\nu}{4\pi d_{\mathrm{L}}^2} = 4\pi^2 R^2 \frac{j_\nu}{\alpha_\nu}(1 - \frac{2}{\tau_\nu{}^2}[1 - e^{-\tau_\nu}(\tau_\nu + 1)]), \tag{I.15}$$

where τ_ν is the optical depth in the blob along the line of sight and expressed as $\tau_\nu = 2\alpha_\nu R$.

I.2   Correction Factor; C_{corr}

We calculate the correction factor in equation (11.3), based on the formulae given in Gould (1979). In a homogeneous model, the electron population is assumed to be *homogeneous* over the source. This results in the synchrotron emissivity j_ν is also homogeneous, however, the number density of photons $n(\epsilon_0)$ should vary depending on the position in the source.

Gould (1979) showed that in a homogeneous source, the number density changes with the radial distance from the center ξ ($\xi \equiv r/R$) as

$$n(\xi) \propto \Phi(\xi), \tag{I.16}$$
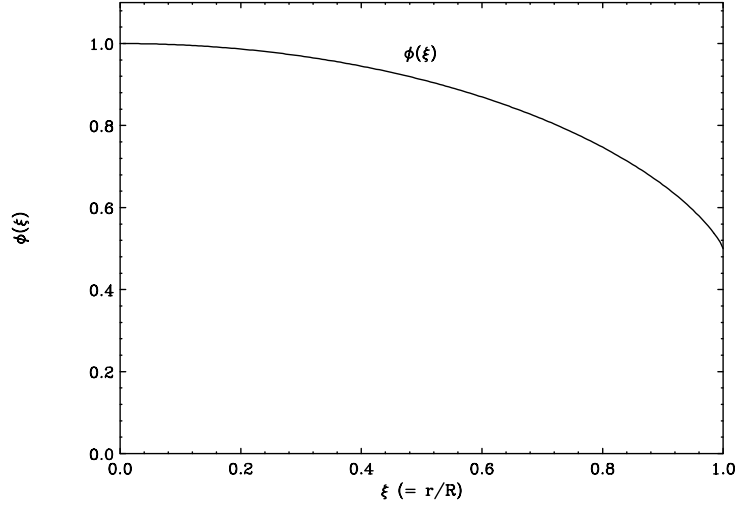
Figure I.2: Function $\Phi(\xi)$, which represents the *density* of synchrotron photon distribution in a homogeneous source ($n(\xi) \propto \Phi(\xi)$). ξ is defined as $\xi \equiv r/R$, and r is the radial distance from the center.

where

$$\Phi(\xi) = \frac{1}{4\xi}(1 - \xi^2)\ln\left|\frac{1+\xi}{1-\xi}\right| + \frac{1}{2}, \tag{I.17}$$

and illustrated in Figure I.2.

The total number of synchrotron self-Compton (SSC) photons produced per unit time per interval of $d\epsilon$ is proportional to integral I, such that

$$\frac{dN_e}{dtd\epsilon} \propto I \equiv 4\int_0^1 d\xi \xi^2 \Phi(\xi) = 1 \tag{I.18}$$

(see, equation (20) and (22) in Gould 1979).

We approximate $n(\xi)$ at the center of the source, which corresponds to

$$\Phi(\xi) \sim \Phi(0) = 1. \tag{I.19}$$

In this case, the integral I_{approx} is replaced by

$$I_{\mathrm{approx}} = 4\int_0^1 d\xi \xi^2 \Phi(0) = 4\int_0^1 d\xi \xi^2 = \frac{4}{3}, \tag{I.20}$$

which makes misreading of absolute SSC flux by a factor of 4/3 from the accurate solution. The invert of this factor, i.e., 0.75, should be multiplied to correct the soft photon density for inverse Compton scattering. We thus correct $n(\epsilon_0)$ by a factor C_{corr} ($\equiv 0.75$), yielding

$$n(\epsilon_0) = \frac{4\pi}{hc\epsilon_0}C_{\mathrm{corr}}\frac{j_\nu}{\alpha_\nu}(1 - e^{-\alpha_\nu R}). \tag{I.21}$$

Appendix J

Numerical Approach to the Kinetic Equation

In general, the kinetic equations of electrons, given in equation (3.55), can not be solved analytically except for very simple cases which do not involve the non-linear processes (e.g., Kardashev 1962). In §4, we derived the approximate solution for time evolution of electrons in the *accelerating region*, while numerical approach was necessary for *emitting region*, because of the high non-linearity of inverse Compton process in the Klein-Nishina regime (equation (3.54)).

We solved the equation (11.7) adopting a fully implicit difference scheme proposed by Chang & Cooper (1970). This method was developed in the study of Fokker-Planck equations which describes an infinite, isotropic, fully ionized plasma. This equation have the form

$$\frac{\partial u}{\partial t} = \frac{1}{A(x)}\frac{\partial}{\partial x}[B(x,t)u + C(x,t)\frac{\partial u}{\partial x}], \tag{J.1}$$

in the domain $0 \leq t \leq t_0$, $0 \leq x \leq \infty$, with A, B, and C are all positive functions. The quantity x usually represents a velocity variable and $u(x,t)$ is the single particle distribution function. The merits of their method are as follows;
(1) particle number is always conserved,
(2) solution is always positive, and never fall in negative values,
(3) significantly reduces the number of mesh points in calculation, with no loss of accuracy.

However, for our purposes, some modifications are required because we are including the additional injection/escape terms, while no diffusion term ($C(x,t)[\partial u/\partial x]$).

We first define the energy mesh points of electrons with equal logarithmic resolution;

$$\gamma_j = \gamma_{\min}\left(\frac{\gamma_{\inf}}{\gamma_{\min}}\right)^{\frac{j}{j_{\max}}} \qquad (0 \le j \le j_{\max}), \tag{J.2}$$

where $j_{\max}$ is the number of the mesh and $\gamma_{\inf}$ is the maximum Lorentz factor of electrons to be used in the calculation. Since we are assuming exponential cut-off at $\gamma = \gamma_{\max}$ for the injection function $Q(\gamma, t)$ (see, e.g., equation (11.20)), $\gamma_{\inf}$ is taken to be much larger than $\gamma_{\max}$. As a default, we used $j_{\max} = 50$ for $\gamma_{\inf} = 10^7 - 10^8$.

The kinetic equation in the emission region is given by equation (11.7)

$$\frac{\partial N(\gamma, t)}{\partial t} = \frac{\partial}{\partial \gamma}[\dot{\gamma} N(\gamma, t)] + Q(\gamma, t) - \frac{N(\gamma, t)}{t_{\rm esc}}, \tag{J.3}$$

where

$$\dot{\gamma} = \dot{\gamma}_{\rm sync} + \dot{\gamma}_{\rm SSC}. \tag{J.4}$$

For the numerical calculation, this can be written as

$$\frac{N_j^{n+1} - N_j^n}{\Delta t} = \frac{\dot{\gamma}_{j+1/2}^n N_{j+1}^{n+1} - \dot{\gamma}_{j-1/2}^n N_j^{n+1}}{\gamma_{j+1/2} - \gamma_{j-1/2}} + Q_j^n - \frac{N_j^{n+1}}{t_{\rm esc}} \tag{J.5}$$

where

$$N_j^n = N(\gamma_j, n\Delta t), \tag{J.6}$$

and quantities with the subscript $j+1/2$ are calculated at half grid points. Δt is the time-step of the calculation. We can rewrite this equation conveniently in the form (Chaiberge & Ghisellini. 1999)

$$V3_j N_{j+1}^{n+1} + V2_j N_j^{n+1} + V1_j N_{j-1}^{n+1} = S_j^n \qquad (1 \le j \le j_{\max}), \tag{J.7}$$

where

$$V1_j = 0, \tag{J.8}$$

$$V2_j = 1 + \frac{\Delta t}{\gamma_{j+1/2} - \gamma_{j-1/2}}\dot{\gamma}_{j-1/2}^n + \frac{\Delta t}{t_{\rm esc}}, \tag{J.9}$$

$$V3_j = -\frac{\Delta t}{\gamma_{j+1/2} - \gamma_{j-1/2}}\dot{\gamma}_{j+1/2}^n, \tag{J.10}$$

$$S_j^n = N_j^n + Q_j^n \Delta t. \tag{J.11}$$

This can be written in a tridiagonal matrix and can be solved numerically (e.g., Press et al. 1989)

$$\begin{pmatrix} V2_0 & V3_0 & 0 & \cdot & \cdot & 0 \\ V1_1 & V2_1 & V3_1 & 0 & \cdot & \cdot \\ \cdot & \cdot & \cdot & \cdot & \cdot & \cdot \\ \cdot & \cdot & \cdot & \cdot & \cdot & \cdot \\ \cdot & \cdot & \cdot & \cdot & \cdot & \cdot \\ \cdot & \cdot & 0 & V1_{j_{\max}-1} & V2_{j_{\max}-1} & V3_{j_{\max}-1} \\ \cdot & \cdot & 0 & 0 & V1_{j_{\max}} & V2_{j_{\max}} \end{pmatrix} \begin{pmatrix} N_0^{n+1} \\ N_1^{n+1} \\ \cdot \\ \cdot \\ \cdot \\ N_{j_{\max}-1}^{n+1} \\ N_{j_{\max}}^{n+1} \end{pmatrix} = \begin{pmatrix} S_0^n \\ S_1^n \\ \cdot \\ \cdot \\ \cdot \\ S_{j_{\max}-1}^n \\ S_{j_{\max}}^n \end{pmatrix} .$$

(J.12)

To obtain a number conserving solution, we have to set the boundary condition in the absence of *sources* (injection term) or *sinks* (escape term) for each trial. This can be written

$$\sum_{j=1}^{j_{\max}} \left(\frac{\dot{\gamma}_{j+1/2}^n N_{j+1}^{n+1} - \dot{\gamma}_{j-1/2}^n N_j^{n+1}}{\gamma_{j+1/2} - \gamma_{j-1/2}} \right) \equiv 0.$$

(J.13)

Summarizing our numerical approach, we first define the electron population $N_j^0 = N(\gamma_j, 0)$ as an initial condition. Next we calculate for this electron population, synchrotron loss $\dot{\gamma}_{\mathrm{sync}}$ and inverse Compton loss $\dot{\gamma}_{\mathrm{IC}}$ by using equation (3.34) and (3.54). We then obtain $\dot{\gamma}_{j-1/2}$ and $\dot{\gamma}_{j+1/2}$, which can be used to produce $V1_j$, $V2_j$ and $V3_j$ (equation (J.9) and (J.10)). The tridiagonal matrix (equation (J.12)) is solved numerically to obtain the electron population at time Δt; $N_j^1 = N(\gamma_j, \Delta t)$. The iteration of above prescription gives the electron population at an arbitrary time t.

Bibliography

[1] Aharonian, F., et al. 1997, A&A, 327, L5

[2] Aharonian, F., et al. 1999a, A & A, 349, 29

[3] Aharonian, F., et al. 1999b, A & A, 350, 757

[4] Angel, J. R. P., & Stockman, H. S., 1980, Annu. Rev. Astron. Astrophysics, 18, 321

[5] Antonucci, R., & Miller, J. 1985, ApJ, 297, 621

[6] Antonucci, R. 1993, Ann. Rev. Astr. Astrophys, 31, 473

[7] Band, D. L., & Grindlay, J. E. 1985, ApJ, 298, 128

[8] Band, D. L., & Grindlay, J. E. 1986, ApJ, 308, 576

[9] Bednarek, W. 1993, ApJ, 402, L29

[10] Bednarek, W., & Protheroe, R. J. 1997, MNRAS, 292, 646

[11] Bednarek, W., & Protheroe, R. J. 1999, MNRAS, submitted, astro-ph/9902050

[12] Belobodorov, A. M., Stern, B & Svensson, R., 1998, ApJ, 508, L25

[13] Blandford, R. D., & Königl, A. 1979, ApJ, 232, 34

[14] Blandford, R. D., & Rees, M. J., 1978, In "Pittsburgh Conference on BL Lac objects", 328, niv Pittsburgh Press

[15] Blandford, R. D., & Eichler, D., Phys. Rep., 1987, 154, 1

[16] Blandford, R. D., & Levinson, A. 1995, ApJ, 441, 79

[17] Blumenthal, G. R., & Gould, R. J. 1970, Rev. Mod. Phys., 42, 237

[18] Bradbury, S. M. 1997, A&A, 320, L5

[19] Buckley, J. H., et al. 1996, ApJ, 472, L9

[20] Burke, B. E., et al. 1991, IEEE Trans. ED-38, 1096

[21] Catanese, M., et al. 1997, ApJ, 487, L143

[22] Catanese. M., et al. 1998, ApJ, 501, 616

[23] Cawley, M. F., & Weekes, T. C. 1995, Exp. Astron., 6, 7

[24] Celloti. A., & Ghisellini. G. 1998, BL Lac Phenomenam June 22-26, Turku, Finland

[25] Chadwick, P. M., et al. 1999, ApJ, 513, 161

[26] Chang, J. S., & Cooper, G. 1970, Journal of Computational Physics, 6, 1

[27] Chiaberge, M., & Ghisellini, G. 1999, MNRAS, 306, 551

[28] Chiappetti, L., et al. 1999, ApJ, 521, 552, astro-ph/9810263

[29] Comastri, A., et al. 1995, MNRAS, 277, 297

[30] Comastri, A., et al. 1997, ApJ, 480, 534

[31] Dar, A., & Laor.,A. 1997, ApJ, 478, L5

[32] Dermer, C. D., & Schlickeiser, R. 1993, ApJ, 416, 458

[33] Dermer, C. D. 1995, ApJ, 446, L63

[34] Dermer, C. D. 1998, ApJ, 501, L157

[35] Dotani, T., et al. 1997, ApJL, 485, L87

[36] Dondi, L.,& Ghisellini, G. 1995, MNRAS, 273, 583

[37] Edelson, R. A. 1987, ApJ, 313, 651

[38] Edelson, R., & Krolik, J. 1988, ApJ, 333, 646

[39] Edelson, R., et al. 1995, ApJ, 438, 120

[40] Elvis, M., et al. 1989, AJ, 97(3), 777

[41] Elvis, M., et al. 1992, ApJS, 80, 257

[42] Fanaroff, B. & Riley, J. 1974 MNRAS, 167, 31

[43] Fabian, A. C., 1979, Proc. R. Soc. London, 366, 449

[44] Fichtel, C. E., et al. 1994, ApJS, 94, 551

[45] Fossati, G., et al. 1998, MNRAS, 299, 433

[46] Funk, B., et al. 1998, Astroparticle Physics, 9, 97

[47] Gaidos, J. A., et al. 1996, Nature, 383, 319

[48] Gaisser, T. K., Cosmic Rays and Prticle Physics, Cambridge University Press, 1990

[49] Gehrels, N. 1997, IL NUOVO CIMENTO, 112 B, 11

[50] Georganopoulos, M., & Marscher, A. P. 1999, ApJ, 506, L11

[51] George, I. M., Warrick, R. S., & Bromage, G. E. 1988, MNRAS, 232, 793

[52] Ghisellini, G., & Maraschi, L. 1989, ApJ, 340, 181

[53] Ghisellini, G., & Maraschi, L. 1996, Blazar Continuum Variability, ASP conferences Series, Vol. 110

[54] Ghisellini, G., & Madau, P., 1996, MNRAS, 280, 67

[55] Ghisellini, G., et al. 1997, A & A, 327, 61

[56] Ghisellini, G., et al. 1998, MNRAS, 301, 451

[57] Ghisellini, G., 1999, Astronomische Nachrichten, proceedings of fourth *ASCA* sympsium

[58] Giommi, P., et al. 1990, ApJ, 356, 432

[59] Giommi, P., et al. 1998, A&A, 333, L5

[60] Giommi, P., et al. 1999, MNRAS, in press

[61] Giovannini, G., et al. 1998, in the proceedings of "BL Lac phenomenon" Turku, Finland

[62] Gould, R. J., et al. 1979, A&A, 76, 306

[63] Gregory, P. C.,& Condon, J. J., 1991, ApJS, 75, 1011

[64] Hartman, R. C., et al. 1996, ApJ, 461, 698

[65] Hartman, R. C., et al. 1999, ApJS, 123, 79

[66] Hayashida, K., et al. 1998, ApJ, 500, 642

[67] Hewitt, A & Burbidge, G. 1993, ApJS, 87, 451

[68] Hughes, P. A., Aller, H. D.,& Aller, M. F., 1992, ApJ, 396, 469

[69] Inoue, S., & Takahara, F. 1996, ApJ, 463, 555

[70] Jahoda, K., et al. 1996, SPIE, 2808, 59

[71] Jahoda, K., et al. 1999,"On Orbit Perormance of the Rossi X-ray Timing Explore Proportional Counter Array", http://lheawww.gsfc.nasa.gov/docs/xray/xte/pca

[72] Jones, F. C. 1968, Phys. Rev., 167, 1159

[73] Jones, T. W., O'Dell, S. L., & Stein, W. A. 1974, ApJ, 188, 353

[74] Kardashev, N, S. 1962, Soviet Astronomy-AJ, 6, 317

[75] Kataoka, J., et al. 1999a, ApJ, 514, 138

[76] Kataoka, J., et al. 1999b, Astroparticle Physics, 11, 149

[77] Kataoka, J., et al. 2000, ApJ, 528, 243

[78] Kawaguchi, T., et al. 1998, ApJ, 504, 671

[79] Kerrick, A. D., et al. 1995, ApJ, 438, L59

[80] Kirk, J. G., Rieger, F. M. & Mastichiadis, A. 1998, A&A, 333, 452

[81] Kohmura, H., et al. 1994, PASJ, 46, 131

[82] Königl, A. 1981, ApJ, 243, 700

[83] Kubo, H., Ph. D. Thesis, University of Tokyo

[84] Kubo, H., et al. 1998, ApJ, 504, 693

[85] Lamer, G., & Wagner, S. J. 1998, A & A, 331, L13

[86] Lin, D. J., et al. 1992, ApJ, 442, 96

[87] Macomb, D. J., et al. 1995, ApJ, 449, L99

[88] Macomb, D. J., et al. 1996, ApJ, 459, L111 (Erratum)

[89] Madejski, G. M., et al. 1999, ApJ, 521, 145

[90] Mannheim, K., & Biermann, P. L., 1992, A & A, 253, L21

[91] Mannheim, K., A & A, 1993, 269, 67

[92] Makino, F, et al. 1987, ApJ, 313, 662

[93] Makino, F., Fink, H. H., & Clavel, J. 1992, in Frontiers of X–ray Astronomy, Universal Academy Press, Y.Tanaka & K.Koyam

[94] Makino, F., et al. 1996, in Röntgenstrahlung from the Universe, eds. H. U. Zimmermann, J. Trűmper and H. Yorke, MPE Report 263, p.413.

[95] Makino, F., et al. 1998, in the proceedings of "BL Lac phenomenon" Turku, Finland

[96] Makishima, K, et al. 1996, PASJ, 48, 171

[97] Maraschi, L, et al. 1994, ApJ, 435, L91

[98] Maraschi, L, et al. 1999a, Proceedings of the 32nd COSPAR Meeting, Nagoya, astro-ph/9902059

[99] Maraschi, L, et al. 1999b, ApJL, in press

[100] Marscher, A. P. 1980, ApJ, 235, 386

[101] Marscher, A. P., & Travis, J. P. 1996, A&AS, 120, 537

[102] Marscher, A. P., 1999, Astroparticle Physics, 11, 19

[103] Mastichiadis, A., & Kirk, J. G. 1997, A&A, 320, 19

[104] Mattox, J. R., et al. 1993, ApJ, 410, 609

[105] Mattox, J. R., et al. 1997, ApJ, 476, 692

[106] McEnergy, J. E., et al. 1997, in proceedings of 25 ICRC (Durban), astro-ph/9706125

[107] Miyoshi, M., et al. 1995, Nature, 373, 127

[108] Mukherjee, R., et al. 1997, ApJ, 490, 116

[109] Morrison, R, & McCammon, D. 1983, ApJ, 270, 119

[110] Ohashi, T., et al. 1996, PASJ, 48, 157

[111] Osterbrock, D. E. 1981, ApJ, 249, 462

[112] Ormes, in Current Perspectives in High Energy Astrophysics, NASA 1391, 1996

[113] Padovani, P., & Giommi, P. 1995, ApJ, 444, 567

[114] Paltani, S., et al. 1997, 327, 539

[115] Patanik, A. R., 1992, 254, 655

[116] Perlman, E. S., et al. 1996, ApJS, 104, 251

[117] Petry, D., et al. 1996, A&A, 311, L13

[118] Petry, D., 1997, PhD thesis, Max-Planck-Institute for Physics, Munich, report MPI-PhE/97-27

[119] Pian, E., et al. 1998, ApJ, 492, L17

[120] Piner, B, G., et al. 1999, ApJ, in press

[121] Press, W, H., et al. 1992, Numerical Recipes in C, Cambridge University Press

[122] Protheroe, R. J., in Towards the Millennium in Astrophysics; Problems and Prospects, Erice 1996, astro-ph/961212

[123] Punch, M., et al. 1992, Nature, 358, 477

[124] Quinn, J., et al. 1996, ApJ, 456, L83

[125] Quinn, J., et al. 1999, ApJ, 518, 693

[126] Rees, M. J., 1984, Annu. Rev. Astron. Astrophys., 22, 471

[127] Rephaeli, Y., 1979, ApJ, 227, 364

[128] Rodriguez-pascual, P. M., 1997, ApJS, 110, 9

[129] Rybicki,G. B., & Lightman, A. P. 1979, Radiative Processes in Astrophysics (New York: Wiley)

[130] Samuelson, F. W., et al. 1998, ApJ, 501, L17

[131] Sembay, S., et al. 1993, ApJ, 404, 112

[132] Sikora, M., Begelman, M. C., & Rees, M. J. 1994, ApJ, 421, 153

[133] Sikora, M. 1994, ApJS, 90, 923

[134] Sikora, M. & Madejski, G. M., Moderski, R., & Poutanen, J, 1997, ApJ, 484, 108

[135] Simonetti, J, H., Cordes, J, M., & Heeschen, D. S., 1985, ApJ, 296, 46

[136] Smith, A. G., et al. 1993, AJ, 105, 437

[137] Sreekumar, P., & Vestrand, W. T., 1997, IAU Circular, 6774

[138] Stark, A. A., et al. 1992, ApJS, 79, 77

[139] Stecker, F. W., de Jager, O. C., & Salamon, M. H. 1992, ApJ, 390, L49

[140] Stecker, F. W., de Jager, O. C. 1998, A & A, 334, L85

[141] Stein, W. A., O'Dell, S. L., & Strittmatter, R., 1976, Annu. Rev. Astron. Astrophysics, 14, 173

[142] Tagliaferri, G., et al. 1991, ApJ, 380, 78

[143] Takahashi, T., et al. 1994, IAU Circular, 5993

[144] Takahashi, T., et al. 1995, IAU Circular, 6167

[145] Takahashi, T., Tashiro, M., Madejski, M., Kubo, H., Kamae, T., Kataoka, J., et al. 1996, ApJ, 470, L89

[146] Takahashi, T., et al. 1998, IAU Circular, 6888

[147] Takahashi, T., et al. 1999, Astroparticle Physics, 11, 177

[148] Tanaka, Y., Inoue, H., and Holt, S. S. 1994, PASJ, 46, L73

[149] Tanaka, Y., et al. 1995, Nature, 375, 659

[150] Tanihata, C., Takahashi, T., Kataoka, J. et al. 1999, submitted to ApJ

[151] Tashiro, M., et al. 1992, Ph. D. Thesis, University of Tokyo

[152] Tashiro, M., et al. 1995, PASJ, 47, 131

[153] Tavecchio, F., Maraschi, L., & Ghisellini, G. 1998, ApJ, 509, 608

[154] Thompson, D. J., et al. 1993, ApJS, 86, 629

[155] Toor, A., & Seward, F. D. 1974, AJ, 79, 995

[156] Treves, A., et al. 1989, ApJ, 341, 733

[157] Ulrich, M. –H., Maraschi, L., & Urry, C. M. 1997, ARAA, 35, 445

[158] Urry, C. M., 1984, PhD Thsis, Johns Hopkins University

[159] Urry, C. M., & Padovani, P., 1995, PASP, 715, 803

[160] Urry, C. M., et al. 1997, ApJ, 486, 799

[161] Urry, C. M. 1998, Proc. of BL Lac Phenomenon, Takalo

[162] Vermeulen, R. C., & Cohen, M. H. 1994, ApJ, 430, 467

[163] Veron-Cetti, M.P. & Veron, P. 1993, ESO Sci. Rep. 13, 1

[164] Vestrand, W. T., Stacy, J. G., & Sreekumar, P. 1995, ApJ, 454, L93

[165] Wagner, S. J., et al. 1993, A & A, 271, 344

[166] von Montigny, C., et al. 1995, ApJ, 440, 525

[167] Yamashita, A. 1997, IEEE Trans Nucl. Sci., 44, 847

[168] Yamashita, A. 1999, Nuclear Instruments And Methods In Physics Research Sect. A Vol. 436 (1), 68

[169] Zhang, Y. H., et al. 1999, ApJ, 527, 719

Acknowledgment